Synthesis, Characterization and Studies on Multicomponent Oxide Materials Based on Vanadium Pentoxide

Ph. D. Thesis submitted to the
University of Calicut, Thenhipalam

for the partial fulfillment of the
requirements for the award of the degree of

DOCTOR OF PHILOSOPHY IN PHYSICS

by

Sabna. M

Under the guidance of
Dr. P. Jayaram
Assistant Professor of Physics

Department of Physics
MES Ponnani College, Ponnani South-670586
August 2026

DEPARTMENT OF PHYSICS

MES PONNANI COLLEGE, PONNANI SOUTH
Recognized Research Centre Under the University of Calicut

CERTIFICATE

This is to certify that the work presented in this thesis, entitled " **Synthesis, Characterization and Studies on Multicomponent Oxide Materials Based on Vanadium Pentoxide ",** is the report of original work done by **Sabna M.,** under my guidance and supervision at the Department of Physics, MES Ponnani College, Ponnani South, Kerala, and no part thereof has been presented for the award of any other degree.

Ponnani
27. 07. 2026

Dr. P. Jayaram
Research Supervisor

MES PONNANI COLLEGE (AUTONOMOUS)

Govt. Aided Institution I Affiliated to the University of Calicut
NAAC Re-accredited (III[rd] Cycle) with A+ Grade (3.46 CGPA) I Estd. : 1968
Recognized under UGC 2(f) & 12(B) I ISO 9001:2015 Certified
Ponnani South P.O., Malappuram Dt, Kerala, India - 679 586

CERTIFICATE

This is to certify that the thesis entitled **"Synthesis, Characterization and Studies on Multicomponent Oxide Materials Based on Vanadium Pentoxide"** embodies the original research work carried out by **Sabna M.** under the guidance and supervision of **Dr. P. Jayaram**, Research Supervisor, at the Department of Physics, MES Ponnani College, Ponnani South, Kerala, recognized research center under University of Calicut.

It is further certified that the candidate has carried out the research work in the Department of Physics, MES Ponnani College (Autonomous) and has fulfilled the requirements prescribed by the University of Calicut for the submission of Ph. D thesis.

Place: Ponnani
Date: 27 July 2026

Principal

MES PONNANI COLLEGE
Ponnani South
Pin. 679 586

DEPARTMENT OF PHYSICS

MES PONNANI COLLEGE, PONNANI SOUTH
Recognized Research Centre Under the University of Calicut

CERTIFICATE

This is to certify that the corrections and suggestions recommended by the adjudicators have been duly incorporated in the thesis entitled **"Synthesis, Characterization and Studies on Multicomponent Oxide Materials Based on Vanadium Pentoxide"** submitted by Sabna. M. It is also certified that the hard and soft copies of the thesis submitted s are identical.

Dr. Jayaram P
Research Supervisor and Assistant Professor
Department of Physics
MES Ponnani College

Date: 11-08-2026

Place: Ponnani

DECLARATION

I hereby declare that the work presented in this thesis, entitled " **Synthesis, Characterization and Studies on Multicomponent Oxide Materials Based on Vanadium Pentoxide ",** is the original work done by me under the guidance of **Dr. P. Jayaram,** Assistant Professor, Department of Physics, MES Ponnani College, Ponnani South, Kerala, and no part thereof has been presented for the award of any other degree. The contents of the thesis have undergone a plagiarism check using iThenticate software at the C.H.M.K. Library, University of Calicut, and the similarity index was found to be within the permissible limit. I also declare that the thesis is free from AI generated contents.

Sabna M.

Ponnani
27. 07. 2026

Dr. P. Jayaram
Research Supervisor
Department of Physics
MES Ponnani College, Ponnani South, Kerala

UNIVERSITY OF CALICUT

CERTIFICATE ON PLAGIARISM CHECK

1.	Name of the Research Scholar	SABNA. M	
2.	Title of thesis / dissertation	Synthesis, Characterization and Studies on Multicomponent Oxide Materials Based on Vanadium Pentoxide	
3.	Name of the Supervisor	Dr. P. Jayaram	
4.	Department/Institution	RESEARCH SCHOLAR, DEPARTMENT OF PHYSICS, MES PONNANI COLLEGE, PONNANI SOUTH, 679586	
5.	Similar content (%) identified	Non Core	Core
		Introduction/ Theoretical overview/Review of literature/ Materials & Methods/ Methodology	**Analysis/Result/Discussion / Summary/Conclusion/ Recommendations**
		5	**5**
	Acceptable maximum limit (%)	10	10
6.	Software used	iThenticate	
7.	Date of verification	17.11.2025	

**Report on plagiarism check, specifying included/excluded items with % of similarity to be attached.*

Dr. Nasirudheen. T
Assistant Librarian
University of Calicut, Kerala.

Checked by (Name, designation & signature)

MOHAMMED KOYA LIBRARY
P.O. CALICUT UNIVERSITY
UNIVERSITY OF CALICUT

Name and signature of the Researcher : Sabna. M,

Name and signature of the Supervisor.

Dr. Jayaram. P,
Asst. Professor, Dept. of Physics,
M.E.S Ponnani College
Ponnani South - 679586
Malappuram Dist., Kerala

The Doctoral Committee* has verified the report on plagiarism check with the contents of the thesis, as summarized above and appropriate measures have been taken to ensure originality of the Research accomplished herein.

Name & Signature of the HoD/HoI (Chairperson of the Doctoral Committee)

Dr. A.A. Zubair
Assistant Professor
in charge of the Principal
MES Ponnani College
P.O. Ponnani South - 679 586

**In case of languages like Malayalam, Tamil etc..on which no software is available for plagiarism check, a manual check shall be made by the Doctoral Committee, for which an additional certificate has to be attached.*

ACKNOWLEDGEMENTS

As I stand at the culmination of my Ph.D. journey, I am profoundly humbled by the realization that this achievement is not solely mine but is the product of the collective support, guidance, and unwavering belief of many individuals who have walked beside me. Their encouragement has been the bedrock upon which this thesis was built, and their presence has significantly enriched both my academic and personal growth. I owe this success to the people who believed in me, inspired me, and provided the strength necessary to overcome the challenges I faced along the way.

I am deeply indebted to my research advisor, ***Dr. P. Jayaram****, whose mentorship has been a cornerstone of my academic journey. His insightful guidance, coupled with his profound knowledge, has shaped my approach to research and scholarship. I am immensely grateful for the time and wisdom he has shared, which has not only expanded my intellectual horizons but also molded me into a more disciplined and thoughtful researcher. I will forever cherish his constant support, whether through his patient listening, his forgiveness of my occasional lapses, or the invaluable freedom he provided, allowing me to navigate my research independently. His encouragement has been the guiding light that propelled me through the most demanding phases of my work.*

I express my thanks to ***Dr. Zubair. A. A****, Principal, as well as all the previous principals during my research period at MES Ponnani College, Ponnani South, for providing all the facilities in the department to accomplish my research work. I extend my gratitude to* ***Dr. K. Jayakrishnan****, head of the Department of Physics, for understanding the difficulties faced by a part-time research scholar and for providing ample support for my research. Thanks to all my colleagues* ***Mohammed Abdurahiman. K, Jumailath. K, Majeesh. M, Sreejalakshmi. S, Riyas. K. M and Sukanya. K*** *of the Physics department, MES Ponnani College for their constant support and understanding. Thanks to all the non- teaching staffs of the department for their help in various situations. Thanks to Head of Aquaculture department for providing different research facilities essential for the advancement of my work.*

Sincere thanks to ***Safna. K, Sona. C. P*** *and* ***Sreedevi. S,*** *the research scholars of the department, for their boundless help and support. It's rare to encounter individuals who offer assistance without seeking personal gain.*

I would like to extend my profound gratitude to ***Dr. Jineesh K. B.****, Department of Physics, IIST Trivandrum, for his invaluable guidance and for providing exceptional instrumentation facilities for thin-film fabrication and analysis of resistive-switching applications. Special thanks are due to* ***Dr. Dayal G****., Research Scholar, for his expert technical assistance in Pulsed Laser Deposition (PLD). I also wish to acknowledge* ***Dr. Rakhi R. B****. NIIST, Trivandrum, for her dedicated support in conducting electrochemical studies. I am deeply grateful to* ***Dr. Pradeep Reddy Venga*** *from Vel Tech Rangarajan Dr. Sagunthala R&D Institute of Science and Technology, Chennai. for his expertise in performing Rietveld refinement on the as-prepared samples, which significantly enhanced the precision of my structural analysis. My sincere appreciation goes to* ***Prof. P. P. Pradyumnan*** *and* ***Prof. Mohammed Shahin Thayyil*** *for facilitating access to the characterization facilities at the Department of Physics, University of Calicut, which were crucial for various analytical techniques. I would like to acknowledge* ***Dr. Rajeev N. E****., Retired Professor, Guruvayoorappan College, for his generous provision of facilities for AC conductivity and dielectric studies, which contributed significantly to my research. I am also thankful to* ***Dr. Fazalurahman K****., Department of Chemistry, University of Calicut, for enabling the photoluminescence studies that were key to understanding the optical properties of my materials. A special mention goes to the Aquaculture Department of MES Ponnani College, particularly* ***Dr. K. M. Mujeeb Rahman*** *and Research Scholar* ***K. R. Aneesa****, for their invaluable assistance in conducting the antimicrobial studies at the microbiology lab, which provided critical insights into the biological applications of my research.*

I dedicate this thesis to my parents ***M. Abbobacker*** *&* ***Sakeena. P. A*** *and my spouse's parents* ***Ismayil. V*** *&* ***Ayishakkutty****, whose unwavering dedication, sacrifices, and unrelenting support have been the guiding lights throughout this journey. I am also deeply grateful to my sisters,* ***Jasmine M****. and* ***Febin M****., for their love, understanding,*

and continual encouragement. My heartfelt thanks extend to all my relatives for their affectionate support, which has been a constant source of strength.

I would like to express my deepest appreciation to ***Lt. Dr. Thoufeeq Rahman V****, my life partner, whose dedicated support, selfless sacrifices, and continuous encouragement have been instrumental in the seamless progress of my Ph.D. journey. His unwavering belief in me, coupled with his own academic accomplishments as a Ph.D. holder, has been a source of inspiration, making this journey more meaningful. A warm embrace to my beloved children,* ***Lehan V., Leyan V., and Leyna V****., whose boundless energy and love have been my solace, even though I know that the demands of my research may have caused some inconvenience. Your presence has been a comforting balm, alleviating stress and reminding me of the true meaning of perseverance and love.*

Finally, I express my gratitude to all other family members and friends who have offered their unwavering support, encouragement, and understanding throughout this endeavor. Your collective love and assistance have made this achievement possible, and for that, I am eternally grateful.

Sabna. M

Dedicated to My Parents

ABSTRACT

This study investigates the synthesis and characterization of multi-cation-incorporated V_2O_5 compounds, specifically Sb-and Ni-incorporated V_2O_5, to enhance their structural, electronic, and photocatalytic properties for advanced applications in energy storage, environmental remediation, and antimicrobial therapies. The compounds $V_{(1-x)2}Ni_{3x}O_{5-\delta}$, $V_{2-x}Sb_{2x}O_{5-\delta}$, and $V_{2-x}Ni_{2x}Sb_xO_{5-\delta}$ were synthesized via high-temperature solid-state reactions, and their structural integrity and phase stability were confirmed using X-ray diffraction, Raman spectroscopy, and X-ray photoelectron spectroscopy. These analyses revealed the coexistence of orthorhombic V_2O_5, monoclinic NiV_2O_6, and tetragonal $SbVO_4$ phases, with varying degrees of lattice distortion and mixed oxidation states (V^{4+}/V^{5+}, Ni^{2+}/Ni^{3+}, Sb^{3+}/Sb^0), which significantly enhanced their defect densities and redox behavior.

The incorporation of Sb and Ni ions into the V_2O_5 lattice altered the materials' electronic properties, including their band gap restructuring, explained with Burstein-Moss effect. These modifications were supported by photoluminescence spectra, which showed defect-induced emissions. The compounds demonstrated substantial improvements in dielectric properties, with frequency-dependent behavior suitable for energy storage applications such as capacitors. AC conductivity was enhanced by polaronic hopping mechanisms, although higher doping concentrations led to a reduction in charge mobility due to increased structural defects.

The photocatalytic activity of Sb-Ni-V_2O_5/g-C_3N_4 heterostructures was significantly improved, facilitating efficient visible-light-driven reactions for organic Methylene Blue dye degradation. The Z-scheme photocatalysts exhibited enhanced charge separation, leading to effective generation of reactive oxygen species, crucial for pollutant mineralization. Additionally, the Sb-Ni-V-O compounds and heterostructures displayed broad-spectrum antimicrobial activity, inhibiting both Gram-positive and Gram-negative bacteria and fungal strains, attributed to oxidative stress and membrane disruption. Overall, the incorporation of Sb and Ni into V_2O_5 yields multi-functional materials with enhanced electronic, photocatalytic, and

antimicrobial properties, paving the way for their application in energy storage devices, environmental remediation, and biomedical fields. Future research should focus on optimizing dopant concentrations, exploring their use in energy storage applications, and assessing their cytotoxicity for potential biomedical use.

Keywords: Vanadium Pentoxide, XRD, Dielectric and AC Conductivity, Photocatalysis, Antimicrobial

സംഗ്രഹം

കാറ്റയോണുകൾ(cations) കൂട്ടിചേർത്തു രൂപപ്പെടുത്തിയ (പ്രത്യേകിച്ച് ആൻറിമണി, നിക്കൽ കാറ്റയോണുകൾ കൂട്ടിച്ചേർത്തു രൂപപ്പെടുത്തിയ) വനേഡിയം പെന്റോക്സൈഡ് സംയുക്തങ്ങളുടെ സംശ്ലേഷണവും സവിശേഷ സ്വഭാവവിശ്ലേഷണവുമാണ് ഈ പഠനത്തിലൂടെ നിർവ്വഹിക്കുന്നത്. ഘടനാപരവും പ്രകാശപ്രേരിതവുമായ (photocatalytic)കഴിവുകളെയും ഇലക്ട്രോണിക് ഗുണങ്ങളെയും വർദ്ധമാനമാക്കുന്നതിലൂടെ ഊർജ്ജസംഭരണം, പാരിസ്ഥിതികപ്രശ്നപരിഹാരങ്ങൾ, രോഗാണു-സുക്ഷ്മാണു നിർമ്മാർജ്ജന ചികിത്സാരീതികൾ എന്നീ മേഖലകളിൽ ഇവ പ്രയോഗക്ഷമമാകുമെന്ന് പ്രതീക്ഷിക്കപ്പെടുന്നു. ഉയർന്ന താപനിലയിൽ ഖരാവസ്ഥയിൽ നടക്കുന്ന പ്രതിപ്രവർത്തനങ്ങളിലൂടെ$V_{(1-x)2}Ni_{3x}O_{5-d}$, $V_{2-x}Sb_{2x}O_{5-d}$, $V_{2-x}Ni_{2x}Sb_xO_{5-d}$എന്നീ സംയുക്തങ്ങളുടെ ഘടനാപരമായ സംയോജിതസ്ഥിതി പഠിക്കുകയും വിവിധഘട്ട(phase)ങ്ങളുടെ സ്ഥിരത ഉറപ്പുവരുത്തുകയും ചെയ്തു. എക്സ്റേ ഡിഫ്രാക്ഷൻ, രാമൻ സ്പെക്ട്രോസ്കോപ്പി, എക്സ്-റേ ഫോട്ടോ ഇലക്ട്രോൺ സ്പെക്ട്രോസ്കോപ്പി എന്നീ മാർഗ്ഗങ്ങൾ ഇതിനായി ഉപയോഗിച്ചു. ഓർത്തോറോംബിക്V_2O_5, മോണോക്ലിനിക് NiV_2O_6, ടെട്രാഗണൽ $SbVO_4$ എന്നിവ ഒരുമിച്ചു നിലനിൽക്കുന്ന അവസ്ഥകളെ ഈ പരീക്ഷണം വെളിപ്പെടുത്തുകയുണ്ടായി. വ്യത്യസ്ത അളവുകളിലും നിലകളിലുമുള്ള ക്രിസ്റ്റൽ ക്രമീകരണവൈകല്യങ്ങളും V^{4+}/V^{5+}, Ni^{2+}/Ni^{3+}, Sb^{3+}/Sb^0എന്നീ മിശ്രിതഓക്സിഡേഷൻ അവസ്ഥകളും ക്രിസ്റ്റൽവൈകല്യങ്ങളുടെ സാന്ദ്രതയും നിരോക്സീകരണ സ്വഭാവവും ഏറെ വർദ്ധിപ്പിക്കുന്നതിനു സഹായിച്ചു. സ്കാനിങ് ഇലക്ട്രോൺ മൈക്രോസ്കോപ്പ് വഴി ഉപരിതലഘടനയെ സവിശേഷമായി പഠിക്കുകയും ഊർജ്ജപ്രകീർണ്ണന എക്സ് റേ സ്പെക്ട്രോസ്കോപ്പി ഉപയോഗിച്ച് രാസമൂലകങ്ങളുടെ ഘടന കൃത്യമായി നിർണ്ണയിക്കുകയും ചെയ്തു.

V_2O_5ന്റെ ക്രിസ്റ്റൽ ഘടനയിൽ Sb, Ni കാറ്റയോണുകൾ കൂട്ടിച്ചേർത്തത് ഇതിന്റെ ഇലക്ട്രോണിക് ഗുണങ്ങളെ പരിവർത്തിപ്പിച്ചു. അവയുടെ ബാൻഡ് വിടവിന്റെ (Band Gap) പുനർനിർമ്മാണവും വ്യത്യാസങ്ങളും ബർസ്റ്റൈൻ-മോസ് ഇഫക്റ്റ് ഉപയോഗിച്ച് വിശദീകരിച്ചു. ക്രിസ്റ്റൽവൈകല്യ(crystal defect)പ്രേരിതമായ ഉത്സർജ്ജന(emission)ങ്ങൾ കാണിക്കുന്ന പ്രകാശദീപ്തിവർണ്ണരാജി (Photo Luminescence Spectra) ഈ മാറ്റങ്ങളെ ഉൾക്കൊള്ളുന്നതും പിന്തുണക്കുന്നതായിരുന്നു. കപ്പാസിറ്ററുകൾ പോലുള്ള ഊർജ്ജ സംഭരണപ്രയോഗങ്ങൾക്ക് അനുയോജ്യമായ ആവൃത്തി-ആശ്രിത സ്വഭാവമുള്ള കുചാലകഗുണങ്ങൾ (dielectric properties) ഈ സംയുക്തങ്ങൾക്ക് ഗണ്യമായി ഉയർന്നതാണ്. വർദ്ധിപ്പിച്ച ഡോപ്പിംഗ് സാന്ദ്രത, വർദ്ധിതമായ ക്രിസ്റ്റൽഘടനാവൈകല്യങ്ങൾ എന്നിവ മൂലം ചാർജിന്റെ ചലനക്ഷമത കുറയുന്നുണ്ടെങ്കിലും പോളറോണിക് ഹോപ്പിംഗ് സംവിധാനങ്ങൾ വഴി എസി ചാലകത (AC Conductivity) വർദ്ധിപ്പിച്ചു.

Sb-Ni-V_2O_{5g}-C_3N_4 ഉഭയഘടനകളുടെ പ്രകാശപ്രേരിതസ്വഭാവങ്ങൾ ഗണ്യമായി മെച്ചപ്പെട്ടു. ഇത് കാര്യക്ഷമമായ ദൃശ്യപ്രകാശപ്രേരിത പ്രതിപ്രവർത്തനങ്ങളിലൂടെ ജൈവ മെത്തിലീൻ ബ്ലൂ ഡൈ ക്ഷയത്തിനു സഹായകമാകുന്നതാണ്. Z-സ്കീം പ്രകാശപ്രേരകങ്ങൾ മെച്ചപ്പെട്ട രീതിയിൽ ചാർജ് വിടവ് പ്രദർശിപ്പിക്കുകയുണ്ടായി. ഇത് മാലിന്യങ്ങളുടെ ധാതുവൽക്കരണത്തിന് സഹായകമായ പ്രതിപ്രവർത്തിത ഓക്സിജൻ ജനുസ്സുകളുടെ ഫലപ്രദമായ ഉൽപ്പാദനത്തിലേക്ക് നയിച്ചേക്കും. കൂടാതെ, Sb-Ni-V-O സംയുക്തങ്ങളും ഉഭയഘടനകളും വിശാലമായ രോഗാണുവിരുദ്ധക്ഷമത സ്പെക്ട്രം പ്രദർശിപ്പിക്കുന്നുണ്ട്. ഓക്സിഡേറ്റീവ് സമ്മർദ്ദം, കോശസംരക്ഷണപാളിയിൽ തടസ്സം എന്നിവയ്ക്ക് കാരണമാകുന്ന ഗ്രാം-പോസിറ്റീവ്, ഗ്രാം-നെഗറ്റീവ് ബാക്ടീരിയകളെയും ഫംഗസ് ജനുസ്സുകളെയും ഇതു തടയുന്നു. സാകല്യത്തിൽ, V_2O_5 ലേക്ക് Sb,Ni എന്നിവയെ സംയോജിപ്പിക്കുന്നത് പ്രകാശഉൾപ്രേരിതവും രോഗാണുനിർമ്മാർജ്ജനസഹായകവുമായ മെച്ചങ്ങളും ഉയർന്ന ഇലക്ട്രോണിക് ഗുണങ്ങളും വഴി ബഹുപ്രയോഗസാദ്ധ്യതകളുള്ള പദാർത്ഥങ്ങളെ നിർമ്മിച്ചു നൽകുമെന്ന് പ്രതീക്ഷിക്കാവുന്നതാണ്. ഇത് ഊർജ്ജസംഭരണോപകരണങ്ങൾക്കും പാരിസ്ഥിതികപ്രശ്നപരിഹാരങ്ങൾക്കും വൈദ്യശാസ്ത്ര മേഖലയിലും പല വിധത്തിലുള്ള പ്രയോഗങ്ങൾക്കും വഴിയൊരുക്കുന്നു. ഭാവിയിലെ ഗവേഷണങ്ങൾ ഡോപന്റ് സാന്ദ്രത വർദ്ധിപ്പിക്കുന്നതിലും ഊർജ്ജസംഭരണപ്രവർത്തനങ്ങളിലെ കൂടുതൽ ഉപയോഗങ്ങൾ പര്യവേക്ഷണം ചെയ്യുന്നതിലും സാദ്ധ്യമായ വൈദ്യശാസ്ത്ര ഉപയോഗങ്ങൾക്കായി ജീവകോശങ്ങൾക്കു എന്തെങ്കിലും കേടുകൾ വരുത്താനുള്ള സാദ്ധ്യതകൾ വിലയിരുത്തുന്നതിലും കൂടുതൽ ശ്രദ്ധ കേന്ദ്രീകരിക്കേണ്ടതാണ്.

പദങ്ങൾ:
വനേഡിയം പെന്റോക്സൈഡ്, കുചാലകങ്ങൾ, എസി ചാലകത, രോഗാണു വിരുദ്ധം.

PREFACE

The exploration of vanadium pentoxide and its derivatives, particularly when doped with transition metals such as antimony (Sb) and nickel (Ni), has garnered significant scientific interest due to their unique and versatile properties. These multi-cations incorporated V_2O_5 compounds are studied for their enhanced properties and potential applications in energy storage, photocatalysis, antimicrobial therapies, and electronic devices. **Chapter 1** introduces the fundamental properties of V_2O_5, particularly its orthorhombic phase and its significance across diverse applications such as photochromic and electrochromic devices, sensors, and lithium-ion batteries. The structure of V_2O_5 is discussed in detail, highlighting its oxygen vacancy-induced defect chemistry, which plays a crucial role in its electrical and catalytic properties. This chapter also sets the context for synthesizing V_2O_5 based complex oxides by incorporating Sb and Ni cations and studying its properties, including its electrical conductivity, photocatalytic efficiency, and antimicrobial activity.

Chapter 2 elaborates on the synthesis of the multi-cation based V_2O_5 compounds, specifically $V_{(1-x)2}Ni_{3x}O_{5-\delta}$, $V_{2-x}Sb_{2x}O_{5-\delta}$, and $V_{2-x}Ni_{2x}Sb_xO_{5-\delta}$, using a high-temperature solid-state reaction. This chapter details the characterization techniques employed to analyze the impact of Sb and Ni incorporation in to the V_2O_5 matrix. Techniques such as X-ray diffraction, Raman spectroscopy, X-ray photoelectron spectroscopy, and scanning electron microscopy are described, alongside methods for synthesizing V_2O_5-based heterostructures with g-C_3N_4 via sonication-hydrothermal processes.

In Chapter 3, the characterization of the Sb-V_2O_5 compounds is presented. Structural analysis reveals the coexistence of orthorhombic V_2O_5 and Sb-related phases, while the incorporation of Sb enhances surface area and dye adsorption capacity. This chapter discusses the frequency-dependent dielectric behavior, AC conductivity, and the impact of Sb doping on polaronic conduction. The antimicrobial activity of the Sb-V-O compounds is also explored, demonstrating their efficacy against both bacterial and fungal strains.

Chapter 4 investigates the incorporation of Ni into the V_2O_5 lattice. The structural changes and formation of mixed phases are analyzed, and the effects of Ni doping on the electronic properties are discussed. This chapter also highlights the compound's potential in energy storage and catalysis, as well as its promising antimicrobial activity, including the generation of reactive oxygen species that enhance microbial damage.

Chapter 5 presents the synthesis and characterization of multi-cation Ni-Sb-V_2O_5 compounds. The chapter delves into the structural modifications induced by the dual doping, revealing a combination of V_2O_5, NiV_2O_6, and $SbVO_4$ phases. The resulting material properties, including dielectric behavior, conductivity, and antimicrobial activity, are analyzed, demonstrating the potential of these compounds for a wide range of applications in energy storage and biofilm-targeted therapies.

Chapter 6 explores the synthesis and characterization of the V_2O_5-based heterostructures with g-C_3N_4. The formation of a Z-scheme photocatalyst is examined, with emphasis on improved charge separation and visible-light absorption. The photocatalytic activity of these heterostructures, including the degradation of methylene blue and antimicrobial efficacy, is discussed, highlighting their potential for environmental remediation and biomedical applications.

In **Chapter 7**, the findings of the study are summarized, emphasizing the enhanced properties of Sb and Ni-incorporated V_2O_5 materials. The successful doping with transition metals has been shown to improve the material's conductivity, photocatalytic efficiency, and antimicrobial activity. The chapter also discusses the potential applications of these materials in photocatalysis and biomedical therapies, highlighting their multifunctionality.

Chapter 8 provides a roadmap for future research, focusing on optimizing Sb and Ni concentrations in V_2O_5 to further enhance photocatalytic and antimicrobial performance. The chapter discusses the potential for these materials in high-frequency devices, antimicrobial coatings, and pollutant degradation reactors. Future studies should explore the cytotoxicity of these compounds for biomedical applications and

investigate their use in energy storage systems, such as supercapacitors and Li-ion batteries. This thesis presents a comprehensive study of multi-cation doped V_2O_5 compounds, highlighting their potential across multiple domains. The findings contribute to the development of next-generation materials with tailored properties for energy, environmental, and biomedical applications.

CONTENTS

Title	*Page No.*
Chapter I	**1-36**
Multi-Cation Incorporated Vanadium Pentoxide Complex Oxides: Unlocking Diverse Applications	
1.1 Introduction	1
1.2 Structure of V_2O_5	1
1.3 Morphology of V_2O_5	2
1.4. Optical Properties	4
1.5. AC Conductivity, Dielectric, and Impedance Studies	5
1.6. Applications of V_2O_5	6
1.6.1. Energy Storage	6
1.6.2. Chromogenic thin films	9
1.6.3. Photocatalysis	11
1.6.4. Gas Sensors	13
1.6.5. Optoelectronic Devices	14
1.6.6. Biomedical Applications	14
1.7. Limitations of pristine Vanadium pentoxide	15
1.8. Methods for Altering the Properties of Vanadium Pentoxides	17
1.8.1. Muti-Cation Incorporation in V_2O_5	17
1.8.2. Composite Formation	19
1.8.3. Heterostructure Engineering	19
1.8.4. Defect Engineering	21
1.8.5. Surface Functionalization	21
1.8.6. Ion Intercalation / Layer Engineering	22
1.9. Objective of the Study	23
1.10. Relevance of the study	23
References:	25
Chapter II	**37-83**
Synthesis And Characterization Techniques	
2.1. Introduction	37
2.2. High Temperature Solid State Reaction Method	37
2.3. Types of solid solutions	38

2.3.1. Substitutional solid solution 38
2.3.2 Interstitial solid solutions 38
2.3.3 Hume-Rothery rule for the selection of precursors in forming solid solutions 39
2.4. Characterization Techniques and Studies 40
2.4.1. X-Ray Diffraction and Bragg's Law 40
2.4.1.1. Structure Factor and Intensity of Diffracted Beams 41
2.4.1.2. Rietveld Refinement: Relevance and Quality Indicators 42
2.4.1.3. Rietveld Refinement Using Full Prof Suite 44
2.4.2. Raman Spectroscopy 45
2.4.3. Infrared Spectroscopy 46
2.4.4. X-Ray Photoelectron Spectroscopy 47
2.4.5 Scanning Electron Microscopy and Energy Dispersive Spectra 49
2.4.6. UV Visible Spectroscopy 52
2.4.7. Photoluminescence Spectroscopy 55
2.4.8. BET Surface Area Measurements 57
2.4.8.1 Principle of BET Method 57
2.4.8.2 Surface Area Calculation 57
2.4.8.3 N_2 Adsorption–Desorption Isotherms 59
2.4.8.4 Applications 59
2.5. Application Studies 60
2.5.1. AC Conductivity and Dielectric Studies 60
2.5.1.1. Principles of AC Conductivity and Dielectric Studies 60
2.5.1.2. Dielectric Properties 60
2.5.1.3. Impedance and Electric Modulus 61
2.5.1.4. AC Conductivity 62
2.5.1.5. LCR Meter 62
2.5.1.6. Impedance Spectroscopy 63
2.5.2. Adsorption Studies 63
2.5.2.1. Adsorption Isotherm Equations with Explanation 64
2.5.2.1.1. Langmuir Isotherm 64
2.5.2.1.2. Freundlich Isotherm 64
2.5.2.1.3. Temkin Isotherm 65

2.5.2.1.4. Dubinin–Radushkevich (D–R) Isotherm 65
2.5.2.2. Adsorption Kinetic Models 66
2.5.2.2.1. Pseudo-First-Order Kinetic Model 67
2.5.2.2.2. Pseudo-Second-Order Kinetic Model 67
2.5.2.2.3. Intra-Particle Diffusion Model 68
2.5.2.2.4. Elovich Kinetic Model 68
2.5.3 Photocatalytic Studies 69
2.5.4 Antimicrobial Studies of Metal Oxides 70
References 72
Chapter III **85-148**
Synthesis, Crystallographic Profiling, Core-Shell Electronic Configurations, Investigations of Frequency-Dependent Dielectric Characteristics, Adsorption and Antimicrobial Studies of Sb_2O_3-V_2O_5 Micro Ceramics
3.1. Introduction 85
3.2. Materials and Methods 91
3.2.1. Adsorption experiments 91
3.2.2. Antimicrobial Studies 95
3.3. Result and Discussion 96
3.3.1. Structural Analysis: X-ray Diffractogram 96
3.3.2. Rietveld Refinement using FULLPROF 98
3.3.3. Surface Morphology and Chemical Composition 104
3.3.4. X-ray Photoelectron Spectroscopy 107
3.3.5. Raman Spectroscopy: Phase, crystallinity, and molecular interactions 109
3.3.6. Optical Analysis: UV-Visible Spectroscopy 111
3.3.7. Photoluminescence Spectroscopy 113
3.3.8. Adsorption studies of Sb-V-O compounds 115
3.3.9. FTIR Spectroscopy 117
3.3.10. N_2 Adsorption Isotherms 118
3.3.11. Kinetic Studies on MB Adsorption 120
3.3.12. AC conductivity and Dielectric studies 123
3.3.13. Antimicrobial Studies 130
3.4. Conclusion 134
References 136

Chapter IV **149-187**

Comprehensive Analysis of Crystallographic, Electrical, Optical, and Antimicrobial Properties of Ni-Incorporated Vanadium Pentoxide($V_{2-x}Ni_{2x}O_{5-\delta}$): A Multifaceted Approach

4.1. Introduction 149

4.2. Materials and Methods 151

4.3. Results and Discussion 152

4.3.1. Structural Analysis and Crystallographic Refinement 152

4.3.2. Lattice dynamics: Raman Spectroscopy 159

4.3.3. Surface morphology and elemental analysis 164

4.3.4. X Ray Photoelectron Spectroscopy (XPS) 166

4.3.5. UV Visible Spectroscopy 167

4.3.6. AC Conductivity 169

4.3.7. Dielectric studies 172

4.3.8. Antimicrobial Studies 173

4.4. Conclusion 179

References 181

Chapter V **189-236**

Correlating Structural, Electronic, and Optical Properties with Energy Dissipation, Polarization Dynamics, Dielectric Responses, and Antimicrobial Applications in V_2O_5-NiO-Sb_2O_3 Micro-Ceramics

5.1. Introduction 189

5.2 Materials and methods 191

5.3 Results and Discussion 192

5.3.1. Microstructural Analysis using XRD 192

5.3.2. Crystallographic Refinement of XRD Data 195

5.3.3. Lattice Dynamics: Raman Spectroscopy 202

5.3.4. Surface Analysis and Elemental Composition 207

5.3.5. X-ray photoelectron spectroscopy (XPS) 209

5.3.6. Optical Studies: UV-Visible spectroscopy 213

5.3.7. Photoluminescence spectroscopy 215

5.3.8. AC Conductivity and Dielectric Studies 217

5.3.9. Anti-Microbial Studies 222

5.4. Conclusion 226

References 229

Chapter VI **237-271**
Development of Z-scheme Sb_2O_3-NiO-V_2O_5/g-C_3N_4 Heterostructures for Visible Light Photocatalysis and Antimicrobial Applications
6.1. Introduction 237
6.2. Materials and Methods 239
6.2.1. Synthesis of $V_{2-x}Ni_{2x}Sb_xO_{5-\delta}$ (Sb-Ni-V_2O_5) for $0.05 \leq x \leq 0.08$ 239
6.2.2. Synthesis of g-C_3N_4 nanoparticles 239
6.2.3. Synthesis of $V_{2-x}Ni_{2x}Sb_xO_{5-\delta}$/g-$C_3N_4$ ($0.05 \leq x \leq 0.08$) heterostructures 239
6.2.4. Characterizations 240
6.2.5. Photocatalytic experiments 241
6.2.6. Photocatalytic efficiency and Kinetic study 241
6.2.7. Active species trapping experiments 242
6.2.8. Antimicrobial studies 242
6.3. Result and Discussion 243
6.3.1. Structural Analysis: X-ray Diffractogram 243
6.3.2. FTIR Spectroscopy 245
6.3.3. Surface Morphology and Chemical Composition 247
6.3.4. X-ray photoelectron spectroscopy (XPS) 249
6.3.5. Optical Analysis: UV- Visible Spectroscopy 253
6.3.6. Photoluminescence Spectroscopy 254
6.3.7. Photocatalytic performance 257
6.3.8. Scavenger testing 259
6.3.9. Discussion of catalytic reaction mechanism 260
6.3.10. Cycling Stability 264
6.3.11. Visible light-induced antimicrobial applications of $V_{2-x}Ni_{2x}Sb_xO_{5-\delta}$/g-$C_3N_4$heterostructures 265
6.4. Conclusion 268
References 270
Chapter 7 **279-280**
General Conclusion
Chapter 8 **281**
Future Prospects
Appendix **283**
Papers Published
Papers Presented **286**
Awards and Recognition **288**

LST OF TABLES

Table No.	*Title*	*Page No.*
3.1.	Structural parameters of $V_{2-x}Sb_{2x}O_{5-d}$ compounds estimated from Scherer equation and WH-plot	98
3.2(a)	Structural Parameters, Cell volume & Compositional Percentage of Orthorhombic V_2O_5 and Tetragonal $SbVO_4$ obtained from Rietveld refinement of $V_{2-x}Sb_{2x}O_{5-\delta}$ for (0.05<=x<=0.08) compounds	100
3.2(b)	Reliability factors obtained from Rietveld refinement of XRD pattern of $V_{2-x}Sb_{2x}O_{5-\delta}$ ($0.05\leq x \leq 0.08$) compounds	101
3.2(c)	Prominent XRD reflections with Miller indices (hkl), corresponding 2θ values and microstructure of $V_{2-x}Sb_{2x}O_{5-\delta}$ compounds at x=0.06	102
3.2(d)	Bond lengths of Orthorhombic V_2O_5 in $V_{2-x}Sb_{2x}O_{5-\delta}$ for (0.05<=x<=0.08)	102
3.2(e)	The Wyckoff positions, atomic positions, and occupancy of each atom of $V_{2-x}Sb_{2x}O_{5-\delta}$ (0.05<=x<=0.08) compounds	103
3.3	Elemental Constituents $V_{2-x}Sb_{2x}O_{5-d}$ compounds obtained from the EDS spectrum	106
3.4	Comparison of Raman active phonon modes (in Wavenumbers, cm^{-1}) obtained for α-V_2O_5, Bi-V_2O_5, Ni-V_2O_5, Cr-V_2O_5, and experimental Raman data of Sb-V-O compound.	111
3.5	Textural parameters of Sb-V-O compounds from N_2 adsorption isotherms and BET analysis	119
3.6	Adsorption parameters for Pseudo first order, Pseudo second order, Intra-particle Diffusion and Elvoich kinetic models for Sb-V-O compound	122
3.7	Parameters derived from Almond West fit for different mole fractions	129
3.8	Zone inhibition values (in mm) of Gram positive bacteria, gram negative bacteria and fungi for Sb-V-O 8 compound systems	131
4.1(a)	Prominent XRD reflections with Miller indices (hkl), corresponding 2θ values and microstructure of $V_{2-x}Ni_{2x}O_{5-\delta}$compounds at x=0.06	153
4.1(b)	Estimated structural parameters and elemental composition of the compounds	155

4.1(c)	Edge Lengths and compositional percentage of Orthorhombic V_2O_5 and Triclinic NiV_2O_6	155
4.1(d)	Summarizes the quantitative phase analysis of the Ni-V-O system. It presents the relative weight fractions of the orthorhombic V_2O_5 and triclinic NiV_2O_6 phases alongside key Rietveld refinement parameters, including profile residuals (R_p, R_{wp}), expected R-value (R_{exp}), and the goodness-of-fit indicator (χ^2)	156
4.1(e)	Showing bond length of Orthorhombic V_2O_5 phase in the $V_{2-x}Ni_{2x}O_{5-\delta}$ for $0.03 \leq x \leq 0.06$	156
4.1(f)	Showing bond angle of Orthorhombic V_2O_5 phase in the $V_{2-x}Ni_{2x}O_{5-\delta}$ for $0.03 \leq x \leq 0.06$	156
4.2	Comparison of Wavenumbers (in cm^{-1}) of Raman active phonon modes obtained theoretically and experimentally for pure V_2O_5 and experimental Raman data of $V_{(1-x)2}Ni_{3x}O_{5-\delta}$	167
4.3	DC conductivity and frequency exponent obtained after JPL fitting of frequency-dependent AC conductivity curve of $V_{(1-x)2}Ni_{3x}O_{5-\delta}$ samples for x=0.04, 0.05 and 0.06	170
4.4	Inhibition Zone Diameters (in mm) of Gram-positive Bacteria, Gram-negative Bacteria, and Fungi, along with Positive and Negative Controls, for Ni-V-O7 Compound Systems.	174
5.1	Estimated grain size, dislocation density, microstrain, lattice parameters, and cell volume of $V_{2-x}Ni_{2x}Sb_xO_{5-\delta}$ (0.05<=x<=0.08) compounds	194
5.2(a)	Edge Lengths of V_2O_5, NiV_2O_6 and $SbVO_4$	198
5.2(b)	Interaxial angles of V_2O_5, NiV_2O_6, and $SbVO_4$	198
5.2(c)	Compositional percentage of V_2O_5, NiV_2O_6, and $SbVO_4$	199
5.3(a)	Bond Lengths (in Å) of the orthorhombic phase of V_2O_5	200
5.3(b)	Bond angles (in degrees) of the orthorhombic phase of V_2O_5	200
5.3(c)	Bond Lengths (in Å) of the triclinic phase of NiV_2O_6	200
5.3(d)	Bond angles (in degrees) of the triclinic phase of NiV_2O_6 -171 Table 5.3(e) Bond Lengths (in Å) of the tetragonal phase of $SbVO_4$	201
5.3(e)	Bond Lengths (in Å) of the tetragonal phase of $SbVO_4$	202
5.3(f)	Bond angles (in degrees) of the tetragonal phase of $SbVO_4$	202
5.4	Comparison of Raman active phonon modes (in Wavenumbers, cm-1) obtained for pure V_2O_5, $V_{2-x}Bi_{2x}O_{5-\delta}$, $V_{(1-x)2}Ni_{3x}O_{5-\delta}$, $Cr_{0.1}V_2O_5$, and experimental Raman data of $V_{2-x}Ni_{2x}Sb_xO_{5-\delta}$ compounds	206

5.5	Displays the Weight% and atomic% of Antimony, Nickel, Vanadium, and Oxygen elements present in the compound $V_{2-x}Ni_{2x}Sb_xO_{5-\delta}$, as obtained from the EDAX spectrum	208
5.6	Almond West fitted parameters of $V_{2-x}Ni_{2x}Sb_xO_{5-\delta}$ samples recorded for different mole concentrations a) x=0.05 b) x=0.06 c) x=0.07 d) x=0.08	222
5.7	Presents the zone inhibition values (in mm) and mic values of gram positive bacteria, gram negative bacteria and fungi for $V_{2-x}Ni_{2x}Sb_xO_{5-\delta}$for x=0.08 compound systems for 50, 100, 150 & 200 µl concentration	224
6.1	Elemental Constituents of $V_{2-x}Ni_{2x}Sb_xO_{5-\delta}$/g-$C_3N_4$ compounds obtained from the EDS	249
6.2	Comparison of photocatalytic performance of V_2O_5 and g-C_3N_4-based heterostructures	259
6.3	Presents the absolute electronegativity (χ)**,** band gap energy (Eg), and the calculated valence band (E_{VB}**)** and conduction band **(**E_{CB}**)** edge potentials (vs. NHE) for each molar fraction (**x**) of the compound $V_{2-x}Ni_{2x}Sb_xO_{5-\delta}$, along with the corresponding values for g-C_3N_4	263
6.4	ZOI values (in mm) for Gram-positive bacteria, Gram-negative bacteria, and fungi treated with Sb–Ni–V_2O_5/g-C_3N_4 compound at 50, 100, 150, and 200 µL concentrations, including positive and negative controls	267

LIST OF FIGURES

Figure No.	*Title*	*Page No.*
1.1	Layered structure of Vanadium Pentoxide	2
2.1	Flow chart of the high-temperature solid-state reaction method	37
2.2	Schematic illustration of Bragg's diffraction. Incident X-rays reflect from successive atomic planes separated by a distance d.	41
2.3	AERIS Panalytical X-ray Diffractogram Instrument	41
2.4	Image of JASCO NRS 4100 Raman Spectrometer used in the study	45
2.5	Schematic representation of an FTIR spectrometer	47
2.6	IRAffinity-1S(A221353), Shimadzu spectrometer	47
2.7	Thermoscientific ESCALAB equipment equipped with Al Kα monochromator	48
2.8	Schematic diagram of X-Ray Photoelectron Spectroscopy	49
2.9	Gemini SEM 300, Carl Zeiss, Scanning Electron Micrograph	50
2.10	Schematic Diagram of Scanning Electron Microscopy	50
2.11	Schematic Diagram of Energy Dispersive X-ray Spectroscopy	51
2.12	Perkin Elmer Lambda 365 UV-Vis spectrophotometer	53
2.13	Schematic diagram of the experimental setup of UV-Visible Spectroscopy	53
2.14	FP-8300 JASCO spectrofluorometer with an excitation wavelength of 330 nm used for PL measurements.	55
2.15	Schematic diagram of Photoluminescence Spectroscopy	56
2.16	Schematic Diagram of BET Surface Area Measurement Instrument	58
2.17	BET surface area, pore volume, pore diameter analyzer: BELSORP-MAX instrument.	58
2.18	Agilent 4294A Precision Impedance Analyzer for the AC conductivity nd dielectric studies of pellet samples	62
3. 1	XRD pattern of $V_{2-x}Sb_{2x}O_{5-d}$ compounds for $0.05 \leq x \leq 0.08$ indicating orthorhombic structure in pmmn space group symmetry	97
3.2(a)	Rietveld Refined XRD Pattern of $V_{2-x}Sb_{2x}O_{5-\delta}$ (0.05<=x<=0.08)	99

3.2(b,c)	Orthorhombic crystal structure of $V_{2-x}Sb_{2x}O_{5-\delta}$ compounds at x=0.05 (c) Orthorhombic V_2O_5 and Tetragonal $SbVO_4$ coexisting in $V_{2-x}Sb_{2x}O_{5-\delta}$ at x=0.08	104
3.3	Scanning Electron Micrographs of $V_{2-x}Sb_{2x}O_{5-d}$ compounds for $0.05 \leq x \leq 0.08$ showing the dense growth of plake and rod like particle (a) x=0.05 (b) x=0.06 (c) x=0.07 and (d) x=0.08	104
3.4	Average particle size of $V_{2-x}Sb_{2x}O_{5-d}$ compounds for $0.05 \leq x \leq 0.08$ from SEM images	105
3.5	Elemental Mapping showing the presence of (a) Oxygen (b) Antimony (c) Vanadium and (d) EDS spectrum of $V_{2-x}Sb_{2x}O_{5-\delta}$ compounds for x=0.08	106
3.6	XPS spectra of V2p in $V_{2-x}Sb_{2x}O_{5-\delta}$ compounds at (a) 0.05, (b) 0.06, (c) 0.07, and (d) 0.08. The asymmetric V2p spectrum of the Sb-V-O5 compounds shows peaks at 517.23 eV and 524.78 eV, which were attributed to V $2p_{3/2}$ and V$2p_{1/2}$ levels.	107
3.7	XPS spectra of Sb*3d* and O*1s* regions of $V_{2-x}Sb_{2x}O_{5-\delta}$ compounds at x=(a) 0.05, (b) 0.06, (c) 0.07 and (d) 0.08	108
3.8	Raman spectrum of the compounds synthesized by high-temperature solid-state reaction technique (b) The relative intensity of four prominent Raman bands at 143cm^{-1}, 285 cm^{-1}, 702 $cm^{-1,}$ and 998 cm^{-1} in $V_{2-x}Sb_{2x}O_{5-\delta}$ for $0.05 \leq x \leq 0.08$	110
3.9	Diffuse Reflectance Spectra obtained from the Sb-V-O compounds for various x values (b) Showing the optical band gap estimated using K-M theory	112
3.10	Photoluminescence spectrum of $V_{2-x}Sb_{2x}O_{5-\delta}$ compounds for (a)x=0.05 (b)x=0.06 (c)x=0.07 & (d)=0.08	114
3.11	MB dye Absorbance spectrum of pure V_2O_5 compound (b) Plot of c/c_0 vs time for $V_{2-x}Sb_{2x}O_{5-d}$ compounds for $0.05 \leq x \leq 0.08$	115
3.12	Bar Diagram depicting % Dye removal of $V_{2-x}Sb_{2x}O_{5-d}$ compounds for x=0.0 and $0.05 \leq x \leq 0.08$	116
3.13	FTIR spectrum showing up $V_{2-x}Sb_{2x}O_{5-d}$ compounds (b) MB adsorbed $V_{2-x}Sb_{2x}O_{5-d}$ compounds for $0.05 \leq x \leq 0.08$	117
3.14	N_2 adsorption isotherm of $V_{2-x}Sb_{2x}O_{5-d}$ micro-flakes for $0.05 \leq x \leq 0.08$ showing type IV curve with H_3 hysteresis	119
3.15	Pseudo second order kinetic model, linear fit of $V_{2-x}Sb_{2x}O_{5-d}$ for 0.05<=x<=0.08 giving R^2=0.99 for all compounds	123
3.16	Frequency-dependent variations of $Sb_{2x}V_{2-x}O_{5-\delta}$samples for all mole fractions a) dielectric constant b) dielectric loss factor c) dissipation factor d) ac conductivity	124

3.17	Almond West fitted Conductivity when a) x=0.05 b) x=0.06 c) x=0.07 d) x=0.08	128
3.18	Representative photographs of zone of growth inhibition against bacteria and fungi for Sb-V-O-8 with positive and negative control:(a) S.aureus, (b) E.coli, (c) Pencillium (d) A. niger, and Zone of growth inhibition against bacteria for $V_{2-x}Sb_{2x}O_{5-\delta}$ compounds (0.05<=x<=0.08) with positive control (e)P. aeroginosa (f) V. harveyi (g) B. cereus, (h)V. cholera	131
3.19	Bar diagram comparing the zone of inhibition of $V_{2-x}Sb_{2x}O_{5-\delta}$ compounds (0.05<=x<=0.08), against the growth of the gram positive-gram, negative bacteria and fungi for 200µl concentration	133
4.1	XRD pattern of the $V_{(1-x)2}Ni_{3x}O_{5-\delta}$ with prominent orientation along (001) direction	152
4.2	Rietveld refinement patterns of $V_{2-x}Ni_{2x}O_{5-\delta}$ samples for $0.03 \leq x \leq 0.06$, (b) orthorhombic V_2O_5 unit cell structure, (c)NiV_2O_6 unit cell and (d) unit cell model of Ni–V–O mixed-phase compounds comprising V_2O_5 and NiV_2O_6 phasesfor x=0.07, all visualized using VESTA software	159
4.3	Micro-Raman spectra of $V_{(1-x)2}\ Ni_{3x}\ O_{5-\delta}$ for $0.04 \geq x \geq 0.06$	160
4.4	Intensity variation of prominent peaks in Raman spectra with varying concentrations of Nickel and b) Variation in the bandwidth of prominent Raman peaks in the Ni-V-O compound	163
4.5	Scanning electron micrographs of $V_{(1-x)2}Ni_{3x}O_{5-\delta}$ powders (a)x=0.03 (b)x= 0.04 (c)x=0.05 and (d)x=0.06	164
4.6	EDS spectrum of $V_{(1-x)2}Ni_{3x}O_{5-\delta}$ powders (a)x=0.03 (b)x= 0.04 (c)x=0.05 (d)x=0.06	165
4.7	Histogram for particle size of distribution of $V_{(1-x)2}Ni_{3x}O_{5-\delta}$ powders (a)x=0.03 (b) x=0.04 (c)x=0.05 & (d)x=0.06	165
4.8	High-resolution X-ray photoelectron spectroscopy (XPS) data for $V_{2-x}Ni_{2x}O_{5-\delta}$, including (a) the survey spectrum and detailed core level spectra of (b) Ni *2p*, (c) V *2p*, and (d) O *1s* regions	166
4.9	Displays the Diffuse Reflectance Spectrum of $V_{(1-x)2}Ni_3O_{5-\delta}$ for various x values (b) Optical band gap energies of $V_{(1-x)2}Ni_{3x}O_{5-\delta}$ bulk powder for varying x values from K-M plot	168
4.10	Jonscher Power Law fit to frequency-dependent AC conductivity Curve of $V_{(1-x)2}Ni_{3x}O_{5-\delta}$ compounds 5 (d)Variation of AC conductivity with frequency for different mole fractions in Ni-VO compounds	171
4.11	Variation of AC conductivity with temperature for x=0.04,0.05 & 0.06 in $V_{(1-x)2}Ni_{3x}O_{5-\delta}$ samples	171

4.12	Variation of Dielectric constant with frequency, (b) Variation of Dielectric constant with temperature	172
4.13	Representative photographs of zone of growth inhibition against bacteria and fungi for Ni-V-O7 compound with positive and negative control: (a) P. Aeroginosa (100µl), (b) P. Aeroginosa (200 µl), (c) S. Aureus (200 µl) (d) S. Aureus (150 and 200 µl), (e)&(f) E. Coli (50 & 100 µl) and Pencillium(150 & 200 µl)	173
4.14	Bar diagram comparing the zone inhibition of $V_{2-x}Ni_{2x}O_{5-\delta}$for $0.03\leq x\leq 0.06$compounds, against the gram-positive and gram-negative bacteria and fungi growth for 200µl concentration.	178
5.1	XRD pattern of$V_{2-x}Ni_{2x}Sb_xO_{5-\delta}$ ceramics indicating the prominent orthorhombic phase of V_2O_5, with asterisk and diamond sign indicating peaks corresponding to Ni and Sb phases, respectively	193
5.2	Representing Rietveld refinements of $V_{2-x}Ni_{2x}Sb_xO_{5-\delta}$ samples for x=0.0, 0.05, 0.06, 0.07 and 0.08 respectively. (b) The unit cell structure of Sb-Ni-V-O compounds, containing the mixed phases of V_2O_5, NiV_2O_6 and $SbVO_4$ (c) The unit cell structure of Orthorhombic V_2O_5 (d) The unit cell structure of NiV_2O_6, (e) The rutile-type crystal structure of $SbVO_4$ characterized by a random distribution of Sb and V atoms within octahedral positions, each atom exhibiting a partial occupancy of 0.5	195
5.3	Raman spectrum of$V_{2-x}Ni_{2x}Sb_xO_{5-\delta}$(0.05<=x<=0.08) compounds (b) depicts the relative intensity of four prominent Raman bands at 143cm-1. 283 cm-1, 700 cm-1 and 997 cm-1 in $V_{2-x}Ni_{2x}Sb_xO_{5-\delta}$ $0.05\leq x\leq 0.08$	204
5.4	SEM micrographs of $V_{2-x}Ni_{2x}Sb_xO_{5-\delta}$ ceramics with x=0.05, 0.06, 0.07 & 0.08 in 2µm magnification. (e)-(h) indicating the histograms representing the average particle size of $V_{2-x}Ni_{2x}Sb_xO_{5-\delta}$ ceramics at x=0.05, 0.06, 0.07 & 0.08 respectively. (i) Displays the Weight% of Antimony, Nickel, Vanadium, and Oxygen elements present in the compound $V_{2-x}Ni_{2x}Sb_xO_{5-\delta}$, as obtained from the EDX spectrum	208
5.5	EDS spectrum of $V_{2-x}Ni_{2x}Sb_xO_{5-\delta}$compounds for x=0.08, elemental mapping showing the presence of (b)Oxygen, (c)Antimony, (d)Vanadium, and (e)Nickel, and(f) Sb, Ni, V & O	209
5.6	Curve fitting of the V2p XPS spectra of $V_{2-x}Ni_{2x}Sb_xO_{5-\delta}$ samples for x=(a)0.05, (b)0.06 (c)0.07 and (d)0.08 respectively	210
5.7	High-resolution XPS spectra of Sb 3d, taking into account of the O1s for Shirley background determination (binding energy relative to the O1s level at 530.0 eV) in $V_{2-x}Ni_{2x}Sb_xO_{5-\delta}$ samples for x=(a)0.05, (b)0.06 (c)0.07 and (d)0.08 respectively	211

5.8	XPS spectra for the Ni 2p in $V_{2-x}Ni_{2x}Sb_xO_{5-\delta}$ samples for x=(a)0.05, (b)0.06, (c)0.07 and (d)0.08 respectively	213
5.9	Diffuse reflectance spectrum of $V_{2-x}Ni_{2x}Sb_xO_{5-\delta}$ samples recorded for different mole concentrations x=0.05, 0.06, 0.07 & 0.08 (b) KM plot showing optical band gap energy variations as a function of mole fraction	214
5.10	Photoluminescence spectrum of $V_{2-x}Ni_{2x}Sb_xO_{5-\delta}$ compounds for (a)x=0.05 (b)x=0.06 (c)x=0.07 & (d)=0.08	216
5.11	Variation of dielectric constant with frequency and b)Tangent loss vs frequency for $V_{2-x}Ni_{2x}Sb_xO_{5-\delta}$ samples recorded for different mole concentrations x=0.05, 0.06, 0.07 & 0.08	218
5.12	Variation of AC conductivity with frequency (b)Variation of impedance with frequency for $V_{2-x}Ni_{2x}Sb_xO_{5-\delta}$ samples recorded for different mole concentrations x=0.05, 0.06, 0.07 & 0.08	221
5.13	Almond west curve fitting for AC conductivity vs frequency for $V_{2-x}Ni_{2x}Sb_xO_{5-\delta}$ samples recorded for different mole concentrations a) x=0.05 b) x=0.06 c) x=0.07 d)x=0.08	222
5.14	Representative photographs of zone of growth inhibition by $V_{2-x}Ni_{2x}Sb_xO_{5-\delta}$ compounds against bacteria and fungi:(a) Pencillium(150 & 200 µl) (b)Aspergillus Niger:(150 & 200 µl), (c) E-Coli (50 and 100 µl) (d) S. Aureus(100 µl) (e) E. coli(200 µl) (f) P. aeruginosa(200 µl)	225
5.15	Bar diagram comparing the zone of inhibition of $V_{2-x}Ni_{2x}Sb_xO_{5-\delta}$ compounds (0.05<=x<=0.08), against the growth of the gram positive-gram negative bacteria and fungi for 200µl concentration	225
6.1	Representing XRD pattern of as prepared hexagonal phase of g-C_3N_4, (b)Mixed phase $V_{2-x}Ni_{2x}Sb_xO_{5-\delta;}$ x =0.05 & (c)$V_{2-x}Ni_{2x}Sb_xO_{5-\delta}$/g-$C_3N_4$ heterostructures for $0.05 \leq x \leq 0.08$	244
6.2	Depicts the FTIR spectrum showing pure g-C_3N_4, $V_{2-x}Ni_{2x}Sb_xO_{5-\delta}$ &$V_{2-x}Ni_{2x}Sb_xO_{5-\delta}$/g-$C_3N_4$ at x=0.05 compounds 2(b) shows up $V_{2-x}Ni_{2x}Sb_xO_{5-\delta}$/g-$C_3N_4$ heterostructures for $0.05 \leq x \leq 0.08$	246
6.3	SEM image of pure g-C_3N_4, (b) SEM image of Sb-Ni-V_2O_5-5 triple phase composite, (c,d,e,f) present the SEM images of $V_{2-x}Ni_{2x}Sb_xO_{5-d}$ /g-C_3N_4 heterostructures for $0.05 \leq x \leq 0.08$	247
6.4	Representing the elemental overlay image of Sb-Ni-V_2O_5/g-C_3N_4-5, Carbon, Nitrogen, Oxygen, Antimony, Vanadium, and Nickel, respectively	248
6.5	EDS spectrum representing the presence of Sb, Ni, V, O, C, and N elements in $V_{2-x}Ni_{2x}Sb_xO_{5-\delta}$ /C_3N_4 heterostructures for $0.05 \leq x \leq 0.08$	248

6.6	High-resolution XPS spectra of (a) V2p (b)C1s (c)N1s (d)Ni2p (e)Sb 3d and (f) Survey spectrum in $V_{2-x}Ni_{2x}Sb_xO_{5-d}$ /g-C_3N_4 heterostructure for x=0.08	251
6.7	Absorbance spectrum and (b)Tauc plot of pure g-C_3N_4 and $V_{2-x}Ni_{2x}Sb_xO_{5-d}$/g-$C_3N_4$ heterostructures	253
6.8	Photoluminescence spectrum of $V_{2-x}Ni_{2x}Sb_xO_{5-\delta}$ /g-C_3N_4 heterostructures for $0.05 \leq x \leq 0.08$ and pristine g-C_3N_4(inset)	255
6.9	UV–Vis absorption spectra of methylene blue (MB) solution during photodegradation using Sb–Ni–V_2O_5/C_3N_4-5 under visible light irradiation. b) The photodegradation performance of the photocatalyst and its precursors for MB dye degradation. c)Bar Diagram depicting % Dye removal and d) Pseudo-first-order reaction kinetics of Sb-Ni-V_2O_5, C_3N_4, $V_{2-x}Ni_{2x}Sb_xO_{5-\delta}$ /g-C_3N_4 compounds for $0.05 \leq x \leq 0.08$	257
6.10	Rate constants for MB degradation (b). Reactive species trapping experiments for the Sb–Ni–V_2O_5/g-C_3N_4-8 photocatalyst showing dye removal efficiency after 1 hour of visible light irradiation	258
6.11	The possible photocatalytic mechanism of Sb-Ni-V_2O_5/g-C_3N_4 heterojunction photocatalysts at x=0.08, for degradation of MB under solar light irradiation	262
6.12	Recyclability test of Sb–Ni–V_2O_5/g-C_3N_4-8 showing a slight reduction in MB degradation efficiency from 100% to 95.3% over five 30-minute sunlight irradiation cycles	264
6.13	Representative images depicting microbial growth inhibition zones induced by Sb–Ni–V_2O_5/g-C_3N_4 heterostructures at x=0.08, against selected bacterial and fungal strains, compared to standard positive controls (streptomycin for bacteria,fluconazole forfungi) and a DMSO negative control, (a)g-C_3N_4: E.Coli(50 & 100µl),(b)g-C_3N_4: A. Niger(150 & 200 µl),and Sb-Ni-V_2O_5/g-C_3N_4 against(c) Pencillium(150 & 200 µl), (d)A.Niger(100 &150 µl), e)P. Aeroginosa(200 µl) (f)B. Cereus(200 µl), (g)S. Aureus (200µl) (h) V. Harveyi (200 µl), (i)V. Cholerae (200 µl)	266
6.14	Comparative bar charts illustrating the antimicrobial efficacy of Sb–Ni–V_2O_5/g-C_3N_4 heterostructures with varying mol fraction x ($0.05 \leq x \leq 0.08$), assessed through zone of inhibition measurements (mm) at a standardized dose of 200 µL encompassing activity against gram-positive and gram-negative bacterial strains and fungal species.	268

Chapter I

Multi-Cation Incorporated Vanadium Pentoxide Complex Oxides: Unlocking Diverse Applications

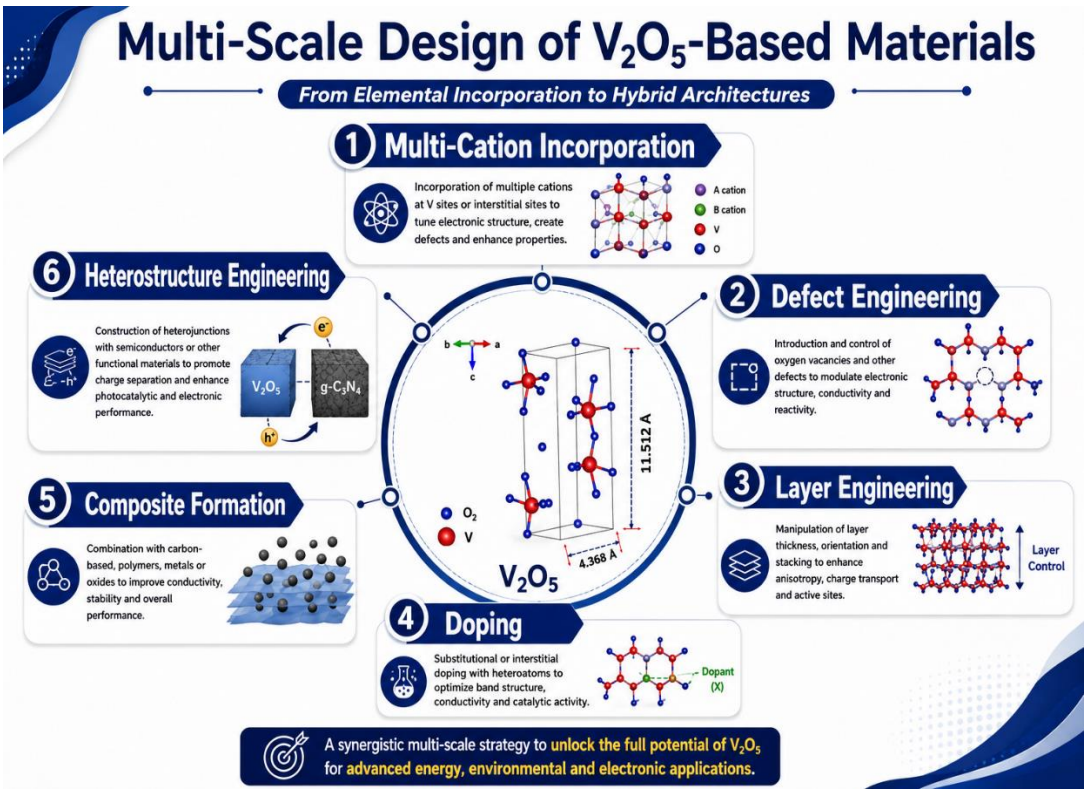

"The future of functional materials lies not in a single component, but in the intelligent synergy of multiple elements working together to create real world technologies."

1.1 Introduction

Vanadium, a transition metal with atomic number 23, belonging to Group 5, has an electronic configuration $[Ar]3d^3 4s^2$. It can exist in multiple oxidation states, varying between -3 to +5, with +2, +3, +4, and +5 being most common [1]. This multivalent nature of vanadium is the reason of it's rich chemistry and color range, with V^{5+} compounds orange-yellow, V^{4+} blue, and V^{3+} green in color. Multiple oxide phases include VO, V_2O_3, V_2O_5, VO_2, and mixed phases, such as the Magneli phase V_nO_{2n-1} (V_3O_5, V_4O_7, V_5O_9, V_6O_{11}, and V_7O_{13}), and the Wadsley phase V_nO_{2n+1} (V_3O_7, V_4O_9, V_5O_{11}, V_6O_{13}, V_7O_{15}, and V_8O_{17}). In these compounds, vanadium is coordinated by oxygen in various polyhedral geometries, such as VO_6 octahedra in V_2O_3 and VO_5 square pyramids in V_2O_5, and they crystallize in distinct lattice structures; for instance, VO adopts a rock-salt structure, V_2O_3 crystallizes in a corundum-type lattice, VO_2 exhibits a rutile-like monoclinic form at low temperatures and transitions to a rutile structure at high temperatures. At the same time, V_2O_5 possesses a layered orthorhombic configuration. In general**,** higher V oxidation state raises the band gap and oxidizing power, while lower V states yield narrower gaps or metallic behavior. For instance, VO_2 (V^{4+}) is a small-gap semiconductor (~0.6 eV when insulating) [1] whereas V_2O_5 (V^{5+}) is a wide-gap oxide (~2.3 eV) [2]. Vanadium oxides exhibit distinct structure-dependent functionalities and pronounced sensitivity to external stimuli, making them promising smart materials for energy conversion and conservation applications [2].

1.2. Structure of V_2O_5

Polymorphic phases of Vanadium pentoxide includes α, β, γ, £, ζ, δ, and ω phases as per the reports in the literature. Among these, the α-V_2O_5 phase represents the most stable form, whereas metastable or mixed V_2O_5 phases can emerge through structural transitions of α-V_2O_5 under high-temperature, high-pressure, or electrochemical conditions [2]. Within the vanadium oxide family, V_2O_5 stands out as the most thermodynamically stable compound, possessing the highest vanadium oxidation state of +5. V_2O_5 crystallizes in a layered orthorhombic structure belonging

to the *Pmnm*(59) space group, characterized by lattice parameters a = 11.510 Å, b = 3.563 Å, and c = 4.369 Å.

On analyzing the crystal structure of V_2O_5, the basic polyhedra consist of VO_5 pyramids, in which four oxygen atoms in the basal plane are interconnected to the vanadium atom by weak V-O bonds of bond length 2 Å, and the oxygen atom at the apex point is coupled with the vanadium atom by a short V=O vanadyl bond of 1.54 Å. As shown in Figure 1.1 [7], the layered structure of V_2O_5 is formed by interconnecting the VO_5 pyramids, forming a continuous layer in the ab-plane that is periodically stacked along the c-axis [3]. Double chains extending along the b-axis are formed from the VO_5 pyramids, which share edges and are joined and oriented in opposing directions. These double chains are oriented in the same direction and are joined along the a-axis through the pyramids' corners. Additionally, along the a-axis, the apices of these pyramids are arranged in an alternating pattern of up-up-down-down [2],[4-6].

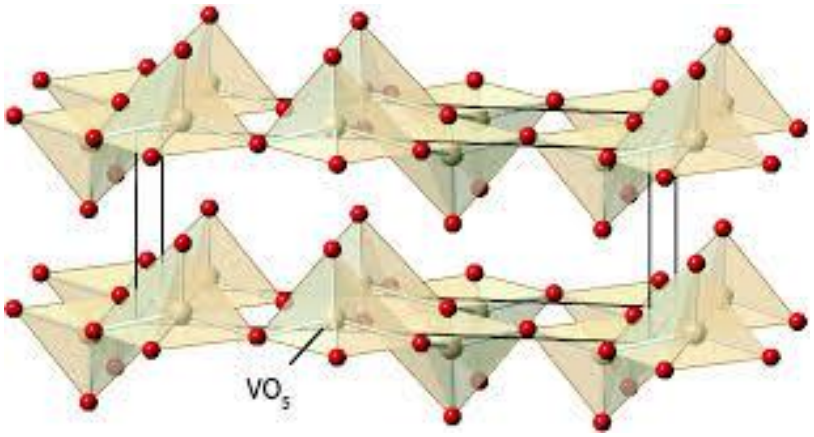

Figure 1.1. Layered structure of Vanadium Pentoxide

1.3. Morphology of V_2O_5

Vanadium pentoxide can be synthesized into various forms, including nanorods, nanowires, nanobelts, nanosheets, nanospheres, and complex three-dimensional (3D) structures. The choice of synthesis method, ranging from hydrothermal and solvothermal techniques to sol-gel processes, electrospinning, chemical vapor deposition (CVD), and template-assisted methods significantly

impacts the resulting nanostructures. For example, hydrothermal and sol-gel approaches are commonly employed to produce one-dimensional (1D) nanorods and nanowires. These methods rely on careful control of variables like precursor concentration, pH, reaction temperature, and the use of surfactants or structure-directing agents to achieve anisotropic crystal growth along specific crystallographic axes. Furthermore, combining electrospinning with post-annealing yields uniform nanowires with high aspect ratios and interconnected networks. Such 1D nanostructures are especially suited for high-performance lithium-ion battery cathodes, as they facilitate enhanced ion diffusion and electron transport [7].

Two-dimensional vanadium pentoxide, in the form of nanosheets and nanobelts, can be produced by exfoliating vanadium oxide precursors. These nanostructures have a high surface-to-volume ratio, which accelerates surface reactions and enhances contact with the electrolyte in electrochemical systems. Their layered structure allows different cations to intercalate, making them useful in zinc-ion and lithium-ion batteries. More exposed active sites also boost their photocatalytic activity [8-10].

Zero-dimensional V_2O_5 nanospheres, which are generally formed under isotropic growth conditions such as CVD or solvothermal reactions with controlled supersaturation, offer uniform morphology and high surface area [10]. V_2O_5 zero-dimensional (0D) nanospheres have a homogeneous shape and a large surface area. They are often grown under isotropic conditions, such as CVD or solvothermal processes with controlled supersaturation [11]. These characteristics are helpful in gas sensing and catalytic applications, where surface adsorption and quick diffusion are essential. Furthermore, microspheres made of aggregated nanoparticles or nanosheets can serve as the foundation for more intricate structures. Precursor chemistry, pH, and reaction kinetics are typically adjusted to form hierarchical 3D structures, such as flower-like, urchin-like, or porous micro- and nanostructures, often without the use of templates. These assemblages combine the functional benefits of their lower-dimensional constituents to produce synergistic effects, such as improved stress

tolerance during repeated charge-discharge cycles, increased ion/electron mobility, and enhanced mechanical integrity.

When researchers alter the shape and structure of V_2O_5 using different synthetic methods, they can improve key properties, such as surface area, electrical conductivity, stability, and interactions with other substances. Adjusting these features not only improves V_2O_5's basic performance but also makes it more useful in real devices. Because these properties can be changed and scaled up, V_2O_5 remains a flexible and popular choice in nanotechnology and energy research [11-16].

1.4. Optical Properties

Pure V_2O_5 is an n-type semiconductor that can show both direct and indirect band gaps, depending on the conditions. Its electronic structure is complex and depends on factors such as morphology, oxygen vacancies, and crystal phase [18]. At room temperature, bulk α-V_2O_5 exhibits a direct bandgap of approximately 2.3–2.4 eV and an indirect bandgap of 1.9-2.0 eV. The valence-band widths were determined to be 5.5 ± 0.5 eV for the bulk and 5.0 ± 0.5 eV for the single-layer configuration. Instead of a single band, the conduction band consists of two bands, a main CB and a split-off CB. These split-off CBs, with a bandwidth of 0.75 eV, are localized 0.6 eV below the main CB [2], [17]. Oxygen-vacancy-induced defects and, hence, non-stoichiometry in $V_2O_{5-\delta}$ leads to changes in the electronic and crystalline microstructure. Removal of oxygen atoms or oxygen deficiency creates extra electrons in the lattice. The V–O bonding environment alters in the crystal owing to the regulated atomic structure and hybridized V*3d*-O*2p* orbitals. Subsequently, the crystal's geometry is altered, forming mid-gap and surface states. Previous literature reported a mid-gap at approximately 0.7–1.0 eV above the VB, caused by oxygen vacancies. The experimental results showed that this gap is 1.8 eV above the valence band. The mid-gap states formed due to O(1), O(2), and O(3) vacancies are identified at 0.95, 0.75, and 0.69 eV, respectively [2]. The theoretical and experimental results showed that the optical bandgap and inter-sub-band transition intensity in V_2O_5 were influenced by numerous factors. In particular, in pure α-V_2O_5 with 3 bands, 4 optical transitions identified are, VB to the main CB, VB to the split-off CB, VB to the mid-

gap state and surface state, and the mid-gap state to the main CB. Therefore, in the literature, the band-gap energy of the optical transition and that obtained from PL of V_2O_5 do not coincide.

1.5. AC Conductivity, Dielectric, and Impedance Studies

The AC conductivity, dielectric, and impedance spectroscopy analyses of V_2O_5 pellets and films are noteworthy, as they are significant for understanding and improving its material properties for various uses. It provides insights into the electrical behavior, charge-transport mechanisms, and dielectric properties of V_2O_5, which are essential for applications in electronics, energy storage, and sensor devices. This knowledge is inevitable for understanding the hopping conduction mechanism, especially in multi-cation doped V_2O_5. Charge-transport mechanism studies clarify whether conduction occurs via polaron hopping or band conduction. AC conductivity measurements can help reveal how intrinsic defects and extrinsic doping affect electrical properties [18]. Incorporation of elements such as Ni, Mn, Bi, and Al can alter conductivity by increasing the number of charge carriers or altering the band structure of vanadium pentoxide. The dielectric constant (ε') and dielectric loss (ε'') obtained from dielectric studies indicate the material's capacity to store and dissipate electrical energy. High dielectric constants are suitable for capacitors, while low dielectric loss materials with minimal energy loss are beneficial for high-frequency applications. These studies also provide insights into different polarization mechanisms, such as electronic, ionic, dipolar, and interfacial polarization, that influence device performance in capacitors, varistors, and electrochromic devices [18].

Impedance spectroscopy enables the identification of the electrical response of V_2O_5 into contributions from grain boundaries, grains, and electrode interfaces. This is achieved by fitting the data to suitable circuit models, which provide detailed insights into the material's resistance, capacitance, and inductance [19]. The relaxation processes can identify defect states in V_2O_5 by analyzing Nyquist plots and Bode plots. The presence of multiple relaxation times can indicate different defect types or heterogeneous regions in the material, such as grain boundaries or phase separations

[19]. The conducting properties can be altered by doping, and impedance spectroscopy can be used to study the effect of doping on the overall conductivity and relaxation behavior of V_2O_5. For instance, the addition of different cations alters the impedance response, which can be correlated with changes in grain boundary resistance or bulk conduction pathways [20], [21]. The dielectric and impedance characteristics of V_2O_5 are essential for identifying its role in gas, humidity, and actuator sensors. The sensitivity of these properties to environmental changes makes V_2O_5 a suitable material for sensing applications [22], [23].

1.6. Applications of V_2O_5

Vanadium pentoxide is a versatile material with a wide range of applications due to its unique physical, chemical, and electronic properties. Below are some of its key applications:

1.6.1. Energy Storage

a) **Lithium-ion Batteries:** Vanadium pentoxide is attracting researchers worldwide for its energy storage applications, especially in lithium-ion batteries. Its high theoretical capacity and layered structure enable it to store and release lithium ions efficiently, making it a strong candidate for cathode materials. But it has a limited use in its pristine form due to poor cycling stability and low conductivity. To address this, researchers have made their particles smaller, to the nanoscale, which improves ion movement and increases the surface area for better contact between the electrode and electrolyte. Creating 2D nanosheets and other nanostructures has also improved their electrochemical properties, like specific capacity, rate capability, and cycling stability. Thus, V_2O_5 is now seen as a promising material for high-energy-density uses in electronics, electric vehicles, and renewable energy storage [8], [24].

Yanwei Li et al. [25] reported a facile, environmentally suitable, and cost-effective synthesis method for producing 2D V_2O_5 nanosheets having leaf-like morphology. These nanosheets exhibit distinctive nanoscale features, including a

hierarchical porous architecture and a high specific surface area, which contribute to their exceptional electrochemical performance as cathode materials for lithium-ion batteries. These unique structural characteristics enhance specific capacity, rate capability, and cycling stability, making them highly efficient for energy storage applications. Yu Chen et al. [26] reported the synthesis of submicron-level spherical V_2O_5 particles, synthesized by thermal decomposition of $(NH_4)_2V_4O_9$, prepared by chemical precipitation using commercially available V_2O_5. X-ray diffraction analysis indicates the formation of V_2O_5 with lower crystallinity and larger lattice parameters than its commercial counterpart. Electrochemical characterization indicated that the as-prepared V_2O_5 sample synthesized at 400°C has an initial discharge capacity of 330 mAh g^{-1}, retaining 263 mAh g^{-1} after 50 cycles, revealing its potential as a noteworthy cathode material for lithium-ion batteries [26], [27]. Aegyeong Kim et al. [28] developed a scalable synthesis method for in situ V_2O_5 nanoparticles using citric acid as a reducing and chelating agent. Nanoparticles annealed at 600°C exhibited superior cycling stability and rate performance, due to an optimal amorphous surface layer with vanadium oxides and C=C structures combined with high crystallinity. This methodology could be extended to enhance the electrochemical performance of other oxide electrode materials, such as Fe_3O_4 and Fe_2O_3, during Li^+ insertion and extraction.

(b) **Supercapacitors:** Supercapacitors, also known as electrochemical capacitors or ultracapacitors, are rigorously studied as they can be considered as an alternative to lithium-ion batteries with higher power density, faster charge/discharge cycles, and longer cycle life. However, their low energy density limits their use as standalone energy storage devices. High-capacitance materials usually have large surface areas and excellent electrical conductivity, which is directly connected to the electrochemical double-layer capacitance and the surface area available for redox reactions, contributing to pseudocapacitive behavior. Many high-surface-area carbon-based materials, such as activated carbon, CNTs, and graphene sheets, have been investigated as electrode materials for supercapacitors. Graphene, a 2D layer of carbon atoms, has shown exceptional potential as a component for 3D structures,

providing improved electrochemical performance essential for advanced energy storage devices [15], [29].

There are reports on the preparation of conductive graphene oxide/V_2O_5 composites using polyvinylpyrrolidone (PVP) as a carrier matrix, yielding well-defined, structurally stable nanofibers. The formation of these fibrous structures was confirmed through X-ray diffraction and scanning electron microscopy. The electrochemical performance of the graphene oxide/V_2O_5 nanofibers was tested in different electrolytes, with neutral KOH showing the best response. These findings indicate that the electrospinning method can improve electrode performance and can be adapted for other transition metal oxides to develop high-efficiency supercapacitor electrodes [30-33]. Many studies have examined V_2O_5 nanostructures for charge storage. For example, highly stable V_2O_5 nanochains were synthesized via a simple hydrothermal method using CTAB, achieving excellent supercapacitance without conductive supports [34].

Arup Choudhury et al. [36] developed a nanohybrid material by growing vanadium pentoxide nanofibers (VNFs) in situ on exfoliated graphene nanosheets for supercapacitor electrode applications. Raman and FTIR analyses confirmed the presence of non-covalent interactions between the VNFs and graphene, alongside XRD showed a highly crystalline structure. The VNF/graphene hybrid exhibited a good specific capacitance (218 Fg^{-1}), energy density (22 Wh kg^{-1}), and power density (3594 W kg^{-1}), outperforming pure VNFs. An asymmetric supercapacitor using this hybrid as the positive electrode demonstrated exceptional performance, with a capacitance of 279 $Fg^{-1,}$ an energy density of 37.2 Wh kg^{-1}, and a power density of 3743 W kg^{-1} [29]. Recent research developed a microwave-initiated method to exfoliate alpha polymorphic orthorhombic V_2O_5 powders into wrinkled nanoribbons. These nanoribbons were further combined with rGO using cation-assisted self-assembly and thermal annealing to create a V_2O_5/rGO hybrid. The resulting material showed a high specific capacitance of 423.6 Fg^{-1}, maintained excellent cycling

stability over 1800 cycles, and achieved an energy density of 58.8 $Whkg^{-1}$, highlighting its strong potential for scalable energy storage applications [36].

1.6.2. Chromogenic thin films

Vanadium pentoxide thin films are used in chromogenic applications, especially in electrochromic devices. V_2O_5 thin films can change color when a voltage is applied, as they can reversibly gain or lose oxygen. This property makes them useful for smart windows, displays, and energy-saving devices. V_2O_5 thin films also offer high optical contrast, fast switching, and good cycling stability, making them promising for energy-saving technologies, sensors, and displays.

(a) **Electrochromic Applications:**

V_2O_5 used in electrochromic devices changes color or transparency when an electric current is applied. This phenomenon occurs due to reversible intercalation of Li^+ ion within the V_2O_5 lattice, altering its optical properties. Key applications include [31]:

i. **Smart Windows:** V_2O_5 thin films enable the dynamic modulation of light transmission, reducing heating and cooling energy requirements in buildings.

ii. **Self-Dimming Rear-View Mirrors**: In automotive applications, electrochromic V_2O_5 thin films adjust the mirror's reflectance based on ambient light, enhancing driving safety.

iii. **Low-Power Displays:** Used in electrochromic displays for devices requiring low power, V_2O_5 enables displays that change color based on electrical stimuli.

Cosmin Romanitan et al. [32] showed a direct relation between the texture coefficient and electrochromism in orthorhombic V_2O_5 nanostructured films synthesized through spray pyrolysis. The larger the texture coefficient, the greater the charge insertion and transmittance contrast, reaching −73.30 $mC\text{-}cm^{-2}$ on coloration and 18.48% transmittance under ±1V, highlighting its significance in optimizing electrochromic performance. Mjejr et al. [33] reported the synthesis of V_2O_5

nanopowders prepared through the polyol process and the fabrication of V_2O_5 thin films using the *Doctor Blade* method. The resulting films exhibited noteworthy electrochromism in Li- and Na-based electrolytes. Junyi Wang et al. [34] reported the synthesis of porous and amorphous V_2O_5 films through a room-temperature photochemical process, with macropores attributed to a bubble-templating mechanism. The films exhibit enhanced multicolored electrochromic properties, attributed to a pseudocapacitive electrochromism that accelerates ion intercalation and deintercalation [34].

(b) Photochromic Applications:

V_2O_5 thin films show photochromic behavior, meaning they change color or transparency when exposed to UV or visible light [2]. This makes them ideal for,

i. **Smart Windows and Lenses**: Photochromic V_2O_5 films can automatically darken or lighten based on sunlight exposure, which is helpful in eyewear (like transition lenses) and adaptive glazing for windows, enhancing user comfort and energy efficiency.

ii. **Optical Data Storage**: V_2O_5's photochromic response to light can be applied in optical data storage technologies where data is recorded and read using light-induced changes.

Hidetoshi Miyazaki et al. [35] reported the fabrication of vanadium pentoxide-based composite films by adding evenly dispersed sub nanometer sized V_2O_5 particles. Upon exposure to ultraviolet light, the film exhibited a broad absorption peak centered around 700 nm. Additionally, the optical band gap of the films increased with prolonged UV irradiation, attributed to the corresponding rise in carrier concentration. This band gap widening occurs due to the Burstein Moss effect, in which an increased carrier concentration shifts the Fermi level into the conduction band. The films reverted to their bleached state when left in darkness, demonstrating reversible photochromic behavior.

(c) Thermochromic Applications:

V_2O_5 thin films exhibit thermochromic behavior, with their optical properties changing with temperature. This capability allows for:

i) **Temperature-Sensitive Smart Windows**: In thermochromic windows, V_2O_5 films can adjust transparency with changing external temperatures, allowing better regulation of heat and light.

ii) **Heat Regulation Coatings**: These films are used in coatings for energy-efficient buildings, allowing the material to transition from transparent to opaque as temperatures rise, reducing the cooling load in hot climates.

Sunil Kumar et al. [36] reported the synthesis of polycrystalline V_2O_5 films that exhibit reversible thermochromism, changing from yellow to orange with temperature, devoid of phase transitions, giving potential applications for tunable thermochromic devices. In conclusion, V_2O_5's photochromic, thermochromic, and electrochromic applications span a wide range of industries, from smart windows and energy-efficient buildings to automobile safety and display technologies [2].

1.6.3. Photocatalysis

V_2O_5 is used as a photocatalyst in environmental remediation applications such as water purification and the degradation of organic pollutants. Its ability to generate reactive oxygen species under UV-Visible light enables it to break down harmful substances in water and air. M.M. Sajid et al. reported the preparation of V_2O_5 nanoparticles through sol gel and hydrothermal methods, with the hydrothermally synthesized particles exhibiting higher crystallinity. The hydrothermal V_2O_5 nanoparticles demonstrated a high surface area of 238.454 cm^2/g and a pore size of 3.405 nm. Photocatalytic degradation of Congo Red (99.1%) and Methyl Orange(82%) was achieved, highlighting the material's potential for visible light driven photocatalytic and photoelectrochemical applications [37].

Sohaimi K. S. A. et al. [38] reviewed V_2O_5 as an efficient photocatalyst due to its exceptional crystallinity, reusability, cost-effectiveness, photo-corrosion

resistance, narrow band gap of 2.3 eV, and enhanced charge carrier mobility. Despite its potential, V_2O_5 suffers from photogenerated carrier recombination, limiting its photocatalytic efficiency. The review explores various synthesis methods, including hydrothermal, sol-gel, co-precipitation, and solvothermal techniques, and focuses on modifications to improve performance. V_2O_5 has been primarily used for dye degradation, though extensive research on its capabilities for pharmaceutical and other pollutants remains underexplored [38].

Bapuso M. Babar et al. [39] reported the successful synthesis of vanadium pentoxide nanoparticles using a straightforward hydrothermal method, where the impact of annealing on the MB dye decomposition was explored. The structural properties of V_2O_5 were confirmed through XRD and Raman spectroscopy, while FTIR spectroscopy identified the presence of functional groups. SEM revealed agglomerated nanoparticle morphology, and the direct band gap of V_2O_5 was obtained from UV-Vis spectra varying between 2.63-2.81 eV. Calcinated V_2O_5 exhibited enhanced photocatalytic activity, achieving 68% MB degradation within 80 minutes with a rate constant of 9.9×10^{-5} s^{-1} [39]. Sanja J. Armaković et al [40] reported that conventional wastewater treatment processes fail to eliminate organic pharmaceutical pollutants, leaving active pharmaceutical compounds, such as β-blockers, in water. He explored the photocatalytic degradation of β-blockers-nadolol (NAD), pindolol (PIN), and metoprolol (MET)—using V_2O_5 nanoparticles synthesized via the hydrothermal method. The tunable band gap of V_2O_5, via structural manipulation or external stimuli, enhances its photocatalytic potential, making it highly promising for water purification applications [40]. Raj et al. [41] reported the synthesis of vanadium pentoxide via surfactant-assisted hydrothermal methods and analyzed the products using structural, morphological, electronic, and optical characterization techniques. Electrochemical studies revealed that V_2O_5 prepared with CTAB exhibited superior charge-discharge cycle stability, while photocatalytic studies showed that V_2O_5 synthesized with SDS had the highest efficiency in degrading Methyl Orange dye under UV light [41].

1.6.4. Gas Sensors

The material's sensitivity to environmental changes, particularly to gases such as ammonia, ethanol, and nitrogen oxides, makes it useful for gas sensing applications. V_2O_5-based sensors are used for detecting toxic and hazardous gases. A. Dhayal Raj et al. [41] successfully synthesized hollow spheres of vanadium pentoxide composed of self-assembled nanorods using a solvothermal method. XRD analysis confirmed the orthorhombic structure of the calcinated V_2O_5 nanorods, which formed hollow spherical structures, as observed in SEM images. The hollow spheres had diameters of 2–3 μm, while the nanorods within them measured 100–200 nm in diameter and several hundred nanometers in length. Gas sensing studies revealed that the resistance of the V_2O_5 nanorods varied with ethanol and ammonia concentrations over time. Sensitivity increased linearly with the concentration of both gases, with the nanorods showing a stronger response to ethanol than to ammonia [42].

Pankaj Singh Chauhan [43] reported the successful synthesis of novel V_2O_5 nanostructures exhibiting rod and floral morphologies via a simple, daylong hydrothermal method using vanadyl sulfate hydrate and potassium bromate as precursors. The V_2O_5 nanostructures were used in thin-film form for room-temperature detection of hydrogen gas, targeting trace levels, with a lower explosive limit of 4% in air. Detailed investigations revealed a 40% increase in sensitivity when transitioning from nanowires to nanostars [43]. Yuxiang Qin et al. [44] reported the synthesis of advanced gas sensors based on hierarchical V_2O_5 structures, synthesized via a direct seed-induced hydrothermal process in which nanostructured V_2O_5 was grown on substrates with patterned Pt electrodes. By varying the precursor concentration, porous flower and honeycomb-like V_2O_5 architectures were fabricated. The flower-like hierarchical network, composed of radially oriented ultrathin nanoneedles, nanoribbons, and overlapping nanowires, exhibited an ideal microstructure for gas sensing applications. Ethanol gas sensing was studied from room temperature to 300°C, across a concentration range of 5 to 1000 ppm. The sensor exhibited a temperature-dependent p-to-n transition, with dual response peaks at 20°C and 250 °C. At 250 °C, the sensor showed heightened sensitivity to ethanol and NH_3, whereas at room temperature it demonstrated excellent ethanol selectivity [44].

1.6.5. Optoelectronic Devices

Vanadium pentoxide's unique optoelectronic properties, including high optical transparency, electrochromic capabilities, semiconducting behavior, and potential for use in memory devices, make it an important material in optoelectronics. Ko-Ying Pan et al. [46] synthesized V_2O5 nanowires on Si substrates using the vapor-solid method, confirmed by SEM, EDS, XRD, and HRTEM. The growth mechanism involves screw dislocations on the (110) crystal plane. Electrical resistivity was 64.62 Ω-cm. Cyclic voltammetry showed strong durability after 10 cycles, demonstrating the potential of V_2O_5 nanowires for optoelectronics and lithium-ion battery cathodes [45]. Advanced electronic, optical, and optoelectronic devices have initiated significant research into the preparation of vanadium oxide thin films. The optical performance and electronic behavior of these coatings are heavily influenced by the sample preparation methods and the films' resultant microstructure. Therefore, an understanding of the relationship between the fabrication process and film properties is crucial for optimizing their use in real-world applications [46].

1.6.6. Biomedical Applications

Vanadium pentoxide micro- and nanostructures are promising for many biomedical applications due to their oxygen-deficient lattice sites, strong oxidative potential, and good biocompatibility. These features make V_2O_5 useful in antimicrobial, antioxidant, and anticancer treatments. V_2O_5 nanoparticles exhibit strong antibacterial and antifungal effects, primarily by generating reactive oxygen species (ROS) that damage microbial membranes and disrupt key cellular processes [47]. Their redox activity has also led to the creation of "nanoisozymes" that mimic enzyme functions, enabling controlled catalytic activity in therapy. Modified V_2O_5 systems, such as those coated with mesoporous carbon, have shown promise for drug delivery by improving drug loading, controlling release, and reducing toxicity, supporting V_2O_5's role in advanced therapies [48], [49]. Huang et al.[50] added V_2O_5 nanowires to electrospun alginate wound dressings, which worked well against *S. aureus* and *E. coli* in lab tests and helped wounds heal faster in animal studies. V_2O_5 nanoparticles also showed antibacterial activity against several human pathogens,

including *Staphylococcus aureus, Escherichia coli, Pseudomonas aeruginosa,* and *Proteus vulgaris*, when tested by K. Karthik et al. Their results suggest that ultrasound-assisted V_2O_5 nanoparticles could be useful in both environmental and medical fields [51]. Although these results are promising in lab and animal studies, more in vivo testing and toxicity studies are needed before V_2O_5-based coatings can be used in clinics [52].

1.7. Limitations of pristine Vanadium pentoxide

Despite its applications, pure vanadium pentoxide exhibits several limitations that prevent its performance in various fields. These limitations include

a) **Low Intrinsic Conductivity:** V_2O_5 possesses inherently low electrical conductivity (~10^{-3} S/cm), which hinders its use in electronic devices and energy storage applications. This disadvantage can lead to poor charge transport and slow kinetics, especially in battery and supercapacitor electrodes, reducing their overall efficiency [53].

b) **Structural Instability:** During lithium-ion intercalation and deintercalation in batteries, V_2O_5 usually undergoes significant volume changes. This creates mechanical stress, structural degradation, and material pulverization, leading to a rapid decline in capacity and cycling stability [54].

c) **Phase Transition:** V_2O_5 undergoes phase transitions at relatively low temperatures, which can adversely affect its structural integrity and performance in high-temperature applications like catalysis and thermoelectrics [54-55].

d) **Photocatalytic Limitations:** Although V_2O_5 possesses a band gap of ~2.3 eV, enabling partial absorption of visible light, its absorption is largely confined to the blue-green region of the visible spectrum. The limited utilization of longer-wavelength visible light, together with rapid electron-hole recombination which suppresses the generation of reactive oxygen species, such as hydroxyl (•OH) and superoxide ($\bullet O_2^-$) radicals and hence restricts its overall photocatalytic efficiency under solar irradiation [56], [57].

e) Mechanical Weakness: Pristine V_2O_5 is brittle and lacks mechanical flexibility, which can be problematic in applications requiring durable and robust materials, such as structural composites and coatings [58].

f) Chemical Stability and Corrosion: V_2O_5 is chemically reactive and can be corroded by acidic and basic environments, leading to dissolution or degradation of the material. This limits its long-term stability and applicability in harsh chemical conditions, such as in catalytic converters and chemical sensors.

g) Catalytic Limitations: V_2O_5 often has limited selectivity and activity because of its specific surface area and few active sites. This lowers its efficiency in selective oxidation and other catalytic processes [56]. The low surface area of bulk V_2O_5 limits its catalytic performance. A high surface area is important for exposing more active sites in catalytic reactions [57].

h) Thermal Stability Issues: V_2O_5 can decompose or lose oxygen at elevated temperatures (>700°C), which affects its catalytic performance and stability in applications such as exhaust gas treatment and high-temperature sensors [59].

i) Biocompatibility and Toxicity: The cytotoxic nature of V_2O_5 limits its use in biomedical applications, such as drug delivery and bioimaging. The release of vanadium ions can be harmful to biological tissues, necessitating careful control and modification of the material for safe use [60].

j) Optoelectronic Limitations: In optoelectronic devices, the low charge carrier mobility in V_2O_5 can impede the efficient transport of electrons and holes, resulting in suboptimal performance in applications like solar cells, photodetectors, and electrochromic devices [61].

Vanadium pentoxide does not dissolve readily and is difficult to process, which makes fabrication challenging. V_2O_5 does not dissolve much in common solvents, so making films or coatings with solution-based methods is challenging. This limits how easily it can be used in different device designs [62]. To address these issues, researchers often use methods such as doping, creating composite materials, forming heterostructures, or altering the material's shape. These changes can improve

V_2O_5's electrical, structural, and chemical properties, making it more useful for advanced applications.

1.8. Methods for Altering the Properties of Vanadium Pentoxides

To optimize its structural, electronic, and chemical properties, researchers have employed a wide range of enhancement strategies. These go beyond traditional doping, encompassing composite formation, heterostructure engineering, and a suite of cutting-edge techniques, including defect engineering, morphology control, and intercalation chemistry. Below is a comprehensive overview of the major approaches used to enhance the performance of V_2O_5-based materials.

1.8.1. Multi-Cation Incorporation in V_2O_5

Suitable cation elements may alter the band structure and modify the E_{opt} of Vanadium Pentoxide. The color of the synthesized V_2O_5 varies with the dopant element and concentration. The E_{opt} increased with increasing Ce-, Sm-, Dy-, and Mg-doping in V_2O_5, whereas Sn-, Nb-, Gd-, Ag-, and Li-doping led to a decrease in optical band gap. For instance, Nd, F, La, Yb, and W incorporation, the optical band gap varies with foreign ion concentration.

E_{opt} decreases when the V:W ratio is below 9:1, but increases again when the ratio is above 7:1. Factors such as solvent, temperature, reaction time, and pressure influence how dopants bind to vanadium precursors, thereby altering the properties of V_2O_5. The size and behavior of the dopant elements make them compete for positions in the V_2O_5 layers, affecting the local and band structures. Dopants can either speed up or slow down crystallization. If the dopant radius is smaller than the host lattice, the lattice constant and crystal size become smaller. If the dopant radius is larger, both increase. These elements can form V–M oxide or local vanadate (MVO_4). Experiments show that the unit-cell volume of M-doped V_2O_5, where M = Na, Ba, and Al, is different from pure V_2O_5 [2]. Dopants can also act as donors in V_2O_5, creating new energy levels below the conduction band. This makes it easier for transitions between the valence band and these new levels, lowering Eg. When there are more donors, the new energy level fills up and E shifts to a higher energy. Adding

an ionic element creates defects and oxygen vacancies, leading to lower oxidation states like V^{4+} and V^{3+}. As the dopant concentration increases, the fraction of V^{4+}/V^{5+} or $(V^{3+}+V^{4+})/V^{5+}$ rises, which means there are more electron carriers. Electrons are also produced when V is replaced by $M^{x+,}$ where x is greater than 5. For example, replacing V with Cr or W adds extra electrons. These electrons can move into the split-off band, which increases Eg and changes the color [2].

Adding various metal cations, such as Mn, Ni, Sb, Al, and Li, to the V_2O_5 lattice alters its crystal structure, enhances redox activity, and improves conductivity. This approach helps increase photocatalytic, antimicrobial, and electrochemical performance. P. Kiran et al. [63] reviewed recent progress in using elemental doping to improve the gas-sensing abilities of vanadium pentoxide sensors. Doping with transition metals, rare-earth elements, and non-metals has been shown to make V_2O_5 sensors more sensitive, selective, and stable, and to speed up their response by altering surface properties, the electronic structure, and catalytic activity. The effectiveness of multi-cation incorporation depends on factors such as the type, amount, and distribution of dopants, as well as the synthesis method and operating conditions. Although doping can greatly improve performance, there are still challenges in controlling the process, managing structural changes, and optimizing the optimal dopant concentration [63].

Hong mei Zeng et al. [64] reported the synthesis of nanostructured Mn^{2+} incorporated V_2O_5 as a cathode material for lithium-ion batteries to improve charge transport. They used a layered vanadium(III) jarosite compound as the precursor, allowing Mn^{2+} ions to be evenly distributed between the vanadium oxide layers. Adding the larger Mn^{2+} ions expanded the cell volume and made it easier for Li^+ ions to move. The presence of multivalent cations created oxygen vacancies, thereby increasing electronic conductivity. When tested, the Mn^{2+} doped V_2O_5 showed much better performance than undoped V_2O_5 made from the same precursor. Further Ni-V_2O_5 nanorods were prepared via a simple sol–gel method, as reported by V. Uma Shankar et al. [65].

Microstructural analysis from XRD results confirmed the formation of an orthorhombic V_2O_5 phase in all samples, and SEM images show that Ni nanoparticles

are uniformly distributed on the surface of the V_2O_5 nanorods. Raman spectra showed V–O vibrational modes without extrinsic phases arising from foreign cations. Both pristine and Ni-incorporated V_2O_5 electrodes exhibited pseudo capacitance, with specific capacitances of 112 $F\,g^{-1}$ and 152 $F\,g^{-1}$ at a scan rate of 10 $mV\,s^{-1}$, respectively, indicating enhanced electrochemical performance upon Ni addition. Zhou et al. [66] developed a high-performance Al-incorporated V_2O_5 cathode for zinc-ion batteries by using a rapid quenching method to induce Al doping and surface oxygen vacancies.

1.8.2. Composite Formation

Many studies show that V_2O_5 can form composites with carbon-based nanomaterials such as graphene, CNTs, polymers, and metal oxides. These combinations improve conductivity, mechanical strength, and stability. As a result, these composites are used in energy storage, photocatalysis, and biomedical coatings. Sneha R. Bhosale and colleagues [67] developed a mesoporous carbo-V_2O_5 composite that works as a biogenic nanocarrier with better drug loading, antioxidant, antibacterial, and anticancer properties. The combination of carbon and V_2O_5 increased surface area and improved interfacial interactions, making it more effective than pure V_2O_5 for biomedical application. Arun Varghese and team developed a polypyrrole-V_2O_5-MnO_2 electrocatalyst for energy applications that performed well in hydrogen evolution and supercapacitor tests. Their composite had a high surface area of 136.3 m^2/g, an overpotential of 192 mV, and a specific capacity of 1736.1 C/g [68]. S. A. Ahamed and colleagues [69] used Morus alba leaf extract to make pure and Fe-doped V_2O_5 for better supercapacitor performance. Adding Fe improved redox activity and stability, with $V_{1.8}Fe_{0.2}O_5$ reaching a capacitance of 719.25 F/g at 2 A/g. A symmetric device kept 94% of its capacitance after 10,000 cycles and delivered an energy density of 49 Wh/kg, showing promise as a sustainable electrode material.

1.8.3. Heterostructure Engineering

Creating heterojunctions with materials such as g-C_3N_4, MoS_2, or TiO_2 can enhance charge separation, light absorption, and photocatalytic activity. V_2O_5-based heterostructures are promising for many applications because their electronic structure

and redox activity can be readily adjusted. These materials improve photodetector performance by increasing light absorption and charge transport, and they offer high capacitance and stable ion intercalation for energy storage. In electrochromic devices, V_2O_5 enables rapid, reversible color changes. Its photocatalytic activity under visible light helps break down pollutants, and its ability to generate reactive oxygen species gives it antimicrobial effects. Combining V_2O_5 with materials such as MXene, graphene, or TiO_2 further improves conductivity, stability, and surface reactivity, making it valuable for new optoelectronic, energy, environmental, and biomedical devices. Junjie Huang and colleagues [70] developed a dual-ion electrochromic capacitor (EDIC) with a V_2O_5/MXene anode and a PANI/TiO_2 cathode, enabling fast ion exchange and improved charge transfer. Their device exhibited multicolor switching, 51% optical modulation, fast response times (2.4/7.2 s), and high coloration efficiency (111 cm2 C^{-1}), outperforming traditional systems and offering a promising approach for efficient electrochromic energy storage.

A. G. Roman and his team made V_2O_5/porous silicon heterostructures for photodetectors using a simple, low-cost process. They produced porous silicon by electrochemical anodization and grew V_2O_5 structures using solvothermal or hydrothermal methods. Their analysis found aligned pores (about 1.4 μm wide and 22 μm long) and V_2O_5 in the form of nanosheets, nanobelts, or hollow microspheres. XRD and Raman studies confirmed the orthorhombic V_2O_5 phase, with crystallite sizes of 31.5 and 16.4 nm. Photoluminescence showed emissions at 550 nm and 707 nm, and the optical band gaps were 1.5 eV and 2.1 eV. Electrical tests showed both rectifying and ohmic behavior, along with a clear photocurrent response, supporting their use as simple, efficient photodetectors [71]. Hu and his team designed a δ-V_2O_5-H_2O/rGO (VOG) heterostructure as a cathode for zinc-ion batteries to solve the conductivity and structural problems of layered vanadium oxides. The VOG electrode showed strong interfacial coupling, improved ion diffusion, and delivered 342 mAh g^{-1} at 1 A g^{-1} with good rate performance [72]. A.E. Hassan and his team [73] created V_2O_5/N-deficient g-C_3N_4 heterostructures that showed efficient visible-light-driven bifunctional photocatalysis for hydrogen production (5892 μ-mol g^{-1} h^{-1},6.5% quantum yield) and pollutant degradation. The improved performance stems from N defects and S-scheme charge transfer, which enhance charge separation, light absorption, and stability.

1.8.4. Defect Engineering

Generating oxygen vacancies or other structural defects in materials creates mid-gap states and improves electronic conductivity, which enhances photocatalysis, battery performance, and gas-sensing capabilities. Ahmed Badreldin and his team [74] produced black V_2O_5 via an eco-friendly reduction method that generated oxygen vacancies, thereby improving its photocatalytic activity under visible light. Their experiments and DFT studies revealed that charge separation improved because of a type-II heterostructure with pure V_2O_5. The new material eliminated 92% of methylene blue in 60 minutes and worked well with other dyes, with surface defects linked to structural changes. Adding sulfur to V_2O_5 has also improved its energy storage and conversion. Sabna et al. team [75] prepared 2D sulfur-doped V_2O_5 flakes via a hydrothermal method, creating lattice defects that narrowed the band gap and improved conductivity. DFT and electrochemical tests showed better ion movement, lower charge resistance, and a high specific capacitance of 749 F/g with strong cycling stability. The doped material also showed about a 4.7 times increase in photocurrent density, making it a strong candidate for advanced energy devices. N. Brijadar [76] reported the making of vanadium pentoxide with maleic acid as a surfactant, then adding palladium nanoparticles onto the surface. They tested different amounts of Pd, including 0.5 wt%, 1 wt%, 3 wt%, and 5 wt%, and compared how plain and Pd-decorated V_2O_5 worked as resistive gas sensors. The 1 wt% Pd@V_2O_5 sample had the best response and selectivity for NO_x, namely NO and NO_2 gases, performing better than other samples tested with organic vapors like SO_x, NH_3, methanol, ethanol, acetone, trimethylamine, triethylamine, and formaldehyde. They tested the sensors at about 30°C, 100°C, and 150°C, with the best results at 150°C. The sensor responded quickly, within about 1 second, and recovered in 2 minutes, detecting NOx concentrations ranging from 10 to 1000 ppm. The improved sensing after adding Pd was similar to previous studies, showing good progress in NO_x gas detection.

1.8.5. Surface Functionalization

Incorporating organic ligands, polymers, or biomolecules into V_2O_5 enhances its dispersion, interfacial charge transfer, and biocompatibility. These materials are

commonly used in biosensors, drug delivery, and tissue engineering. L. T. B Mendoca et al. [77] created V_2O_5/PANI nanocomposites using laser ablation in water. With PANI, the interlayer spacing increased from 7.95 to 13.6 Å. Adding H_2O_2 changed the material's shape, leading to fiber formation in V_2O_5/PANI. Raman and electrochemical tests showed a strong interaction between V_2O_5 and PANI, with changes in redox behavior and a stronger current response. A.Shoukat et al. [78] prepared a flexible PVA/V_2O_5/$BaTiO_3$ nanocomposite film with improved optical, dielectric, and mechanical properties. The film had a lower bandgap of 2.61 eV and a higher Young's modulus, making it suitable for optoelectronic applications. G.J. Thangamani et al. [79] produced poly vinylalcohol(PVA)/polypyrrole/ vanadiumpentoxide nanocomposite films using solution casting. Mechanical tests showed the films were flexible and strong. For gas sensing, PVA/WPPy/V_2O_5 nanocomposites containing 15% V_2O_5 showed the highest sensitivity of 1.16% to liquid petroleum gas at 600 ppm at room temperature, with quick response and recovery times of about 10 and 8 seconds, respectively. This combination also showed excellent selectivity for LPG over other volatile organic compounds, suggesting it could be effective as a chemi-resistive sensor for LPG detection.

Yen-Lin Pan [80] developed a new ammonia gas sensor by combining a radio-frequency-sputtered vanadium pentoxide thin film with platinum nanoparticles. The Pt NP/V_2O_5 sensor exhibited unusual p-type conductivity, likely due to an inversion layer of holes at the n-type V_2O_5 surface. Adding Pt nanoparticles increased the surface area and catalytic activity, which increases ammonia detection. The sensor achieved a high response ratio of 83.2% at 1000 ppm NH_3/air and could detect as little as 100 ppb, with fast response times at 300°C. The device was also selective, simple, stable, and easy to make, making it a strong candidate for high-performance ammonia sensing [80].

1.8.6. Ion Intercalation / Layer Engineering

Intercalating ions like Li^+, Na^+, or Zn^{2+} between V_2O_5 layers increases interlayer spacing and improves ionic/electronic conductivity, particularly in batteries [81]. Incorporating multiple metal cations, such as Mn, Mg, Ni, Bi, Al, Li, and Sb, into Vanadium Pentoxide can significantly enhance its physical, chemical, and

electronic properties [82]. These multi-cation incorporations can induce modifications in the crystal structure, improve electrical conductivity, boost catalytic performance, and increase the thermal and chemical stability of V_2O_5-based metal oxide complexes. Such synergistic tuning of V_2O_5's properties enhances its suitability for advanced applications across fields such as photocatalysis, energy storage, antimicrobial systems, and sensing technologies. Each incorporated cation contributes uniquely to the structural and functional enhancement of the V_2O_5 matrix, offering a versatile platform for performance optimization.

1.9. Objective of the Study

- **Unraveling Electrical and Dielectric Properties**: Conduct A.C. conductivity and dielectric studies on Sb and Ni-incorporated V_2O_5 compounds, providing insights into their suitability for advanced electronic and energy storage applications.

- **Advancing Adsorption Capabilities:** Examine the adsorption properties of Sb-V_2O_5 compounds to understand their potential for adsorbing the cationic Methylene Blue dye.

- **Enhancing Photocatalytic Performance:** Explore the enhanced photocatalytic activity of Sb-Ni-V_2O_5/g-C_3N_4 heterostructures for environmental remediation, leveraging their unique structural identity for efficient light-driven reactions

- **Exploring Antimicrobial Potential:** Investigate the antimicrobial efficacy of Sb-V-O, Ni-V-O, and Sb-Ni-V-O multi-cation incorporated oxides, along with Sb-Ni-V_2O_5/g-C_3N_4 heterostructures, to uncover their potential as next-generation antibacterial agents.

1.10. Relevance of the study

The present investigation is of substantial scientific relevance, as it bridges fundamental materials science with advanced functional applications. By elucidating the electrical and dielectric behavior of Sb- and Ni-incorporated V_2O_5 compounds, the study provides crucial insights into charge transport and polarization mechanisms, with implications for next-generation electronic and energy-storage devices.

Furthermore, exploring the adsorptive properties of Sb–V_2O_5 for cationic methylene blue reveals its potential for wastewater purification through efficient dye sequestration. The photocatalytic performance of Sb–Ni–V_2O_5/g-C_3N_4 heterostructures highlights the synergy between multi-cation oxides and graphitic carbon nitride in enhancing visible-light-driven catalytic efficiency**,** offering sustainable solutions for environmental remediation**.** Additionally, the assessment of antimicrobial activity in Sb–V–O, Ni–V–O, and Sb–Ni–V–O systems, as well as in their g-C_3N_4 composites, expands the material's functionality toward biomedical and hygienic applications. Collectively, this research advances the multidisciplinary understanding of doped V_2O_5 systems, aligning structural modification, optical response, and surface reactivity with the design of high-performance, eco-efficient, and multifunctional materials**.**

References:

[1] P. Hu *et al.*, "Vanadium Oxide: Phase Diagrams, Structures, Synthesis, and Applications," *Chem. Rev.*, vol. 123, no. 8, pp. 4353–4415, Apr. 2023, doi: 10.1021/acs.chemrev.2c00546.

[2] T. K. Le *et al.*, "Recent advances in vanadium pentoxide (V_2O_5) towards related applications in chromogenics and beyond: fundamentals, progress, and perspectives," *J. Mater. Chem. C*, vol. 10, no. 11, pp. 4019–4071, 2022, doi: 10.1039/D1TC04872D.

[3] F. Liu, S. Song, D. Xue, and H. Zhang, "Selective crystallization with preferred lithium-ion storage capability of inorganic materials," *Nanoscale Res. Lett.*, vol. 7, no. 1, p. 149, Dec. 2012, doi: 10.1186/1556-276X-7-149.

[4] H. G. Bachmann, F. R. Ahmed, and W. H. Barnes, "The crystal structure of vanadium pentoxide," *Z. Für Krist.*, vol. 115, no. 1–2, pp. 110–131, May 1961, doi: 10.1524/zkri.1961.115.1-2.110.

[5] N. A. Chernova, M. Roppolo, A. C. Dillon, and M. S. Whittingham, "Layered vanadium and molybdenum oxides: batteries and electrochromics," *J. Mater. Chem.*, vol. 19, no. 17, p. 2526, 2009, doi: 10.1039/b819629j.

[6] C. Delmas, H. Cognacauradou, J. Cocciantelli, M. Menetrier, and J. Doumerc, "The LixV2O5 system: An overview of the structure modifications induced by the lithium intercalation," *Solid State Ion.*, vol. 69, no. 3–4, pp. 257–264, Aug. 1994, doi: 10.1016/0167-2738(94)90414-6.

[7] A. Cao, J. Hu, H. Liang, and L. Wan, "Self-Assembled Vanadium Pentoxide (V_2O_5) Hollow Microspheres from Nanorods and Their Application in Lithium-Ion Batteries," *Angew. Chem. Int. Ed.*, vol. 44, no. 28, pp. 4391–4395, July 2005, doi: 10.1002/anie.200500946.

[8] Y. Yue and H. Liang, "Micro- and Nano-Structured Vanadium Pentoxide (V_2O_5) for Electrodes of Lithium-Ion Batteries," *Adv. Energy Mater.*, vol. 7, no. 17, p. 1602545, Sept. 2017, doi: 10.1002/aenm.201602545.

[9] X. Wang *et al.*, "Vanadium pentoxide nanosheets as cathodes for aqueous zinc-ion batteries with high rate capability and long durability," *Appl. Surf. Sci.*, vol. 502, p. 144207, Feb. 2020, doi: 10.1016/j.apsusc.2019.144207.

[10] J. Mu *et al.*, "Hydrothermal synthesis and electrochemical properties of V2O5 nanomaterials with different dimensions," *Ceram. Int.*, vol. 41, no. 10, pp. 12626–12632, Dec. 2015, doi: 10.1016/j.ceramint.2015.06.091.

[11] A. Pan *et al.*, "Facile synthesized nanorod structured vanadium pentoxide for high-rate lithium batteries," *J. Mater. Chem.*, vol. 20, no. 41, p. 9193, 2010, doi: 10.1039/c0jm01306d.

[12] F. Zhou, X. Zhao, C. Yuan, and L. Li, "Vanadium Pentoxide Nanowires: Hydrothermal Synthesis, Formation Mechanism, and Phase Control Parameters," *Cryst. Growth Des.*, vol. 8, no. 2, pp. 723–727, Feb. 2008, doi: 10.1021/cg060816x.

[13] R. K. Sharma, P. Kumar, and G. B. Reddy, "Synthesis of vanadium pentoxide (V2O5) nanobelts with high coverage using plasma assisted PVD approach," *J. Alloys Compd.*, vol. 638, pp. 289–297, July 2015, doi: 10.1016/j.jallcom.2015.02.178.

[14] J. Zhu *et al.*, "Building 3D Structures of Vanadium Pentoxide Nanosheets and Application as Electrodes in Supercapacitors," *Nano Lett.*, vol. 13, no. 11, pp. 5408–5413, Nov. 2013, doi: 10.1021/nl402969r.

[15] H. Bai, Z. Liu, D. D. Sun, and S. H. Chan, "Hierarchical 3D micro-/nano-V2O5 (vanadium pentoxide) spheres as cathode materials for high-energy and high-power lithium ion-batteries," *Energy*, vol. 76, pp. 607–613, Nov. 2014, doi: 10.1016/j.energy.2014.08.058.

[16] L. Yao, C. Zhang, N. Hu, L. Zhang, Z. Zhou, and Y. Zhang, "Three-dimensional skeleton networks of reduced graphene oxide nanosheets/vanadium pentoxide nanobelts hybrid for high-performance supercapacitors," *Electrochimica Acta*, vol. 295, pp. 14–21, Feb. 2019, doi: 10.1016/j.electacta.2018.10.134.

[17] L. Top, M. Kang, and S. Kim, "A review on the optical characterization of V2O5 micro-nanostructures," *Ceram. Int.*, vol. 45, May 2019, doi: 10.1016/j.ceramint.2019.05.339.

[18] A. Ray, A. Roy, S. De, S. Chatterjee, and S. Das, "Frequency and temperature dependent dielectric properties of TiO2-V2O5 nanocomposites," *J. Appl. Phys.*, vol. 123, no. 10, Mar. 2018, doi: 10.1063/1.5012586.

[19] P. Rosaiah, G. L. Sandhya, and O. M. Hussain, "Impedance Spectroscopy and Electrochemical Properties of Nano-Crystalline Vanadium Pentoxide (V_2O_5) Synthesized by Co-Precipitation Method," *Adv. Sci. Eng. Med.*, vol. 8, no. 2, pp. 83–90, Feb. 2016, doi: 10.1166/asem. 2016.1839.

[20] J. Wu *et al.*, "Influence of Dopants on Electrical Properties of ZnO-V2O5 Varistors Deduced from AC Impedance and Variable-Temperature Dielectric Spectroscopy," *J. Electron. Mater.*, vol. 41, no. 7, pp. 1970–1977, July 2012, doi: 10.1007/s11664-012-1935-7.

[21] A. Sivakumar *et al.*, "Shock wave recovery experiments on α-V2O5 nano-crystalline materials: A potential material for energy storage applications," *J. Alloys Compd.*, vol. 929, p. 167180, Dec. 2022, doi: 10.1016/j.jallcom.2022.167180.

[22] "VO nanofibres: novel gas sensors with extremely high sensitivity and selectivity to amines," *Sens. Actuators B Chem.*, vol. 106, no. 2, pp. 730–735, May 2005, doi: 10.1016/j.snb.2004.09.024.

[23] V. Modafferi *et al.*, "Highly sensitive ammonia resistive sensor based on electrospun V2O5 fibers," *Sens. Actuators B Chem.*, vol. 163, no. 1, pp. 61–68, Mar. 2012, doi: 10.1016/j.snb.2012.01.007.

[24] Y. Zhu *et al.*, "V_2O_5 Textile Cathodes with High Capacity and Stability for Flexible Lithium-Ion Batteries," *Adv. Mater.*, vol. 32, no. 7, Feb. 2020, doi: 10.1002/adma.201906205.

[25] Y. Li *et al.*, "Leaf-Like V_2O_5 Nanosheets Fabricated by a Facile Green Approach as High Energy Cathode Material for Lithium-Ion Batteries," *Adv. Energy Mater.*, vol. 3, no. 9, pp. 1171–1175, Sept. 2013, doi: 10.1002/aenm.201300188.

[26] Y. Chen, C. Chen, W. Chen, H. Liu, and J. Zhu, "Influence of thermal-decomposition temperatures on structures and properties of V2O5 as cathode materials for lithium ion battery," *Prog. Nat. Sci. Mater. Int.*, vol. 25, no. 1, pp. 42–46, Feb. 2015, doi: 10.1016/j.pnsc.2015.01.015.

[27] H. Wang, D. Ma, Y. Huang, and X. Zhang, "Electrospun V_2O_5 Nanostructures with Controllable Morphology as High-Performance Cathode Materials for Lithium-Ion Batteries," *Chem. – Eur. J.*, vol. 18, no. 29, pp. 8987–8993, July 2012, doi: 10.1002/chem.201200434.

[28] T. Kim, J. Shin, T.-S. You, H. Lee, and J. Kim, "Thermally Controlled V2O5 Nanoparticles as Cathode Materials for Lithium-Ion Batteries with Enhanced Rate Capability," *Electrochimica Acta*, vol. 164, pp. 227–234, May 2015, doi: 10.1016/j.electacta.2015.02.208.

[29] A. Choudhury, J. S. Bonso, M. Wunch, K. S. Yang, J. P. Ferraris, and D. J. Yang, "In-situ synthesis of vanadium pentoxide nanofibre/exfoliated graphene nanohybrid and its supercapacitor applications," *J. Power Sources*, vol. 287, pp. 283–290, Aug. 2015, doi: 10.1016/j.jpowsour.2015.04.062.

[30] Y. Chen, K. Muthukumar, L. Leban, and J. Li, "Microwave-assisted high-yield exfoliation of vanadium pentoxide nanoribbons for supercapacitor applications," *Electrochimica Acta*, vol. 330, p. 135200, Jan. 2020, doi: 10.1016/j.electacta.2019.135200.

[31] Y. Wang, K. Takahashi, H. Shang, and G. Cao, "Synthesis and Electrochemical Properties of Vanadium Pentoxide Nanotube Arrays," *J. Phys. Chem. B*, vol. 109, no. 8, pp. 3085–3088, Mar. 2005, doi: 10.1021/jp044286w.

[32] C. Romanitan *et al.*, "Structural Investigations in Electrochromic Vanadium Pentoxide Thin Films," *Phys. Status Solidi A*, vol. 219, no. 16, p. 2100431, Aug. 2022, doi: 10.1002/pssa.202100431.

[33] I. Mjejri, L. M. Manceriu, M. Gaudon, A. Rougier, and F. Sediri, "Nano-vanadium pentoxide films for electrochromic displays," *Solid State Ion.*, vol. 292, pp. 8–14, Sept. 2016, doi: 10.1016/j.ssi.2016.04.023.

[34] J. Wang *et al.*, "Pseudocapacitive porous amorphous vanadium pentoxide with enhanced multicolored electrochromism," *Chem. Eng. J.*, vol. 452, p. 139655, Jan. 2023, doi: 10.1016/j.cej.2022.139655.

[35] H. Miyazaki, T. Matsuura, and T. Ota, "Vanadium oxide-based photochromic composite film," *RSC Adv.*, vol. 7, no. 5, pp. 2388–2391, 2017, doi: 10.1039/C6RA25892A.

[36] S. Kumar, A. Qadir, F. Maury, and N. Bahlawane, "Visible Thermochromism in Vanadium Pentoxide Coatings," *ACS Appl. Mater. Interfaces*, vol. 9, no. 25, pp. 21447–21456, June 2017, doi: 10.1021/acsami.7b04484.

[37] M. M. Sajid *et al.*, "Preparation and characterization of Vanadium pentoxide (V2O5) for photocatalytic degradation of monoazo and diazo dyes," *Surf. Interfaces*, vol. 19, p. 100502, June 2020, : 10.1016/j.surfin.2020.100502.

[38] K. S. A. Sohaimi, J. Jaafar, and N. Rosman, "Synthesis, Properties, and Applications of Vanadium Pentoxide (V2O5) as Photocatalyst: A Review," *Malays. J. Fundam. Appl. Sci.*, vol. 19, no. 5, pp. 901–914, Oct. 2023, doi: 10.11113/mjfas.v19n5.2774.

[39] Department of Physics, Yashavantrao Chavan Institute of Science, Satara, Maharashtra 415 001, India *et al.*, "Hydrothermally Prepared Vanadium Oxide Nanostructures for Photocatalytic Application," *ES Energy Environ.*, 2022, doi: 10.30919/esee8c639.

[40] S. J. Armaković *et al.*, "Photocatalytic Activity of the V2O5 Catalyst toward Selected Pharmaceuticals and Their Mixture: Influence of the Molecular Structure on the Efficiency of the Process," *Molecules*, vol. 28, no. 2, p. 655, Jan. 2023, doi: 10.3390/molecules28020655.

[41] A. T. Raj, K. Ramanujan, S. Thangavel, S. Gopalakrishan, N. Raghavan, and G. Venugopal, "Facile Synthesis of Vanadium-Pentoxide Nanoparticles and Study on Their Electrochemical, Photocatalytic Properties," *J. Nanosci. Nanotechnol.*, vol. 15, no. 5, pp. 3802–3808, May 2015, doi: 10.1166/jnn.2015.9543.

[42] A. Dhayal Raj, T. Pazhanivel, P. Suresh Kumar, D. Mangalaraj, D. Nataraj, and N. Ponpandian, "Self assembled V2O5 nanorods for gas sensors," *Curr. Appl. Phys.*, vol. 10, no. 2, pp. 531–537, Mar. 2010, doi: 10.1016/j.cap.2009.07.015.

[43] P. S. Chauhan and S. Bhattacharya, "Vanadium Pentoxide Nanostructures for Sensitive Detection of Hydrogen Gas at Room Temperatur," *J. Energy Environ. Sustain.*, vol. 2, pp. 69–74, July 2016, doi: 10.47469/JEES.2016.v02.100022.

[44] Y. Qin, G. Fan, K. Liu, and M. Hu, "Vanadium pentoxide hierarchical structure networks for high performance ethanol gas sensor with dual working temperature characteristic," *Sens. Actuators B Chem.*, vol. 190, pp. 141–148, Jan. 2014, doi: 10.1016/j.snb.2013.08.061.

[45] K.-Y. Pan and D.-H. Wei, "Optoelectronic and Electrochemical Properties of Vanadium Pentoxide Nanowires Synthesized by Vapor-Solid Process," *Nanomaterials*, vol. 6, no. 8, p. 140, July 2016, doi: 10.3390/nano6080140.

[46] E. E. Chain, "Optical properties of vanadium dioxide and vanadium pentoxide thin films," *Appl. Opt.*, vol. 30, no. 19, p. 2782, July 1991, doi: 10.1364/AO.30.002782.

[47] S. Das *et al.*, "Anti-angiogenic vanadium pentoxide nanoparticles for the treatment of melanoma and their *in vivo* toxicity study," *Nanoscale*, vol. 12, no. 14, pp. 7604–7621, 2020, doi: 10.1039/D0NR00631A.

[48] S. Nivetha *et al.*, "Nickel-doped vanadium pentoxide (Ni@V2O5) nanocomposite induces apoptosis targeting PI3K/AKT/mTOR signaling pathway in skin cancer: An in vitro and in vivo study," *Colloids Surf. B Biointerfaces*, vol. 234, p. 113763, Feb. 2024, doi: 10.1016/j.colsurfb.2024.113763.

[49] H. S. Lalithamba, A. D. Nagaraja, A. Siddekha, G. K. Prashanth, and G. Nagendra, "Green synthesis of V2O5 nanoparticles: Anticancer, antioxidant activity, application in biodiesel production and amino acid derived thioacids," *Results Chem.*, vol. 15, p. 102260, May 2025, doi: 10.1016/j.rechem.2025.102260.

[50] L. Huang, L. Yu, X. Yin, Y. Lin, Y. Xu, and Y. Niu, "Silver nanoparticles with vanadium oxide nanowires loaded into electrospun dressings for efficient healing of

bacterium-infected wounds," *J. Colloid Interface Sci.*, vol. 622, pp. 117–125, Sept. 2022, doi: 10.1016/j.jcis.2022.04.026.

[51] K. Karthik, M. P. Nikolova, A. Phuruangrat, S. Pushpa, V. Revathi, and M. Subbulakshmi, "Ultrasound-assisted synthesis of $V_2 O_5$ nanoparticles for photocatalytic and antibacterial studies," *Mater. Res. Innov.*, vol. 24, no. 4, pp. 229–234, June 2020, doi: 10.1080/14328917.2019.1634404.

[52] N. Anicic, M. Vukomanovic, and D. Suvorov, "Design of a multifunctional vanadium pentoxide/polymer biocomposite for implant-coating applications," *RSC Adv.*, vol. 7, no. 61, pp. 38647–38658, 2017, doi: 10.1039/C7RA06471C.

[53] B. Walls *et al.*, "Optical anisotropy of pristine and reduced V2O5(010)," *Sci. Rep.*, vol. 15, no. 1, July 2025, doi: 10.1038/s41598-025-07519-z.

[54] G. A. Horrocks *et al.*, "Mitigating Cation Diffusion Limitations and Intercalation-Induced Framework Transitions in a 1D Tunnel-Structured Polymorph of V_2O_5," *Chem. Mater.*, vol. 29, no. 24, pp. 10386–10397, Dec. 2017, doi: 10.1021/acs.chemmater.7b03800.

[55] R. Verrelli *et al.*, "On the strange case of divalent ions intercalation in V2O5," *J. Power Sources*, vol. 407, pp. 162–172, Dec. 2018, doi: 10.1016/j.jpowsour.2018.08.024.

[56] R. Saravanan, V. K. Gupta, E. Mosquera, and F. Gracia, "Preparation and characterization of V2O5/ZnO nanocomposite system for photocatalytic application," *J. Mol. Liq.*, vol. 198, pp. 409–412, Oct. 2014, doi: 10.1016/j.molliq.2014.07.030.

[57] Y. Li, S. Chen, W. Duan, Y. Nan, D. Ding, and G. Xiao, "Research progress of vanadium pentoxide photocatalytic materials," *RSC Adv.*, vol. 13, no. 33, pp. 22945–22957, 2023, doi: 10.1039/d3ra03648k.

[58] R. Mirabal-Rojas, S. E. Rodil, G. Ramirez, T. Polcar, E. Camps, and A. Erdemir, "Effect of the addition of Si into V2O5 coatings: Structure and tribo-mechanical properties," *Surf. Coat. Technol.*, vol. 349, pp. 111–118, Sept. 2018, doi: 10.1016/j.surfcoat.2018.05.052.

[59] F. Xia *et al.*, "Thermal transition behaviors of vanadium pentoxide film during post-deposition annealing," *Surf. Coat. Technol.*, vol. 405, p. 126637, Jan. 2021, doi: 10.1016/j.surfcoat.2020.126637.

[60] L. S. Rhoads, W. T. Silkworth, M. L. Roppolo, and M. S. Whittingham, "Cytotoxicity of nanostructured vanadium oxide on human cells in vitro," *Toxicol. In Vitro*, vol. 24, no. 1, pp. 292–296, Feb. 2010, doi: 10.1016/j.tiv.2009.08.010.

[61] A. S. Altowyan, J. Hakami, H. Algarni, and M. Shkir, "Enhancing the optoelectronic properties of V2O5 thin films through Tb doping for photodetector applications," *J. Alloys Compd.*, vol. 960, p. 170911, Oct. 2023, doi: 10.1016/j.jallcom.2023.170911.

[62] S. Sutrave *et al.*, "A simple solution combustion method for the synthesis of V2O5 nanostructures for supercapacitor applications," *Appl. Surf. Sci. Adv.*, vol. 12, p. 100331, Dec. 2022, doi: 10.1016/j.apsadv.2022.100331.

[63] P. Kiran *et al.*, "Vanadium pentoxide gas sensors: An overview of elemental doping strategies and their effect on sensing performance," *Catal. Commun.*, vol. 187, p. 106838, Feb. 2024, doi: 10.1016/j.catcom.2023.106838.

[64] H. Zeng *et al.*, "Nanostructured Mn-Doped V_2 O_5 Cathode Material Fabricated from Layered Vanadium Jarosite," *Chem. Mater.*, vol. 27, no. 21, pp. 7331–7336, Nov. 2015, doi: 10.1021/acs.chemmater.5b02840.

[65] V. Uma Shankar, D. Govindarajan, P. Christuraj, M. J. Salethraj, F. J. Johanson, and M. D. Raja, "Enhanced the electrochemical properties of Ni doped V2O5 as a electrode material for supercapacitor applications," *Mater. Today Proc.*, vol. 50, pp. 2675–2678, 2022, doi: 10.1016/j.matpr.2020.08.213.

[66] H. Jiang *et al.*, "Quench-tailored Al-doped V2O5 nanomaterials for efficient aqueous zinc-ion batteries," *J. Energy Chem.*, vol. 70, pp. 52–58, July 2022, doi: 10.1016/j.jechem.2022.02.030.

[67] S. R. Bhosale, R. R. Bhosale, R. P. Dhavale, G. B. Kolekar, V. B. Shimpale, and P. V. Anbhule, "Nanomaterials Based Multifunctional Bioactivities of V_2 O_5 and Mesoporous Carbon@V_2 O_5 Composite: Preparation and Characterization," *Langmuir*, vol. 40, no. 12, pp. 6471–6483, Mar. 2024, doi: 10.1021/acs.langmuir.4c00010.

[68] A. Varghese, K. R. P. Sunajadevi, D. Pinheiro, B. Saravanakumar, and M. Selvaraj, "Advancing energy production and storage: Polypyrrole/V2O5/MnO2 composite as a high-performance electrocatalyst," *Int. J. Hydrog. Energy*, vol. 123, pp. 238–246, Apr. 2025, doi: 10.1016/j.ijhydene.2025.03.419.

[69] S. A. Ahmad, F. Mashkoor, M. A. Ansari, A. A. Alothman, M. Shoeb, and C. Jeong, "Morus alba-mediated defect-rich Fe-doped V2O5 nanoparticles on woven carbon fiber for high-performance supercapacitor with enhanced charge storage mechanism," *J. Alloys Compd.*, vol. 1020, p. 179515, Mar. 2025, doi: 10.1016/j.jallcom.2025.179515.

[70] J. Huang, S. Zhang, Q. Qin, Z. Wang, and G. Cai, "Designing V2O5/MXene van der Waals heterostructure for complementary electrochromic dual-ion capacitor," *Chem. Eng. J.*, vol. 476, p. 146626, Nov. 2023, doi: 10.1016/j.cej.2023.146626.

[71] A. Garzon-Roman *et al.*, "Fabrication of V2O5/porous silicon heterostructures by simple and low-cost methods, morphological, structural, optical, and electrical characterization, and their first application as photodetectors," *Sens. Actuators Phys.*, vol. 387, p. 116471, June 2025, doi: 10.1016/j.sna.2025.116471.

[72] X. Hu *et al.*, "Two-dimensional heterostructure of MXene-derived V2O5·H2O and graphene with enhanced Zn-ion storage capability," *Electrochimica Acta*, vol. 507, p. 145093, Dec. 2024, doi: 10.1016/j.electacta.2024.145093.

[73] A. E. Hassan *et al.*, "V2O5 nanoribbons/N-deficient g-C3N4 heterostructure for enhanced visible-light photocatalytic performance," *Int. J. Hydrog. Energy*, vol. 48, no. 26, pp. 9620–9635, Mar. 2023, doi: 10.1016/j.ijhydene.2022.12.009.

[74] A. Badreldin *et al.*, "Surface microenvironment engineering of black V2O5 nanostructures for visible light photodegradation of methylene blue," *J. Alloys Compd.*, vol. 871, p. 159615, Aug. 2021, doi: 10.1016/j.jallcom.2021.159615.

[75] W. Young Jang *et al.*, "Novel 2D sulfur-doped V2O5 flakes and their applications in photoelectrochemical water oxidation and high-performance energy storage supercapacitors," *Chem. Eng. J.*, vol. 461, p. 141935, Apr. 2023, doi: 10.1016/j.cej.2023.141935.

[76] S. N. Birajdar and P. V. Adhyapak, "Palladium-decorated vanadium pentoxide as NOx gas sensor," *Ceram. Int.*, vol. 46, no. 17, pp. 27381–27393, Dec. 2020, doi: 10.1016/j.ceramint.2020.07.223.

[77] L. T. Boaes Mendonça, A. G. Bezerra, and W. Mendes De Azevedo, "Preparation and characterization of V2O5 and V2O5/PANI nanocomposite by laser ablation technique in liquid," *Mater. Chem. Phys.*, vol. 273, p. 125084, Nov. 2021, doi: 10.1016/j.matchemphys.2021.125084.

[78] A. Shoukat, M. Aslam, Z. Mustafa, M. Basit, and S. M. A. Zaidi, "Fabrication and analysis of PVA/V2O5/BaTiO3 nanocomposite film for flexible optoelectronics," *Phys. B Condens. Matter*, vol. 678, p. 415777, Apr. 2024, doi: 10.1016/j.physb.2024.415777.

[79] G. J. Thangamani, K. Deshmukh, N. A. Nambiraj, and S. K. K. Pasha, "Chemiresistive gas sensors based on vanadium pentoxide reinforced polyvinyl alcohol/polypyrrole blend nanocomposites for room temperature LPG sensing," *Synth. Met.*, vol. 273, p. 116687, Mar. 2021, doi: 10.1016/j.synthmet.2020.116687.

[80] Y.-L. Pan and W.-C. Liu, "Study of a Platinum (Pt) Nanoparticle (NP)/Vanadium Pentoxide (V_2 O_5) Thin Film-Based Ammonia Gas Sensor," *IEEE Trans. Electron Devices*, vol. 67, no. 5, pp. 2126–2132, May 2020, doi: 10.1109/TED.2020.2981113.

[81] J. Światowska-Mrowiecka, V. Maurice, S. Zanna, L. Klein, and P. Marcus, "XPS study of Li ion intercalation in V2O5 thin films prepared by thermal oxidation of vanadium metal," *Electrochimica Acta*, vol. 52, no. 18, pp. 5644–5653, May 2007, doi: 10.1016/j.electacta.2006.12.050.

[82] H. Si *et al.*, "Impact of the Morphology of V_2 O_5 Electrodes on the Electrochemical Na^+ -Ion Intercalation," *J. Electrochem. Soc.*, vol. 165, no. 11, pp. A2709–A2717, 2018, doi: 10.1149/2.0621811jes.

[83] T. P. Jaya, P. Jayaram, T. Ramachandran, P. Hajira, C. N. Anumol, and P. P. Pradyumnan, "Synthesis of solid solutions of Mn and Bi substituted V2O5 and substitutional effect in structural and optoelectronic behavior," *Phys. B Condens. Matter*, vol. 407, no. 8, pp. 1214–1218, Apr. 2012, doi: 10.1016/j.physb.2012.01.098.

[84] R. Abaira, T. Dammak, A. Matoussi, and A. Younes, "Structural and optical properties of zinc oxide doped by V2O5 synthesized by solid-state reaction," *Superlattices Microstruct.*, vol. 91, pp. 365–374, Mar. 2016, doi: 10.1016/j.spmi.2016.01.008.

[85] W. D. Callister and D. G. Rethwisch, *Materials Science and Engineering: An Introduction, ., .*, 9th ed. Wiley, 2014.

[86] K. McColl, I. Johnson, and F. Corà, "Thermodynamics and defect chemistry of substitutional and interstitial cation doping in layered α-V_2 O_5," *Phys. Chem. Chem. Phys.*, vol. 20, no. 22, pp. 15002–15006, 2018, doi: 10.1039/C8CP02187B.

[87] T. Chen, C. Foo, and S. C. Edman Tsang, "Interstitial and substitutional light elements in transition metals for heterogeneous catalysis," *Chem. Sci.*, vol. 12, no. 2, pp. 517–532, 2021, doi: 10.1039/D0SC06496C.

[88] G. K. Williamson and W. H. Hall, "X-ray line broadening from filed aluminium and wolfram," *Acta Metall.*, vol. 1, no. 1, pp. 22–31, Jan. 1953, doi: 10.1016/0001-6160(53)90006-6.

[89] O. A. Bulavchenko and Z. S. Vinokurov, "In Situ X-ray Diffraction as a Basic Tool to Study Oxide and Metal Oxide Catalysts," *Catalysts*, vol. 13, no. 11, p. 1421, Nov. 2023, doi: 10.3390/catal13111421.

[90] Cullity, B. D., & Stock, S. R., *Elements of X-ray Diffraction (3rd ed.)*. Prentice Hall., 2001.

[91] A. L. Patterson, "The Scherrer Formula for X-Ray Particle Size Determination," *Phys. Rev.*, vol. 56, no. 10, pp. 978–982, Nov. 1939, doi: 10.1103/PhysRev.56.978.

[92] J. I. Langford and A. J. C. Wilson, "Scherrer after sixty years: A survey and some new results in the determination of crystallite size," *J. Appl. Crystallogr.*, vol. 11, no. 2, pp. 102–113, Apr. 1978, doi: 10.1107/S0021889878012844.

[93] A. Monshi, M. R. Foroughi, and M. R. Monshi, "Modified Scherrer Equation to Estimate More Accurately Nano-Crystallite Size Using XRD," *World J. Nano Sci. Eng.*, vol. 02, no. 03, pp. 154–160, 2012, doi: 10.4236/wjnse.2012.23020.

[94] H. M. Rietveld, "A profile refinement method for nuclear and magnetic structures," *J. Appl. Crystallogr.*, vol. 2, no. 2, pp. 65–71, June 1969, doi: 10.1107/S0021889869006558.

[95] R. A. YOUNG, *The Rietveld Method*. International Union of Crystallography. Oxford University Press.

[96] B. H. Toby, "*R* factors in Rietveld analysis: How good is good enough?," *Powder Diffr.*, vol. 21, no. 1, pp. 67–70, Mar. 2006, doi: 10.1154/1.2179804.

[97] J. Rodríguez-Carvajal, "Recent advances in magnetic structure determination by neutron powder diffraction," *Phys. B Condens. Matter*, vol. 192, no. 1–2, pp. 55–69, Oct. 1993, doi: 10.1016/0921-4526(93)90108-I.

[98] L. B. McCusker, R. B. Von Dreele, D. E. Cox, D. Louër, and P. Scardi, "Rietveld refinement guidelines," *J. Appl. Crystallogr.*, vol. 32, no. 1, pp. 36–50, Feb. 1999, doi: 10.1107/S0021889898009856.

[99] E. N. Kaufmann, *Characterization of Materials*. in Characterization of Materials, no. v. 1. John Wiley & Sons, Incorporated, 2012. [Online]. Available: https://books.google.co.in/books?id=Ke8nLgEACAAJ

[100] L. A. Gribov, "The Theory of Raman Spectra: A New Approach," *High Energy Chem.*, vol. 54, no. 4, pp. 233–236, July 2020, doi: 10.1134/S0018143920040062.

[101] "Infrared Spectroscopy," in *ACS Reagent Chemicals*, Washington, DC: American Chemical Society, 2017. doi: 10.1021/acsreagents.2008.

[102] M. El-Azazy, A. S. El-Shafie, and K. Al-Saad, "Introductory Chapter: Infrared Spectroscopy - Principles and Applications," in *Infrared Spectroscopy - Perspectives and Applications*, M. El-Azazy, K. Al-Saad, and A. S. El-Shafie, Eds., IntechOpen, 2023. doi: 10.5772/intechopen.109139.

[103] B. Faramarzi, M. Moggio, N. Diano, M. Portaccio, and M. Lepore, "A Brief Review of FT-IR Spectroscopy Studies of Sphingolipids in Human Cells," *Biophysica*, vol. 3, no. 1, pp. 158–180, Mar. 2023, doi: 10.3390/biophysica3010011.

[104] F. A. Stevie and C. L. Donley, "Introduction to x-ray photoelectron spectroscopy," *J. Vac. Sci. Technol. Vac. Surf. Films*, vol. 38, no. 6, p. 063204, Dec. 2020, doi: 10.1116/6.0000412.

[105] N. Alov, D. Kutsko, I. Spirovová, and Z. Bastl, "XPS study of vanadium surface oxidation by oxygen ion bombardment," *Surf. Sci.*, vol. 600, no. 8, pp. 1628–1631, Apr. 2006, doi: 10.1016/j.susc.2005.12.052.

[106] J. Biener, M. Bäumer, J. Wang, and R. J. Madix, "Electronic structure and growth of vanadium on TiO2(110)," *Surf. Sci.*, vol. 450, no. 1–2, pp. 12–26, Apr. 2000, doi: 10.1016/S0039-6028(99)01216-9.

[107] Y. Okano, "Scanning Electron Microscopy," in *Compendium of Surface and Interface Analysis*, The Surface Science Society Of Japa, Ed., Singapore: Springer Singapore, 2018, pp. 563–569. doi: 10.1007/978-981-10-6156-1_91.

[108] M. T. Postek, A. E. Vladár, O. C. Wells, and J. L. Lowney, "Application of the low-loss scanning electron microscope image to integrated circuit technology. Part 1–applications to accurate dimension measurements," *Scanning*, vol. 23, no. 5, pp. 298–304, Sept. 2001, doi: 10.1002/sca.4950230502.

[109] M. Schreiner and M. Melcher, "Scanning Electron Microscopy," in *The Encyclopedia of Archaeological Sciences*, 1st ed., S. L. López Varela, Ed., Wiley, 2018, pp. 1–4. doi: 10.1002/9781119188230.saseas0518.

[110] K. Tsuji, "X-ray Fluorescence and Emission: X-ray Fluorescence Theory," in *Reference Module in Chemistry, Molecular Sciences and Chemical Engineering*, Elsevier, 2018, p. B9780124095472144749. doi: 10.1016/B978-0-12-409547-2.14474-9.

[111] J. Zheng, K. Nagashima, D. Parmiter, J. De La Cruz, and A. K. Patri, "SEM X-Ray Microanalysis of Nanoparticles Present in Tissue or Cultured Cell Thin Sections," in *Characterization of Nanoparticles Intended for Drug Delivery*, vol. 697, S. E. McNeil, Ed., in Methods in Molecular Biology, vol. 697. , Totowa, NJ: Humana Press, 2011, pp. 93–99. doi: 10.1007/978-1-60327-198-1_9.

[112] M. A. K. Abdelhalim and M. M. Mady, "Physical Properties of Different Gold Nanoparticles: Ultraviolet-Visible and Fluorescence Measurements," *J. Nanomedicine Nanotechnol.*, vol. 03, no. 03, 2012, doi: 10.4172/2157-7439.1000133.

[113] A. K. Brisdon, "UV-visible spectroscopy," in *Inorganic Spectroscopic Methods*, Oxford University Press, 1998. doi: 10.1093/hesc/9780198559498.003.0004.

[114] B. W. Montag, N. Platt, N. M. Boag, J. I. Brand, and K. A. Nelson, "Doped Wide Bandgap Materials and Devices from Semiconducting Boron Carbide," *ECS Trans.*, vol. 3, no. 5, pp. 429–435, Oct. 2006, doi: 10.1149/1.2357234.

[115] P. Makuła, M. Pacia, and W. Macyk, "How To Correctly Determine the Band Gap Energy of Modified Semiconductor Photocatalysts Based on UV–Vis Spectra," *J. Phys. Chem. Lett.*, vol. 9, no. 23, pp. 6814–6817, Dec. 2018, doi: 10.1021/acs.jpclett.8b02892.

[116] J. E. Toney, "Photoluminescence Spectroscopy," in *Characterization of Materials*, 1st ed., E. N. Kaufmann, Ed., Wiley, 2003. doi: 10.1002/0471266965.com058.

[117] Q. Li, M. Anpo, J. You, T. Yan, and X. Wang, "Photoluminescence (PL) Spectroscopy," in *Springer Handbook of Advanced Catalyst Characterization*, I. E. Wachs and M. A. Bañares, Eds., in Springer Handbooks. , Cham: Springer International Publishing, 2023, pp. 295–321. doi: 10.1007/978-3-031-07125-6_14.

[118] J. R. Lakowicz, Ed., *Principles of Fluorescence Spectroscopy*. Boston, MA: Springer US, 2006. doi: 10.1007/978-0-387-46312-4.

[119] S. Sanguinetti, M. Guzzi, and M. Gurioli, "Accessing structural and electronic properties of semiconductor nanostructures via photoluminescence," in *Characterization of Semiconductor Heterostructures and Nanostructures*, Elsevier, 2008, pp. 175–208. doi: 10.1016/B978-0-444-53099-8.00006-3.

[120] S. Shimizu and N. Matubayasi, "Surface Area Estimation: Replacing the Brunauer–Emmett–Teller Model with the Statistical Thermodynamic Fluctuation Theory," *Langmuir*, vol. 38, no. 26, pp. 7989–8002, July 2022, doi: 10.1021/acs.langmuir.2c00753.

[121] F. Ambroz, T. J. Macdonald, V. Martis, and I. P. Parkin, "Evaluation of the BET Theory for the Characterization of Meso and Microporous MOFs," *Small Methods*, vol. 2, no. 11, p. 1800173, Nov. 2018, doi: 10.1002/smtd.201800173.

[122] S. Saitzek, J. -F. Blach, S. Villain, and J. -R. Gavarri, "Nanostructured ceria: a comparative study from X-ray diffraction, Raman spectroscopy and BET specific surface measurements," *Phys. Status Solidi A*, vol. 205, no. 7, pp. 1534–1539, July 2008, doi: 10.1002/pssa.200723419.

[123] K. S. W. Sing, "Reporting physisorption data for gas/solid systems with special reference to the determination of surface area and porosity (Recommendations 1984)," *Pure Appl. Chem.*, vol. 57, no. 4, pp. 603–619, Jan. 1985, doi: 10.1351/pac198557040603.

[124] J. W. M. Osterrieth *et al.*, "How Reproducible are Surface Areas Calculated from the BET Equation?," *Adv. Mater.*, vol. 34, no. 27, p. 2201502, July 2022, doi: 10.1002/adma.202201502.

[125] S. Lowell, J. E. Shields, M. A. Thomas, and M. Thommes, *Characterization of Porous Solids and Powders: Surface Area, Pore Size and Density*, vol. 16. in Particle Technology Series, vol. 16. Dordrecht: Springer Netherlands, 2004. doi: 10.1007/978-1-4020-2303-3.

[126] Jean Rouquerol, Françoise Rouquerol, Philip Llewellyn, Guillaume Maurin, Kenneth Sing, *Adsorption by Powders and Porous Solids Principles, Methodology and Applications*, 2nd Edition-September 6, 2013.

[127] R. Bardestani, G. S. Patience, and S. Kaliaguine, "Experimental methods in chemical engineering: specific surface area and pore size distribution measurements—BET, BJH,

and DFT," *Can. J. Chem. Eng.*, vol. 97, no. 11, pp. 2781–2791, Nov. 2019, doi: 10.1002/cjce.23632.

[128] A. Debnath, M. Majumder, M. Pal, N. S. Das, K. K. Chattopadhyay, and B. Saha, "Enhanced Adsorption of Hexavalent Chromium onto Magnetic Calcium Ferrite Nanoparticles: Kinetic, Isotherm, and Neural Network Modeling," *J. Dispers. Sci. Technol.*, vol. 37, no. 12, pp. 1806–1818, Dec. 2016, doi: 10.1080/01932691.2016.1141100.

[129] Z. Ying, D. Zhao, H. Li, X. Liu, and J. Zhang, "Efficient Adsorption of Deoxynivalenol by Porous Carbon Prepared from Soybean Dreg," *Toxins*, vol. 13, no. 7, p. 500, July 2021, doi: 10.3390/toxins13070500.

[130] A. K. Jonscher, "Dielectric relaxation in solids," *J. Phys. Appl. Phys.*, vol. 32, no. 14, pp. R57–R70, July 1999, doi: 10.1088/0022-3727/32/14/201.

[131] M. M. El-Nahass, H. A. M. Ali, M. Saadeldin, and M. Zaghllol, "AC conductivity and dielectric properties of bulk tungsten trioxide (WO3)," *Phys. B Condens. Matter*, vol. 407, no. 22, pp. 4453–4457, Nov. 2012, doi: 10.1016/j.physb.2012.07.043.

[132] C. Thirmal, S. D. Ramarao, L. S. Rao, and V. R. K. Murthy, "Study of structural, dielectric and AC conductivity properties of SrMoO4," *Mater. Res. Bull.*, vol. 146, p. 111618, Feb. 2022, doi: 10.1016/j.materresbull.2021.111618.

[133] A. H. Bashal, N. S. Alkayal, J. Aslam, and K. D. Khalil, "Investigation of structure, dielectric properties, and AC conductivity at high temperature for chitosan capped metal oxides nanocomposites," *J. Taibah Univ. Sci.*, vol. 19, no. 1, p. 2490411, Dec. 2025, doi: 10.1080/16583655.2025.2490411.

[134] A. Syifaurrahma, A. Arnelli, and Y. Astuti, "LiOH/Coconut Shell Activated Carbon Ratio Effect on the Electrical Conductivity of Lithium Ion Battery Anode Active Material," *Molekul*, vol. 16, no. 3, p. 235, Nov. 2021, doi: 10.20884/1.jm.2021.16.3.805.

[135] Y. Şafak-Asar, T. Asar, Ş. Altındal, and S. Özçelik, "Investigation of dielectric relaxation and ac electrical conductivity using impedance spectroscopy method in (AuZn)/TiO2/p-GaAs(110) schottky barrier diodes," *J. Alloys Compd.*, vol. 628, pp. 442–449, Apr. 2015, doi: 10.1016/j.jallcom.2014.12.170.

[136] Aakansha, B. Deka, S. Ravi, and D. Pamu, "Impedance spectroscopy and ac conductivity mechanism in Sm doped Yttrium Iron Garnet," *Ceram. Int.*, vol. 43, no. 13, pp. 10468–10477, Sept. 2017, doi: 10.1016/j.ceramint.2017.05.089.

[137] M. A. Al-Ghouti and D. A. Da'ana, "Guidelines for the use and interpretation of adsorption isotherm models: A review," *J. Hazard. Mater.*, vol. 393, p. 122383, July 2020, doi: 10.1016/j.jhazmat.2020.122383.

[138] S. Azizian and S. Eris, "Adsorption isotherms and kinetics," in *Interface Science and Technology*, vol. 33, Elsevier, 2021, pp. 445–509. doi: 10.1016/B978-0-12-818805-7.00011-4.

[139] M. M. Sabzehmeidani, S. Mahnaee, M. Ghaedi, H. Heidari, and V. A. L. Roy, "Carbon based materials: a review of adsorbents for inorganic and organic compounds," *Mater. Adv.*, vol. 2, no. 2, pp. 598–627, 2021, doi: 10.1039/D0MA00087F.

[140] M. Náfrádi, G. Veréb, D. S. Firak, and T. Alapi, "Photocatalysis: Introduction, Mechanism, and Effective Parameters," in *Green Photocatalytic Semiconductors*, S.

Garg and A. Chandra, Eds., in Green Chemistry and Sustainable Technology. , Cham: Springer International Publishing, 2022, pp. 3–31. doi: 10.1007/978-3-030-77371-7_1.

[141] U. G. Akpan and B. H. Hameed, "Parameters affecting the photocatalytic degradation of dyes using TiO2-based photocatalysts: A review," *J. Hazard. Mater.*, vol. 170, no. 2–3, pp. 520–529, Oct. 2009, doi: 10.1016/j.jhazmat.2009.05.039.

[142] M. Nemiwal, T. C. Zhang, and D. Kumar, "Recent progress in g-C3N4, TiO2 and ZnO based photocatalysts for dye degradation: Strategies to improve photocatalytic activity," *Sci. Total Environ.*, vol. 767, p. 144896, May 2021, doi: 10.1016/j.scitotenv.2020.144896.

[143] M. Aslam, I. M. I. Ismail, N. Salah, S. Chandrasekaran, M. T. Qamar, and A. Hameed, "Evaluation of sunlight induced structural changes and their effect on the photocatalytic activity of V2O5 for the degradation of phenols," *J. Hazard. Mater.*, vol. 286, pp. 127–135, Apr. 2015, doi: 10.1016/j.jhazmat.2014.12.022.

[144] I. A. Mkhalid, A. A. Ismail, M. A. Hussein, and R. H. M. Al Thomali, "Visible-light-induced V2O5 -TiO2 photocatalysts with high photocatalytic ability for degradation of tetracycline," *Opt. Mater.*, vol. 135, p. 113263, Jan. 2023, doi: 10.1016/j.optmat.2022.113263.

[145] M. M. Khan, S. F. Adil, and A. Al-Mayouf, "Metal oxides as photocatalysts," *J. Saudi Chem. Soc.*, vol. 19, no. 5, pp. 462–464, Sept. 2015, doi: 10.1016/j.jscs.2015.04.003.

[146] Y. Wang, W. Yang, X. Chen, J. Wang, and Y. Zhu, "Photocatalytic activity enhancement of core-shell structure g-C3N4@TiO2 via controlled ultrathin g-C3N4 layer," *Appl. Catal. B Environ.*, vol. 220, pp. 337–347, Jan. 2018, doi: 10.1016/j.apcatb.2017.08.004.

[147] W.-K. Jo and T. S. Natarajan, "Influence of TiO2 morphology on the photocatalytic efficiency of direct Z-scheme g-C3N4/TiO2 photocatalysts for isoniazid degradation," *Chem. Eng. J.*, vol. 281, pp. 549–565, Dec. 2015, doi: 10.1016/j.cej.2015.06.120.

[148] Z. Sun, Z. Yu, Y. Liu, C. Shi, M. Zhu, and A. Wang, "Construction of 2D/2D BiVO4/g-C3N4 nanosheet heterostructures with improved photocatalytic activity," *J. Colloid Interface Sci.*, vol. 533, pp. 251–258, Jan. 2019, doi: 10.1016/j.jcis.2018.08.071.

[149] J. Pasquet, Y. Chevalier, J. Pelletier, E. Couval, D. Bouvier, and M.-A. Bolzinger, "The contribution of zinc ions to the antimicrobial activity of zinc oxide," *Colloids Surf. Physicochem. Eng. Asp.*, vol. 457, pp. 263–274, Sept. 2014, doi: 10.1016/j.colsurfa.2014.05.057.

[150] A. Yousef, M. M. El-Halwany, N. A. M. Barakat, M. N. Al-Maghrabi, and H. Y. Kim, "Cu0- doped TiO2 nanofibers as potential photocatalyst and antimicrobial agent," *J. Ind. Eng. Chem.*, vol. 26, pp. 251–258, June 2015, doi: 10.1016/j.jiec.2014.11.036.

[151] Y. Li, W. Zhang, J. Niu, and Y. Chen, "Mechanism of Photogenerated Reactive Oxygen Species and Correlation with the Antibacterial Properties of Engineered Metal-Oxide Nanoparticles," *ACS Nano*, vol. 6, no. 6, pp. 5164–5173, June 2012, doi: 10.1021/nn300934k.

[152] M. M. Khan, S. N. Matussin, and A. Rahman, "Recent development of metal oxides and chalcogenides as antimicrobial agents," *Bioprocess Biosyst. Eng.*, vol. 46, no. 9, pp. 1231–1249, Sept. 2023, doi: 10.1007/s00449-023-02878-1.

Chapter II

Synthesis And Characterization Techniques

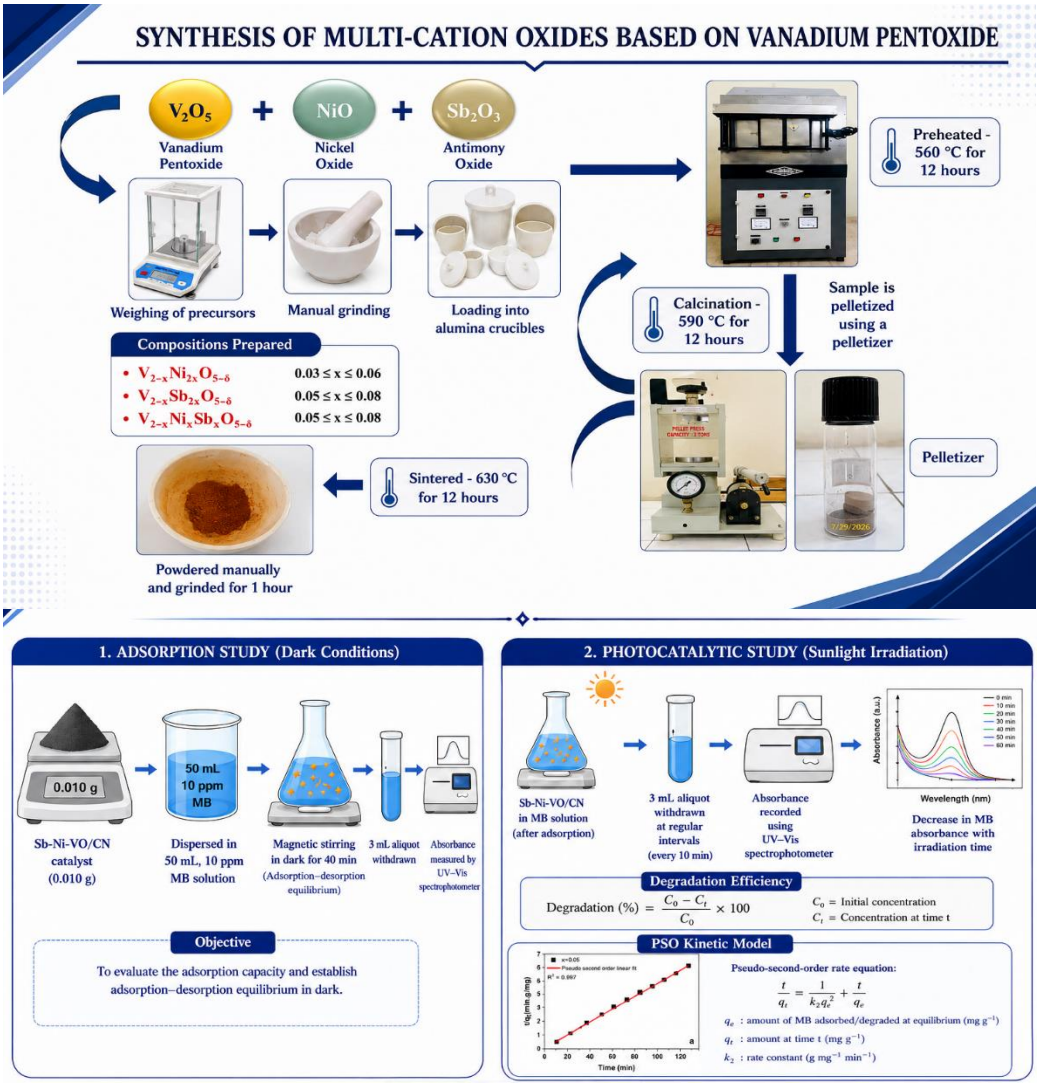

"The journey from precursor to functional material is guided by synthesis and understood through characterization; together they unlock the hidden potential of vanadium pentoxide-based complex oxides."

2.1 Introduction

Multi-cation metal oxide compounds have attracted significant interest in materials science due to their unique physical, electrochemical, and catalytic properties. These compounds, which have more than one metal cation in the oxide lattice, exhibit greater stability and adjustable electronic properties, and benefit from the interactions among the different cations. There are several ways to synthesize multi-cation metal oxides, each with its own pros and cons for composition, phase purity, and structural control. Of these methods, the high-temperature solid-state reaction is considered the most suitable

2.2. High Temperature Solid State Reaction Method

The high-temperature solid-state reaction method starts by selecting high-purity solid precursors (NiO, Sb_2O_3, and V_2O_5) in the correct ratios, then grinding them thoroughly to ensure uniform mixing. The mixture is pre-calcinated by heating at a moderate temperature (usually 300 to 500°C) to remove volatile parts and make it more reactive.

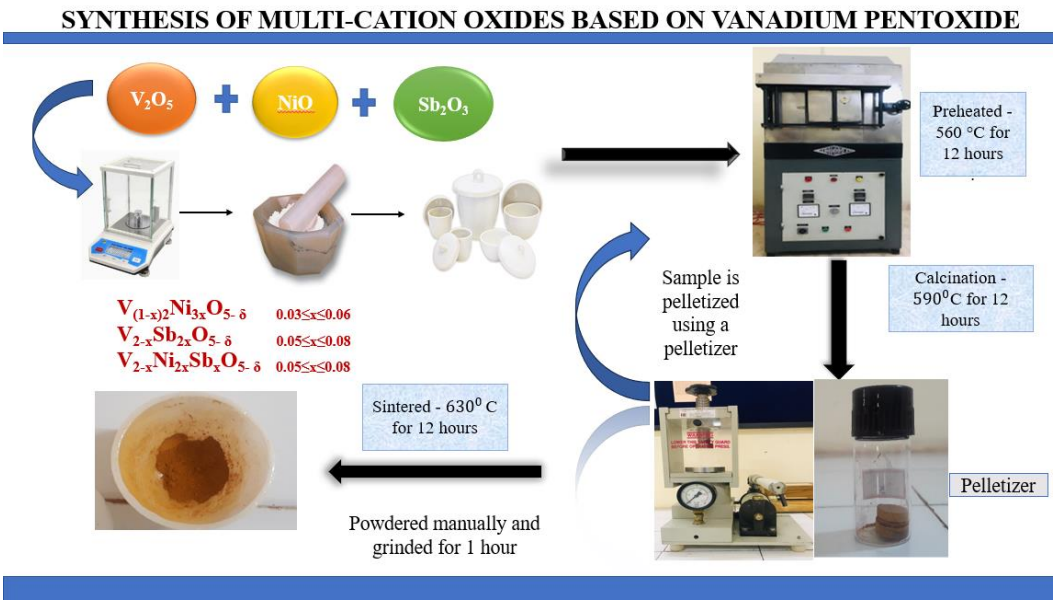

Figure 2.1: Flow chart of the high-temperature solid-state reaction method

After this step, the powder is ground again and calcined at a higher temperature (typically 500 to 700 °C) for several hours to help the materials react and mix fully

[83]. Additional grinding and heating cycles can be done to improve the purity and structure of the final product. The powders are pressed into 14 mm pellets and sintered at high temperature to improve pellet density and homogeneity. Finally, the product is cooled to room temperature, ground into a fine powder, and stored for later use or analysis[84]. The flow chart of high-temperature solid-state reaction is shown in figure (2.1).

2.3. Types of solid solutions

2.3.1. Substitutional solid solution

Substitutional solid solutions among the transition-metal oxides enable foreign cations such as Ni, Mn, Al, Li, Bi, and Sb to substitute for host metal ions within the lattice, occupying specific crystal sites while retaining a single-phase structure. Such dopants can occupy tetrahedral or octahedral sites in layered vanadium pentoxide frameworks, often triggering charge-compensation mechanisms that create cation/anion vacancies or alter adjacent cation valences. The structural and electronic perturbations from cation doping, including lattice distortions, defect formation, and valence-state adjustments, critically influence material behavior. For example, Ni^{2+} substitution for Mn^{3+} in a spinel-like $LiMn_2O_4$ raises the average Mn oxidation state by converting Mn^{3+} to Mn^{4+}, thereby suppressing Jahn–Teller distortion, stabilizing the structure, and enhancing battery cyclability [3]. In sum, cation doping in transition metal oxides tailors and optimizes the lattice and electronic structures, enabling the design of materials with enhanced catalytic activity, energy storage performance, sensor responsiveness, thermoelectric efficiency, and tunable magnetic/electronic functionalities.

2.3.2 Interstitial solid solutions

An interstitial solid solution in transition metal oxides is formed when small atoms or ions, such as hydrogen, lithium, or oxygen anions in excess, occupy the interstitial sites of the oxide lattice without swapping the primary metal or oxygen ions from their lattice positions. These interstitial cations and anions can significantly modify the oxide's structural, electronic, and ionic transport properties. For example, Ni interstitials in transition-metal oxides can alter electronic conductivity and induce

changes in valence states of cations, while interstitial oxygen in oxides such as TiO_{2-x} or WO_{3-x} contributes to non-stoichiometry and enhances carrier mobility [87]. The formation of such interstitial solid solutions is strongly governed by factors such as the size of the interstitial species relative to available lattice voids, defect chemistry, surface chemistry, and thermodynamic stability. Importantly, interstitial solid solutions find applications ranging from solid oxide fuel cells (SOFCs), hydrogen storage, and catalysis to electrochromic devices, where interstitially accommodated ions play a decisive role in determining functional performance.

2.3.3 Hume-Rothery rule for the selection of precursors in forming solid solutions

The Hume-Rothery rules are a set of well-defined rules used for the selection of precursors in solid solutions, checking if two elements will form a solid solution when mixed, either by one element substituting for the other in the crystal lattice (substitutional solid solution) or by occupying interstitial sites (interstitial solid solution) [4]. These rules, originally formulated by William Hume-Rothery, provide guidelines based on atomic size, crystal structure, electronegativity, and valence for achieving significant solubility in alloys. Below, we discuss the rules for both substitutional and interstitial solid solutions [87]**.**

a) **Atomic Size Similarity:** The atomic radii of the two species must be within about ±15% of each other. A small size mismatch minimizes lattice distortion. If the size difference exceeds ~15%, solubility will be limited because a large size mismatch induces significant lattice strain, making extensive substitution energetically unfavorable**.**

b) **Crystal Structure Compatibility:** The solvent and solute should share the same (or at least highly similar) crystal structure. For example, two face-centered cubic (FCC) metals or two body-centered cubic (BCC) metals can more likely form a substitutional solution than an FCC metal with a BCC metal. A common lattice framework allows the solute atoms to fit into the host lattice without creating a new phase. If the crystal structures differ, only limited solubility or formation of a separate phase, e.g., intermetallic compound tends to occur.

c) **Valency Factor**: Ideally, the two elements should have the same valence or at least not vastly different valencies. Metals with the same valency tend to be more soluble in each other. If other factors are favorable, complete solubility is often observed when the solvent and solute have identical valence. Additionally, a metal can typically dissolve another metal of higher valency more readily than one of lower valency. A significant difference in valence can limit solubility because it often drives the formation of electron-compensating compounds.

d) **Electronegativity Similarity:** The electronegativities of the two elements should be similar. When there is a large electronegativity difference, the elements tend to form intermetallic compounds or other ordered phases rather than a random solid solution. A small difference (close to zero) in electronegativity favors the formation of a disordered solid solution as neither element strongly attracts electrons from the other to form ionic like bonds.

2.4. Characterization Techniques and Studies

In this thesis, the various characterization techniques used to analyze and calculate the parameters and properties of V_2O_5-based multi-cation compounds and heterostructures are discussed.

2.4.1. X-Ray Diffraction and Bragg's Law

When X-rays interact with a crystalline solid, the periodic atomic arrangement causes constructive interference, resulting in scattered radiation in specific directions. Unlike individual atoms, which scatter X-rays weakly, the crystal lattice amplifies scattering in certain directions and cancels it in others, resulting in X-ray diffraction (XRD). The powder technique, used in X-ray diffractometers with monochromatic radiation, enhances experimental results, aiding in the determination of the structural properties of crystalline materials [8]. A simple yet powerful way to understand this scattering is through Bragg's Law, which considers the crystal as a set of parallel planes of atoms (fig. 2.2). There occurs constructive interference when the path difference between rays reflected from successive planes equals an integer multiple of the X-ray wavelength [90]

$$n\lambda=2d\sin\theta \quad (1)$$

Here, n is the order of reflection, λ is the wavelength of the incident X-rays, d is the interplanar spacing, and θ is the angle between the incident X-ray and the lattice plane.

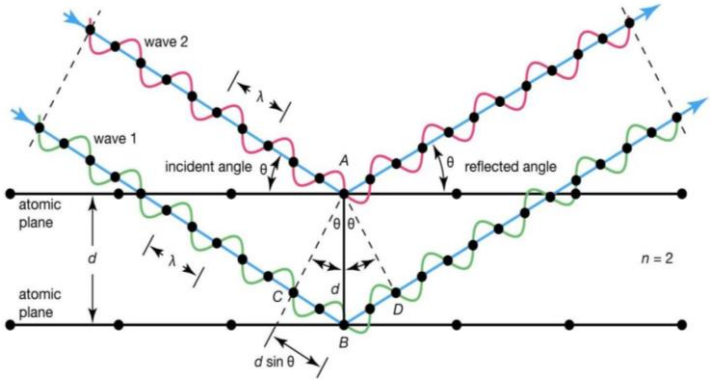

Figure 2.2: Schematic illustration of Bragg's diffraction. Incident X-rays reflect from successive atomic planes separated by a distance d.

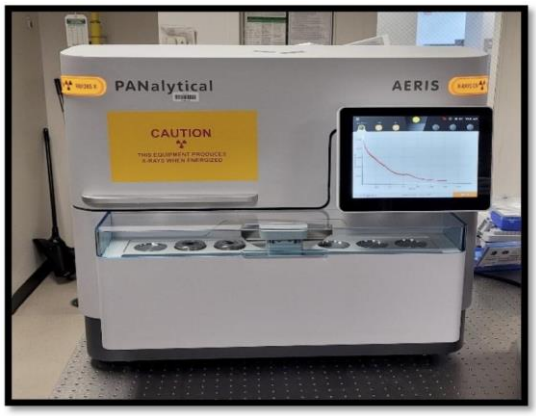

Figure 2.3: AERIS Panalytical X-ray Diffractogram Instrument

We analyzed the crystal structures of the prepared samples using X-ray diffraction (XRD) with Cu Kα radiation (λ = 1.541 Å). Measurements were taken over a 2θ range of 15 to 55 degrees using an *AERIS PANalytical* instrument. (fig. 2.3).

2.4.1.1. Structure Factor and Intensity of Diffracted Beams

Although Bragg's Law defines the angles at which diffraction peaks occur, the intensity of these peaks is governed by the structure factor F_{hkl} which depends on the arrangement and types of atoms in the unit cell [89]

$$F_{hkl} = \sum_{j=1}^{N} f_j \, exp[2\pi i(hxj + kyj + lzj)] \quad (2)$$

where:

- f_j is the atomic scattering factor of the j^{th} atom
- x_j, y_j, z_j are the fractional coordinates of that atom within the unit cell
- h,k,l are the miller indices of the corresponding diffracting plane and $I_{hkl} \propto |F_{hkl}|^2$

This means that even if Bragg's Law is satisfied, a reflection may be absent or weak if the structure factor approaches zero. Hence, both geometric and atomic considerations are essential in interpreting XRD patterns and determining crystal structures [91]. The line broadening value gives the measure of the average size of the crystallites by using the Scherrer formula [91],

$$\text{Grain Size} = K\lambda/\beta \cos\theta \quad (3)$$

Where D is the average particle size, λ is the wavelength of the radiation and **β** is the FWHM (full width at half maximum) of the reflection peak that has the same maximum intensity in the diffraction pattern (integral breadth of the peak located at angle θ). K is the Scherrer constant in the formula, which accounts for particle shape and is generally taken to be 0.9. The grain size obtained from the Scherrer equation gives the average particle size of a material [10].

2.4.1.2. Rietveld Refinement: Relevance and Quality Indicators

While X-ray diffraction provides qualitative insights into the phase composition and crystal structure of materials, it also yields quantitative, highly accurate structural information, such as lattice parameters, atomic positions, site occupancies, and microstructural features, which requires additional computational analysis. This is achieved through Rietveld refinement, a powerful technique that fits a calculated diffraction pattern to the experimentally observed pattern by minimizing the difference between them via least-squares optimization [94]. Hugo Rietveld developed the Rietveld refinement in 1969. This method models the diffraction profile rather than just individual peak positions, enabling more accurate analysis of crystalline materials, even in complex multiphase systems [95].

Key Objectives of Rietveld Refinement:

- Accurate determination of unit cell parameters
- Refinement of atomic positions**,** occupancies**,** and thermal factors
- Estimation of crystallite size and microstrain
- Quantitative phase analysis in multiphase mixtures

In practice, the calculated intensity I_{calc} at each point in the diffraction pattern is obtained from a structural model and compared with the observed intensity I_{obs}. The refinement process adjusts model parameters to minimize the residual through repeated calculations**,** usually the weighted sum of squared differences:

$$\text{Residual}=\sum w_i(I_{obs,i}-I_{calc,i})^2 \quad (4)$$

where w_i is a weighting factor for each data point.

- **Goodness of Fit and Quality Indicators**

In Rietveld refinement, several statistical parameters, known as R-factors and the goodness-of-fit indicator **(χ^2\chi^2)**, are used to assess the quality of the fit: [96]

1. **Profile R-factor (Rp)**

$$Rp = \frac{\sum \text{Iobs} - \text{Icalc}}{\sum \text{Iobs}} \times 100\% \quad (5)$$

Represents the absolute value of the difference between observed and calculated intensities. Lower values indicate a better fit.

2. Weighted Profile R-factor (R_{wp})

$$R_{wp} = \sqrt{\frac{\sum w_i (I_{i(obs)} - I_{i(calc)})^2}{\sum w_i I_{i(obs)}^2}} \text{ X } 100\% \quad (6)$$

Represents the statistical weight of each data point, offering a more reliable measure than R_p.

3. Expected R-factor (R_{exp})

$$R_{exp} = \frac{N-P+C}{\sum w_i I_{i(obs)}^2} \times 100\% \quad (7)$$

Where:

- N is the number of observations (data points),
- P is the number of parameters refined.
- Number of constraints applied during the refinement process

4. Goodness of Fit (GoF or χ^2\chi^2)

The chi-squared value is crucial for evaluating the quality of the refinement. A value of χ^2 equals 1 suggests a statistically good fit, and larger values may indicate issues such as low-quality background correction, problems in phase identification, or incorrect peak shape modelling function used for fitting the experimental data [96].

2.4.1.3. Rietveld Refinement Using Full Prof Suite

The FullProf Suite is a widely used software package for Rietveld refinement, suitable for both powder and neutron diffraction data. It offers good control over background modelling, peak shape functions like pseudo-Voigt, Thompson-Cox-Hastings, and allows simultaneous multiphase refinement in compounds having multiple phases [97].

During refinement using FullProf, attention must be given to [97]:

a) **Convergence criteria**: Minimal changes in parameters during consecutive iterations

b) **R-factor values**: Low Rp, Rwp, and a χ2 value close to 1.

c) **Difference plot**: The residual curve, that is observed – calculated, should be flat

Rietveld refinement, especially when using tools like FullProf Suite, plays a key role in modern materials science by helping researchers get detailed structural information from powder XRD data [98].

2.4.2. Raman Spectroscopy

Raman spectroscopy uses inelastic light scattering to analyze gases, liquids, and solids, whether amorphous or crystalline. This method can study very small samples, even under high temperatures or pressures. In a typical experiment, monochromatic light shines on the sample, and the resulting inelastic scattering creates a spectrum showing intensity versus wavenumber shift. Each peak in the spectrum corresponds to a specific vibrational mode, revealing details about bonding, strain, and molecular structure. This makes the spectrum a unique fingerprint for each material [99].

In a Raman experiment, a sample is exposed to monochromatic laser light, and the scattered light is measured with a spectrometer to detect intensity changes corresponding to the Raman spectral shift in cm^{-1}. Each peak in the Raman spectrum corresponds to a different vibrational phonon mode, and its position and intensity provide details about chemical bonds, molecular symmetry, and crystal structure. Whether a Raman-active mode appears depends on the molecular or crystal symmetry.

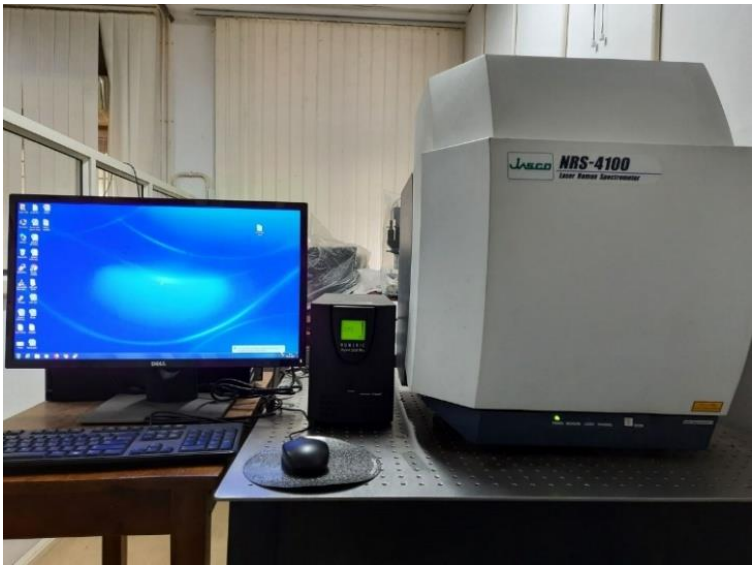

Figure 2.4: Image of JASCO NRS 4100 Raman Spectrometer used in the study

Some vibrational modes might not be detected if their signals are too weak or overlap with others. Raman spectroscopy is especially useful for studying solid

materials, identifying crystal phases, structural disorder, and small changes in bonding [99]. It works well in extreme conditions, requires little sample preparation, and complements X-ray diffraction by providing information on short-range order, defects, and local distortions. This makes it very useful for studying nanomaterials and complex systems [100]. For this study, Raman measurements were recorded using a JASCO-B005161822 micro spectrometer, with a laser power of 2.9 mW, an exposure time of 2 seconds, and an excitation wavelength of 540 nm as depicted in figure 2.4

2.4.3 Infrared Spectroscopy

Infrared (IR) spectroscopy is a powerful technique for identifying and studying chemical substances by analyzing how their molecules vibrate. When molecules absorb infrared light, their chemical bonds vibrate in specific ways, such as stretching, bending, or twisting. These vibrations are unique to certain bonds and functional groups, giving each compound its own molecular fingerprint [101]. The IR part of the electromagnetic spectrum ranges from about 4000 to 400 cm^{-1} and is divided into three sections: near-infrared (14000–4000 cm^{-1}), mid-infrared (4000–400 cm^{-1}), and far-infrared (400–10 cm^{-1}). Most IR spectroscopy uses the mid-IR region because it is best for detecting the main vibrations of molecular bonds [102]. In an IR spectrometer, IR light is shone on the sample under study. The molecules in the sample absorb light at certain frequencies that match their vibrations, and a detector measures the intensity of the light that passes through or is reflected from the sample. This process, as shown in the schematic diagram in figure 2.5, produces an IR spectrum. The spectrum shows transmittance or absorbance versus wavenumber, which helps identify the functional groups and bonding within the compound [102].

IR spectroscopy is especially useful for studying metal oxides and doped materials. It helps identify metal–oxygen bonds, hydroxyl groups, and other vibrations in the material's structure. Changes in peak positions or intensities can indicate structural changes due to doping or phase transitions. Because of this, IR spectroscopy is an important method for understanding the chemical structure, bonding, and composition of advanced materials [99]. FTIR studies were carried out using

IRAffinity-1S(A221353), Shimadzu spectrometer within the range, 500 to 4000 cm^{-1} (fig. 2.6)

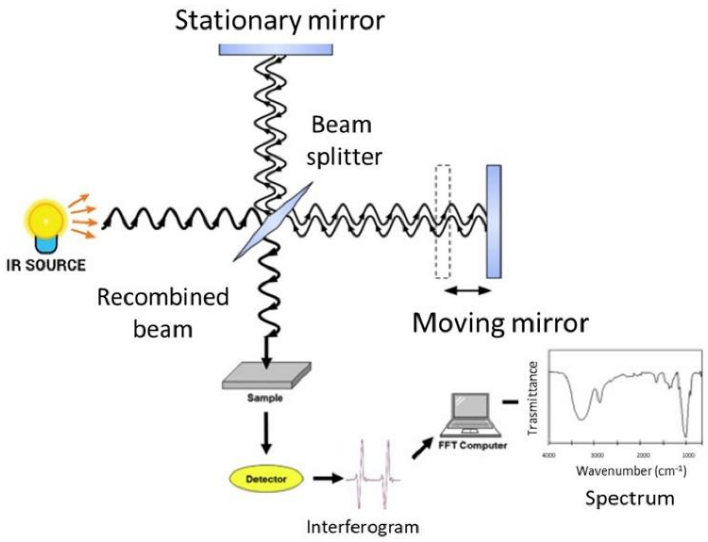

Figure 2.5. Schematic representation of an FTIR spectrometer[103]

Figure 2 6. IRAffinity-1S(A221353), Shimadzu spectrometer

2.4.4. X-Ray Photoelectron Spectroscopy

X-ray Photoelectron Spectroscopy is a technique used to study the surface science of materials. It helps to identify the elements and their surface chemical and electronic states. To obtain the XPS spectra, a material is shone with X-rays, and the photoelectron spectrometer instrument measures the energy and number of electrons emitted from the top 0 to 10 nanometers of the surface [104]. XPS works on the principle of the photoelectric effect. When X-rays fall on a material sample, they

knock out core-level electrons from its atoms. The spectrometer then measures the kinetic energy of these electrons. You can find the binding energy of the electron with this equation [99]:

$$BE = h\upsilon - KE - \phi \quad (8)$$

Where $h\upsilon$ is the energy of the photon of x-ray, and ϕ is the work function of the spectrometer. The binding energy is characteristic of a specific element and its chemical state.

Figure 2.7. Thermoscientific ESCALAB equipment equipped with Al Kα monochromator

By analyzing the binding energies and intensities of the photoelectron peaks, the elemental composition and chemical states of the sample can be determined [99]. XPS analysis was recorded with Thermo Scientific ESCALAB equipment using an *Al* Kαmonochromator (1486 A^0), as shown in figure 2.7. Survey scans were performed at a constant pass energy of 100 eV, and high-resolution measurements were performed at 20 eV. The schematic diagram of the X-ray Photoelectron Spectroscopy setup is shown in figure. 2.8 [104]. Casa XPS software was used to examine the XPS data, and mixed Lorentzian-Gaussian curves were employed to fit the data.

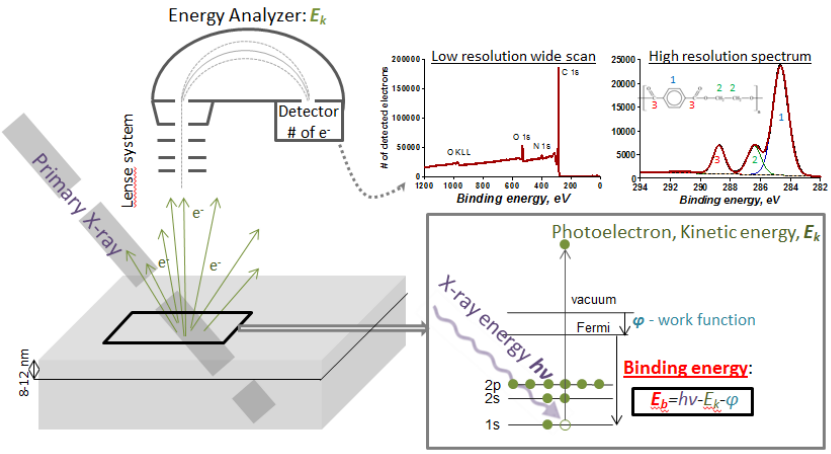

Figure 2 8: Schematic diagram of X-Ray Photoelectron Spectroscopy

Information Obtained from XPS

a) **Elemental Composition:** XPS can identify all elements present on the sample surface, except for hydrogen and helium.

b) **Chemical State Identification:** The chemical state of an element is identified by the binding energy of its core-level electrons. Slight variations in this energy, known as chemical shifts, reveal details about the element's oxidation state and bonding environment [105].

c) **Quantitative Analysis:** The photoelectron peaks' intensity is directly proportional to the concentration of the element in the sample. By quantifying the peak areas, the elemental composition of the sample can be easily identified [99].

d) **Depth Profiling:** By the variation of the analyzing angle, the depth-dependent sample's compositional variations within the sample could be identified. This method, known as angle-resolved XPS, is particularly effective for investigating thin films and layered materials [106].

2.4.5. Scanning Electron Microscopy and Energy Dispersive Spectra

The scanning electron microscopy imaging technique is widely used to study surface morphology and composition at high magnification. A focused electron beam is used to scan the sample surface, and the resulting interactions create detailed images

of the sample. SEM finds applications in all fields, including materials science, biology, and nanotechnology for analyzing materials.

Figure.2.9: Gemini SEM 300, Carl Zeiss, Scanning Electron Micrograph

When the electron beam reaches the sample surface, it produces secondary electrons, backscattered electrons, and X-rays. Secondary electrons originate at the surface and reveal the topography of materials. Backscattered electrons depend on the sample's atomic number. X-rays are produced when the beam removes core electrons, which helps to identify the elements. In this study, surface morphology was examined using a Gemini SEM 300 (Carl Zeiss), and chemical composition was measured with energy dispersive spectra (VEGA-TESCAN analyzer) at a 30-KeV accelerating potential (Fig.2.9). Figure 2.10 shows the SEM schematic diagram [107].

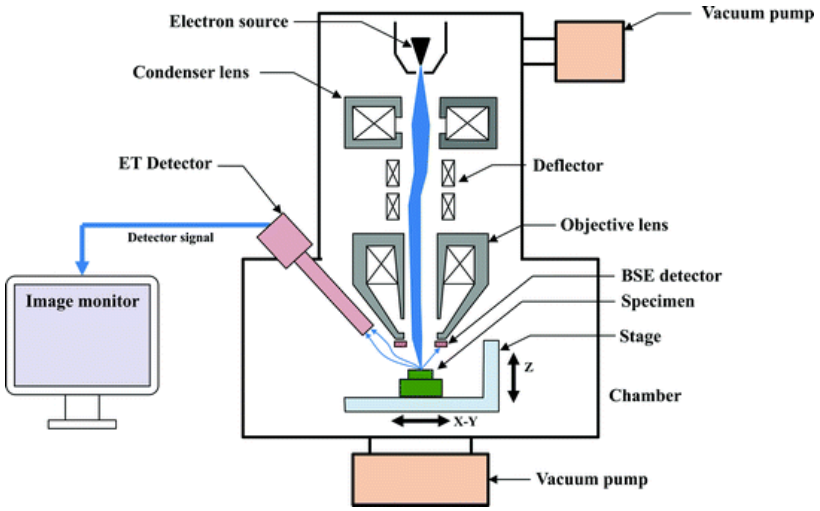

Figure. 2.10: Schematic Diagram of Scanning Electron Microscopy[107]

Signals and Image Formation

a) **Secondary Electron Imaging:** SE imaging is the most common mode of image formation using SEM. SEs provide high-resolution images of the sample's surface topography. Variations in the number of secondary electrons emitted from different areas of the sample create contrast in the image, revealing details about the surface features [108].

b) **Backscattered Electron Imaging:** BSE imaging shows what elements are in a sample. Areas with heavier elements look brighter because they produce more backscattered electrons, while regions with lighter elements look darker [109].

c) **Energy-Dispersive X-ray Spectroscopy:** Besides imaging, SEM can work with EDS to analyze elements. EDS finds X-rays coming from the sample and identifies the elements by their unique X-ray energies [109].

Figure 2.11 represents the Schematic Diagram of Energy Dispersive X-ray Spectroscopy [109].

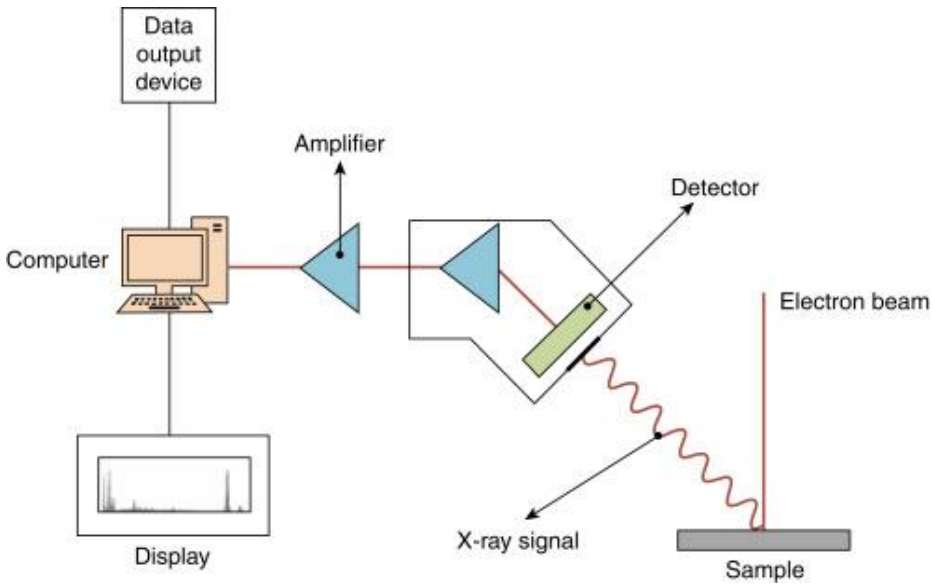

Figure 2.11: Schematic Diagram of Energy Dispersive X-ray Spectroscopy

Information Obtained from EDS

a) **Qualitative Analysis:** An EDS spectrum usually appears as a graph showing X-ray intensity against energy. The peaks on this graph match the energies of the characteristic X-rays given off by the elements in the sample. By finding where these peaks are, you can tell which elements are present [99].

b) **Quantitative Analysis:** The strength of each X-ray peak matches the amount of that element in the sample. Measuring the peak areas lets us figure out what elements are present. For accurate results, it is important to consider matrix effects like absorption and secondary excitation [111].

c) **Elemental Mapping:** EDS can create elemental maps that show where different elements are found in a sample. To do this, the electron beam scans over the sample's surface, and an X-ray spectrum is recorded at each spot. The intensity of X-rays for each element is then used to build a map showing how that element is spread across the sample [111].

2.4.6. UV Visible Spectroscopy

UV-Visible spectroscopy is a common technique in chemistry and materials science for studying how materials absorb and transmit light in the ultraviolet and visible parts of the spectrum. This method provides important details about a material's electronic structure and is useful for both qualitative and quantitative analysis. In this technique, UV or visible light is passed through a sample under investigation, and the absorption at different wavelengths is measured from the device. When electrons are excited from the ground state to higher energy levels, they absorb photons with energy equal to the energy difference between the ground and excited states. The main parameters measured are absorbance (A), transmittance (T), and reflectance (R) [101]. In the samples under present investigations optical reflectance or absorbance was measured from 200 to 700 nm using a Perkin Elmer Lambda 365 UV-Vis spectrophotometer (fig. 2.12). Figure 2.13 shows the schematic diagram of the UV-Visible spectrometer [99].

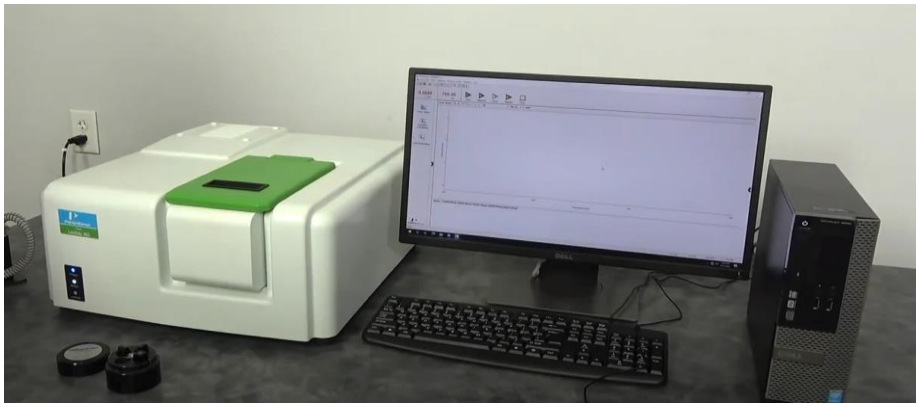

Figure 2.12: Perkin Elmer Lambda 365 UV-Vis spectrophotometer

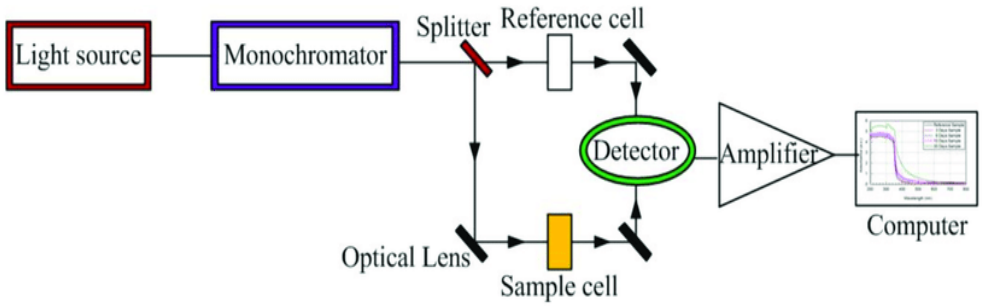

Figure 2.13: Schematic diagram of the experimental setup of UV-Visible Spectroscopy [99].

Information Obtained from UV-Vis Spectroscopy

- **Qualitative Analysis:** UV-Vis spectra help identify certain compounds by showing their unique absorption patterns. The position and strength of these absorption bands depend on the molecule's electronic structure [112].
- **Quantitative Analysis:** The Beer-Lambert law explains that a solution's absorbance increases with both the amount of the substance present and the distance the light travels through it. This makes it useful for finding out how much of a substance is in a sample [113].
- **Band Gap Determination:** UV-Vis spectroscopy helps measure the optical band gap in solid-state materials. This band gap is the smallest amount of energy needed to move an electron from the valence band to the conduction band [114].

a) Tauc Plot Method

The Tauc plot method is a widely used technique to estimate the optical band gap of semiconductors from their UV-Visible absorption spectra. It is based on the Tauc relation, which describes the dependence of the absorption coefficient (α) on the photon energy (hν) [115]:

$$(\alpha h\nu)^n = A(h\nu - Eg) \quad (9)$$

Where: α is the absorption coefficient, hν is the photon energy, A is a proportionality constant, Eg is the optical band gap, n depends on the nature of the electronic transition:

- n=1/2 for direct allowed transitions,
- n=2 for indirect allowed transitions.

To determine the band gap:

1. Calculate the absorption coefficient from the absorbance data.
2. Plot $(\alpha h\nu)^n$ versus hν.
3. Extrapolate the linear portion of the plot to intersect the energy axis, and the intercept corresponds to the band gap energy, Eg.

b) Kubelka-Munk Plot Method

The Kubelka-Munk (K-M) function is particularly useful for determining the band gap of powdered or highly scattering materials using diffuse reflectance spectra (DRS). It transforms the reflectance data into an equivalent absorption spectrum using the Kubelka-Munk function [115]:

$$F(R) = \frac{(1-R)^2}{2R} \quad (10)$$

Where R is the reflectance of the sample and F(R) is proportional to the absorption coefficient α for sufficiently thick samples.

To determine the band gap:

1. Measure the diffuse reflectance (R) using a UV-Vis spectrophotometer equipped with an integrating sphere.

2. Convert the reflectance data into F(R).

3. Apply the Tauc relation by replacing α with F(R): $[F(R)\cdot h\nu]^n = A(h\nu - Eg)$

4. Plot $[F(R)\cdot h\nu]^n$ versus hν, and extrapolate the linear region to the x-axis to obtain Eg.

2.4.7 Photoluminescence Spectroscopy

Photoluminescence spectroscopy is a non-destructive, contactless method for investigating the electronic structure and properties of materials by analyzing the light emitted after a material absorbs photons. It is based on the phenomenon where a material absorbs light (or other electromagnetic radiation) and then re-emits light [116]. Photoluminescence analysis was conducted using an FP-8300 JASCO spectrofluorometer with an excitation wavelength of 330 nm (fig. 2.14).

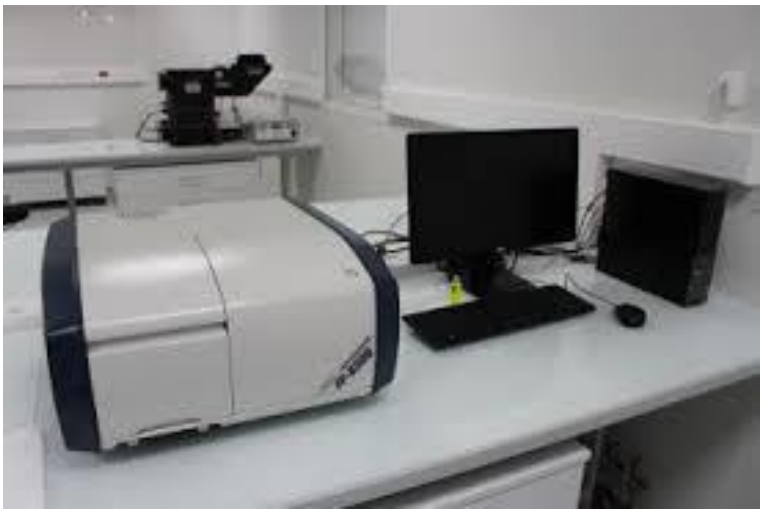

Figure 2.14: FP-8300 JASCO spectrofluorometer with an excitation wavelength of 330 nm used for PL measurements.

In photoluminescence (PL) spectroscopy, a sample is excited with monochromatic light, elevating electrons to higher energy levels. As the electrons

return to lower states, they emit photons. The emitted light is analyzed by a spectrometer to determine its intensity and wavelength, revealing the material's electronic and defect characteristics. Figure 2.15 shows the schematic diagram of PL spectrophotometer [117].

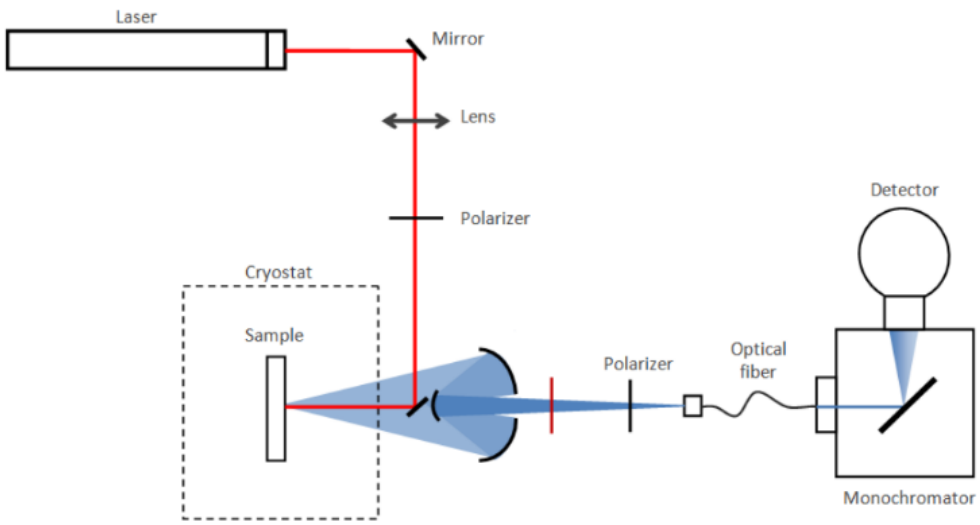

Figure 2.15: Schematic diagram of Photoluminescence Spectroscopy[117]

Information Obtained from PL Spectroscopy

a) **Energy Levels and Band Gaps:** The wavelengths (or energies) of the emitted photons provide information about the energy levels within the material. In semiconductors, PL spectroscopy can be used to determine the band gap energy, which is a crucial parameter for characterizing their electronic properties [118].

b) **Defect and Impurity Identification:** PL spectra often reveal the presence of defects and foreign particles within a material. These imperfections can restructure the energy levels within the band gap, leading to additional emission peaks at specific wavelengths. By analyzing these peaks, one can identify the types and concentrations of defects present [119].

c) **Material Quality Assessment:** The intensity and shape of the PL peaks are sensitive to the quality and purity of the material. A high-quality material with

few defects will typically exhibit a strong, narrow PL peak, while a defective material will show weaker and broader peaks [119].

d) **Surface Properties:** PL is sensitive to surface properties and can be enhanced or modified by surface treatments.

2.4.8. BET Surface Area Measurements

2.4.8.1. Principle of BET Method

The Brunauer–Emmett–Teller (BET) theory is an important method in surface science for measuring the specific surface area of porous and finely divided solids by gas adsorption, usually with nitrogen at 77 K [120]. Unlike Langmuir's model, which considers only a single layer, BET accounts for multilayer adsorption, making it a more realistic model for describing gas adsorption on surfaces. The theory assumes the first layer of adsorbate attaches with the heat of adsorption, while the next layers form with the heat of liquefaction. This approach accounts for the fact that surfaces are not uniform and have different types of sites. In practice, a degassed sample is exposed to different pressures of an inert gas, and the amount adsorbed is measured as the relative pressure (P/P_0) changes [121]. Since this method avoids chemical interactions, it provides accurate surface area measurements, which are important for studies in catalysis and adsorption [122].

The BET equation is given as[122].:

$$\frac{1}{v\left(\frac{P_0}{P}-1\right)} = \frac{c-1}{v_m c} * \frac{P}{P_0} + \frac{1}{v_m c} \qquad (11)$$

Where v is the volume of gas at equilibrium pressure P, vm is the monolayer adsorbed gas volume, P_0 is the saturation pressure of adsorbate gas at 77K, and c is the BET constant related to the heat of adsorption.

2.4.8.2. Surface Area Calculation

The specific surface area (S-BET) is calculated from the monolayer capacity using the following formula [41]

$$S_{BET} = \frac{v_m N_A A}{V_m * m} \quad (12)$$

Where, S_{BET} = surface area (m^2/g), v_m = monolayer volume of gas adsorbed (cm^3 STP/g), N_A = Avogadro's number (6.022×10^{23} mol^{-1}), A = cross-sectional area of a N_2 molecule (~0.162 nm^2), V_m = molar volume of gas at STP (~22414 cm^3/mol), m = mass of the adsorbent (g).

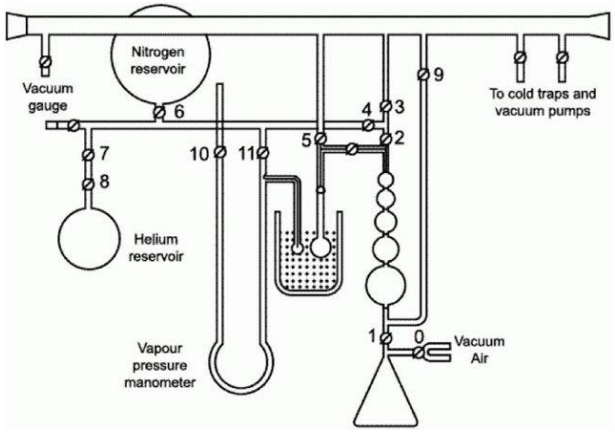

Figure 2.16: Schematic Diagram of BET Surface Area Measurement Instrument

Figure 2.17: BET surface area, pore volume, pore diameter analyzer: BELSORP-MAX instrument.

A typical BET surface area analyzer includes a degassing unit to remove moisture and pre-adsorbed gases, and a sample holder suitable for powders or pellets. A liquid nitrogen bath maintains the standard 77 K measurement temperature, while vacuum and pressure transducers regulate gas flow. The gas inlet system introduces high-purity nitrogen as the adsorbate. Advanced instruments, such as the Micromeritics ASAP 2020, Quantachrome Autosorb, or BELSORP-max, integrate

automated software to record adsorption isotherms and compute BET parameters, pore volume, and pore size distribution efficiently(fig. 2.17) [125]. Figure 2.16 presents a schematic diagram of the BET surface area measurement instrument [125].

2.4.8.3 N_2 Adsorption–Desorption Isotherms

The adsorption–desorption isotherm is a graphical representation of the amount of gas adsorbed (v) as a function of relative pressure (P/P_0). The IUPAC classifies isotherms into six types [126]:

Type I	:	Microporous solids (high affinity at low P/P_0).
Type II	:	Non-porous or macroporous solids (monolayer multilayer adsorption).
Type III	:	Weak adsorbent–adsorbate interactions (no point of inflection).
Type IV	:	Mesoporous solids (capillary condensation).
Type V	:	Weak interaction + mesopores (with hysteresis).
Type VI	:	Stepwise multilayer adsorption (uniform non-porous surfaces).

Hysteresis loops in Types IV and V indicate mesoporous structures and can provide information about pore shape and adsorption mechanisms [127].

2.4.8.4. Applications

BET analysis is widely used to [46] :

a) Quantify surface area of nanomaterials**,** adsorbents**,** catalysts**,** and electrode materials**.**

b) Analyze pore filling mechanisms.

c) Assess adsorption capacity and photocatalytic performance**.**

d) Evaluate changes in porosity and surface area due to doping**,** calcination**,** or composite formation.

In this study, the BET surface area of multi-cation-doped V_2O_5 was measured to correlate porosity and surface area with enhanced photocatalytic efficiency.

2.5. Application Studies

2.5.1. AC Conductivity and Dielectric Studies

2.5.1.1. Principles of AC Conductivity and Dielectric Studies

AC conductivity and dielectric studies reveal how materials behave electrically, which is important for devices such as capacitors, sensors, and batteries. These studies explain how charge moves, how energy is stored, and how it is lost when an alternating current is applied. AC conductivity tells us how well a material carries an alternating current, which depends on the current's frequency and the material's properties, such as conductivity, permittivity, and temperature. This is especially important for materials used in energy storage, semiconductors, and conductive polymers [130]. Dielectric studies examine how a material reacts to an electric field and how well it stores energy. Dielectrics are insulators that become polarized in an electric field. These studies provide information about a material's dielectric constant, loss tangent, and relaxation times, which are important for making capacitors, insulators, and other electronic parts.

2.5.1.2 Dielectric Properties

Capacitance (C) is the basic property that describes the ability of a material to store electrical energy in the presence of an electric field. The capacitance of a parallel plate capacitor is given by the equation [130],

$$C = \frac{\varepsilon_0 \varepsilon_r A}{d} \tag{13}$$

Here, ε_0 is the permittivity of free space (8.85×10^{-12} F/m), ε_r is the relative permittivity, A is the area of the plates (in m^2), and d is the distance between the plates (in meters). Capacitance goes up when the dielectric constant ε_r of the material increases. Materials with higher dielectric constants can store more energy per unit volume. Dielectric constant (ε_r) is a measure of the material's ability to store

electrical energy relative to a vacuum. It is given by the ratio of the material's capacitance (C) to the capacitance of a vacuum(C_0) [131]:

$$\varepsilon_r = \frac{C}{C_0} \tag{14}$$

where C_0 is the capacitance of a vacuum, which is typically 8.854 x 10^{-12} F/m. Dielectric loss (tan δ) measures the energy dissipated as heat in the dielectric material. The loss tangent is the ratio of the imaginary part of the permittivity (ε") to the real part (ε'):

$$\tan\delta = \frac{\varepsilon''}{\varepsilon'} \tag{15}$$

where ε' is the real part (dielectric constant) and ε" is the imaginary part (dielectric loss) of the complex permittivity. A higher value of tan δ indicates a material with more loss and lower efficiency in energy storage.

2.5.1.3. Impedance and Electric Modulus

Impedance (Z) is a complex quantity that describes the total opposition to current flow in a material. It is given by [132]:

$$Z = R + jX \tag{16}$$

where, R is the resistance, and X is the reactance (which can be inductive or capacitive). j is the imaginary unit ($j^2 = -1$). The impedance is frequency-dependent and provides valuable information about the charge transport and relaxation processes in the material. Electric Modulus (M) is the reciprocal of the complex permittivity and is particularly useful for describing materials with non-Debye-type relaxation behavior. It is defined as:

$$M^*(\omega) = 1 / \varepsilon^*(\omega) \tag{17}$$

where ε*(ω) is the complex permittivity of the material, which can be expressed as:

$$\varepsilon^*(\omega) = \varepsilon'(\omega) - j\varepsilon''(\omega) \tag{18}$$

The modulus provides a more direct way of analyzing the material's response in cases of complex dielectric relaxation and charge transport phenomena.

2.5.1.4 AC Conductivity

AC conductivity (σ_{ac}) represents a material's ability to conduct an alternating current, which varies with frequency. It is related to the impedance of the material and is given by [133]:

$$\sigma_{ac} = (\omega * \varepsilon_0 * \varepsilon_r) / Z \quad (19)$$

where, ω is ($2\pi f$) is the angular frequency, ε_0 is the permittivity of free space, ε_r is the relative permittivity of the material, Z is the impedance. The conductivity increases with frequency in many materials, reflecting the frequency-dependent behavior of charge carriers.

2.5.1.5. LCR Meter

An LCR meter measures the inductance (L), capacitance (C), and resistance (R) of a material. It works by applying a small AC signal to the material under test and measuring the resulting response. The meter measures the sample's impedance and determines its dielectric properties. The LCR meter can measure the real and imaginary components of the impedance and, in turn, the dielectric constant, loss tangent, and other material properties [134].

Figure 2.18: Agilent 4294A Precision Impedance Analyzer for the AC conductivity nd dielectric studies of pellet samples

LCR meters are widely used in dielectric studies because they provide high-precision measurements of capacitance and resistance across a range of frequencies. The instrument typically provides data that can be used to calculate the frequency-dependent behavior of the dielectric constant and loss [134]. AC conductivity and

dielectric studies of the prepared pellets were also carried out using an Agilent 4294A Precision Impedance Analyzer at room temperature, with measurements taken over a frequency range from 10 Hz to 10 MHz (fig. 2.18).

2.5.1.6. Impedance Spectroscopy

Impedance Spectroscopy is a spectroscopic technique in which an AC voltage is applied to a material, and the resulting current is measured to determine the impedance at various frequencies. By looking at a wide range of frequencies, this technique helps us understand how a material responds electrically. It is especially helpful for studying complex materials, since their behavior is not just resistive or capacitive but can also involve relaxation, charge movement, and diffusion. Impedance spectroscopy enables separating the effects within the material from those at its surface, making it useful for studying ionic and electronic conductors, semiconductors, and dielectrics. By analyzing how impedance changes with frequency, we can determine properties such as relaxation times and conductivity [134].

2.5.2. Adsorption Studies

Adsorption is a basic physicochemical process in which atoms, ions, or molecules from a liquid or gaseous phase adhere to the surface of a solid, called the adsorbent [135-136]. Unlike absorption, which involves a substance spreading throughout the material, adsorption occurs only on the surface and is therefore a surface phenomenon. Features such as porosity, surface area, surface energy, pore volume and temperature are important for the efficiency of adsorption [137]. Recently, adsorption has become more popular because it is simple, affordable, and effective in many areas, including environmental remediation, catalysis, and sensor technology. It is commonly used to remove pollutants such as heavy metals, dyes, and organic contaminants from wastewater, as well as for gas separation, purification, and storage.

Several factors influence adsorption mechanisms, including the interaction between the adsorbent and adsorbate at the interface, pH, temperature, contact time,

and the initial concentration of the adsorbent. Researchers use models like Langmuir, Freundlich, Temkin, and Dubinin–Radushkevich to study equilibrium behavior [138]. Carbon-based materials such as activated carbon, graphene, nanotubes, and biochar are becoming popular adsorbents because they have large surface areas, well-defined pores, and strong stability. Looking ahead, scientists are focusing on adding metal oxides, polymers, or biomolecules to these materials and combining them with systems like membrane filtration and photocatalysis. These approaches aim to develop eco-friendly, reusable, and scalable solutions for wastewater treatment [139].

2.5.2.1. Adsorption Isotherm Equations with Explanation

2.5.2.1.1. Langmuir Isotherm

Assumptions:

- Adsorption occurs at specific homogeneous sites on the adsorbent surface.
- Once a site is occupied, no further adsorption can occur at that site (monolayer coverage).
- No interaction between adsorbed molecules [137].

$$q_e = \frac{q_{max} K_L C_e}{1 + K_L C_e} \tag{20}$$

Explanation of Terms:

q_e – Amount adsorbed at equilibrium (mg/g)

q_{max} – Maximum monolayer adsorption capacity (mg/g)

K_L – Langmuir constant related to binding affinity (L/mg)

C_e – Equilibrium concentration (mg/L)

2.5.2.1.2. Freundlich Isotherm

Assumptions:

- Empirical model for heterogeneous surfaces.
- Surface sites have different affinities (heterogeneous energy distribution).
- Suitable for multilayer adsorption [139].

Equation:

$$q_e = K_F C_e^{1/n} \quad (21)$$

Explanation of Terms:

q_e – Amount adsorbed at equilibrium (mg/g)

C_e – Equilibrium concentration (mg/L)

K_F – Freundlich constant indicative of adsorption capacity

1/n – Heterogeneity factor; adsorption intensity

2.5.2.1.3. Temkin Isotherm

Assumptions

- Heat of adsorption of all molecules in the layer decreases linearly with coverage due to adsorbent–adsorbate interactions.
- Valid for moderate ranges of adsorption concentrations [139].

Equation:

$$q_e = \left(\frac{RT}{b}\right) \ln(K_T C_e) \quad (22)$$

Explanation of Terms:

q_e – Amount adsorbed at equilibrium (mg/g)

R – Universal gas constant (8.314 J/mol·K)

T – Temperature in Kelvin (K)

b – Related to heat of adsorption (J/mol)

K_T – Temkin isotherm constant (L/g),

C_e – Equilibrium concentration (mg/L)

2.5.2.1.4. Dubinin–Radushkevich (D–R) Isotherm

Assumptions:

- Useful to distinguish between physical and chemical adsorption.
- Does not assume a homogeneous surface or constant adsorption potential [139].

Equation

$$q_e = q_s \exp(-B\varepsilon^2)\, where, \varepsilon = RTln(1 + \frac{1}{C_e}) \quad (23)$$

Explanation of Terms:

q_e – Amount adsorbed at equilibrium (mg/g)

qs – Theoretical saturation capacity (mg/g)

B – Constant related to adsorption energy (mol²/kJ²)

ε – Polanyi potential

R – Universal gas constant

T – Temperature in Kelvin

C_e – Equilibrium concentration (mg/L)

Mean Free Energy of Adsorption (E):

$$E = \frac{1}{\sqrt[2]{2B}} \quad (23)$$

- If E<8 kJ/mol, the adsorption is physisorption.
- If E>8 kJ/mol, the adsorption is chemisorption.

In the context of V_2O_7 based adsorbents, studies have shown good agreement with both Langmuir and Freundlich models, indicating the coexistence of mono and multilayer adsorption phenomena, depending on surface morphology and functionalization.

2.5.2.2. Adsorption Kinetic Models

Understanding the kinetics of adsorption is essential to decipher the mechanism and rate-limiting steps of the process, whether they involve film diffusion, pore diffusion, or surface chemical interactions. Kinetic models are mathematical tools used to interpret experimental adsorption data and evaluate the rate at which

adsorbate molecules are removed from a solution by the adsorbent. The following are the most commonly applied adsorption kinetic models in research involving metal oxides and doped vanadium pentoxide systems [137].

2.5.2.2.1. Pseudo-First-Order Kinetic Model

Proposed by Lagergren in 1898, this model assumes that the rate of occupation of adsorption sites is proportional to the number of unoccupied sites. It is often applied to the initial stages of adsorption where the driving force is the concentration gradient [138].

Equation:

$$\ln(q_e - q_t) = \ln(q_e) - k_1 * t \quad (24)$$

Explanation of Terms:

q_e – Amount of adsorbate adsorbed at equilibrium (mg/g)

q_t – Amount of adsorbate adsorbed at time t (mg/g)

k_1 – Rate constant of pseudo-first-order adsorption (1/min)

t – Contact time (min)

Limitations: This model often fails to accurately predict behavior throughout the adsorption process, especially at longer time scales and for chemisorption systems.

2.5.2.2.2. Pseudo-Second-Order Kinetic Model

This model assumes that adsorption follows second-order kinetics based on the assumption that chemisorption is the rate-controlling step, involving valence forces through electron sharing or exchange between adsorbent and adsorbate [139]

Equation:

$$\frac{t}{q_t} = \frac{1}{k_2 q_e^2} + \frac{t}{q_e} \quad (25)$$

Explanation of Terms:

q_e – Amount of adsorbate adsorbed at equilibrium (mg/g)

q_t – Amount of adsorbate adsorbed at time t (mg/g)

k_2 – Rate constant of pseudo-second-order adsorption (g/mg·min)

t – Contact time (min)

Advantages: It provides a better fit for chemisorption processes and is widely accepted in describing the adsorption of dyes and heavy metals by metal oxides.

2.5.2.2.3. Intra-Particle Diffusion Model

This model evaluates the influence of intra-particle diffusion on the overall adsorption rate. And explains the role of pore diffusion as a rate-limiting step. Adsorption is not necessarily limited to a single phase; solute molecules can diffuse into the internal structure of the adsorbent. If the plot of q_t versus $t^{0.5}$ is linear and passes through the origin, intra-particle diffusion is the sole rate-limiting step. If not, multiple mechanisms are involved [138].

Equation

$$q_t = k_i t^{0.5} + C \quad (26)$$

Explanation of Terms:

q_t – Amount of adsorbate adsorbed at time t (mg/g)

k_i – Intra-particle diffusion rate constant (mg/g·$min^{0.5}$)

t – Contact time (min)

C – Intercept related to boundary layer thickness

2.5.2.2.4. Elovich Kinetic Model

The Elovich equation is helpful in describing adsorption on highly heterogeneous surfaces. It assumes that the adsorption sites increase exponentially

with adsorption, leading to a decrease in the adsorption rate over time. This model is applicable when chemisorption is the dominant process and is often observed in systems involving activated carbon, metal oxides, or hybrid materials [139].

$$q_t = \frac{1}{\beta}\ln(\alpha\beta) + \frac{1}{\beta}\ln(t) \quad (27)$$

Explanation of Terms:

q_t – Amount of adsorbate adsorbed at time t (mg/g)

α – Initial adsorption rate (mg/g·min)

β – Desorption constant related to surface coverage (g/mg)

t – Contact time (min)

2.5.3. Photocatalytic Studies

Photocatalysis is a catalytic process that uses light to speed up chemical reactions, leading to decomposition, and is important for cleaning the environment and converting solar energy. Photocatalyst materials absorb light and create electron-hole pairs, which help break down pollutants and produce clean fuels. Many industrial wastewaters, especially from textile, leather, and paper factories, contain organic dyes that are difficult to remove and can harm the environment and health. Dyes such as methylene blue (MB), rhodamine B (RhB), and methyl orange (MO) do not readily break down due to their complex structures. As a result, they stay in water for a long time, blocking light, slowing photosynthesis, and harming aquatic life, causing an acute danger to living organisms [140].

Photocatalysis is thus an advanced oxidation process (AOP), offering an eco-friendly and sustainable method for degrading organic dyes into harmless end products such as Carbon di oxide water. Metal oxides such as TiO_2 [141], ZnO [142], and V_2O_5 [66] have been widely studied for this application due to their photochemical stability, low cost, and non-toxic nature. However, their large bandgap energies and high electron-hole recombination rates limit their photocatalytic efficiencies under visible light. To overcome these limitations, the formation of heterojunctions with polymeric semiconductors has been proposed [143-145].

Graphitic carbon nitride (g-C_3N_4), a polymeric semiconductor with a narrow bandgap (~2.7 eV), has emerged as a promising candidate for visible-light-driven photocatalysis. Because of its layered structure and the positions of its conduction and valence bands, this material is well-suited for making heterostructures with metal oxides. Creating these heterojunctions helps separate charges and increases light absorption, which boosts photocatalytic activity. Systems such as TiO_2/g-C_3N_4 [142], ZnO/g-C_3N_4 [146], and $BiVO_4$/g-C_3N_4 [76] have demonstrated improved performance in degrading dyes, drugs, and other toxic substances under visible light. When a photocatalyst absorbs photons with energy equal to or greater than its bandgap, electrons in the valence band move to the conduction band, leaving holes in the valence band. This process can be summarized as: Excited-photocatalyst + hυ = e− (CB) + h+ (VB). These charge carriers then participate in surface redox reactions whereby electrons reduce molecular oxygen: and holes oxidize water or hydroxide ions. Photocatalysts can be classified into several categories based on their chemical composition, dimensionality, bandgap energy, and heterostructure configuration. Main categories of photocatalysts are Type I, Type II, Z scheme, S-scheme etc

2.5.4. Antimicrobial Studies of Metal Oxides

Metal Oxides as Antimicrobial Agents: Metal oxides, such as ZnO, TiO_2, CuO, and Ag_2O, have attracted attention as potential antimicrobial agents due to their intrinsic properties. These materials exhibit a wide range of antimicrobial activities against both bacteria and fungi, with some also demonstrating antiviral effects. The antimicrobial action of metal oxides is attributed to several mechanisms that can be influenced by factors such as particle size, morphology, surface charge, redox potential, electronic heterogeneity, and the rate of electron-hole recombination [149], [150].

1. **Generation of Reactive Oxygen Species (ROS):** The mechanisms by which metal oxides exert antimicrobial activity is the generation of reactive oxygen species (ROS), such as hydroxyl radicals (•OH), superoxide anion ($O_2•^-$), and hydrogen peroxide (H_2O_2). These ROS can damage bacterial cell components, including the cell membrane, DNA, and proteins, leading to cell death. ROS

are generated when metal oxide particles are exposed to light, remarkably UV light, or when they come into contact with moisture or biological fluids [151].

2. **Membrane Damage and Disruption:** Metal oxide particles can interact directly with microbial cell membranes, causing mechanical damage. Positively charged metal ions, such as Zn^{2+} or Cu^{2+}, can bind to the negatively charged microbial cell membrane, disrupting its integrity. This can lead to leakage of cellular contents and ultimately to cell death [151].

3. **Metal Ion Release:** Metal ions such as Cu^{2+}, Ag^{+}, $Zn^{2+,}$ and V^{5+} released from metal oxides can exert antimicrobial effects by interfering with microbial metabolic pathways. For example, copper ions can bind to proteins and enzymes, disrupting their normal function, while silver ions can inhibit cellular respiration by interacting with sulfur-containing proteins [152]

References

[1] P. Hu *et al.*, "Vanadium Oxide: Phase Diagrams, Structures, Synthesis, and Applications," *Chem. Rev.*, vol. 123, no. 8, pp. 4353–4415, Apr. 2023, doi: 10.1021/acs.chemrev.2c00546.

[2] T. K. Le *et al.*, "Recent advances in vanadium pentoxide (V_2O_5) towards related applications in chromogenics and beyond: fundamentals, progress, and perspectives," *J. Mater. Chem. C*, vol. 10, no. 11, pp. 4019–4071, 2022, doi: 10.1039/D1TC04872D.

[3] F. Liu, S. Song, D. Xue, and H. Zhang, "Selective crystallization with preferred lithium-ion storage capability of inorganic materials," *Nanoscale Res. Lett.*, vol. 7, no. 1, p. 149, Dec. 2012, doi: 10.1186/1556-276X-7-149.

[4] H. G. Bachmann, F. R. Ahmed, and W. H. Barnes, "The crystal structure of vanadium pentoxide," *Z. Für Krist.*, vol. 115, no. 1–2, pp. 110–131, May 1961, doi: 10.1524/zkri.1961.115.1-2.110.

[5] N. A. Chernova, M. Roppolo, A. C. Dillon, and M. S. Whittingham, "Layered vanadium and molybdenum oxides: batteries and electrochromics," *J. Mater. Chem.*, vol. 19, no. 17, p. 2526, 2009, doi: 10.1039/b819629j.

[6] C. Delmas, H. Cognacauradou, J. Cocciantelli, M. Menetrier, and J. Doumerc, "The LixV2O5 system: An overview of the structure modifications induced by the lithium intercalation," *Solid State Ion.*, vol. 69, no. 3–4, pp. 257–264, Aug. 1994, doi: 10.1016/0167-2738(94)90414-6.

[7] A. Cao, J. Hu, H. Liang, and L. Wan, "Self-Assembled Vanadium Pentoxide (V_2O_5) Hollow Microspheres from Nanorods and Their Application in Lithium-Ion Batteries," *Angew. Chem. Int. Ed.*, vol. 44, no. 28, pp. 4391–4395, July 2005, doi: 10.1002/anie.200500946.

[8] Y. Yue and H. Liang, "Micro- and Nano-Structured Vanadium Pentoxide (V_2O_5) for Electrodes of Lithium-Ion Batteries," *Adv. Energy Mater.*, vol. 7, no. 17, p. 1602545, Sept. 2017, doi: 10.1002/aenm.201602545.

[9] X. Wang *et al.*, "Vanadium pentoxide nanosheets as cathodes for aqueous zinc-ion batteries with high rate capability and long durability," *Appl. Surf. Sci.*, vol. 502, p. 144207, Feb. 2020, doi: 10.1016/j.apsusc.2019.144207.

[10] J. Mu *et al.*, "Hydrothermal synthesis and electrochemical properties of V2O5 nanomaterials with different dimensions," *Ceram. Int.*, vol. 41, no. 10, pp. 12626–12632, Dec. 2015, doi: 10.1016/j.ceramint.2015.06.091.

[11] A. Pan *et al.*, "Facile synthesized nanorod structured vanadium pentoxide for high-rate lithium batteries," *J. Mater. Chem.*, vol. 20, no. 41, p. 9193, 2010, doi: 10.1039/c0jm01306d.

[12] F. Zhou, X. Zhao, C. Yuan, and L. Li, "Vanadium Pentoxide Nanowires: Hydrothermal Synthesis, Formation Mechanism, and Phase Control Parameters," *Cryst. Growth Des.*, vol. 8, no. 2, pp. 723–727, Feb. 2008, doi: 10.1021/cg060816x.

[13] R. K. Sharma, P. Kumar, and G. B. Reddy, "Synthesis of vanadium pentoxide (V2O5) nanobelts with high coverage using plasma assisted PVD approach," *J. Alloys Compd.*, vol. 638, pp. 289–297, July 2015, doi: 10.1016/j.jallcom.2015.02.178.

[14] J. Zhu *et al.*, "Building 3D Structures of Vanadium Pentoxide Nanosheets and Application as Electrodes in Supercapacitors," *Nano Lett.*, vol. 13, no. 11, pp. 5408–5413, Nov. 2013, doi: 10.1021/nl402969r.

[15] H. Bai, Z. Liu, D. D. Sun, and S. H. Chan, "Hierarchical 3D micro-/nano-V2O5 (vanadium pentoxide) spheres as cathode materials for high-energy and high-power lithium ion-batteries," *Energy*, vol. 76, pp. 607–613, Nov. 2014, doi: 10.1016/j.energy.2014.08.058.

[16] L. Yao, C. Zhang, N. Hu, L. Zhang, Z. Zhou, and Y. Zhang, "Three-dimensional skeleton networks of reduced graphene oxide nanosheets/vanadium pentoxide nanobelts hybrid for high-performance supercapacitors," *Electrochimica Acta*, vol. 295, pp. 14–21, Feb. 2019, doi: 10.1016/j.electacta.2018.10.134.

[17] L. Top, M. Kang, and S. Kim, "A review on the optical characterization of V2O5 micro-nanostructures," *Ceram. Int.*, vol. 45, May 2019, doi: 10.1016/j.ceramint.2019.05.339.

[18] A. Ray, A. Roy, S. De, S. Chatterjee, and S. Das, "Frequency and temperature dependent dielectric properties of TiO2-V2O5 nanocomposites," *J. Appl. Phys.*, vol. 123, no. 10, Mar. 2018, doi: 10.1063/1.5012586.

[19] P. Rosaiah, G. L. Sandhya, and O. M. Hussain, "Impedance Spectroscopy and Electrochemical Properties of Nano-Crystalline Vanadium Pentoxide (V_2O_5) Synthesized by Co-Precipitation Method," *Adv. Sci. Eng. Med.*, vol. 8, no. 2, pp. 83–90, Feb. 2016, doi: 10.1166/asem. 2016. 1839.

[20] J. Wu *et al.*, "Influence of Dopants on Electrical Properties of ZnO-V2O5 Varistors Deduced from AC Impedance and Variable-Temperature Dielectric Spectroscopy," *J. Electron. Mater.*, vol. 41, no. 7, pp. 1970–1977, July 2012, doi: 10.1007/s11664-012-1935-7.

[21] A. Sivakumar *et al.*, "Shock wave recovery experiments on α-V2O5 nano-crystalline materials: A potential material for energy storage applications," *J. Alloys Compd.*, vol. 929, p. 167180, Dec. 2022, doi: 10.1016/j.jallcom.2022.167180.

[22] "VO nanofibres: novel gas sensors with extremely high sensitivity and selectivity to amines," *Sens. Actuators B Chem.*, vol. 106, no. 2, pp. 730–735, May 2005, doi: 10.1016/j.snb.2004.09.024.

[23] V. Modafferi *et al.*, "Highly sensitive ammonia resistive sensor based on electrospun V2O5 fibers," *Sens. Actuators B Chem.*, vol. 163, no. 1, pp. 61–68, Mar. 2012, doi: 10.1016/j.snb.2012.01.007.

[24] Y. Zhu *et al.*, "V_2O_5 Textile Cathodes with High Capacity and Stability for Flexible Lithium-Ion Batteries," *Adv. Mater.*, vol. 32, no. 7, Feb. 2020, doi: 10.1002/adma.201906205.

[25] Y. Li *et al.*, "Leaf-Like V_2O_5 Nanosheets Fabricated by a Facile Green Approach as High Energy Cathode Material for Lithium-Ion Batteries," *Adv. Energy Mater.*, vol. 3, no. 9, pp. 1171–1175, Sept. 2013, doi: 10.1002/aenm.201300188.

[26] Y. Chen, C. Chen, W. Chen, H. Liu, and J. Zhu, "Influence of thermal-decomposition temperatures on structures and properties of V2O5 as cathode materials for lithium ion battery," *Prog. Nat. Sci. Mater. Int.*, vol. 25, no. 1, pp. 42–46, Feb. 2015, doi: 10.1016/j.pnsc.2015.01.015.

[27] H. Wang, D. Ma, Y. Huang, and X. Zhang, "Electrospun V_2O_5 Nanostructures with Controllable Morphology as High-Performance Cathode Materials for Lithium-Ion Batteries," *Chem. – Eur. J.*, vol. 18, no. 29, pp. 8987–8993, July 2012, doi: 10.1002/chem.201200434.

[28] T. Kim, J. Shin, T.-S. You, H. Lee, and J. Kim, "Thermally Controlled V2O5 Nanoparticles as Cathode Materials for Lithium-Ion Batteries with Enhanced Rate Capability," *Electrochimica Acta*, vol. 164, pp. 227–234, May 2015, doi: 10.1016/j.electacta.2015.02.208.

[29] A. Choudhury, J. S. Bonso, M. Wunch, K. S. Yang, J. P. Ferraris, and D. J. Yang, "In-situ synthesis of vanadium pentoxide nanofibre/exfoliated graphene nanohybrid and its supercapacitor applications," *J. Power Sources*, vol. 287, pp. 283–290, Aug. 2015, doi: 10.1016/j.jpowsour.2015.04.062.

[30] Y. Chen, K. Muthukumar, L. Leban, and J. Li, "Microwave-assisted high-yield exfoliation of vanadium pentoxide nanoribbons for supercapacitor applications," *Electrochimica Acta*, vol. 330, p. 135200, Jan. 2020, doi: 10.1016/j.electacta.2019.135200.

[31] Y. Wang, K. Takahashi, H. Shang, and G. Cao, "Synthesis and Electrochemical Properties of Vanadium Pentoxide Nanotube Arrays," *J. Phys. Chem. B*, vol. 109, no. 8, pp. 3085–3088, Mar. 2005, doi: 10.1021/jp044286w.

[32] C. Romanitan *et al.*, "Structural Investigations in Electrochromic Vanadium Pentoxide Thin Films," *Phys. Status Solidi A*, vol. 219, no. 16, p. 2100431, Aug. 2022, doi: 10.1002/pssa.202100431.

[33] I. Mjejri, L. M. Manceriu, M. Gaudon, A. Rougier, and F. Sediri, "Nano-vanadium pentoxide films for electrochromic displays," *Solid State Ion.*, vol. 292, pp. 8–14, Sept. 2016, doi: 10.1016/j.ssi.2016.04.023.

[34] J. Wang *et al.*, "Pseudocapacitive porous amorphous vanadium pentoxide with enhanced multicolored electrochromism," *Chem. Eng. J.*, vol. 452, p. 139655, Jan. 2023, doi: 10.1016/j.cej.2022.139655.

[35] H. Miyazaki, T. Matsuura, and T. Ota, "Vanadium oxide-based photochromic composite film," *RSC Adv.*, vol. 7, no. 5, pp. 2388–2391, 2017, doi: 10.1039/C6RA25892A.

[36] S. Kumar, A. Qadir, F. Maury, and N. Bahlawane, "Visible Thermochromism in Vanadium Pentoxide Coatings," *ACS Appl. Mater. Interfaces*, vol. 9, no. 25, pp. 21447–21456, June 2017, doi: 10.1021/acsami.7b04484.

[37] M. M. Sajid *et al.*, "Preparation and characterization of Vanadium pentoxide (V2O5) for photocatalytic degradation of monoazo and diazo dyes," *Surf. Interfaces*, vol. 19, p. 100502, June 2020, doi: 10.1016/j.surfin.2020.100502.

[38] K. S. A. Sohaimi, J. Jaafar, and N. Rosman, "Synthesis, Properties, and Applications of Vanadium Pentoxide (V2O5) as Photocatalyst: A Review," *Malays. J. Fundam. Appl. Sci.*, vol. 19, no. 5, pp. 901–914, Oct. 2023, doi: 10.11113/mjfas.v19n5.2774.

[39] Department of Physics, Yashavantrao Chavan Institute of Science, Satara, Maharashtra 415 001, India *et al.*, "Hydrothermally Prepared Vanadium Oxide Nanostructures for Photocatalytic Application," *ES Energy Environ.*, 2022, doi: 10.30919/esee8c639.

[40] S. J. Armaković *et al.*, "Photocatalytic Activity of the V2O5 Catalyst toward Selected Pharmaceuticals and Their Mixture: Influence of the Molecular Structure on the Efficiency of the Process," *Molecules*, vol. 28, no. 2, p. 655, Jan. 2023, doi: 10.3390/molecules28020655.

[41] A. T. Raj, K. Ramanujan, S. Thangavel, S. Gopalakrishan, N. Raghavan, and G. Venugopal, "Facile Synthesis of Vanadium-Pentoxide Nanoparticles and Study on Their Electrochemical, Photocatalytic Properties," *J. Nanosci. Nanotechnol.*, vol. 15, no. 5, pp. 3802–3808, May 2015, doi: 10.1166/jnn.2015.9543.

[42] A. Dhayal Raj, T. Pazhanivel, P. Suresh Kumar, D. Mangalaraj, D. Nataraj, and N. Ponpandian, "Self assembled V2O5 nanorods for gas sensors," *Curr. Appl. Phys.*, vol. 10, no. 2, pp. 531–537, Mar. 2010, doi: 10.1016/j.cap.2009.07.015.

[43] P. S. Chauhan and S. Bhattacharya, "Vanadium Pentoxide Nanostructures for Sensitive Detection of Hydrogen Gas at Room Temperatur," *J. Energy Environ. Sustain.*, vol. 2, pp. 69–74, July 2016, doi: 10.47469/JEES.2016.v02.100022.

[44] Y. Qin, G. Fan, K. Liu, and M. Hu, "Vanadium pentoxide hierarchical structure networks for high performance ethanol gas sensor with dual working temperature characteristic," *Sens. Actuators B Chem.*, vol. 190, pp. 141–148, Jan. 2014, doi: 10.1016/j.snb.2013.08.061.

[45] K.-Y. Pan and D.-H. Wei, "Optoelectronic and Electrochemical Properties of Vanadium Pentoxide Nanowires Synthesized by Vapor-Solid Process," *Nanomaterials*, vol. 6, no. 8, p. 140, July 2016, doi: 10.3390/nano6080140.

[46] E. E. Chain, "Optical properties of vanadium dioxide and vanadium pentoxide thin films," *Appl. Opt.*, vol. 30, no. 19, p. 2782, July 1991, doi: 10.1364/AO.30.002782.

[47] S. Das *et al.*, "Anti-angiogenic vanadium pentoxide nanoparticles for the treatment of melanoma and their *in vivo* toxicity study," *Nanoscale*, vol. 12, no. 14, pp. 7604–7621, 2020, doi: 10.1039/D0NR00631A.

[48] S. Nivetha *et al.*, "Nickel-doped vanadium pentoxide (Ni@V2O5) nanocomposite induces apoptosis targeting PI3K/AKT/mTOR signaling pathway in skin cancer: An in vitro and in vivo study," *Colloids Surf. B Biointerfaces*, vol. 234, p. 113763, Feb. 2024, doi: 10.1016/j.colsurfb.2024.113763.

[49] H. S. Lalithamba, A. D. Nagaraja, A. Siddekha, G. K. Prashanth, and G. Nagendra, "Green synthesis of V2O5 nanoparticles: Anticancer, antioxidant activity, application in biodiesel production and amino acid derived thioacids," *Results Chem.*, vol. 15, p. 102260, May 2025, doi: 10.1016/j.rechem.2025.102260.

[50] L. Huang, L. Yu, X. Yin, Y. Lin, Y. Xu, and Y. Niu, "Silver nanoparticles with vanadium oxide nanowires loaded into electrospun dressings for efficient healing of

bacterium-infected wounds," *J. Colloid Interface Sci.*, vol. 622, pp. 117–125, Sept. 2022, doi: 10.1016/j.jcis.2022.04.026.

[51] K. Karthik, M. P. Nikolova, A. Phuruangrat, S. Pushpa, V. Revathi, and M. Subbulakshmi, "Ultrasound-assisted synthesis of $V_2 O_5$ nanoparticles for photocatalytic and antibacterial studies," *Mater. Res. Innov.*, vol. 24, no. 4, pp. 229–234, June 2020, doi: 10.1080/14328917.2019.1634404.

[52] N. Anicic, M. Vukomanovic, and D. Suvorov, "Design of a multifunctional vanadium pentoxide/polymer biocomposite for implant-coating applications," *RSC Adv.*, vol. 7, no. 61, pp. 38647–38658, 2017, doi: 10.1039/C7RA06471C.

[53] B. Walls *et al.*, "Optical anisotropy of pristine and reduced V2O5(010)," *Sci. Rep.*, vol. 15, no. 1, July 2025, doi: 10.1038/s41598-025-07519-z.

[54] G. A. Horrocks *et al.*, "Mitigating Cation Diffusion Limitations and Intercalation-Induced Framework Transitions in a 1D Tunnel-Structured Polymorph of V_2O_5," *Chem. Mater.*, vol. 29, no. 24, pp. 10386–10397, Dec. 2017, doi: 10.1021/acs.chemmater.7b03800.

[55] R. Verrelli *et al.*, "On the strange case of divalent ions intercalation in V2O5," *J. Power Sources*, vol. 407, pp. 162–172, Dec. 2018, doi: 10.1016/j.jpowsour.2018.08.024.

[56] R. Saravanan, V. K. Gupta, E. Mosquera, and F. Gracia, "Preparation and characterization of V2O5/ZnO nanocomposite system for photocatalytic application," *J. Mol. Liq.*, vol. 198, pp. 409–412, Oct. 2014, doi: 10.1016/j.molliq.2014.07.030.

[57] Y. Li, S. Chen, W. Duan, Y. Nan, D. Ding, and G. Xiao, "Research progress of vanadium pentoxide photocatalytic materials," *RSC Adv.*, vol. 13, no. 33, pp. 22945–22957, 2023, doi: 10.1039/d3ra03648k.

[58] R. Mirabal-Rojas, S. E. Rodil, G. Ramirez, T. Polcar, E. Camps, and A. Erdemir, "Effect of the addition of Si into V2O5 coatings: Structure and tribo-mechanical properties," *Surf. Coat. Technol.*, vol. 349, pp. 111–118, Sept. 2018, doi: 10.1016/j.surfcoat.2018.05.052.

[59] F. Xia *et al.*, "Thermal transition behaviors of vanadium pentoxide film during post-deposition annealing," *Surf. Coat. Technol.*, vol. 405, p. 126637, Jan. 2021, doi: 10.1016/j.surfcoat.2020.126637.

[60] L. S. Rhoads, W. T. Silkworth, M. L. Roppolo, and M. S. Whittingham, "Cytotoxicity of nanostructured vanadium oxide on human cells in vitro," *Toxicol. In Vitro*, vol. 24, no. 1, pp. 292–296, Feb. 2010, doi: 10.1016/j.tiv.2009.08.010.

[61] A. S. Altowyan, J. Hakami, H. Algarni, and M. Shkir, "Enhancing the optoelectronic properties of V2O5 thin films through Tb doping for photodetector applications," *J. Alloys Compd.*, vol. 960, p. 170911, Oct. 2023, doi: 10.1016/j.jallcom.2023.170911.

[62] S. Sutrave *et al.*, "A simple solution combustion method for the synthesis of V2O5 nanostructures for supercapacitor applications," *Appl. Surf. Sci. Adv.*, vol. 12, p. 100331, Dec. 2022, doi: 10.1016/j.apsadv.2022.100331.

[63] P. Kiran *et al.*, "Vanadium pentoxide gas sensors: An overview of elemental doping strategies and their effect on sensing performance," *Catal. Commun.*, vol. 187, p. 106838, Feb. 2024, doi: 10.1016/j.catcom.2023.106838.

[64] H. Zeng *et al.*, "Nanostructured Mn-Doped V_2 O_5 Cathode Material Fabricated from Layered Vanadium Jarosite," *Chem. Mater.*, vol. 27, no. 21, pp. 7331–7336, Nov. 2015, doi: 10.1021/acs.chemmater.5b02840.

[65] V. Uma Shankar, D. Govindarajan, P. Christuraj, M. J. Salethraj, F. J. Johanson, and M. D. Raja, "Enhanced the electrochemical properties of Ni doped V2O5 as a electrode material for supercapacitor applications," *Mater. Today Proc.*, vol. 50, pp. 2675–2678, 2022, doi: 10.1016/j.matpr.2020.08.213.

[66] H. Jiang *et al.*, "Quench-tailored Al-doped V2O5 nanomaterials for efficient aqueous zinc-ion batteries," *J. Energy Chem.*, vol. 70, pp. 52–58, July 2022, doi: 10.1016/j.jechem.2022.02.030.

[67] S. R. Bhosale, R. R. Bhosale, R. P. Dhavale, G. B. Kolekar, V. B. Shimpale, and P. V. Anbhule, "Nanomaterials Based Multifunctional Bioactivities of V_2 O_5 and Mesoporous Carbon@V_2 O_5 Composite: Preparation and Characterization," *Langmuir*, vol. 40, no. 12, pp. 6471–6483, Mar. 2024, doi: 10.1021/acs.langmuir.4c00010.

[68] A. Varghese, K. R. P. Sunajadevi, D. Pinheiro, B. Saravanakumar, and M. Selvaraj, "Advancing energy production and storage: Polypyrrole/V2O5/MnO2 composite as a high-performance electrocatalyst," *Int. J. Hydrog. Energy*, vol. 123, pp. 238–246, Apr. 2025, doi: 10.1016/j.ijhydene.2025.03.419.

[69] S. A. Ahmad, F. Mashkoor, M. A. Ansari, A. A. Alothman, M. Shoeb, and C. Jeong, "Morus alba-mediated defect-rich Fe-doped V2O5 nanoparticles on woven carbon fiber for high-performance supercapacitor with enhanced charge storage mechanism," *J. Alloys Compd.*, vol. 1020, p. 179515, Mar. 2025, doi: 10.1016/j.jallcom.2025.179515.

[70] J. Huang, S. Zhang, Q. Qin, Z. Wang, and G. Cai, "Designing V2O5/MXene van der Waals heterostructure for complementary electrochromic dual-ion capacitor," *Chem. Eng. J.*, vol. 476, p. 146626, Nov. 2023, doi: 10.1016/j.cej.2023.146626.

[71] A. Garzon-Roman *et al.*, "Fabrication of V2O5/porous silicon heterostructures by simple and low-cost methods, morphological, structural, optical, and electrical characterization, and their first application as photodetectors," *Sens. Actuators Phys.*, vol. 387, p. 116471, June 2025, doi: 10.1016/j.sna.2025.116471.

[72] X. Hu *et al.*, "Two-dimensional heterostructure of MXene-derived V2O5·H2O and graphene with enhanced Zn-ion storage capability," *Electrochimica Acta*, vol. 507, p. 145093, Dec. 2024, doi: 10.1016/j.electacta.2024.145093.

[73] A. E. Hassan *et al.*, "V2O5 nanoribbons/N-deficient g-C3N4 heterostructure for enhanced visible-light photocatalytic performance," *Int. J. Hydrog. Energy*, vol. 48, no. 26, pp. 9620–9635, Mar. 2023, doi: 10.1016/j.ijhydene.2022.12.009.

[74] A. Badreldin *et al.*, "Surface microenvironment engineering of black V2O5 nanostructures for visible light photodegradation of methylene blue," *J. Alloys Compd.*, vol. 871, p. 159615, Aug. 2021, doi: 10.1016/j.jallcom.2021.159615.

[75] W. Young Jang *et al.*, "Novel 2D sulfur-doped V2O5 flakes and their applications in photoelectrochemical water oxidation and high-performance energy storage supercapacitors," *Chem. Eng. J.*, vol. 461, p. 141935, Apr. 2023, doi: 10.1016/j.cej.2023.141935.

[76] S. N. Birajdar and P. V. Adhyapak, "Palladium-decorated vanadium pentoxide as NOx gas sensor," *Ceram. Int.*, vol. 46, no. 17, pp. 27381–27393, Dec. 2020, doi: 10.1016/j.ceramint.2020.07.223.

[77] L. T. Boaes Mendonça, A. G. Bezerra, and W. Mendes De Azevedo, "Preparation and characterization of V2O5 and V2O5/PANI nanocomposite by laser ablation technique in liquid," *Mater. Chem. Phys.*, vol. 273, p. 125084, Nov. 2021, doi: 10.1016/j.matchemphys.2021.125084.

[78] A. Shoukat, M. Aslam, Z. Mustafa, M. Basit, and S. M. A. Zaidi, "Fabrication and analysis of PVA/V2O5/BaTiO3 nanocomposite film for flexible optoelectronics," *Phys. B Condens. Matter*, vol. 678, p. 415777, Apr. 2024, doi: 10.1016/j.physb.2024.415777.

[79] G. J. Thangamani, K. Deshmukh, N. A. Nambiraj, and S. K. K. Pasha, "Chemiresistive gas sensors based on vanadium pentoxide reinforced polyvinyl alcohol/polypyrrole blend nanocomposites for room temperature LPG sensing," *Synth. Met.*, vol. 273, p. 116687, Mar. 2021, doi: 10.1016/j.synthmet.2020.116687.

[80] Y.-L. Pan and W.-C. Liu, "Study of a Platinum (Pt) Nanoparticle (NP)/Vanadium Pentoxide (V_2 O_5) Thin Film-Based Ammonia Gas Sensor," *IEEE Trans. Electron Devices*, vol. 67, no. 5, pp. 2126–2132, May 2020, doi: 10.1109/TED.2020.2981113.

[81] J. Światowska-Mrowiecka, V. Maurice, S. Zanna, L. Klein, and P. Marcus, "XPS study of Li ion intercalation in V2O5 thin films prepared by thermal oxidation of vanadium metal," *Electrochimica Acta*, vol. 52, no. 18, pp. 5644–5653, May 2007, doi: 10.1016/j.electacta.2006.12.050.

[82] H. Si *et al.*, "Impact of the Morphology of V_2 O_5 Electrodes on the Electrochemical Na^+ -Ion Intercalation," *J. Electrochem. Soc.*, vol. 165, no. 11, pp. A2709–A2717, 2018, doi: 10.1149/2.0621811jes.

[83] T. P. Jaya, P. Jayaram, T. Ramachandran, P. Hajira, C. N. Anumol, and P. P. Pradyumnan, "Synthesis of solid solutions of Mn and Bi substituted V2O5 and substitutional effect in structural and optoelectronic behavior," *Phys. B Condens. Matter*, vol. 407, no. 8, pp. 1214–1218, Apr. 2012, doi: 10.1016/j.physb.2012.01.098.

[84] R. Abaira, T. Dammak, A. Matoussi, and A. Younes, "Structural and optical properties of zinc oxide doped by V2O5 synthesized by solid-state reaction," *Superlattices Microstruct.*, vol. 91, pp. 365–374, Mar. 2016, doi: 10.1016/j.spmi.2016.01.008.

[85] W. D. Callister and D. G. Rethwisch, *Materials Science and Engineering: An Introduction, ., .*, 9th ed. Wiley, 2014.

[86] K. McColl, I. Johnson, and F. Corà, "Thermodynamics and defect chemistry of substitutional and interstitial cation doping in layered α-V_2 O_5," *Phys. Chem. Chem. Phys.*, vol. 20, no. 22, pp. 15002–15006, 2018, doi: 10.1039/C8CP02187B.

[87] T. Chen, C. Foo, and S. C. Edman Tsang, "Interstitial and substitutional light elements in transition metals for heterogeneous catalysis," *Chem. Sci.*, vol. 12, no. 2, pp. 517–532, 2021, doi: 10.1039/D0SC06496C.

[88] G. K. Williamson and W. H. Hall, "X-ray line broadening from filed aluminium and wolfram," *Acta Metall.*, vol. 1, no. 1, pp. 22–31, Jan. 1953, doi: 10.1016/0001-6160(53)90006-6.

[89] O. A. Bulavchenko and Z. S. Vinokurov, "In Situ X-ray Diffraction as a Basic Tool to Study Oxide and Metal Oxide Catalysts," *Catalysts*, vol. 13, no. 11, p. 1421, Nov. 2023, doi: 10.3390/catal13111421.

[90] Cullity, B. D., & Stock, S. R., *Elements of X-ray Diffraction (3rd ed.)*. Prentice Hall., 2001.

[91] A. L. Patterson, "The Scherrer Formula for X-Ray Particle Size Determination," *Phys. Rev.*, vol. 56, no. 10, pp. 978–982, Nov. 1939, doi: 10.1103/PhysRev.56.978.

[92] J. I. Langford and A. J. C. Wilson, "Scherrer after sixty years: A survey and some new results in the determination of crystallite size," *J. Appl. Crystallogr.*, vol. 11, no. 2, pp. 102–113, Apr. 1978, doi: 10.1107/S0021889878012844.

[93] A. Monshi, M. R. Foroughi, and M. R. Monshi, "Modified Scherrer Equation to Estimate More Accurately Nano-Crystallite Size Using XRD," *World J. Nano Sci. Eng.*, vol. 02, no. 03, pp. 154–160, 2012, doi: 10.4236/wjnse.2012.23020.

[94] H. M. Rietveld, "A profile refinement method for nuclear and magnetic structures," *J. Appl. Crystallogr.*, vol. 2, no. 2, pp. 65–71, June 1969, doi: 10.1107/S0021889869006558.

[95] R. A. YOUNG, *The Rietveld Method*. International Union of Crystallography. Oxford University Press.

[96] B. H. Toby, "*R* factors in Rietveld analysis: How good is good enough?," *Powder Diffr.*, vol. 21, no. 1, pp. 67–70, Mar. 2006, doi: 10.1154/1.2179804.

[97] J. Rodríguez-Carvajal, "Recent advances in magnetic structure determination by neutron powder diffraction," *Phys. B Condens. Matter*, vol. 192, no. 1–2, pp. 55–69, Oct. 1993, doi: 10.1016/0921-4526(93)90108-I.

[98] L. B. McCusker, R. B. Von Dreele, D. E. Cox, D. Louër, and P. Scardi, "Rietveld refinement guidelines," *J. Appl. Crystallogr.*, vol. 32, no. 1, pp. 36–50, Feb. 1999, doi: 10.1107/S0021889898009856.

[99] E. N. Kaufmann, *Characterization of Materials*. in Characterization of Materials, no. v. 1. John Wiley & Sons, Incorporated, 2012. [Online]. Available: https://books.google.co.in/books?id=Ke8nLgEACAAJ

[100] L. A. Gribov, "The Theory of Raman Spectra: A New Approach," *High Energy Chem.*, vol. 54, no. 4, pp. 233–236, July 2020, doi: 10.1134/S0018143920040062.

[101] "Infrared Spectroscopy," in *ACS Reagent Chemicals*, Washington, DC: American Chemical Society, 2017. doi: 10.1021/acsreagents.2008.

[102] M. El-Azazy, A. S. El-Shafie, and K. Al-Saad, "Introductory Chapter: Infrared Spectroscopy - Principles and Applications," in *Infrared Spectroscopy - Perspectives and Applications*, M. El-Azazy, K. Al-Saad, and A. S. El-Shafie, Eds., IntechOpen, 2023. doi: 10.5772/intechopen.109139.

[103] B. Faramarzi, M. Moggio, N. Diano, M. Portaccio, and M. Lepore, "A Brief Review of FT-IR Spectroscopy Studies of Sphingolipids in Human Cells," *Biophysica*, vol. 3, no. 1, pp. 158–180, Mar. 2023, doi: 10.3390/biophysica3010011.

[104] F. A. Stevie and C. L. Donley, "Introduction to x-ray photoelectron spectroscopy," *J. Vac. Sci. Technol. Vac. Surf. Films*, vol. 38, no. 6, p. 063204, Dec. 2020, doi: 10.1116/6.0000412.

[105] N. Alov, D. Kutsko, I. Spirovová, and Z. Bastl, "XPS study of vanadium surface oxidation by oxygen ion bombardment," *Surf. Sci.*, vol. 600, no. 8, pp. 1628–1631, Apr. 2006, doi: 10.1016/j.susc.2005.12.052.

[106] J. Biener, M. Bäumer, J. Wang, and R. J. Madix, "Electronic structure and growth of vanadium on TiO2(110)," *Surf. Sci.*, vol. 450, no. 1–2, pp. 12–26, Apr. 2000, doi: 10.1016/S0039-6028(99)01216-9.

[107] Y. Okano, "Scanning Electron Microscopy," in *Compendium of Surface and Interface Analysis*, The Surface Science Society Of Japa, Ed., Singapore: Springer Singapore, 2018, pp. 563–569. doi: 10.1007/978-981-10-6156-1_91.

[108] M. T. Postek, A. E. Vladár, O. C. Wells, and J. L. Lowney, "Application of the low-loss scanning electron microscope image to integrated circuit technology. Part 1–applications to accurate dimension measurements," *Scanning*, vol. 23, no. 5, pp. 298–304, Sept. 2001, doi: 10.1002/sca.4950230502.

[109] M. Schreiner and M. Melcher, "Scanning Electron Microscopy," in *The Encyclopedia of Archaeological Sciences*, 1st ed., S. L. López Varela, Ed., Wiley, 2018, pp. 1–4. doi: 10.1002/9781119188230.saseas0518.

[110] K. Tsuji, "X-ray Fluorescence and Emission: X-ray Fluorescence Theory," in *Reference Module in Chemistry, Molecular Sciences and Chemical Engineering*, Elsevier, 2018, p. B9780124095472144749. doi: 10.1016/B978-0-12-409547-2.14474-9.

[111] J. Zheng, K. Nagashima, D. Parmiter, J. De La Cruz, and A. K. Patri, "SEM X-Ray Microanalysis of Nanoparticles Present in Tissue or Cultured Cell Thin Sections," in *Characterization of Nanoparticles Intended for Drug Delivery*, vol. 697, S. E. McNeil, Ed., in Methods in Molecular Biology, vol. 697. , Totowa, NJ: Humana Press, 2011, pp. 93–99. doi: 10.1007/978-1-60327-198-1_9.

[112] M. A. K. Abdelhalim and M. M. Mady, "Physical Properties of Different Gold Nanoparticles: Ultraviolet-Visible and Fluorescence Measurements," *J. Nanomedicine Nanotechnol.*, vol. 03, no. 03, 2012, doi: 10.4172/2157-7439.1000133.

[113] A. K. Brisdon, "UV-visible spectroscopy," in *Inorganic Spectroscopic Methods*, Oxford University Press, 1998. doi: 10.1093/hesc/9780198559498.003.0004.

[114] B. W. Montag, N. Platt, N. M. Boag, J. I. Brand, and K. A. Nelson, "Doped Wide Bandgap Materials and Devices from Semiconducting Boron Carbide," *ECS Trans.*, vol. 3, no. 5, pp. 429–435, Oct. 2006, doi: 10.1149/1.2357234.

[115] P. Makuła, M. Pacia, and W. Macyk, "How To Correctly Determine the Band Gap Energy of Modified Semiconductor Photocatalysts Based on UV–Vis Spectra," *J. Phys. Chem. Lett.*, vol. 9, no. 23, pp. 6814–6817, Dec. 2018, doi: 10.1021/acs.jpclett.8b02892.

[116] J. E. Toney, "Photoluminescence Spectroscopy," in *Characterization of Materials*, 1st ed., E. N. Kaufmann, Ed., Wiley, 2003. doi: 10.1002/0471266965.com058.

[117] Q. Li, M. Anpo, J. You, T. Yan, and X. Wang, "Photoluminescence (PL) Spectroscopy," in *Springer Handbook of Advanced Catalyst Characterization*, I. E. Wachs and M. A. Bañares, Eds., in Springer Handbooks. , Cham: Springer International Publishing, 2023, pp. 295–321. doi: 10.1007/978-3-031-07125-6_14.

[118] J. R. Lakowicz, Ed., *Principles of Fluorescence Spectroscopy*. Boston, MA: Springer US, 2006. doi: 10.1007/978-0-387-46312-4.

[119] S. Sanguinetti, M. Guzzi, and M. Gurioli, "Accessing structural and electronic properties of semiconductor nanostructures via photoluminescence," in *Characterization of Semiconductor Heterostructures and Nanostructures*, Elsevier, 2008, pp. 175–208. doi: 10.1016/B978-0-444-53099-8.00006-3.

[120] S. Shimizu and N. Matubayasi, "Surface Area Estimation: Replacing the Brunauer–Emmett–Teller Model with the Statistical Thermodynamic Fluctuation Theory," *Langmuir*, vol. 38, no. 26, pp. 7989–8002, July 2022, doi: 10.1021/acs.langmuir.2c00753.

[121] F. Ambroz, T. J. Macdonald, V. Martis, and I. P. Parkin, "Evaluation of the BET Theory for the Characterization of Meso and Microporous MOFs," *Small Methods*, vol. 2, no. 11, p. 1800173, Nov. 2018, doi: 10.1002/smtd.201800173.

[122] S. Saitzek, J. -F. Blach, S. Villain, and J. -R. Gavarri, "Nanostructured ceria: a comparative study from X-ray diffraction, Raman spectroscopy and BET specific surface measurements," *Phys. Status Solidi A*, vol. 205, no. 7, pp. 1534–1539, July 2008, doi: 10.1002/pssa.200723419.

[123] K. S. W. Sing, "Reporting physisorption data for gas/solid systems with special reference to the determination of surface area and porosity (Recommendations 1984)," *Pure Appl. Chem.*, vol. 57, no. 4, pp. 603–619, Jan. 1985, doi: 10.1351/pac198557040603.

[124] J. W. M. Osterrieth *et al.*, "How Reproducible are Surface Areas Calculated from the BET Equation?," *Adv. Mater.*, vol. 34, no. 27, p. 2201502, July 2022, doi: 10.1002/adma.202201502.

[125] S. Lowell, J. E. Shields, M. A. Thomas, and M. Thommes, *Characterization of Porous Solids and Powders: Surface Area, Pore Size and Density*, vol. 16. in Particle Technology Series, vol. 16. Dordrecht: Springer Netherlands, 2004. doi: 10.1007/978-1-4020-2303-3.

[126] Jean Rouquerol, Françoise Rouquerol, Philip Llewellyn, Guillaume Maurin, Kenneth Sing, *Adsorption by Powders and Porous Solids Principles, Methodology and Applications*, 2nd Edition-September 6, 2013.

[127] R. Bardestani, G. S. Patience, and S. Kaliaguine, "Experimental methods in chemical engineering: specific surface area and pore size distribution measurements—BET, BJH,

and DFT," *Can. J. Chem. Eng.*, vol. 97, no. 11, pp. 2781–2791, Nov. 2019, doi: 10.1002/cjce.23632.

[128] A. Debnath, M. Majumder, M. Pal, N. S. Das, K. K. Chattopadhyay, and B. Saha, "Enhanced Adsorption of Hexavalent Chromium onto Magnetic Calcium Ferrite Nanoparticles: Kinetic, Isotherm, and Neural Network Modeling," *J. Dispers. Sci. Technol.*, vol. 37, no. 12, pp. 1806–1818, Dec. 2016, doi: 10.1080/01932691.2016.1141100.

[129] Z. Ying, D. Zhao, H. Li, X. Liu, and J. Zhang, "Efficient Adsorption of Deoxynivalenol by Porous Carbon Prepared from Soybean Dreg," *Toxins*, vol. 13, no. 7, p. 500, July 2021, doi: 10.3390/toxins13070500.

[130] A. K. Jonscher, "Dielectric relaxation in solids," *J. Phys. Appl. Phys.*, vol. 32, no. 14, pp. R57–R70, July 1999, doi: 10.1088/0022-3727/32/14/201.

[131] M. M. El-Nahass, H. A. M. Ali, M. Saadeldin, and M. Zaghllol, "AC conductivity and dielectric properties of bulk tungsten trioxide (WO3)," *Phys. B Condens. Matter*, vol. 407, no. 22, pp. 4453–4457, Nov. 2012, doi: 10.1016/j.physb.2012.07.043.

[132] C. Thirmal, S. D. Ramarao, L. S. Rao, and V. R. K. Murthy, "Study of structural, dielectric and AC conductivity properties of SrMoO4," *Mater. Res. Bull.*, vol. 146, p. 111618, Feb. 2022, doi: 10.1016/j.materresbull.2021.111618.

[133] A. H. Bashal, N. S. Alkayal, J. Aslam, and K. D. Khalil, "Investigation of structure, dielectric properties, and AC conductivity at high temperature for chitosan capped metal oxides nanocomposites," *J. Taibah Univ. Sci.*, vol. 19, no. 1, p. 2490411, Dec. 2025, doi: 10.1080/16583655.2025.2490411.

[134] A. Syifaurrahma, A. Arnelli, and Y. Astuti, "LiOH/Coconut Shell Activated Carbon Ratio Effect on the Electrical Conductivity of Lithium Ion Battery Anode Active Material," *Molekul*, vol. 16, no. 3, p. 235, Nov. 2021, doi: 10.20884/1.jm.2021.16.3.805.

[135] Y. Şafak-Asar, T. Asar, Ş. Altındal, and S. Özçelik, "Investigation of dielectric relaxation and ac electrical conductivity using impedance spectroscopy method in (AuZn)/TiO2/p-GaAs(110) schottky barrier diodes," *J. Alloys Compd.*, vol. 628, pp. 442–449, Apr. 2015, doi: 10.1016/j.jallcom.2014.12.170.

[136] Aakansha, B. Deka, S. Ravi, and D. Pamu, "Impedance spectroscopy and ac conductivity mechanism in Sm doped Yttrium Iron Garnet," *Ceram. Int.*, vol. 43, no. 13, pp. 10468–10477, Sept. 2017, doi: 10.1016/j.ceramint.2017.05.089.

[137] M. A. Al-Ghouti and D. A. Da'ana, "Guidelines for the use and interpretation of adsorption isotherm models: A review," *J. Hazard. Mater.*, vol. 393, p. 122383, July 2020, doi: 10.1016/j.jhazmat.2020.122383.

[138] S. Azizian and S. Eris, "Adsorption isotherms and kinetics," in *Interface Science and Technology*, vol. 33, Elsevier, 2021, pp. 445–509. doi: 10.1016/B978-0-12-818805-7.00011-4.

[139] M. M. Sabzehmeidani, S. Mahnaee, M. Ghaedi, H. Heidari, and V. A. L. Roy, "Carbon based materials: a review of adsorbents for inorganic and organic compounds," *Mater. Adv.*, vol. 2, no. 2, pp. 598–627, 2021, doi: 10.1039/D0MA00087F.

[140] M. Náfrádi, G. Veréb, D. S. Firak, and T. Alapi, "Photocatalysis: Introduction, Mechanism, and Effective Parameters," in *Green Photocatalytic Semiconductors*, S. Garg and A. Chandra, Eds., in Green Chemistry and Sustainable Technology. , Cham: Springer International Publishing, 2022, pp. 3–31. doi: 10.1007/978-3-030-77371-7_1.

[141] U. G. Akpan and B. H. Hameed, "Parameters affecting the photocatalytic degradation of dyes using TiO2-based photocatalysts: A review," *J. Hazard. Mater.*, vol. 170, no. 2–3, pp. 520–529, Oct. 2009, doi: 10.1016/j.jhazmat.2009.05.039.

[142] M. Nemiwal, T. C. Zhang, and D. Kumar, "Recent progress in g-C3N4, TiO2 and ZnO based photocatalysts for dye degradation: Strategies to improve photocatalytic activity," *Sci. Total Environ.*, vol. 767, p. 144896, May 2021, doi: 10.1016/j.scitotenv.2020.144896.

[143] M. Aslam, I. M. I. Ismail, N. Salah, S. Chandrasekaran, M. T. Qamar, and A. Hameed, "Evaluation of sunlight induced structural changes and their effect on the photocatalytic activity of V2O5 for the degradation of phenols," *J. Hazard. Mater.*, vol. 286, pp. 127–135, Apr. 2015, doi: 10.1016/j.jhazmat.2014.12.022.

[144] I. A. Mkhalid, A. A. Ismail, M. A. Hussein, and R. H. M. Al Thomali, "Visible-light-induced V2O5 -TiO2 photocatalysts with high photocatalytic ability for degradation of tetracycline," *Opt. Mater.*, vol. 135, p. 113263, Jan. 2023, doi: 10.1016/j.optmat.2022.113263.

[145] M. M. Khan, S. F. Adil, and A. Al-Mayouf, "Metal oxides as photocatalysts," *J. Saudi Chem. Soc.*, vol. 19, no. 5, pp. 462–464, Sept. 2015, doi: 10.1016/j.jscs.2015.04.003.

[146] Y. Wang, W. Yang, X. Chen, J. Wang, and Y. Zhu, "Photocatalytic activity enhancement of core-shell structure g-C3N4@TiO2 via controlled ultrathin g-C3N4 layer," *Appl. Catal. B Environ.*, vol. 220, pp. 337–347, Jan. 2018, doi: 10.1016/j.apcatb.2017.08.004.

[147] W.-K. Jo and T. S. Natarajan, "Influence of TiO2 morphology on the photocatalytic efficiency of direct Z-scheme g-C3N4/TiO2 photocatalysts for isoniazid degradation," *Chem. Eng. J.*, vol. 281, pp. 549–565, Dec. 2015, doi: 10.1016/j.cej.2015.06.120.

[148] Z. Sun, Z. Yu, Y. Liu, C. Shi, M. Zhu, and A. Wang, "Construction of 2D/2D BiVO4/g-C3N4 nanosheet heterostructures with improved photocatalytic activity," *J. Colloid Interface Sci.*, vol. 533, pp. 251–258, Jan. 2019, doi: 10.1016/j.jcis.2018.08.071.

[149] J. Pasquet, Y. Chevalier, J. Pelletier, E. Couval, D. Bouvier, and M.-A. Bolzinger, "The contribution of zinc ions to the antimicrobial activity of zinc oxide," *Colloids Surf. Physicochem. Eng. Asp.*, vol. 457, pp. 263–274, Sept. 2014, doi: 10.1016/j.colsurfa.2014.05.057.

[150] A. Yousef, M. M. El-Halwany, N. A. M. Barakat, M. N. Al-Maghrabi, and H. Y. Kim, "Cu0- doped TiO2 nanofibers as potential photocatalyst and antimicrobial agent," *J. Ind. Eng. Chem.*, vol. 26, pp. 251–258, June 2015, doi: 10.1016/j.jiec.2014.11.036.

[151] Y. Li, W. Zhang, J. Niu, and Y. Chen, "Mechanism of Photogenerated Reactive Oxygen Species and Correlation with the Antibacterial Properties of Engineered Metal-Oxide Nanoparticles," *ACS Nano*, vol. 6, no. 6, pp. 5164–5173, June 2012, doi: 10.1021/nn300934k.

[152] M. M. Khan, S. N. Matussin, and A. Rahman, "Recent development of metal oxides and chalcogenides as antimicrobial agents," *Bioprocess Biosyst. Eng.*, vol. 46, no. 9, pp. 1231–1249, Sept. 2023, doi: 10.1007/s00449-023-02878-

Chapter III

Synthesis, Crystallographic Profiling, Core-Shell Electronic Configurations, Investigations of Frequency-Dependent Dielectric Characteristics, Adsorption and Antimicrobial Studies of Sb_2O_3-V_2O_5 Micro Ceramics

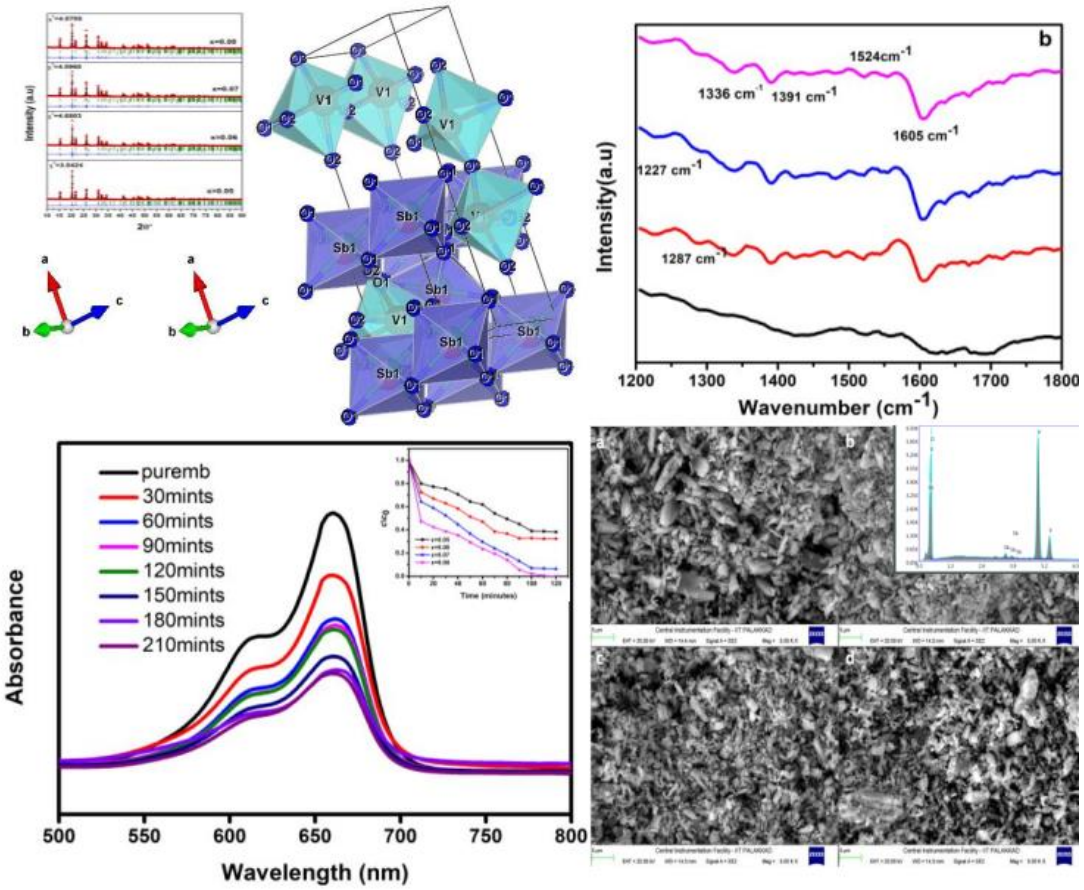

***Melethil Sabna**, K Safna, Sona C P, P Jayaram, Surface-Modified Mesoporous $V_{2-x}Sb_{2x}O_{5-\delta}$ Ceramics for Improving the Electrostatic Chemisorption of Methylene Blue, Chemistry Select 9 (29), e202400862, https://doi.org/10.1002/slct.202400862, 29/2024*

***Melethil Sabna**, Peediyekkal Jayaram, K. Safna, Riyas K. M, Sona C. P, Crystallographic profiling, core-shell electronic configurations, and investigations of frequency-dependent dielectric characteristics of Sb_2O_3–V_2O_5 micro ceramics, Materials Chemistry and Physics, Volume 332, 2025, 130172, ISSN 0254-0584,* https://doi.org/10.1016/j. matchemphys.2024.130172

***Sabna Melethil**, Jayaram, P., Aneesa, K.R. Mujeeb Rahman. K. M, Investigations on the Antimicrobial Activity of V2–xSb2xO5–δ Compound Systems Against the Gram-Positive, Gram-Negative Bacteria, Penicillium, and Aspergillus niger Fungi, J Appl Spectrosc 92, 680–687 (2025).* https://doi.org/10.1007/s10812-025-01958-212

3.1. Introduction

Among the various oxides of vanadium, the orthorhombic phase of V_2O_5 (α-V_2O_5) is notable for its high degree of crystallinity and strong absorption in the ultraviolet (UV) and visible regions of the electromagnetic spectrum which renders α-V_2O_5 particularly suitable for use as a UV-blocking material in coatings and sunscreens, along with its widespread applications in photochromic and electrochromic devices, sensors, supercapacitors and Li-ion batteries [1-4]. The structure and properties of V_2O_5 are determined by the three types of oxygen atoms in its lattice: vanadyl oxygen atoms O(1), which are coordinated to a single vanadium atom, and bridging oxygen atoms O(2) and O(3), which are coordinated to two and three vanadium atoms, respectively. The equilibration of gas-phase oxygen with vanadium oxides leads to the formation of the intrinsic defect structure of V_2O_5, characterized by the presence of oxygen vacancies [5]. Oxygen vacancies are equilibrium defects in the vanadium pentoxide system that facilitate polaronic hopping transport via V^{4+} charge-compensating defects. These vacancies are generated at the surface and migrate into the bulk, with a corresponding reduction in metal cations.

During reoxidation, V_2O_5 replenishes these vacancies with oxygen from the gas phase, potentially at different sites, which then diffuses through the oxide lattice. The interaction of reacting molecules with the surface induces surface reconstruction, governed by the intrinsic defect structure of the solid and oxygen vacancies are generally considered the primary point defects in the V_2O_5 lattice [6-5]. The formation of oxygen vacancies in the V_2O_5 lattice results in the appearance of nonstoichiometry, which may be expressed by the formula $V_2O_{5-\delta}$ [5]. The addition of n-valent impurity cations, where n can be +2, +3, +4, +5, or +6 allows for the creation of compounds with different oxidation states, as these cations can either replace vanadium ions in the lattice or occupy interstitial sites [7-11]. Incorporating n-valent impurity cations into the layered vanadium pentoxide matrix, leveraging its capacity to accommodate nonstoichiometry, results in a versatile and promising area of research that produces multi-cation, phase-pure, and mixed-phase compounds with varied structural and

electrical properties, potentially leading to novel defect structures and applications. V_2O_5 based multi-cation compounds are thus used in solar cells, optoelectronic devices, electrochromic devices, microelectronics, gas detectors, and as antimicrobial agents [8], [10], [12].

Previous reports have elucidated the electrical conduction mechanism in V_2O_5-based materials, attributing it to the hopping of unpaired 3d1 electrons between V^{4+} and V^{5+} valence states, which contributes to AC conductivity [13]. Studies have also shown that doping with alkali metal oxides can alter vanadium's oxidation state, creating oxygen vacancies and altering electrical conductivity [14]. Structural changes, such as those induced by the addition of Bi_2O_3 and NiO have also been reported to impact dielectric constant and electrical conductivity [10], [15]. Notably, AC conductivity studies have consistently shown a decrease in conductivity with increasing MgO concentration in $V_{2-x}Mg_xO_{5-\delta}$ systems [16]. According to Savidh Khan et al., the incorporation of Li_2O into $V_{2-x}Li_xO_{5-\delta}$ samples resulted in an enhancement of both AC and DC conductivity at a temperature of 450°C, highlighting the increased hopping sites [17].

Amid its captivating practical uses, the adsorption and photocatalytic prowess of bulk V_2O_5 also make it a compelling candidate for effectively eliminating methylene blue, methyl orange, rhodamine 6G, acetone, crystal violet, and various other deleterious dyes and hydrocarbons from water [18]. The narrow band gap (of approximately 2.3–2.8 eV), high exciton energy, magnificent light absorption capacity, excellent carrier transportation, and electronic structure invigorate V_2O_5 as a favorable candidate for the adsorption mediated degradation of dyes [19]. Despite its strong catalytic properties, V_2O_5's performance can be hindered by a high recombination rate, low adsorption capacity for hydrophobic contaminants, and a tendency to aggregate, which leads to decreased adsoptive/photocatalytic efficiency due to heat conversion. To address these limitations, V_2O_5 is frequently combined with other metal oxides, inorganic semiconductors, and polymers. Ahmed Kangmenna et al [20] reported V_2O_5-functionalized starch grafted polyacrylonitrile (PAN) adsorbent to remove methylene blue dye from water. This method achieved

90% removal efficiency of methylene blue at pH 9 using an optimal dose of 200 mg in 50 mL of 50 mg/mL methylene blue solution. Bernice Y**.** Danu et al [21] also reported V_2O_5/chitosan graft sodium alginate nanocomposite for the adsorption of model dye, methyl violet, from water and the effects of adsorption parameters were investigated and analyzed by different adsorption isotherms [21]. V_2O_5 compounds intercalated with alkylimidazolium, the cation of an ionic liquid, exhibit lower adsorption capacities for dyes such as methyl orange and rhodamine B. However, their adsorption efficiency for methylene blue is higher, reaching 81 wt% within a short time frame, and they completely removed 10 ppm of methylene blue within 80 minutes [22]. Smriti Bansal et al [19] investigated the adsorption and photocatalytic properties of chitosan and its alkylated derivative integrated with vanadium pentoxide which was stabilized using gallic acid, specifically focusing on methylene blue.

According to a review of existing literature, V_2O_5-based compounds demonstrated optimal performance in the adsorption of methylene blue. Thus we chose methylene blue as the model pollutant in our studies. Methylene Blue (MB), a widely employed cationic thiazine dye in diverse industries and medical applications, showcases a stable structure due to its three aromatic rings, defying natural biological degradation processes. When these dyes interact with other pollutants in wastewater, they engender deleterious by-products that pose threats to both aquatic ecosystems and human well-being. Regrettably, water tainted with MB often reaches water bodies without undergoing proper treatment, exacerbating the environmental predicament and so these dyes are to be removed from wastewater for safety [23-27]. For this purpose, biological, physical as well and chemical methods like coagulation, flocculation, biodegradation, adsorption, ion exchange, photocatalysis, and advanced oxidation are usually used [28]. Among these methods, adsorption is recognized as one of the most efficient and cost-effective way, as it is easy to operate and can be adapted to various scales, from small laboratory setups to large industrial applications. Many adsorbents can be regenerated and reused, reducing waste and operating costs [29]. Adsorbents such as fly ash [30-31], charcoal [32], peat [33], sawdust [34], lignite [35], wood [36], chitosan [37], [21] have attracted greater interest, mainly because of their natural availability and low cost. In addition, graphene-based materials [25],

polymers [38], zeolites [39], and structurally and morphologically engineered semiconducting metal oxides like NiO [40], Fe_2O_3 [41], MnO_2 [42], ZnO [43], V_2O_5 [27], [44-45], Co_3O_4 [46], CuO [47-48] are another category of adsorbents/catalysts which possess better physicochemical stability when compared to classical adsorbents and have found various applications in the removal of cationic/anionic dyes [45], [27], [49], [51].

The bactericidal and fungicidal properties of metal oxide nanoparticles, such as CuO [52], ZnO [53], MgO [54], TiO_2[55], CeO_2 [56-57], V_2O_5 [58] and carbon nanotubes [59] have been extensively researched due to their potential applications in wastewater treatment and the preparation of practical application surfaces involving the production of reactive oxygen species (ROS) destroying genetic material within the micro-organism. Given the inefficacy of commercial antimicrobial drugs and the rapid spread of bacterial infections, these metal oxides offer promising solutions due to their non-toxicity, stability, direct bandgap, low cost, and excellent chemical and thermal stability, making them effective bactericidal agents [60]. Human pathogenic bacteria, including *Escherichia coli* (associated with diarrhea and urinary tract infections), *Staphylococcus* species (causing skin, bloodstream infections, and food poisoning), *Vibrio* species (responsible for acute intestinal diarrheal infections), and Pseudomonas species (linked to infections of the blood, ear, and eye), are known to cause a range of illnesses. The primary spoilage fungi include *Aspergillus sp., Fusarium sp., Penicillium sp., and Candida sp.,* which can produce toxic mycotoxins, posing significant health risks to humans and animals [58]. These fungi cause grain discoloration, alter chemical and nutritional properties, and reduce germination in plants. *Aspergillus* species, particularly *A. fumigatus, A. flavus, and A. niger*, are notorious for causing invasive aspergillosis, with high mortality rates. The rise of antifungal-resistant Aspergillus strains underscores the urgent need for novel antifungal therapies, potentially leveraging nanomaterials to combat resistant fungal pathogens [61]. In summary, the interaction of metal oxides (MOs) with the cell surface induces morphological alterations in the membrane, initiating the activation of membrane phospholipases. This enzymatic activity compromises the integrity of the outer membrane, leading to pore formation and subsequently releasing metal ions

(M^+) through both spontaneous processes and enzyme-mediated reactions. These ions penetrate the plasma membrane via ionic transport proteins and once internalized, M+ engage with various intracellular enzymes, inhibiting their function and triggering a cascade of metabolic disruptions. This series of events elevates intracellular reactive oxygen species (ROS) levels, causing oxidative stress, metabolic dysregulation, leakage of cellular components, and ultimately, cell death [62]. One of the promising metal cation studied is vanadium found in blood plasma at around 200 nM and in tissues at approximately 0.3 mg/kg, with higher concentrations in the liver, kidney, and bone, and while most dietary vanadium is excreted through feces, minimizing the risk of accumulation-related hazards. its various oxidation states play crucial roles in numerous biological functions, including respiratory and enzymatic activities, in both eukaryotes and prokaryotes [63].

Vanadium Pentoxide with pentavalent vanadium, with their high cytotoxicity and antitumor activity, hold significant therapeutic potential demonstrated in anti microbial, anti-diabetic properties, anti-cancer activity, leading to further investigation into their anti-angiogenic properties, and are extensively used in various biomedical applications including drug delivery, imaging, diagnosis, cell separation, purification, and cancer treatment [63]. P.Suma. et al. [64] elucidated the anti-cancer efficacy of vanadium pentoxide nanoparticles, demonstrating their activity against triple-negative breast cancer cells. Sunil Kumar et al. [65] highlighted the promising prospects of vanadium complexes as antitumor agents, noting their high selectivity and low toxicity, which surpass the limitations of conventional platinum-based chemotherapeutics. Vanadium complexes are also being increasingly recognized as potent metal-based antimicrobial agents, as reviewed in recent literature [66]. In another study, Ali J. Hadi et al. [67] showcased the antibacterial and anti-proliferative potential of V_2O_5 nanoparticles against MCF-7 breast cancer cells, further underscoring their therapeutic versatility. Moreover, Selvaraju Nivetha et al. [68] reported that nickel-doped vanadium pentoxide ($Ni@V_2O_5$) exhibits antibacterial potential and excellent cytotoxic activity against skin cancer cells, inducing apoptosis in B16F10 melanoma cells as well as in BALB/c mice models. Additionally, Sourav Das et al [63]. explored the anti-angiogenic properties of vanadium nanoparticles,

demonstrating both their in vitro and in vivo anti-cancer activities. Collectively, these findings underscore the diverse biomedical applications of vanadium compounds, positioning them as valuable candidates for next-generation therapeutic agents.

On an added account introduction of foreign cation to V_2O_5 is always a versatile area of research [69-71], and there are plenty of reports on Li, Ni, Bi, Co, Mn, and Mo-doped vanadium pentoxide systems creating single-phase as well as mixed-phase compounds, composites and alloys with enhanced physical and catalytic properties [7], [11], [72-73]. But there are no much reports on AC conductivity, dielectric studies, enhanced dye adsorption and antimicrobial studies of Sb incorporated V_2O_5 based multi-cation compounds synthesized through traditional high-temperature solid-state reaction technique.

The synthesis process involves the integration of trivalent antimony ions into an orthorhombic vanadium pentoxide matrix, following a formulated chemical empirical formula denoted as $V_{2-x}Sb_{2x}O_{5-\delta}$, where $0.05 \leq x \leq 0.08$. Crystallographic parameters were determined via X-ray diffraction (XRD) coupled with Rietveld refinement, providing detailed structural insights, while phonon modes and lattice vibrational dynamics were probed through Raman spectroscopy. Furthermore, electronic transitions and band-gap characteristics were systematically investigated using UV–visible absorption spectroscopy. Further elucidation of the structural morphology, the weight percentage of constituent atoms and elemental mapping were attained through Scanning Electron Micrograph (SEM) and Energy Dispersive X-ray Spectroscopy (EDS). A comprehensive analysis of textural characteristics and the adsorption properties of Sb-V-O catalysts for methylene blue, utilized for water purification, were conducted through N_2 adsorption isotherm studies, BET analysis, and FTIR spectra. This process involved a thorough examination of absorption spectra of catalyst-embedded MB dye solution using a UV–visible spectrophotometer. The adsorption kinetic studies and isotherm studies were carried out using the adsorption data. Alongside X-ray photoelectron spectroscopy was employed for determining elemental oxidation states, and AC conductivity and dielectric measurements were done for evaluating their electrical performance. Herein we also present an application

study of the compound involving comprehensive antimicrobial evaluations, elucidating its multifaceted properties and potential applications

3.2. Materials and Methods

$V_{2-x}Sb_{2x}O_{5-\delta}$ powders were synthesized by high temperature solid state reaction for $0.05 \leq x \leq 0.08$ using V_2O_5 (99.99% trace metal basis) and Sb_2O_3(99.99% pure,) as precursors from Sigma-Aldrich Chemicals Co. USA. As per Hume Rothery rules, the stoichiometric proportion of Sb_2O_3 solute is adjusted so as not to exceed 12% with respect to solvent concentration [75]. Initially, the materials were finely ground for 2 hours with an agate mortar and pestle before being transferred to alumina crucibles for calcination in a programmable high-temperature furnace at 550°C for 12 hours under controlled heat flow [76]. The finely ground powders were then compacted into circular disc pellets of 14 mm diameter with thicknesses of 2 mm using coaxial pressing and subsequent sintering at 650°C for 12 hours. Finally, the resulting pellets were ground again to achieve uniform powder samples. The ground powder was again compressed into a 1.5 mm thick, 13 mm diameter disk by adding poly vinyl alchohol (PVA) as the binder. After polishing, the pellet was positioned between two copper electrodes, and frequency-dependent measurements of capacitance, dissipation factor, impedance, and phase were recorded over a frequency range from 10 Hz to 1 MHz.

3.2.1. Adsorption experiments

Methylene Blue (MB, $C16H18ClN3S2{\cdot}3H_2O$, M.W: 319.85), from Merk Chemical Reagent Company, was used as received. The MB dye adsorption experiments of all samples were carried out in the dark. Firstly, the adsorbent concentration was optimized for 10 ppm Methylene Blue dye concentration. In a typical experiment ~ 75 mg and 50 mg of pristine V_2O_5 microcrystals were added to 50 mL of 10 ppm MB aqueous solution and 50 mg was the optimized adsorbent amount selected. The experiment was repeated for 50 mg of Sb-V-O compounds for dye solution concentration varying from 5 ppm to 40 ppm, with a step size of 5 ppm. To gauge MB adsorption onto microcrystals, beaker wall adsorption of the dye was examined without Sb-V-O catalysts as a reference followed by the assessment of dye

concentration changes spectrophotometrically with catalysts, at 664 nm within the Lambert-Beer regime. Dye removal percentage (R%) was determined using the specified equation.

$$R\% = \left(\frac{C_0 - C_e}{C_0}\right) X100 \quad (1)$$

Co and Ce are the initial and equilibrium concentrations of dye solution respectively in (mg/L) [23]. The amount of the adsorbed MB, qe (mg/g) was obtained using the equation given below

$$q_e = \frac{(C_0 - C_e)V}{m} \quad (2)$$

The variable 'm' represents the weight of the adsorbent in grams (g), and V indicates the solution volume in liters (L) [23], [77]. To gain insights into the intricate features of the adsorption process, researchers typically employ a range of kinetic models, including the pseudo–first–order, pseudo–second–order, Elovich, and Weber's intraparticle diffusion models. The first and second-order pseudo-kinetic models were used to assess the dynamics indicating whether the reaction process is chemical or physical and unveil a connection between the quantity of adsorbate eliminated and the duration needed for its removal from an aqueous solution. The pseudo-first-order model (PFO) was introduced under the assumption that the adsorption rate is directly related to the count of unoccupied adsorption sites. Here, the adsorption rate was calculated using the linear form of PFO [23] given by eqn (3)

$$\ln(q_e - q_t) = \ln(q_e) - k_1 t \quad (3)$$

where q_e (mg/g) and q_t (mg/g) denotes adsorption capacity at equilibrium and at time t respectively and K_1 (min^{-1}) is the first order rate constant. The pseudo-first-order model is typically employed for rapid adsorption, achieving equilibrium within 20-30 minutes, while the second-order model is reserved for slower adsorption mechanisms, as is the case in our study [50]. As documented in existing literature, the pseudo-second-order kinetic (PSO) model posits the occurrence of a chemisorption process and was introduced under the assumption that the adsorption rate is directly

proportional to the square of the unoccupied adsorption sites and the interactions between the adsorbate and adsorbents result from the adsorbate's robust binding to the surface of the adsorbent. The linear representation of this model can be expressed as equation 4 [50].

$$\frac{t}{q_t} = \frac{1}{k_2 q_e^2} + \frac{t}{q_e} \tag{4}$$

where k_2 is the pseudo-second-order rate constant (g mg^{-1} min^{-1})

The linear form of Intra Particle Diffusion model is given as

$$q_t = k_{id}\, t^{1/2} + C \tag{5}$$

where k_{id} is the intraparticle diffusion rate constant (mg g^{-1} $min^{-1/2}$), and C is a constant for any experiment (mg/g) The linear form of the Elvoich model of adsorption is given as,

$$q = \frac{1}{\alpha}\ln(\alpha\beta) + \frac{1}{\alpha}\ln(t) \tag{6}$$

α is the initial adsorption rate and β is the desorption constant during each experiment. The basic assumptions of the Elovich model are the increase in the activation energy with adsorption time and that the surface of the adsorbent was heterogeneous. The linear form is given in eqn. (6) is the most frequently applied form of the Elovich model, which has been successfully used for modeling the adsorption of metal ions and organic pollutants on adsorbents [78]. Mechanisms of adsorption encompass chemical adsorption, involving chemical bond formation, physical adsorption driven by Van der Waals forces, and ion exchange. Understanding these mechanisms is pivotal for designing both adsorbents and adsorption systems. Various investigative approaches such as modeling of adsorption equilibrium data, characterization of adsorbents pre- and post-adsorption, molecular dynamics studies, and density functional theory calculations have been employed. Among these, isotherm model-based data modeling is particularly prevalent and convenient, offering insights into maximum adsorption capacity, crucial for assessing adsorbent performance. The adsorption data obtained from 50 mg of Sb-V-O-8 compound in 5

ppm to 40 ppm (5 ppm step size) of MB dye solution was fitted to the Freundlich, Langmuir and Dubinin-Radushkevich (D-R)and Temkin adsorption isotherm models [21].

Langmuir isotherm model showcases a uniform surface adsorption. The linear form is [79]

$$\frac{c_e}{q_e} = \frac{c_e}{q_m} + \frac{1}{q_m}\frac{1}{K_L} \tag{7}$$

where Ce is the residual dye concentration at equilibrium (mg/L), q_e is the amount of MB removed at equilibrium per unit mass (mg/g), q_m is the monolayer adsorption capacity of the adsorbent and K_L is the Langmuir constant (L/mg). In Freundlich adsorption isotherm model the absorbates form a mono molecular layer as well as multilayer on the surface of the absorbent. The Freundlich model expression shows the heterogeneity of the surface of the molecules as well as the exponential distribution of active sites and their energies [79]. The linear equation is

$$log\ q_e = \frac{1}{n}\log c_e + \log K_F \tag{8}$$

where q_e is the quantity of dye adsorbed at equilibrium per unit mass (mg/g), C_e is the residual concentration at equilibrium (mg/L), K_F is the adsorbent capacity (mg/g)(L/mg) and 1/n is the heterogeneity factor. A linear plot of log q_e against log C_e determines the value of 1/n and K_F.

Dubinin-Radushkevich (D-R) isotherm is used to ascertain the mean free energy and nature of adsorption as to whether it is physical or chemical in nature. The linear form is:

$$\ln q_e = \ln q_{DR} - \beta\varepsilon^2 \tag{9}$$

where q_{DR} is the D-R maximum monolayer adsorption capacity (mg/g), β is the activity coefficient ($mol^2\ J^2$) related to the mean adsorption energy and ε can be estimated using the relation:

$$\varepsilon = RT\ln\left(1 + \frac{1}{C_e}\right) \tag{10}$$

where R is the molar gas constant (8.314 J/mol-K), T is the temperature (K) and Ce is the residual concentration of the adsorbate at equilibrium (mg/L). The mean free energy E, can be determined using

$$E = \frac{1}{\sqrt{2\beta}} \tag{11}$$

B and q_{DR} values can be obtained from a plot of ln q_e against ε^2. E is frequently applied to determine whether the adsorption is dominated by a physical process (E < 8 kJ·mol-1) or a chemical process (E > 8 kJ·mol^{-1}) [80].

The Temkin isotherm model posits a linear decrease in adsorption heat with increasing surface coverage, assuming uniform binding energy distribution up to a maximum value. It incorporates the impact of indirect adsorbate/adsorbate interactions and is valid only for an intermediate range of ion concentrations. The linear form of the Temkin isotherm model is given by the following [79], [80].

$$q_e = B \ln A + B \log C_e \tag{12}$$

q_e is the amount adsorbed at equilibrium(mg/g), c_e is the equilibrium concentration (mg/L), A is the Temkin isotherm constant in L/g, B=RT/b, B is the constant related to heat adsorption, b is the Temkin constant (J/mol), T is the absolute temperature in kelvin and R is the gas constant (8.314 J/mol-K).

3.2.2. Antimicrobial Studies

The antibacterial and antifungal activities of the Sb-V-O compound were evaluated against various microorganisms, including Gram-positive bacteria (Staphylococcus aureus, Bacillus cereus, Staphylococcus agalactiae), Gram-negative bacteria (Escherichia coli, Pseudomonas aeruginosa, Vibrio species), and fungi (Penicillium and Aspergillus niger). The antibacterial test was conducted using the agar well diffusion method on Mueller Hinton Agar (MHA) plates. Bacterial cultures were grown in Luria Bertani broth at 37°C for 24 hours to ensure purity. These cultures were then swabbed onto the MHA plates, and wells (6 mm in diameter) were created with sterile cork borers. The Sb-V-O compound, dissolved in DMSO at 5 mg/ml concentration was added to the wells at volumes of 50, 100, 150, and 200 µL. Streptomycin (10 µg) served as the positive control, while DMSO was used as the negative control. Following incubation at 37°C for 24 hours, the inhibition zones were

measured to evaluate antimicrobial activity. The minimum inhibitory concentration (MIC) was identified as the lowest concentration of the compound that prevented visible bacterial growth.

For antifungal testing, Penicillium and Aspergillus niger were inoculated into sterile saline and vortexed to achieve a uniform suspension, adjusted to a 0.5 McFarland standard. Sabouraud's dextrose agar (SDA) plates were prepared and sterilized. The Sb-V-O compound was transferred to sterile discs, which were placed onto the SDA plates along with Fluconazole as a positive control and a DMSO solvent disc as a negative control. After incubation, the inhibition zone diameters were measured. All tests were performed in triplicate, and average values were used for analysis.

3.3. Result and Discussion

3.3.1. Structural Analysis: X-ray Diffractogram

The XRD pattern of the samples shown in figure. 3.1, can be indexed as the orthorhombic V_2O_5 phase with excellent crystallinity (ICDD No. 41-1426) in *Pmmn* space group symmetry and all concentrations of $V_{2-x}Sb_{2x}O_{5-\delta}$ ($0.05 \leq x \leq 0.08$) are plotted along with the pure V_2O_5 [73]. The pattern exhibits distinct peaks at various 2θ angles, including 15.46°, 20.37°, 21.83°, 26.26°, 29.01°, 31.05°, 32.33°, 33.27°, 34.29°, 41.25°, 42.01°, 45.46°, 47.29°, 47.89° and 48.80°, corresponding to reflection directions along different crystal planes, such as (200), (001), (101), (110), (301), (400), (011), (111), (310), (002), (102), (411), (600), (302) and (012), respectively with prominent orientation along the thermodynamically stable surface (001) of V_2O_5 [81-82]. V_2O_5 has a unique crystal structure that is orthorhombic in shape, with lattice parameters of a = 11.48 Å, b = 3.58 Å, and c = 4.36 Å [73]. The crystal structure is composed of VO_5 pyramids arranged in alternating double chains along the b-axis. These chains are made up of pyramids facing up and pyramids facing down, connected laterally by bridging oxygens to form a sheet or ribbon in the a-b plane. The planes are held together by van der waals bonds, which are relatively weak, resulting in easy cleavage along these planes [83]. There are three different oxygen atoms, O1, O2, and O3, in a single layer of V_2O_5, and a weak vanadium-oxygen interaction is responsible for connecting adjacent V_2O_5 sheets, creating an interlayer space suitable for guest ions to intercalate [84]. As the mole fraction x increases, the XRD peaks show a shift

towards lower 2θ values. This shift is attributed to the substitution of Sb^{3+} cation at the vanadyl site, which induces lattice strain and causes an increase in the interplanar spacing. To compensate for this increase, the diffraction angle 2θ decreases, resulting in a shift of the position of 2θ towards lower angles after the substitution of Sb^{3+} [11]. The lattice parameters, grain size, micro-strain, and dislocation density were calculated and recorded in Table 3.1.

The Debye-Scherrer equation and the uniform deformation model, using the Williamson-Hall (W-H) plot, were employed for these estimations [85]. The addition of Sb^{3+} induces variations in the lattice constants, showing slightly expanded lattice along both a- and c-axes, and constant along the b-axis. The increase in lattice constants and strain in the substituted V_2O_5 lattice is attributed to the larger ionic radius of Sb^{3+}ions compared to V^{5+}. The accommodation of Sb^{3+} ions may stabilize the VO_5 layers and potentially improve the intercalation properties within the V_2O_5 layers [86]. Hence, the introduction of Sb_2O_3 into V_2O_5 results in the substitutional incorporation of Sb^{3+} ions into the vanadium position within the crystal lattice (CCDC: 2357624-2357627). The increase in molar concentration leads to a noticeable change in grain size within the micrometer range. This variation is primarily caused by the collective influence of lattice distortions, strain, and limited atom mobility during the process of grain growth [7].

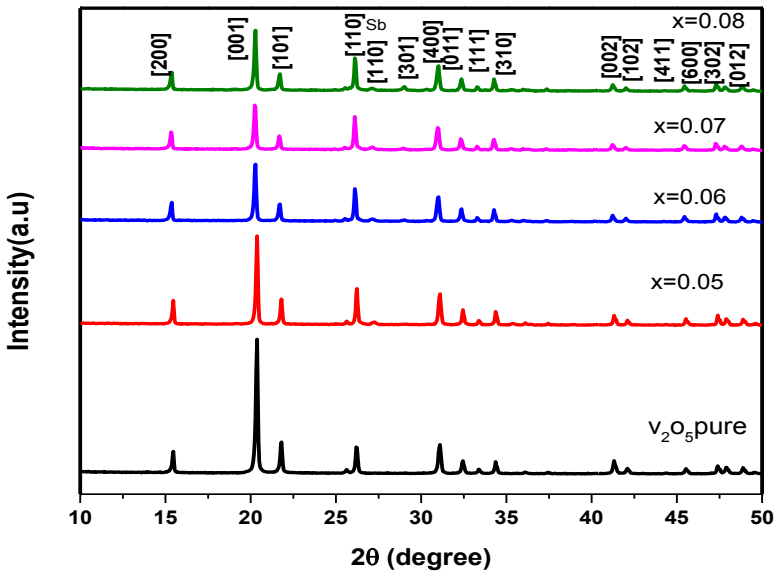

Figure.3.1: XRD pattern of $V_{2-x}Sb_{2x}O_{5-\delta}$ compounds for $0.05 \leq x \leq 0.08$ indicating orthorhombic structure in pmmn space group symmetry

Table.3.1: Structural parameters of $V_{2-x}Sb_{2x}O_{5-\delta}$ compounds estimated from Scherer equation and WH-plot

X values	***Sherrer Equation***		***Uniform Deformation Model, W-H plot***			***Lattice parameters***			**CCDC Number**
	Grain size D (nm)	***Dislocation Density (δ) × 10^{-3} nm^{-2}***	***Grain size D (nm)***	***Dislocation Density (δ) ×10^{-3} nm^{-2}***	***Micro strain (ε) ×10^{-3}***	***a(Å)***	***b(Å)***	***c(Å)***	
0.05	72.60	0.190	63.87	0.245	0.171	11.48	3.56	4.36	2357624
0.06	64.94	0.237	69.30	0.208	0.188	11.55	3.57	4.38	2357625
0.07	62.66	0.254	63.00	0.252	0.049	11.56	3.57	4.39	2357626
0.08	60.35	0.275	66.95	0.223	0.137	11.55	3.57	4.38	2357627

3.3.2. Rietveld Refinement using FULLPROF

For a more thorough structural analysis, Rietveld refinement was performed on the X-ray diffraction (XRD) data of the $V_{2-x}Sb_{2x}O_{5-\delta}$ compounds (where $0.05 \leq x \leq 0.08$). Figure 3.2(a) presents the graphical output of the Rietveld refinement, displaying both the experimental and calculated diffraction patterns. The calculations were performed over 15 cycles using FULLPROF software, with symmetry considerations for space group *Pmmn* (No. 59) and space group *P42/mnm* (No. 136). For the refinement process, the Thompson-Cox-Hastings pseudo-voigt* axial divergence asymmetry was employed as the peak shape function, as depicted in Figure 3.2(a) with red dotted lines. The refinement yielded a satisfactory alignment of the peak positions, encompassing the peak profile, atomic positions, lattice parameters, background parameters, instrument factors, and site occupancy parameters [74]. Table 3.2(b) displays the important reliability factors, like goodness factor (χ^2), R expected (R_{exp}), profile factor (R_p), and weighted profile factor (R_{wp}), which are employed in the quantitative analysis of X-ray diffraction (XRD) patterns using Rietveld refinement to assess how well the refined parameters and the proposed structural model explain the experimental results [87-88]. The final R_{wp} value should come close to R_{exp} but it should not exceed it. From the data, it is clear that R_{wp} is greater than R_{exp} and they are in good agreement, which indicates that the refined structure is credible [89].

At a molar fraction of x=0.05, the compound exhibited phase purity, displaying a well-defined orthorhombic crystal structure with symmetry consistent with the *Pmmn* space group. Although a low-intensity, indistinct peak associated with the $SbVO_4$ phase was observed at $2\theta=27.21^0$, its prominence remained minimal and increasingly diverged during refinement for x=0.05, indicating a negligible presence of the $SbVO_4$ phase. The χ^2 value for this composition excluding the $SbVO_4$ phase is notably lower at 3.04 compared to higher concentrations, suggesting that, x = 0.05 represents the solubility limit of Sb_2O_3 within the V_2O_5 matrix (Table 3.2(b)). However, as the molar fraction increases from x = 0.06 to 0.08, the appearance of the tetragonal $SbVO_4$ phase becomes more pronounced.

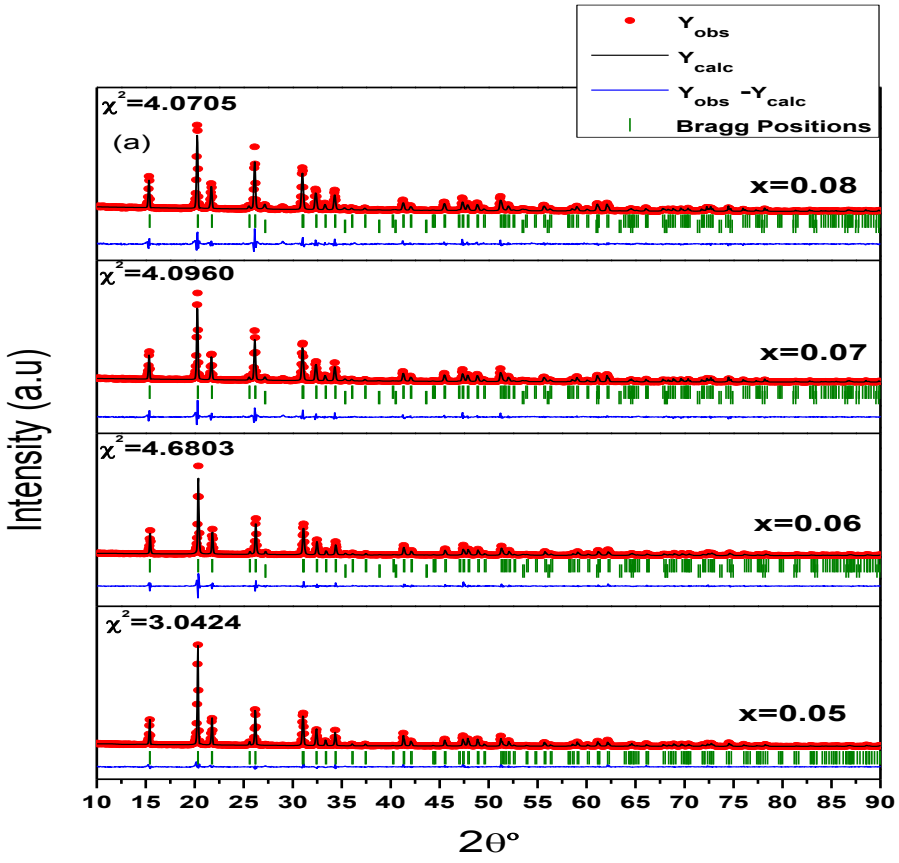

Figure.3.2 (a): Rietveld Refined XRD Pattern of $V_{2-x}Sb_{2x}O_{5-\delta}$ (0.05<=x<=0.08)

The compositional percentage of this secondary phase rises from 3.61% at x = 0.06 to 5.74% at x = 0.08, signifying a progressive deviation from phase purity and indicating the onset of phase separation as the solubility limit is exceeded. The refinement result indicates that the orthorhombic phase of V_2O_5 and tetragonal phase

of $SbVO_4$ coexist for mol fractions x=0.06, 0,07, 0.08, and χ^2 value of dual-phase refinement of the sample decreases again as the concentration of the Sb atoms increases (Table 3.2(b)). As the molar fraction x increases from 0.05 to 0.06, the lattice parameters and cell volume of the orthorhombic V_2O_5 phase decrease initially, allowing for the emergence of the distinct $SbVO_4$ phase at x=0.06.

With further increase in x from 0.06 to 0.08, a linear relationship develops between the molar fraction, lattice parameters and unit cell volume, in both the orthorhombic V_2O_5 and tetragonal $SbVO_4$ phases, reflecting a systematic structural adaptation in response to Sb incorporation (Table 3.2(a)). Table 3.2(c) presents the Miller indices (hkl) along with their corresponding 2θ values and microstructures of the prominent XRD reflections for $V_{2-x}Sb_{2x}O_{5-\delta}$ compounds at x=0.06.

Table.3.2(a) Structural Parameters, Cell volume & Compositional Percentage of Orthorhombic V_2O_5 and Tetragonal $SbVO_4$ obtained from Rietveld refinement of $V_{2-x}Sb_{2x}O_{5-\delta}$ for (0.05≤ x ≤0.08) compounds

Mol fraction x	V_2O_5 orthorhombic					$SbVO_4$ Tetragonal				
	Phase%	Lattice Parameter(Å)			Cell Volume (Å^3)	Phase%	Lattice parameters (Å)			Cell Volume (Å^3)
		a	b	c			a	b	c	
0.05	100	11.504	3.562	4.369	179.049	0	-	-	-	-
0.06	96.39	11.496	3.559	4.366	178.606	3.61	4.636	4.636	3.033	65.191
0.07	95.73	11.513	3.564	4.372	179.406	4.27	4.641	4.641	3.033	65.320
0.08	94.26	11.517	3.565	4.373	179.513	5.74	4.640	4.640	3.037	65.377

Figures 3.2(b) & 3.2(c) depicts the crystal structure obtained from the refinement of $V_{2-x}Sb_{2x}O_{5-\delta}$ (0.05≤x≤0.08) compounds at concentrations x=0.05 and x=0.08 respectively. Figure 3.2(b) represents orthorhombic V_2O_5 with space group *Pmmn* and in figure 3.2(c) the Orthorhombic phase of V_2O_5 with *Pmmn* space group and tetragonal phase of $SbVO_4$ with space group symmetry *P42/mnm* is found to coexist. The structure has edge and corner-sharing VO_5 octahedral square pyramidal shapes, with edge-sharing VO_6 octahedral pyramids sharing an edge having an opposite orientation in the b-direction. In contrast, corner-sharing pyramids have the same orientation [90]. The Wyckoff position, atomic coordinates, and occupancy of

each atom of Sb_2O_3-V_2O_5 ceramics with different concentrations are tabulated in Table 3.2(e). In V_2O_5 one vanadium atom is connected to six oxygen atoms with five bond lengths.

Table 3.2.(b) Reliability factors obtained from Rietveld refinement of XRD pattern of $V_{2-x}Sb_{2x}O_{5-\delta}$ ($0.05 \leq x \leq 0.08$) compounds

Mol fraction	Rietveld Refinement Parameters			
	χ^2	R_{exp}	R_{wp}	R_p
0.05	3.0424	10.89	19.0	20.4
0.06	4.6803	10.83	23.4	24.8
0.07	4.0950	12.40	25.3	28.7
0.08	4.0705	13.07	26.4	30.9

The vanadyl oxygen atom (O1), bridging oxygen atom (O3), coordinated oxygen atom (O2) and vanadium atom (V1) occupy 4f, 2a, 4f and 4f Wyckoff positions respectively [90]. At a low molar fraction of x=0.0, the $V_{2-x}Sb_{2x}O_{5-\delta}$ compound exhibits phase purity with an orthorhombic V_2O_5 structure, where the O1 atom at the 4f position is double-bonded to V1 along the c-axis, displaying the shortest bond length of approximately 1.604 Å. There is a nonlinear trend in the variation of this bond length with increase in mol fraction from x=0.05 to 0.08. The O3 atom at the 2a position, bonded to two vanadium atoms along the a-axis, shows a bond length of 1.784 Å for x=0.05, which decreases to 1.757 Å as x increases to 0.06, and then slightly increases as the molar fraction escalates.

The coordinated oxygen O2 at the 4f position forms two shorter bonds, V-$O2_1$ and V-$O2_2$, with lengths of 1.855 Å, which also decrease with rising x before increasing to around 1.876 Å at x=0.08. The longer V–O2 bond along the a-axis, initially 2.054 Å, follows a similar trend, first decreasing then increasing with the higher Sb molar fraction [91]. This behavior reflects how the orthorhombic V_2O_5 lattice adjusts to the incorporation of antimony, particularly at lower concentrations (x=0.05), where the structure remains intact but begins to show slight reductions in V–O bond lengths as Sb partially substitutes vanadium sites. When x reaches 0.06, a mixed-phase structure emerges, introducing the tetragonal $SbVO_4$ phase alongside

orthorhombic V_2O_5. Thus further incorporation of Sb induces local lattice strain, resulting in slight elongation of the V–O bonds as the lattice balances expansion and contraction forces.

Table.3.2(c). Prominent XRD reflections with Miller indices (hkl), corresponding 2θ values and microstructure of $V_{2-x}Sb_{2x}O_{5-\delta}$ compounds at x=0.06

SL. No	2θ°	(hkl)	Phase(Microstructure)
1.	15.46°	(200)	Orthorhombic V_2O_5
2.	20.37°	(001)	Orthorhombic V_2O_5
3.	21.83°	(101)	Orthorhombic V_2O_5
4.	26.26°	(110)	Orthorhombic V_2O_5
5.	27.21°	(110)	Tetragonal $SbVO_4$
5.	29.01°	(301)	Orthorhombic V_2O_5
6.	31.05°	(400)	Orthorhombic V_2O_5
7.	33.27°	(011)	Orthorhombic V_2O_5
8.	32.33°	(111)	Orthorhombic V_2O_5
9.	34.29°	(310)	Orthorhombic V_2O_5
10.	41.25°	(002)	Orthorhombic V_2O_5
11.	42.01°	(102)	Orthorhombic V_2O_5
12.	45.46°	(411)	Orthorhombic V_2O_5
13.	47.29°	(600)	Orthorhombic V_2O_5
14.	47.89°	(302)	Orthorhombic V_2O_5
15.	48.80°	(012)	Orthorhombic V_2O_5

Table 3.2 (d) Bond lengths of Orthorhombic V_2O_5 in $V_{2-x}Sb_{2x}O_{5-\delta}$ for ($0.05 \leq x \leq 0.08$)

Bond Length(Å)				
Bond Type	x=0.05	x=0.06	x=0.07	x=0.08
V-O2	1.855	1.854	1.869	1.876
V-O2	2.054	2.042	2.046	2.058
V-O3	1.784	1.757	1.764	1.784
V-O1	1.604	1.591	1.576	1.604

At higher Sb concentrations (x=0.07 to 0.08), the $SbVO_4$ phase becomes increasingly dominant, leading to a more systematic trend in bond length modifications within the orthorhombic V_2O_5 phase. Here, the lattice parameters exhibit a linear relationship with increasing x, resulting in gradual adjustments in V–

O1, V–O2, and V–O3 bond lengths. The bond length details for the orthorhombic V_2O_5 phase across all concentrations are summarized in Table 3.2(d) [91] [92].

Table.3.2(e) The Wyckoff positions, atomic positions, and occupancy of each atom of $V_{2-x}Sb_{2x}O_{5-\delta}$ ($0.05 \leq x \leq 0.08$) compounds

Mol fraction x	Atoms	Wyckoff Positions	Atomic coordinates			Occupancy
			x	y	z	
0.05	O2	4f	0.323	0.250	-0.009	0.500
	O3	2a	0.250	0.250	0.002	0.250
	O1	4f	0.146	0.250	0.472	0.500
	V1	4f	0.157	0.250	0.105	0.500
0.06	O2	4f	0.323	0.250	-0.011	0.641
	O3	2a	0.250	0.250	0.010	0.303
	O1	4f	0.144	0.250	0.469	0.601
	V1	4f	0.149	0.250	0.105	0.598
	O1	4f	0.704	0.704	0.000	0.286
	Sb1	2a	0.000	0.000	0.000	0.062
	V1	2a	0.000	0.000	0.000	0.062
0.07	O2	8g	0.321	0.250	-0.006	0.499
	O3	8g	0.250	0.250	0.00980	0.235
	O1	8g	0.143	0.250	0.46611	0.440
	V1	8g	0.148	0.250	0.10759	0.463
	O1	4f	0.311	0.311	0.00000	0.352
	Sb1	2a	0.000	0.000	0.00000	0.062
	V1	2a	0.000	0.000	0.00000	0.062
0.08	O2	8g	0.322	0.250	-0.00084	0.678
	O3	8g	0.250	0.250	0.00482	0.326
	O1	8g	0.142	0.250	0.46758	0.638
	V1	8g	0.148	0.250	0.10698	0.646
	O1	4f	0.303	0.303	0.00000	0.420

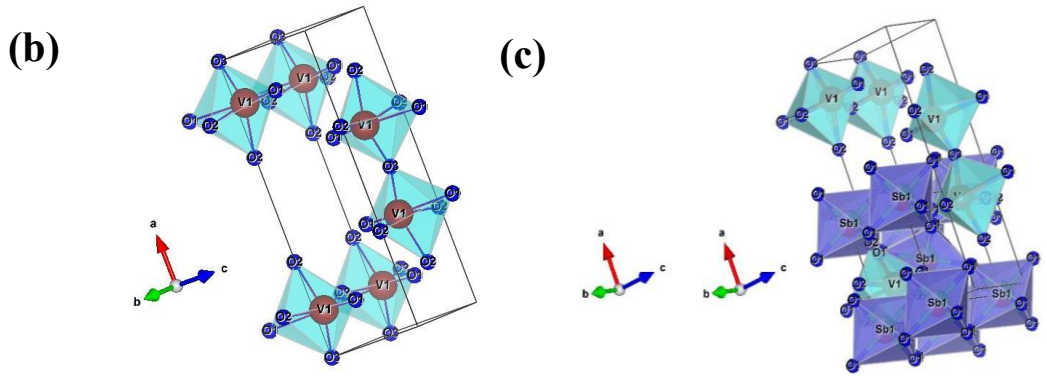

Figure 3.2 (b) Orthorhombic crystal structure of $V_{2-x}Sb_{2x}O_{5-\delta}$ compounds at x=0.05 (c) Orthorhombic V_2O_5 and Tetragonal $SbVO_4$ coexisting in $V_{2-x}Sb_{2x}O_{5-\delta}$ at x=0.08

3.3.3. Surface Morphology and Chemical Composition

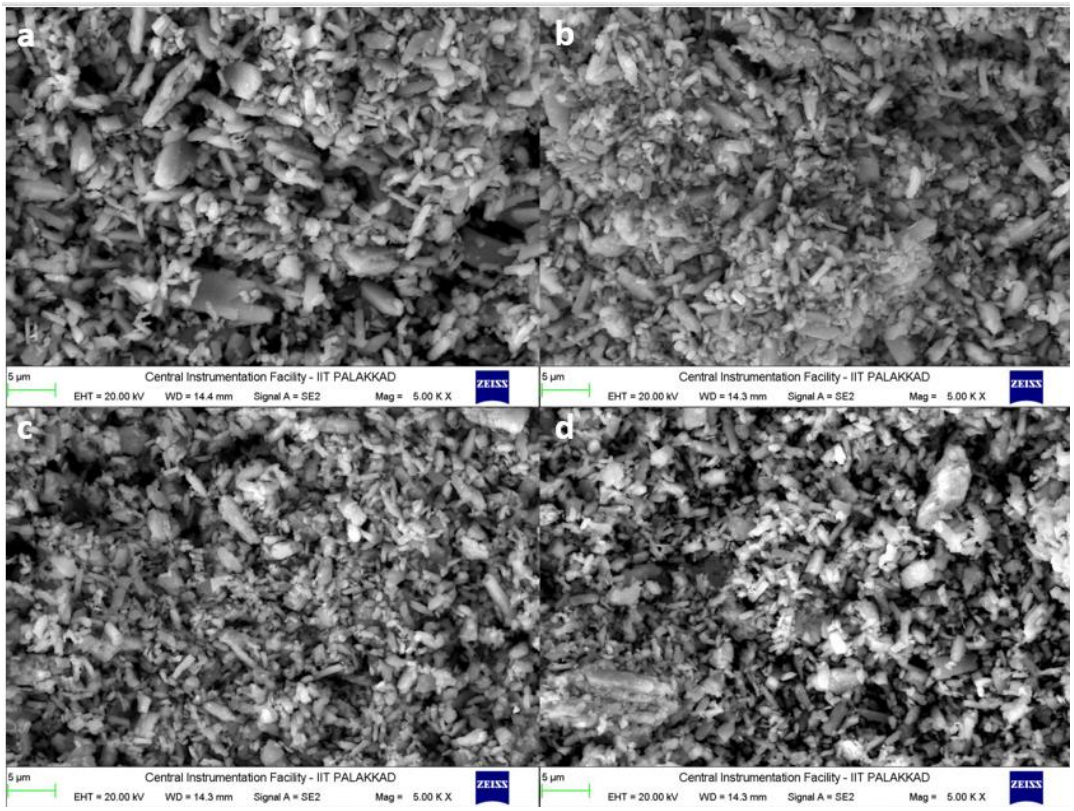

Fig. 3.3 Scanning Electron Micrographs of $V_{2-x}Sb_{2x}O_{5-\delta}$ compounds for $0.05 \leq x \leq 0.08$ showing the dense growth of plake and rod like particle (a) x=0.05 (b) x=0.06 (c) x=0.07 and (d) x=0.08

Morphological studies of Sb-V-O compounds were done by SEM microscopy. The SEM micrograph of $V_{2-x}Sb_{2x}O_{5-\delta}$ ($0.05 \leq x \leq 0.08$) compounds, (figure.3.3), reveals the presence of microrods of compact and dense morphology along with

randomly distributed flakes. The frequency polygon in Figure 3.4 shows up the particle size distribution in terms of diameter of the rods obtained through ImageJ software. For x=0.05, the average diameter of rods is 0.69 μm (Figure 3.4a) [93]. As the value of x increases, the diameter of rods shrinks and for the mol fraction x=0.06, rods have lowest diameter, that is 0.66 μm and are distributed more densely. The non-linear variation in the diameter of rods with mol fraction x can be attributed to the inhomogeneous mechanical ball milling and the agglomeration of rods is observed in higher concentrations. Comparing grain size calculated using XRD data and particle size from SEM, the as-prepared samples contain particles with polycrystalline microrod-like structures [94]. The micro rods are projected straight up and several non-ordered voids can be observed in the SEM micrograph, which can accommodate gas molecules and act as a porous material [95]. The elemental constituents obtained from the EDS spectrum (Table 3.3) revealed the weight ratios of the precursors in stoichiometric proportions as per the formulated chemical empirical formulae [82].

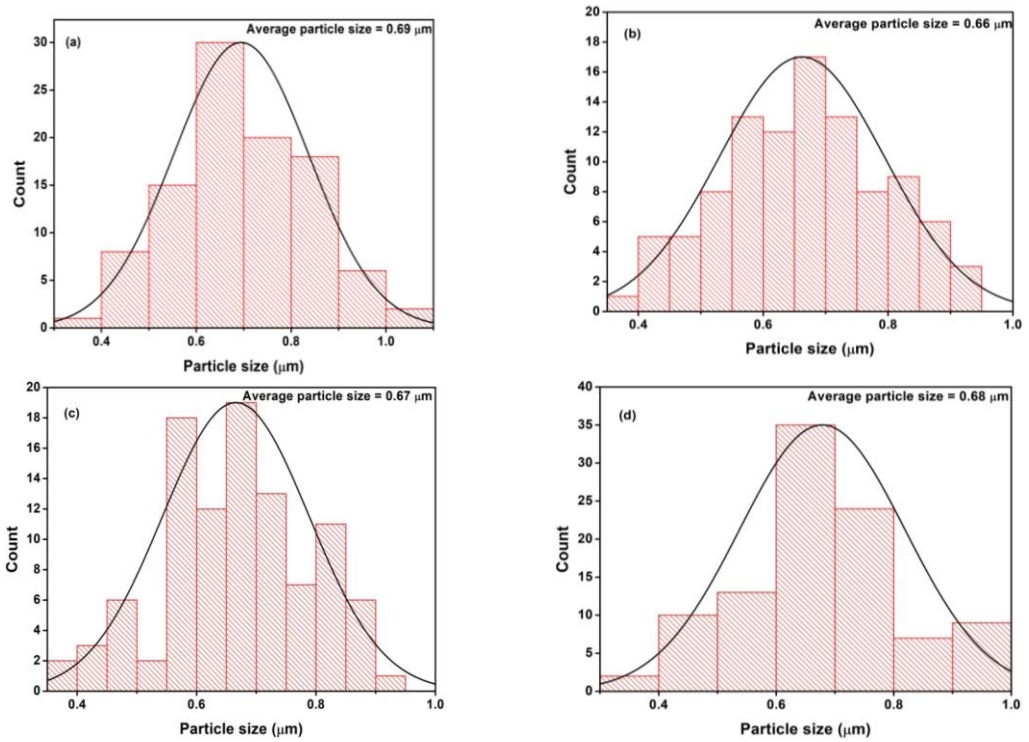

Figure. 3.4.(a,b,c,d) Average particle size of $V_{2-x}Sb_{2x}O_{5-\delta}$ compounds for $0.05 \leq x \leq 0.08$ from SEM images

Figure 3.5 shows the elemental scanning image of the Sb-V-O-8 compound, in which figure 3.5(a, b & c) indicate the presence of elements Vanadium, Oxygen, and Antimony, respectively, and figure 3.5(d) presents the EDS spectrum of the Sb-

V-O-8 compound system [60]. The elemental mapping results indicate that the estimates derived from the EDX measurements are consistent with the elemental compositions used in the study.

The EDX spectrum (Figure 3.5 d) of Sb-V-O microparticles displays characteristic peaks corresponding to vanadium (V), oxygen (O), and antimony (Sb). The absence of extraneous peaks in the EDS spectrum further confirms the compound's purity [74].

Table 3.3: Elemental Constituents $V_{2-x}Sb_{2x}O_{5-\delta}$ compounds obtained from the EDS spectrum

X values	**0.05**		**0.06**		**0.07**		**0.08**	
Elements	Wt %	At%	Wt %	At %	Wt %	At%	Wt %	At %
O	22.05	47.61	21.38	46.96	22.81	39.76	23.96	45.12
Sb	1.16	0.33	3.00	0.87	3.62	1.12	4.69	1.39
V	76.79	52.06	5.62	52.17	73.57	59.12	71.35	53.49

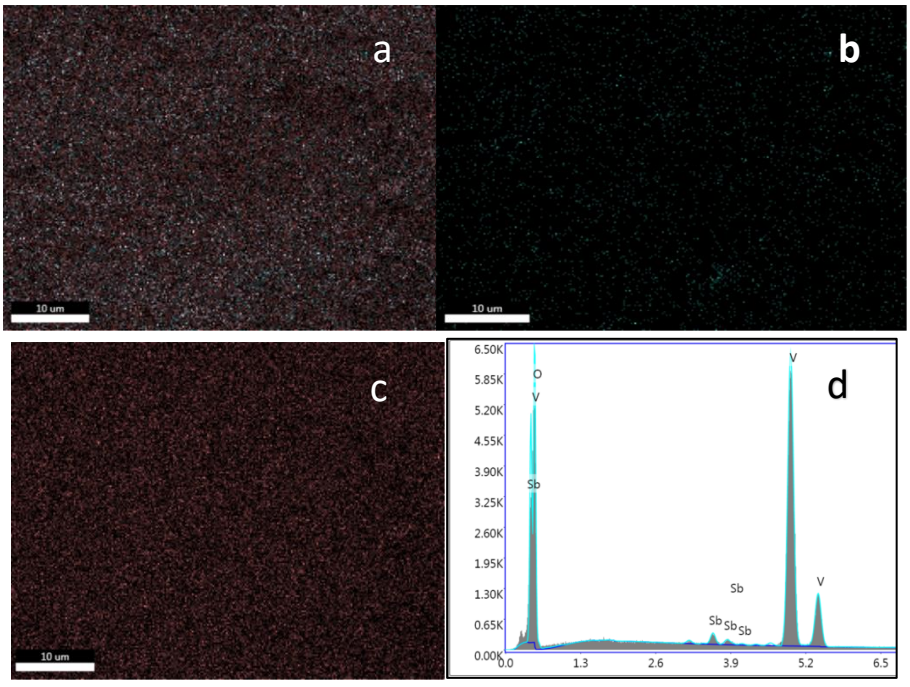

Figure.3.5. Elemental Mapping showing the presence of (a) Oxygen (b) Antimony (c) Vanadium and (d) EDS spectrum of $V_{2-x}Sb_{2x}O_{5-\delta}$ compounds for x=0.08

3.3.4. X-ray Photoelectron Spectroscopy

The elemental state and surface chemical composition of $V_{2-x}Sb_{2x}O_{5-\delta}$ compounds were investigated using X-ray Photoelectron Spectroscopy (XPS). The analysis of the narrow scans of core-shell electron emission spectra from the V*2p* region of vanadium, the Sb*3d* region of antimony, and the O*1s* spectra are illustrated in Figures 3.6 and 3.7. The absence of satellite peaks in the spectrum indicates that the synthesized Sb-V-O compound retains its stability, showing no notable chemical shifts or signs of decomposition. Figure 3.6(a) illustrates the asymmetrical V*2p* spectrum, featuring peaks at 517.23 eV and 524.78 eV, which correspond to the V$2p_{3/2}$ and V$2p_{1/2}$ energy levels, respectively [96]. The binding energy of the V$2p_{3/2}$ core level electron is influenced by the oxidation state of the vanadium cation. To identify the various oxidation states of vanadium cations in Sb_2O_3-V_2O_5 ceramics, curve fitting of the V$2p_{3/2}$ and V$2p_{1/2}$ XPS signals was performed using CASA XPS. Fig. 3.6(a) shows the result of the fitting in the Sb-V-O5 compound, showing up distribution of V^{5+}, V^{4+} ions.

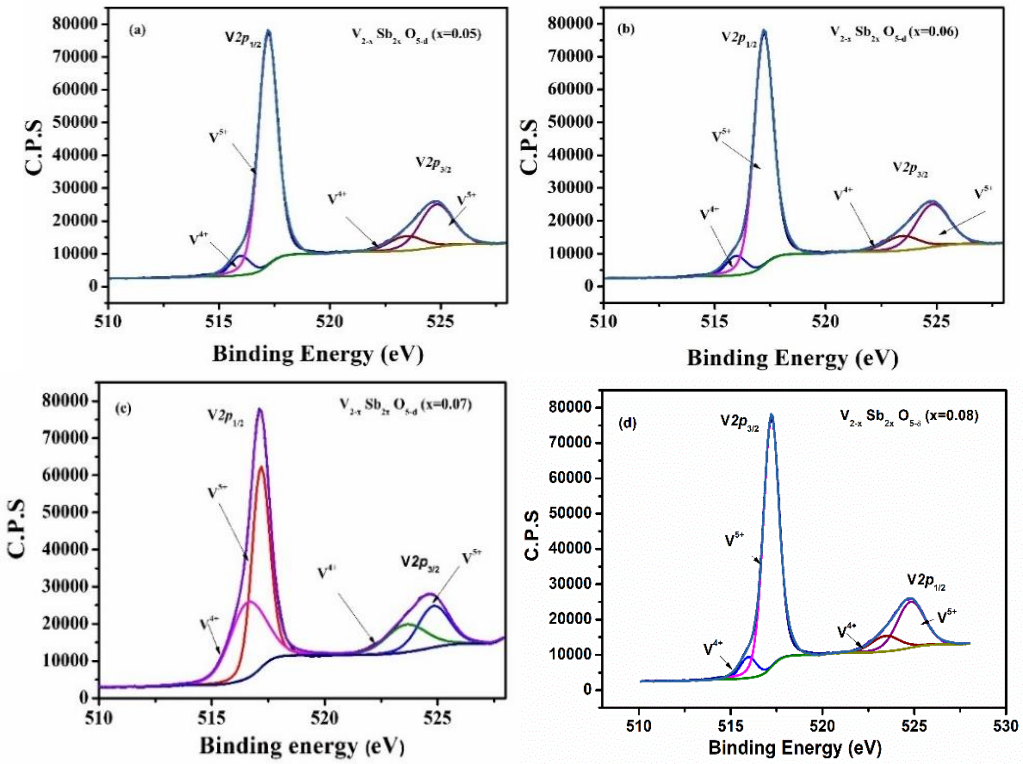

Figure.3.6: XPS spectra of V2p in $V_{2-x}Sb_{2x}O_{5-\delta}$ compounds at (a) 0.05, (b) 0.06, (c) 0.07, and (d) 0.08.

The deconvoluted spectral components reveal the presence of minor quantities of V^{4+} ions alongside a predominant population of V^{5+} ions, with their respective V2p$_{3/2}$ peak positions appearing at 517 eV and 516 eV. In the V$2p_{1/2}$ spectral state V^{4+} and V^{5+} ions are identified at 523.5eV and 524.86 eV. The V^{4+} ions identified from the deconvolution of V$2p_{3/2}$ and V$2p_{1/2}$ spectral states might be generated from the partial reduction of V^{5+} to V^{4+} during the solid-state reaction process. In Fig. 3.7, the asymmetrical peak centered around 530 eV and symmetrical peak at 540.4 eV correspond to the Sb $3d_{5/2}$ and Sb $3d_{3/2}$ binding energies, respectively. In the Sb-V-O-5 compound, the XPS spectrum (fig. 3.7a) displays a photoemission line at 530.12 eV, which is resolved into two distinct components: a line at 529.9 eV corresponding to the combined $Sb^{3+}3d_{5/2}$ and O$1s$ levels, indicating antimony ions in the +3 oxidation state, and a separate line at 530.9 eV, representing the O$1s$ electron exclusively [22], [97].

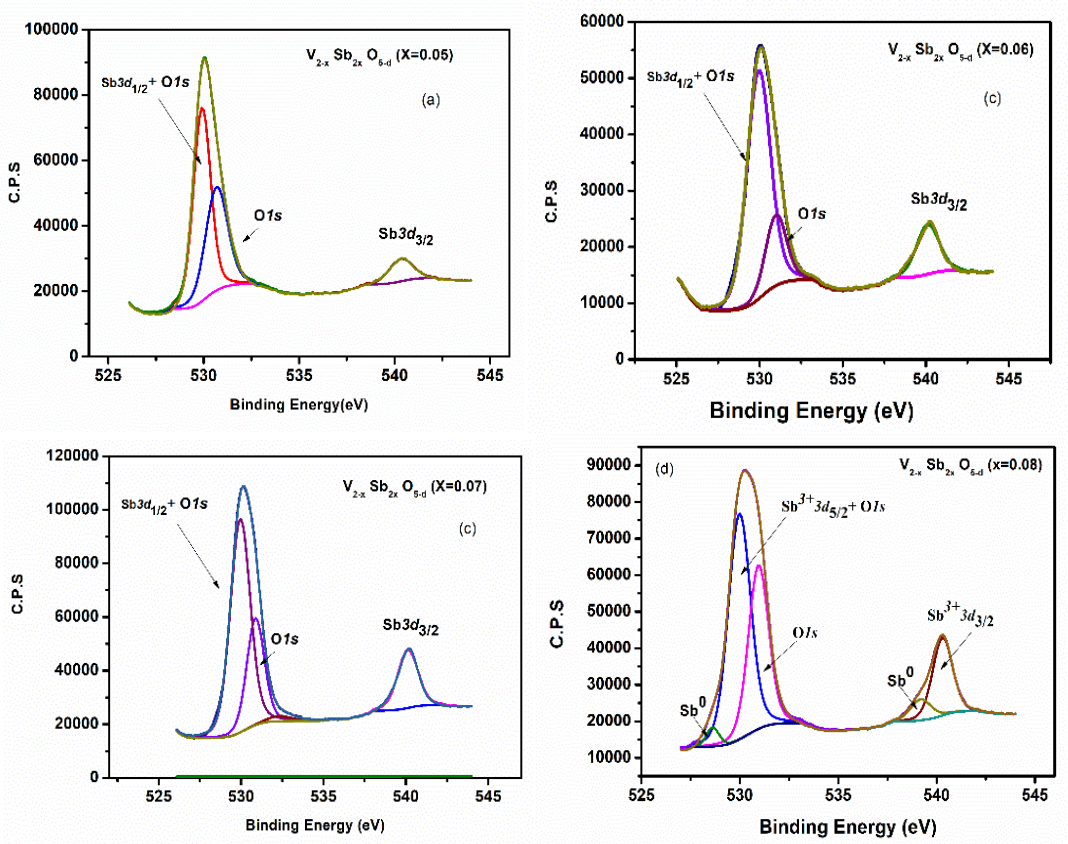

Figure 3.7: XPS spectra of Sb3d and O1s regions of $V_{2-x}Sb_{2x}O_{5-\delta}$ compounds at x=(a) 0.05, (b) 0.06, (c) 0.07 and (d) 0.08

The overlap of the Sb $3d_{5/2}$ binding energy with the O*1s* binding energy signals a substantial presence of antimony oxide, making the Sb $3d_{3/2}$ binding energy more reliable for chemical state analysis. In the Sb-V-O-5 compounds, the Sb $3d_{3/2}$ peak for Sb_2O_3 appears at 540.4 eV, indicating an oxidation state of +3 for Sb. This value is consistent with literature reports, which cite a similar binding energy of 539.35 eV [97-101].

The valence state of the Sb ions in the compound is confirmed as Sb^{3+} for all mole fractions from x=0.05 to 0.07(figures 3.7.a, b & c) in $V_{2-x}Sb_{2x}O_{5-\delta}$ compounds. Figure 3.7(d) presents the deconvoluted spectrum of Sb *3d* and O*1s* spectral levels in the Sb-V-O-8 compound indicating the photoemission lines at 528.6 eV (Sb$3d_{5/2}$) and 539.2 eV (Sb$3d_{3/2}$) attributed to the presence of metallic antimony as well (Sb^0) [96-97], [102-103]. In this study, the binding energies of V*2p*, Sb*3d*, and O*1s* in the Sb-V-O compounds showed a slight blue shift with increasing molar fraction x, attributed to the size effects of trivalent antimony as a foreign particle within the V_2O_5 host matrix. This shift is consistent with established findings in the literature [101], [104-105].

3.3.5. Raman Spectroscopy: Phase, crystallinity, and molecular interactions

Figure 3.8(a) represents the Raman spectra of the samples. The Raman peak position and intensity coincide with the reference peaks of the α-polymorphic phase of orthorhombic V_2O_5 material. Ten Raman bands observed at 102, 143, 197, 285, 307, 406, 482, 530, 703, and 998 cm^{-1} correspond to the Raman characteristic vibrations modes of the orthorhombic structure of V_2O_5 in the as prepared Sb-V-O ceramics and is in well agreement with the polycrystalline nature of the Sb-V-O layer. The major vibrational modes of V_2O_5 were in the range of 100–1100 cm^{-1}. This region consisted of 3 parts, including the V–O terminal stretching in the range of 520–1100 cm^{-1}, the V–O–V stretching region in the range of 300–500 cm^{-1}, and bending mode in the range of 200–300 cm^{-1}. In addition, the lattice vibrations were present at 150 cm^{-1} which is attributed to the crystalline nature of V_2O_5 [106]. Ten Raman active phonon modes attributed to the Sb-V-O compounds are represented as $V_{2-x}Sb_{2x}O_{5-\delta}$: Γ-Raman = $6\ A_g+2B_{1g}+1B_{2g}+1B_{3g}$.

In Figure 3.8, the prominent Raman peak observed at 143 cm^{-1} is attributed to the B_{3g} skeletal bending vibration mode, while the weaker intensity band at 102 cm^{-1},

corresponding to the Ag mode, provides evidence for the layered structure of the $V_{2-x}Sb_{2x}O_{5-\delta}$ compounds. Additional Raman peaks identified at 197 cm^{-1} and 287 cm^{-1} are ascribed to the A_g and B_{2g} modes, respectively, and are associated with the bending vibrations of the O-V-O bonds. Furthermore, the bands at 307 cm^{-1} and 703 cm^{-1} are linked to V-O bending and stretching vibrations in the A_g and B_{2g} modes, respectively. V-O-V bond's bending and stretching vibrations corresponding to the Ag modes are distinctly observed at 406 cm^{-1} and 530 cm^{-1}, reinforcing the vibrational characteristics of the compound's lattice structure. The Ag mode corresponding to the symmetric stretching of the V—O—V bridging bond was found at 482 cm^{-1} [106]. The other sharp peak located at 998 cm^{-1} originates from V=O stretching mode, which is also a confirmation for the layered structure of Sb-V-O ceramics [102]. No Raman bands associated with Sb-O vibration are observed in the figure 3.8(a).

As the compositional percentage of the V_2O_5 phase exceeds 94% for all concentrations, no significant Raman bands attributed to Sb can be excited in the Raman spectrum which was however evident in the XRD [74] (CCDC:2357624-2357627). The progressive reduction in peak intensity of the Sb-V-O Raman spectra, as illustrated in figure 3. 8(b), correlates with increasing concentrations of Sb dopant cations for all prominent Raman bands.

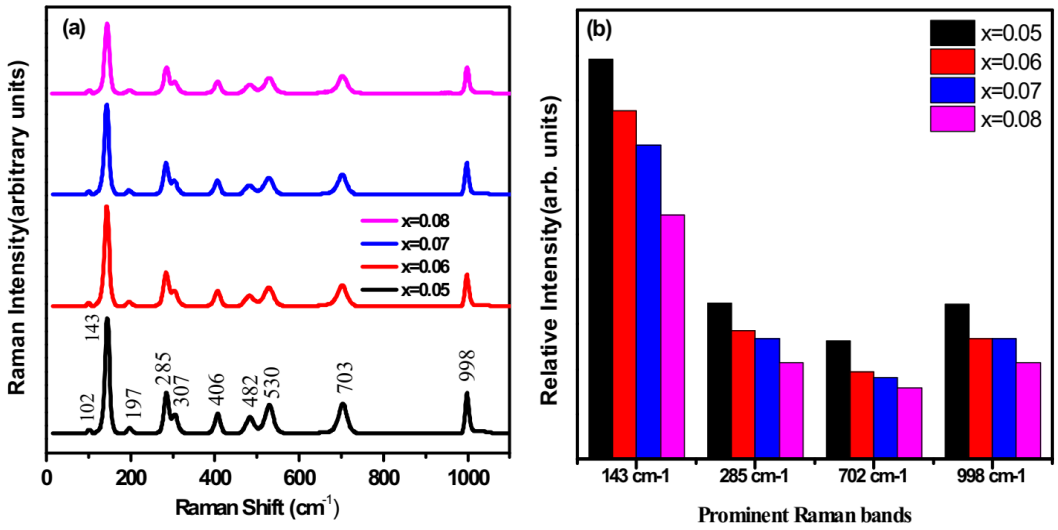

Fig.3.8. (a) Raman spectra and (b) The relative intensity of four prominent Raman bands at 143cm^{-1}, 285 cm^{-1}, 702 cm^{-1}, and 998 cm^{-1} in $V_{2-x}Sb_{2x}O_{5-\delta}$ for $0.05 \leq x \leq 0.08$.

This decline is likely due to a reduction in the aggregation and crystallinity of vanadium pentoxide species as the molar fraction (x) of Sb increases. The pronounced skeletal bending vibration at 143 cm^{-1}, along with the strong stretching vibration at 998 cm^{-1}, serves as a definitive fingerprint, confirming the presence of a well-ordered layered structure within the Sb-V-O matrix. Table 3.4 exhibits the comparison of the Raman bands observed in α-V_2O_5 [107], Bi-V_2O_5 [11], Ni-V_2O_5 [10], Cr-V_2O_5 [108], and the present Sb-V-O compound. The Sb-V-O Raman spectra thus exhibited only slight deviations from the characteristic vibrational modes of V_2O_5 corresponding to the increasing concentration of Sb^{3+} cations (Table 3.4) [102], [109].

Table 3.4: Comparison of Raman active phonon modes (in Wavenumbers, cm^{-1}) obtained for α-V_2O_5, Bi-V_2O_5, Ni-V_2O_5, Cr-V_2O_5, and experimental Raman data of Sb-V-O compound.

Mode	Single crystal of V_2O_5[107]		$V_{2-x}Bi_{2x}O_{5-\delta}$ cm^{-1}[11]	$V_{(1-x)2}Ni_{3x}O_{5-\delta}$ x=0.04 cm^{-1}[10]	$Cr_{0.1}V_2O_5$ cm^{-1} [108]	Sb-V-O x=0.05 cm^{-1}
	Experimental cm^{-1}	Calculate cm^{-1}				
A_g	104	97	98	99	-	102
	304	315	304	302	303	307
	404	406	406	406	406	406
	480	489	480	476	483	482
	526	527	528	527	527	530
	994	1001	997	995	995	998
B_{1g}	146	149	143	142	143	143
	700	700	702	700	698	703
B_{2g}	200	191	196	193	196	197
	-	848	-	856	-	-
B_{3g}	280	297	283	283	282	285
	701	701	-	787	-	-

3.3.7 Optical Analysis: UV- Visible Spectroscopy

Pure V_2O_5 is a semiconductor characterized by an ionic configuration, with occupied O*2p* orbitals and vacant V*3d* orbitals in its band structure, with a band gap of 2.3eV. This structure gives rise to three distinct bands above the valence band (O*2p* states), which include V*3d* states, V*3d* split-off states, and mid-gap states. A strong deviation of VO_6 octahedra from the cubic coordination led to a narrow split-off conduction band [110]. These states exhibit varying electron transition properties and when Sb_2O_3 is doped in V_2O_5 the coexistence of different valence phases can occur, such as a mixture of V^{4+}, V^{5+} along with Sb^{3+} phases.

This will influence factors like morphology, ionic configuration and carrier trap centers that will eventually lead to alterations in the absorption band [111]. The diffuse reflectance spectra of $V_{2-x}Sb_{2x}O_{5-\delta}$ compounds for $0.05 \leq x \leq 0.08$ are shown in figure 3.10(a). All compounds shows intense absorption in visible region (400–520 nm) with slight blue-shift in the absorption threshold edge, with increase in concentration of antimony ions. Band gap energy of the samples is obtained from the Kubelka–Munk model [10] (eqn. 13),

$$[F(R_\infty)h\upsilon]^2 = A(h\upsilon - Eg) \tag{13}$$

where R is the absolute reflectance of the samples. The Kubelka monk plot of $V_{2-x}Sb_{2x}O_{5-\delta}$ compounds for $0.05 \leq x \leq 0.08$ is shown in figure 3.10(b). The energy band gap of Sb-V-O samples rises proportionally with an increase in Sb ion concentration. The introduction of trivalent Sb ions into the V_2O_5 lattice is anticipated to create impurities with energy levels resulting from the hybridization of Sb's *5p* orbitals and oxygen's *2p* orbital, situated between the valence band (VB) and conduction band (CB).

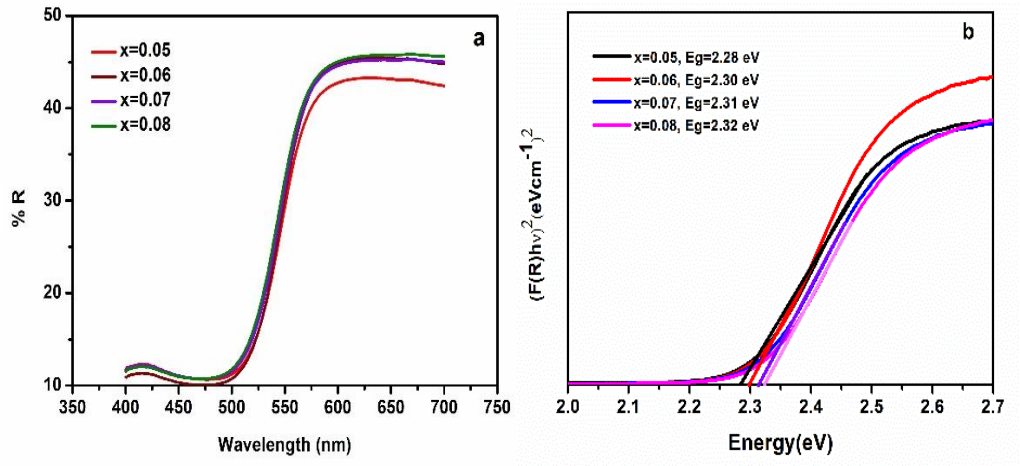

Figure.3.10. (a) Diffuse Reflectance Spectra obtained from the Sb-V-O compounds for various x values (b) Showing the optical band gap estimated using K-M theory

Consequently, alterations in optical absorption are due to the emergence of band edge states induced by the bonding and antibonding molecular Sb–O orbitals. The Sb ions occupying vanadyl site in the O=V=O double bonds, will have deficiency of electrons making holes as the majority carriers. As the mole

fraction x increases from 0.05 to 0.08, a large number of holes are created, dragging fermi level down, below the top of the valence band. As a result, the band gap energy experiences a slight increase from 2.28-2.32 eV with a rise in Sb ion concentration. The shift in the band gap, however, is marginal, likely attributable to the low doping rates. Nevertheless, the impact of the foreign cation, Sb is clearly manifested in the structural and electronic properties of V_2O_5. Here, this leads to altered optical gap with $E_g = E_{g0} + \Delta E_g$, where E_{g0} is the optical band gap of pure V_2O_5, and ΔE_g is the Burstein Moss shift due to the presence of Sb^{3+} ions [112-113].

3.3.6. Photoluminescence Spectroscopy

The photoluminescence characteristics of V_2O_5 are widely recognized for their sensitivity to imperfections present in the materials. Within V_2O_5 materials, the photoluminescence phenomenon encompasses both phosphorescence and fluorescence, with their respective values being linked to the vibrational states of the V=O double bond. Specifically, when light shines on a V=O double bond situated on the surface, an electron is transferred from oxygen to vanadium ions, which leads to the formation of excited singlet and triplet states. These states subsequently recombine with the ground hole states, resulting in the fluorescence and phosphorescence processes [114].

PL spectroscopy was carried out on $V_{2-x}Sb_{2x}O_{5-\delta}$ compounds, to confirm the band gap energy, electron-hole pair generation dynamics and electron-trapping due to defects production by doping [115]. V_2O_5 has a V*3d* split-off conduction band structure with gap widths of 0.6 eV and 0.75 eV from the higher conduction band level. Oxygen vacancies (V−O2) are the most significant defects in the V_2O_5 crystal and lead to the wide formation of defect levels between the conduction band and the valance band [116]. Therefore, many recombination paths have been identified among the conduction band, valence band and defect levels. The conduction band and valence band of V_2O_5 contribute to the *3d* bands of vanadium (V*3d*) and the *2p* bands of oxygen (O*2p*), respectively [117]. Figure 3.9(a,b,c & d) depicts the room temperature photoluminescence spectra of $V_{2-x}Sb_{2x}O_{5-\delta}$ compounds recorded from 400 to 600 nm at an excitation wavelength of 330 nm.

The PL emission spectrum of V_2O_5 exhibits prominent bands, including a blue-green emission at 450 nm, 466 nm, 481 nm, and 492 nm, as well as a broad green emission at 546 nm and 564 nm. The emissions at 450 nm, 466 nm, 481 nm, and 492 nm are attributed to band-to-band transitions, specifically involving electronic transitions from the shallow donor levels of vanadium interstitials to the valence band [118-119]. The defect formations due to the induction of foreign Sb atoms catalysis the splitting of such bands in Sb_2O_3-V_2O_5 ceramics and more peaks are observed in this region with slightly varying intensities. The strong PL emissions at 546 nm and 564 nm which is created by point defects correspond to the radial recombination of the electron-hole pair from the lowest split-off V*3d* conduction bands to the top of the O*2p* valence bands [118-120]. T.K. Le et al. [121] identified a photoluminescence peak at 530 nm (2.34 eV) in V_2O_5, attributing it to the band edge transition consistent with its bandgap energy range of 2.3–2.4 eV. In Sb-V-O compounds, the corresponding PL peaks are observed at 563–564 nm (2.20 eV) and 540–546 nm (2.27–2.29 eV), indicating band edge transitions in Sb-incorporated V_2O_5 compounds with a bandgap energy of 2.2–2.3 eV.

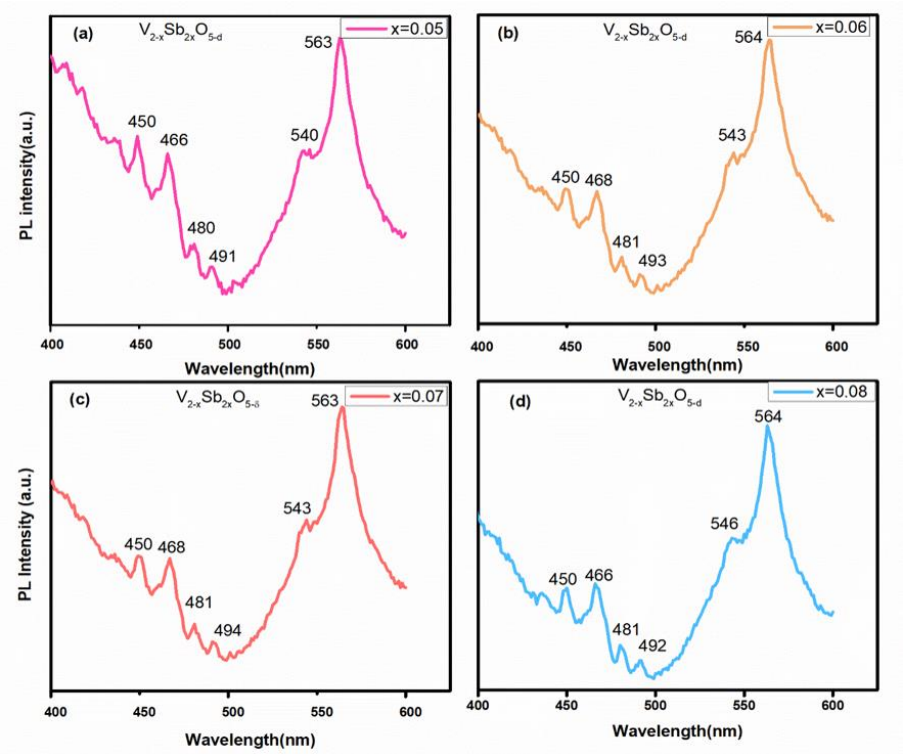

Figure. 3.9. Photoluminescence spectrum of $V_{2-x}Sb_{2x}O_{5-\delta}$ compounds for (a)x=0.05 (b)x=0.06 (c)x=0.07 & (d)=0.08

This aligns with the bandgap values derived from Kubelka-Munk plots for Sb-V-O compounds, as reported in prior studies [74]. The slight shifting in the band edge peak with increase in the Sb ions (increase in x value) confirmed the existence of doping states of V_2O_5.

3.3.8 Adsorption studies of Sb-V-O compounds

The potential of Antimony Trioxide (Sb_2O_3) to enhance the capacity of V_2O_5 to adsorb methylene blue is investigated here. To initiate the investigation, the absorbance spectra of pristine 50 mg and 75 mg V_2O_5 powders were determined as catalysts, in 50 ml Methylene Blue dye solutions with a concentration of 10 ppm. Within 210 minutes, an efficacy of 60% and 65% in dye removal was respectively observed for the samples. The absorbance spectrum of the 50 mg V_2O_5 catalyst under these conditions is illustrated in figure 3.11(a), leading to the optimized condition of concentration of Sb-V-O compounds as 50 mg. The experiment is standardized by fixing 50 mg of Sb-V-O microcrystals to 50 ml of a 10 ppm Methylene Blue aqueous solution for the adsorption kinetic studies. This solution had an initial concentration of 2.3×10^{-5} M, a basic *pH* of 7.5, and was maintained at room temperature. Magnetic stirring at 1000 rpm for 10 minutes ensured proper dispersion of Sb-V-O powder within the dye solution. Identical adsorption tests were conducted concurrently for each sample.

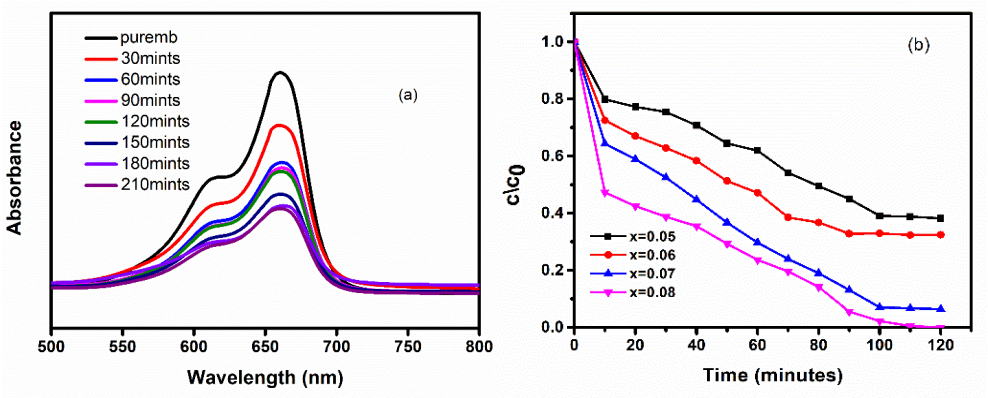

Figure.3.11. (a) MB dye Absorbance spectrum of pure V_2O_5 compound (b) Plot of c/c_0 vs time for $V_{2-x}Sb_{2x}O_{5-d}$ compounds for $0.05 \leq x \leq 0.08$

At 10-minute intervals, 3ml of the aliquots was collected, and after centrifugation at 10000 rpm for 5 minutes, the catalysts were separated and the remaining dye concentration was then measured from the absorbance spectrum

using a spectrophotometer, and the amount of dye removed was calculated [45]. Figure 3.11(b) presents the effect of varying concentrations of antimony ions to the $V_{2-x}Sb_{2x}O_{5-\delta}$ micro-composites on MB dye removal. The initial dye concentration(10 ppm), contact time(120 minutes), and catalyst loading(50 mg), were examined as influences on the adsorption process [122]. Figure 3.12 divulges the bar diagram indicating the MB dye removal percentage of $V_{2-x}Sb_{2x}O_{5-\delta}$ compounds for 0.05<=x<=0.08 for a contact time of 120 minutes. It can be seen that the increasing level of doping translates into higher percentage of dye removal in 120 min of contact time attaining 100%, 93%, 82%, and 61% for mol fractions x = 0.08, 0.07, 0.06, and 0.05 respectively [23]. The study highlights that Sb_2O_3 modification significantly augments the adsorption capacity of V_2O_5 microcrystals, wherein, an increase in the concentration of Antimony ions corresponds to an escalation in the MB dye adsorption rate.

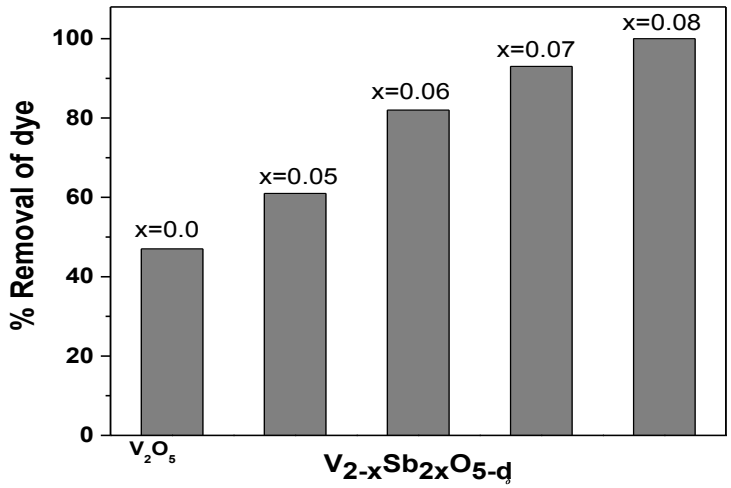

Figure.3.12. Bar Diagram depicting % Dye removal of $V_{2-x}Sb_{2x}O_{5-\delta}$ compounds for x=0.0 and 0.05 ≤ x ≤ 0.08

This trend culminates in 100% dye removal for $V_{2-x}Sb_{2x}O_{5-\delta}$ compounds at x=0.08 (Fig. 3.12). This heightened adsorption can be ascribed to the expanded surface area of Sb-V-O compounds, as confirmed by BET analysis when contrasted with pure V_2O_5. It is also noted that as per the previous studies, the efficiency of dye adsorption decreases with increasing solution temperature. This is because the active sites on the adsorbent shrink and change at higher temperatures, reducing the active adsorbent surface. The dyes then leach into the solution due to the increased separation between

the dye molecules and the adsorbent at high temperatures. We studied this experimentally with the Sb-V-O-8 compound which showed 100% adsorption within a contact time of 90 minutes., We observed a 5% leaching of dye back into the solution at a temperature of 40^{0}C which increased to 20% when the temperature was increased up to 80^{0}C[123].

3.3.9. FTIR Spectroscopy

To qualitatively assess adsorption, we procured FTIR spectra for both Sb-V-O samples and Sb-V-O samples infused with adsorbed MB, which are elucidated in Figure 3.13 (a) and (b) respectively. In the FTIR spectra of Sb-V-O samples as depicted in Figure 3.13 (a), two prominent absorption bands are discernible at 813 and 1003 cm^{-1}, corresponding to the asymmetric stretching modes of V–O–V, and the stretching vibration of V=O respectively. Noteworthy is the absence of notable IR excitations attributed to Sb-O bonds, attributable to the relatively low concentration of Sb^{3+} cations within the Sb-V-O compounds [38], [124]. In Figure 3.13 (b) the FTIR spectra of MB-adsorbed Sb-V-O catalysts scanned between 1200 cm^{-1} to 1800 cm^{-1} reveal IR modes linked to Methylene Blue.

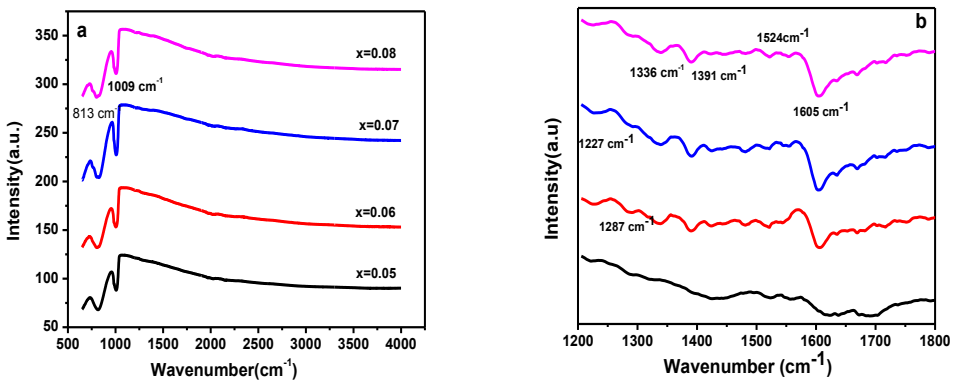

Figure.3.13. (a) FTIR spectrum showing up $V_{2-x}Sb_{2x}O_{5-\delta}$ compounds (b) MB adsorbed $V_{2-x}Sb_{2x}O_{5-\delta}$ compounds for $0.05 \leq x \leq 0.08$

In essence, it is plausible that the removal of color is primarily attributable to adsorption and not to the degradation of the chromophore group [45], [51]. The adsorption behavior was readily discernible by observing the C=C stretching mode of Methylene Blue (MB) at approximately 1605 cm^{-1} [41]. The emergence of this

spectral band post-adsorption unmistakably confirmed the successful sequestration of MB. This characteristic band was consistently evident across all samples [50].

The identified functional groups related to the MB absorption peaks encompass C=C side ring stretching within the range of 1500 cm^{-1} to 1400 cm^{-1}, –CH2 /–CH3 stretching spanning from 1400 cm^{-1} to 1300 cm^{-1}, as well as C–N and N–N stretching absorption peaks at 1287 cm^{-1} and 1227 cm^{-1}, respectively. Additional MB absorption peaks include C–H out-of-plane bending vibrations of the ring, observed between 800 cm^{-1} and 900 cm^{-1} [125], [126]. From figure 3.13(b) when we look at the data, it's clear that for mol fraction of x=0.05, the IR bands related to the MB dye are not very distinct. This matches the lower dye adsorption as seen in the bar diagram (fig. 3.12). But as x goes up from 0.06 to 0.08, the strong band at 1605 cm^{-1} becomes more visible.

3.3.10. N_2 Adsorption Isotherms

While the molecules penetrate a three-dimensional matrix in absorption, the molecules attach to a two-dimensional matrix usually between phase boundaries in adsorption [30], [42]. And hence surface area is an important parameter in determining the adsorption rate. The International Union of Pure and Applied Chemistry (IUPAC) classified N_2 adsorption isotherms into six types, type I to type VI and the detailed description provided by the IUPAC classified hysteresis loops into four types, each representing a different pore shape [127]. Out of the hysteresis loops, Type H1 represents cylindrical pores in which both ends are open and capillary condensation occurs in the middle of the relative pressure; Type H2 is associated with ink-bottle-shaped pores with poor connectivity and uneven pore structure, Type H3 is attributed to wedge-shaped pores formed by the loose stacking of flaky particles, and Type H4 is a result of slit-shaped pores resulting from internal parallel pore structure [128].

In figure 3.14 (a, b, c, and d), the N_2 adsorption isotherms, reveals that all Sb-V-O micro-rods/flakes, to be typical IV-type curves with a clear H_3-type hysteresis, which resulted from capillary condensation in the mesopores (diameter, $2 < d < 7$ nm) at the relative pressure range of 0.45–0.9 P/P_0 [128]. The adsorption isotherms of all

the investigated samples rose progressively during the relative pressure range of 0–0.7 P/P_0, which means mono-molecule layer adsorption occurring on the Sb-V-O surface.

Table.3.5: Textural parameters of Sb-V-O compounds from N_2 adsorption isotherms and BET analysis

$V_{2-x}Sb_{2x}O_{5-\delta}$	x=0.05	x=0.06	x=0.07	x=0.08
Pore Volume(cm^3/g)	0.0284	0.0295	0.0326	0.0356
Pore Diameter(nm)	6.83	5.958	5.37	4.96
BET surface area(m^2/g)	16.67	19.83	24.32	28.74

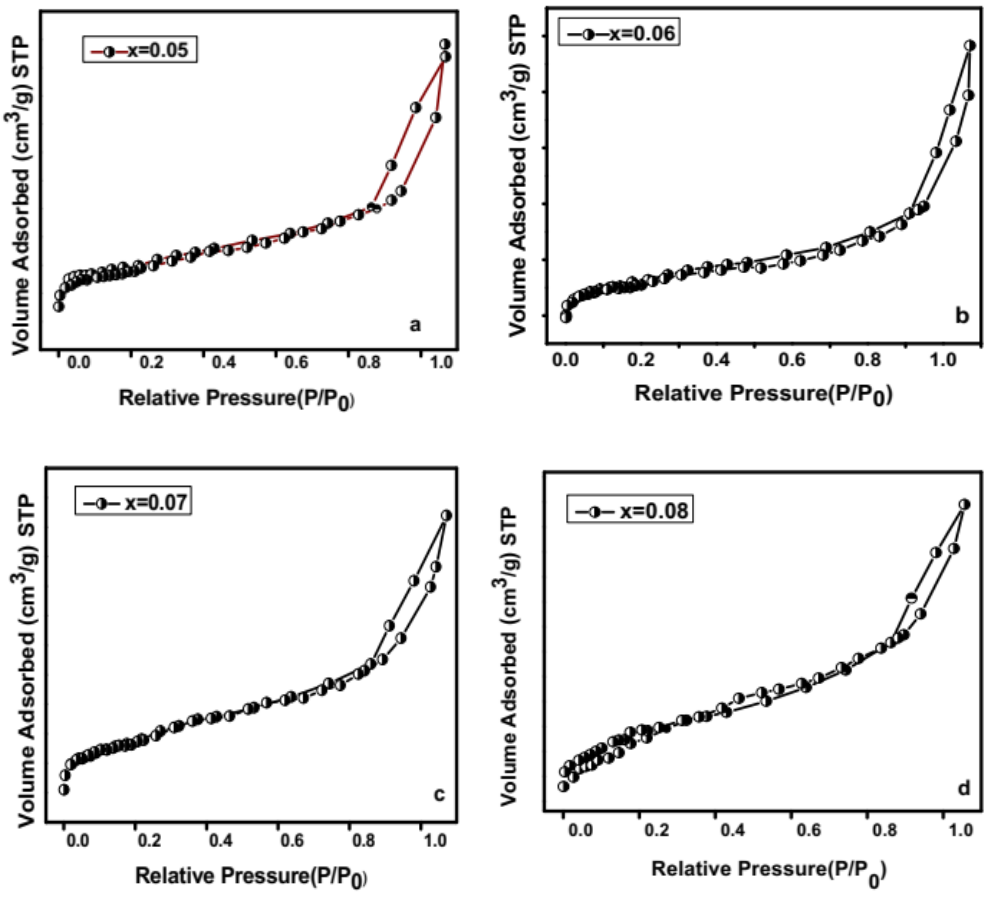

Figure.3.14. (a, b, c & d): N_2 adsorption isotherm of $V_{2-x}Sb_{2x}O_{5-d}$ micro-flakes for $0.05 \leq x \leq 0.08$ showing type IV curve with H_3 hysteresis

Then, the adsorption curves rose steadily, resulting in the saturation of mono-molecule layer adsorption followed by the multi-molecular layer adsorption. When the relative

pressure was 0.7–0.9 P/P_0, the desorption branch was obviously higher than the adsorption branch, along with the appearance of capillary condensation, which resulted in the hysteresis loop. At the relative pressure of 0.9–1.0 P/P_0, the adsorption branch and desorption branch suddenly rose and coincided at the end. Therefore, the occurrences of hysteresis loops indicate that all Sb-V-O compounds had a lot of mesopores [45], [129].

This trend is characteristic of mesoporous materials, suggesting that the Sb-V-O samples is in the form of non-rigid aggregates of platelet-like particles or rods in agreement with the result of SEM [38], [128], [130-131]. Similarly, the smaller adsorption amount at $P/P_0 < 0.4$ and the large adsorption amount at $P/P_0 > 0.9$ show that all Sb-V-O compounds had a certain number of macropores ($d > 50$ nm) and a small amount of micropores ($d < 2$ nm) [81]. The table 3.5 shows the specific surface area, calculated using BET method, increases from 16.67 m^2/g to 28.74 m^2/g for $0.05 \leq x \leq 0.08$. Here there is an enhancement in the surface area of Sb-V-O compounds as compared to BET surface area of 6-7 m^2/g for pure V_2O_5 microparticles as per the previous reports [122], [132-133]. Thus greater adsorption rate for the Sb-V-O-8 compound can be attributed to the increase in specific surface area. An increase in pore volume from 0.0284 to 0.0356 cm^3/g with increase in Sb ion concentration also supplements the increase in adsorption (Table 3.5). Thus, the enhanced porosity characteristic of $V_{2-x}Sb_{2x}O_{5-\delta}$ composites is revealed by the increased specific surface area. A higher pore volume will boost adsorption activity owing to more available active sites at the surface [27], [38].

3.3.11. Kinetic Studies on MB Adsorption

Adsorption kinetic modeling is an especially useful tool to interpret the mechanism of the MB adsorption to Sb-V-O compounds. To determine the sorption mechanism in detail, various models can be deployed. Here, we made comparative studies of pseudo-first-order, pseudo-second-order, intra particle diffusion and elvoich models [27], [45], [78], [122]. Table 3.6 shows the kinetic constants (q_e, K_1, K_2, K_{id}, α, β) derived from the slope and intercept of the four regression equations of adsorption models.

The pseudo-first-order kinetic response is obtained as a linear relationship between $\log(q_t - q_e)$ with time t (eqn.3) and gives a low value for regression coefficient, R^2 for all the mol fractions (Table. 6). The plot of q_t vs $t^{1/2}$ as per the Weber and Morris Intra particle diffusion model (eqn. 5) is a straight line that do not pass through the origin for the MB adsorption by Sb-V-O compounds giving R^2 between 0.91 to 0.93 [122] (Table 3.6). The plot of q_e vs ln(t), (eqn. 8), the linear form of elvoich model gives R^2 in the range 0.85-0.89 (Table 3.6), which gives the worst fit among all the discussed models. The pseudo-second-order (PSO) adsorption kinetic model reveals a positive relationship between t/q_t and time (eqn.4), with 0.99 as R^2 (Table. 3.6) for x=0.05, 0.06, 0.07 & 0.08 in $V_{2-x}Sb_{2x}O_{5-\delta}$ compounds (Fig. 3.15. a, b, c and d). Thus PSO is the best fitting kinetic model for representing the adsorption kinetics of Sb-V-O catalysts on MB dye [78]. The PSO model operates under the premise that the determining factor in the rate of adsorption is chemisorption process and offers predictions that are applicable across the entire spectrum of adsorption. In this scenario, the rate of adsorption hinges on the adsorption capacity rather than the concentration of the adsorbate [23], [78], [134].

The plot of t/q_t as a function of time gives a linear relationship (Fig. 3.15). From the slope, $1/q_e$ and the intercept, $1/(k_2q_e^2)$, the amount of adsorbate adsorbed at equilibrium (q_e) and k_2, the second-order rate coefficient (Table 6) were calculated. Here the equilibrium adsorbate concentration q_e (mg/g) exactly matches with the experimentally observed values for all concentration. Sb-V-O-8 compound shows highest q_e of 21 mg/g in comparison with 4.8 mg/g for V_2O_5/MWCNTs composites [135]. Alessandro Di Mauro et al [50] reported the equilibrium adsorption capacity of pure V_2O_5 as 7 mg/g and SnO_2/TiO_2 modified V_2O_5 as 7.4 mg/g. Sb modification on V_2O_5 enhances both the adsorption rate and equilibrium adsorbate concentration when compared to pristine V_2O_5. We studied the Langmuir (eqn 7), Freudlich (8), D-R (eqn 9,10,11) and Temkin (eqn 12) adsorption isotherm models for Sb-V-O-8 compound [26], [80], [136]. Sb-V-O-8 compound was selected as it showed maximum adsorption with minimum contact time and the comparatively best adsorption isotherm that fits the data was Freudlich adsorption isotherm model with the regression coefficient value of R^2 =0.98 [37], [136] .

Table 3. 6: Adsorption parameters for Pseudo first order, Pseudo second order, Intra-particle Diffusion and Elvoich kinetic models for Sb-V-O compound

Sb-V-O	**x=0.05 q_e (exp)= 17.60mg/g**			**x=0.06 q_e(exp)=18 mg/g**			**x=0.07 q_e(exp)=20 mg/g**			**x=0.08 q_e(exp)=20.5 mg/g**		
Parameters	R^2	K	q_e mg/g	R^2	K	q_e mg/g	R^2	K	q_e mg/g	R^2	K	q_e mg/g
Pseudo First order Kinetic Model	0.84	0.038	9.68	0.91	0.05	9.88	0.89	0.04	11.12	0.88	0.031	8.37
Pseudo Second order kinetic model	0.99	0.008	18.3	0.99	0.017	18.73	0.99	0.0065	20.96	0.99	0.0077	21.18
Parameters	R^2	K_{id}	C	R^2	K_{id}	C	R^2	k_{id}	C	R^2	k_{id}	C
Intra particle model	0.92	0.45	12.57	0.91	0.44	13.49	0.93	0.62	13.54	0.92	0.51	14.87
Parameters	R^2	B	α	R^2	B	A	R_2	B	α	R^2	β	α
Elvoich	0.85	1922	0.69	0.89	4058	0.71	0.89	3410	0.598	0.87	4191	0.63

The value of K_f=3.52 indicates extend of interaction between adsorbate and the surface. All other compounds in the Sb-V-O series shows the same trend. Waldir Avansi Jr et al [45] reported the synthesis and adsorptive/photocatalytic study of 1D vanadium pentoxide nanostructures prepared under hydrothermal conditions at temperature of 180 and 200 ^{0}C and the mechanism of adsorption was reported to occur via interaction of NMe^{2+} of the MB dye with the negatively charged surface of the 1D-V_2O_5 samples. Previous investigations suggest that the efficiency of adsorption on vanadium pentoxide-based compounds is based on the electronic characteristic of the pollutants given by cationic dye (MB) > neutral dye (RhB) > anionic dye (MO) [45], [50].

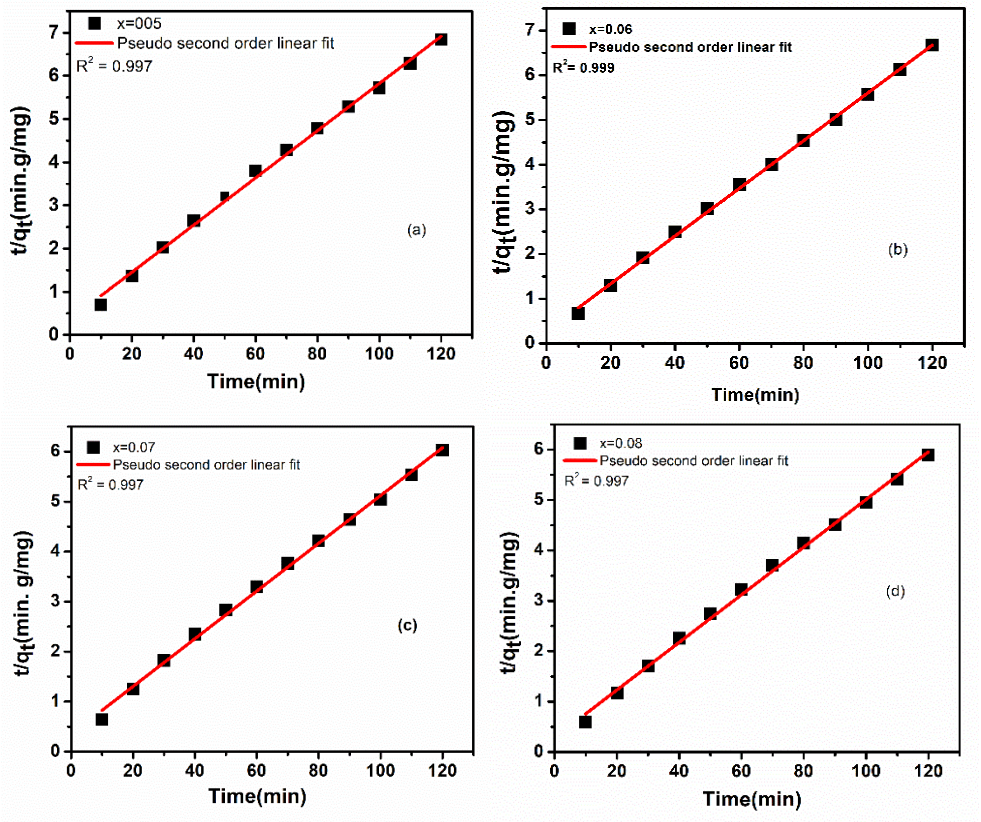

Figure.3.15. (a, b, c & d). Pseudo second order kinetic model, linear fit of $V_{2-x}Sb_{2x}O_{5-\delta}$ for $0.05 \leq x \leq 0.08$ giving R^2=0.99 for all compounds

3.3.12. AC conductivity and Dielectric studies

To investigate the frequency-dependent dielectric dispersion of the $V_{2-x}Sb_{2x}O_{5-\delta}$ ($0.05 \leq x \leq 0.08$) compound, the dielectric constant was plotted against

frequency, as shown in figure. 3.17(a). The dielectric constant for each composition was calculated using the following equation (14) [137]

$$\varepsilon_r' = \frac{C_p d}{\varepsilon_0 A} \tag{14}$$

where ε_r' represents the dielectric constant, d the thickness of the pellet, ε_0 is the electric permittivity of free space, C_p is the parallel capacitance obtained directly from the impedance analyzer instrument, and A is the cross-sectional area of the pellet. Across all concentrations from x=0.05 to x=0.08, the dielectric measurements of the samples display consistent behavior, offering valuable insights into the material's electrical properties. At low frequencies, the dielectric constant begins at a high value and decreases as frequency increases, eventually stabilizing at a lower constant value at higher frequencies.

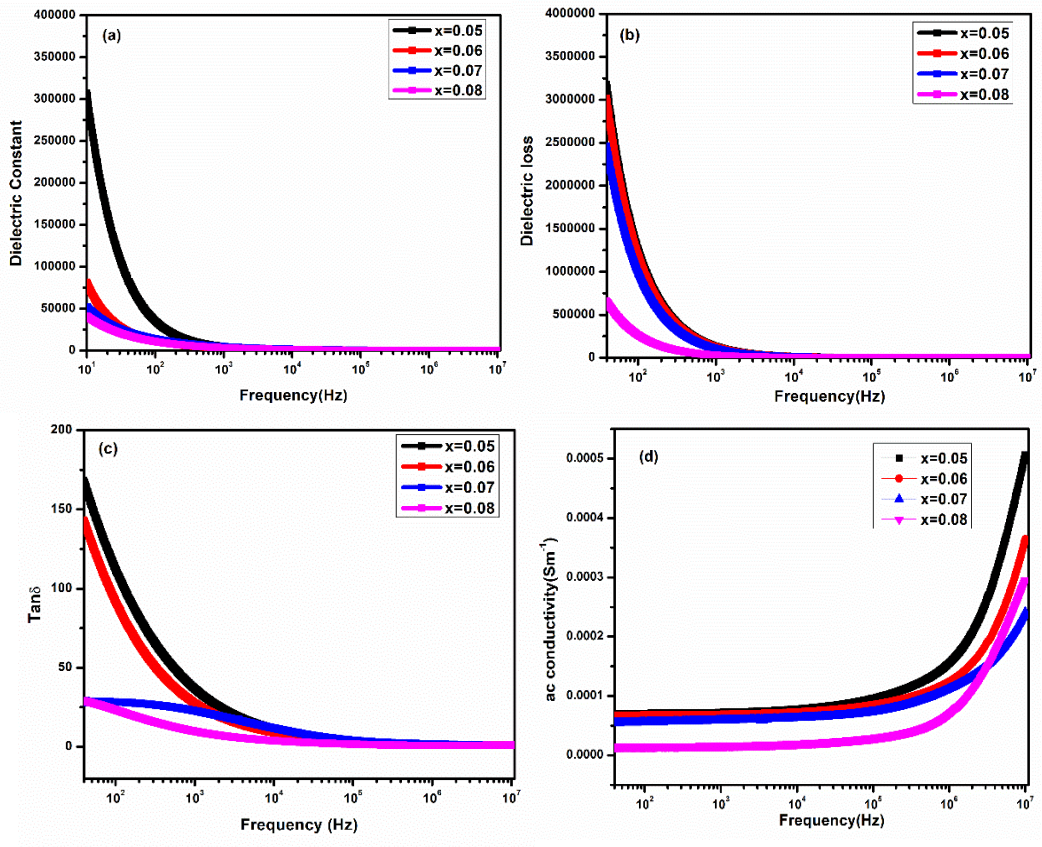

Figure.3.16: Frequency-dependent variations of $Sb_{2x}V_{2-x}O_{5-\delta}$ samples for all mole fractions a) dielectric constant b) dielectric loss factor c) dissipation factor d) ac conductivity

This phenomenon is attributed to the behavior of charge carriers in response to the applied alternating electric field. At lower frequencies, the field changes direction relatively slowly, allowing charge carriers within the material sufficient time to align with the electric field direction, leading to higher values of ε_r' . However, as frequency increases, the rapid reversal of the electric field direction outpaces the carriers' ability to realign synchronously with the field, causing a drop in the dielectric constant. At even higher frequencies, when the alignment of carriers is effectively frozen due to the quick oscillation of the electric field, ε_r' stabilizes [88], [138- 140].

In the low-frequency range, the grain boundaries, known for their high resistivity, dominate the dielectric response. Their resistive nature impedes the flow of charge, which enhances polarization within the boundaries and results in a high dielectric constant ε_r'. In contrast, at high frequencies, the response shifts toward the highly conductive grains, which promote conduction and reduce the dielectric constant. This frequency-dependent transition aligns with the boundary-grain model, which postulates that at lower frequencies, conduction is controlled by resistive grain boundaries, while at higher frequencies, conductive grains govern the behavior of the material's dielectric response [141-142]. From figure 3.16 (a) it is evident that the value of the dielectric constant at 10 Hz decreases from 309640 to 40712 as x varies from 0.05 to 0.08. When Sb^{3+} ions replace V^{5+} ions, the lattice structure may be distorted due to the dissimilar ionic radii and oxidation states of antimony in comparison to vanadium along with the formation of the $SbVO_4$ phase at higher mol fractions. These distortions in the lattice due to Sb substitution lead to a reduction in the material's overall polarizability. As the ionic size and charge of Sb^{3+} differ significantly from those of V^{5+} the replacement disrupts the alignment of electric dipoles, lowering the ability of the material to polarize under an electric field. This lowered polarizability, in turn, reduces the dielectric constant ε_r' of the material, particularly noticeable at higher frequencies, where only intrinsic polarization contribute to the dielectric behavior [143].

The dielectric loss factor ε_r'' is the imaginary component of the complex permittivity. When a material is subjected to an electric field, it causes displacement

of charge carriers, leading to energy loss. This lost energy is converted into heat, a phenomenon referred to as dielectric loss [144]. Figure 3.16 (b) represents the frequency dependence of the dielectric loss factor. The dielectric loss behavior resembles the real part of electrical permittivity. The variation of the loss factor with frequency can be explained by ion migration within the material at low frequencies. At moderate frequencies, the dielectric loss values are influenced by ion jumps, conduction losses due to ion migration, and ion polarization losses. As frequency increases, the dielectric loss factor falls from a relatively high value in the low-frequency zone. Migrating charge carriers are the source of substantial dielectric loss in the low-frequency area; charge carrier migration decreases as frequency rises. This frequency-dependent behavior is characteristic of charge carrier-dominated dielectric relaxation processes [8], [144].

As the loss factor is much greater than the dielectric constant, it can be deduced that the Sb-V-O compounds have lossy properties in the low-frequency range (10 Hz to 1 kHz). On the other hand, for frequencies greater than 10 kHz, all molar fractions ε_r'' values stay constant, indicating reduced energy dissipation in the dielectric system [145]. This phenomenon underscores the potential of Sb_2O_3-V_2O_5 ceramics for energy storage applications, where materials with high dielectric constants at low frequencies are favorable for capacitors and high-energy storage devices. At low frequencies, grain boundaries impede conduction, leading to a high dielectric constant, while at high frequencies, the grains dominate, promoting conduction and decreasing the dielectric constant. This frequency-dependent transition aligns well with Koop's phenomenological theory and suggests potential applications in multi-layer ceramic capacitors, where high dielectric permittivity is essential [8], [143].

The behavior of tan δ with frequency is depicted in Figure 3.16 (c). The term tangent loss (tanδ) describes the energy dissipation in dielectrics. The tangent loss (eqn. 15) is defined as the ratio of the imaginary part of the permittivity to the real part of the permittivity [140], [146].

$$tan\delta = \frac{\epsilon_r^{"}}{\epsilon_r^{'}} \tag{15}$$

Impurities, flaws, and irregularities in the crystal lattice are typically the source of tangent losses in materials, which cause polarization to lag behind the applied external field. At higher frequencies, the Maxwell-Wagner model of polarization and Koop's phenomenological theory predict that energy loss and dielectric constant are nearly frequency-independent. This phenomenon indicates that polarization in any polycrystalline material arises from well-conducting grains separated by weak grain boundaries. At lower frequencies, space charges can follow the applied field due to their longer relaxation times, but at higher frequencies, they cannot keep up with the field. As a result, both tangent loss and dielectric constant increase at lower frequencies, but they exhibit frequency-independent behavior at higher frequencies [8], [142]. It is also noticed that tanδ decreases as Sb concentration increases since the incorporation of Sb into the V_2O_5 lattice can decrease the material's overall polarizability. This frequency-independent behaviour at elevated frequencies, as per the Maxwell-Wagner polarization and Koop's theory, indicates reduced energy dissipation, suggesting that Sb_2O_3-V_2O_5 compounds is suitable for high-frequency applications such as RF and microwave devices. Here, minimal dielectric loss is essential to maintain signal integrity and avoid unwanted energy dissipation. Additionally, the incorporation of Sb in V_2O_5 leads to a decrease in tan δ, likely due to the reduced polarizability within the lattice. This reduction in dielectric loss minimizes dielectric heating, enhancing the material's suitability for dielectric resonators, particularly in frequency-stable, low-loss filters used in telecommunication systems [147-148].

The AC conductivity spectra demonstrate high-frequency dispersion that adheres to a power-law [150] while at lower frequencies, the conductivity remains fundamentally flat and frequency-independent. Typically, the AC conductivity follows the Almond-West formalism, which is expressed as [151],

$$\sigma(\omega) = \sigma_{dc}\left[1 + \left(\frac{\omega}{\omega_H}\right)^n\right] \tag{16}$$

Here, σ_{dc} represents the DC conductivity, ω_H is the crossover or hopping frequency of charge carriers that separates the DC regime from the dispersive region, and n is

the frequency exponent, which typically falls within the range of 0 to 1 and indicates the interaction between ions. The values of σ_{dc}, ω_H, and n were estimated by fitting the experimentally measured frequency-dependent conductivity data at different mole concentrations using equation (16) [144], [145].

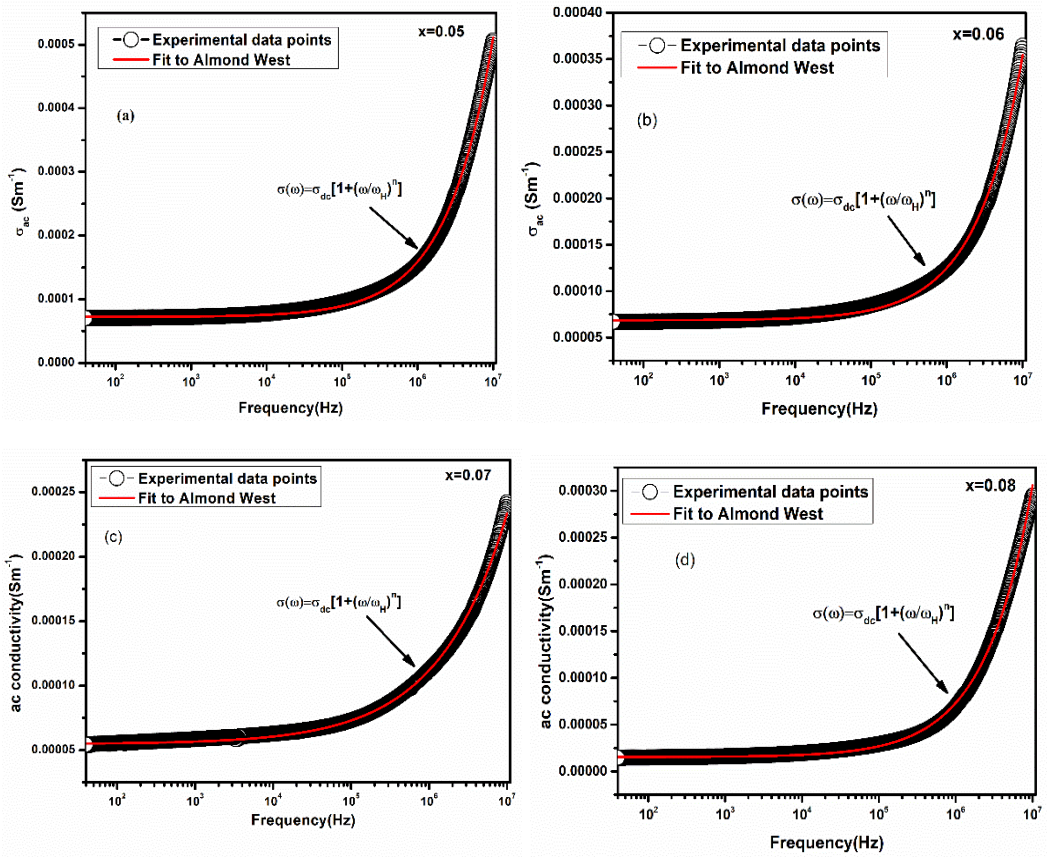

Figure.3.17. Almond West fitted Conductivity when a) x=0.05 b) x=0.06 c) x=0.07 d) x=0.08

To comprehend the frequency dependency of the material's electrical properties, ac conductivity measurement is performed. Information on the characteristics of charge carriers can also be obtained from the frequency dependence of AC conductivity. The empirical formula (eqn.17) used to compute the AC electrical conductivity is [149]

$$\sigma_{ac} = \omega \epsilon_0 \epsilon_r^{"} \tag{17}$$

where ω is the angular frequency, ϵ_0 is permittivity in free space and is the $\epsilon_r^{"}$d ielectric loss factor. Figure 3.16.d shows the variation of room temperature ac

conductivity with frequency for all Sb concentrations. The frequency-dependent conductivity consists of two distinct regions. The first region occurs at low frequencies, where $\sigma(\omega)$ remains nearly independent of frequency. The second region is characterized by a strong frequency dependence of $\sigma(\omega)$.

The Almond west fits to the experimental data are shown in Figure 3.17(a, b, c, and d). It describes the flow of ions in the material when an alternating electric field is present. As illustrated in Figure 3.17, the experimental data for all samples were well-fitted with the universal power law, achieving a high parameter fit adj.(R^2) between 0.997 and 0.999 and a least square fit error factor (Chi-square) ranging from 1.157×10^{-11} to 9.42×10^{-12}. The Almond West formalism was found to be applicable to all the samples studied in this work. The Almond fit yields the hopping or crossover frequency values for each mole fraction and is tabulated (Table 3.7). At 10MHz, σ_{ac} decreases from 5.08×10^{-4} S/m to 2.40×10^{-4} S/m as x values vary from 0.05 to 0.08 while σ_{dc} decreases from 7.22×10^{-5} S/m to 1.55×10^{-5} S/m. This decrease in ac conductivity is due to the result of structural changes brought about by the substitution of Sb^{3+} ions for V^{5+} ions and the formation of new $SbVO_4$ phase.

Table 3.7. Parameters derived from Almond West fit for different mole fractions

Almond West Fitted parameters	**x=0.05**	**x=0.06**	**x=0.07**	**x=0.08**
$\boldsymbol{\sigma dc}$**(Sm^{-1})**	7.22E-5	6.58E-5	5.48E-5	1.55E-5
$\boldsymbol{WH}$	770978	132000	923525	153105
n	0.7037	0.7051	0.4961	0.7018
Chi-square	1.157E-11	9.42E-12	3.84E-12	4.26E-12
Adj. R-Square	0.998	0.997	0.998	0.999

This substitution causes a large reduction in the number of nearest free pair O_2 ions and interferes with the polaronic conduction of vanadium ions. Therefore, the obstruction that polarons experienced on their journey can be responsible for the decrease in sample conductivity [16]. At low frequencies, conductivity remains nearly frequency-independent, indicating a stable DC component, which is valuable in

applications requiring consistent charge retention, such as batteries and supercapacitors. At high frequencies, however, conductivity exhibits a significant frequency dependence, which could be advantageous in applications that rely on tunable conductivity. This behavior of AC conductivity not only aligns with known models of charge transport but also highlights the potential for Sb_2O_3-V_2O_5 ceramics in applications where controlled conductivity is essential, such as in electrochemical sensors and resistive switching devices [152-153]

3.3.13. Antimicrobial Studies

$V_{2-x}Sb_{2x}O_{5-\delta}$ compounds ($0.05 \leq x \leq 0.08$) was tested for its antibacterial activity against the Gram positive bacteria (*Staphylococcus aureus and agalactia, Bacillus cereus*), Gram negative bacteria (*Escherichia coli, Pseudomonas aeroginosa Vibrio harveyi and Vibrio cholerae)* and Fungus (*Pencillium, Aspergillus niger*) by using Agar well diffusion method on Mueller Hinton Agar (MHA) plates for bacteria and Disk diffusion method for fungi as shown in figure 3.18. The broth cultures of a single bacterial species were uniformly inoculated onto the surface of Mueller-Hinton agar (MHA) plates using the sterile cotton swab technique. The wells of 6 mm are made out of sterile cork borers in those plates. The compound dispersed in DMSO solvent media is introduced into the wells in the concentration of 50, 100, 150 and 200 micro litres. The positive control used was streptomycin disc (10 mcg) and the negative control was pure DMSO solvent media. After 24 hours of incubation at 37^{o}C, measurement of the diameter of inhibition zones was taken. The antimicrobial activities of the Sb-V-O microflakes were assessed by evaluating the zone of growth inhibition against the employed bacteria and by adjusting the concentration of the synthesized compounds in DMSO solvent [60].

Bacteria are characterized by distinct structural components, including the cell membrane, cell wall, and cytoplasm. The cell wall, located external to the cell membrane, primarily consists of peptidoglycan—a robust matrix of amino acids and sugars that confers mechanical strength and maintains osmotic balance. In Gram-positive bacteria, the cell wall is notably thick and multilayered, measuring approximately 20–80 nm, with a single underlying cytoplasmic membrane. In

contrast, Gram-negative bacteria exhibit a thinner peptidoglycan layer (7–8 nm), situated between an outer membrane and an inner plasma membrane.

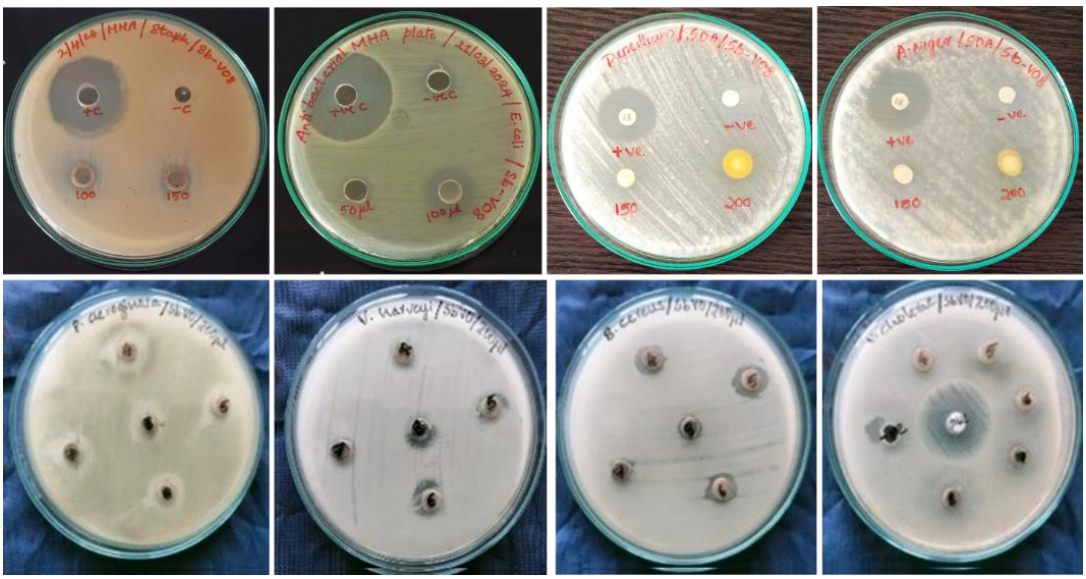

Figure 3.18. Representative photographs of zone of growth inhibition against bacteria and fungi for Sb-V-O-8 with positive and negative control:(a) S.aureus, (b) E.coli, (c) Pencillium (d) A. niger, and Zone of growth inhibition against bacteria for $V_{2-x}Sb_{2x}O_{5-\delta}$ *compounds (0.05<=x<=0.08) with positive control (e) P. aeroginosa (f) V. harveyi (g) B. cereus, (h)V. cholerae*

Table 3.8 Zone inhibition values (in mm) of Gram positive bacteria, gram negative bacteria and fungi for Sb-V-O-8 compound systems

Sl. No	Name of Bacteria/Fungus	50 µl	100 µl	150 µl	200 µl	+ve	-ve
1	Escherichia coli	R	19	20	24	23	7
2	Staphylococus aureus	R	11	12	15	24	R
3	Pseudomonas aeroginosa	R	11	13	15	22	7
4	Bacillus cereus	R	10	12	15	21	7
5	Vibrio harveyi	R	10	11	12	20	7
6	Vibrio cholerae	R	15	16	16	20	7
7	Staphylococus agalactia	R	R	R	R	20	R
8	Pencillium	R	R	15	17	22	R
9	Aspergillus niger	R	R	R	18	23	R

The cytoplasm, comprising proteins, carbohydrates, nucleic acids, salts, ions, and about 80% water, is critical for maintaining cellular functions, including electrical conductivity. The net negative charge of bacterial cell walls attracts positively charged

ions such as V^{5+}, V^{4+} and Sb^{3+} from the Sb-V-O compounds, facilitating their interaction with the bacterial cell surface [74]. These ions, suspended in a DMSO solution, adhere to the cell surface, disrupting the charge balance and leading to cell rupture and bacterial death. Chakradhar Sridhar B et al reported the 10 mm & 11 mm Zone inhibition of V_2O_5 and V_2O_5 /Pani against *S. aureus* at 250 µg and 19 mm and 9 mm for V_2O_5 and V_2O_5/Pani against *A. Niger* at 250 [58].

The sharp edges of Sb-V-O microparticles mechanically disrupt bacterial cell membranes, releasing V^{5+}, V^{4+}, Sb^{3+}, and O^{2-} ions. These ions interfere with the bacterial NADH redox cycle, crucial for respiration, and catalyze Haber-Weiss and Fenton-type reactions, generating reactive oxygen species (ROS). The ROS, in turn, attack lipopolysaccharides (LPS) in *E. coli* membranes, leading to further membrane disruption [109]. The release of reactive ionic species (V^{5+}, V^{4+}, Sb^{3+}, OH^-, O^{2-}) from the Sb-V-O composite targets bacterial cells. For example although *S. aureus* typically resists damage due to its thick peptidoglycan, Sb-V-O-8 induced clumping, enabling extended interaction and redox alterations, inhibiting growth by 15 mm at 200 µl [109]. Conducting antimicrobial experiments with fungi poses additional difficulties due to the resilience of their cell walls, which are more resistant to harsh conditions compared to bacteria. Ilkhechi et. al [154] reported the antifungal activity of zinc oxide related to the formation of free radicals on the surface of nanoparticles that damage the fungal cell membrane lipids, which lead to protein leakage through the membrane disruption. ZnO and TiO_2 is reported to produce reactive oxygen species (ROS), such as hydrogen peroxide and hydroxyl radicals, which induce oxidative stress. This oxidative stress disrupts fungal cell membranes and damages biomolecules including DNA, proteins, and lipids leading to the destruction of microbial enzymes and ultimately killing the fungi[154]. Sb-V-O microparticles in higher concentrations might attach to and saturate fungal hyphae, leading to the destruction of fungal cells. This inhibitory effect is likely due to the presence of V^{5+}, V^{4+}, Sb^{3+}, and O^{2-} ions, which disrupt the function of membrane-bound enzymes, particularly those involved in the respiratory chain, and other microbial proteins. Additionally, Sb-V-O particles may engage in competitive inhibition with substrates, rendering enzymes inactive and thereby blocking the synthesis of products essential for cellular activity [61], [155].

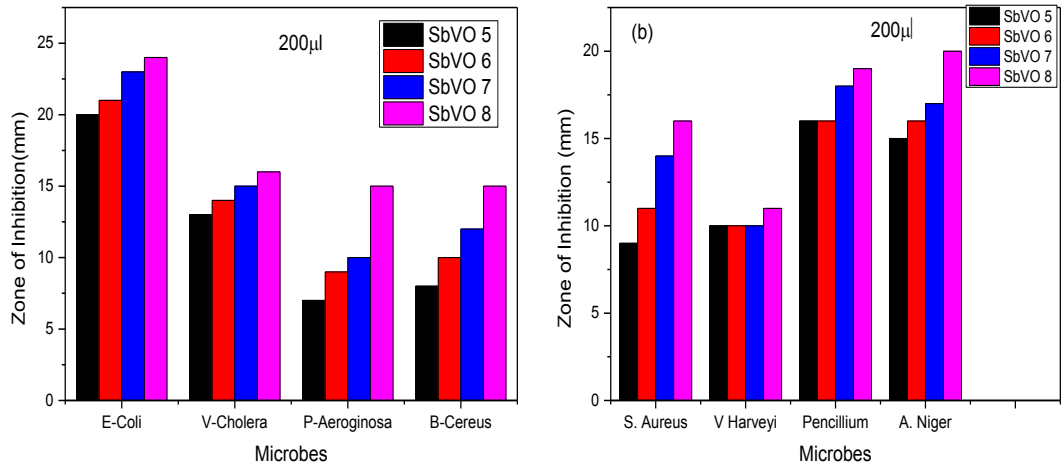

Fig.3.19 (a & b) Bar diagram comparing the zone of inhibition of $V_{2-x}Sb_{2x}O_{5-\delta}$ compounds ($0.05 \leq x \leq 0.08$), against the growth of the gram positive-gram, negative bacteria and fungi for 200 µl concentration

Table 3.8 shows up the antibacterial and antifungal effects of Sb-V-O-8 compounds against the gram negative, gram positive bacteria and fungus. The results showed that Sb-V-O-8 is more effective in inhibiting the growth of Escherichia coli with a zone inhibition diameter of 24 mm at 200 µl concentration. Other bacterial species like *S. Aureus, P. Aeroginosa, B. cereus* shows a inhibition zone of 15 mm, *V. harveyi* and *V. cholerae* showed a zone inhibition of 12 mm & 16 mm respectively, while the funguses, *Pencillium & Aspergillus niger* shows a zone inhibition of 18 mm and 19 mm respectively. However *Staphylococcus Agalactia* is resistant to Sb-V-O compounds for all mol fractions. Figure 3.19 (a & b) reveals the bar diagram depicting the inhibition zone produced by $V_{2-x}Sb_{2x}O_{5-\delta}$ compounds ($0.05 \leq x \leq 0.08$) against the growth of all the 7 bacteria and 2 fungi at 200 µl concentration. The zone of inhibition increases with increase in mol fraction from x=0.05 to x=0.08 for all the microbes, indicating the effect of the Antimony ions in inhibiting the growth of microbes because of the electrostatic interaction between the Sb-V-O compounds and the microbial surface leading to the attachment of microbes to the treated surface resulting in oxidization of microbes and finally death [109], [156].

3.4. Conclusion

In this research, four different concentrations of $V_{2-x}Sb_{2x}O_{5-\delta}$ compounds ($0.05 \leq x \leq 0.08$) were synthesized by high temperature solid state reaction. A variety of characterization techniques were deployed to analyze the effect of integration of antimony ions to the V_2O_5 matrix. Structural analysis using Rietveld refinement of the compounds using XRD data through the fullproof software reveal the presence of tetragonal $SbVO_4$ structures along with the prominent orthorhombic V_2O_5 structures for mol fraction x=0.06, 0.07 and 0.08. The Raman spectra, characterized by a prominent skeletal bending vibration at 143 cm^{-1} and a robust stretching vibration at 998 cm^{-1}, unequivocally confirm the presence of a well-ordered layered structure within the Sb-V-O matrix. Elemental mapping using EDAX spectrum reveals the presence of V, O, and Sb atoms in the compound. PL spectra of the as-prepared compound revealed significant transitions in the blue-green regions as a result of symmetry distortions and defects induced by the incorporation of Sb ions into the V_2O_5 matrix.

In the XPS studies, the deconvoluted V*2p* spectra further reveal a predominant population of V^{5+} ions, accompanied by a minor population of V^{4+} ions. XPS spectra of the Sb *3d* region confirm a strong presence of antimony oxide, as evidenced by the overlap of the Sb $3d_{5/2}$ binding energy with the O*1s* binding energy. Furthermore, a distinct component in the Sb*3d* signal, with a separation of 539.2 eV observed in the x=0.08 composition, indicates the presence of metallic antimony (Sb^0). The band gap energy, extracted from the Kubelka-Monk plot, escalates from 2.28 eV to 2.32 eV with an augmented concentration of trivalent antimony ions, explained using the Moss-Burstein effect. The materials display a combination of rod and flake-like morphologies, significantly elevating the surface area to 28 m^2/g for x = 0.08. Consequently, this results in 100% Methylene Blue dye adsorption within 90 minutes of contact time for the Sb-V-O-8 compound giving qe of 21 mg/g in comparison with 7 mg/g for pristine V_2O_5.

The surface-modified Sb-V-O forms mesoporous microcrystals, observable through the Type IV, N_2 adsorption isotherm with typical H3 hysteresis, enhancing the adsorption capacity. The pseudo-second-order kinetic model effectively characterizes the cationic MB dye chemisorption on Sb-V-O catalysts, with a high correlation coefficient ($R^2 = 0.99$) across all concentrations. The adsorption data fitted well with the Freundlich isotherm model indicating multilayer adsorption on heterogeneous surfaces. The effects of antimony concentration on the electrical properties of $Sb_{2x}V_{2-x}O_{5-\delta}$ compounds were examined at room temperature across a broad frequency range of 10 Hz to 10 MHz. The dielectric behavior of the $Sb_{2x}V_{2-x}O_{5-\delta}$ compound, as investigated in this study, exhibits a frequency-dependent response that is characteristic of polycrystalline materials. The dielectric constant of the sample decreases with increasing frequency due to charge carrier alignment limitations. This behavior highlights Sb_2O_3-V_2O_5 ceramics' potential for energy storage, particularly in capacitors needing high dielectric constants at low frequencies. This frequency-dependent shift aligns with Koop's theory, making these ceramics promising candidates for multi-layer capacitors where high dielectric permittivity is essential. As Sb concentration increases in the V_2O_5 lattice, tanδ also decreases due to reduced polarizability, resulting in frequency-independent behavior at elevated frequencies.

The AC conductivity shows a power-law behavior at high frequencies and is frequency-independent at low frequencies. The Almond-West formalism fits the experimental data well, allowing for the estimation of hopping frequency values. Sb substitution reduces AC conductivity due to structural changes and interference with polaronic conduction. The study underscores the potential of Sb-incorporated V_2O_5 compounds for advanced applications, particularly in microwave absorption technologies. The incorporation of Sb induces structural distortions that diminish AC conductivity by disrupting polaronic transport pathways and altering the local electronic environment, thus reducing charge carrier mobility. Antimicrobial studies also demonstrated broad-spectrum activity against Gram-positive, Gram-negative bacteria, and fungi

References

[1] D. Tadeu Cestarolli and E. Maria Guerra, "Vanadium Pentoxide (V_2O_5): Their Obtaining Methods and Wide Applications," in *Transition Metal Compounds - Synthesis, Properties, and Application*, S. Haider and A. Haider, Eds., IntechOpen, 2021. doi: 10.5772/intechopen.96860.

[2] A. Cao, J. Hu, H. Liang, and L. Wan, "Self-Assembled Vanadium Pentoxide (V_2O_5) Hollow Microspheres from Nanorods and Their Application in Lithium-Ion Batteries," *Angew. Chem. Int. Ed.*, vol. 44, no. 28, pp. 4391–4395, July 2005, doi: 10.1002/anie.200500946.

[3] T. K. Le *et al.*, "Recent advances in vanadium pentoxide (V_2O_5) towards related applications in chromogenics and beyond: fundamentals, progress, and perspectives," *J. Mater. Chem. C*, vol. 10, no. 11, pp. 4019–4071, 2022, doi: 10.1039/D1TC04872D.

[4] Y. Tang *et al.*, "Vanadium pentoxide cathode materials for high-performance lithium-ion batteries enabled by a hierarchical nanoflower structure via an electrochemical process," *J Mater Chem A*, vol. 1, no. 1, pp. 82–88, 2013, doi: 10.1039/C2TA00351A.

[5] J. Haber, M. Witko, and R. Tokarz, "Vanadium pentoxide I. Structures and properties," *Appl. Catal. Gen.*, vol. 157, no. 1–2, pp. 3–22, Sept. 1997, doi: 10.1016/S0926-860X(97)00017-3.

[6] T. Sarkar, S. Majumder, S. Biswas, S. S. Rose, and V. Kamble, "Engineering lattice oxygen defects and polaronic transport in vanadium pentoxide via isovalent phosphorus doping," *Appl. Phys. Lett.*, vol. 123, no. 22, p. 222106, Nov. 2023, doi: 10.1063/5.0178546.

[7] T. P. Jaya, P. Jayaram, T. Ramachandran, P. Hajira, C. N. Anumol, and P. P. Pradyumnan, "Synthesis of solid solutions of Mn and Bi substituted V2O5 and substitutional effect in structural and optoelectronic behavior," *Phys. B Condens. Matter*, vol. 407, no. 8, pp. 1214–1218, Apr. 2012, doi: 10.1016/j.physb.2012.01.098.

[8] S. K, J. Peediyekkal, S. M, S. S, and M. Chennabasappa, "Rietveld refinement, core level electron shell structure and frequency-dependent dielectric behavior of vanadium bismuth oxide microstructures," *Phys. B Condens. Matter*, vol. 691, p. 416318, Oct. 2024, doi: 10.1016/j.physb.2024.416318.

[9] M. Sabna, K. Safna, J. Mayandi, S. Zh. Karazhanov, and P. Jayaram, "Microstructure profiling and photoluminescence characteristics of V(1-x)2 Ni3xO5-δ compound systems," *Mater. Lett.*, vol. 266, p. 127507, May 2020, doi: 10.1016/j.matlet.2020.127507.

[10] M. Sabna and P. Jayaram, "Reformed dielectric features in single phase orthorhombic nickel vanadate complex oxides and the significance of the lattice dynamics in the optoelectrical features," *J. Phys. Chem. Solids*, vol. 180, p. 111428, Sept. 2023, doi: 10.1016/j.jpcs.2023.111428.

[11] K. Safna, P. Jayaram, M. Sabna, P. Prasannan, J. Mayandi, and P. P. Pradyumnan, "Microstructure profiling, lattice dynamics, and morphological studies on multi-excitonic vanadium bismuth oxide compound systems," *J. Aust. Ceram. Soc.*, vol. 58, no. 4, pp. 1129–1136, Sept. 2022, doi: 10.1007/s41779-022-00766-7.

[12] H. Wu *et al.*, "One step synthesis of vanadium pentoxide sheets as cathodes for lithium ion batteries," *Electrochimica Acta*, vol. 206, pp. 301–306, July 2016, doi: 10.1016/j.electacta.2016.04.169.

[13] A. Al-Hajry, A. Al-Shahrani, and M. M. El-Desoky, "Structural and other physical properties of barium vanadate glasses," *Mater. Chem. Phys.*, vol. 95, no. 2–3, pp. 300–306, Feb. 2006, doi: 10.1016/j.matchemphys.2005.06.041.

[14] J. Wang, Z. Yang, X. He, Y. Chen, Z. Lei, and S. Peng, "Effect of humidity on La0.4Sr0.6Co0.2Fe0.7Nb0.1O3−δ cathode of solid oxide fuel cells," *Int. J. Hydrog. Energy*, vol. 44, no. 5, pp. 3055–3062, Jan. 2019, doi: 10.1016/j.ijhydene.2018.10.193.

[15] R. Punia, R. S. Kundu, M. Dult, S. Murugavel, and N. Kishore, "Temperature and frequency dependent conductivity of bismuth zinc vanadate semiconducting glassy system," *J. Appl. Phys.*, vol. 112, no. 8, p. 083701, Oct. 2012, doi: 10.1063/1.4759356.

[16] S. Khan and K. Singh, "Effect of MgO on structural, thermal and conducting properties of V2-Mg O5- (x = 0.05–0.30) systems," *Ceram. Int.*, vol. 45, no. 1, pp. 695–701, Jan. 2019, doi: 10.1016/j.ceramint.2018.09.231.

[17] S. Khan and K. Singh, "Structural, optical, thermal and conducting properties of V2−xLixO5−δ ($0.15 \leq x \leq 0.30$) systems," *Sci. Rep.*, vol. 10, no. 1, p. 1089, Jan. 2020, doi: 10.1038/s41598-020-57836-8.

[18] M. M. Sajid *et al.*, "Preparation and characterization of Vanadium pentoxide (V2O5) for photocatalytic degradation of monoazo and diazo dyes," *Surf. Interfaces*, vol. 19, p. 100502, June 2020, doi: 10.1016/j.surfin.2020.100502.

[19] S. Bansal, A. Singh, D. Poddar, and P. Jain, "Fabrication and photocatalytic evaluation of functionalized chitosan decorated vanadium pentoxide nano-adsorbents for water remediation," *Ceram. Int.*, vol. 49, no. 6, pp. 8871–8885, Mar. 2023, doi: 10.1016/j.ceramint.2022.11.043.

[20] A. Kangmennaa, H. Yakubu, A. Tutuwaa, C. O. Agyapong, M. Toku, and E. S. Agorku, "Methylene blue adsorption on vanadium pentoxide nanorods dispersed in starch-grafted polyacrylonitrile," *Int. J. Polym. Anal. Charact.*, vol. 28, no. 8, pp. 697–713, Nov. 2023, doi: 10.1080/1023666X.2023.2274661.

[21] B. Y. Danu *et al.*, "Chitosan-Graft-Sodium Alginate Encapsulated Vanadium Pentoxide (V2 O5) Nanocomposite for Adsorption and Antimicrobial Studies," *J. Adv. Mater. Sci. Eng.*, vol. 1, no. 1, Dec. 2021, doi: 10.33425/2771-666X.1006.

[22] A. Kong, Y. J. Ding, P. Wang, H. Q. Zhang, F. Yang, and Y. K. Shan, "Novel alkylimidazolium/vanadium pentoxide intercalation compounds with excellent adsorption performance for methylene blue," *J. Solid State Chem.*, vol. 184, no. 2, pp. 331–336, Feb. 2011, doi: 10.1016/j.jssc.2010.12.008.

[23] M. H. Ashery, M. Elnouby, E. M. EL-Maghraby, and E. M. Elsehly, "Structural control of V2O5 nanoparticles via a thermal decomposition method for prospective photocatalytic applications," *Beni-Suef Univ. J. Basic Appl. Sci.*, vol. 12, no. 1, p. 12, Jan. 2023, doi: 10.1186/s43088-023-00350-3.

[24] "BET N2 adsorption–desorption isotherms of (a) 2-V2O5 and (b) 3-V2O5 and...," ResearchGate. Accessed: Apr. 04, 2023. [Online]. Available: https://www.researchgate.net/figure/BET-N2-adsorption-desorption-isotherms-of-a-2-V2O5-and-b-3-V2O5-and-their_fig5_359638015

[25] M. Shanmugam, A. Alsalme, A. Alghamdi, and R. Jayavel, "Enhanced Photocatalytic Performance of the Graphene-V $_2$ O $_5$ Nanocomposite in the Degradation of Methylene Blue Dye under Direct Sunlight," *ACS Appl. Mater. Interfaces*, vol. 7, no. 27, pp. 14905–14911, July 2015, doi: 10.1021/acsami.5b02715.

[26] T. H. Tran *et al.*, "Adsorption isotherms and kinetic modeling of methylene blue dye onto a carbonaceous hydrochar adsorbent derived from coffee husk waste," *Sci. Total Environ.*, vol. 725, p. 138325, July 2020, doi: 10.1016/j.scitotenv.2020.138325.

[27] M. H. Saghi *et al.*, "Vanadium oxide nanoparticles for methylene blue water remediation: Exploring the effect of physicochemical parameters by process modeling," *J. Mol. Liq.*, vol. 318, p. 114046, Nov. 2020, doi: 10.1016/j.molliq.2020.114046.

[28] V. Katheresan, J. Kansedo, and S. Y. Lau, "Efficiency of various recent wastewater dye removal methods: A review," *J. Environ. Chem. Eng.*, vol. 6, no. 4, pp. 4676–4697, Aug. 2018, doi: 10.1016/j.jece.2018.06.060.

[29] H. M. Nassef, G. A. A. M. Al-Hazmi, A. A. Alayyafi, M. G. El-Desouky, and A. A. El-Bindary, "Synthesis and characterization of new composite sponge combining of metal-organic framework and chitosan for the elimination of Pb(II), Cu(II) and Cd(II) ions from aqueous solutions: Batch adsorption and optimization using Box-Behnken design," *J. Mol. Liq.*, vol. 394, p. 123741, Jan. 2024, doi: 10.1016/j.molliq.2023.123741.

[30] I. D. Mall, V. C. Srivastava, and N. K. Agarwal, "Removal of Orange-G and Methyl Violet dyes by adsorption onto bagasse fly ash—kinetic study and equilibrium isotherm analyses," *Dyes Pigments*, vol. 69, no. 3, pp. 210–223, Jan. 2006, doi: 10.1016/j.dyepig.2005.03.013.

[31] S. Wang and H. Wu, "Environmental-benign utilisation of fly ash as low-cost adsorbents," *J. Hazard. Mater.*, vol. 136, no. 3, pp. 482–501, Aug. 2006, doi: 10.1016/j.jhazmat.2006.01.067.

[32] M. J. Iqbal and M. N. Ashiq, "Adsorption of dyes from aqueous solutions on activated charcoal," *J. Hazard. Mater.*, vol. 139, no. 1, pp. 57–66, Jan. 2007, doi: 10.1016/j.jhazmat.2006.06.007.

[33] L. Sepúlveda, K. Fernández, E. Contreras, and C. Palma, "Adsorption of Dyes using Peat: Equilibrium and Kinetic Studies," *Environ. Technol.*, vol. 25, no. 9, pp. 987–996, Sept. 2004, doi: 10.1080/09593332508618390.

[34] P. K. Malik, "Use of activated carbons prepared from sawdust and rice-husk for adsorption of acid dyes: a case study of Acid Yellow 36," *Dyes Pigments*, vol. 56, no. 3, pp. 239–249, Mar. 2003, doi: 10.1016/S0143-7208(02)00159-6.

[35] Q. He, G. Wang, Z. Chen, Z. Miao, K. Wan, and S. Huang, "Adsorption of anionic azo dyes using lignite coke by one-step short-time pyrolysis," *Fuel*, vol. 267, p. 117140, May 2020, doi: 10.1016/j.fuel.2020.117140.

[36] F. Ferrero, "Dye removal by low cost adsorbents: Hazelnut shells in comparison with wood sawdust," *J. Hazard. Mater.*, vol. 142, no. 1–2, pp. 144–152, Apr. 2007, doi: 10.1016/j.jhazmat.2006.07.072.

[37] G. A. A. M. Al-Hazmi, A. A. Alayyafi, M. G. El-Desouky, and A. A. El-Bindary, "Chitosan-nano CuO composite for removal of mercury (II): Box-Behnken design optimization and adsorption mechanism," *Int. J. Biol. Macromol.*, vol. 261, p. 129769, Mar. 2024, doi: 10.1016/j.ijbiomac.2024.129769.

[38] S. M. Saleh, A. E. A. E. Albadri, M. A. B. Aissa, and A. Modwi, "Fabrication of Mesoporous V2O5@g-C3N4 Nanocomposite as Photocatalyst for Dye Degradation," *Crystals*, vol. 12, no. 12, p. 1766, Dec. 2022, doi: 10.3390/cryst12121766.

[39] I. Ali, E. N. Al-Shafei, A. A. Al-Arfaj, and T. A. Saleh, "Influence of titanium oxide on the performance of molybdenum catalysts loaded on zeolite toward hydrodesulfurization reactions," *Microporous Mesoporous Mater.*, vol. 303, p. 110188, Aug. 2020, doi: 10.1016/j.micromeso.2020.110188.

[40] N. M. Hosny, I. Gomaa, A. Abd El-Moemen, and Z. M. Anwar, "Synthesis, magnetic and adsorption of dye onto the surface of NiO nanoparticles," *J. Mater. Sci. Mater. Electron.*, vol. 31, no. 11, pp. 8413–8422, June 2020, doi: 10.1007/s10854-020-03376-w.

[41] S. Noreen *et al.*, "Iron oxide (Fe2O3) prepared via green route and adsorption efficiency evaluation for an anionic dye: kinetics, isotherms and thermodynamics studies," *J. Mater. Res. Technol.*, vol. 9, no. 3, pp. 4206–4217, May 2020, doi: 10.1016/j.jmrt.2020.02.047.

[42] Q. Qin, T. Sun, W. Yin, and Y. Xu, "Rapid and efficient removal of methylene blue by freshly prepared manganese dioxide," *Cogent Eng.*, vol. 4, no. 1, p. 1345289, Jan. 2017, doi: 10.1080/23311916.2017.1345289.

[43] W. S. Al-Arjan, "Zinc Oxide Nanoparticles and Their Application in Adsorption of Toxic Dye from Aqueous Solution," *Polymers*, vol. 14, no. 15, p. 3086, July 2022, doi: 10.3390/polym14153086.

[44] T. A. Abdullah *et al.*, "V2O5 Nanoparticles for Dyes Removal from Water," *Chem. J. Mold.*, vol. 16, no. 2, pp. 102–111, Dec. 2021, doi: 10.19261/cjm.2021.911.

[45] W. Avansi, V. R. de Mendonça, O. F. Lopes, and C. Ribeiro, "Vanadium pentoxide 1-D nanostructures applied to dye removal from aqueous systems by coupling adsorption and visible-light photodegradation," *RSC Adv.*, vol. 5, no. 16, pp. 12000–12006, Jan. 2015, doi: 10.1039/C4RA12788A.

[46] P. B. Koli, K. H. Kapadnis, U. G. Deshpande, and M. R. Patil, "Fabrication and characterization of pure and modified Co3O4 nanocatalyst and their application for photocatalytic degradation of eosine blue dye: a comparative study," *J. Nanostructure Chem.*, vol. 8, no. 4, pp. 453–463, Dec. 2018, doi: 10.1007/s40097-018-0287-0.

[47] N. M. Hosny, I. Gomaa, and M. G. Elmahgary, "Adsorption of polluted dyes from water by transition metal oxides: A review," *Appl. Surf. Sci. Adv.*, vol. 15, p. 100395, June 2023, doi: 10.1016/j.apsadv.2023.100395.

[48] T. B. Vidovix, H. B. Quesada, R. Bergamasco, M. F. Vieira, and A. M. S. Vieira, "Adsorption of Safranin-O dye by copper oxide nanoparticles synthesized from *Punica granatum* leaf extract," *Environ. Technol.*, vol. 43, no. 20, pp. 3047–3063, Sept. 2022, doi: 10.1080/09593330.2021.1914180.

[49] S. Homaeigohar, A. Zillohu, R. Abdelaziz, M. Hedayati, and M. Elbahri, "A Novel Nanohybrid Nanofibrous Adsorbent for Water Purification from Dye Pollutants," *Materials*, vol. 9, no. 10, p. 848, Oct. 2016, doi: 10.3390/ma9100848.

[50] A. Di Mauro, A. Landström, I. Concina, G. Impellizzeri, V. Privitera, and M. Epifani, "Surface modification by vanadium pentoxide turns oxide nanocrystals into powerful adsorbents of methylene blue," *J. Colloid Interface Sci.*, vol. 533, pp. 369–374, Jan. 2019, doi: 10.1016/j.jcis.2018.08.070.

[51] O. Ifguis, Y. Ziat, H. Belkhanchi, F. Ammou, A. Moutcine, and C. Laghlimi, "Adsorption mechanism of Methylene Blue from polluted water by Opuntia ficus indica of Beni Mellal and Sidi Bou Othmane areas: A comparative study," *Chem. Phys. Impact*, vol. 6, p. 100235, June 2023, doi: 10.1016/j.chphi.2023.100235.

[52] S. Meghana, P. Kabra, S. Chakraborty, and N. Padmavathy, "Understanding the pathway of antibacterial activity of copper oxide nanoparticles," *RSC Adv.*, vol. 5, no. 16, pp. 12293–12299, 2015, doi: 10.1039/C4RA12163E.

[53] R. Dadi, R. Azouani, M. Traore, C. Mielcarek, and A. Kanaev, "Antibacterial activity of ZnO and CuO nanoparticles against gram positive and gram negative strains," *Mater. Sci. Eng. C*, vol. 104, p. 109968, Nov. 2019, doi: 10.1016/j.msec.2019.109968.

[54] N.-Y. T. Nguyen, N. Grelling, C. L. Wetteland, R. Rosario, and H. Liu, "Antimicrobial Activities and Mechanisms of Magnesium Oxide Nanoparticles (nMgO) against Pathogenic Bacteria, Yeasts, and Biofilms," *Sci. Rep.*, vol. 8, no. 1, p. 16260, Nov. 2018, doi: 10.1038/s41598-018-34567-5.

[55] M. Azizi-Lalabadi, A. Ehsani, B. Divband, and M. Alizadeh-Sani, "Antimicrobial activity of Titanium dioxide and Zinc oxide nanoparticles supported in 4A zeolite and evaluation the morphological characteristic," *Sci. Rep.*, vol. 9, no. 1, p. 17439, Nov. 2019, doi: 10.1038/s41598-019-54025-0.

[56] S. N. Matussin, M. H. Harunsani, and M. M. Khan, "CeO2 and CeO2-based nanomaterials for photocatalytic, antioxidant and antimicrobial activities," *J. Rare Earths*, vol. 41, no. 2, pp. 167–181, Feb. 2023, doi: 10.1016/j.jre.2022.09.003.

[57] S. Kumar, F. Ahmed, N. M. Shaalan, and O. Saber, "Biosynthesis of CeO2 Nanoparticles Using Egg White and Their Antibacterial and Antibiofilm Properties on Clinical Isolates," *Crystals*, vol. 11, no. 6, p. 584, May 2021, doi: 10.3390/cryst11060584.

[58] C. Sridhar, N. Gunvanthrao Yernale, and M. V. N. A. Prasad, "Synthesis, Spectral Characterization, and Antibacterial and Antifungal Studies of PANI/V_2O_5 Nanocomposites," *Int. J. Chem. Eng.*, vol. 2016, pp. 1–6, 2016, doi: 10.1155/2016/3479248.

[59] M. A. Saleemi, Y. L. Kong, P. V. C. Yong, and E. H. Wong, "An Overview of Antimicrobial Properties of Carbon Nanotubes-Based Nanocomposites," *Adv. Pharm. Bull.*, vol. 12, no. 3, pp. 449–465, May 2022, doi: 10.34172/apb.2022.049.

[60] L. K. Abdul Karem and A. T. Ali, "Biosynthesis, Characterization, Adsorption and Antimicrobial studies of Vanadium Oxide Nanoparticles Using Punica Granatum Extract," *Baghdad Sci. J.*, July 2023, doi: 10.21123/bsj.2023.8114.

[61] A. H. Hashem *et al.*, "Antifungal Activity of Biosynthesized Silver Nanoparticles (AgNPs) against Aspergilli Causing Aspergillosis: Ultrastructure Study," *J. Funct. Biomater.*, vol. 13, no. 4, p. 242, Nov. 2022, doi: 10.3390/jfb13040242.

[62] A. Carrapiço, M. R. Martins, A. T. Caldeira, J. Mirão, and L. Dias, "Biosynthesis of Metal and Metal Oxide Nanoparticles Using Microbial Cultures: Mechanisms, Antimicrobial Activity and Applications to Cultural Heritage," *Microorganisms*, vol. 11, no. 2, p. 378, Feb. 2023, doi: 10.3390/microorganisms11020378.

[63] S. Das *et al.*, "Anti-angiogenic vanadium pentoxide nanoparticles for the treatment of melanoma and their *in vivo* toxicity study," *Nanoscale*, vol. 12, no. 14, pp. 7604–7621, 2020, doi: 10.1039/D0NR00631A.

[64] P. R. Pillai Suma *et al.*, "Paradigm of Vanadium pentoxide nanoparticle-induced autophagy and apoptosis in triple-negative breast cancer cells," Oct. 18, 2019, *Scientific Communication and Education*. doi: 10.1101/810200.

[65] S. Kumar, S. Kumari, R. Karan, A. Kumar, R. K. Rawal, and P. Kumar Gupta, "Anticancer perspectives of vanadium complexes," *Inorg. Chem. Commun.*, vol. 161, p. 112014, Mar. 2024, doi: 10.1016/j.inoche.2023.112014.

[66] M. Kumari *et al.*, "Vanadium complexes as potential metal-based antimicrobial drugs," *JBIC J. Biol. Inorg. Chem.*, vol. 29, no. 7–8, pp. 685–706, Nov. 2024, doi: 10.1007/s00775-024-02084-8.

[67] A. J. Hadi, U. M. Nayef, M. S. Jabir, and F. A.-H. Mutlak, "Synthesis of vanadium pentoxide nanoparticles via laser ablation for biomedical applications," *Int. J. Mod. Phys. B*, vol. 38, no. 18, p. 2450230, July 2024, doi: 10.1142/S0217979224502308.

[68] S. Nivetha *et al.*, "Nickel-doped vanadium pentoxide (Ni@V2O5) nanocomposite induces apoptosis targeting PI3K/AKT/mTOR signaling pathway in skin cancer: An in vitro and in vivo study," *Colloids Surf. B Biointerfaces*, vol. 234, p. 113763, Feb. 2024, doi: 10.1016/j.colsurfb.2024.113763.

[69] M. Jayalakshmi, M. M. Rao, N. Venugopal, and K.-B. Kim, "Hydrothermal synthesis of SnO2–V2O5 mixed oxide and electrochemical screening of carbon nano-tubes (CNT), V2O5, V2O5–CNT, and SnO2–V2O5–CNT electrodes for supercapacitor applications," *J. Power Sources*, vol. 166, no. 2, pp. 578–583, Apr. 2007, doi: 10.1016/j.jpowsour.2006.11.025.

[70] J. Liu, X. Wang, Q. Peng, and Y. Li, "Vanadium Pentoxide Nanobelts: Highly Selective and Stable Ethanol Sensor Materials," *Adv. Mater.*, vol. 17, no. 6, pp. 764–767, Mar. 2005, doi: 10.1002/adma.200400993.

[71] A. G. Temam *et al.*, "Recent progress on V2O5 based electroactive materials: Synthesis, properties, and supercapacitor application," *Curr. Opin. Electrochem.*, vol. 38, p. 101239, Apr. 2023, doi: 10.1016/j.coelec.2023.101239.

[72] S. Khan and K. Singh, "Influence of Al3+ doping for V5+ on the structural, optical, thermal and electrical properties of V2-Al O5- (x=0–0.20) ceramics," *Ceram. Int.*, vol. 47, no. 8, pp. 10724–10732, Apr. 2021, doi: 10.1016/j.ceramint.2020.12.188.

[73] M. Sabna, K. Safna, J. Mayandi, S. Zh. Karazhanov, and P. Jayaram, "Microstructure profiling and photoluminescence characteristics of V(1-x)2 Ni3xO5-δ compound systems," *Mater. Lett.*, vol. 266, p. 127507, May 2020, doi: 10.1016/j.matlet.2020.127507.

[74] M. Sabna, K. Safna, S. C P, and P. Jayaram, "Surface-Modified Mesoporous V_{2-x} Sb_{2x} $O_{5-\delta}$ Ceramics for Improving the Electrostatic Chemisorption of Methylene Blue," *ChemistrySelect*, vol. 9, no. 29, p. e202400862, Aug. 2024, doi: 10.1002/slct.202400862.

[75] A. Martin and M. Thuo, "Beyond Hume-Rothery Rules," *Acc. Mater. Res.*, vol. 4, no. 10, pp. 809–813, Oct. 2023, doi: 10.1021/accountsmr.3c00126.

[76] J. Khelifi, M. Nasri, and E. Dhahri, "Magnetic, Magnetocaloric and Master Curve Behaviors for La0.6Sr0.4Mn0.9V0.1O3 Compound," *J. Supercond. Nov. Magn.*, vol. 29, no. 3, pp. 753–758, Mar. 2016, doi: 10.1007/s10948-015-3338-5.

[77] J. Vidya, A. John Bosco, K. Haribaaskar, and P. Balamurugan, "Polyaniline - BiVO4 nanocomposite as an efficient adsorbent for the removal of methyl orange from aqueous solution," *Mater. Sci. Semicond. Process.*, vol. 103, p. 104645, Nov. 2019, doi: 10.1016/j.mssp.2019.104645.

[78] J. Wang and X. Guo, "Adsorption kinetic models: Physical meanings, applications, and solving methods," *J. Hazard. Mater.*, vol. 390, p. 122156, May 2020, doi: 10.1016/j.jhazmat.2020.122156.

[79] N. Ayawei, A. N. Ebelegi, and D. Wankasi, "Modelling and Interpretation of Adsorption Isotherms," *J. Chem.*, vol. 2017, pp. 1–11, 2017, doi: 10.1155/2017/3039817.

[80] J. Wang and X. Guo, "Adsorption isotherm models: Classification, physical meaning, application and solving method," *Chemosphere*, vol. 258, p. 127279, Nov. 2020, doi: 10.1016/j.chemosphere.2020.127279.

[81] H. Song, C. Zhang, Y. Liu, C. Liu, X. Nan, and G. Cao, "Facile synthesis of mesoporous V2O5 nanosheets with superior rate capability and excellent cycling stability for lithium ion batteries," *J. Power Sources*, vol. 294, pp. 1–7, Oct. 2015, doi: 10.1016/j.jpowsour.2015.06.055.

[82] V. Uma Shankar, D. Govindarajan, P. Christuraj, M. J. Salethraj, F. J. Johanson, and M. D. Raja, "Enhanced the electrochemical properties of Ni doped V2O5 as a electrode material for supercapacitor applications," *Mater. Today Proc.*, vol. 50, pp. 2675–2678, 2022, doi: 10.1016/j.matpr.2020.08.213.

[83] A. Mauger, C. M. Julien, and Sorbonne Universités, Institut de Minéralogie, de Physique des Matériaux et de Cosmologie (IMPMC), UMR 7590, 4 place Jussieu,

75252 Paris, France, "V_2O_5 thin films for energy storage and conversion," *AIMS Mater. Sci.*, vol. 5, no. 2, pp. 349–401, 2018, doi: 10.3934/matersci.2018.3.349.

[84] R. B. Darling and S. Iwanaga, "Structure, properties, and MEMS and microelectronic applications of vanadium oxides," *Sadhana*, vol. 34, no. 4, pp. 531–542, Aug. 2009, doi: 10.1007/s12046-009-0025-x.

[85] S. Devesa, A. P. Rooney, M. P. Graça, D. Cooper, and L. C. Costa, "Williamson-hall analysis in estimation of crystallite size and lattice strain in Bi1.34Fe0.66Nb1.34O6.35 prepared by the sol-gel method," *Mater. Sci. Eng. B*, vol. 263, p. 114830, Jan. 2021, doi: 10.1016/j.mseb.2020.114830.

[86] Y. Li *et al.*, "Sn-Doped V $_2$ O $_5$ Film with Enhanced Lithium-Ion Storage Performance," *J. Phys. Chem. C*, vol. 117, no. 45, pp. 23507–23514, Nov. 2013, doi: 10.1021/jp406927m.

[87] S. Mandal, A. Pramanick, S. Chakraborty, and P. Pratim Dey, "Phase determination of ZrB2-B4C ceramic composite material using XRD and rietveld refinement analysis," *Mater. Today Proc.*, vol. 33, pp. 5664–5666, 2020, doi: 10.1016/j.matpr.2020.04.124.

[88] Karim. Souifi *et al.*, "Synthesis, structural and magnetic behavior and theoretical approach to study the magnetic and magnetocaloric properties of the half-doped perovskite Nd0.5Ba0.5CoO3," *J. Mater. Sci. Mater. Electron.*, vol. 32, no. 11, pp. 15291–15306, June 2021, doi: 10.1007/s10854-021-06079-y.

[89] A. A. Bagade, V. V. Ganbavle, S. V. Mohite, T. D. Dongale, B. B. Sinha, and K. Y. Rajpure, "Assessment of structural, morphological, magnetic and gas sensing properties of CoFe 2 O 4 thin films," *J. Colloid Interface Sci.*, vol. 497, pp. 181–192, July 2017, doi: 10.1016/j.jcis.2017.02.067.

[90] J. Goclon, R. Grybos, M. Witko, and J. Hafner, "Relative stability of low-index V $_2$ O $_5$ surfaces: a density functional investigation," *J. Phys. Condens. Matter*, vol. 21, no. 9, p. 095008, Mar. 2009, doi: 10.1088/0953-8984/21/9/095008.

[91] C.-C. Wang, C.-L. Lu, F.-S. Shieu, and H. C. Shih, "Structure and Photoluminescence Properties of Thermally Synthesized V2O5 and Al-Doped V2O5 Nanostructures," *Materials*, vol. 14, no. 2, p. 359, Jan. 2021, doi: 10.3390/ma14020359.

[92] X. Yang, Z. Dong, and C. Q. Sun, "Effects of doping concentration on bond length and bond energy studied by Raman shift," *Appl. Phys. Lett.*, vol. 123, no. 5, p. 053101, July 2023, doi: 10.1063/5.0160714.

[93] S. Pavasupree, Y. Suzuki, A. Kitiyanan, S. Pivsa-Art, and S. Yoshikawa, "Synthesis and characterization of vanadium oxides nanorods," *J. Solid State Chem.*, vol. 178, no. 6, pp. 2152–2158, June 2005, doi: 10.1016/j.jssc.2005.03.034.

[94] M. Michalska, A. Jain, S. R. Manippady, H. Nishihara, R. Tang, and K. Sobczak, *Data_V2O5.docx*. figshare, 2022, p. 2560853 Bytes. doi: 10.6084/M9.FIGSHARE.21155236.

[95] Y. Zhou, Z. Qiu, M. Lü, A. Zhang, and Q. Ma, "Preparation and characterization of porous Nb2O5 nanoparticles," *Mater. Res. Bull.*, vol. 43, no. 6, pp. 1363–1368, June 2008, doi: 10.1016/j.materresbull.2007.06.053.

[96] E. Hryha, E. Rutqvist, and L. Nyborg, "Stoichiometric vanadium oxides studied by XPS," *Surf. Interface Anal.*, vol. 44, no. 8, pp. 1022–1025, Aug. 2012, doi: 10.1002/sia.3844.

[97] J. Chen *et al.*, "Electrochemical Performance and Stress Distribution of Sb/Sb2O3 Nanoparticles as Anode Materials for Sodium-Ion Batteries," *Batteries*, vol. 9, no. 2, p. 98, Jan. 2023, doi: 10.3390/batteries9020098.

[98] Q. Han *et al.*, "Synthesis of one-dimensional yolk-shell Sb2O3/TiO2 composite as an anode material for enhanced lithium-storage properties," *Ionics*, vol. 26, no. 3, pp. 1221–1228, Mar. 2020, doi: 10.1007/s11581-019-03300-1.

[99] H. Xue *et al.*, "S-Doped Sb2O3 Nanocrystal: an Efficient Visible-Light Catalyst for Organic Degradation," *Nanoscale Res. Lett.*, vol. 13, no. 1, p. 114, Dec. 2018, doi: 10.1186/s11671-018-2522-5.

[100] Q. Zhao, X. Zhang, Q. Yang, and Y. Xie, "One-step synthesis of Sb $_2$ O $_3$ broom-like belts with controllable morphology," *Can. J. Chem.*, vol. 83, no. 8, pp. 1093–1097, Aug. 2005, doi: 10.1139/v05-123.

[101] G. Silversmit, D. Depla, H. Poelman, G. B. Marin, and R. De Gryse, "Determination of the V2p XPS binding energies for different vanadium oxidation states (V5+ to V0+)," *J. Electron Spectrosc. Relat. Phenom.*, vol. 135, no. 2–3, pp. 167–175, Apr. 2004, doi: 10.1016/j.elspec.2004.03.004.

[102] A. Choudhury, J.-H. Kim, K.-S. Yang, and D.-J. Yang, "Facile synthesis of self-standing binder-free vanadium pentoxide-carbon nanofiber composites for high-performance supercapacitors," *Electrochimica Acta*, vol. 213, pp. 400–407, Sept. 2016, doi: 10.1016/j.electacta.2016.06.111.

[103] B. Ávila-Bolívar, V. Montiel, and J. Solla-Gullón, "On the activity and stability of Sb2O3/Sb nanoparticles for the electroreduction of CO2 toward formate," *J. Electroanal. Chem.*, vol. 895, p. 115440, Aug. 2021, doi: 10.1016/j.jelechem.2021.115440.

[104] N. Asim, S. Radiman, M. A. Yarmo, and M. S. Banaye Golriz, "Vanadium pentoxide: Synthesis and characterization of nanorod and nanoparticle V2O5 using CTAB micelle solution," *Microporous Mesoporous Mater.*, vol. 120, no. 3, pp. 397–401, Apr. 2009, doi: 10.1016/j.micromeso.2008.12.013.

[105] B. P. Barbero, L. E. Cadús, and L. Hilaire, "XPS studies for vanadium pentoxide along the catalytic bed: oxidative dehydrogenation of propane," *Appl. Catal. Gen.*, vol. 246, no. 2, pp. 237–242, June 2003, doi: 10.1016/S0926-860X(03)00025-5.

[106] P. Nakhanivej, S. K. Park, K. H. Shin, S. Yun, and H. S. Park, "Hierarchically structured vanadium pentoxide/reduced graphene oxide composite microballs for lithium ion battery cathodes," *J. Power Sources*, vol. 436, p. 226854, Oct. 2019, doi: 10.1016/j.jpowsour.2019.226854.

[107] L. Abello, E. Husson, Y. Repelin, and G. Lucazeau, "Vibrational spectra and valence force field of crystalline V2O5," *Spectrochim. Acta Part Mol. Spectrosc.*, vol. 39, no. 7, pp. 641–651, Jan. 1983, doi: 10.1016/0584-8539(83)80040-3.

[108] S. Zhan, G. Chen, D. Liu, A. Li, C. Wang, and Y. Wei, "Effects of Cr doping on the structural and electrochemical properties of V2O5," *J. Alloys Compd.*, vol. 479, no. 1–2, pp. 652–656, June 2009, doi: 10.1016/j.jallcom.2009.01.023.

[109] P. R. P. Suma, R. V. Nair, W. Paul, and R. S. Jayasree, "Vanadium pentoxide nanoplates: Synthesis, characterization and unveiling the intrinsic anti-bacterial activity," *Mater. Lett.*, vol. 269, p. 127673, June 2020, doi: 10.1016/j.matlet.2020.127673.

[110] K. Schneider, "Optical properties and electronic structure of V2O5, V2O3 and VO2," *J. Mater. Sci. Mater. Electron.*, vol. 31, no. 13, pp. 10478–10488, July 2020, doi: 10.1007/s10854-020-03596-0.

[111] L. Top, M. Kang, and S. Kim, "A review on the optical characterization of V2O5 micro-nanostructures," *Ceram. Int.*, vol. 45, May 2019, doi: 10.1016/j.ceramint.2019.05.339.

[112] V. I. Merupo, S. Velumani, G. Oza, M. Makowska-Janusik, and A. Kassiba, "Structural, electronic and optical features of molybdenum-doped bismuth vanadium oxide," *Mater. Sci. Semicond. Process.*, vol. 31, pp. 618–623, Mar. 2015, doi: 10.1016/j.mssp.2014.12.057.

[113] P. Jayaram, P. P. Pradyumnan, S. Zh. Karazhanov, R. J. Choudary, and S. N. Potty, "Pulsed laser deposition and optical band gap engineering in multinary transparent conducting oxide thinfilms," *Mater. Sci. Semicond. Process.*, vol. 31, pp. 624–629, Mar. 2015, doi: 10.1016/j.mssp.2014.12.062.

[114] Department of Physics, Kongunadu Arts and Science College, Coimbatore641029 Tamil Nadu, India *et al.*, "Characterization of pure and Cu doped V2O5 nanostructures and their Cu:V2O5/p-Si photodiode applications," *Dig. J. Nanomater. Biostructures*, vol. 18, no. 1, pp. 131–143, Jan. 2023, doi: 10.15251/DJNB.2023.181.131.

[115] C.-C. Wang, C.-L. Lu, F.-S. Shieu, and H. C. Shih, "Enhanced photoluminescence properties of Ga-doped V2O5 nanorods via defect structures," *Chem. Phys. Lett.*, vol. 738, p. 136864, Jan. 2020, doi: 10.1016/j.cplett.2019.136864.

[116] P. Srilakshmi, A. U. Maheswari, V. Sajeev, and M. Sivakumar, "Tuning the optical bandgap of V2O5 nanoparticles by doping transition metal ions," *Mater. Today Proc.*, vol. 18, pp. 1375–1379, 2019, doi: 10.1016/j.matpr.2019.06.603.

[117] F. C. Kalangestani, M. Simiari, and F. E. Ghodsi, "Fabrication of V2O5/NiO double-layer film with hydrophilic property and evaluation of the effects of V2O5 coating on electro-optical parameters of NiO film," *Appl. Phys. A*, vol. 128, no. 5, p. 395, May 2022, doi: 10.1007/s00339-022-05545-6.

[118] K.-Y. Pan and D.-H. Wei, "Optoelectronic and Electrochemical Properties of Vanadium Pentoxide Nanowires Synthesized by Vapor-Solid Process," *Nanomaterials*, vol. 6, no. 8, p. 140, July 2016, doi: 10.3390/nano6080140.

[119] S. Usharani and V. Rajendran, "Size Controlled Synthesis and Characterization of V2O5/Al2O3 Nanocomposites," *Colloid Interface Sci. Commun.*, vol. 24, pp. 7–12, May 2018, doi: 10.1016/j.colcom.2018.03.001.

[120] K. M. Shafeeq, V. P. Athira, C. H. R. Kishor, and P. M. Aneesh, "Structural and optical properties of V2O5 nanostructures grown by thermal decomposition technique," *Appl. Phys. A*, vol. 126, no. 8, p. 586, Aug. 2020, doi: 10.1007/s00339-020-03770-5.

[121] C. W. Zou and W. Gao, "Fabrication, Optoelectronic and Photocatalytic Properties of Some Composite Oxide Nanostructures," *Trans. Electr. Electron. Mater.*, vol. 11, no. 1, pp. 1–10, Feb. 2010, doi: 10.4313/TEEM.2010.11.1.001.

[122] A. N. Oliveros, J. A. I. Pimentel, M. D. G. de Luna, S. Garcia-Segura, R. R. M. Abarca, and R.-A. Doong, "Visible-light photocatalytic diclofenac removal by tunable vanadium pentoxide/boron-doped graphitic carbon nitride composite," *Chem. Eng. J.*, vol. 403, p. 126213, Jan. 2021, doi: 10.1016/j.cej.2020.126213.

[123] N. F. Alharby, R. S. Almutairi, and N. A. Mohamed, "Adsorption Behavior of Methylene Blue Dye by Novel CrossLinked O-CM-Chitosan Hydrogel in Aqueous Solution: Kinetics, Isotherm and Thermodynamics," *Polymers*, vol. 13, no. 21, p. 3659, Oct. 2021, doi: 10.3390/polym13213659.

[124] H. Ali and A. M. Ismail, "Honeycomb-like V2O5 Based Films: Synthesis, Structural, Thermal, and Optical Properties for Environmental Applications," *J. Inorg. Organomet. Polym. Mater.*, vol. 32, no. 8, pp. 3012–3029, Aug. 2022, doi: 10.1007/s10904-022-02331-y.

[125] A. A. Alshehri and M. A. Malik, "Biogenic fabrication of ZnO nanoparticles using Trigonella foenum-graecum (Fenugreek) for proficient photocatalytic degradation of methylene blue under UV irradiation," *J. Mater. Sci. Mater. Electron.*, vol. 30, no. 17, pp. 16156–16173, Sept. 2019, doi: 10.1007/s10854-019-01985-8.

[126] X. Liang *et al.*, "The remarkable effect of vanadium doping on the adsorption and catalytic activity of magnetite in the decolorization of methylene blue," *Appl. Catal. B Environ.*, vol. 97, no. 1–2, pp. 151–159, June 2010, doi: 10.1016/j.apcatb.2010.03.035.

[127] J. Rouquerol *et al.*, "Recommendations for the characterization of porous solids (Technical Report)," *Pure Appl. Chem.*, vol. 66, no. 8, pp. 1739–1758, Jan. 1994, doi: 10.1351/pac199466081739.

[128] L. Xu *et al.*, "Pore Structure and Fractal Characteristics of Different Shale Lithofacies in the Dalong Formation in the Western Area of the Lower Yangtze Platform," *Minerals*, vol. 10, p. 72, Jan. 2020, doi: 10.3390/min10010072.

[129] F. Gao *et al.*, "The states of vanadium species in V-SBA-15 synthesized under different pH values," *Microporous Mesoporous Mater.*, vol. 110, no. 2, pp. 508–516, Apr. 2008, doi: 10.1016/j.micromeso.2007.06.041.

[130] Danmei Yu,*ab Changguo Chen,b Shuhong Xie,cd Yanyi Liu,a Kwangsuk Park,a Xiaoyuan Zhou,a and Qifeng Zhang,a Jiangyu Lic and Guozhong Cao*a, "Mesoporous vanadium pentoxide nanofibers with significantly enhanced Li-ion storage properties by electrospinning," *Energy Environ. Sci.*, vol. 4, pp. 858–861, Nov. 2011, doi: DOI:%2010.1039/c0ee00313a.

[131] A. M. Elfadly, A. M. Badawi, F. Z. Yehia, Y. A. Mohamed, M. A. Betiha, and A. M. Rabie, "Selective nano alumina supported vanadium oxide catalysts for oxidative

dehydrogenation of ethylbenzene to styrene using CO2 as soft oxidant," *Egypt. J. Pet.*, vol. 22, no. 3, pp. 373–380, Dec. 2013, doi: 10.1016/j.ejpe.2013.10.007.

[132] M. Xue, H. Chen, J. Ge, and J. Shen, "Preparation and characterization of thermally stable high surface area mesoporous vanadium oxides," *Microporous Mesoporous Mater.*, vol. 131, no. 1–3, pp. 37–44, 2010.

[133] H. Yin *et al.*, "Self-Assembled Vanadium Oxide Nanoflakes for p-Type Ammonia Sensors at Room Temperature," *Nanomaterials*, vol. 9, no. 3, Art. no. 3, Mar. 2019, doi: 10.3390/nano9030317.

[134] T. R. Sahoo and B. Prelot, "Adsorption processes for the removal of contaminants from wastewater," in *Nanomaterials for the Detection and Removal of Wastewater Pollutants*, Elsevier, 2020, pp. 161–222. doi: 10.1016/B978-0-12-818489-9.00007-4.

[135] M. H. Ashery, E. M. Elsehly, M. Elnouby, and E. M. EL-Maghraby, "Controlled synthesis of MWCNTs/V2O5 nanocomposite by hydrothermal approach for adsorption and photodegradation processes," *Water Sci. Technol.*, vol. 88, no. 2, pp. 392–407, July 2023, doi: 10.2166/wst.2023.217.

[136] G. A. A. M. Al-Hazmi, A. A. Alayyafi, M. G. El-Desouky, and A. A. El-Bindary, "Guava seed activated carbon loaded calcium alginate aerogel for the adsorption of diclofenac sodium: Characterization, isotherm, kinetics, and optimization via Box-Behnken design," *Int. J. Biol. Macromol.*, vol. 262, p. 129995, Mar. 2024, doi: 10.1016/j.ijbiomac.2024.129995.

[137] M. Uzair *et al.*, "Effect of Mn Doped on Structural, Optical, and Dielectric Properties of $BiFe_{1-x}Mn_xO_3$ for Efficient Antioxidant Activity," *ACS Omega*, vol. 8, no. 45, pp. 42390–42397, Nov. 2023, doi: 10.1021/acsomega.3c04714.

[138] D. Sahoo, S. Senapati, S. Samal, S. Varadharajaperumal, and R. Naik, "Optical and Dielectric Characterization of Nanoparticle-Based $Cu_2Ni_{1+x}Sn_{1-x}S_4$ Nanosphere Synthesized by Facile Solvothermal Method," *ACS Appl. Eng. Mater.*, vol. 1, no. 3, pp. 1001–1012, Mar. 2023, doi: 10.1021/acsaenm.2c00269.

[139] H. Bouaamlat *et al.*, "Dielectric Properties, AC Conductivity, and Electric Modulus Analysis of Bulk Ethylcarbazole-Terphenyl," *Adv. Mater. Sci. Eng.*, vol. 2020, pp. 1–8, Jan. 2020, doi: 10.1155/2020/8689150.

[140] A. Yadav, M. S. Dahiya, P. Narwal, A. Hooda, A. Agarwal, and S. Khasa, "Electrical characterization of lithium bismuth borate glasses containing cobalt/vanadium ions," *Solid State Ion.*, vol. 312, pp. 21–31, Dec. 2017, doi: 10.1016/j.ssi.2017.10.006.

[141] H. Van Swygenhoven, "Grain Boundaries and Dislocations," *Science*, vol. 296, no. 5565, pp. 66–67, Apr. 2002, doi: 10.1126/science.1071040.

[142] S. Riaz, S. M. H. Shah, A. Akbar, S. Atiq, and S. Naseem, "Effect of Mn doping on structural, dielectric and magnetic properties of BiFeO3 thin films," *J. Sol-Gel Sci. Technol.*, vol. 74, no. 2, pp. 329–339, May 2015, doi: 10.1007/s10971-014-3461-y.

[143] F. Ragot, J. C. Badot, N. Baffier, and A. Fourrier-Lamer, "Influence of the microstructure on dielectric and conducting properties of vanadium pentoxide," *J. Mater. Chem.*, vol. 5, no. 8, p. 1155, 1995, doi: 10.1039/jm9950501155.

[144] F. K. Tan, J. Hassan, Z. Abd. Wahab, and R. S. Azis, "Electrical conductivity and dielectric studies of MnO 2 doped V 2 O 5," *Results Phys.*, vol. 6, pp. 420–427, 2016, doi: 10.1016/j.rinp.2016.07.011.

[145] F. K. Tan, J. Hassan, Z. Abd. Wahab, and R. S. Azis, "Electrical conductivity and dielectric behaviour of manganese and vanadium mixed oxide prepared by conventional solid state method," *Eng. Sci. Technol. Int. J.*, vol. 19, no. 4, pp. 2081–2087, Dec. 2016, doi: 10.1016/j.jestch.2016.08.002.

[146] M. Nasri *et al.*, "Temperature and Frequency Dependence of Negative Capacitance, Dielectric and Electric Properties in La0.57Nd0.1Sr0.13Ag0.2MnO3 Ceramic," *J. Low Temp. Phys.*, vol. 206, no. 3–4, pp. 250–268, Feb. 2022, doi: 10.1007/s10909-021-02656-x.

[147] Y. Higuchi and H. Tamura, "Recent progress on the dielectric properties of dielectric resonator materials with their applications from microwave to optical frequencies," *J. Eur. Ceram. Soc.*, vol. 23, no. 14, pp. 2683–2688, Jan. 2003, doi: 10.1016/S0955-2219(03)00193-6.

[148] M. Hussain, H. Zahra, S. M. Abbas, and Y. Zhu, "Flexible Dielectric Materials: Potential and Applications in Antennas and RF Sensors," *Adv. Electron. Mater.*, p. 2400240, June 2024, doi: 10.1002/aelm.202400240.

[149] B. N. Parida, P. R. Das, R. Padhee, S. Behera, and R. N. P. Choudhary, "Structural, dielectric and electrical properties of a new tungsten bronze ferroelectric ceramics," *J. Mater. Sci. Mater. Electron.*, vol. 25, no. 6, pp. 2618–2626, June 2014, doi: 10.1007/s10854-014-1920-4.

[150] A. K. Jonscher, "The 'universal' dielectric response," *Nature*, vol. 267, no. 5613, pp. 673–679, June 1977, doi: 10.1038/267673a0.

[151] A. S. Das and D. Biswas, "Investigation of Ac conductivity mechanism and dielectric relaxation of semiconducting neodymium-vanadate nanocomposites: temperature and frequency dependency," *Mater. Res. Express*, vol. 6, no. 7, p. 075206, Apr. 2019, doi: 10.1088/2053-1591/ab13ee.

[152] G. D. Khattak and A. Mekki, "Structure and electrical properties of SrO-borovanadate (V2O5)0.5(SrO)0.5−y(B2O3)y glassses," *J. Phys. Chem. Solids*, vol. 70, no. 10, pp. 1330–1336, Oct. 2009, doi: 10.1016/j.jpcs.2009.06.023.

[153] R. V. Barde, K. R. Nemade, and S. A. Waghuley, "AC conductivity and dielectric relaxation in V_2O_5–P_2O_5–B_2O_3 glasses," *J. Asian Ceram. Soc.*, vol. 3, no. 1, pp. 116–122, Mar. 2015, doi: 10.1016/j.jascer.2014.11.006.

[154] N. N. Ilkhechi, M. Mozammel, and A. Y. Khoroushahi, "Antifungal effects of ZnO, TiO2 and ZnO-TiO2 nanocomposite on Aspergillus flavus," Dec. 10, 2020. doi: 10.21203/rs.3.rs-123795/v1.

[155] Y. Shao, Y. Luan, C. Hao, J. Song, L. Li, and F. Song, "Antimicrobial protection of two controlled release silver nanoparticles on simulated silk cultural relic," *J. Colloid Interface Sci.*, vol. 652, pp. 901–911, Dec. 2023, doi: 10.1016/j.jcis.2023.08.116.

[156] S. Altimime, S. Q. Mohammed, M. H. Hassoni, and A. N. Abd, "Properties and Biomedical Applications of Hydrothermal method Synthesized of Vanadium Oxide nanoparticles," *J. Phys. Conf. Ser.*, vol. 1963, no. 1, p. 012043, July 2021, doi: 10.1088/1742-6596/1963/1/012043.

Chapter IV

Comprehensive Analysis of Crystallographic, Electrical, Optical, and Antimicrobial Properties of Ni-Incorporated Vanadium Pentoxide($V_{2-x}Ni_{2x}O_{5-\delta}$): A Multifaceted Approach

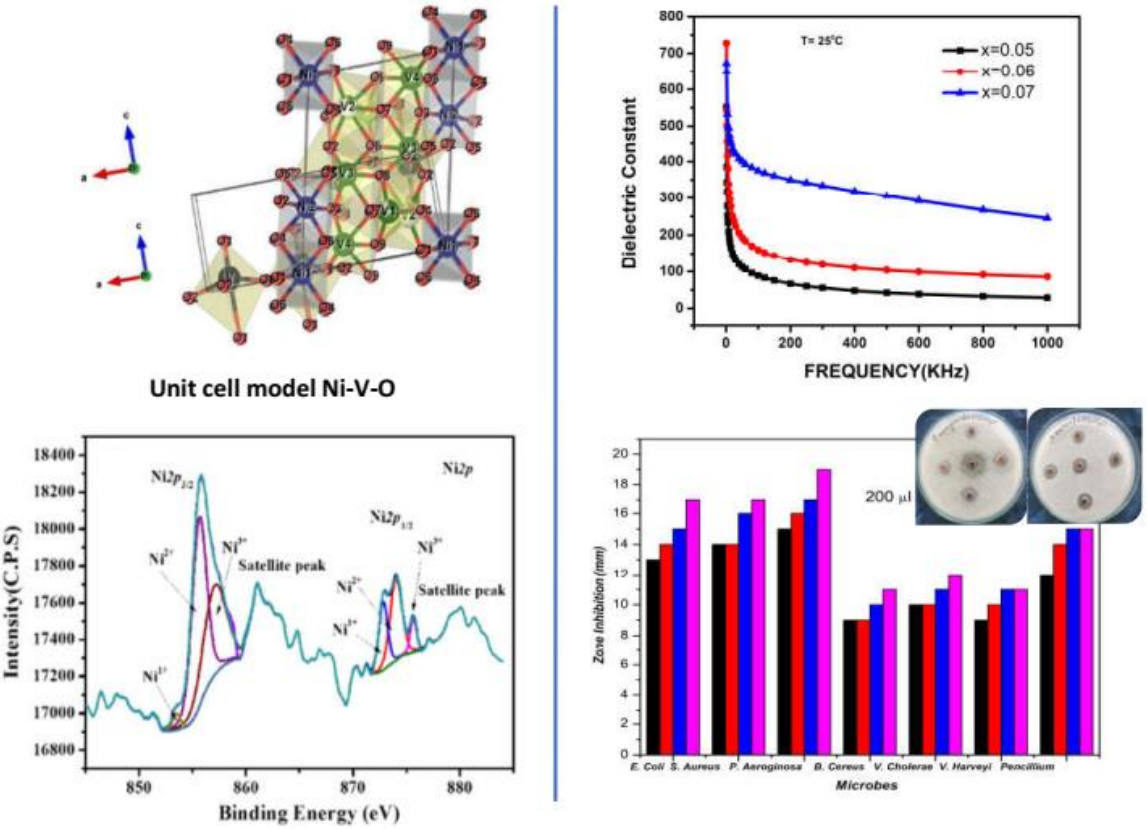

***Sabna, Melethil**, Jayaram, Pi, Sreedevi, Vanga, Pradeep Reddy, S, Sreejalakshmi, Aneesa Ko, Mujeeb Rahiman K and Safna, K. "Phase evolution, surface chemistry, and antimicrobial performance of Ni-incorporated vanadium pentoxide complex oxides" Zeitschrift für Physikalische Chemie, vol. 240, no. 1-2, 2026, pp. 219-237. https://doi.org/10.1515/zpch-2025-0076*

***Melethil Sabna**, P. Jayaram,Reformed dielectric features in single phase orthorhombic nickel vanadate complex oxides and the significance of the lattice dynamics in the optoelectrical features, Journal of Physics and Chemistry of Solids, Volume 180, 2023, 111428, ISSN 00223697, https://doi.org/10.1016/j.jpcs.2023.111428*

***Melethil. Sabna**, K. Safna , J Mayandi , S.Zh. Karazhanov P Jayaram, Microstructure profiling and photoluminescence characteristics of $V_{(1-x)2}Ni_{3x}O_{5-\delta}$ compound systems, Materials Letters 266 (2020) 127507, https://doi.org/10.1016/j.matlet.2020.127507*

4.1. Introduction

Recent researches focus on the synthesis of multi-cation pentavalent vanadium-based flexible frameworks with stable structural geometry, as the replacement of V^{5+} ions with other suitable metal cations, say X, forming V-X-O, leading to low valence ionic state of vanadium (V^{4+}, V^{3+}), causing increased electronic conductivity [1], [2]. As the orthorhombic structure of V_2O_5 is compatible with distorted [VO_6] octahedral units, effective replacement of the V^{5+} ion chooses the formation of [XO6] octahedral chains within the V_2O_5 framework, increasing the three-dimensional structural stability of the compounds that are inevitable for electrochemical cycling [3], [4].

The foreign ion concentration can alter vanadium valency by generating oxygen vacancies, thereby maintaining electrical neutrality in vanadate systems [5], [6]. Benorita Prusty et al. [7] reported the hydrothermal synthesis of V-Ni-O rods with excellent phase purity, retaining the orthorhombic structure, and with enhanced energy and power densities suitable for supercapacitor applications. Electrical conductivity in V_2O_5-based materials arises by *3d* electron hopping between V^{4+} and V^{5+} valence states thus forming polarons by the induced polarization of *3d* electrons at the positive vanadyl ions [8], [9]. Savidh Khan et al. [8] reported the rise in the AC conductivity up to $0.11Sm^{-1}$ in $V_{2-x}Mg_xO_{5-\delta}$ at x= 0.05 at 300^0C. Small polaron hopping between pentavalent and tetra-valent sites is regarded as a significant contributor to the conductivity of vanadate materials. Low valent cations replacing V^{5+} ions creates more oxygen vacancies leading to increased hopping of ions, and hence conductivity [8], [9].

The escalating global health crisis of antimicrobial resistance, driven by the overuse and misuse of antibiotics, is exacerbated by bacteria's ability to form biofilms, which act as physical and chemical barriers, hindering antibiotic efficacy. In response, researchers are focusing on inorganic antimicrobial agents, such as metal oxide nanomaterials, which enhance surface reactivity and generate reactive oxygen species to disrupt bacterial membranes and cellular integrity, providing an effective solution

to multidrug-resistant pathogens like *Staphylococcus aureus, Pseudomonas aeruginosa*, and *Escherichia coli* [10], [11], [12].

Numerous studies have documented the antimicrobial properties of various metal oxide nanoparticles, including silver oxide (Ag_2O), copper oxide (CuO), zinc oxide (ZnO), and titanium dioxide (TiO_2), which exhibit broad-spectrum activity by generating reactive oxygen species and disrupting microbial membranes [13]. However, fewer investigations have focused on the antimicrobial potential of less-explored transition metal oxides, such as oxides of vanadium, which have shown promising antibacterial activity, particularly in the form of vanadium pentoxide. The enhanced antimicrobial performance of V_2O_5 is attributed to its high redox potential, surface reactivity, and its ability to induce oxidative stress in microbial cells. V_2O_5, with its well-defined orthorhombic structure, reversible redox activity, and low toxicity, stands out as a versatile material in biomedical applications. Its antibacterial, antifungal, and anticancer properties have been demonstrated, with recent advancements in its use for drug delivery, where composites such as mesoporous carbon-coated V_2O_5 derivatives show improved loading capacity and controlled release profiles [12], [13], [16].

To overcome limitations such as low surface area and rapid charge carrier recombination, cation substitution has been widely investigated to enhance V_2O_5's structural stability, electrical conductivity, and bioactivity [17], [18]. Substituted systems often exhibit increased V^{4+} content due to charge compensation, suggesting a nuanced alteration in the local environment and oxidation states [19]. Such modifications can significantly influence the biological performance and redox behavior of V_2O_5-based materials. Haiyun Sun et. al [17] reported the synthesis of ZnO nanoflower-decorated vanadium pentoxide nanowire heterojunction, efficient for the generation of reactive oxygen species under both illuminated and dark conditions, achieving antibacterial efficacy rates of 99.8% and 99.0% against *Staphylococcus aureus*, respectively. Arunachalam Vinothini et al. [18] reported the enhanced antibacterial efficacy of Ag, Cd, and Ru doped Vanadium Pentoxide. Sneha R. Bhosale et al. [20] reported that the mesoporous carbon@V_2O_5 (C@V) composite

exhibited enhanced antibacterial activity, attributed to the synergistic effect of mesoporous carbon and V_2O_5, which increased surface area and active sites for interaction with microbial cells. This structural enhancement facilitated stronger interfacial interactions, improving bioactivity and disrupting bacterial membranes more effectively than pure V_2O_5. The $ZnO–V_2O_5–WO_3$ heterostructured nanocomposites demonstrated superior antibacterial activity against *Klebsiella pneumoniae*, *Staphylococcus aureus*, *Proteus vulgaris*, and *Pseudomonas aeruginosa*, This enhanced performance is attributed to the synergistic effect of the tri-metal oxide system, which promotes efficient reactive oxygen species generation under sunlight, thereby improving antibacterial efficacy compared to the individual components [21-22].

In this context, nickel-substituted vanadium pentoxide offers a promising pathway to tailor both structural, optical, electrical and biomedical properties. This study thus aims to investigate the structural evolution, surface morphology, surface chemistry, diffuse reflectance spectrum, electrical and antimicrobial behavior of V_2O_5 substituted with varying nickel concentrations. This multifaceted approach offers insight into the design of functional metal oxide materials for electrical and therapeutic applications.

4.2. Materials and Methods

Solid ceramic compounds were synthesized by mixing stoichiometric amounts of NiO (Nickel Oxide, 99.99% purity) and V_2O_5 (Vanadium Pentoxide, 99.99% purity), both procured from Sigma-Aldrich. The compositions followed the general formula $V_{(1-x)2}Ni_{3x}O_{5-\delta}$, with x ranging from 0.03 to 0.06. The precursor powders were thoroughly ground in an agate mortar and pestle for 2 h to ensure homogeneity. The resulting mixture was subjected to multiple cycles of high-temperature treatment and grinding, with heating performed at temperatures between 550 °C and 630 °C for a total duration of 24 h. Afterwards, the powders were coaxially pressed into pellets, which were then calcined at 650 °C for 12 h. To ensure high phase purity, the pellets underwent heating for 12 h after pressing. The structural characterization of the samples was done using powder X-ray diffraction ,the Rietveld refinement of the

diffraction data was carried out using the FullProf Suite software to extract detailed crystallographic parameters. VESTA software was utilized to visualize and analyze the crystal structures. Lattice dynamics was analyzed using microraman spectroscopy. Surface morphology of the samples was studied using SEM and elemental mapping confirmed the presence of constituent elements. Surface chemical state of samples were analyzed using X-ray Photoelectron Spectroscopy. The XPS data were analyzed using Casa XPS software. Optical properties were analyzed using Diffuse reflectance spectra, and band gap energy was determined using Kubelka-Munk plots. Dielectric and AC conductivity studies were carried out to determine the electrical measurements of the 14 mm sample pellets. Antimicrobial studies of the as prepared Ni-V-O compounds were carried out using the same methodology as discussed in chapter 3.

4.3. Results and Discussion

4.3.1. Structural Analysis and Crystallographic Refinement

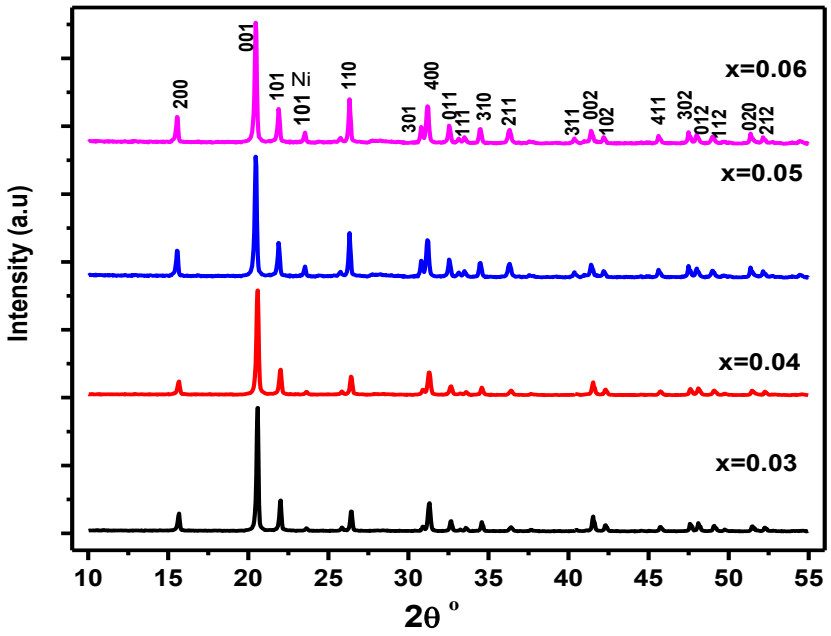

Figure 4.1. XRD pattern of the $V_{(1-x)2}Ni_{3x}O_{5-\delta}$ with prominent orientation along (001) direction.

The diffractogram of the synthesized $V_{(1-x)2}Ni_{3x}O_{5-\delta}$ ($0.03 \leq x \leq 0.06$) microparticles reveals an orthorhombic phase, as evidenced by distinct diffraction peaks observed at 2θ values of 15.62^0, 20.61°, 22.08°, 26.31°, 27.21°, 31.28°, 32.67°, 33.19°, 34.57°, 41.56°, 42.29°, 45.68°, 47.48°, 48.11°, 49.07° as shown in Figure. 4.1 [1]. The planes corresponding to these diffraction peaks are indicated in Table 4.1(a). These peaks correspond to specific lattice planes alligning with the characteristic planes documented in the JCPDS No. 41–1426 database, affirming the presence of the *Pmmn* (59) space group in the synthesized Ni-V-O compounds [23], [81-82]. As a result of Ni incorporation into the V_2O_5 lattice, a new peak arises at 23.57° corresponding to the 101 plane, indicating the *Triclinic* NiV_2O_6 phase with $P1$ space group symmetry [14-16], [29].

Table. 4.1(a). Prominent XRD reflections with Miller indices (hkl), corresponding 2θ values and microstructure of $V_{(1-x)2}Ni_{3x}O_{5-\delta}$ compounds at x=0.06

Sl. No	2θ°	(hkl)	Phase (Microstructure)
1.	15.62°	(200)	Orthorhombic V_2O_5
2.	20.61°	(001)	Orthorhombic V_2O_5
3.	22.08°	(101)	Orthorhombic V_2O_5
4.	23.57°	(101)	Triclinic NiV2O6
5.	26.31°	(110)	Orthorhombic V_2O_5
6.	31.28°	(400)	Orthorhombic V_2O_5
7.	32.67°	(111)	Orthorhombic V_2O_5
8.	33.19°	(011)	Orthorhombic V_2O_5
9.	34.57°	(310)	Orthorhombic V_2O_5
10.	41.56°	(002)	Orthorhombic V_2O_5
11.	42.29°	(102)	Orthorhombic V_2O_5
12.	45.68°	(411)	Orthorhombic V_2O_5
13.	47.48°	(600)	Orthorhombic V_2O_5
14.	48.11°	(302)	Orthorhombic V_2O_5
15.	49.07°	(012)	Orthorhombic V_2O_5

The estimated crystallite size, micro strain dislocation density and lattice parameters corresponding to V_2O_5 orthorhombic phase obtained from Scherrer equation and WH plot are given in table 4.1(b) [1], [2]. Rietveld refinement was conducted on each sample using the FullProf software for more in-depth analysis, as illustrated in Figure 4.2 presenting key crystallographic data and structural models of the Ni-V-O system. Figure. 4.2(a) displays the Rietveld refinement patterns of $V_{(1-x)2}Ni_{3x}O_{5-\delta}$ samples for compositions within the range of $0.03 \leq x \leq 0.06$, highlighting the refinement results for these Ni-doped vanadium oxide phases. Figure.4.2(b) showcases the orthorhombic unit cell structure of V_2O_5, visualized using VESTA software, figure 4.2(c) shows the unit cell of NiV_2O_6 simulated using optimized crystallographic data, also generated with VESTA, illustrating the structural features of the Ni-doped phase & figure 4.2 (d) depicts a unit cell model of the Ni–V–O mixed-phase compounds, combining both V_2O_5 and NiV_2O_6 phases for $x = 0.07$, offering a comprehensive visual representation of the phase composition and its structural evolution. The peak shape was modeled with the *Pseudo-Voigt* axial divergence asymmetry function, while a 6-coefficient polynomial function was employed to fit the background profile accurately. The refinement process involved optimizing several parameters, including scale factors, lattice parameters, full width at half maximum (FWHM)/shape factors, asymmetry parameters, and atomic coordinates. The Rietveld refinement thus revealed the presence of a dominant V_2O_5 phase with an orthorhombic structure, followed by the detection of a minor NiV_2O_6 phase exhibiting a triclinic structure [30].

The refined lattice parameters and unit cell volumes corresponding to the orthorhombic V_2O_5 phase and triclinic NiV_2O_6 phase, along with their respective phase fractions (in wt.%) at varying mole fractions (x), are summarized in Table 4.1(c). As NiO is incorporated into V_2O_5, the larger Ni^{2+} ions substitute for the smaller V^{5+} ions in the lattice, causing a distortion that expands the unit cell, increasing the lattice parameters and unit cell volume of the orthorhombic V_2O_5 phase with higher NiO concentration (Table 4.1(b & c)).

Table 4. 1(b) Estimated structural parameters and elemental composition of the compounds

x values	Sherrar Equation		Uniform Deformation Model W-H plot			Lattice Parameters			Constituent Elements Atomic %		
	Crystallite size D (nm)	Dislocation Density (δ) x 10^{-3} nm^{-2}	Crystallite size D (nm)	Dislocation Density (δ) x 10^{-3} nm^{-2}	Micro strain x(ε) 10^{-3}	a(Å)	b(Å)	C(Å)	Ni	V	O
0.03	66.91	0.224	59.15	0.286	0.190	11.32	3.54	4.31	3.52	31.59	64.89
0.04	64.27	0.242	57.97	0.298	0.181	11.32	3.54	4.31	4.91	39.43	55.66
0.05	61.57	0.264	58.91	0.288	0.093	11.36	3.55	4.33	8.24	16.19	75.57
0.06	59.64	0.281	58.92	0.288	0.026	11.39	3.55	4.34	13.03	35.30	51.67

Table 4.1(c) Edge Lengths and compositional percentage of Orthorhombic V_2O_5 and Triclinic NiV_2O_6

Mol Fraction	Orthorhombic V_2O_5				Triclinic NiV_2O_6						
	a	b	c	V=a*b*c	a	b	c	V=a*b*c	α	β	γ
x=0.00	11.514	3.566	4.374	179.572							
x=0.03	11.518	3.567	4.376	179.796	7.135	4.793	8.831	302.015	90	102.01	94.20
x=0.04	11.519	3.568	4.375	179.807	7.136	4.794	8.832	301.971	90	102.00	94.22
x=0.05	11.523	3.569	4.380	180.097	7.140	4.800	8.838	302.890	90	101.98	94.21
x=0.06	11.526	3.570	4.381	180.189	7.129	4.793	8.830	301.791	90	101.98	94.22

Table 4.1(d) Summarizes the quantitative phase analysis of the Ni-V-O system. It presents the relative weight fractions of the orthorhombic V_2O_5 and triclinic NiV_2O_6 phases alongside key Rietveld refinement parameters, including profile residuals (R_p, R_{wp}), expected R-value (R_{exp}), and the goodness-of-fit indicator (χ^2).

$V_{2-x}Ni_{2x}O_{5-\delta}$	V_2O_5	NiV_2O_6	Rp	Rwp	Rexp	χ^2
x=0.03	95.21 (1.36)	4.79 (0.24)	21.2	19.4	17.28	1.53
x=0.04	94.07 (1.22)	5.93 (0.24)	19.3	19.1	16.13	1.40
x=0.05	87.84 (1.60)	12.16 (0.64)	29.3	19.8	17.53	1.94
x=0.06	88.73 (1.24)	11.27 (0.31)	20.6	19.4	17.09	1.29

Table 4.1(e): Showing bond length of Orthorhombic V_2O_5 phase in the $V_{(1-x)2}Ni_{3x}O_{5-\delta}$ for $0.03 \leq x \leq 0.06$

Bond Type	x= 0.03	x= 0.04	x= 0.05	x= 0.06
	Bond Length in Å			
V - O1	1.654(7)	1.654(7)	1.643(9)	1.620(8)
V - O3	1.802(4)	1.802(4)	1.792(5)	1.796(5)
V - O2	1.830(2)	1.830(2)	1.848(3)	1.837(2)
V - O2	2.093(12)	2.093(12)	2.073(13)	2.078(12)

Table 4.1(f): Showing bond angle of Orthorhombic V_2O_5 phase in the $V_{(1-x)2}Ni_{3x}O_{5-\delta}$ for $0.03 \leq x \leq 0.06$

Angle Type	x=0.03	x=0.04	x=0.05	x=0.06
	Angle [°]			
O2-V-O2	80.4(6)	80.4(6)	78.6(7)	79.3(6)
O3-V-O2	94.5(6)	94.5(6)	95.3(7)	95.2(6)
O1-V-O3	100.9(6)	100.9(6)	100.5(7)	101.5(7)
O1-V- O2	100.9(6)	100.9(6)	102.9(8)	101.7(6)
O1-V-O2	107.0(6)	107.0(6)	107.8(7)	106.7(6)
O3-V-O2	152.1(5)	152.1(5)	149.7(7)	151.6(6)
O2-V-O2	154.3(6)	154.3(6)	151.7(7)	152.2(7)
V-O2-V	99.60(6)	99.60(6)	101.4(7)	100.7(7)
V-O2-V	154.3(8)	154.3(8)	149.7(10)	152.2(9)
V-O3-V	153.4(7)	153.4(7)	151.6(9)	152.4(7)

Additionally, the non-linear trend observed in the variation of unit cell volume for the triclinic NiV_2O_6 phase can be explained by the complex interactions between the nickel and vanadium species (Table 4.1(c)). As the NiO concentration increases, there is a competing effect between the formation of the NiV_2O_6 phase and the continuing presence of the V_2O_5 phase, leading to a non-linear variation in the unit cell volume of NiV_2O_6. The presence of multiple oxidation states of nickel, as evident from the XPS results (Ni^{2+}, Ni^{3+}, and Ni^{1+}), introduces complexity in the crystallography of NiV_2O_6. The non-linear trend could arise from changes in the electronic configuration and oxidation state distribution, which affect the crystallographic packing and local atomic arrangements within the NiV_2O_6 phase. The incorporation of Ni into the matrix of V_2O_5, added the impurity levels as defects, that will decrease the intensity and increase the full width half maximum , corresponding to a decrease in crystallite size with an increase in percentage of dopant.

Additionally, the quality of the Rietveld refinement is quantified by the corresponding goodness-of-fit parameters, including the R-factors (Rwp, Rp, Rexp) and the chi-squared (χ^2) values as shown in Table 4.1(d). At the lowest doping concentration (x=0.03), the orthorhombic V_2O_5 phase remains dominant at 95.2 wt.%, while a minor fraction of 4.8 wt.% NiV_2O_6 emerges, indicating the onset of Ni incorporation and secondary phase formation. A similar trend persists at x=0.04, with a slight decrease in V_2O_5 content (94.1 wt.%) and a corresponding increase in NiV_2O_6 (5.9 wt.%), suggesting gradual phase segregation as doping increases. A significant compositional shift occurs at x = 0.05, where the V_2O_5 content drops sharply to 87.8 wt.% and NiV_2O_6 increases to 12.2 wt.%. This sharp increase in secondary phase content likely reflects the solubility limit of Ni^{2+} within the V_2O_5 lattice, beyond which phase separation becomes more pronounced. Interestingly, at x = 0.06, a marginal increase in V_2O_5 fraction (88.7 wt.%) is observed, with a slight reduction in NiV_2O_6 content (11.3 wt.%), which may be attributed to improved dopant distribution or enhanced structural ordering. The refinement quality metrics are within acceptable limits across all samples, with R_{wp} values ranging from 19.3 to 29.3 and χ^2 values between 1.29 and 1.94. Notably, the best fit was achieved at x = 0.06 (χ^2 = 1.29), indicating a well-resolved diffraction pattern and high crystallographic order. In contrast, the highest R_{wp} (29.3) and χ^2 (1.94) at x = 0.05 may reflect increased

microstructural disorder or strain arising from phase coexistence and dopant-induced lattice distortion. Thus, phase evolution and refinement statistics confirm the progressive transformation to a biphasic composite, with a critical transitional behavior observed near x = 0.05.

The NiO-incorporated V_2O_5 compound, as determined through Rietveld refinement, exhibits a biphasic structure consisting of orthorhombic V_2O_5 with *Pmmn* space group symmetry and triclinic NiV_2O_6 with $P\bar{1}$ symmetry. The orthorhombic V_2O_5 phase is defined by lattice parameters a ≈ 11.512 Å, b ≈ 3.563 Å, and c ≈ 4.368 Å, with vanadium atoms occupying the 4e Wyckoff positions at approximately (0.000, 0.250, 0.457), while oxygen atoms are distributed across 4e and 4f positions. Structurally V_2O_5 consists of distorted VO_5 square pyramids, where each vanadium is coordinated to five oxygen atoms, four in a basal plane and one apical oxygen, forming layers that stack along the c-axis. These pyramidal units are connected via shared corners and edges, creating two-dimensional sheets weakly bonded by Van der Waals forces, leading to high anisotropy in electrical and ionic conductivity. The interlayer spacing provides pathways for ion intercalation, making V_2O_5 a promising candidate in energy storage and catalys applications [31].

The NiV_2O_6 phase crystallizes in a triclinic system with lattice parameters a ≈ 9.24 Å, b ≈ 3.44 Å, c ≈ 6.18 Å, and angles α ≈ 90.2°, β ≈ 106.6°, γ ≈ 94.5°, consistent with the *P-1* space group (Fig 4.2 c). Its structure comprises distorted MO_6 (M = Ni, V) octahedra interconnected through edge and corner sharing, forming a complex three-dimensional framework [32]. In this phase, vanadium atoms exist in mixed oxidation states (V^{4+}/V^{5+}), contributing to electron hopping and redox activity. The presence of Ni^{2+} in octahedral coordination introduces additional distortion and modifies the electronic environment, enhancing structural diversity. Unlike the layered nature of V_2O_5, the arrangement in NiV_2O_6 favors a more rigid, interconnected lattice, which can influence the material's magnetic and electrochemical behavior. The successful refinement of both phases is supported by low residual factors (R_p, R_{wp}) and a χ^2 value close to unity, confirming the coexistence and structural integrity of the biphasic NiO-V_2O_5 system. Tables 4.1 (e,f) provide the bond lengths and angles of V_2O_5 phase [33].

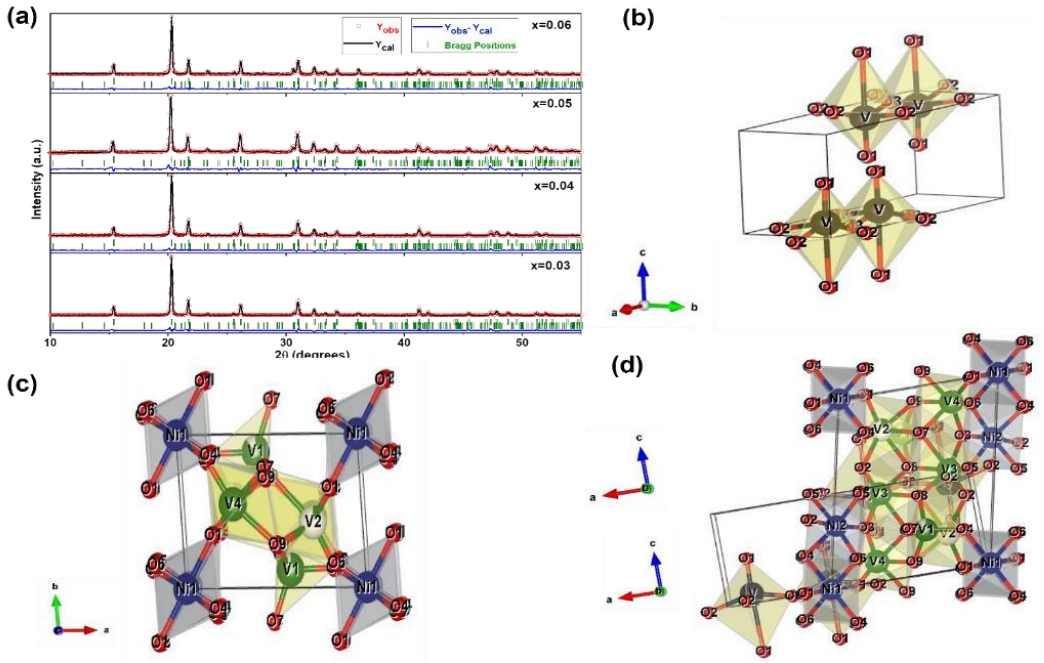

Figure 4.2.(a) Rietveld refinement patterns of $V_{(1-x)2}Ni_{3x}O_{5-\delta}$ samples for $0.03 \leq x \leq 0.06$, (b) orthorhombic V_2O_5 unit cell structure, (c)NiV_2O_6 unit cell and (d) unit cell model of Ni–V–O mixed-phase compounds comprising V_2O_5 and NiV_2O_6 phases for x=0.07, all visualized using VESTA software

3.2. Lattice dynamics: Raman Spectroscopy

Figure 4.3. Divulges the Raman spectrum of $V_{(1-x)2}Ni_{3x}O_{5-\delta}$ for $0.03 \geq x \geq 0.06$ with a series of well-resolved peaks with the most intense peak at 142cm^{-1} and the least intense at 787cm^{-1}. The observed Raman shifts are comparable with the previously reported α-V_2O_5 polymorphic phase of Vanadium Pentoxide [34], [35]. The basic α-V_2O_5 orthorhombic crystal with *Pmmn* space group symmetry and D_{13}^{2h} point group structures contain two formula units per unit cell accommodating 14 atoms with [VO_5] square pyramids arranged in up-up-down-down sequence connected to each other by sharing edges and corners [36]. In a single V_2O_5 slab O_1, O_2 and O_3 atoms exist [34], [37]**.** R.Baddour-Hadjean et al. [34] , reported that out of the 39 optical zone center modes obtained through factor group analysis, 21 Raman-active phonon modes exist for the α-V_2O_5 polymorph which is represented as α- V_2O_5:

$\Gamma_{Raman} = 7A_g + 7B_{2g} + 3B_{1g} + 4B_{3g}$

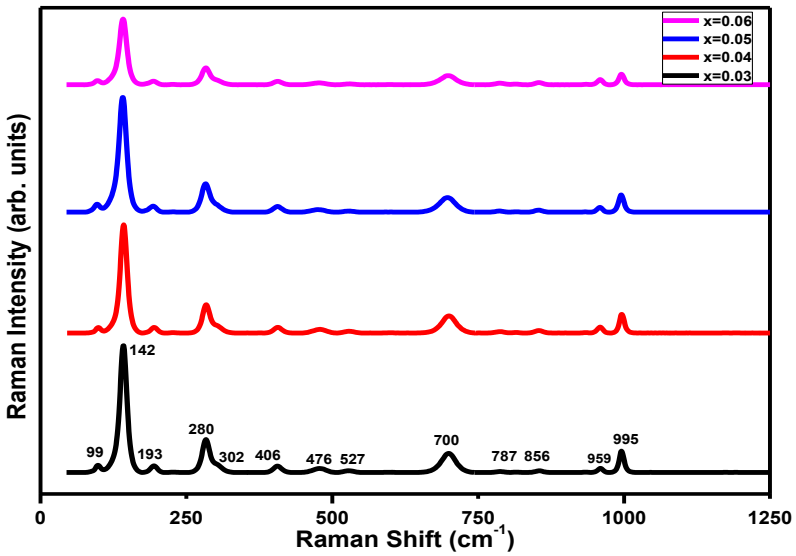

Figure 4.3: Micro-Raman spectra of $V_{(1-x)2}Ni_{3x}O_{5-\delta}$ for $0.03 \geq x \geq 0.06$

Previous studies shows that for the α-V_2O_5 structure, vibrational modes involving atomic displacements in the x-z plane belong to A_g and B_{2g} species and out-of-plane vibrations with y displacements indicate B_{1g} and B_{3g} species [34]. A comparison report of Raman active phonon modes of pure V_2O_5 powders and previously reported Density Functional Perturbation calculations along with present results is shown in table 4.2 [35], [38].

13 Raman active phonon modes are observed to be excited in the sample specimen in the study and are given as $V_{(1-x)2}Ni_{3x}O_{5-\delta}$: Γ-Raman = 6 A_g+2B_{1g}+2B_{2g}+2B_{3g}+1. The intense peak at 995cm^{-1} is in best agreement with the predicted Ag mode implying V-O_1 double bond stretching vibration along the y-direction involving the terminal unshared O1 atom. This highest peak in the larger wavenumber region showcases the strongest V-O_1 bonds in the sample. But the intensity of this peak is inversely proportional to the mole fraction x (Fig 4.2), suggesting a weakening of the bonds with the increasing concentration of Nickel [35-36]. The mode at 700 cm^{-1} is purely an antisymmetric stretching vibration of a doubly coordinated V-O2-V bridging bond involving corner shared O_2 atom along the y-direction [37] and the peak at 527 cm^{-1} is probably due to the stretching of V-O2 interconnecting bonds attaching V_2O_5 units [37].

Table 4.2: Comparison of Wavenumbers (in cm^{-1}) of Raman active phonon modes obtained theoretically and experimentally for pure V_2O_5 and experimental Raman data of $V_{(1-x)2}Ni_{3x}O_{5-\delta}$

Mode	Single crystal of V_2O_5[35]		Experimental Raman spectrum α- V_2O_5 precursor [38] cm^{-1}	Calculated Raman spectrum of pure V_2O_5[39] cm^{-1}	Experimental Raman spectrum of $Cr_{0.1}V_2O_5$ [40] cm^{-1}	Present Work $V_{(1-x)2}Ni_{3x}O_{5-\delta}$ x=0.03, cm^{-1}
	Experimental cm^{-1}	Calculated cm^{-1}				
A_g	104	97	104	108	-	99
	304	315	306	294	303	302
	404	406	406	382	406	406
	480	489	483	528	483	476
	526	527	528	543	527	527
	994	1001	996	1029	995	995
B_{1g}	146	149	146	167	143	142
	700	700	701	772	698	700
B_{2g}	200	191	198	199	196	193
	-	848	-	1010	-	856
B_{3g}	280	297	285	279	282	283
	701	701	-	772	-	787
No assigned modes					956	959

The blunt peak at 856 cm^{-1} is assumed to be the quasi-silent mode due to the antisymmetric stretching of V-O3-V bridging bonds in the x-z plane which is theoretically predicted at 848 cm^{-1} for pristine V_2O_5 and hence the blueshift is attributed to Ni being substituted at the lattice site [38]. A low intense peak due to B_{3g} mode at 787 cm^{-1} is likely due to the V-O_3 stretching vibration along the z-axis [35]. It is the only peak for which a drastic blue shift occurs in comparison with 710 cm^{-1} [35] and 772 cm^{-1} [17] for V_2O_5 from DFT simulations, bringing light to the occurrence of Ni-O3 bonds [35], [39]. A blunt shoulder band occurs at 959 cm^{-1}, not attributed to orthorhombic V_2O_5, but resembles the V^{4+}-O_1 stretching vibration in $Cr_{0.1}V_2O_5$ and $CuV_2O_{5-\delta}$ [40] due to oxygen deficiency. This confirms the presence of V^{4+} ions in $V_{(1-x)2}Ni_{3x}O_{5-\delta}$ samples. Analyzing the structural features in the low-frequency part of the spectrum is rather difficult as the vibrational modes in these regions may contain contributions of angle-bending coordinates and other coupling effects. As per the present investigations, the highest peak at 142 cm^{-1} is attributed to the vibrational excitation owing to the translational and bending vibrational modes of neighboring V-Ni-O layers and it fits well with the predicted and experimental values in these regions. The high intensity of this mode reflects the long-range order in the plane of the vanadium oxygen layers. However, there is a reduction in intensity for this band at x= 0.06 compared to x= 0.04 (fig 4.3) revealing disruption of long-range order due to the higher concentration of Nickel [37], [41], [42].

A small shoulder at 99 cm^{-1} further confirms the layered structure [15]. A low-frequency B1g mode at 193cm^{-1} is an external mode originating from the relative motion of V-Ni-O/V-O units indicating the layered structure [35], [39], [42] The peak at 302cm^{-1} is attributed to the V-O1 bond angle deformation [42], [35]. Raktima Basu et al. [43] reported a peak at 403 cm^{-1} owing to the vibration of the V-O1 molecule along the z-axis and in the present work corresponding Raman modes are observed at 406 cm^{-1}. Veronica Brazdova et al. [44] reported peaks for bulk V_2O_5 at 290cm^{-1} and 483 cm^{-1} predicting V-O2-V bond angle deformation which is in tune with the excitation at 283 cm^{-1} and 476 cm^{-1} respectively in $V_{(1-x)2}Ni_{3x}O_{5-\delta}$ for all x values. However, all these peaks show a slight redshift for ascending x values. Such spectral

variations reveal induced structural changes due to an increase in the concentration of Nickel creating oxygen vacancies by valency variation of vanadium [45], [25].

It is well evident from figure 4.4(a) that the intensity of all the Raman peaks decreases from x=0.03 to 0.04, but almost remains the same for x=0.04 and 0.05. The initial decreasing trend indicated the reduction of crystallinity of the sample for the higher concentration of Nickel. The nonlinear trend observed in moving from mole fraction x=0.05 to 0.06 can be rationalized by the discontinuity in the composition of Vanadium as obtained from EDS data reported in Table 4.2. The broadening of prominent Raman peaks (fig.4.4(b)) exposes the diminishing of Raman features with increasing mole fractions(x). The width of the Raman bands has greater values for x=0.06 at 283 cm^{-1} and 700 cm^{-1} frequencies corresponding to V-O2 stretching and bending, affirming the reduction in crystallinity with increasing concentration of Ni ions. It implies that the increased concentration of Ni^{2+} cation can effectively inhibit the orthorhombic V_2O_5 crystalline grain growth and hence widen the Raman peaks.

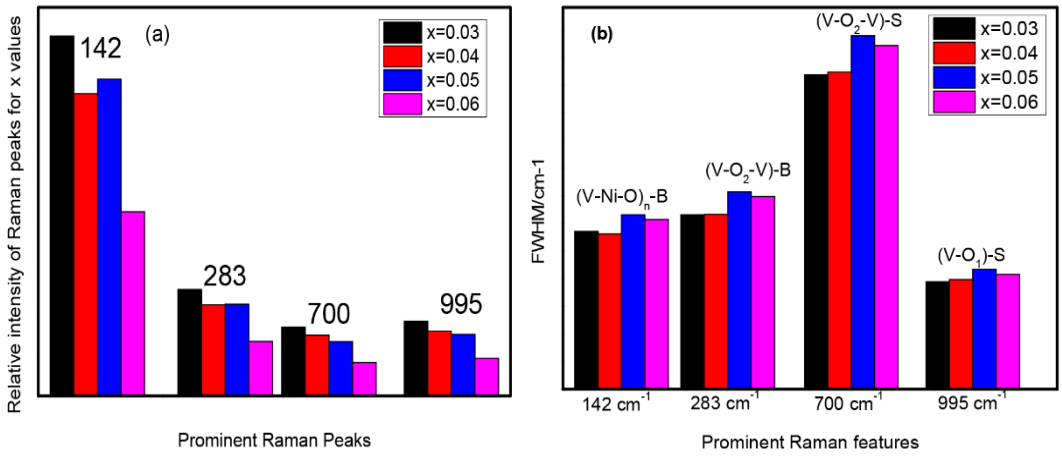

Figure 4.4. (a). Intensity variation of prominent peaks in Raman spectra with varying concentrations of Nickel and b) Variation in the bandwidth of prominent Raman peaks in the Ni-V-O compound

The absence of new vibrational modes corresponding to Ni is due to the low doping concentration of NiO. Here the nickel ions might have occupied the substitutional lattice sites retaining the orthorhombic structure of vanadium pentoxide with induced

oxygen deficiency and defective sites which may be probably because of Ni^{2+} occupancy within the V_2O_5 lattice as the ionic radius of Ni^{2+} (0.70Å) is comparable to V^{5+} (0.60 Å). The absence of high-frequency phonon modes at wavenumbers greater than 600 cm^{-1} corresponding to Ni^{2+} ions or Nickel Oxide vibrations further justifies the formation of phase pure Ni-V-O compounds as evidenced from XRD [23], [38-39], [42-43], [46] .

4.3.3 Surface morphology and elemental analysis

Figure 4.5(a-d) presents scanning electron micrographs of the $V_{(1-x)2}Ni_{3x}O_{5-\delta}$ powders, showcasing the morphology of the particles. The particle size is observed to fall within the micrometer range, indicating a larger scale than nanometer-sized particles. The particles are randomly distributed and exhibit a flake-like structure, which is a characteristic feature of the synthesized material.

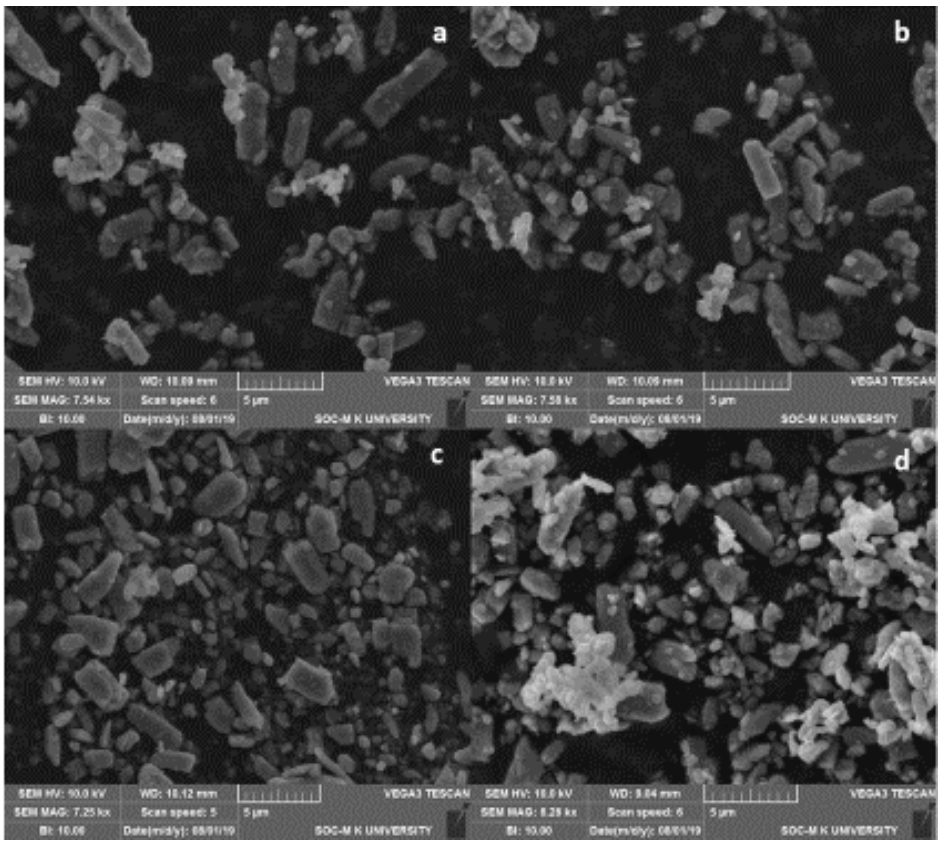

Figure 4.5. Scanning electron micrographs of $V_{(1-x)2}Ni_{3x}O_{5-\delta}$ powders (a)x=0.03 (b)x= 0.04 (c)x=0.05 and (d)x=0.06.

The EDS spectrum in figure 4.6(a-d) give the elemental constituents of the sample for all mol fractions.

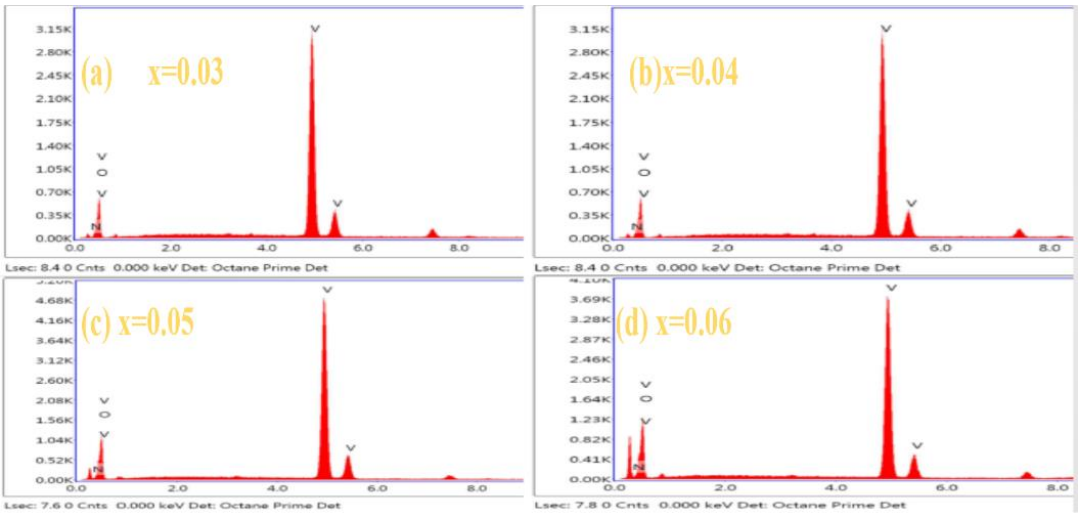

Figure.4.6 EDS spectrum of $V_{(1-x)2}Ni_{3x}O_{5-\delta}$ powders (a)x=0.03 (b)x= 0.04 (c)x=0.05 (d)x=0.06.

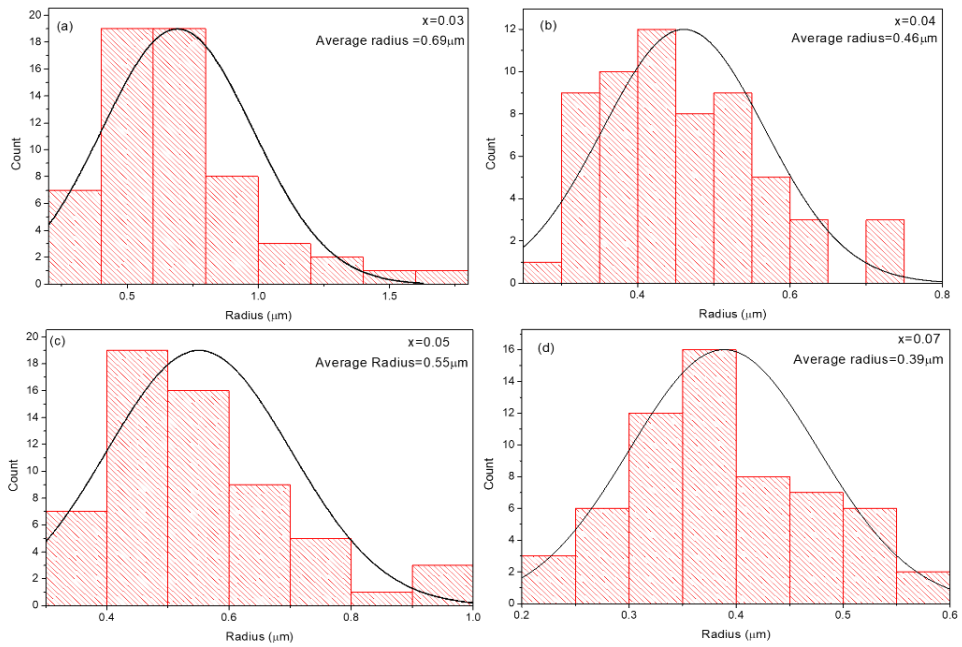

Figure. 4.7. Histogram for particle size of distribution of $V_{(1-x)2}Ni_{3x}O_{5-\delta}$ powders (a)x=0.03 (b) x=0.04 (c)x=0.05 & (d)x=0.06

The size distribution of these particles was quantitatively analyzed using histogram analysis with ImageJ software, as illustrated in Figure 4.7(a-d). The results reveal

that the particle size varies between 0.69 µm and 0.39 µm for the compositions within the range of 0.03≤x≤0.06.

4.3.4. X Ray Photoelectron Spectroscopy

X-ray photoelectron spectroscopy measurements were further employed to characterize the detailed elemental composition and electronic structure of the as-prepared $V_{(1-x)2}Ni_{3x}O_{5-\delta}$ compound, where x=0.06. The survey analysis of $V_{(1-x)2}Ni_{3x}O_{5-\delta}$ for compounds within the 0.03≤ x ≤0.06 range identified the elements Ni, V, O, and C present in the material (Figure 4.8 a). A Gaussian fitting method was utilized to assess the oxidation states of these elements thoroughly. The peak-fitted XPS spectrum for the Ni*2p* region revealed two spin-orbit peaks, Ni$2p_{3/2}$ and Ni$2p_{1/2}$, with binding energies of 857.3 and 875.6 eV, respectively, indicating the presence of Ni^{3+} ions (Figure 4.8 b). These findings are consistent with previous studies on Ni-related compounds, confirming the successful integration of Ni^{3+} ions into the vanadium pentoxide lattice. .

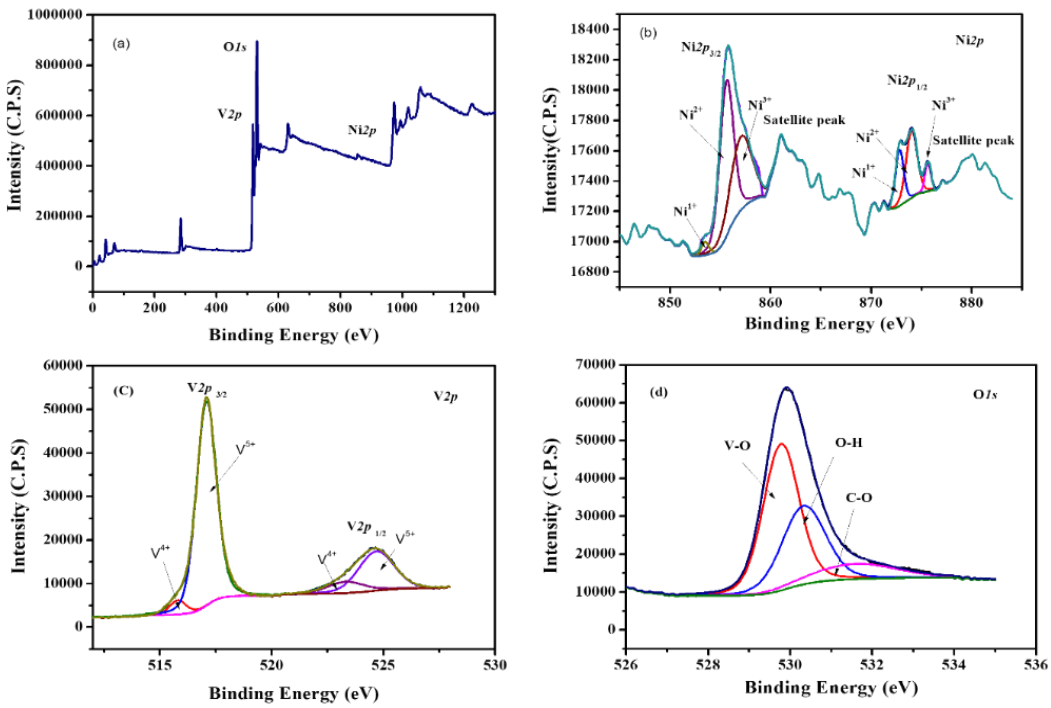

Figure 4.8: High-resolution X-ray photoelectron spectroscopy data for $V_{(1-x)2}Ni_{3x}O_{5-\delta}$ including (a) the survey spectrum and detailed core level spectra of (b) Ni2p, (c) V2p, and (d) O1s regions.

Additionally, the characteristic satellite peaks observed at elevated binding energies further validated the assignment of the Ni^{3+} oxidation state, which is recognized for enhancing the electrochemical properties of these materials through improved charge transfer dynamics and redox activity [47-48]. The observed shift in the Ni$2p_{3/2}$ binding energy from 858 eV to 855 eV indicates a partial reduction of Ni^{2+} to a lower oxidation state, such as Ni^0 (metallic nickel) or Ni^{1+} [49]. This shift can be attributed to factors such as oxygen vacancies, electron donation from surrounding elements, or the formation of a Ni-metallic phase. Lower oxidation states increase the electron density around the Ni nucleus, leading to enhanced shielding effects and a consequent reduction in binding energy. The detection of a minor peak at 853 eV indicates the presence of Ni^{1+} species in the analyzed compound, while the significant peaks for Ni^{3+} at 857.3 and 875.6 eV provide further evidence of the presence of mixed oxidation states in the sample [50-51].

Figure 4.8(c) illustrates that the high-resolution spectrum of the V*2p* region can be separated into distinct peaks at binding energies of 517.2 eV and 524.0 eV. These peaks are characteristic signatures corresponding to the oxidation states of vanadium, specifically V^{5+} and V^{4+}, thereby indicating the presence of mixed-valence states within the sample. This finding is consistent with prior literature, reinforcing the notion of these oxidation states coexisting and implying their possible impact on the electronic properties of the material [52]. The O*1s* spectrum at the core level, illustrated in Figure 4.8(d), is analyzed and separated into three unique peaks with binding energies of 529.9 eV, 530.7 eV, and 533.0 eV. The peak at 529.9 eV is associated with V–O bonding, confirming interactions between vanadium and oxygen in the sample matrix, consistent with earlier studies. The peak at 530.7 eV is associated with chemisorbed hydroxyl (OH) groups, suggesting the presence of surface hydroxyls that could affect the material's surface reactivity and electrochemical properties. The third peak, found at 533.0 eV, is related to ambient C–O adsorption. These deconvoluted peaks provide significant insights into the chemical environment of oxygen in the sample, highlighting the roles of various oxygen species in its overall electronic properties [53].

4.3.5. UV Visible Spectroscopy

UV-Visible Spectroscopy scanning done in the 200 nm to 900 nm range exhibits the diffused reflectance spectra of the samples and projects a sharp absorption edge from the 500 to 650 nm range as displayed in Figure 4.9(a). It is clear that light absorption increases with the concentration of foreign elements in the compounds. The redshifts in the absorption onset appear typically due to the decrease in band gap energy of the specimen. The optical band gap is a significant property of semiconducting material and is calculated using Kubelka Munk's theory. Kubelka-Munk equation at any wavelength can be written as [54].

$$[\mathrm{F}(R_\infty)h\upsilon]^2 = A(h\upsilon - Eg) \quad (1)$$

In order to determine the optical band gap in bulk powder sample the parameter $[\mathrm{F}(R_\infty)h\upsilon]^2$ versus photon energy $h\upsilon$ is plotted in Figure 4.9(b). To obtain the direct band gap values the straight line portion of the plot is extended to intercept at $h\upsilon$ axis. The above results show a slight decrease in band gap energy from 2.28 eV to 2.25 eV corresponding to direct optical transition with an increase in x values from x=0.04 to 0.06 respectively, suggesting an increase in the doping concentration that could lead to an excess carrier concentration in samples (fig. 4.9(b)).

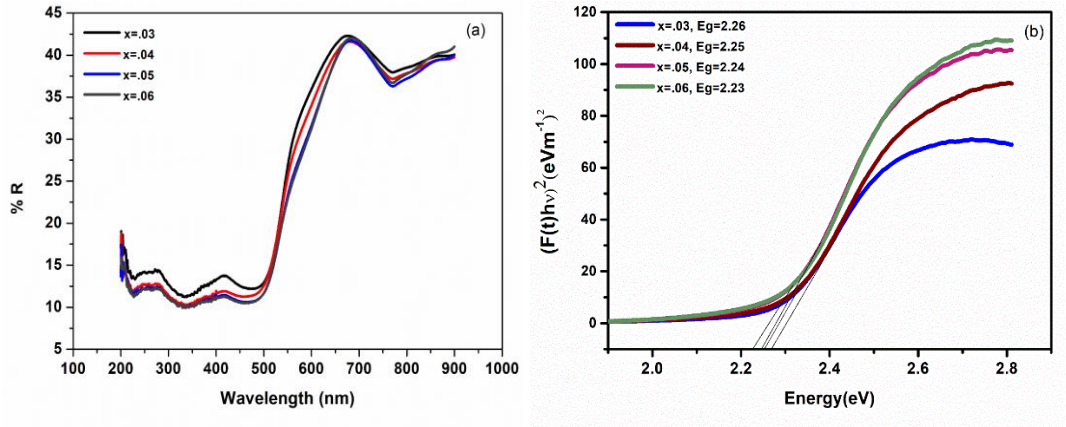

Figure 4.9 (a) Displays the Diffuse Reflectance Spectrum of $V_{(1-x)2}Ni_3O_{5-\delta}$ for various x values (b) Optical band gap energies of $V_{(1-x)2}Ni_{3x}O_{5-\delta}$ bulk powder for varying x values from K-M plot

Bulk V_2O_5 is a diamagnetic semiconductor with a band gap of about 2.3eV, which is based on the ionic configuration with filled O*2p* and unoccupied V*3d* orbitals

[55], [56]. Top Khac Le et al [55] investigated and reviewed that bulk diamagnetic semiconductor α-V_2O_5 at room temperature when pure can absorb the photon from an excitation source and electrons can jump to a higher state in four ways namely, (a) from VB to V*3d* split-off states of CB (b) from VB to V*3d* states of CB, (c) from mid-gap states to CB (c) from VB to mid-gap states.

The frequency of the aforesaid process and it's intensity depend on the microstructure of V_2O_5 and the excitation wavelengths of the source. Evidently reports [57], divulge that the absorption of V_2O_5 is based on the transition between O*2p* and V*3d* split-off bands corresponding to the band edge at about 2.3 eV. R. Suresh et al [41] reported the band gap reduction in Ni-V_2O_5 particles synthesized hydrothermally for higher Ni concentration. The observed decrease in the direct band gap with increasing Ni concentration with x = 0.03–0.06 can be attributed to the combined effects of substitutional Ni incorporation and the formation of the NiV_2O_6 phase. Substitution of Ni^{2+} ions at V^{5+} lattice sites introduces acceptor-like states, resulting in an increased hole concentration and an inverse Burstein–Moss effect, which broadens the valence band and consequently narrows the band gap. In addition, Rietveld refinement confirms the formation of the triclinic NiV_2O_6 phase, whose electronic structure arises from the hybridization of Ni *3d*, V *3d*, and O *2p* orbitals. The coexistence of α-V_2O_5 and NiV_2O_6 modifies the overall electronic band structure by introducing additional electronic states near the band edges, thereby further reducing the effective optical band gap. Thus, the band gap narrowing is attributed to the synergistic influence of Ni substitution and NiV_2O_6 phase formation [58], [59].

4.3.6. AC Conductivity

The AC conductivity of Ni-V-O binary oxide is studied by varying temperatures and frequencies. Figure 4.10 displays the variation of AC conductivity with frequency studied in the range 1KHz to 1MHz and at temperature 25^0C. AC conductivity is calculated using the equations [2] and [3] given below [60].

$$\sigma_{ac}(\omega)=\omega\varepsilon_o\varepsilon'', \text{ where } \varepsilon'' =\varepsilon'Tan\delta \quad [2]$$

$$\sigma_{ac}(\omega)=2\pi f\varepsilon_o\varepsilon'Tan\delta \quad [3]$$

where, ε_0 ε', ε'', f, and tan δ are the permittivity of free space (8.854×10^{-12} Fm^{-1}), dielectric constant, dielectric loss, frequency (in Hz) of the applied electric field and loss tangent respectively. AC conductivity is independent of frequency in the low-frequency region indicating a plateau for all mole fractions as shown in figure 4.10(d) and is attributed to the DC-like conductivity due to the short-range paired carrier hopping between the neighboring particles [60]. In the high-frequency realm up to 1MHz, there is an increasing trend in the dispersion region attributed to the hopping relaxation model whereby the charge carriers hop to the neighboring vacant site existing in the low-frequency region [60], [61]. As frequency increases, the probability of the correlated back-and-forth hopping causes the relaxation of the charge carriers [61]. It is observed that the AC conductivity at 1MHz shows an elevation from 1.6 x 10^{-03} Sm^{-1} through 4.8 x 10^{-03} Sm^{-1} reaching 13.6 x10^{-03} Sm^{-1} for the increasing concentration of Ni^{2+} ions for mole fractions x=0.04, 0.05, 0.06 respectively indicating a hike in carrier concentration at higher mole fraction. All these observations are congruent to the Jonscher's universal power law (Fig 4.10(a, b & c) represented as equation 4 [62].

$$\sigma\ (\omega)= \sigma_{dc}(0) + A\omega^{s} \qquad [4]$$

where σ_T is the total conductivity, σ_{dc} is the DC conductivity, A is constant, ω is the angular frequency and s is the frequency exponent where $0<s<1$. Table 4.3 gives the σ_{dc} and s values obtained after JPL fitting σ_{dc} is observed to increase with increasing mole fraction x.

Table 4.3. DC conductivity and frequency exponent obtained after JPL fitting of frequency-dependent AC conductivity curve of $V_{(1-x)2}Ni_{3x}O_{5-\delta}$ samples for x=0.04, 0.05 and 0.06

JPL parameters	**x=0.04**	**x=0.05**	**x=0.06**
$\sigma_{dc(S/m)}$	1.013 x 10^{-5}	6.87 x10^{-5}	2.037 x 10^{-4}
s	0.7314	0.4809	0.7636

Figure 4.11(a) projects the increase in AC conductivity with increase in temperature as the mole fraction increases. The mobility of charge carriers increases with

temperature (50 ^{0}C to 250 ^{0}C) elevating the overall conductivity and revealing the semiconducting behavior of all samples as per the previous reports [60], [62].

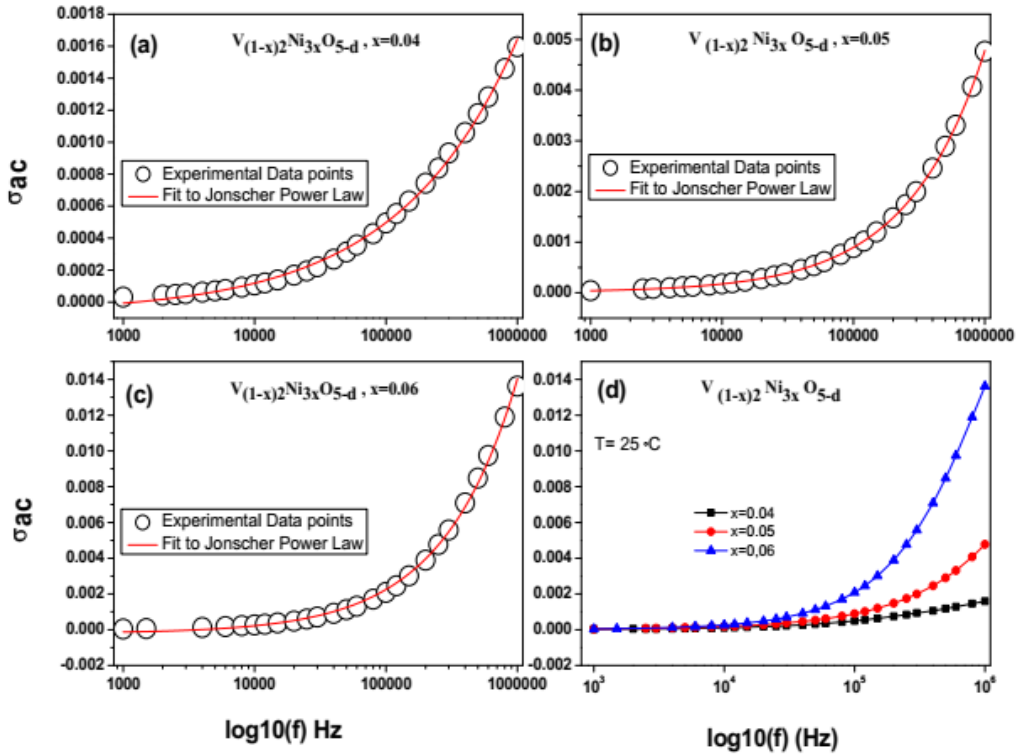

Figure 4.10. (a), (b) & (c) Jonscher Power Law fit to frequency-dependent AC conductivity Curve of $V_{(1-x)2}Ni_{3x}O_{5-\delta}$ compounds for x=0.04,0.05,0.06 respectively (d) Variation of AC conductivity with frequency for different mole fractions in Ni-VO compounds

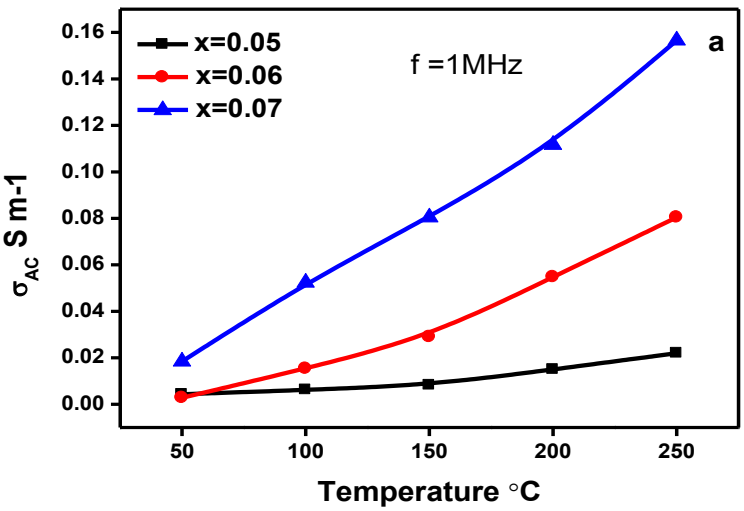

Figure 4.11. Variation of AC conductivity with temperature for x=0.04, 0.05 & 0.06 in $V_{(1-x)2}Ni_{3x}O_{5-\delta}$ samples

4. 3.7. Dielectric studies

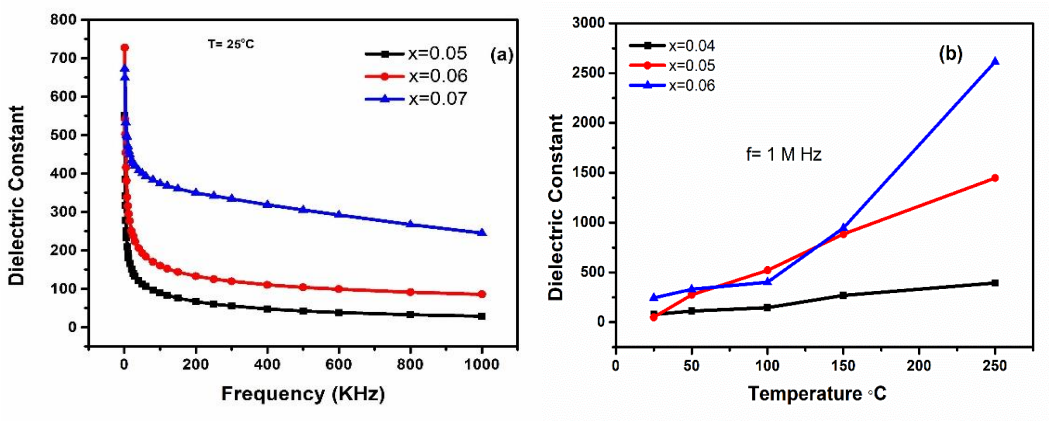

Fig: 4.12 (a) Variation of Dielectric constant with frequency, (b) Variation of Dielectric constant with temperature

Dielectric constant is calculated using the equation, ε'=where, C is the capacitance of the sample, d is thickness of the pellet, A is area of the pellet and εo is the free space permittivity. Generally deformational (electronic and ionic) and relaxation (orientational and interfacial) polarization determines the dielectric behaviour of samples. Electronic, Ionic, Orientational and Interfacial polarization is dominant up to frequencies 10^{16},10^{13},10^{10},10^{3} Hz respectively. The displacement of valence electrons relative to the positive nucleus is the source of electronic polarization [59], [60], [63], [64]. Displacement of positive and negative ions, concerning each other contributes to the ionic polarization which is not considered in the present sample, due to the covalent type boding in vanadium pentoxide-based compounds [59], [63], [64]. Dipolar or Orientational polarization arises in materials having permanent dipole moment which changes orientation in an applied electric field Space charge or interfacial polarization occurs due to the impedance of mobile charge carriers at the interface [59], [60]. Interfacial polarization contributes the highest at low frequencies and as frequency rises up, dipolar polarization becomes the major contributor in the present compounds [61], [65].

At low frequencies, the dielectric constant has a high value for all the mole fractions, and then at higher frequencies from 300 KHz to 1MHz dielectric constant doesn't vary for samples studied at room temperature 25 ^{o}C (fig. 4.12(a)). A steep decrease in permittivity observed over the frequency range of 10-40 kHz is attributed to the tendency of dipoles to orient themselves in the direction of the applied field in

the low-frequency range. On an added account the dipoles can hardly orient themselves in the direction of the applied field in the high-frequency range and hence the value of the permittivity decreases [66]. At the plateaus of the curve, the corresponding dielectric constant is at 50, 150, and 350 for x=0.04, 0.05, and 0.06 respectively. In Ni-V-O compounds, the dielectric constant increases with an increase in temperature studied in the temperature range from 25 ^{0}C to 250 ^{0}C (fig. 4.12(b), step size 50 ^{0}C). Tan Foo Khoon et al [61] previously reported the increase in dielectric constant with temperature in Mn-VO mixed oxides. In the present study, the dielectric constant at 250 ^{0}C, is observed to increase from 395, through 1447 to 2614, for mole fractions 0.04, 0.05 and 0.06 respectively. This phenomenon can be explained by using dielectric polarization. The charge carriers are at low energy at room temperature and show little movement to follow the direction of the applied field resulting in a low contribution to polarization and dielectric behavior [61], [65]. With the rise in temperature, the charge carriers are excited and have enough energy to follow the change of the applied field, consequently increasing the dielectric constant.

4.3.8. Antimicrobial Studies

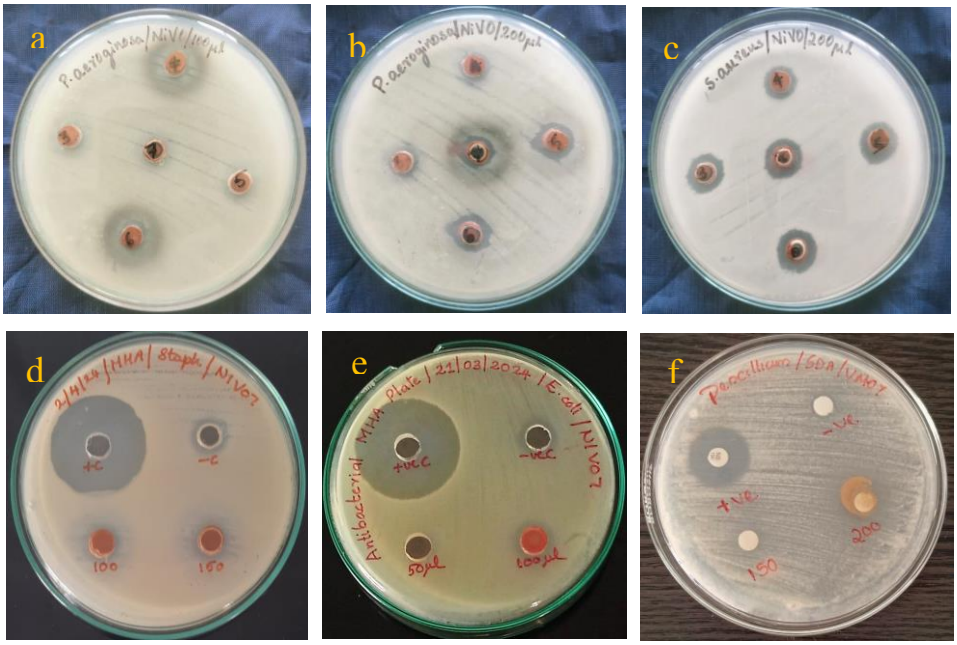

Figure 4.13. Representative photographs of zone of growth inhibition against bacteria and fungi for Ni-V-O-6 compound with positive and negative control: (a) P. Aeroginosa (100µl), (b) P. Aeroginosa (200 µl), (c) S. Aureus (200 µl) (d) S. Aureus (150 and 200 µl), (e)&(f) E. Coli (50 & 100 µl) and Pencillium(150 & 200 µl).

The antimicrobial efficacy of nickel-incorporated vanadium pentoxide-based multi-cationic compounds has been demonstrated against a range of microbial pathogens, including two Gram-positive bacteria—*Staphylococcus aureus* and *Bacillus cereus*—and four Gram-negative strains—*Escherichia coli*, *Pseudomonas aeruginosa*, *Vibrio harveyi*, and *Vibrio cholerae*. In addition to these bacterial species, these compounds also exhibited antifungal activity against *Penicillium*, a filamentous fungus characterized by septate hyphae, branched conidiophores, and brush-like conidia formations, which contribute to its resistance and persistence in diverse environments. Figure 4.13 presents the representative images depicting the antimicrobial activity of the Ni–V–O compound against bacterial and fungal strains, alongside appropriate positive and negative controls.

Table 4.4 Inhibition Zone Diameters (in mm) of Gram-positive Bacteria, Gram-negative Bacteria, and Fungi, along with Positive and Negative Controls, for Ni-V-O-6 Compound Systems.

Sl. No.	Name of Bacteria/Fungus	50 µl	100 µl	150 µl	200 µl	+ve	-ve
1.	*Escherichia coli*	R	12	15	17	20	7
2.	*Staphylococus aureus*	R	R	12	17	24	7
3.	*Pseudomonas aeroginosa*	R	11	13	19	22	7
4.	*Bacillus cereus*	R	R	10	11	21	7
5.	*Vibrio harveyi*	R	8	10	11	20	7
6.	*Vibrio cholerae*	R	10	11	12	20	7
7.	*Pencillium*	R	R	12	15	22	7

The agar well diffusion assay and disc diffusion method assessed inhibition zones under varying compound concentrations for bacterial and fungal strains. Specifically, the test conditions included: (a) *Pseudomonas aeruginosa* treated with 100 µL, (b) *P. aeruginosa* with 200 µL, (c) *Staphylococcus aureus* with 200 µL, (d) *S. aureus* with 150 and 200 µL, (e) *Escherichia coli* with 50 and 100 µL, and *Penicillium* spp. with 150 and 200 µL of the Ni–V–O-6 solution. The concentration

values refer to the volume of the compound solution introduced into each well and disc. Streptomycin (10 µg/disc) was employed as the positive control for bacterial strains, while fluconazole served as the antifungal positive control. Dimethyl sulfoxide (DMSO), the solvent used to dissolve the compound, was used as the negative control for both bacterial and fungal assays. These photographs visually confirm the concentration-dependent antimicrobial efficacy of the Ni–V–O-6 compound against the tested microorganisms. The inhibition zone diameters (in mm) observed for Gram-positive bacteria, Gram-negative bacteria, and fungi, along with the corresponding positive and negative controls, for the Ni–V–O-6 compound system, are systematically presented in Table 4.4. It is well evident that as the concentration increases, the diameter of the zone of inhibition also increases for all microbial strains.

These findings underscore the broad-spectrum antimicrobial potential of multi-cationic V_2O_5-based nanomaterials, including their effectiveness against structurally and morphologically diverse pathogens [67]. The incorporation of NiO introduces additional valence states (Ni^{+}, Ni^{2+}, Ni^{3+}), as confirmed by XPS, alongside the V^{5+} and V^{4+} states of vanadium, enabling a highly reactive surface capable of continuous redox cycling and generation of reactive oxygen species (ROS). *Pseudomonas aeruginosa* is a Gram-negative, opportunistic pathogen with a robust outer membrane, efflux pumps, and a notably high clinical isolation frequency, particularly in nosocomial settings [69]. It can colonize and infect various anatomical sites, including the ocular and auditory systems, urinary tract, respiratory tract, and dermal tissues, especially in burn wounds. One of the most clinically significant manifestations of *P. aeruginosa* infection occurs in patients with cystic fibrosis (CF), where it establishes chronic, biofilm-associated pulmonary infections. These infections are notoriously difficult to eradicate due to the bacterium's intrinsic resistance mechanisms and its ability to acquire multidrug resistance [13]. Persistent colonization by multidrug-resistant *P. aeruginosa* in CF patients contributes to progressive lung function decline and is a major determinant of morbidity and reduced life expectancy. Its adaptability and resistance profile underscore the urgent need for alternative antimicrobial strategies targeting this pathogen. The ROS generated from

redox cycling between V^{5+}/V^{4+} and Ni^{2+}/Ni^{3+} could penetrate the lipopolysaccharide (LPS) layer and damage the inner membrane. The •OH radicals and superoxide species peroxidize membrane lipids, leading to leakage of cytoplasmic content and eventual lysis. Moreover, the electron transport chain could be disrupted due to ROS interaction with cytochrome complexes, inducing metabolic arrest. The high inhibition zone (19 mm) for Ni-V-O-6 compound (Table 4.4) indicates effective penetration and destruction, supported by the structural advantage of V_2O_5's high surface area and the catalytic role of Ni ions [70], [71].

S. aureus, a Gram-positive bacterium, lacks an outer membrane but has a thick peptidoglycan layer [72] and is a predominant opportunistic pathogen implicated in a wide spectrum of infections, ranging from superficial wound colonization to severe device-associated biofilm infections involving catheters, endotracheal tubes, and other implanted biomaterials. Its escalating resistance to multiple classes of antibiotics, including β-lactams, tetracyclines, macrolides, and even glycopeptides like vancomycin, poses a significant clinical challenge. Consequently, the development of alternative, site-targeted therapeutic strategies that bypass conventional antibiotics and minimize the emergence of resistance is of critical importance in managing *S. aureus* infections [73]. Upon exposure to the microbial environment, the Ni-doped vanadium pentoxide system exhibits pronounced photocatalytic and redox activity, primarily through the efficient separation of photogenerated electron–hole (e^-/h^+) pairs. This charge carrier separation facilitates subsequent surface redox reactions involving molecular oxygen and water adsorbed onto the catalyst surface. Under the experimental conditions of the agar well diffusion assay, this photocatalytic mechanism leads to the in situ formation of reactive oxygen species (ROS), including superoxide anions (O_2^-), hydroxyl radicals (•OH), hydrogen peroxide (H_2O_2), and singlet oxygen ($^1O_2$). Specifically, ROS-mediated oxidative stress compromises cellular integrity and metabolic function in *Staphylococcus aureus*, ultimately leading to cell death. Additionally, V^{4+} species can interfere with DNA replication by forming adducts with phosphate backbones. The 17 mm inhibition zone for Ni-V-O-6 suggests that, despite the peptidoglycan barrier, the particles redox-active surface is highly efficient at bacterial eradication.

Escherichia coli, a Gram-negative bacterium, exhibits moderate sensitivity to the composite, similar to *Pseudomonas aeruginosa*, with the antimicrobial mechanism primarily involving ROS-mediated outer membrane disruption [74]. However, the efficiency is slightly reduced in *E. coli* due to differences in membrane composition and more robust antioxidant defense mechanisms. Additionally, Ni^{2+} ions are likely to chelate intracellular thiol groups, impairing key enzymatic functions, while vanadium species contribute to cytotoxicity by depolarizing the inner membrane and disrupting ATP synthesis. The observed inhibition zone of 16 mm for the composite at a molar fraction of x = 0.06 indicates effective synergy between ROS generation, metal ion activity, and membrane-targeting mechanisms in bacterial suppression [22], [71-72], [75].

The Ni-V_2O_5 compound produces comparatively lower anti-bacterial activity against *Vibrio cholerae* (12 mm), *Vibrio harveyi* (11 mm), and *Bacillus cereus* (11 mm) through the synergistic multi-modal mechanism. *Vibrio cholerae* is a Gram-negative, comma-shaped pathogen responsible for cholera, a severe diarrheal disease, and exhibits adaptability through three distinct lifestyles planktonic, pellicle biofilm (PB), and surface-attached biofilm (SB). Biofilm formation enhances its environmental persistence, virulence, and antibiotic resistance, making infections more challenging to treat [76-77]. *Vibrio harveyi* is a Gram-negative, luminous, opportunistic pathogen responsible for significant economic losses in aquaculture, particularly affecting penaeid shrimp under stress conditions such as overcrowding and poor water quality. It causes luminous vibriosis, characterized by symptoms like appetite loss, retarded growth, and high mortality [78]. The Ni-V-O particles, with an average size of 60 nm, exhibited strong antibacterial activity attributed to surface-mediated interactions and intracellular disruption [79-80]. The multi- cations present in the compound could facilitate dynamic electron transfer processes and the generation of reactive oxygen species such as •OH and O_2^-, known to induce oxidative stress and irreversible damage to bacterial membranes, DNA, and proteins. The high surface area and defect-rich structure of the NiV_2O_6 phase further enhance ROS yield and active site density. Gram-negative bacteria (*V. cholerae*, *V. harveyi*) are particularly susceptible to ROS and electrostatic disruption due to their negatively

charged lipopolysaccharide membranes, which interact strongly with positively charged Ni ions, leading to membrane permeabilization and cytoplasmic leakage [81]. Despite a thicker peptidoglycan wall in the Gram-positive *B. cereus*, the porous cell envelope permits ROS penetration. At the same time, intracellular Ni ion uptake may disrupt enzymatic pathways and metal ion homeostasis, ultimately inducing apoptosis-like death. This combination of redox-driven ROS generation, metal ion toxicity, and physical membrane disruption presents a scientifically substantiated and highly effective antibacterial mechanism against both Gram-negative and Gram-positive pathogens [82-84].

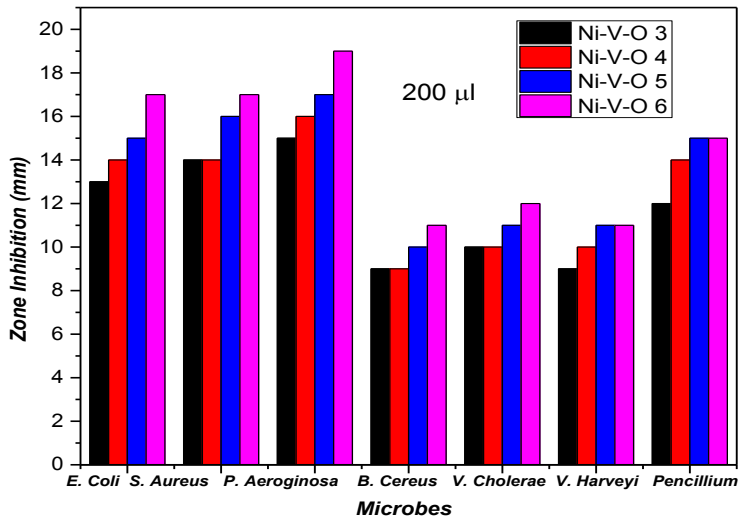

Figure 4.14. Bar diagram comparing the zone inhibition of $V_{2-x}Ni_{2x}O_{5-\delta}$ for $0.03 \leq x \leq 0.06$ compounds, against the gram-positive and gram-negative bacteria and fungi growth for 200µl concentration.

Pencillium, a filamentous fungus, exhibits a different response mechanism [85]. The ROS generated from the microparticle surface could disrupt the chitin and β-glucan structure of the fungal cell wall. Ni^{2+} ions possibly displace essential metal ions like Zn^{2+} and Mg^{2+} required for enzymatic processes, inhibiting spore germination and hyphal elongation [86]. Simultaneously, oxidative stress leads to mitochondrial damage and apoptosis-like features in fungal cells. The 15 mm inhibition zone for Ni-V-O-6 compound at 200 µl concentration signifies substantial

antifungal activity, a valuable attribute considering the rising fungal resistance in clinical and environmental settings [87]. The bar diagram in Figure. 4.14 shows that as the molar fraction (x) increases, there is a slight but consistent increase in the diameter of the zone of inhibition for all six bacterial strains and one fungal strain. This trend indicates that the increasing concentration of Ni ions in the $V_{2-2x}Ni_{3x}O_{5-\delta}$ matrix positively enhances its antimicrobial efficacy, likely due to improved interaction with microbial membranes or enhanced generation of reactive oxygen species (ROS).

4.4. Conclusion

In conclusion, incorporating vanadium pentoxide with nickel using a high-temperature solid-state reaction for x=0.03 to 0.06 in $V_{(1-x)2}Ni_{3x}O_{5-\delta}$, produced a composite with notable structural and functional enhancements. Rietveld refinement confirmed a biphasic material comprising orthorhombic V_2O_5 and triclinic NiV_2O_6, with lattice parameters expanding progressively as Ni content increased, showing clear evidence that Ni^{2+} ions substituted into V_2O_5 by replacing V^{5+} sites. This substitution induced defects and multiple oxidation states, as revealed by X-ray photoelectron spectroscopy (XPS), which showed mixed Ni and V valence states and thereby increased the material's redox flexibility and electronic heterogeneity.Micro-Raman spectroscopy further corroborated these structural modifications by displaying 13 well-resolved phonon modes characteristic of V_2O_5; notably, a subtle shoulder band at 959 cm^{-1} emerged, corresponding to V^{4+}-O stretching vibrations associated with oxygen vacancies introduced by Ni doping. These structural and electronic adjustments had direct implications on the material's electronic properties: the band gap of V_2O_5 was effectively narrowed due to a negative Burstein–Moss shift, and both AC and DC electrical conductivities were markedly enhanced. The presence of Ni created additional hopping sites for charge carriers, facilitating charge transport via a small-polaron hopping mechanism between V^{4+} and V^{5+} ions and thereby boosting overall conductivity. Importantly, beyond electronic improvements, Ni incorporation also conferred significant antimicrobial activity to the V_2O_5-based compounds. The Ni-V-O materials demonstrated potent biocidal effects against both Gram-positive

and Gram-negative bacteria, even against strains known for antibiotic resistance, indicating their promise for biomedical and environmental applications. XPS analysis of the samples confirmed that Ni incorporation leads to the generation of reactive oxygen species (ROS) at the material's surface. These ROS induce oxidative stress in microbial cells, leading to structural damage and cell death, with higher Ni content producing more pronounced ROS-mediated antimicrobial effects. Such a material could be advantageous in advanced electronic devices or energy systems that simultaneously demand high conductivity and stability, as well as in applications where inherent antimicrobial properties are beneficial, underscoring the broader applicability of Ni-V-O compounds discovered in this work. This work not only advances fundamental understanding of Ni-V_2O_5 complex systems, but also opens avenues for designing multipurpose oxide materials that address both technological and healthcare challenges.

References

[1] M. Sabna, K. Safna, J. Mayandi, S. Zh. Karazhanov, and P. Jayaram, "Microstructure profiling and photoluminescence characteristics of V(1-x)2 Ni3xO5-δ compound systems," *Mater. Lett.*, vol. 266, p. 127507, May 2020, doi: 10.1016/j.matlet.2020.127507.

[2] R. Abazari, S. Sanati, and L. A. Saghatforoush, "Non-aggregated divanadium pentoxide nanoparticles: A one-step facile synthesis. Morphological, structural, compositional, optical properties and photocatalytic activities," *Chem. Eng. J.*, vol. 236, pp. 82–90, Jan. 2014, doi: 10.1016/j.cej.2013.09.056.

[3] X. Huang, X. Rui, H. H. Hng, and Q. Yan, "Vanadium Pentoxide-Based Cathode Materials for Lithium-Ion Batteries: Morphology Control, Carbon Hybridization, and Cation Doping," *Part. Part. Syst. Charact.*, vol. 32, no. 3, pp. 276–294, Mar. 2015, doi: 10.1002/ppsc.201400125.

[4] J. Yao, Y. Li, R. C. Massé, E. Uchaker, and G. Cao, "Revitalized interest in vanadium pentoxide as cathode material for lithium-ion batteries and beyond," *Energy Storage Mater.*, vol. 11, pp. 205–259, Mar. 2018, doi: 10.1016/j.ensm.2017.10.014.

[5] R. Vannier, "Bi4V2O11 polymorph crystal structures related to their electrical properties," *Solid State Ion.*, vol. 157, no. 1–4, pp. 147–153, Feb. 2003, doi: 10.1016/S0167-2738(02)00202-3.

[6] I. Abrahams *et al.*, "Effects of preparation parameters on oxygen stoichiometry in Bi4V2O11−δ," *J. Mater. Chem.*, vol. 8, no. 5, pp. 1213–1217, 1998, doi: 10.1039/a801614c.

[7] B. Prusty, M. Adhikary, and C. Das, "Supercapacitor Electrode Material Based on Nickel Vanadium Oxide," *Am. Chem. Sci. J.*, vol. 6, no. 2, pp. 91–95, Jan. 2015, doi: 10.9734/ACSJ/2015/15866.

[8] S. Khan and K. Singh, "Effect of MgO on structural, thermal and conducting properties of V2-Mg O5- (x = 0.05–0.30) systems," *Ceram. Int.*, vol. 45, no. 1, pp. 695–701, Jan. 2019, doi: 10.1016/j.ceramint.2018.09.231.

[9] A. Al-Hajry, A. Al-Shahrani, and M. M. El-Desoky, "Structural and other physical properties of barium vanadate glasses," *Mater. Chem. Phys.*, vol. 95, no. 2–3, pp. 300–306, Feb. 2006, doi: 10.1016/j.matchemphys.2005.06.041.

[10] A. A. Sharfalddin *et al.*, "Therapeutic Properties of Vanadium Complexes," *Inorganics*, vol. 10, no. 12, p. 244, Dec. 2022, doi: 10.3390/inorganics10120244.

[11] K. H. Thompson, J. H. McNeill, and C. Orvig, "Vanadium Compounds as Insulin Mimics," *Chem. Rev.*, vol. 99, no. 9, pp. 2561–2572, Sept. 1999, doi: 10.1021/cr980427c.

[12] L. M. P. F. Amaral, T. Moniz, A. M. N. Silva, and M. Rangel, "Vanadium Compounds with Antidiabetic Potential," *Int. J. Mol. Sci.*, vol. 24, no. 21, p. 15675, Oct. 2023, doi: 10.3390/ijms242115675.

[13] Y. Zhan *et al.*, "Therapeutic strategies for drug-resistant *Pseudomonas aeruginosa* : Metal and metal oxide nanoparticles," *J. Biomed. Mater. Res. A*, vol. 112, no. 9, pp. 1343–1363, Sept. 2024, doi: 10.1002/jbm.a.37677.

[14] C. D. Shilpa, H. Nagarajaiah, M. M. Swamy, A. S. Sowmyashree, and M. Chougala, "Synthesis, characterization, and application of vanadium pentoxide nanoparticles: insights from green extraction methods, photocatalytic, and antibacterial studies," *Can. Metall. Q.*, pp. 1–13, Mar. 2025, doi: 10.1080/00084433.2025.2471634.

[15] R. Ramadan and M. K. Ahmed, "Impact of adding vanadium pentoxide to Mn-doped magnetite for technological uses," *Appl. Phys. A*, vol. 128, no. 12, p. 1056, Dec. 2022, doi: 10.1007/s00339-022-06197-2.

[16] P. G. Pawar *et al.*, "Binder free vanadium pentoxide by ammonium metavanadate for supercapacitor application," *Mater. Sci. Eng. B*, vol. 316, p. 118118, June 2025, doi: 10.1016/j.mseb.2025.118118.

[17] H. Sun *et al.*, "Zinc oxide/vanadium pentoxide heterostructures with enhanced day-night antibacterial activities," *J. Colloid Interface Sci.*, vol. 547, pp. 40–49, July 2019, doi: 10.1016/j.jcis.2019.03.061.

[18] A. Vinothini, A. Mathavan Conceptulaization, E. Arulkumar, C. Vedhi, and S. Thanikaikarasan, "Green route synthesis of transition metal doped V2O5 nanoparticles, with emerging biomedical applications," *Results Chem.*, vol. 7, p. 101373, Jan. 2024, doi: 10.1016/j.rechem.2024.101373.

[19] Q. Fu *et al.*, "Preferred Site Occupation of Doping Cation and Its Impact on the Local Structure of V_2 O_5," *Chem. Mater.*, vol. 34, no. 22, pp. 9844–9853, Nov. 2022, doi: 10.1021/acs.chemmater.2c01695.

[20] S. R. Bhosale, R. R. Bhosale, R. P. Dhavale, G. B. Kolekar, V. B. Shimpale, and P. V. Anbhule, "Nanomaterials Based Multifunctional Bioactivities of V_2 O_5 and Mesoporous Carbon@V_2 O_5 Composite: Preparation and Characterization," *Langmuir*, vol. 40, no. 12, pp. 6471–6483, Mar. 2024, doi: 10.1021/acs.langmuir.4c00010.

[21] F. Mukhtar, T. Munawar, M. S. Nadeem, M. N. U. Rehman, M. Riaz, and F. Iqbal, "Dual S-scheme heterojunction ZnO–V2O5–WO3 nanocomposite with enhanced photocatalytic and antimicrobial activity," *Mater. Chem. Phys.*, vol. 263, p. 124372, Apr. 2021, doi: 10.1016/j.matchemphys.2021.124372.

[22] S. Shadi Saeidi, P. Sanati, G. Rezaei, and B. Vaseghi, "Synthesis and improving antibacterial effectiveness of Ag/Co3V2O8 nanocomposites by graphene oxide for biomedical applications," *Mater. Sci. Eng. B*, vol. 306, p. 117457, Aug. 2024, doi: 10.1016/j.mseb.2024.117457.

[23] M. Sabna, K. Safna, J. Mayandi, S. Zh. Karazhanov, and P. Jayaram, "Microstructure profiling and photoluminescence characteristics of V(1-x)2 Ni3xO5-δ compound systems," *Mater. Lett.*, vol. 266, p. 127507, May 2020, doi: 10.1016/j.matlet.2020.127507.

[24] H. Song, C. Zhang, Y. Liu, C. Liu, X. Nan, and G. Cao, "Facile synthesis of mesoporous V2O5 nanosheets with superior rate capability and excellent cycling stability for lithium ion batteries," *J. Power Sources*, vol. 294, pp. 1–7, Oct. 2015, doi: 10.1016/j.jpowsour.2015.06.055.

[25] V. Uma Shankar, D. Govindarajan, P. Christuraj, M. J. Salethraj, F. J. Johanson, and M. D. Raja, "Enhanced the electrochemical properties of Ni doped V2O5 as a electrode material for supercapacitor applications," *Mater. Today Proc.*, vol. 50, pp. 2675–2678, 2022, doi: 10.1016/j.matpr.2020.08.213.

[26] D. Fang *et al.*, "BiVO4-rGO with a novel structure on steel fabric used as high-performance photocatalysts," *Sci. Rep.*, vol. 7, no. 1, p. 7979, Aug. 2017, doi: 10.1038/s41598-017-07342-1.

[27] R. Ran, J. G. McEvoy, and Z. Zhang, "Synthesis and Optimization of Visible Light Active $BiVO_4$ Photocatalysts for the Degradation of RhB," *Int. J. Photoenergy*, vol. 2015, pp. 1–14, 2015, doi: 10.1155/2015/612857.

[28] D. Errandonea, "High pressure crystal structures of orthovanadates and their properties," *J. Appl. Phys.*, vol. 128, no. 4, p. 040903, July 2020, doi: 10.1063/5.0016323.

[29] Q. Zhou, Y. Gong, and J. Lin, "Low temperature synthesis of sponge-like NiV2O6/C composite by calcining Ni-V-based coordination polymer for supercapacitor application," *J. Electroanal. Chem.*, vol. 823, pp. 80–91, Aug. 2018, doi: 10.1016/j.jelechem.2018.05.037.

[30] P. M. Aiswarya, S. Narang, R. Dawar, P. D. Babu, P. Banerjee, and R. Mishra, "Thermodynamic insights of ternary compounds of NiO - V2O5 system," *J. Alloys Compd.*, vol. 994, p. 174646, Aug. 2024, doi: 10.1016/j.jallcom.2024.174646.

[31] B. Singh *et al.*, "Anomalous lattice behavior of vanadium pentaoxide (V_2O_5): X-ray diffraction, inelastic neutron scattering and ab initio lattice dynamics," *Phys. Chem. Chem. Phys.*, vol. 19, no. 27, pp. 17967–17984, 2017, doi: 10.1039/C7CP01904A.

[32] D. Nandi, M. Gnanaseelan, F. Simon, and J. Pionteck, "Unique nanopetals of nickel vanadate: crystal structure elucidation and supercapacitive performance," *New J. Chem.*, vol. 41, no. 13, pp. 5620–5627, 2017, doi: 10.1039/C6NJ03427F.

[33] F. Haaß, A. H. Adams, T. Buhrmester, G. Schimanke, M. Martin, and H. Fuess, "X-Ray absorption and X-ray diffraction studies on molybdenum doped vanadium pentoxide," *Phys Chem Chem Phys*, vol. 5, no. 19, pp. 4317–4324, 2003, doi: 10.1039/B307158H.

[34] R. Baddour-Hadjean *et al.*, "Lattice Dynamics of β-V_2O_5: Raman Spectroscopic Insight into the Atomistic Structure of a High-Pressure Vanadium Pentoxide Polymorph," *Inorg. Chem.*, vol. 51, no. 5, pp. 3194–3201, Mar. 2012, doi: 10.1021/ic202651b.

[35] L. Abello, E. Husson, Y. Repelin, and G. Lucazeau, "Vibrational spectra and valence force field of crystalline V2O5," *Spectrochim. Acta Part Mol. Spectrosc.*, vol. 39, no. 7, pp. 641–651, Jan. 1983, doi: 10.1016/0584-8539(83)80040-3.

[36] Y. Wang and G. Cao, "Synthesis and Enhanced Intercalation Properties of Nanostructured Vanadium Oxides," *Chem. Mater.*, vol. 18, no. 12, pp. 2787–2804, June 2006, doi: 10.1021/cm052765h.

[37] G. Faggio, V. Modafferi, G. Panzera, D. Alfieri, and S. Santangelo, "Micro-Raman and photoluminescence analysis of composite vanadium oxide/poly-vinyl acetate fibres

synthesised by electro-spinning," *J. Raman Spectrosc.*, vol. 43, no. 6, pp. 761–768, June 2012, doi: 10.1002/jrs.3089.

[38] R. Baddour-Hadjean and J.-P. Pereira-Ramos, "Raman Microspectrometry Applied to the Study of Electrode Materials for Lithium Batteries," *Chem. Rev.*, vol. 110, no. 3, pp. 1278–1319, Mar. 2010, doi: 10.1021/cr800344k.

[39] B. Zhou and D. He, "Raman spectrum of vanadium pentoxide from density-functional perturbation theory," *J. Raman Spectrosc.*, vol. 39, no. 10, pp. 1475–1481, Oct. 2008, doi: 10.1002/jrs.2025.

[40] S. Zhan, G. Chen, D. Liu, A. Li, C. Wang, and Y. Wei, "Effects of Cr doping on the structural and electrochemical properties of V2O5," *J. Alloys Compd.*, vol. 479, no. 1–2, pp. 652–656, June 2009, doi: 10.1016/j.jallcom.2009.01.023.

[41] R. Suresh *et al.*, "New electrochemical sensor based on Ni-doped V2O5 nanoplates modified glassy carbon electrode for selective determination of dopamine at nanomolar level," *Sens. Actuators B Chem.*, vol. 202, pp. 440–447, Oct. 2014, doi: 10.1016/j.snb.2014.05.095.

[42] R. Baddour-Hadjean, S. Bach, N. Emery, and J. P. Pereira-Ramos, "The peculiar structural behaviour of β-Na0.33V2O5 upon electrochemical lithium insertion," *J. Mater. Chem.*, vol. 21, no. 30, p. 11296, 2011, doi: 10.1039/c1jm11393c.

[43] R. Basu, A. K. Prasad, S. Dhara, and A. Das, "Role of Vanadyl Oxygen in Understanding Metallic Behavior of $V_2 O_5$ (001) Nanorods," *J. Phys. Chem. C*, vol. 120, no. 46, pp. 26539–26543, Nov. 2016, doi: 10.1021/acs.jpcc.6b08452.

[44] V. Brázdová, M. V. Ganduglia-Pirovano, and J. Sauer, "Periodic density functional study on structural and vibrational properties of vanadium oxide aggregates," *Phys. Rev. B*, vol. 69, no. 16, p. 165420, Apr. 2004, doi: 10.1103/PhysRevB.69.165420.

[45] A. Jin, W. Chen, Q. Zhu, Y. Yang, V. L. Volkov, and G. S. Zakharova, "Structural and electrochromic properties of molybdenum doped vanadium pentoxide thin films by sol–gel and hydrothermal synthesis," *Thin Solid Films*, vol. 517, no. 6, pp. 2023–2028, Jan. 2009, doi: 10.1016/j.tsf.2008.10.001.

[46] A. H. Hashem *et al.*, "Antifungal Activity of Biosynthesized Silver Nanoparticles (AgNPs) against Aspergilli Causing Aspergillosis: Ultrastructure Study," *J. Funct. Biomater.*, vol. 13, no. 4, p. 242, Nov. 2022, doi: 10.3390/jfb13040242.

[47] X. Zheng *et al.*, "In Situ Fabrication of Heterostructure on Nickel Foam with Tuned Composition for Enhancing Water-Splitting Performance," *Small*, vol. 14, no. 50, p. 1803666, Dec. 2018, doi: 10.1002/smll.201803666.

[48] S. Anantharaj, J. Kennedy, and S. Kundu, "Microwave-Initiated Facile Formation of Ni_3 Se_4 Nanoassemblies for Enhanced and Stable Water Splitting in Neutral and Alkaline Media," *ACS Appl. Mater. Interfaces*, vol. 9, no. 10, pp. 8714–8728, Mar. 2017, doi: 10.1021/acsami.6b15980.

[49] H. Ali-Löytty *et al.*, "Ambient-Pressure XPS Study of a Ni–Fe Electrocatalyst for the Oxygen Evolution Reaction," *J. Phys. Chem. C*, vol. 120, no. 4, pp. 2247–2253, Feb. 2016, doi: 10.1021/acs.jpcc.5b10931.

[50] Z. Wang *et al.*, "Interfacial and Vacancies Engineering of Copper Nickel Sulfide for Enhanced Oxygen Reduction and Alcohols Oxidation Activity," *ENERGY Environ. Mater.*, vol. 6, no. 5, p. e12409, Sept. 2023, doi: 10.1002/eem2.12409.

[51] B.-O. Shalom *et al.*, "Chemical state of nickel nanoparticles during the oxygen evolution reaction in a carbonate-bicarbonate buffer solution," *Cell Rep. Phys. Sci.*, vol. 5, no. 9, p. 102165, Sept. 2024, doi: 10.1016/j.xcrp.2024.102165.

[52] G. Silversmit, D. Depla, H. Poelman, G. B. Marin, and R. De Gryse, "Determination of the V2p XPS binding energies for different vanadium oxidation states (V5+ to V0+)," *J. Electron Spectrosc. Relat. Phenom.*, vol. 135, no. 2–3, pp. 167–175, Apr. 2004, doi: 10.1016/j.elspec.2004.03.004.

[53] M. Cheng, H. Fan, Y. Song, Y. Cui, and R. Wang, "Interconnected hierarchical $NiCo_2O_4$ microspheres as high-performance electrode materials for supercapacitors," *Dalton Trans*, vol. 46, no. 28, pp. 9201–9209, 2017, doi: 10.1039/C7DT01289F.

[54] M. Beaudoin, M. Meunier, and C. J. Arsenault, "Blueshift of the optical band gap: Implications for the quantum confinement effect in *a* -Si:H/ *a* - SiN x :H multilayers," *Phys. Rev. B*, vol. 47, no. 4, pp. 2197–2202, Jan. 1993, doi: 10.1103/PhysRevB.47.2197.

[55] L. Top, M. Kang, and S. Kim, "A review on the optical characterization of V2O5 micro-nanostructures," *Ceram. Int.*, vol. 45, May 2019, doi: 10.1016/j.ceramint.2019.05.339.

[56] R. Basu and S. Dhara, "Spectroscopic study of native defects in the semiconductor to metal phase transition in V2O5 nanostructure," *J. Appl. Phys.*, vol. 123, no. 16, p. 161550, Apr. 2018, doi: 10.1063/1.5011112.

[57] R.-P. Blum *et al.*, "Surface Metal-Insulator Transition on a Vanadium Pentoxide (001) Single Crystal," *Phys. Rev. Lett.*, vol. 99, no. 22, p. 226103, Nov. 2007, doi: 10.1103/PhysRevLett.99.226103.

[58] P. K. Chakraborty, G. C. Datta, and K. P. Ghatak, "The simple analysis of the Burstein–Moss shift in degenerate n-type semiconductors," *Phys. B Condens. Matter*, vol. 339, no. 4, pp. 198–203, Dec. 2003, doi: 10.1016/j.physb.2003.07.001.

[59] Z. M. Gibbs, A. LaLonde, and G. J. Snyder, "Optical band gap and the Burstein–Moss effect in iodine doped PbTe using diffuse reflectance infrared Fourier transform spectroscopy," *New J. Phys.*, vol. 15, no. 7, p. 075020, July 2013, doi: 10.1088/1367-2630/15/7/075020.

[60] S. Khan and K. Singh, "Structural, optical, thermal and conducting properties of V2−xLixO5−δ ($0.15 \leq x \leq 0.30$) systems," *Sci. Rep.*, vol. 10, no. 1, p. 1089, Jan. 2020, doi: 10.1038/s41598-020-57836-8.

[61] F. K. Tan, J. Hassan, Z. Abd. Wahab, and R. S. Azis, "Electrical conductivity and dielectric studies of MnO 2 doped V 2 O 5," *Results Phys.*, vol. 6, pp. 420–427, 2016, doi: 10.1016/j.rinp.2016.07.011.

[62] N. Shukla and D. K. Dwivedi, "Dielectric relaxation and AC conductivity studies of $Se_{90}\ Cd_{10-x}\ In_x$ glassy alloys," *J. Asian Ceram. Soc.*, vol. 4, no. 2, pp. 178–184, June 2016, doi: 10.1016/j.jascer.2016.02.003.

[63] A. A. Kadam, S. S. Shinde, S. P. Yadav, P. S. Patil, and K. Y. Rajpure, "Structural, morphological, electrical and magnetic properties of Dy doped Ni–Co substitutional spinel ferrite," *J. Magn. Magn. Mater.*, vol. 329, pp. 59–64, Mar. 2013, doi: 10.1016/j.jmmm.2012.10.008.

[64] T. Sankarappa, M. P. Kumar, G. B. Devidas, N. Nagaraja, and R. Ramakrishnareddy, "AC conductivity and dielectric studies in V2O5–TeO2 and V2O5–CoO–TeO2 glasses," *J. Mol. Struct.*, vol. 889, no. 1–3, pp. 308–315, Oct. 2008, doi: 10.1016/j.molstruc.2008.02.009.

[65] F. K. Tan, J. Hassan, Z. Abd. Wahab, and R. S. Azis, "Electrical conductivity and dielectric behaviour of manganese and vanadium mixed oxide prepared by conventional solid state method," *Eng. Sci. Technol. Int. J.*, vol. 19, no. 4, pp. 2081–2087, Dec. 2016, doi: 10.1016/j.jestch.2016.08.002.

[66] W. E. Mahmoud and A. A. Al-Ghamdi, "The influence of vanadium pentoxide on the structure and dielectric properties of poly(vinyl alcohol)," *Polym. Int.*, vol. 59, no. 9, pp. 1282–1288, Sept. 2010, doi: 10.1002/pi.2866.

[67] L. Alaya, A. M. Saeedi, A. A. Alsaigh, M. H. K. Almalki, N. H. Alonizan, and M. Hjiri, "ZnO:V Nanoparticles with Enhanced Antimicrobial Activities," *J. Compos. Sci.*, vol. 7, no. 5, p. 190, May 2023, doi: 10.3390/jcs7050190.

[68] K. Zamani *et al.*, "Antibacterial effect of cerium oxide nanoparticle against Pseudomonas aeruginosa," *BMC Biotechnol.*, vol. 21, no. 1, p. 68, Dec. 2021, doi: 10.1186/s12896-021-00727-1.

[69] G. Senthil Kumar, A. Sakthivelu, M. A. Rahman, S. P. Ramachandran, and P. Parameswari, "Biocidal Properties of Vanadium, ZnO Nanoparticles Prepared Via Green Process," *BioNanoScience*, vol. 13, no. 4, pp. 2458–2468, Dec. 2023, doi: 10.1007/s12668-023-01224-9.

[70] B.-E. Sadoq *et al.*, "Metal and Metal Oxide Nanoparticles: Computational Analysis of Their Interactions and Antibacterial Activities Against Pseudomonas aeruginosa," *BioNanoScience*, vol. 15, no. 1, p. 60, Mar. 2025, doi: 10.1007/s12668-024-01625-4.

[71] B. Salehi, E. Mortaz, and P. Tabarsi, "Comparison of antibacterial activities of cadmium oxide nanoparticles against Pseudomonas Aeruginosa and Staphylococcus Aureus bacteria," *Adv. Biomed. Res.*, vol. 4, no. 1, p. 105, 2015, doi: 10.4103/2277-9175.157805.

[72] L. C. Ann *et al.*, "Antibacterial responses of zinc oxide structures against Staphylococcus aureus, Pseudomonas aeruginosa and Streptococcus pyogenes," *Ceram. Int.*, vol. 40, no. 2, pp. 2993–3001, Mar. 2014, doi: 10.1016/j.ceramint.2013.10.008.

[73] T. J. Thomas Webster, "Bactericidal effect of iron oxide nanoparticles on Staphylococcus aureus," *Int. J. Nanomedicine*, p. 277, Apr. 2010, doi: 10.2147/IJN.S9220.

[74] Q. Qin, J. Li, and J. Wang, "Antibacterial Activity Comparison of Three Metal Oxide Nanoparticles and their Dissolved Metal Ions," *Water Environ. Res.*, vol. 89, no. 4, pp. 378–383, Apr. 2017, doi: 10.2175/106143017X14839994523262.

[75] Y. H. Leung *et al.*, "Mechanisms of Antibacterial Activity of MgO: Non-ROS Mediated Toxicity of MgO Nanoparticles Towards *Escherichia coli*," *Small*, vol. 10, no. 6, pp. 1171–1183, Mar. 2014, doi: 10.1002/smll.201302434.

[76] A. Meza-Villezcas, A. L. Gallego-Hernández, F. H. Yildiz, O. E. Jaime-Acuña, O. Raymond-Herrera, and A. Huerta-Saquero, "Effect of antimicrobial nanocomposites on Vibrio cholerae lifestyles: Pellicle biofilm, planktonic and surface-attached biofilm," *PLOS ONE*, vol. 14, no. 6, p. e0217869, June 2019, doi: 10.1371/journal.pone.0217869.

[77] M. Kitaoka, S. T. Miyata, D. Unterweger, and S. Pukatzki, "Antibiotic resistance mechanisms of Vibrio cholerae," *J. Med. Microbiol.*, vol. 60, no. 4, pp. 397–407, Apr. 2011, doi: 10.1099/jmm.0.023051-0.

[78] J. Chen, Y. Lu, X. Ye, M. Emam, H. Zhang, and H. Wang, "Current advances in Vibrio harveyi quorum sensing as drug discovery targets," *Eur. J. Med. Chem.*, vol. 207, p. 112741, Dec. 2020, doi: 10.1016/j.ejmech.2020.112741.

[79] K. V. Anand *et al.*, "Biomass extract of green macroalga Halimeda opuntia assisted ZnO nanoparticles: preparation, physico-chemical characterization, and antibacterial activity against Vibrio harveyi," *Biomass Convers. Biorefinery*, vol. 14, no. 2, pp. 2225–2233, Jan. 2024, doi: 10.1007/s13399-022-02397-1.

[80] H. A. Mansouri-Tehrani, M. Keyhanfar, M. Behbahani, and G. Dini, "Synthesis and characterization of algae-coated selenium nanoparticles as a novel antibacterial agent against Vibrio harveyi, a Penaeus vannamei pathogen," *Aquaculture*, vol. 534, p. 736260, Mar. 2021, doi: 10.1016/j.aquaculture.2020.736260.

[81] L. Guo *et al.*, "Extraction, identification and mechanism of action of antibacterial substances from *Galla chinensis* against *Vibrio harveyi*," *Biotechnol. Biotechnol. Equip.*, vol. 34, no. 1, pp. 1215–1223, Jan. 2020, doi: 10.1080/13102818.2020.1827980.

[82] M. Diao *et al.*, "Antibacterial activity and mechanism of monolauroyl-galactosylglycerol against Bacillus cereus," *Food Control*, vol. 85, pp. 339–344, Mar. 2018, doi: 10.1016/j.foodcont.2017.10.019.

[83] C.-L. Moo *et al.*, "Antibacterial Activity and Mode of Action of β-caryophyllene on *Bacillus cereus*," *Pol. J. Microbiol.*, vol. 69, no. 1, pp. 49–54, Sept. 2020, doi: 10.33073/pjm-2020-007.

[84] P. Le and A. Desbois, "Antibacterial Effect of Eicosapentaenoic Acid against Bacillus cereus and Staphylococcus aureus: Killing Kinetics, Selection for Resistance, and Potential Cellular Target," *Mar. Drugs*, vol. 15, no. 11, p. 334, Nov. 2017, doi: 10.3390/md15110334.

[85] Y. N. Slavin and H. Bach, "Mechanisms of Antifungal Properties of Metal Nanoparticles," *Nanomaterials*, vol. 12, no. 24, p. 4470, Dec. 2022, doi: 10.3390/nano12244470.

[86] C. G. Baigorria *et al.*, "Antifungal Action of Metallic Nanoparticles Against Fungicide-Resistant Pathogens Causing Main Postharvest Lemon Diseases," *J. Fungi*, vol. 10, no. 11, p. 782, Nov. 2024, doi: 10.3390/jof10110782.

[87] S. Parveen, A. H. Wani, M. A. Shah, H. S. Devi, M. Y. Bhat, and J. A. Koka, "Preparation, characterization and antifungal activity of iron oxide nanoparticles," *Microb. Pathog.*, vol. 115, pp. 287–292, Feb. 2018, doi: 10.1016/j.micpath. 2017.12.068.

Chapter V

Correlating Structural, Electronic, and Optical Properties with Energy Dissipation, Polarization Dynamics, Dielectric Responses, and Antimicrobial Applications in V_2O_5-NiO-Sb_2O_3 Micro-Ceramics

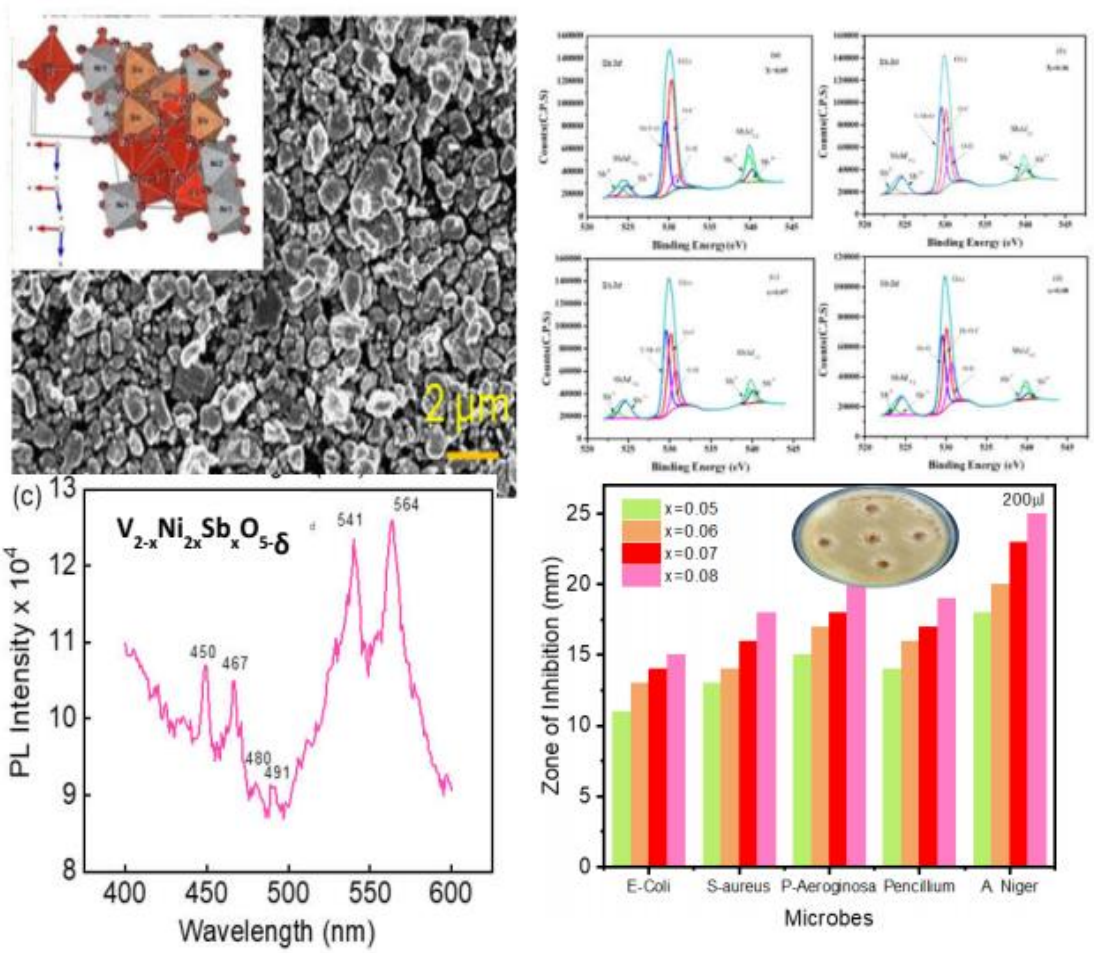

***Sabna, Melethil**., Jayaram, P., Safna, K. et al. Synergistic Effects of Nickel and Antimony Integration into V_2O_5 Matrix: Insights into Microstructural Evolution, Oxygen Defect-Mediated Photoluminescence, Lattice Dynamics and Enhanced Antimicrobial Activity. J Inorg Organomet Polym (2026). https://doi.org/10.1007/s10904-026-04317-6*

***Melethil Sabna**, Peediyekkal Jayaram, K. Safna, S. Sreedevi, Faheema S, Correlating structural and electronic properties with energy dissipation, polarization dynamics, and dielectric responses in V_2O_5-NiO-Sb_2O_3 micro-ceramics, Physica B: Condensed Matter, Volume 704, 2025, 417010, ISSN 0921-4526, https://doi.org/10.1016/j.physb.2025.417010*

5.1. Introduction

Vanadium, abundant in the earth's crust, demonstrates a diverse range of valence states, giving rise to various oxides such as vanadium monoxide (VO), vanadium sesquioxide (V_2O_3), vanadium dioxide (VO_2), and vanadium pentoxide (V_2O_5). These oxides span oxidation states from V^{2+} to V^{5+} [1], [2]. Environmental factors, including temperature, pressure, phase, and concentration, influence the oxidation states of vanadium. The V_2O_5 compound stands out as the prominent and thermodynamically stable member within the family of layered vanadium oxides, characterized by the formula V_nO_{2n+1} with a distinctive layered structure and porous morphology, rendering it highly versatile for numerous applications such as electrochemistry, photocatalysis, sensors, chromogenics, and optoelectronic devices [3], [4].

With a band gap within the visible light spectrum (2.2 eV - 2.3 eV), it holds promise for photodetection purposes. The layered characteristic of vanadium pentoxide facilitates the introduction of various ions into the lamellar spacing, thereby altering the crystalline structure and resulting in diverse properties [4]. Its layered architecture, coupled with a range of available phases, endows it with favorable electrical and optical characteristics, making it a material of considerable interest in scientific exploration [5]. Its distinctive electronic structure, featuring three bands, imparts unique optical properties and a multi-color appearance, making it an intriguing choice for various smart and multifunctional uses [3].

Moreover, oxides exhibit potential as host matrices for rare-earth ion implantation, facilitated by their oxygen incorporation and wide bandgap characteristics, thereby restructuring the bandgap and enhancing photoluminescence emission [6]. Addressing the challenge of improving the electrical and optical conductivity of metal oxides, alloying with suitable elements presents another avenue. Bandgap engineering, achieved through the introduction of defects into the V_2O_5 lattice using extrinsic dopants such as Al, Zn, Cu, Ni, Mn, Bi, and Co as donors, can significantly enhance its electrical and optical properties [7- 9].

Studies have shown that doping V_2O_5 with aliovalent ions, such as Li^{2+}, Mn^{4+}, and Mg^{2+} can significantly enhance electrical conductivity [6], [10-11]. For instance, Li-doped $V_{2-x}Li_xO_{5-\delta}$ exhibits increased AC and DC conductivity at elevated

temperatures [10]. Similarly, Tan Foo Khoon et al. [12] reported a temperature-dependent increase in conductivity and dielectric constant in MnO_2-doped V_2O_5 mixed oxides. Khan C et al. [11] observed an AC conductivity of 0.11 S/m in $V_{2-x}Mg_xO_{5-\delta}$ at x= 0.05 at 300°C. Safna et al. [13] also demonstrated that the electrical conductivity of bismuth-substituted V_2O_5 increases with the concentration of Bi^{3+} ions. In our previous chapters, we studied the frequency dependent conductivity of Ni & Sb substituted V_2O_5 [1]. Building on these findings, this study explores the electrical properties of Sb-Ni-V-O oxides, focusing on the impact of Sb and Ni mole fraction on dielectric behavior, AC conductivity, and impedance studies. Among the dopants, nickel (Ni) [5] emerges as a prominent choice, while antimony (Sb) serves as a less common metalloid dopant [14-15]. Notably, NiO and Sb_2O_3 have garnered substantial interest in this study due to their analogous electronic shell structure, as well as comparable physical and chemical properties to those of V_2O_5.

On an added account, there are some reports on the antimicrobial efficacy of pristine V_2O_5[16] as well as composites like V_2O_5/PANI [17], V_2O_5/ZnO [18], and V_2O_5-loaded TiO_2 [19]. The incidence of nosocomial infections among patients undergoing surgical interventions, compounded by biofilm formation on prosthetic implants and the alarming rise of multidrug-resistant bacterial strains, poses a formidable challenge to healthcare systems. In response, advanced engineered micro and nanoparticles exhibiting enhanced antibacterial properties have emerged as potent coating materials for surgical instruments and implants, significantly mitigating the risk of implant-associated infections. These micro- and nanostructured surfaces inhibit bacterial adhesion and diminish microbial colonization by inducing the generation of reactive oxygen species within the bacterial cells. Suma et al. [16] reported the generation of reactive oxygen species in E. coli biofilms and the prospects of vanadium pentoxide as a potential surface coating agent to impart antibacterial activity.

Fungi such as *Aspergillus sp., Fusarium sp., Penicillium sp., and Candida sp.* are known to produce harmful mycotoxins, affecting human and animal health by causing grain discoloration, chemical and nutritional degradation, and reduced germination rates [20]. Among these, Aspergillus species are prevalent, constituting up to 22% of airborne spores. Notably, A. niger, a prevalent pathogenic species, can lead to invasive respiratory infections with high mortality rates, especially in

immunocompromised individuals. The emergence of drug-resistant Aspergillus isolates further underscores the urgent need for novel antifungal treatments [21]. *Pseudomonas aeruginosa*, a Gram-negative opportunistic pathogen, also presents significant treatment challenges, especially in clinical settings where it contributes to ventilator-associated pneumonia and chronic infections in cystic fibrosis patients. Known for its adaptability and resistance to multiple antibiotics, *P. aeruginosa* forms biofilms that enhance its persistence and resist antibiotic action. The World Health Organization has identified carbapenem-resistant P. aeruginosa as a high-priority pathogen, urging the development of innovative antimicrobial strategies [22]. The exploration of the microbicidal potential of vanadium pentoxide-based compounds presents a vast and promising research avenue, given their multifaceted antimicrobial properties and potential for innovative therapeutic applications.

The previous chapters reported the synthesis, microstructural analysis, optical studies, electrical conductivity, dielectric, and adsorptive studies of NiO-V_2O_5 [29], [30], Sb_2O_3-V_2O_5 [14-15], [24]. Multi-cation vanadium pentoxide-based compounds. Consequently, this study focuses on investigating the microstructural analysis, lattice dynamics, surface morphology, surface chemical states, optical studies, AC conductivity, dielectric studies, and antimicrobial studies of the Sb_2O_3-NiO-V_2O_5 complex compound system [25].

5.2 Materials and methods

The complex ceramic powders of $V_{2-x}Ni_{2x}Sb_xO_{5-\delta}$ ($0.05 \leq x \leq 0.08$) were synthesized via the conventional solid-state reaction method, with antimony oxide (Sb_2O_3, 99.99%) and nickel oxide (NiO, 99.99%) serving as guest metal oxides introduced into the vanadium pentoxide (V_2O_5, 99.99%) host matrix. All precursor materials were sourced from Sigma Aldrich Chemicals Co., USA. The synthesis commenced with the thorough grinding of the oxide materials for 3 h using an agate mortar and pestle to ensure the formation of a homogeneous mixture. The ground mixture was then placed in alumina crucibles and calcined in a programmable high-temperature furnace at 550 °C for 12 h. After calcination, the fine powders were compacted into 14 mm diameter discs with a thickness of 2 mm using a uniaxial press. These compacted pellets were then sintered at 630 °C for 12 to promote the formation of the desired crystalline phases. The sintered pellets were reground to ensure

homogeneity of the powder samples [15], [26]. For AC conductivity and dielectric studies, the powdered materials were thoroughly ground and subsequently compressed into a disk with a thickness of 2 mm and a diameter of 14 mm, utilizing polyvinyl alcohol as a binder to ensure structural integrity.

The resulting pellet underwent surface polishing to achieve optimal flatness and smoothness, enhancing the contact between the sample and the measurement electrodes. Once polished, the pellet was carefully positioned between two copper electrodes, facilitating the acquisition of frequency-dependent data. Measurements were conducted across a broad frequency range, spanning from 10 Hz to 1 MHz, capturing key electrical parameters including capacitance, tangent loss, impedance, and phase angle. This comprehensive approach allowed for a detailed characterization of the material's dielectric behavior and AC conductivity over varying frequencies. The characterizations and antimicrobial studies of the samples were carried out using the instruments and methodologies as mentioned in chapters 3 and 4.

5.3 Results and Discussion

5.3.1. Microstructural Analysis using XRD

The X-ray diffraction patterns of $V_{2-x}Ni_{2x}Sb_xO_{5-\delta}$ ($0.05 \leq x \leq 0.08$) ceramics synthesized by the solid-state reaction method are shown in Figure. 5.1. The XRD pattern of pristine V_2O_5, with an orthorhombic layered crystalline structure, with standard ICDD No. 41–1426 [4] with lattice parameters a = 1.151 nm, b = 0.356 nm and c = 0.437 nm [28] is taken as the reference. The X-Ray Diffraction pattern of the Sb-Ni-V-O ceramic system exhibits prominent diffraction peaks at 15.49°, 20.30°, 21.79°, 26.19°, 30.99°, 32.41°, 34.37° and 41.36°, corresponding to the (200), (001), (101), (110), (301), (011), (110), and (002) crystallographic planes, respectively. These reflections align precisely with the orthorhombic structure of V_2O_5 [2], [4], [14] ,[23], [29]. However, additional reflections at 23.40° and 27.30° were observed, which deviate from the standard orthorhombic V_2O_5 and are attributed to reflections arising from the incorporation of NiO and Sb_2O_3 into the V_2O_5 lattice, indicating the formation of secondary phases within the structure. Upon closer examination, the minor peak around 2θ of 23.40° corresponds to the (101) plane of triclinic NiV_2O_6 phase (JCPDS card no. 45-1053) and ICSD:33881, and the reflection at 27.3° is a

characteristic indication of the formation of vanadate, specifically $SbVO_4$ species [14-16], [33].

The lattice parameters, crystallite size, microstrain, and dislocation density were determined, as detailed in Table 5.1. The estimation was carried out using the Scherrer equation, while the Williamson-Hall (W-H) plot was employed to analyze microstructural properties through the uniform deformation model [23], [34]. Here, the crystallite size decreases with an increase in mol fraction x. The incorporation of Ni^{2+} and Sb^{3+} into the V_2O_5 lattice increases the number of defects, such as vacancies and dislocations, as evidenced by the increase in dislocation density presented in Table 5.1. These defects act as additional nucleation sites during the crystallization process, preventing the growth of larger grains. The presence of more nucleation sites results in the formation of numerous smaller grains instead of fewer, larger ones. Alongside, higher Ni and Sb concentrations with increasing mol fraction 'x', secondary phases such as NiV_2O_6 and $SbVO_4$ can further inhibit grain growth by interrupting the continuity of the V_2O_5 phase.

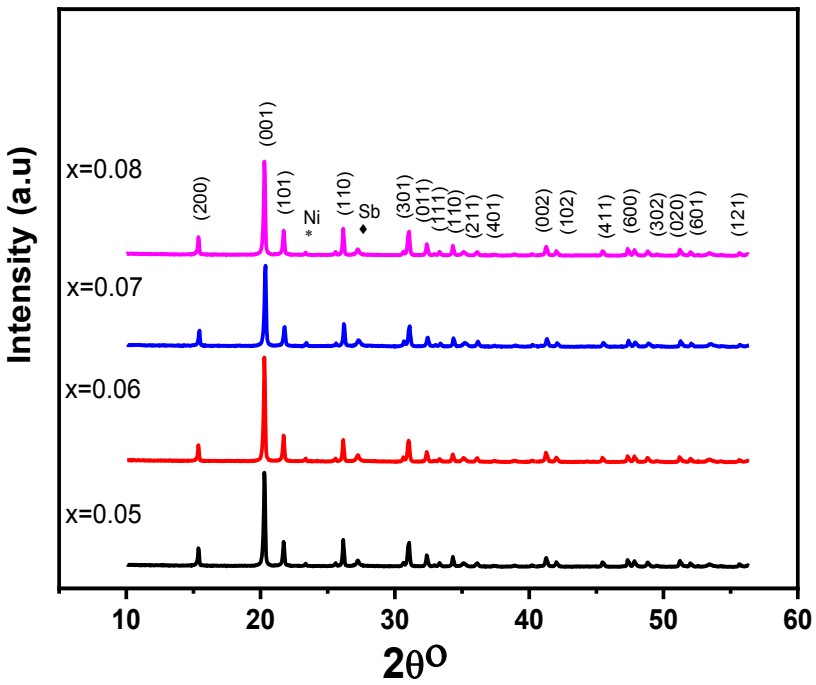

Figure.5.1 XRD pattern of $V_{2-x}Ni_{2x}Sb_xO_{5-\delta}$ ceramics indicating the prominent orthorhombic phase of V_2O_5, with asterisk and diamond sign indicating peaks corresponding to Ni and Sb phases, respectively.

Table 5.1. Estimated grain size, dislocation density, microstrain, lattice parameters, and cell volume of $V_{2-x}Ni_{2x}Sb_xO_{5-\delta}$ ($0.05 \leq x \leq 0.08$) compounds

X values	**Sherrer Equation**		**Uniform Deformation Model W-H plot**			**Lattice Parameters**			**Cell Volume**	**Band Gap Energy**
	Crystallite size D (nm)	**Dislocation Density (δ) x 10^{-3} nm^{-2}**	**Crystallite size D (nm)**	**Dislocation Density (δ) x 10^{-3} nm^{-2}**	**Micro strain (ε) 10^{-3}**	**a(Å)**	**b(Å)**	**c(Å)**	**a*b*c $(Å)^3$**	**(eV)**
0.05	66.95	0.224	62.32	0.257	0.190	11.32	3.53	4.31	172.23	2.28
0.06	65.77	0.242	61.22	0.267	0.181	11.36	3.54	4.33	174.13	2.26
0.07	64.29	0.264	60.91	0.269	0.093	11.39	3.54	4.34	174.99	2.24
0.08	62.75	0.281	59.52	0.285	0.026	11.40	3.56	4.36	176.95	2.22

These secondary phases create boundaries that limit the coalescence and growth of V_2O_5 crystallites, contributing to a reduction in crystallite size. As the concentration of NiO and Sb_2O_3 precursors increases with an increase in mol fraction x, excess nickel and antimony may not be fully incorporated into the V_2O_5 lattice and form separate secondary phases of NiV_2O_6 and $SbVO_4$. These secondary phases can act as strain-relieving agents by providing a mechanism for the redistribution of strain within the system, effectively reducing the strain within the main V_2O_5 crystallites, from 0.190×10^{-3} to 0.026×10^{-3} [2].

5.3.2. Crystallographic Refinement of XRD Data

For deeper examinations, the Rietveld refinement was executed on each sample, employing the FullProf software [35] as depicted in figure 5.2(a). The Peak shape was modelled using the pseudo-Voigt axial divergence asymmetry function, and a 6-coefficient polynomial function was applied to fit the background pattern.

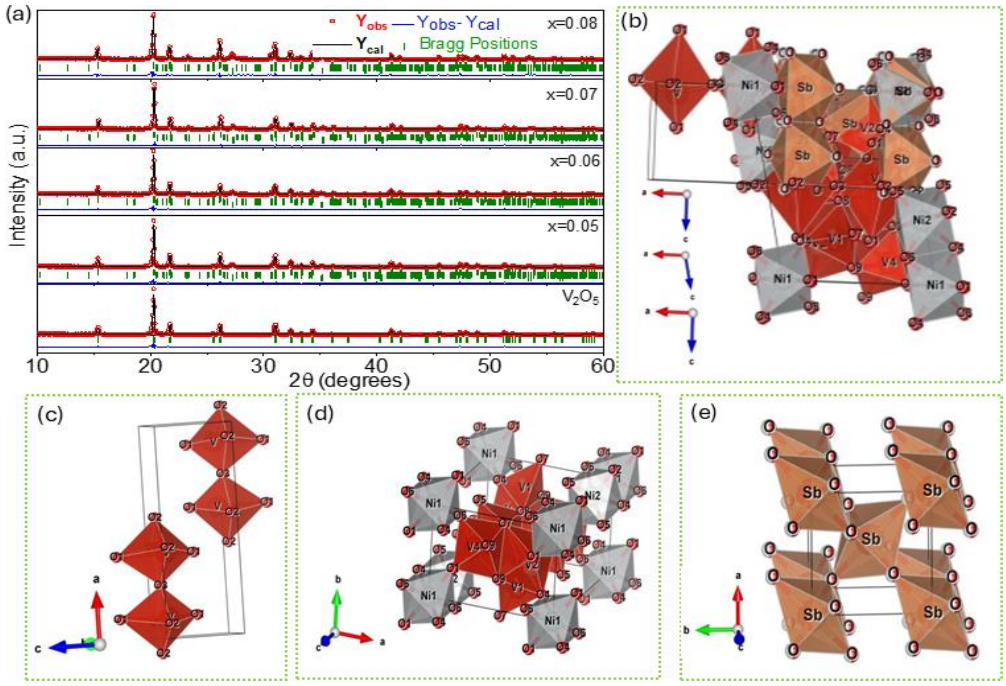

Figure.5.2: (a) representing Rietveld refinements of $V_{2-x}Ni_{2x}Sb_xO_{5-\delta}$ samples for x=0.0, 0.05, 0.06, 0.07 and 0.08 respectively (b)The unit cell structure of Sb-Ni-V-O compounds, containing the mixed phases of V_2O_5, NiV_2O_6 and $SbVO_4$ (c) The unit cell structure of Orthorhombic V_2O_5 (d) The unit cell structure of NiV_2O_6, (e) The rutile-type crystal structure of $SbVO_4$ characterized by a random distribution of Sb and V atoms within octahedral positions, each atom exhibiting a partial occupancy of 0.5.

The refinement process involved adjustments of several parameters, including scale, lattice parameters, full-width half-maximum shape parameters, asymmetry parameters, and atomic positions [15],[36]. Rietveld refinement unveiled the emergence of a prominent V_2O_5 phase characterized by the orthorhombic structure in the *Pmmn* space group, succeeded by a NiV_2O_6 phase exhibiting a monoclinic structure with *P-1* space group, and the $SbVO_4$ phase, distinguished by a tetragonal structure with *P42/mnm* space group, observed to have the least representation in terms of compositional percentage.

The crystal structure of the combined phases modelled using VESTA software [37] is depicted in Figure. 5.2(b-e). Figure. 5.2(c) presents the unit cell structure of orthorhombic V_2O_5 obtained after Rietveld refinement using the Vesta software. Within the orthorhombic unit cell of V_2O_5, V chains intertwine with oxygen along the XYZ axis, resulting in the formation of VO_5 pyramids [28]. The structure is characterized by zig-zag double chains of VO_5 square-based pyramids oriented along the b-axis. These pyramids alternate their directions, sharing an edge along the [010] direction of the chain. Along the b-axis, corner-sharing oxygen atoms bridge these chains, forming a 2D layered structure in the x-y plane. Weak bonding along the c-axis is established through V-O Van der Waals interactions [38].

Three distinct oxygen atom types exist, namely vanadyl (O1), binding singularly to vanadium at the pyramid apex chain (O3), binding to three vanadium atoms; and bridge (O1), linked to two vanadium atoms, thereby connecting the chains[4]. Table 5.2(a) presents the lattice parameters for different molar fractions (x = 0.05, 0.06, 0.07, and 0.08), showing a nonlinear trend with increasing molar fraction. Table 5.2(b) details the interfacial angles, which are crucial for understanding the grain boundary characteristics and phase interactions within the samples**.** Table 5.2(c) provides the compositional percentages of the V_2O_5, NiV_2O_6, and $SbVO_4$ phases, highlighting the phase distribution and relative stability of synthesized compounds. The compositional percentage of the V_2O_5 phase decreases from 92% to 82% with the escalation in mol fraction from x=0.05 to x=0.08. Tables 5.3 (a) & (b) present the bond angles (in°) and bond lengths(in Å) of V_2O_5 in $V_{2-x}Ni_{2x}Sb_xO_{5-\delta}$

ceramics at x=0.05 [39]. The various V-O bond lengths vary between 1.6 to 2 Å. The O-V-O & V-O-V bond angles (in°) range between 77-151 & 103–152, respectively [40]. In all sample compositions, the NiV_2O_6 phase exhibited a triclinic crystal system (space group: *P-1*), as determined through Rietveld refinement [33]. The peaks corresponding to the Ni phase are marked in XRD by * as in Figure 5.1.

The lattice parameters of the triclinic NiV_2O_6 for all mol fractions are elucidated in Table 5.2 (a and b). The compositional percentage of the NiV_2O_6 phase is found to increase from 5 % to 12 %, as evidenced by Table 5.2(c), in line with the stoichiometric proportions used during synthesis. In the NiV_2O_6 unit cell, the crystallographic analysis revealed the distribution of Ni^{2+} cations across two distinct lattice positions, V^{5+} cations across four discrete lattice sites, and O^{2-} anions distributed across nine discrete lattice sites, collectively constituting the entirety of the crystal structure [41]. As in Fig. 5.1(d), the NiV_2O_6 unit cell, delineated within the space group *P-1*, was elucidated through optimized data via diamond crystal analysis. Eight corners of the parallelepiped unit cell were occupied by Ni(1) sites. Ni(1) coordinated with one V(4) site and three distinct O(6), O(1), and O(3) sites from the unit cell corners. This lattice configuration belonged to the centrosymmetric type pinacoidal class, devoid of internal mirror planes [41]. The bond distances (Å) of Ni-O & V-O span over 2.00 to 2.12 and 1.55 to 2.23, respectively (Table 5.3 (c)). All the bond angles, including O-Ni-O, V-V-O, O-V-O, Ni-O-Ni & V-O-Ni, are tabulated in Table 5.3 (d)

The least prevalent phase observed in Sb-Ni-V-O ceramics is the tetragonal $SbVO_4$, characterized by the *P42/mnm* space group. Table 5.2 (a and b) outline the edge lengths and interaxial angles, respectively, while Table 5.2(c) illustrates the compositional percentage of $SbVO_4$, increasing from 2.89 % to 5.49 % as x ranges from 0.05 to 0.08. Figure.5.1(e) illustrates the rutile-type crystal structure of $SbVO_4$, where the positions of Sb and V atoms within octahedral sites are randomized, each atom having a partial occupancy of 0.5. This configuration was determined through computational analysis employing VESTA software. Moreover, the bond lengths and angles in $SbVO_4$ orthovanadates are detailed in Table 5.3 (e & f) respectively.

Table 5.2 (a) Edge Lengths of V_2O_5, NiV_2O_6 and $SbVO_4$

$V_{2-x}Ni_{2x}Sb_xO_{5-\delta}$	V_2O_5 (Orthorhombic)			NiV_2O_6 (Triclinic)			$SbVO_4$ (Tetragonal)		
	a[Å]	b[Å]	c[Å]	a[Å]	b[Å]	c[Å]	a[Å]	b[Å]	c[Å]
x=0	11.514(8)	3.5656(3)	4.3739(9)						
x=0.05	11.511(2)	3.5644(7)	4.3738(0)	7.1337(2)	4.7858(6)	8.8270(1)	4.6265(4)	4.6265(4)	3.0621(5)
x=0.06	11.513(3)	3.5652(3)	4.3742(3)	7.1338(5)	4.7866(2)	8.8297(7)	4.6205(4)	4.6205(4)	3.0562(7)
x=0.07	11.501(2)	3.5612(1)	4.3693(0)	7.1218(4)	4.7856(9)	8.8206(1)	4.6205(4)	4.6205(4)	3.0562(7)
x=0.08	11.518(7)	3.5666(6)	4.3758(3)	7.1296(2)	4.7949(4)	8.8325(6)	4.6289(0)	4.6289(0)	3.0582(9)

Table 5.2 (b) Interaxial angles of V_2O_5, NiV_2O_6, and $SbVO_4$

$V_{2-x}Ni_{2x}Sb_xO_{5-\delta}$	V_2O_5 (Orthorhombic)			NiV_2O_6 (Triclinic)			$SbVO_4$ (Tetragonal)		
	α	β	γ	α	β	γ	α	β	γ
x=0	90	90	90						
x=0.05	90	90	90	90.109(7)	101.967(3)	94.164(6)	90	90	90
x=0.06	90	90	90	90.100(3)	101.978(4)	94.171(2)	90	90	90
x=0.07	90	90	90	90.053(7)	101.974(1)	94.193(2)	90	90	90
x=0.08	90	90	90	90.064(0)	101.981(8)	94.203(0)	90	90	90

Daniel Errandonea et al. [32] investigated and reported less commonly studied vanadates, including $SbVO_4$, $RhVO_4$, and $NbVO_4$. $SbVO_4$ adopts a disordered rutile-type structure, where trivalent Sb atoms and pentavalent V atoms occupy cationic sites randomly, with a 50 % partial occupation [32]. Both cations are arranged in octahedral coordination within the structure, which is characterized by the space group *P42/mnm* [42]. Historically, orthovanadates have been predominantly observed to crystallize in a tetragonal configuration akin to the crystal structure of zircon (space group *I41/amd*) [32]. An alternative structure for these vanadates may involve a transition under relatively low pressures into a zircon- or scheelite-type arrangement, where the metal cations occupy 2a sites in a randomized manner. This arrangement consists of chains of octahedra that share opposite edges along the c-direction and corners in all other directions [43]. The zircon structure, *I41/amd*, represents a subgroup within the rutile space group, *P42/mnm*.

Remarkably, the zircon structure can be derived from doubling the rutile unit cell along the c-axis and redistributing half of the cations (Sb) to achieve dodecahedral coordination, while the remaining half (V atoms) assume tetrahedral coordination. Consequently, both zircon and scheelite structures are credible contenders for the high-pressure phases of $SbVO_4$ based on considerations of crystal chemistry [32], [42]. The Sb-O, O-O & V-O bond lengths (in Å) vary in the range 1.92 to 2.35 (Table 5.3(e)). The O-Sb-O, O-V-O, Sb-O-Sb & Sb-O-O bond angles (in^o) vary between 52.8 to 180 (Table 5.3(f)).

Table 5.2 (c) Compositional percentage of V_2O_5, NiV_2O_6, and $SbVO_4$

$V_{2-x}Ni_{2x}Sb_xO_{5-\delta}$	**V_2O_5 (Orthorhombic)**	**NiV_2O_6 (Triclinic)**	**$SbVO_4$ (Tetragonal)**
x=0.05	92.42(1.41)	4.69(0.29)	2.89(0.12)
x=0.06	91.76(1.37)	5.16(0.37)	3.08(0.13)
x=0.07	88.37(1.29)	7.95(0.45)	3.68(0.14)
x=0.08	82.07(1.38)	12.43(0.63)	5.49(0.20)

Table 5.3(a) Bond Lengths (in Å) of the orthorhombic phase of V_2O_5

Bond Type	Length [Å]
V - O1	1.556(11)
V - O3	1.795(6)
V - O2	1.847(3)
V - O2	2.018(15)

Table 5.3(b)Bond angles (in degrees) of the orthorhombic phase of V_2O_5

Angle Type	Angle [°]	Angle Type	Angle [°]	Angle Type	Angle [°]
O2 - V - O2	77.4(8)	O1 - V - O2	106.7(9)	V - O2 -V	149.6(11)
O3 - V - O2	97.0(8)	O2 – V - O2	149.6(9)	V - O3 - V	152.4(10)
O1 - V - O2	101.6(9)	O3 - V - O2	151.1(8)		
O1 - V - O3	102.1(9)	V - O2 - V	102.6(9)		

Table 5.3(c)Bond Lengths (in Å) of the triclinic phase of NiV_2O_6

Bond Type	Length [Å]	Bond Type	Length [Å]	Bond Type	Length [Å]
Ni1 - O6	2.002(1)	V1 - V2	1.611(88)	V3 - O5	1.659(1)
Ni1 - O1	2.064(175)	V1 - O9	1.749(115)	V3 - O3	1.883(1)
Ni1 - O4	2.068(1)	V1 - O7	1.815(87)	V3 - O8	1.974(1)
Ni2 - O5	2.017(92)	V1 - O8	1.844(118)	V4 - O1	1.582(125)
Ni2 - O4	2.031(93)	V2 - O4	1.655(1)	V4 - O6	1.712(1)
Ni2 - O3	2.048(88)	V2 - O1	2.016(98)	V4 - O3	1.819(1)
Ni2 - O6	2.058(91)	V2 - O9	2.059(1)	V4 - O9	2.046(1)
Ni2 - O5	2.084(91)	V2 - O2	2.228(1)	V4 - O9	2.132(1)
Ni2 - O2	2.123(86)	V2 - O8	2.238(1)	V4 - O7	2.233(1)
V1 - O4	1.557(103)	V3 - O2	1.648(1)		

Table 5.3 (d)Bond angles (in degrees) of the triclinic phase of NiV_2O_6

Angle Type	Angle [°]	Angle Type	Angle [°]	Angle Type	Angle [°]
O6 - Ni1 - O1	82.8(78)	V2 - V1 - O7	177.9(122)	V3 - O5 - Ni2	127.6(44)
O6 - Ni1 - O4	86.4(1)	V1 - V2 - O8	54.4(64)	V3 - O5 - Ni2	136.0(43)
O1 - Ni1 - O4	89.5(78)	V1 - V2 - O9	55.3(64)	O9 - V4 - O9	74.1(1)
O1 - Ni1 - O4	90.5(78)	V1 - V2 - O4	56.9(64)	O3 - V4 - O7	79.6(1)
O6 - Ni1 - O4	93.6(1) 2	O2 - V2 - O8	73.7(1)	O9 - V4 - O7	81.2(1)
O6 - Ni1 - O1	180.0(2)	O1 - V2 - O9	80.0(80)	O9 - V4 - O7	83.6(1)
O4 - Ni1 - O4	180.0(1)	O4 - V2 - O8	84.8(1)	O6 - V4 - O7	84.3(1)
O1 - Ni1 - O1	180.0(111)	O9 - V2 - O8	90.8(1)	O3 - V4 - O9	86.4(1)
O6 - Ni1 - O6	180.0(1)	O4 - V2 - O9	97.3(1)	O1 - V4 - O9	87.5(10
O5 - Ni2 - O2	79.9(55)	O4 - V2 - O2	99.2(1)	O1 - V4 - O9	91.6(10
O4 - Ni2 - O2	85.0(58)	O1 - V2 - O2	108.2(80)	O6 - V4 - O9	94.2(1)
O5 - Ni2 - O2	85.0(59)	O4 - V2 - O1	114.8(80)	O6 - V4 - O3	101.1(1)
O4 - Ni2 - O6	85.9(60)	V1 - V2 - O2	122.3(64)	O1 - V4 - O3	101.7(10
O6 - Ni2 - O2	88.2(60)	V1 - V2 - O1	129.3(103)	O1 - V4 - O6	106.4(10
O5 - Ni2 - O5	88.8(61)	O9 - V2 - O2	156.1(1)	O3 - V4 - O9	155.9(1)
O5 - Ni2 - O4	90.3(63)	O1 - V2 - O8	159.1(80)	O6 - V4 - O9	162.3(1)
O3 - Ni2 - O6	91.9(63)	O5 - V3 - O8	92.3(1)	O1 - V4 - O7	168.6(102)
O6 - Ni2 - O5	93.1(63)	O2 - V3 - O8	94.9(1)	V4 - O1 - V2	97.5(138)
O3 - Ni2 - O5	93.8(63)	O5 - V3 - O3	98.8(1)	V2 - O1 - Ni1	118.1(136)
O5 - Ni2 - O3	95.2(65)	O2 - V3 - O5	103.0(1)	V4 - O1 - Ni1	144.0(171)
O4 - Ni2 - O3	101.3(68)	O2 - V3 - O3	103.0(1)	V3 - O2 - V2	98.8(1)
O4 - Ni2 - O5	164.9(86)	O3 - V3 - O8	156.1(1)	Ni2 - O2 - V2	120.1(42)
O5 - Ni2 - O6	172.6(88)	V1 - O9 - V2	49.2(59)	V3 - O2 - Ni2	140.8(42)
O3 - Ni2 - O2	173.7(86)	V4 - O9 - V2	83.0(1)	V4 - O3 - V3	116.5(1)
O4 - V1 - V2	62.9(68)	V4 - O9 - V4	105.9(1)	V3 - O3 - Ni2	120.1(44)
V2 - V1 - O9	75.4(76)	V2 - O9 - V4	110.1(1)	V4 - O3 - Ni2	123.0(44)
V2 - V1 - O8	80.4(78)	V1 - O9 - V4	118.2(59)	V1 - O4 - V2	60.1(67)
O7 - V1 - O8	101.5(88)	V1 - O9 - V4	124.1(59)	Ni2 - O4 - Ni1	92.4(44)
O4 - V1 - O8	102.5(96)	V1 - O8 - V3	123.6(56)	V2 - O4 - Ni1	118.2(1)
O9 - V1 - O7	104.1(92)	Ni1 - O6 -Ni2	93.6(43)	V1 - O4 - Ni1	123.1(67)
O4 - V1 - O9	115.7(107)	V4 - O6 -Ni1	129.0(1)	V2 - O4 - Ni2	128.4(44)
O4 - V1 - O7	115.8(105)	V4 - O6 -Ni2	132.7(43)	V1 - O4 - Ni2	135.8(80)
O9 - V1 - O8	116.8(98)	Ni2 - O5 -Ni2	91.2(62)		

Table 5.3(e) Bond Lengths (in Å) of the tetragonal phase of $SbVO_4$

Bond Type	Length [Å]	Bond Type	Length [Å]	Bond Type	Length [Å]
Sb - O	1.922(32)	O - O	2.325(74)	V - O	2.109(52)
Sb - O	2.109(52)	V - O	1.922(32)		

Table 5.3(f) Bond angles (in degrees) of the tetragonal phase of $SbVO_4$

Angle Type	Angle [°]	Angle Type	Angle [°]	Angle Type	Angle [°]
O - Sb - O	74.4(31)	O - V - O	74.4(31)	Sb - O - O	52.8(26)
O - Sb - O	90.0(30)	O - V - O	90.0(30)	Sb - O - Sb	105.6(35)
O - Sb - O	105.6(31)	O - V - O	105.6(31)	Sb - O - Sb	127.2(38)
O - Sb - O	180.0(29)	O - V - O	180.0(29)	Sb - O - O	180.0(43)

5.3.3. Lattice Dynamics: Raman Spectroscopy

Figure. 5.3(a) illustrates the Raman spectrum of $V_{2-x}Ni_{2x}Sb_xO_{5-\delta}$ within the $0.05 \leq x \leq 0.08$ range, exhibiting distinct peaks. These observed Raman shifts closely resemble those documented for the α-V_2O_5 polymorphic phase of Vanadium Pentoxide in previous studies. The foundational crystal structure of α-V_2O_5 exhibits an orthorhombic lattice with *Pmmn* space group symmetry and D_{13}^{2h} point group configurations, accommodating two formula units per unit cell comprising a total of 14 atoms. This arrangement consists of [VO_5] square pyramids connected through shared edges and corners, following an alternating up-up-down-down sequence. Within a single V_2O_5 layer, distinct oxygen atoms (O1, O2, and O3) are positioned. The architecture of α-V_2O_5 contains parallel chains of V_2O_5 extending along the b-axis, wherein each chain segment comprises a pair of parallel V=O(1) vanadyl bonds joined by a V─O(3)─V bridge, while V─O(2)─V bridges interconnect these segments. Intervening interchain V─O(2) contacts, denoted as "ladder steps" (LS), establish linkages between adjacent V_2O_5 chains. These chain layers are orthogonally connected to the c-axis [44]. As per the previous reports, among the 39 optical zone center modes derived from factor group analysis, there are 21 Raman-active phonon modes identified within the α-V_2O_5 polymorph [1], which is represented as α- V_2O_5: $\Gamma_{Raman} = 7A_g + 7B_{2g} + 3B_{1g} + 4B_{3g}$

Prior research has established that within the α-V_2O_5 configuration, vibrational modes characterized by atomic displacements in the x-z plane are ascribed to the A_g and B_{2g} species, while out-of-plane vibrations with displacements along the y-axis correspond to the B_{1g} and B_{3g} species [30[,[46],[49]. Twelve Raman active phonon modes are observed to be excited in the sample specimen in the study, and are given as $V_{2-x}Ni_{2x}Sb_xO_{5-\delta}$: Γ-Raman = 6 A_g+2B_{1g}+2B_{2g}+1B_{3g}+1

Out of the 12 Raman active phonon modes obtained for $V_{2-x}Ni_{2x}Sb_xO_{5-\delta}$ compound systems, 11 vibrational modes are characteristic of the α-polymorphic phase of the orthorhombic V_2O_5 compound system. Table 5.4 presents a comparison study of the Raman bands in cm^{-1} of pure V_2O_5 powders [46], $V_{2-x}Bi_{2x}O_{5-\delta}$ [2] compounds, $V_{(1-x)2}Ni_{3x}O_{5-\delta}$ [1] compounds, $Cr_{0.1}V_2O_5$ [47] compounds and the present $V_{2-x}Ni_{2x}Sb_xO_{5-\delta}$ compound systems.

As per the previous reports from the factor group analysis of the α-polymorphic phase of V_2O_5. Raman active phonon modes in the 150-400 cm^{-1} range correspond to the bending mode, 500-800 cm^{-1} corresponds to the V−O−V stretching region, and 770-1050 cm^{-1} indicates V−O terminal stretching [3]. The lower frequency modes at 100 cm^{-1} (A_g), 143 cm^{-1} and 194 cm^{-1} (A_g/B_{2g}), are due to displacements of [VO_5] units in the layered structure of Sb-Ni-V-O compounds [1]. The apex of utmost intensity observed at 143 cm^{-1} (potentially of B_{1g} or B_{3g} symmetry; B_{1g}/B_{3g}) is ascribed to the vibrational stimulation stemming from the translational and bending vibrational modes inherent to the adjacent Sb-Ni-V-O strata. Its congruence with both reported and experimental data within these spectral domains is notable. The heightened magnitude of this resonance underscores the extensive spatial coherence prevailing within the multi-cationic oxygen planes.

Figure 5.3(b) shows the variation in the relative intensity of prominent Raman peaks with increasing mol fraction, and it is well evident that the intensity of the Raman mode at 143cm^{-1} is maximum at mol fraction x= 0.05, and it decreases almost linearly with an increase in the concentration of divalent nickel and trivalent antimony cations. This suggests that elevated levels of exogenous cations can proficiently impede the growth of orthorhombic V_2O_5 crystalline grains, consequently diminishing

the magnitude of discernible Raman peaks [48]. Previous studies documented Raman modes pertinent to $V_{(1-x)2}Ni_{3x}O_{5-\delta}$, highlighting vibrational excitations at 283 cm^{-1} and 476 cm^{-1} indicative of V-O2-V bond angle deformation. These findings align closely with the observed excitations at 282 cm^{-1} and 481 cm^{-1}, within the $V_{2-x}Ni_{2x}Sb_xO_{5-\delta}$ system across all x values [49]. Nonetheless, a subtle displacement is observed in all these peaks as the x values ascend. These spectral alterations unveil induced structural modifications stemming from heightened concentrations of Nickel and Antimony, precipitating oxygen vacancies through the valency variation of Vanadium. Figure 5.3(b) illustrates a 58 % reduction in relative intensity of Raman bands at 283 cm^{-1} corresponding to an escalation in mol fraction from 0.05 to 0.08. At 481 cm^{-1}, the observed peak denotes the Ag mode, arising from the bending vibration of the V-O(3)-V bridge unit. Concurrent oscillations of ladder puckering (involving oscillation of O(2) atoms along the c-axis) and V-O(1) swinging (involving oscillation of O(1) atoms along the a-axis) are discerned at 302 cm^{-1}(Ag) [45]. An Ag line, attributed to V-O(3)-V angle-bending, emerges at 405 cm^{-1} [45]. Furthermore, the Ag mode at 528 cm^{-1} is ascribed to the vibrations associated with ladder-stretching V-O(2) bonds that connect the V_2O_5 chains. Lastly, the B_{1g}/B_{3g} vibrations at 700 cm^{-1} are attributed to the asymmetric stretching of V-O(2)-V bridges, delineating the "rails" of the ladders [30], [49]. Furthermore, the intensity of these Raman bands diminishes with an increase in the concentration of foreign cations.

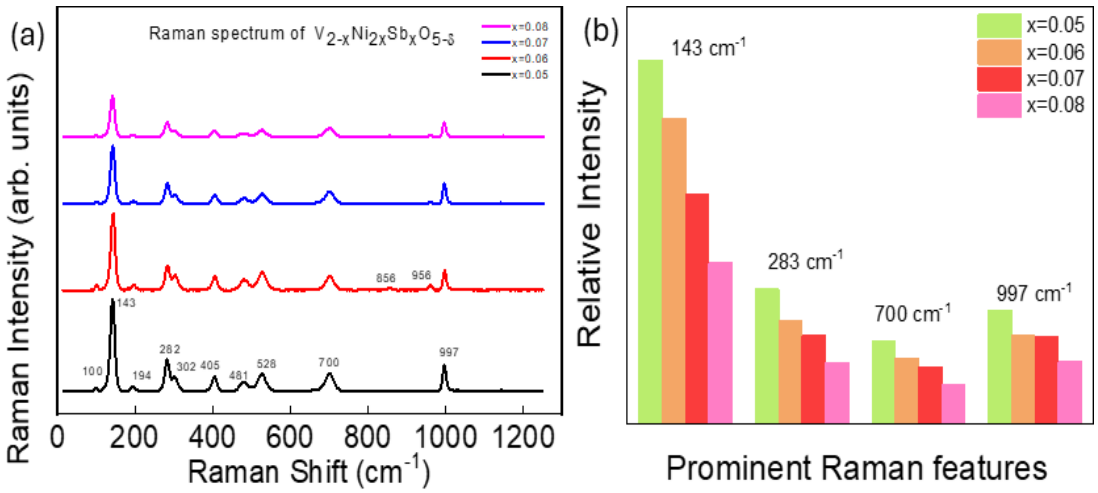

Fig 5.3: (a) Raman spectrum of $V_{2-x}Ni_{2x}Sb_xO_{5-\delta}$ (0.05<=x<=0.08) compounds (b) depicts the relative intensity of four prominent Raman bands at 143cm^{-1}, 283 cm^{-1}, 700 cm^{-1} and 997 cm^{-1} in $V_{2-x}Ni_{2x}Sb_xO_{5-\delta}$ $0.05 \leq x \leq 0.08$.

This decrease in intensity suggests a reduction in the stretching of V-O(2)-V bridges, consequently impeding the growth of the orthorhombic phase of V_2O_5, as corroborated by XRD analysis. The observed broad absorption band at 856 cm^{-1} is presumed to correspond to the less intense mode associated with the antisymmetric stretching vibrations of V-O(3)-V linkages within the x-z plane. Theoretical calculations estimate this mode at 848 cm^{-1} for pristine V_2O_5 [46]. Deviations from the predicted frequency (a blueshift) are attributable to doping the vanadium pentoxide lattice with antimony and nickel ions. The pronounced peak observed at 997 cm^{-1} corresponds to the Ag mode, elucidating the stretching vibration along the y-direction of the V-O(1) double bond, notably involving the terminal unshared O(1) atom. This conspicuous peak, situated in the higher wavenumber spectrum, underscores one of the most robust V-O(1) bonds present within the sample. However, the intensity of this peak exhibits an inverse relationship with the mole fraction x (see Fig 5.3(b)), indicative of a bond weakening trend with escalating concentrations of Nickel and Antimony, and is consistent with previous investigations on multi-cation-based vanadium pentoxide compounds [3]. Wang et al. [7] reported the decrease in the intensity of the Raman peaks upon the addition of Al dopant. Jung et al. [50] reported a decrease in the Raman intensity from V_2O_5 upon the insertion of Li into the $Li_xV_2O_5$ lattice owing to the formation of negative charge carriers by the reduction of V^{5+} to V^{4+}.

A blunt Raman band present at 956 cm^{-1}, not characteristic of the orthorhombic phase of V_2O_5, emulates the V^{4+}- O_1 vibrational stretch observed in both $Cr_{0.1}V_2O_5$ [47] and Cu-doped $V_2O_{5-\delta}$ [51]. This spectral signature indicates oxygen vacancies and corroborates the existence of V^{4+} species within the $V_{(1-x)2}Ni_{3x}O_{5-\delta}$ composition. Furthermore, it is noteworthy that the observable Raman spectrum of vanadates, such as $FeVO_4$ and $AlVO_4$, features a distinct Raman excitation at 954 cm^{-1}, referring to the symmetric stretching mode of the shortest V=O bond located at the VO_4 sites [52], [53]. This observation provides additional evidence supporting the presence of vanadates within the Sb-Ni-V-O ceramics, which aligns with the identification of the $SbVO_4$ tetragonal phase as determined from the Rietveld refinement analysis of the samples. A discernible blue shift is evident across all Raman bands of $V_{2-x}Ni_{2x}Sb_xO_{5-\delta}$ as the molar fraction x increases.

Table 5.4 Comparison of Raman active phonon modes (in Wavenumbers, cm^{-1}) obtained for pure V_2O_5, $V_{2-x}Bi_{2x}O_{5-\delta}$, $V_{(1-x)2}Ni_{3x}O_{5-\delta}$, $Cr_{0.1}V_2O_5$, and experimental Raman data of $V_{2-x}Ni_{2x}Sb_xO_{5-\delta}$ compounds

Mode	Single crystal of V_2O_5 [46]		$V_{2-x}Bi_{2x}O_{5-\delta}$ cm^{-1}[2]	$V_{(1-x)2}Ni_{3x}O_{5-\delta}$ x=0.04 cm^{-1}[1]	$Cr_{0.1}V_2O_5$ cm^{-1} [35]	Sb-Ni-V-O x=0.05
	Experimental cm^{-1}	Calculated cm^{-1}				
A_g	104	97	98	99	-	100
	304	315	304	302	303	302
	404	406	406	406	406	405
	480	489	480	476	483	481
	526	527	528	527	527	528
	994	1001	997	995	995	997
B_{1g}	146	149	143	142	143	143
	700	700	702	700	698	700
B_{2g}	200	191	196	193	196	194
	-	848	-	856	-	856
B_{3g}	280	297	283	283	282	282
	701	701	-	787	-	
Other				959	956	956

This shift signifies the incremental presence of foreign additives and a corresponding elevation in the proportion of associated phases, as elucidated in Table 5.4

5.3.4. Surface Analysis and Elemental Composition

Figure. 5.4(a-d) displays scanning electron microscope images of $V_{2-x}Ni_{2x}Sb_xO_{5-\delta}$ for $0.05 \leq x \leq 0.08$ compounds exhibiting a flake/plate-like architectural morphology. All SEM images were captured at a magnification of 2 μm for all molar fractions. The mean particle size decreases as the molar fraction increases from x=0.05 to 0.08. The assessment of irregular flake size distribution was investigated through histogram analysis employing the Image J software, revealing a Gaussian profile [31], [46]. The particle sizes fall within the micrometer scale, ranging from 0.58 μm, 0.47 μm,0.46 μm, and 0.45 μm for x = 0.05, 0.06, 0.07, and 0.08, respectively, as shown in Fig. 5.4(e-h). Fig. 5.4(i) displays the bar diagram showing the weight % of Antimony, Nickel, Vanadium, and Oxygen elements present in the compound $V_{2-x}Ni_{2x}Sb_xO_{5-\delta}$, as obtained from the EDX spectrum. Table 5.5 displays the weight % and atomic % of Antimony, Nickel, Vanadium, and Oxygen elements present in the compound $V_{2-x}Ni_{2x}Sb_xO_{5-\delta}$, as obtained from the EDAX spectrum. The bar diagram provides detailed insights into the elemental composition of the material, confirming the successful incorporation of Ni and Sb into the V_2O_5 matrix, and the measured values reflect the stoichiometric ratios intended during synthesis, which are critical for understanding the influence of NiO and Sb_2O_3 on the material's structural and electrical properties, correlating elemental content with NiV_2O_6 and $SbVO_4$ phase formation. The discrepancy between the crystallite size obtained from XRD and the particle size measured from a SEM histogram often occurs since XRD provides the crystallite size, which is the size of coherently diffracting domains within a particle. These crystallites are single, continuous regions of the same crystal structure. However, a single particle seen in SEM can be composed of multiple smaller crystallites, and SEM gives the physical dimensions of the entire particle, which can be larger than the crystallites measured by XRD, especially if the particle is made of multiple crystallites aggregated together [54].

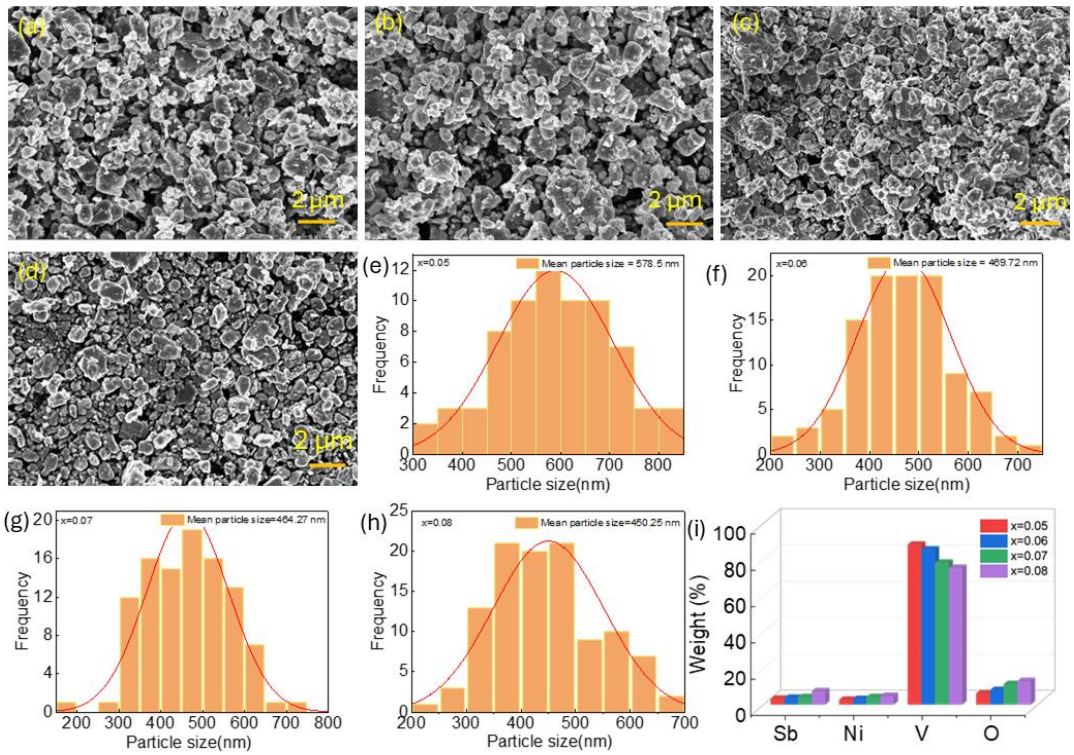

Figure.5.4: (a)–(d)) depicting the SEM micrographs of $V_{2-x}Ni_{2x}Sb_xO_{5-\delta}$ ceramics with x=0.05, 0.06, 0.07 & 0.08 in 2µm magnification. (e)-(h) indicating the histograms representing the average particle size of $V_{2-x}Ni_{2x}Sb_xO_{5-\delta}$ ceramics at x=0.05, 0.06, 0.07 & 0.08 respectively. (i) Displays the Weight% of Antimony, Nickel, Vanadium, and Oxygen elements present in the compound $V_{2-x}Ni_{2x}Sb_xO_{5-\delta}$, as obtained from the EDX spectrum.

Table. 5.5: Displays the Weight% and atomic% of Antimony, Nickel, Vanadium, and Oxygen elements present in the compound $V_{2-x}Ni_{2x}Sb_xO_{5-\delta}$, as obtained from the EDAX spectrum

X values	**0.05**		**0.06**		**0.07**		**0.08**	
Constituent Elements	***Weight %***	***Atomic %***	***Weight %***	***Atomic %***	***Weight%***	***Atomic%***	***Weight%***	***Atomic %***
Sb	3.18	1.19	3.67	1.40	4.01	1.30	07.25	02.85
Ni	2.60	2.06	2.97	2.31	4.05	2.37	04.65	03.57
V	88.08	80.18	85.43	78.01	78.08	67.19	75.21	62.41
O	6.14	16.57	7.93	18.28	11.18	29.14	12.89	31.17

The EDX spectrum and mapping of Sb-Ni-V-O microparticles are given in Figure. 5.5(a-f). Figure. 5.5(a) reveals the EDX spectrum with distinct peaks corresponding to V, O, Sb, and Ni, indicating the successful incorporation of these

elements into the compound. The absence of extraneous signals in the EDAX spectrum corroborates the chemical purity of the synthesized material. Figure 5.5 (f) displays the elemental mapping of the Sb-Ni-V-O-8 sample, while Figure 5.5 (b, c, d & e) illustrate the spatial distribution of oxygen, antimony, vanadium, and nickel, respectively. The elemental mapping data aligns well with the theoretical stoichiometric ratios, confirming the reliability of the EDX analysis for compositional validation in this study.

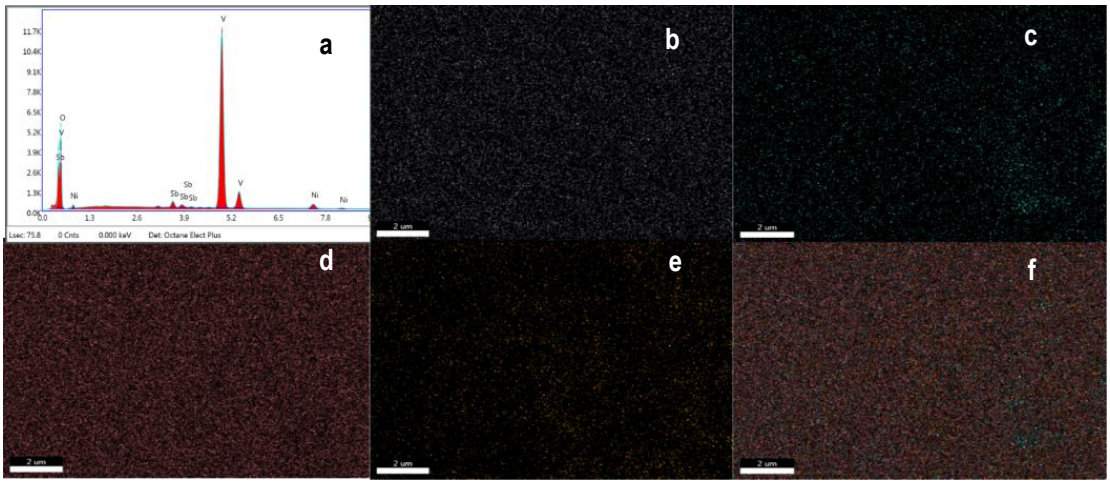

Fig.5.5(a) EDS spectrum of $V_{2-x}Ni_{2x}Sb_xO_{5-\delta}$ compounds for x=0.08, elemental mapping showing the presence of (b)Oxygen, (c)Antimony, (d)Vanadium, and (e)Nickel, and(f) Sb, Ni, V & O

5.3.5. X-ray photoelectron spectroscopy (XPS)

Figures 5.6, 5.7 & 5.8 present the high-resolution X-ray photoelectron spectra of $V_{2-x}Ni_{2x}Sb_xO_{5-\delta}$ compounds, with the molar concentration x varying from 0.05 to 0.08. The spectral peaks have been meticulously deconvoluted using CASA XPS software to analyze the valence stability and electronic states of the V*2p*, Sb*3d*, and Ni*2p* orbitals. Specifically, figure 5.6(a–d) displays the deconvoluted XPS spectra of the V*2p* orbitals, providing insights into the oxidation states and chemical environments of vanadium within the $V_{2-x}Ni_{2x}Sb_xO_{5-\delta}$ system ($0.05 \leq x \leq 0.08$). The V*2p* energy levels exhibit a distinct splitting into two components due to the spin-orbit coupling of the V $2p_{3/2}$ and V$2p_{1/2}$ states, with an energy separation constant ΔE =7.6 eV, aligning with the characteristic ΔE value observed for orthorhombic V_2O_5 structures[7]. This splitting reflects the intrinsic strength of electronic interactions and

the extent of orbital energy separation within the vanadium-based system. The area ratio of these two components remains fixed at 2:1 across all molar fractions (x), indicating a higher population of the V$2p_{3/2}$ level relative to the V$2p_{1/2}$ level. This consistent asymmetry is emblematic of the electronic configuration in many transition-metal systems and underscores the pronounced spin-orbit coupling characteristic of vanadium compounds [7].

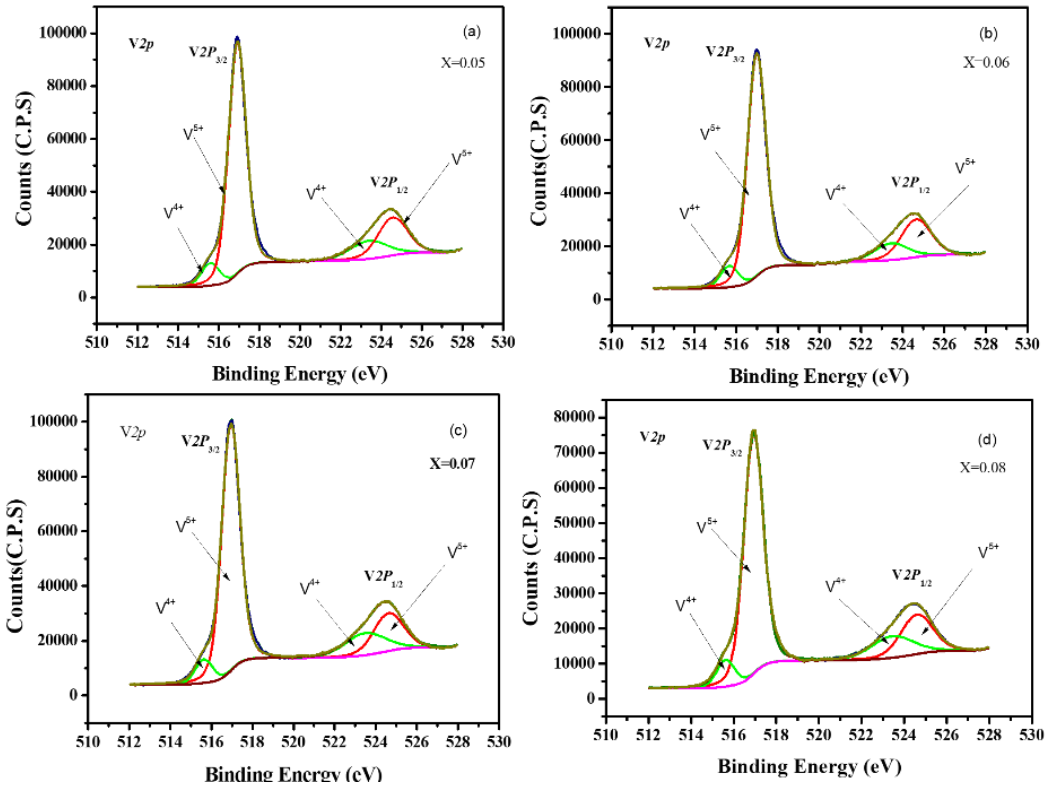

Figure 5.6(a-d): Curve fitting of the V2p XPS spectra of $V_{2-x}Ni_{2x}Sb_xO_{5-\delta}$ samples for x=(a)0.05, (b)0.06 (c)0.07 and (d)0.08 respectively

Peak analysis was performed using advanced deconvolution techniques to resolve the asymmetry in the peak profile of the V$2p_{3/2}$ spectral state. The dominant peak, positioned at a binding energy of 516.9 eV, was attributed to the V^{5+} oxidation state, whereas the peak corresponding to the V^{4+} oxidation state was observed at 516.1 eV. This finding underscores the minimal presence of the V^{4+} state across all molar fractions (x) in the sample. Additionally, a consistent binding energy shift of 0.8 eV between the V^{4+} and V^{5+} states was identified for all compositions, signifying the coexistence of both oxidation states within the material. The observed energy

separation highlights the subtle modifications in electronic configuration, reflecting the interplay between oxidation states and the material's electronic structure.

Figure 5.7(a–d) presents the spectral profiles corresponding to the Sb*3d* core levels in the $V_{2-x}Ni_{2x}Sb_xO_{5-\delta}$ samples ($0.05 \leq x \leq 0.080$). The spectra distinctly exhibit the characteristic peaks associated with the Sb*3d* core levels, which are further resolved into the Sb$3d_{3/2}$ and Sb $3d_{5/2}$ components as a result of spin-orbit coupling. This splitting is indicative of the inherent electronic structure and the spin-orbit interaction within the antimony species embedded in the material matrix [55].

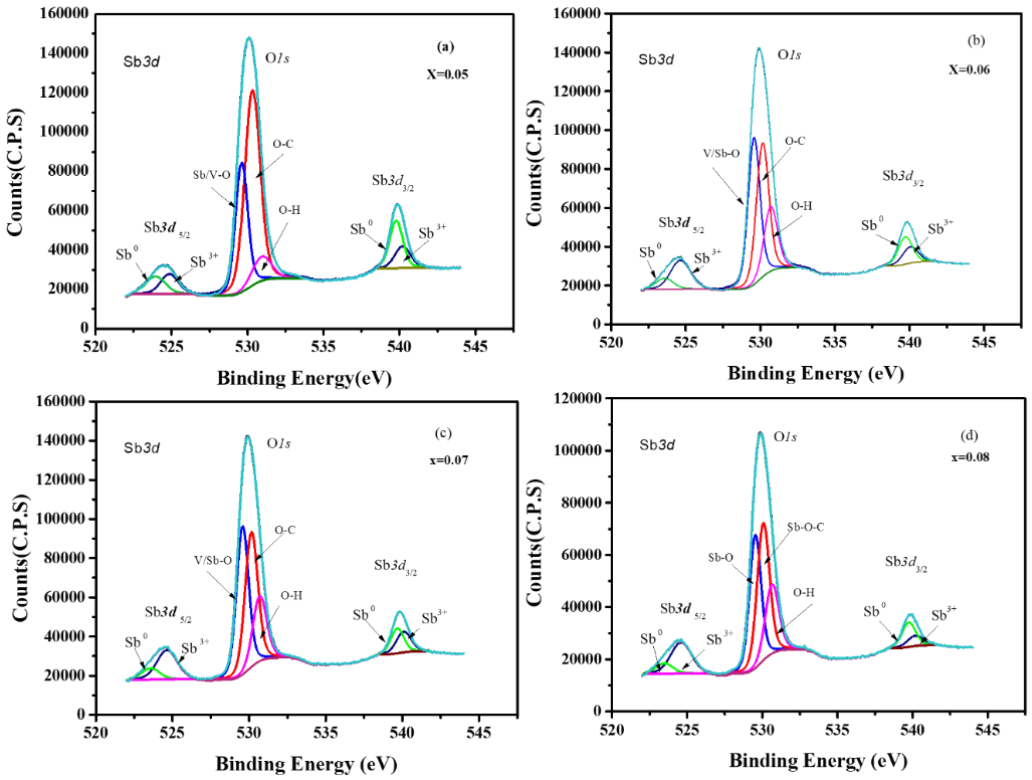

Figure 5.7(a-d): High-resolution XPS spectra of Sb3d, taking into account of the O1s for Shirley background determination (binding energy relative to the O1s level at 530.0 eV) in $V_{2-x}Ni_{2x}Sb_xO_{5-\delta}$ samples for x=(a)0.05, (b)0.06 (c)0.07 and (d)0.08 respectively

In the spectra, the Sb$3d_{5/2}$ peak is the more intense peak in the Sb *3d* doublet and hence would be the preferred peak for quantification purposes and chemical state identification. The Sb*3d* spectrum displays distinct peaks associated with Sb^0 metal atom and Sb^{3+}ion. The peaks observed at binding energies of 523.9 eV and 539.6 eV are attributed to the Sb $3d_{5/2}$ and Sb $3d_{3/2}$ states of Sb^{3+}, confirming the presence of

Sb_2O_3. Additionally, two peaks at 524.0 eV and 540.2 eV correspond to the $3d_{5/2}$ and $3d_{3/2}$ states of Sb^0, respectively, indicating the presence of metallic Sb [56], [57]. For instance, shifts in the binding energy can indicate changes in the oxidation state, while the relative intensities of the peaks can provide information about the local environment and coordination of the Sb atoms. The intensity of the O*1s* peak is sufficiently strong with a binding energy of 530.2 eV, placing it close to the Sb$3d_{5/2}$ level, as illustrated in Figure 5.7.

Prior research indicated that the O*1s* peak, frequently overlaps with the Sb$3d_{5/2}$ level [57], [58] . Here, there is a binding energy difference of 5eV, allowing for the deconvolution of the Sb$3d_{5/2}$ and O*1s* peaks separately. The proximity of the O*1s* peak to the Sb$3d_{3/2}$ level indicates a correlation or coupling between oxygen and antimony states, which may be an indication of chemical bonding or coordination in the antimony oxide structure. O*1s* core level peak has three different oxygen contributions located at 529.5 eV, 530.35 eV, and 531.56 eV. While the first component at 529.5 eV corresponds to oxygen ions associated with vanadium/antimony-oxygen bonds in V_2O_5, the peaks at 530.35eV and 531.56 eV are associated with surface oxygen defective sites and chemisorbed hydroxyl groups (OH), respectively [30], [57], [59]. In this study, the binding energies of Sb*3d* and O*1s* orbitals in the compounds exhibited a minor blue shift as the molar fraction x is increased, which is associated with the effects of foreign particle size, as noted in earlier studies.

Figure 5.8(a-d) illustrates the peak-fitted XPS spectrum of the Ni*2p* region, revealing two distinct spin-orbit split peaks corresponding to Ni$2p_{3/2}$ and Ni$2p_{1/2}$, positioned at binding energies of 855.5 eV and 873.1 eV, respectively. The presence of these primary peaks is corroborated by the appearance of two characteristic satellite peaks, observed at binding energies 5-7 eV higher than the principal peaks. These features are consistent across the $V_{2-x}Ni_{2x}Sb_xO_{5-\delta}$ samples for the composition range $0.05 \leq x \leq 0.08$ providing critical insights into the electronic structure and oxidation states of nickel within the system. The distinct doublet splitting observed in the Ni$2p_{3/2}$ and Ni$2p_{1/2}$ peaks indicates the coexistence of Ni^{2+} and Ni^{3+} ions within the Ni*2p* region. The binding energies associated with Ni^{3+} are centered at 856.8±0.1 eV and 873.6±0.01 eV, while those for Ni^{2+} are located at 855.5±0.01 eV and 872.7±0.01 eV, consistent across all molar fractions (x). Furthermore, the presence of satellite peaks confirms that Ni^{2+} is the predominant species in the system, aligning with previously

reported values in the literature [60], [61]. It is well established that the intensity of the peak at 856 eV increases due to defects arising from various surface treatments. Consequently, it is posited that the defect structure contributes to the specific final state represented by the peak at 856 eV, although it does not directly indicate Ni [62].

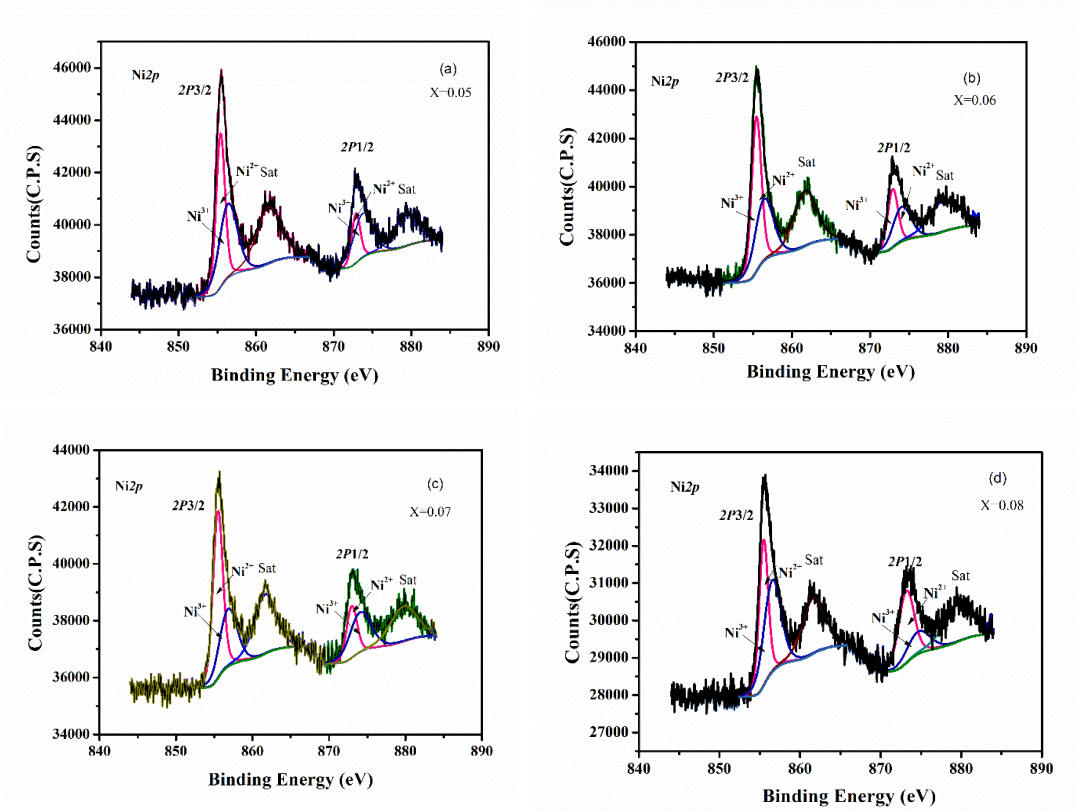

Figure 5.8(a-d): XPS spectra for the Ni 2p in $V_{2-x}Ni_{2x}Sb_xO_{5-\delta}$ samples for x=(a)0.05, (b)0.06, (c)0.07 and (d)0.08 respectively

5.3.6. Optical Studies: UV-Visible spectroscopy

The UV-Visible diffuse reflectance spectrum of the synthesized $V_{2-x}Ni_{2x}Sb_xO_{5-\delta}$ samples recorded for different mole concentrations x=0.05, 0.06, 0.07 & 0.08 is depicted in Figure 5.9(a). Upon analyzing the diffuse reflectance spectra, it is observed that there's an absorption onset around 500 nm, with a transition to higher reflectance occurring in the 700 nm range. A subtle decrease in the reflectance edge is observed as the mole concentration corresponding to Sb and Ni ions increases. This minor variation is caused by band gap restructuring, which influences the conducting behavior of the sample. The redshifts in the absorption onset with mol fraction indicate a decrease in the band gap energy of the specimen [63]. The Kubelka-Munk equation

was utilized to transform the reflectance data, and subsequently, the optical bandgap energy value was calculated [64]. The investigation reveals a decrease in the optical band gap (Eg) from 2.28 eV to 2.22 eV (Table. 5.1) as the mole concentration increases from x = 0.05 to 0.08 as in Figure 5.9(b). This intimates a straightforward optical transition, hinting at a surge in doping concentration, thereby instigating an augmentation in the surplus carrier concentration within the specimens. The rise in Sb^{3+} and Ni^{2+} ions is concurrent with an increase in V^{4+} or V^{5+} ions. The presence of V^{4+} ions, known for their absorption band centered at 770 nm, contributes to band gap narrowing [29].

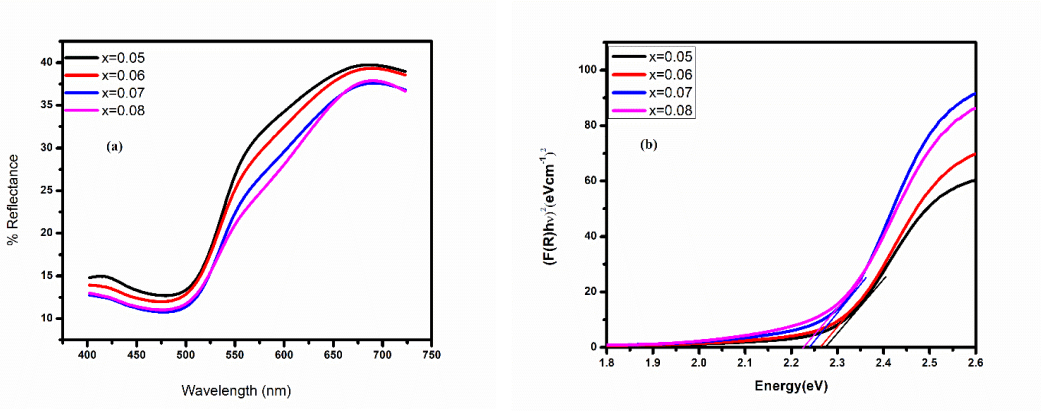

Figure. 5.9(a)Diffuse reflectance spectrum of $V_{2-x}Ni_{2x}Sb_xO_{5-\delta}$ samples recorded for different mole concentrations x=0.05, 0.06, 0.07 & 0.08 (b) KM plot showing optical band gap energy variations as a function of mole fraction

This phenomenon can likely be attributed to the inverse Burstein-Moss effect. Typically, the Burstein-Moss shift is recognized as a key factor in band gap widening in degenerate semiconductors doped with donor impurities. In the case of our complex compound, $V_{2-x}Ni_{2x}Sb_xO_{5-\delta}$, the substitution of divalent Ni ions and trivalent Sb ions for pentavalent vanadium ions induces electron vacancies in the Ni *3d*, Sb *5p*, and O *2p* bonding orbitals. As a result, holes become the predominant charge carriers within the material [1]. As the concentration of free carriers escalates, the widening of the bandgap is offset by a narrowing effect induced by the correlated movement of charge carriers and their scattering due to interactions with ionized impurities [2]. Thus, within Sb-Ni-V-O compounds, Ni^{2+} and Sb^{3+} ions serve as donor impurities, resulting in the occupation of hole states at the top of the valence band. This occupancy induces an expansion of the valence band and a corresponding reduction in the bandwidth.

The samples may have excellent optical behavior, according to this result. Thus, these materials find wide use in various optoelectronic and electrochemical devices [29].

5.3.7. Photoluminescence spectroscopy

Figure. 5.10(a-d) shows the room temperature PL spectra of $V_{2-x}Ni_{2x}Sb_xO_{5-\delta}$ compounds, recorded in the 400-600 nm range under an excitation wavelength of 330 nm. The photoluminescence (PL) properties of V_2O_5 are well-known for their high sensitivity to defects and imperfections within the material's structure [65]. In V_2O_5, photoluminescence encompasses both phosphorescence and fluorescence, which are directly influenced by the vibrational states of the V=O double bond. Upon illumination, the V=O bond facilitates an electron transfer from oxygen to vanadium ions, particularly on the surface, creating excited singlet and triplet states [66]. These excited states eventually recombine with ground-state holes, resulting in fluorescence and phosphorescence emissions. Photoluminescence spectroscopy was employed to investigate the $V_{2-x}Ni_{2x}Sb_xO_{5-\delta}$ compounds, focusing on the evaluation of bandgap energy, electron-hole recombination dynamics, and electron trapping phenomena induced by the incorporation of NiO and Sb_2O_3 into the V_2O_5 matrix [6].

In pristine V_2O_5, the conduction band (CB) is split into V*3d* sub-bands with energy gaps of approximately 0.6 eV and 0.75 eV, while the valence band (VB) is primarily composed of O*2p* orbitals [65]. The introduction of oxygen vacancies (V_{O_2}) in the V_2O_5 lattice creates defect states within the bandgap, acting as trapping sites for charge carriers and forming intermediate energy levels between the CB and VB [67]. These defect levels contribute to multiple recombination pathways involving the VB, CB, and defect states. The doping of Ni and Sb is expected to modify these band structures and recombination [23]. The PL emission spectrum of Sb-Ni-V-O compounds exhibits prominent bands in the blue-green region, including 417 nm, 425 nm, 435 nm, 450 nm, 467 nm, 481 nm, and 492 nm, along with broad green emissions at 541 nm and 564 nm. As per previous reports [68], the PL emission peaks located between 400 and 570 nm belong to an intrinsic transition, and the PL peaking occurs owing to the recombination of an electron-hole pair from the bottom of the V*3d* conduction band to the top of the O*2p* valence band [66], [69]. Specifically, the emissions between 417 nm and 492 nm are attributed to band-to-band transitions from

the shallow donor levels associated with vanadium interstitials to the valence band [70].

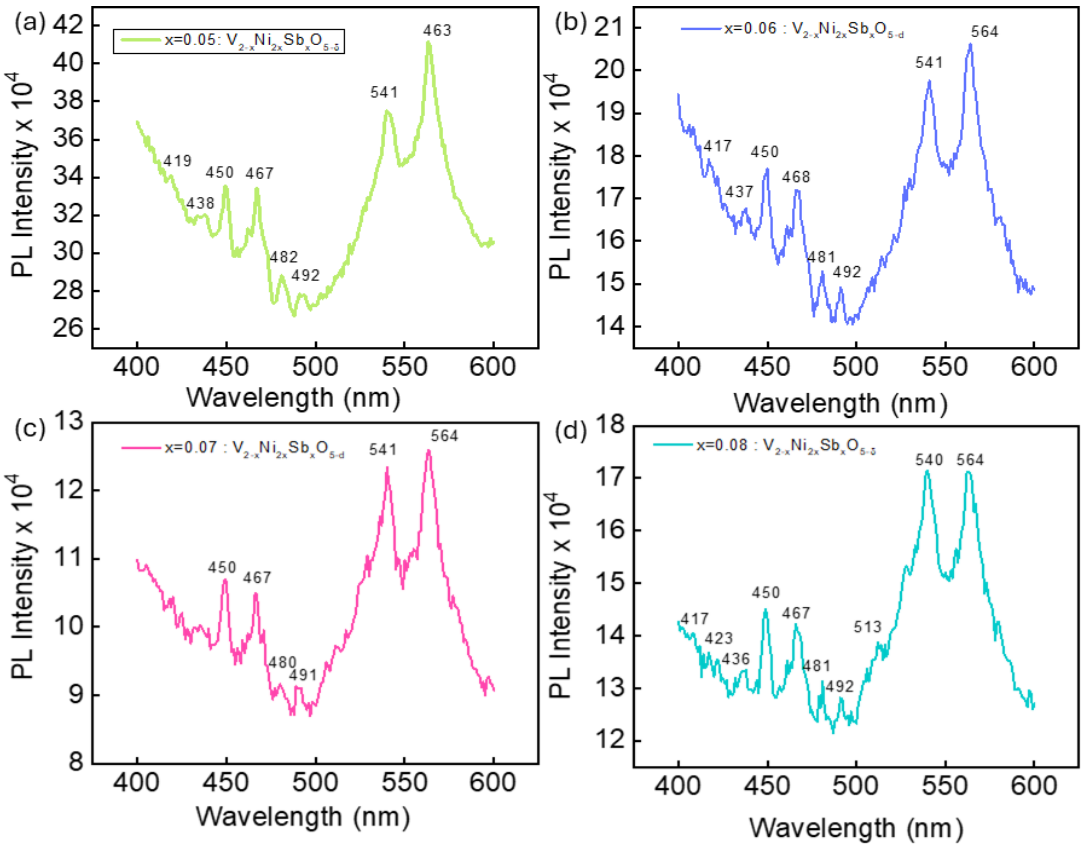

Figure.5.10: (a) Photoluminescence spectrum of $V_{2-x}Ni_{2x}Sb_xO_{5-\delta}$ compounds for (a)x=0.05 (b)x=0.06 (c)x=0.07 & (d)=0.08.

Incorporating Sb and Ni ions induces defect formation, which promotes splitting of these emission bands, yielding additional peaks with varying intensities. Strong PL emissions at 541 nm and 564 nm are ascribed to point defects, representing the radiative recombination of electron-hole pairs from the lowest split-off V*3d* conduction band to the O*2p* valence band top [69]. The PL peaks centered at 564 nm (2.20 eV) and 541 nm (2.29 eV) correspond to band-edge transitions in V_2O_5, aligning with the bandgap energy of 2.2–2.3 eV, as reported from Kubelka-Munk analysis of Sb-Ni-V-O compounds [25]. The slight shifts in the band-edge peak with increasing Sb and Ni concentration, represented by the increase in mol fraction x from 0.05 to 0.08, further confirm the presence of doping states in the V_2O_5 structure [65], [66].

AC Conductivity and Dielectric Studies

Figure 5.11(a & b) illustrates the variation of room temperature dielectric constant and dielectric loss factor (tanδ) with frequency for $V_{2-x}Ni_{2x}Sb_xO_{5-\delta}$ samples recorded for different mole concentrations x= 0.05, 0.06, 0.07 & 0.08. A clear dielectric dispersion is observed at lower frequencies, indicative of dipole relaxation [1],[13]. At lower frequencies, both the dielectric constant and loss exhibit high values, attributed to the sufficient time allowed for dipoles to align with the applied electric field and to the contribution of space-charge polarization at the electrode-electrolyte interface [71]. As frequency increases, the dielectric constant and loss factor decrease monotonically, eventually reaching a constant value. This transition is due to the diminishing space charge polarization and reduced ionic diffusion in the direction of the applied field, resulting in decreased contributions to the dielectric properties. This behavior confirms the non-Debye-type nature of the Sb-Ni-V-O samples [72]. At higher frequencies (f>1 KHz), the dielectric constant and dielectric loss remained relatively constant, suggesting that the dipoles are unable to rotate quickly enough to follow the alternating field [73], [71].

These findings align with the Maxwell-Wagner polarization model, which explains that such interfacial polarization contributes significantly at lower frequencies, particularly in polycrystalline materials, where grain boundaries act as barriers to charge carriers [13], [74]. Furthermore, the observed dielectric behavior could also be influenced by space charge polarization, which tends to dominate at lower frequencies, as seen in similar mixed metal oxide systems [1], [13], [75]. From Figure 5.11(a), it is evident that as the mole concentration of Sb and Ni increases from x=0.05 to x=0.06, the dielectric constant decreases from 32,359 to 6,335 at 10 Hz. However, with further increase in mole fraction, the dielectric constant rises to 18,316 for x=0.07 and 25,577 for x=0.08. The dielectric constant is greatly improved by the addition of Ni ions at x = 0.05, because of the increased concentration of charge carriers and electronic polarization. However, at x=0.06 the incorporation of Sb ions introduces structural distortions and reduces carrier density, hindering dipolar and interfacial polarization. This, combined with increased grain boundaries that scatter

charge carriers, leads to a substantial decrease in the dielectric constant [13]. As the concentration increases further to x = 0.07 and x = 0.08, the dielectric constant rises again due to stabilization of the lattice and possible formation of larger conductive grains. This reduces grain boundary resistance and enhances polarization [1], [15].

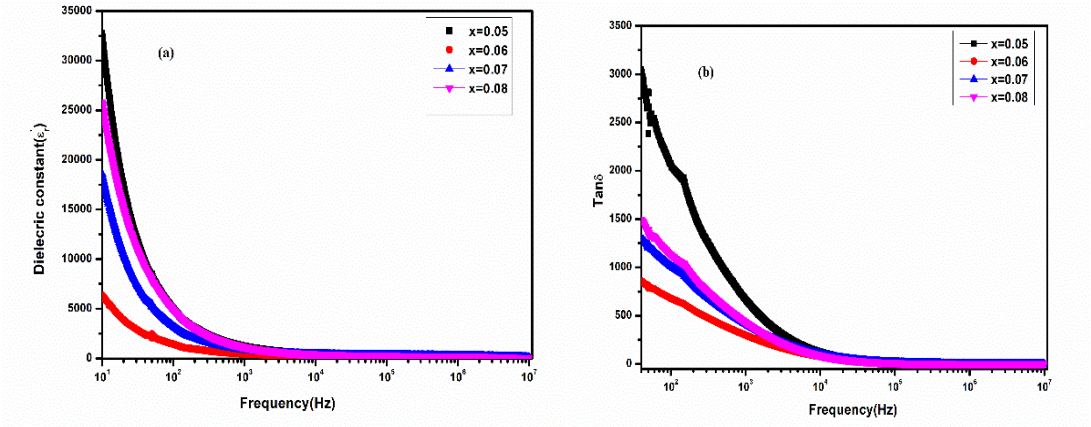

Figure 5.11 a) Variation of dielectric constant with frequency and b) Tangent loss vs frequency for $V_{2-x}Ni_{2x}Sb_xO_{5-\delta}$ samples recorded for different mole concentrations x=0.05, 0.06, 0.07 & 0.08

The tangent loss represents the ratio of the energy dissipated per radian in the material to the energy stored at the peak of polarization, providing insight into the underlying mechanisms of AC conduction and dielectric relaxation. This critical parameter serves as a gauge for understanding the energy losses and polarization dynamics in the system, offering valuable information on the material's dielectric properties and behavior [76]. A similar non-linear trend like the dielectric constant is observed in the tangent loss factor, as depicted in the figure. 5.11(b). At x = 0.05, the high tangent loss is primarily due to the significant polarization effects and enhanced charge carrier density introduced by Ni ions, which increase energy dissipation within the material. At x = 0.06, the incorporation of Sb ions introduces structural distortions and increased grain boundaries, reducing carrier mobility and hindering polarization mechanisms. This leads to lower energy dissipation and, consequently, a reduced tangent loss. With a further increase in mole concentration, the lattice becomes more stabilized, grain boundary resistance decreases, and larger conductive grains are likely to form. This enhances polarization efficiency, leading to greater energy dissipation and consequently a higher tangent loss. These observations highlight notable

modifications in the dielectric properties of Sb-Ni-V-O compounds, underscoring the importance of mole fraction on their electrical behavior [13], [15].

The AC conductivity of the as-prepared Sb-Ni-V-O samples was investigated as a function of frequency using the measured values of dielectric permittivity and tangent loss following Equation [1] at room temperature [13]. The results are presented in Figure. 5.12(a)

$$\sigma_{ac}(\omega) = \omega\, \varepsilon_0\, \varepsilon_r' tan\delta \quad (1)$$

Our analysis revealed that the AC conductivity of Sb-Ni-V-O compounds remains constant within the frequency range of 10 Hz to 1 MHz. Beyond this range, at higher frequencies, the conductivity increases linearly. This low-frequency independent behavior is characteristic of many semiconducting materials [11], [73], [77-78]. Furthermore, figure.5.12(a) demonstrates a non-linear variation in the AC conductivity values as the mole concentration of Sb and Ni is increased. As the mol concentration of Sb and Ni increases from x = 0.05 to 0.06, the AC conductivity initially increases and reaches a maximum value. However, further increments in the 'x' lead to decreased conductivity. This observed trend can be attributed to the competing influences of Ni and Sb ions on the material's conductivity. Our findings are consistent with previous reports on the conductivity variation with Ni concentration in V_2O_5, where conductivity increases with increasing Ni ion concentration [1]. In the present Sb-Ni-V-O compounds, the presence of Ni ions initially dominates the conductivity behavior, leading to the observed increase at lower concentrations. However, as the Sb concentration is further increased, its influence becomes more prominent, resulting in a decrease in conductivity [15]. This interplay between Sb and Ni ions effectively modifies the AC conductivity properties of Sb-Ni-V-O as their concentrations are varied. By adding nickel ions into the V_2O_5 lattice, Ni ions function as electron donors. This addition improves conductivity because it improves the availability of charge carriers, such as electrons or tiny polarons. Additionally, because of their smaller ionic radius than V^{5+}, which promotes improved charge carrier mobility, Ni ions tend to lessen lattice distortion. In contrast, Sb ions have a greater ionic radius than V^{5+}, which might cause lattice distortions and

interfere with the conducting routes in the V_2O_5 matrix. Furthermore, at higher concentrations, Sb ions may act as charge-carrier traps, reducing the mobility and total conductivity of the carriers. Thus, the observed non-linear fluctuations in electrical conductivity and dielectric properties were caused by the interaction between the distortion effects of Sb and the electron-donating behaviour of Ni [1], [15].

The variation of impedance (Z) with the frequency of Sb-Ni-V-O samples, presented in Figure 5.12(b), exhibits a consistent trend across various mole concentrations. The impedance of the prepared samples decreases significantly with increasing frequency, indicating a transition from predominantly ionic to electronic conductivity. At lower frequencies, Z values are significantly higher but decrease steadily as frequency increases, indicating an enhancement of AC conductivity. This trend is ascribed to the relaxation of space charge at higher frequencies [79]. As the frequency increases, trapped charges are released, reducing the overall impedance. At very high frequencies, the electronic component dominates, leading to the convergence of impedance curves. This understanding suggests that Sb-Ni-V-O materials could be particularly well-suited for applications involving alternating currents, such as capacitors or high-frequency components [13]. The frequency-dependent conductivity data, obtained experimentally for various mole fractions, were fitted using the Almond-West formalism to estimate the values of dc conductivity, hopping frequency and frequency exponent 'n' [80]. The Almond West formalism can be represented as

$$\sigma(w) = \sigma_{dc}\left[1 + \left(\frac{\omega}{\omega_H}\right)^n\right] \quad (2)$$

The fitting results, presented in Figure. 5.13 (a-d), demonstrate excellent agreement between the experimental data and the Almond-West model, with adj R-squared values ranging from 0.9963 to 0.9991 and Chi-squared values between 2.09E-11 and 6.54E-12. These findings confirm that the Almond-West formalism applies to all the investigated Sb-Ni-V-O compositions, providing valuable insights into the electrical properties of these materials [81]. The Almond fit analysis yields the crossover frequency values, which separate the dc and ac regions, for each mole fraction 'x'. As shown in Table 5.6, the AC conductivity at 10 MHz exhibits a

significant increase from 4.48×10^{-4} S/m to 7.78×10^{-4} S/m as x increases from 0.05 to 0.06. However, further increase in 'x' from 0.07 to 0.08 result in a decrease in to 6.94×10^{-4} S/m and 6.25×10^{-4} S/m, respectively. The DC conductivity exhibits a similar behavior, with values summarized in Table 5.6. The addition of Ni and Sb to the V_2O_5 lattice initially enhances the DC conductivity due to an increase in charge carrier concentration and improved electron hopping between adjacent vanadium sites. The dopants, substituting for vanadium, introduce localized states that facilitate the hopping of electrons between V^{4+} and V^{5+}, which is a key conduction mechanism in V_2O_5. This process increases the overall charge carrier mobility, leading to a higher conductivity as observed in the initial increase in σ_{dc} from 1.63×10^{-4} to 2.79×10^{-4} S/m on increasing x from 0.05 to 0.06. However, as the concentration of Ni and Sb is further increased, the lattice becomes increasingly disrupted, leading to the formation of defects such as oxygen vacancies and lattice strain. These defects can trap charge carriers and scatter the hopping electrons, effectively reducing the mobility of the charge carriers and, consequently, the DC conductivity.

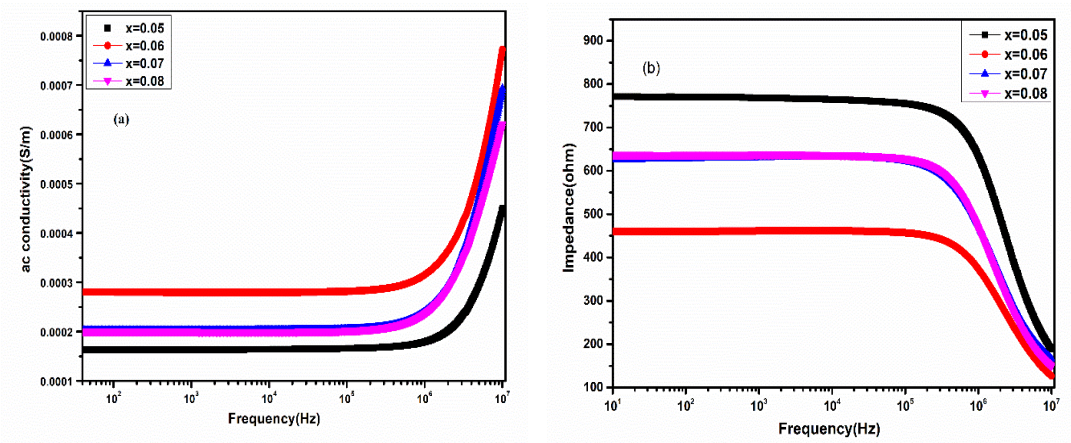

Figure.5.12 (a)Variation of AC conductivity with frequency (b)Variation of impedance with frequency for $V_{2-x}Ni_{2x}Sb_xO_{5-\delta}$ samples recorded for different mole concentrations x=0.05, 0.06, 0.07 & 0.08

This results in a decrease in σ_{dc} to 2×10^{-4} S/m at higher dopant concentration x= 0.08, as the negative effects of increased doping and disorder outweigh the benefits of enhanced electron hopping [1], [15], [81]. These findings provide valuable insights into the optimization of Sb-Ni-V-O compositions for specific applications, highlighting the importance of careful control over the mole fraction to achieve desired electrical properties.

Table 5.6. Almond West fitted parameters of $V_{2-x}Ni_{2x}Sb_xO_{5-\delta}$ samples recorded for different mole concentrations a) x=0.05 b) x=0.06 c) x=0.07 d) x=0.08

x	σ_{dc}(S/m)	ω_H (Hz)	n	Chi^2	Adj R^2
0.05	1.63x10^{-04}	6.13x10^6	1.219	1.92x10^{-12}	0.999
0.06	2.79 x10^{-04}	5.78 x10^6	1.103	6.54 x10^{-12}	0.999
0.07	2.01 x10^{-04}	3.96 x10^6	1.041	2.15 x10^{-11}	0.997
0.08	2.00 x10^{-04}	4.42 x10^6	1.004	2.09 x10^{-11}	0.996

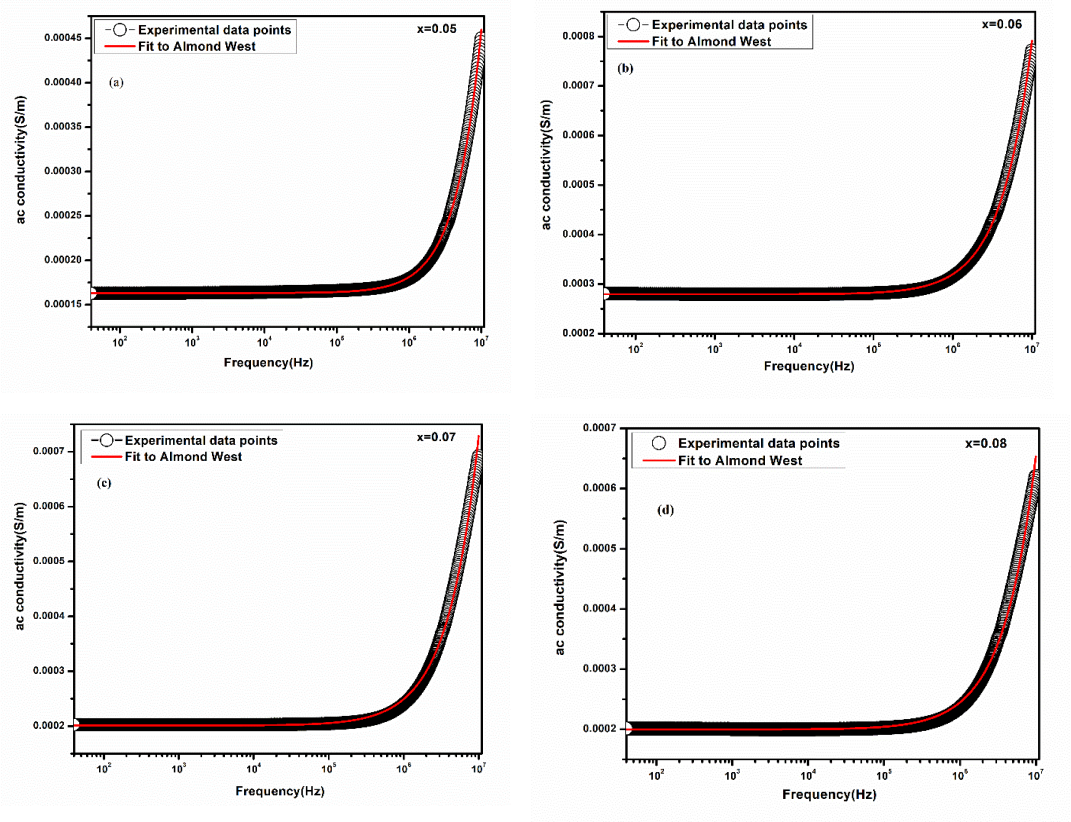

Figure 5.13(a-d). Almond west curve fitting for AC conductivity vs frequency for $V_{2-x}Ni_{2x}Sb_xO_{5-\delta}$ samples recorded for different mole concentrations a) x=0.05 b) x=0.06 c) x=0.07 d)x=0.08

5.3.9. Anti-Microbial Studies

In this section, we explore the antimicrobial efficacy of $V_{2-x}Ni_{2x}Sb_xO_{5-\delta}$ compounds against a spectrum of microbial organisms, including the fungi *Penicillium* and *Aspergillus niger*, as well as gram-positive bacteria (*Staphylococcus aureus* and *Bacillus cereus*) and gram-negative bacteria (*Escherichia coli* and

Pseudomonas aeruginosa). The $V_{2-x}Ni_{2x}Sb_xO_{5-\delta}$ ($0.05 \leq x \leq 0.08$) compounds exhibit potent broad-spectrum antimicrobial efficacy against both fungal and bacterial strains. Dispersed in dimethyl sulfoxide (DMSO) and assessed via the disc diffusion assay, the synthesized compounds exhibited substantial antifungal activity, yielding inhibition zones of 25 mm against *Aspergillus niger* and 19 mm against *Penicillium* spp. Antibacterial efficacy was evaluated using the well diffusion method, demonstrating inhibition zones of 18 mm for *Staphylococcus aureus*, 15 mm for *Escherichia coli*, and 20 mm for *Pseudomonas aeruginosa* at a concentration of 200µl. However, gram-positive aerobic bacteria, Bacillus cereus (6 mm), exhibited marked resistance. Figure.5.14(a-f) displays the representative photographs of zone of growth inhibition by $V_{2-x}Ni_{2x}Sb_xO_{5-\delta}$ compounds against bacteria and fungi with (a) *Pencillium* (150 & 200 µl) (b)*Aspergillus Niger*:(150 & 200 µl), (c) *E-Coli* (50 and 100 µl) (d) *S. Aureus* (100 µl) (e) *E. coli* (200 µl) (f*) P. aeruginosa*(200 µl). Figure.5.15 presents the bar diagram comparing the zone of inhibition of $V_{2-x}Ni_{2x}Sb_xO_{5-\delta}$ compounds (0.05<=x<=0.08) against the growth of gram-positive and gram-negative bacteria and fungi for 200 µl concentration. From the bar diagram, it is evident that as the mol fraction 'x' increases, the zone inhibition against bacteria and fungi increases with an increase in Sb and Ni ion concentration. Table.5.7 inpresents the zone inhibition values (in mm) and minimum inhibitory concentration(mic) values of gram-positive bacteria, gram-negative bacteria, and fungi for $V_{2-x}Ni_{2x}Sb_xO_{5-\delta}$ compound systems for x=0.08 at 50, 100, 150, & 200 µl concentration

The antimicrobial activity stems from a combination of oxidative stress, membrane disruption, enzyme inhibition, and structural damage mechanisms, which are effective against both fungal and bacterial cells [26-27]. The antimicrobial mechanism of $V_{2-x}Ni_{2x}Sb_xO_{5-\delta}$ compounds against fungi, gram-negative and gram-positive bacteria is likely multifaceted, involving several biochemical and cellular disruptions. All these microbes have distinct structural and metabolic characteristics that are targeted by the Ni and Sb incorporated V_2O_5 compound. The primary antifungal mechanism of action involves the generation of reactive oxygen species, such as superoxide anions (O_2^-), hydroxyl radicals (OH•), and hydrogen peroxide (H_2O_2), upon interaction with the microbial cells [20].

Table.5.7 presents the zone inhibition values (in mm) and mic values of gram positive bacteria, gram negative bacteria and fungi for $V_{2-x}Ni_{2x}Sb_xO_{5-\delta}$ for x=0.08 compound systems for 50, 100, 150 & 200 µl concentration

SI. No	Name of Bacteria/Fungus	50µl	100 µl	150 µl	200 µl	+ve	-ve
1.	*Escherichia coli*	R	12	12	15	23	7
2.	*Staphylococus aureus*	12	15	16	18	30	10
3.	*Pseudomonas aeroginosa*	R	16	18	20	22	7
4.	*Bacillus cereus*	R	R	R	R	21	7
5.	*Pencillium*	R	R	R	19	22	7
6.	*Aspergillus niger*	R	R	12	25	23	10

V_2O_5 is known for its redox activity, which facilitates electron transfer, promoting ROS generation [82]. When doped with Ni and Sb, this redox cycling of V_2O_5 is enhanced, leading to an increased production of ROS. *Aspergillus niger, Penicillium, Staphylococcus aureus, Escherichia coli,* and *Pseudomonas aeruginosa* are sensitive to oxidative stress, and the excess ROS damages their cellular components, including lipids, proteins, and nucleic acids [26],[67-68]. This results in membrane disruption, mitochondrial dysfunction, and eventual cell death. Despite *Pseudomonas Aeruginosa's* lower outer-membrane permeability due to the absence of nonspecific porins, which typically makes it more resistant to hydrophilic antimicrobial agents [83], our results demonstrated a significant inhibition zone of 20 mm at a 200 µL concentration. This suggests that the Sb-Ni-V-O-8 compound effectively penetrates the outer membrane, overcoming *P.aeruginosa's* defense mechanisms. The large inhibition zone of 20 mm observed indicates the bacterium's heightened susceptibility, likely due to its thin peptidoglycan layer and lipid-rich outer membrane, which may facilitate the compound's action at the tested concentration. In addition, the cell membranes of fungi are composed mainly of ergosterol and phospholipids, which are crucial for maintaining cell integrity and regulating permeability [84]. Ni^{2+}, Ni^{3+}, and Sb^{3+}, along with V^{5+} and V^{4+} ions in the compound matrix, may interact with the fungal membrane, thereby destabilizing its structure [85]. These metal ions can bind to negatively charged components of the cell membrane, leading to increased membrane permeability. Nickel ions destabilize

bacterial cell membranes by interacting with negatively charged phospholipids, increasing permeability, and causing leakage of intracellular content.

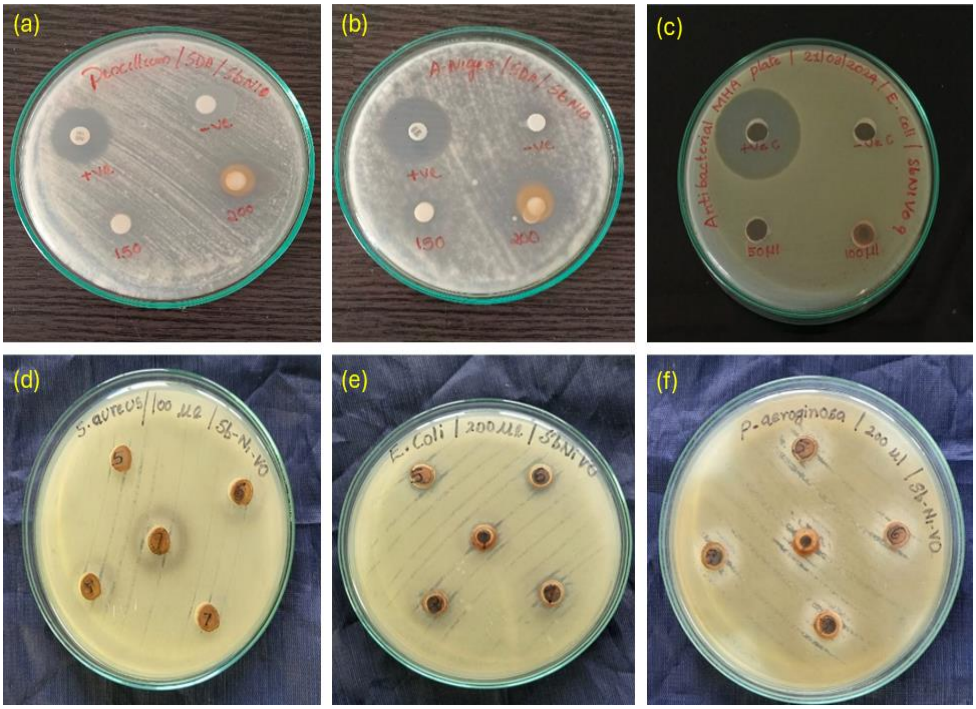

Figure. 5.14 Representative photographs of zone of growth inhibition by $V_{2-x}Ni_{2x}Sb_xO_{5-\delta}$ compounds against bacteria and fungi:(a) Pencillium(150 & 200 µl) (b)Aspergillus Niger:(150 & 200 µl), (c) E-Coli (50 and 100 µl) (d) S. Aureus(100 µl) (e) E. Coli(200 µl) (f) P. aeruginosa(200 µl).

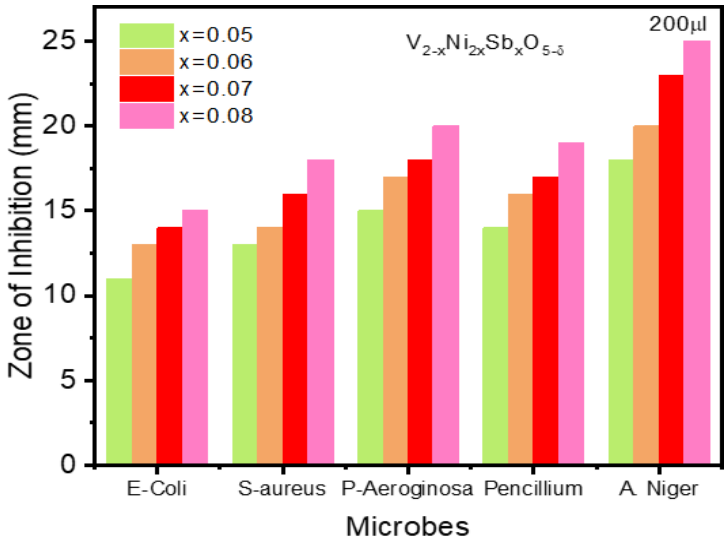

Figure. 5.15: Bar diagram comparing the zone of inhibition of $V_{2-x}Ni_{2x}Sb_xO_{5-\delta}$ compounds (0.05<=x<=0.08), against the growth of the gram positive-gram negative bacteria and fungi for 200µl concentration.

This effect is more pronounced in Gram-negative bacteria, such as *E. coli* and *Pseudomonas aeruginosa*, which have thinner cell walls and an outer membrane that is more easily disrupted [86]. Additionally, vanadium, nickel, and antimony ions can interfere with the enzymatic machinery of microbes. The doped vanadium pentoxide compounds inhibit several key metabolic enzymes, particularly those involved in energy production and macromolecule synthesis. Nickel ions are known to interfere with the function of metalloenzymes by replacing essential metal cofactors, such as magnesium or iron, which are critical for enzyme activity [86-87]. Antimony ions can disrupt protein folding by interacting with thiol groups, thus inactivating enzymes [88]. This interference is particularly effective against *Penicillium, Aspergillus niger* and bacteria, which have complex metabolic pathways that rely on enzymatic activities for cellular growth and spore germination.

ROS generated by $V_{2-x}Ni_{2x}Sb_xO_{5-\delta}$ can also lead to oxidative damage to fungal DNA and RNA. In *Aspergillus niger* and *Penicillium*, which have high replication and transcription rates, oxidative damage to nucleic acids results in breaking of DNA strands, impairing replication and inducing apoptosis in fungal cells [21], [26]. This also causes RNA oxidation, which disrupts protein synthesis by damaging mRNA and ribosomal RNA, preventing the proper translation of essential proteins. This ultimately halts fungal growth and leads to cell death. ROS can also cause oxidative damage to bacterial DNA and RNA, inhibiting cell division and protein synthesis. This damage is particularly detrimental to rapidly dividing bacteria like *Staphylococcus aureus and E. coli* [21]. Iran Sheikhshoaie et al. [90] reported the prospects of vanadium complexes impairing the formation of biofilms of some bacteria, which are critical for microbial survival and resistance. Ni and Sb incorporated V_2O_5 could interfere with the production of extracellular polymeric substances that form the structural basis of biofilms, leading to weakened biofilm formation. By disrupting biofilms, Sb-Ni-V-O compounds would make bacterial cells more susceptible to conventional antibiotics, potentially improving the efficacy of combination therapies.

5.4. Conclusion

In conclusion, we have successfully synthesized multi-cation complex metal oxides of $V_{2-x}Ni_{2x}Sb_xO_{5-\delta}$ for $0.05 \leq x \leq 0.08$, as evidenced by X-ray diffractogram

patterns displaying the standard orthorhombic alpha polymorphic phase of Vanadium Pentoxide along with two low-intensity extra peaks corresponding to Ni and Sb phases. Lattice parameters, crystallite size, microstrain, and dislocation density were estimated, showing a decrease in crystallite size with increasing Ni and Sb dopants due to enhanced defect formation. These defects inhibit grain growth, while secondary phases like NiV_2O_6 and $SbVO_4$ relieve strain, reducing microstrain from 0.190×10^{-3} to 0.026×10^{-3}. Additionally, cell volume is increased from 172 Å³ to 177 Å³ due to lattice expansion. Rietveld refinement analysis of the X-ray diffractogram data confirmed the coexistence of three phases: the prominent V_2O_5 phase with an orthorhombic structure, the NiV_2O_6 monoclinic, and the tetragonal $SbVO_4$ structures. Histogram analysis of SEM images using Image J revealed a Gaussian distribution of particle sizes, ranging from 0.58 μm to 0.45 μm for increasing molar concentration 'x'.

Raman spectroscopy identified 11 vibrational modes characteristic of the α-polymorphic phase of orthorhombic V_2O_5, alongside a blunt Raman band at 956 cm^{-1}, indicative of oxygen vacancies and V^{4+} species within the $V_{2-x}Ni_{2x}Sb_xO_{5-\delta}$ composition, corroborating the presence of vanadates and confirming the identification of the $SbVO_4$ tetragonal phase through Rietveld refinement analysis. XPS analysis of $V_{2-x}Ni_{2x}Sb_xO_{5-\delta}$ compounds confirms the dominant oxidation states of vanadium (+5), antimony (+3), and nickel (+2). Deconvolution of the spectra, necessitated by peak asymmetry, reveals minor contributions from V^{4+}, metallic Sb, and Ni^{3+} ions. The O*1s* core level spectrum shows three distinct peaks, attributed to oxygen atoms in vanadium/antimony-oxygen bonds, oxygen vacancies at surface defect sites, and chemisorbed hydroxyl groups, respectively. The presence of satellite peaks in the Ni*2p* spectrum suggests valence fluctuations in Nickel. Analysis of diffuse reflectance spectra from UV-visible spectroscopy indicated a subtle decrease in reflectance edge with increasing mole concentration of Sb and Ni ions, accompanied by a redshift in absorption onset, indicative of a decrease in band gap energy from 2.28 eV to 2.22 eV, as mole concentration increased from x = 0.05 to 0.08. The PL emission spectrum of Sb-Ni-V-O compounds shows blue-green emissions between 417 nm and 492 nm due to band-to-band transitions, while strong

green emissions at 541 nm and 564 nm are linked to point defects and radiative recombination. Shifts in the band-edge peaks with increasing Sb and Ni concentrations confirm doping states in the V_2O_5 structure The dielectric properties of the compounds were found to be significantly influenced by their mole fraction. The dielectric dispersion at lower frequencies and constant behavior at higher frequencies align with the Maxwell-Wagner polarization model. The non-monotonic dependence of the dielectric constant on Sb and Ni concentration suggests a complex interplay between dipole relaxation and space charge polarization. The tangent loss factor mirrored this trend, highlighting the dependence of energy dissipation and polarization dynamics on mole fraction.

Furthermore, the AC conductivity of $V_{2-x}Ni_{2x}Sb_xO_{5-\delta}$ compounds exhibited a non-linear dependence on mole fraction, with an initial increase followed by a decrease. This behavior suggests a competing influence between Sb and Ni ions on the conductivity. Impedance analysis revealed a transition from ionic to electronic conductivity with increasing frequency, suggesting the potential suitability of these materials for applications involving alternating currents. The Almond-West formalism effectively described the observed conductivity behavior, providing valuable insights into the electrical properties and their dependence on mole fraction. The $V_{2-x}Ni_{2x}Sb_xO_{5-\delta}$ compounds exhibit broad-spectrum antimicrobial activity, effectively inhibiting fungal strains such as *Aspergillus niger*, *Penicillium*, and bacterial pathogens including *E. Coli*, *Staphylococcus aureus* and *Pseudomonas aeruginosa*. The antimicrobial efficacy arises from oxidative stress, membrane disruption, and enzyme inhibition mechanisms. Additionally, the possibility of disruption of biofilm formation enhances bacterial susceptibility to antibiotics, suggesting that these Sb-Ni-V-O compounds hold potential for advanced antimicrobial and biofilm-targeted therapeutic applications.

References

[1] M. Sabna and P. Jayaram, "Reformed dielectric features in single-phase orthorhombic nickel vanadate complex oxides and the significance of the lattice dynamics in the optoelectrical features," *J. Phys. Chem. Solids*, vol. 180, p. 111428, Sept. 2023, doi: 10.1016/j.jpcs.2023.111428.

[2] K. Safna, P. Jayaram, M. Sabna, P. Prasannan, J. Mayandi, and P. P. Pradyumnan, "Microstructure profiling, lattice dynamics, and morphological studies on multi-excitonic vanadium bismuth oxide compound systems," *J. Aust. Ceram. Soc.*, vol. 58, no. 4, pp. 1129–1136, Sept. 2022, doi: 10.1007/s41779-022-00766-7.

[3] T. K. Le *et al.*, "Recent advances in vanadium pentoxide (V_2O_5) towards related applications in chromogenics and beyond: fundamentals, progress, and perspectives," *J. Mater. Chem. C*, vol. 10, no. 11, pp. 4019–4071, 2022, doi: 10.1039/D1TC04872D.

[4] D. Tadeu Cestarolli and E. Maria Guerra, "Vanadium Pentoxide (V_2O_5): Their Obtaining Methods and Wide Applications," in *Transition Metal Compounds - Synthesis, Properties, and Application*, S. Haider and A. Haider, Eds., IntechOpen, 2021. doi: 10.5772/intechopen.96860.

[5] V. Uma Shankar, D. Govindarajan, P. Christuraj, M. J. Salethraj, F. J. Johanson, and M. D. Raja, "Enhanced the electrochemical properties of Ni doped V2O5 as a electrode material for supercapacitor applications," *Mater. Today Proc.*, vol. 50, pp. 2675–2678, 2022, doi: 10.1016/j.matpr.2020.08.213.

[6] Department of Physics, Kongunadu Arts and Science College, Coimbatore641029 Tamil Nadu, India *et al.*, "Characterization of pure and Cu doped V2O5 nanostructures and their Cu:V2O5/p-Si photodiode applications," *Dig. J. Nanomater. Biostructures*, vol. 18, no. 1, pp. 131–143, Jan. 2023, doi: 10.15251/DJNB.2023.181.131.

[7] C.-C. Wang, C.-L. Lu, F.-S. Shieu, and H. C. Shih, "Structure and Photoluminescence Properties of Thermally Synthesized V2O5 and Al-Doped V2O5 Nanostructures," *Materials*, vol. 14, no. 2, p. 359, Jan. 2021, doi: 10.3390/ma14020359.

[8] S. Sharma, Prashant, and N. Kondal, "Recent advancement in doped vanadium pentoxide for energy storage devices," *Mater. Today Proc.*, p. S2214785323007204, Mar. 2023, doi: 10.1016/j.matpr.2023.02.181.

[9] H. Yu *et al.*, "Cu doped V2O5 flowers as cathode material for high-performance lithium ion batteries," *Nanoscale*, vol. 5, no. 11, p. 4937, 2013, doi: 10.1039/c3nr00548h.

[10] S. Khan and K. Singh, "Structural, optical, thermal and conducting properties of V2−xLixO5−δ ($0.15 \leq x \leq 0.30$) systems," *Sci. Rep.*, vol. 10, no. 1, p. 1089, Jan. 2020, doi: 10.1038/s41598-020-57836-8.

[11] S. Khan and K. Singh, "Effect of MgO on structural, thermal and conducting properties of V2-Mg O5- (x = 0.05–0.30) systems," *Ceram. Int.*, vol. 45, no. 1, pp. 695–701, Jan. 2019, doi: 10.1016/j.ceramint.2018.09.231.

[12] F. K. Tan, J. Hassan, Z. Abd. Wahab, and R. S. Azis, "Electrical conductivity and dielectric studies of MnO 2 doped V 2 O 5," *Results Phys.*, vol. 6, pp. 420–427, 2016, doi: 10.1016/j.rinp.2016.07.011.

[13] S. K, J. Peediyekkal, S. M, S. S, and M. Chennabasappa, "Rietveld refinement, core level electron shell structure and frequency-dependent dielectric behavior of vanadium bismuth oxide microstructures," *Phys. B Condens. Matter*, vol. 691, p. 416318, Oct. 2024, doi: 10.1016/j.physb.2024.416318.

[14] M. Sabna, K. Safna, S. C P, and P. Jayaram, "Surface-Modified Mesoporous V_{2-x} Sb_{2x} $O_{5-\delta}$ Ceramics for Improving the Electrostatic Chemisorption of Methylene Blue," *ChemistrySelect*, vol. 9, no. 29, p. e202400862, Aug. 2024, doi: 10.1002/slct.202400862.

[15] M. Sabna, P. Jayaram, K. Safna, Riyas. K. M, Sona. C. P, and S. Sreedevi, "Crystallographic Profiling, Core-Shell Electronic Configurations, and Investigations of Frequency-Dependent Dielectric Characteristics of Sb2O3-V2O5 Micro Ceramics," *Mater. Chem. Phys.*, p. 130172, Nov. 2024, doi: 10.1016/j.matchemphys.2024.130172.

[16] P. R. P. Suma, R. V. Nair, W. Paul, and R. S. Jayasree, "Vanadium pentoxide nanoplates: Synthesis, characterization and unveiling the intrinsic anti-bacterial activity," *Mater. Lett.*, vol. 269, p. 127673, June 2020, doi: 10.1016/j.matlet.2020.127673.

[17] C. Sridhar, N. Gunvanthrao Yernale, and M. V. N. A. Prasad, "Synthesis, Spectral Characterization, and Antibacterial and Antifungal Studies of PANI/V_2O_5 Nanocomposites," *Int. J. Chem. Eng.*, vol. 2016, pp. 1–6, 2016, doi: 10.1155/2016/3479248.

[18] P. S. Sundara Selvam, G. S. Chinnadurai, D. Ganesan, and V. Kandan, "Eggshell membrane-mediated V2O5/ZnO nanocomposite: synthesis, characterization, antibacterial activity, minimum inhibitory concentration, and its mechanism," *Appl. Phys. A*, vol. 126, no. 11, p. 893, Nov. 2020, doi: 10.1007/s00339-020-04076-2.

[19] Y. S. Kim, M. Y. Song, E. S. Park, S. Chin, G.-N. Bae, and J. Jurng, "Visible-Light-Induced Bactericidal Activity of Vanadium-Pentoxide (V2O5)-Loaded TiO2 Nanoparticles," *Appl. Biochem. Biotechnol.*, vol. 168, no. 5, pp. 1143–1152, Nov. 2012, doi: 10.1007/s12010-012-9847-9.

[20] N. N. Ilkhechi, M. Mozammel, and A. Y. Khoroushahi, "Antifungal effects of ZnO, TiO2 and ZnO-TiO2 nanocomposite on Aspergillus flavus," Dec. 10, 2020. doi: 10.21203/rs.3.rs-123795/v1.

[21] A. H. Hashem *et al.*, "Antifungal Activity of Biosynthesized Silver Nanoparticles (AgNPs) against Aspergilli Causing Aspergillosis: Ultrastructure Study," *J. Funct. Biomater.*, vol. 13, no. 4, p. 242, Nov. 2022, doi: 10.3390/jfb13040242.

[22] M. Paulsson *et al.*, "Peptidoglycan-Binding Anchor Is a Pseudomonas aeruginosa OmpA Family Lipoprotein With Importance for Outer Membrane Vesicles, Biofilms, and the Periplasmic Shape," *Front. Microbiol.*, vol. 12, p. 639582, Feb. 2021, doi: 10.3389/fmicb.2021.639582.

[23] M. Sabna, K. Safna, J. Mayandi, S. Zh. Karazhanov, and P. Jayaram, "Microstructure profiling and photoluminescence characteristics of V(1-x)2 Ni3xO5-δ compound systems," *Mater. Lett.*, vol. 266, p. 127507, May 2020, doi: 10.1016/j.matlet.2020.127507.

[24] M. Sabna, P. Jayaram, K. R. Aneesa, and K. M. M. Rahiman, "Investigations on the Antimicrobial Activity of V2–xSb2xO5–δ Compound Systems Against the Gram-Positive, Gram-Negative Bacteria, Penicillium, and Aspergillus niger Fungi," *J. Appl. Spectrosc.*, July 2025, doi: 10.1007/s10812-025-01958-2.

[25] M. Sabna, P. Jayaram, K. Safna, S. Sreedevi, and F. S, "Correlating structural and electronic properties with energy dissipation, polarization dynamics, and dielectric responses in V2O5-NiO-Sb2O3 micro-ceramics," *Phys. B Condens. Matter*, vol. 704, p. 417010, May 2025, doi: 10.1016/j.physb.2025.417010.

[26] S. Sreedevi, J. Peediyekkal, S. Melethil, A. Mallikarjun, A. Biju, and N. Kalarikkal, "Microstructure, fluorescence emission, and nonlinear optical limiting properties of ZnO-Bi2O3-Nb2O5 compound systems," *Ceram. Int.*, p. S0272884224053720, Nov. 2024, doi: 10.1016/j.ceramint.2024.11.275.

[27] R. Dadi, R. Azouani, M. Traore, C. Mielcarek, and A. Kanaev, "Antibacterial activity of ZnO and CuO nanoparticles against gram positive and gram negative strains," *Mater. Sci. Eng. C*, vol. 104, p. 109968, Nov. 2019, doi: 10.1016/j.msec.2019.109968.

[28] H. Dutta and S. K. Pradhan, "Microstructure characterization of high energy ball-milled nanocrystalline V2O5 by Rietveld analysis," *Mater. Chem. Phys.*, vol. 77, no. 3, pp. 868–877, Jan. 2003, doi: 10.1016/S0254-0584(02)00169-4.

[29] T. P. Jaya, P. Jayaram, T. Ramachandran, P. Hajira, C. N. Anumol, and P. P. Pradyumnan, "Synthesis of solid solutions of Mn and Bi substituted V2O5 and substitutional effect in structural and optoelectronic behavior," *Phys. B Condens. Matter*, vol. 407, no. 8, pp. 1214–1218, Apr. 2012, doi: 10.1016/j.physb.2012.01.098.

[30] D. Fang *et al.*, "BiVO4-rGO with a novel structure on steel fabric used as high-performance photocatalysts," *Sci. Rep.*, vol. 7, no. 1, p. 7979, Aug. 2017, doi: 10.1038/s41598-017-07342-1.

[31] R. Ran, J. G. McEvoy, and Z. Zhang, "Synthesis and Optimization of Visible Light Active BiVO $_4$ Photocatalysts for the Degradation of RhB," *Int. J. Photoenergy*, vol. 2015, pp. 1–14, 2015, doi: 10.1155/2015/612857.

[32] D. Errandonea, "High pressure crystal structures of orthovanadates and their properties," *J. Appl. Phys.*, vol. 128, no. 4, p. 040903, July 2020, doi: 10.1063/5.0016323.

[33] Q. Zhou, Y. Gong, and J. Lin, "Low temperature synthesis of sponge-like NiV2O6/C composite by calcining Ni-V-based coordination polymer for supercapacitor application," *J. Electroanal. Chem.*, vol. 823, pp. 80–91, Aug. 2018, doi: 10.1016/j.jelechem.2018.05.037.

[34] R. Abazari, S. Sanati, and L. A. Saghatforoush, "Non-aggregated divanadium pentoxide nanoparticles: A one-step facile synthesis. Morphological, structural,

compositional, optical properties and photocatalytic activities," *Chem. Eng. J.*, vol. 236, pp. 82–90, Jan. 2014, doi: 10.1016/j.cej.2013.09.056.

[35] X. Cui *et al.*, "*AutoFP* : a GUI for highly automated Rietveld refinement using an expert system algorithm based on *FullProf*," *J. Appl. Crystallogr.*, vol. 48, no. 5, pp. 1581–1586, Oct. 2015, doi: 10.1107/S1600576715015125.

[36] S. Mandal, A. Pramanick, S. Chakraborty, and P. Pratim Dey, "Phase determination of ZrB2-B4C ceramic composite material using XRD and rietveld refinement analysis," *Mater. Today Proc.*, vol. 33, pp. 5664–5666, 2020, doi: 10.1016/j.matpr.2020.04.124.

[37] K. Momma and F. Izumi, "*VESTA 3* for three-dimensional visualization of crystal, volumetric and morphology data," *J. Appl. Crystallogr.*, vol. 44, no. 6, pp. 1272–1276, Dec. 2011, doi: 10.1107/S0021889811038970.

[38] Y. L. Cheah, N. Gupta, S. S. Pramana, V. Aravindan, G. Wee, and M. Srinivasan, "Morphology, structure and electrochemical properties of single phase electrospun vanadium pentoxide nanofibers for lithium ion batteries," *J. Power Sources*, vol. 196, no. 15, pp. 6465–6472, Aug. 2011, doi: 10.1016/j.jpowsour.2011.03.039.

[39] B. Singh *et al.*, "Anomalous lattice behavior of vanadium pentaoxide (V_2O_5): X-ray diffraction, inelastic neutron scattering and ab initio lattice dynamics," *Phys. Chem. Chem. Phys.*, vol. 19, no. 27, pp. 17967–17984, 2017, doi: 10.1039/C7CP01904A.

[40] F. Haaß, A. H. Adams, T. Buhrmester, G. Schimanke, M. Martin, and H. Fuess, "X-Ray absorption and X-ray diffraction studies on molybdenum doped vanadium pentoxide," *Phys Chem Chem Phys*, vol. 5, no. 19, pp. 4317–4324, 2003, doi: 10.1039/B307158H.

[41] D. Nandi, M. Gnanaseelan, F. Simon, and J. Pionteck, "Unique nanopetals of nickel vanadate: crystal structure elucidation and supercapacitive performance," *New J. Chem.*, vol. 41, no. 13, pp. 5620–5627, 2017, doi: 10.1039/C6NJ03427F.

[42] J. Isasi, M. L. López, M. L. Veiga, and C. Pico, "Structure and conductivity of RhVO4: Relationship between the MM′O4 oxides derived from the rutile-type," *J. Alloys Compd.*, vol. 232, no. 1–2, pp. 36–42, Jan. 1996, doi: 10.1016/0925-8388(95)01968-5.

[43] V. Singh, M. Seshadri, M. S. Pathak, and N. Singh, "Sm3+ doped calcium orthovanadate Ca3(VO4)2 - A spectral study," *Spectrochim. Acta. A. Mol. Biomol. Spectrosc.*, vol. 217, pp. 315–321, June 2019, doi: 10.1016/j.saa.2019.03.041.

[44] P. Shvets, O. Dikaya, K. Maksimova, and A. Goikhman, "A review of Raman spectroscopy of vanadium oxides," *J. Raman Spectrosc.*, vol. 50, no. 8, pp. 1226–1244, Aug. 2019, doi: 10.1002/jrs.5616.

[45] R. Baddour-Hadjean *et al.*, "Lattice Dynamics of β-V_2O_5 : Raman Spectroscopic Insight into the Atomistic Structure of a High-Pressure Vanadium Pentoxide Polymorph," *Inorg. Chem.*, vol. 51, no. 5, pp. 3194–3201, Mar. 2012, doi: 10.1021/ic202651b.

[46] L. Abello, E. Husson, Y. Repelin, and G. Lucazeau, "Vibrational spectra and valence force field of crystalline V2O5," *Spectrochim. Acta Part Mol. Spectrosc.*, vol. 39, no. 7, pp. 641–651, Jan. 1983, doi: 10.1016/0584-8539(83)80040-3.

[47] S. Zhan, G. Chen, D. Liu, A. Li, C. Wang, and Y. Wei, "Effects of Cr doping on the structural and electrochemical properties of V2O5," *J. Alloys Compd.*, vol. 479, no. 1–2, pp. 652–656, June 2009, doi: 10.1016/j.jallcom.2009.01.023.

[48] J. P. Peña, P. Bouvier, M. Hneda, C. Goujon, and O. Isnard, "Raman spectra of vanadates M V 2 O 6 (M = Mn, Co, Ni, Zn) crystallized in the non-usual columbite-type structure," *J. Phys. Chem. Solids*, vol. 154, p. 110034, July 2021, doi: 10.1016/j.jpcs.2021.110034.

[49] K. Pradeeswari, A. Venkatesan, P. Pandi, and R. Mohan Kumar, "Effect of Zn2+, Ti2+ dopants on structural, optical and electrochemical properties of V2O5 nanoparticles synthesized via non-aqueous sol–gel route," *J. Mater. Sci. Mater. Electron.*, vol. 29, no. 23, pp. 19689–19696, Dec. 2018, doi: 10.1007/s10854-018-0094-x.

[50] H. Jung, K. Gerasopoulos, A. A. Talin, and R. Ghodssi, "A platform for in situ Raman and stress characterizations of V2O5 cathode using MEMS device," *Electrochimica Acta*, vol. 242, pp. 227–239, July 2017, doi: 10.1016/j.electacta.2017.04.160.

[51] Y. Wei, K. Nam, G. Chen, C. Ryu, and K. Kim, "Synthesis and structural properties of stoichiometric and oxygen deficient CuVO prepared via co-precipitation method," *Solid State Ion.*, vol. 176, no. 29–30, pp. 2243–2249, Sept. 2005, doi: 10.1016/j.ssi.2005.06.018.

[52] H. Tian, I. E. Wachs, and L. E. Briand, "Comparison of UV and Visible Raman Spectroscopy of Bulk Metal Molybdate and Metal Vanadate Catalysts," *J. Phys. Chem. B*, vol. 109, no. 49, pp. 23491–23499, Dec. 2005, doi: 10.1021/jp053879j.

[53] R. L. Frost, K. L. Erickson, M. L. Weier, and O. Carmody, "Raman and infrared spectroscopy of selected vanadates," *Spectrochim. Acta. A. Mol. Biomol. Spectrosc.*, vol. 61, no. 5, pp. 829–834, Mar. 2005, doi: 10.1016/j.saa.2004.06.006.

[54] S. Sahoo, V. Jain, D. V. Shah, R. Das, and A. Pathak, "Effect of Mo doping in vanadium pentoxide (V2O5) for dye degradation," *J. Cryst. Growth*, vol. 627, p. 127491, Feb. 2024, doi: 10.1016/j.jcrysgro.2023.127491.

[55] A. J. "Skip" Schwoeble *et al.*, "Application of X-ray Photoelectron Spectroscopy (XPS) for the Surface Characterization of Gunshot Residue (GSR)," *Microsc. Today*, vol. 19, no. 2, pp. 40–45, Mar. 2011, doi: 10.1017/S1551929511000113.

[56] S. Kumar Pandey *et al.*, "*p* -type conduction from Sb-doped ZnO thin films grown by dual ion beam sputtering in the absence of oxygen ambient," *J. Appl. Phys.*, vol. 114, no. 16, p. 163107, Oct. 2013, doi: 10.1063/1.4827379.

[57] J. Chen *et al.*, "Electrochemical Performance and Stress Distribution of Sb/Sb2O3 Nanoparticles as Anode Materials for Sodium-Ion Batteries," *Batteries*, vol. 9, no. 2, p. 98, Jan. 2023, doi: 10.3390/batteries9020098.

[58] A. Kong, Y. J. Ding, P. Wang, H. Q. Zhang, F. Yang, and Y. K. Shan, "Novel alkylimidazolium/vanadium pentoxide intercalation compounds with excellent

adsorption performance for methylene blue," *J. Solid State Chem.*, vol. 184, no. 2, pp. 331–336, Feb. 2011, doi: 10.1016/j.jssc.2010.12.008.

[59] H. T. T. Nguyen, D. Jung, C.-Y. Park, and D. J. Kang, "Synthesis of single-crystalline sodium vanadate nanowires based on chemical solution deposition method," *Mater. Chem. Phys.*, vol. 165, pp. 19–24, Sept. 2015, doi: 10.1016/j.matchemphys.2015.05.053.

[60] H. Reddy Inta, H. V. S. R. M. Koppisetti, S. Ghosh, A. Roy, and V. Mahalingam, "Ni $_3$ Se $_4$ Nanostructure as a Battery-type Positive Electrode for Hybrid Capacitors," *ChemElectroChem*, vol. 10, no. 2, p. e202201041, Jan. 2023, doi: 10.1002/celc.202201041.

[61] G.-X. Huang *et al.*, "Effect of Niobium Doping on Structural Stability and Electrochemical Properties of LiNiO $_2$ Cathode for Li-Ion Batteries," *J. Electrochem. Soc.*, vol. 169, no. 4, p. 040533, Apr. 2022, doi: 10.1149/1945-7111/ac653e.

[62] M. Oku, H. Tokuda, and K. Hirokawa, "Final states after Ni2p photoemission in the nickel—oxygen system," *J. Electron Spectrosc. Relat. Phenom.*, vol. 53, no. 4, pp. 201–211, Jan. 1991, doi: 10.1016/0368-2048(91)85039-V.

[63] N. M. Abd-Alghafour, Naser. M. Ahmed, Z. Hassan, and M. A. Almessiere, "Hydrothermal Synthesis and Structural Properties of V $_2$ O $_5$ Nanoflowers at Low Temperatures," *J. Phys. Conf. Ser.*, vol. 1083, p. 012036, Aug. 2018, doi: 10.1088/1742-6596/1083/1/012036.

[64] S. Landi, I. R. Segundo, E. Freitas, M. Vasilevskiy, J. Carneiro, and C. J. Tavares, "Use and misuse of the Kubelka-Munk function to obtain the band gap energy from diffuse reflectance measurements," *Solid State Commun.*, vol. 341, p. 114573, Jan. 2022, doi: 10.1016/j.ssc.2021.114573.

[65] C.-C. Wang, C.-L. Lu, F.-S. Shieu, and H. C. Shih, "Enhanced photoluminescence properties of Ga-doped V2O5 nanorods via defect structures," *Chem. Phys. Lett.*, vol. 738, p. 136864, Jan. 2020, doi: 10.1016/j.cplett.2019.136864.

[66] K.-Y. Pan and D.-H. Wei, "Optoelectronic and Electrochemical Properties of Vanadium Pentoxide Nanowires Synthesized by Vapor-Solid Process," *Nanomaterials*, vol. 6, no. 8, p. 140, July 2016, doi: 10.3390/nano6080140.

[67] P. Srilakshmi, A. U. Maheswari, V. Sajeev, and M. Sivakumar, "Tuning the optical bandgap of V2O5 nanoparticles by doping transition metal ions," *Mater. Today Proc.*, vol. 18, pp. 1375–1379, 2019, doi: 10.1016/j.matpr.2019.06.603.

[68] T. K. Le, M. Kang, S. W. Han, and S. W. Kim, "Highly intense room-temperature photoluminescence in V $_2$ O $_5$ nanospheres," *RSC Adv.*, vol. 8, no. 72, pp. 41317–41322, 2018, doi: 10.1039/C8RA06861E.

[69] F. C. Kalangestani, M. Simiari, and F. E. Ghodsi, "Fabrication of V2O5/NiO double-layer film with hydrophilic property and evaluation of the effects of V2O5 coating on electro-optical parameters of NiO film," *Appl. Phys. A*, vol. 128, no. 5, p. 395, May 2022, doi: 10.1007/s00339-022-05545-6.

[70] K. M. Shafeeq, V. P. Athira, C. H. R. Kishor, and P. M. Aneesh, "Structural and optical properties of V2O5 nanostructures grown by thermal decomposition

technique," *Appl. Phys. A*, vol. 126, no. 8, p. 586, Aug. 2020, doi: 10.1007/s00339-020-03770-5.

[71] R. M. Mohammed, "Effect of Antimony Oxide Nanoparticles on Structural, Optical and AC Electrical Properties of (PEO-PVA) Blend for Antibacterial Applications," *Int. J. Emerg. Trends Eng. Res.*, vol. 8, no. 8, pp. 4726–4738, Aug. 2020, doi: 10.30534/ijeter/2020/107882020.

[72] D. K. Pati, S. Bhattacharjee, M. Mahapatra, B. N. Parida, P. R. Das, and R. Padhee, "Structural, optical and magnetic characteristics of multiferroic [Pb(Fe0.5Nb0.5)O3]0.4 - [(Ca0.2Sr0.8)TiO3]0.6," *Appl. Phys. A*, vol. 128, no. 8, p. 673, Aug. 2022, doi: 10.1007/s00339-022-05816-2.

[73] B. Sannakki and Anita, "Dielectric Properties of PMMA and its Composites with ZrO2," *Phys. Procedia*, vol. 49, pp. 15–26, 2013, doi: 10.1016/j.phpro.2013.10.006.

[74] M. Uzair *et al.*, "Effect of Mn Doped on Structural, Optical, and Dielectric Properties of $BiFe_{1-x}Mn_xO_3$ for Efficient Antioxidant Activity," *ACS Omega*, vol. 8, no. 45, pp. 42390–42397, Nov. 2023, doi: 10.1021/acsomega.3c04714.

[75] S. Riaz, S. M. H. Shah, A. Akbar, S. Atiq, and S. Naseem, "Effect of Mn doping on structural, dielectric and magnetic properties of BiFeO3 thin films," *J. Sol-Gel Sci. Technol.*, vol. 74, no. 2, pp. 329–339, May 2015, doi: 10.1007/s10971-014-3461-y.

[76] Ş. Çavdar, H. Koralay, and Ş. Altındal, "Effect of Vanadium Substitution on the Dielectric Properties of Glass Ceramic Bi-2212 Superconductor," *J. Low Temp. Phys.*, vol. 164, no. 1–2, pp. 102–114, July 2011, doi: 10.1007/s10909-011-0361-1.

[77] S. Khan and K. Singh, "Influence of Al3+ doping for V5+ on the structural, optical, thermal and electrical properties of V2-Al O5- (x=0–0.20) ceramics," *Ceram. Int.*, vol. 47, no. 8, pp. 10724–10732, Apr. 2021, doi: 10.1016/j.ceramint.2020.12.188.

[78] A. Yadav, M. S. Dahiya, P. Narwal, A. Hooda, A. Agarwal, and S. Khasa, "Electrical characterization of lithium bismuth borate glasses containing cobalt/vanadium ions," *Solid State Ion.*, vol. 312, pp. 21–31, Dec. 2017, doi: 10.1016/j.ssi.2017.10.006.

[79] A. Dhahri, E. Dhahri, and E. K. Hlil, "Electrical conductivity and dielectric behaviour of nanocrystalline $La_{0.6}Gd_{0.1}Sr_{0.3}Mn_{0.75}Si_{0.25}O_3$," *RSC Adv.*, vol. 8, no. 17, pp. 9103–9111, 2018, doi: 10.1039/C8RA00037A.

[80] A. S. Das and D. Biswas, "Investigation of Ac conductivity mechanism and dielectric relaxation of semiconducting neodymium-vanadate nanocomposites: temperature and frequency dependency," *Mater. Res. Express*, vol. 6, no. 7, p. 075206, Apr. 2019, doi: 10.1088/2053-1591/ab13ee.

[81] S. Dahiya, R. Punia, S. Murugavel, and A. S. Maan, "Conductivity and modulus formulation in lithium modified bismuth zinc borate glasses," *Solid State Sci.*, vol. 55, pp. 98–105, May 2016, doi: 10.1016/j.solidstatesciences.2016.02.013.

[82] M. Aureliano, A. L. De Sousa-Coelho, C. C. Dolan, D. A. Roess, and D. C. Crans, "Biological Consequences of Vanadium Effects on Formation of Reactive Oxygen Species and Lipid Peroxidation," *Int. J. Mol. Sci.*, vol. 24, no. 6, p. 5382, Mar. 2023, doi: 10.3390/ijms24065382.

[83] J. Ude *et al.*, "Outer membrane permeability: Antimicrobials and diverse nutrients bypass porins in *Pseudomonas aeruginosa*," *Proc. Natl. Acad. Sci.*, vol. 118, no. 31, p. e2107644118, Aug. 2021, doi: 10.1073/pnas.2107644118.

[84] H. L. Choy, E. A. Gaylord, and T. L. Doering, "Ergosterol distribution controls surface structure formation and fungal pathogenicity," *mBio*, pp. e01353-23, July 2023, doi: 10.1128/mbio.01353-23.

[85] L. K. Abdul Karem and A. T. Ali, "Biosynthesis, Characterization, Adsorption and Antimicrobial studies of Vanadium Oxide Nanoparticles Using Punica Granatum Extract," *Baghdad Sci. J.*, July 2023, doi: 10.21123/bsj.2023.8114.

[86] J. Chang *et al.*, "A Nickel-Containing Polyoxomolybdate as an Efficient Antibacterial Agent for Water Treatment," *Int. J. Mol. Sci.*, vol. 23, no. 17, p. 9651, Aug. 2022, doi: 10.3390/ijms23179651.

[87] L. Wang, C. Hu, and L. Shao, "The antimicrobial activity of nanoparticles: present situation and prospects for the future," *Int. J. Nanomedicine*, vol. Volume 12, pp. 1227–1249, Feb. 2017, doi: 10.2147/IJN.S121956.

[88] R. Wysocki, J. I. Rodrigues, I. Litwin, and M. J. Tamás, "Mechanisms of genotoxicity and proteotoxicity induced by the metalloids arsenic and antimony," *Cell. Mol. Life Sci.*, vol. 80, no. 11, p. 342, Nov. 2023, doi: 10.1007/s00018-023-04992-5.

[89] M. Claudel, J. V. Schwarte, and K. M. Fromm, "New Antimicrobial Strategies Based on Metal Complexes," *Chemistry*, vol. 2, no. 4, pp. 849–899, Oct. 2020, doi: 10.3390/chemistry2040056.

[90] I. Sheikhshoaie, S. Y. Ebrahimipour, N. Lotfi, J. T. Mague, and M. Khaleghi, "Synthesis, spectral characterization, X-ray crystal structure and antimicrobial activities of two cis dioxido-vanadium(V) complexes incorporating unsymmetrical dimalonitrile-based (NNO) Schiff base ligands," *Inorganica Chim. Acta*, vol. 442, pp. 151–157, Mar. 2016, doi: 10.1016/j.ica.2015.11.026.

Chapter VI

Development of Z-scheme Sb_2O_3-NiO-V_2O_5/g-C_3N_4 Heterostructures for Visible Light Photocatalysis and Antimicrobial Applications

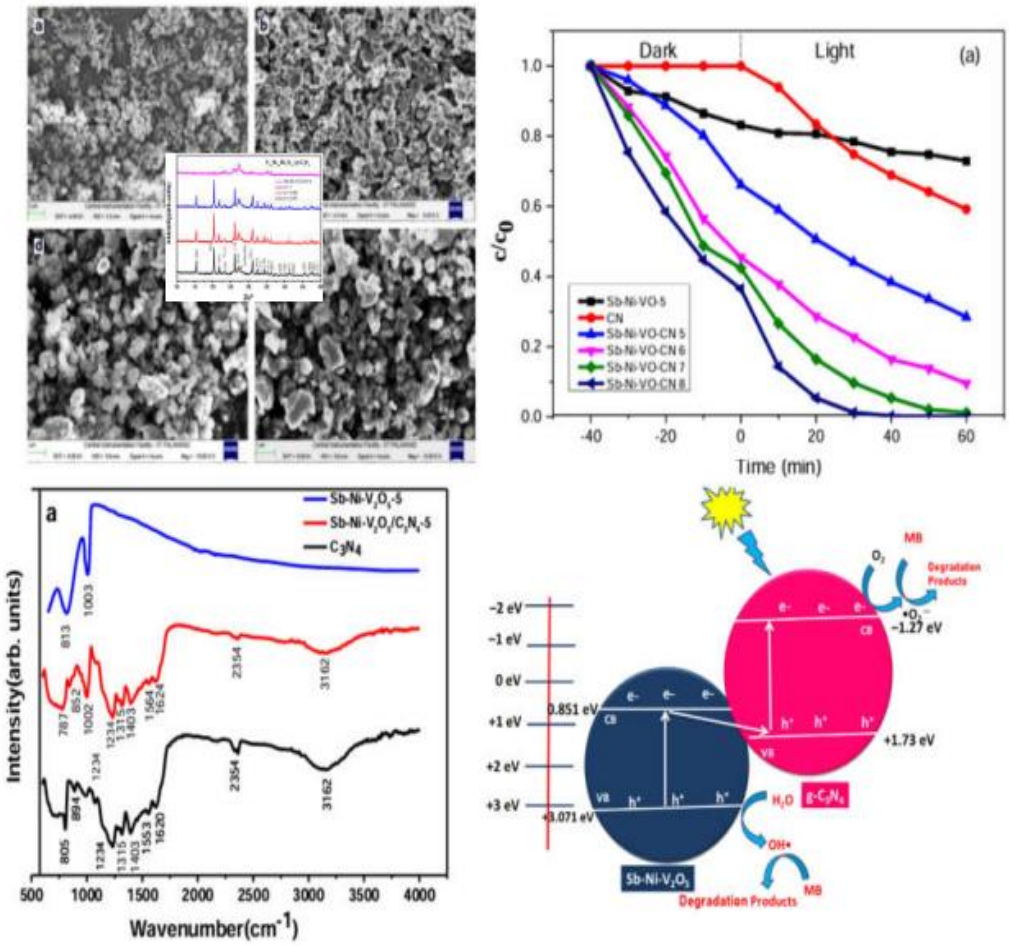

Melethil Sabna, *Peediyekkal Jayaram, Vandana P. Viswanathan, S. Sreedevi, K. Safna, Development of Z-scheme Sb2O3–NiO–V2O5/g-C3N4 heterostructures for visible light photocatalysis and antimicrobial applications, Journal of the Indian Chemical Society, Volume 103, Issue 6, 2026, 102637, ISSN 0019-4522, https://doi.org/10.1016/j.jics.2026.102637.*

Introduction

Semiconductor-based photocatalysis has emerged as a highly promising and eco-friendly strategy for the degradation of organic and inorganic pollutants, harnessing solar energy for advanced wastewater treatment [1], [2]. The photocatalytic efficiency of such materials is primarily determined by their intrinsic physicochemical properties, including band gap energy, specific surface area, pore architecture, and morphological characteristics [3]. Conventional photocatalysts such as titanium dioxide (TiO_2) [4-5], zinc oxide (ZnO) [6], and tin oxide (SnO_2) [7] possess wide band gaps of 3.0 to 3.6 eV, rendering them active predominantly under ultraviolet irradiation. Consequently, their limited visible-light absorption with < 5% of the solar spectrum significantly hampers real-world applicability.Graphitic carbon nitride (g-C_3N_4), a metal-free polymeric semiconductor, is extensively studied for photocatalysis due to its structural stability, tri-s-triazine-based architecture, and visible-light activity [8], [9]. With a band gap of ~2.7 eV, g-C_3N_4 efficiently absorbs visible light for applications such as hydrogen evolution and antimicrobial action. Its porous, amine-rich morphology enhances charge transfer and pollutant adsorption [10-11].

But pristine graphitic carbon nitride suffers from limited light absorption, low quantum yield, fast exciton recombination, poor charge mobility, and photocorrosion during extended photocatalysis [12], [13], [14]. To overcome these limitations, approaches like elemental doping, surface modification, co-catalyst loading, and defect engineering have been employed to modulate its band structure and enhance charge separation. Particularly constructing Type I, Type II, p–n junctions, and Z or S scheme heterojunctions with semiconductors like TiO_2 and ZnO significantly improves interfacial charge transfer, redox ability, and light absorption across a broader spectral range [14-16]. Recent efforts have focused on coupling graphitic carbon nitride with semiconductors possessing compatible band alignments to construct direct Z-scheme photocatalysts with improved visible-light utilization such as g-C_3N_4/MoS_2 [17],[18], g-C_3N_4/Ag_3VO_4 [19], g-C_3N_4/ZnO [20], $ZnIn_2S_4$/g-C_3N_4 [21], g-C_3N_4/InSe [22], g-C_3N_4-CuSe [23], g-C_3N_4/$BaTiO_3$ [24], g-C_3N_4/Bi_2O_3 [25], g-C_3N_4/BiOBr [26], g-C_3N_4/Bi_2O_3/$BiPO_4$ [27], g-C_3N_4/$CoTiO_3$ [28], g-C_3N_4/Ag_2WO_4

[29], ZnO/g-C_3N_4[30], TiO_2/g-C_3N_4 [31], $BiOIO_3$/g-C_3N_4 [32] Bi_2O_3/g-C_3N_4 [33], Ag@AgBr/g-C_3N_4 [34], $FeTiO_3$/Fe doped g-C_3N_4 [35], TiO_2/$NiCo_2O_4$/ g-C_3N_4 [36], $NiFe_2O_4$/g-C_3N_4 [37].

Selecting semiconductors with band structures compatible with g-C_3N_4 offers limited progress in enhancing g-C_3N_4-based Z-scheme photocatalytic systems, as materials like TiO_2 and BiOCl, with band gaps greater than 3.0 eV, cannot absorb visible light. Among the viable candidates, vanadium pentoxide has garnered attention owing to its relatively narrow band gap of 2.3 eV, enabling effective absorption of visible light. Its band edge positions with $E_{CB} \approx 0.47$ eV and $E_{VB} \approx 2.73$ eV, exhibit excellent energetic alignment with that of g-C_3N_4, having $E_{CB} \approx -1.2$ eV & $E_{VB} \approx$ 1.5 eV, rendering it a promising counterpart for constructing an all-solid-state direct Z-scheme photocatalyst. In such a configuration, the photoexcited electrons in the CB of g-C_3N_4 retain potent reducing power, while the holes in the VB of V_2O_5 maintain strong oxidative potential, synergistically promoting charge carrier separation and enhancing the redox activity essential for advanced photocatalytic performance [38]. Thus V_2O_5/g-C_3N_4 Z-scheme photocatalyst enhances charge carrier separation, boosting ROS generation (•OH and $O_2^{\bullet -}$) capable of disrupting microbial membranes, damage proteins and nucleic acids, ensuring broad-spectrum antimicrobial activity. It improves visible-light harvesting, is reusable, and avoids toxic byproducts, making it ideal for sustainable sanitation and water purification [39-40].

We have previously reported the synthesis of NiO incorporated V_2O_5 ($V_{2-x}Ni_{3x}O_{5-\delta}$,$0.03 \leq x \leq 0.06$) [41-42], Sb_2O_3 incorporated V_2O_5 ($V_{2-x}Sb_{2x}O_{5-\delta}$, $0.05 \leq x \leq 0.08$) [43-45], NiO and Sb_2O_3 incorporated V_2O_5 ($V_{2-x}Ni_{2x}Sb_xO_{5-\delta}$ for $0.05 \leq x \leq 0.08$) [46], and analyzed its microstructural, optical, adsorptive, dielectric, and antimicrobial applications. In the present study, we prepared the direct solid-state Z-scheme $V_{2-x}Ni_{2x}Sb_xO_{5-\delta}$/g-$C_3N_4$ heterojunction photocatalysts by a sonication-hydrothermal method. The structural and optical properties of the $V_{2-x}Ni_{2x}Sb_xO_{5-\delta}$/g-$C_3N_4$ heterostructures were investigated using XRD, FTIR, UV–Vis DRS, and photoluminescence spectroscopy, confirming heterojunction formation, superior light absorption, and efficient charge separation. Photocatalytic performance was evaluated

through Methylene Blue degradation, and the prepared heterostructures also demonstrated significant antibacterial and antifungal activity.

6.1. Materials and Methods

6. 2.1. Synthesis of $V_{2-x}Ni_{2x}Sb_xO_{5-\delta}$ (Sb-Ni-V_2O_5) for $0.05 \leq x \leq 0.08$

We have reported the synthesis of $V_{2-x}Ni_{2x}Sb_xO_{5-\delta}$ (Sb-Ni-V_2O_5), where x is the mol fraction with $0.05 \leq x \leq 0.08$, via a conventional solid-state reaction route where high-purity reagents, V_2O_5, NiO, and Sb_2O_3 (all 99.99%, Sigma-Aldrich, USA) were weighed in precise stoichiometric proportions and thoroughly ground for 3 hours in an agate mortar to ensure homogeneity [46]. The blended powders were calcined in alumina crucibles at 550 °C for 12 hours to initiate phase formation. The calcined powders were then uniaxially pressed into 14 mm diameter, ~2 mm thick pellets and sintered at 630 °C for 12 hours to promote densification and crystallinity. Finally, the sintered pellets were reground to obtain uniform, fine powders for subsequent analysis [46].

6.2.2. Synthesis of g-C_3N_4 nanoparticles

Bulk graphitic carbon nitride was synthesized through the thermal polycondensation of urea, purchased from Sigma Aldrich. Specifically, 10 grams of urea were placed in a silica crucible, which was then loosely covered with aluminum foil to control the release of gaseous byproducts. The sample was subjected to calcination in a muffle furnace at 550 °C for 4h, employing a controlled heating rate of 3 °C per minute. Upon natural cooling to ambient temperature, the resulting yellow solid was finely ground using an agate mortar and pestle to yield powdered bulk g-C_3N_4. This bulk material was subsequently exfoliated to enhance its surface area and reactivity for further applications [11].

6.2.3. Synthesis of $V_{2-x}Ni_{2x}Sb_xO_{5-\delta}$/g-$C_3N_4$ ($0.05 \leq x \leq 0.08$) heterostructures

The reagents were precisely measured using an analytical balance, with 70 mg of $V_{2-x}Ni_{2x}Sb_xO_{5-\delta}$ ($0.05 \leq x \leq 0.08$) and 70 mg of g-C_3N_4 accurately weighed, preparing four sample compositions for varying mol fraction x. Solution A was prepared by dispersing 70 mg of Sb-Ni-V_2O_5 into 30 mL of methanol. This mixture was

magnetically stirred for 30 minutes, followed by 80 minutes of sonication, with intervals of 10 minutes of rest after every 20 minutes of sonication. Similarly, solution B was prepared by dispersing 70 mg of g-C_3N_4 into methanol, following the same procedure of 30 minutes of magnetic stirring and 80 minutes of sonication with intermittent breaks as described for solution A. Subsequently, solution A was gradually added dropwise to solution B under continuous magnetic stirring, which was maintained for an additional 20 minutes to ensure thorough mixing. The combined solution was then subjected to an extended sonication process for 1 hour and 30 minutes to achieve a homogeneous dispersion. The samples were then prepared through high-temperature treatment using an autoclave. Before use, the autoclave was meticulously cleaned with chromic acid to ensure purity. The prepared solution was then transferred into the autoclave, which was sealed tightly. Hydrothermal conditions were applied at 100 °C for a duration of 18 hours. Upon completion, the resulting heterostructures were collected, washed, dried, and subjected to further calcination at 300 ^{0}C for 3 hours in an air atmosphere. Finally, the heated heterostructures were finely ground using an agate mortar and pestle to achieve coarse exfoliation. In this way, $V_{2-x}Ni_{2x}Sb_xO_{5-\delta}$/g-$C_3N_4$ heterostructures of four compositions were prepared for mol fractions at x= 0.05, 0.06, 0.07 & 0.08 and named as Sb-Ni-V_2O_5/g-C_3N_4-5, Sb-Ni-V_2O_5/g-C_3N_4-6, Sb-Ni-V_2O_5/g-C_3N_4-7, Sb-Ni-V_2O_5/g-C_3N_4-8 with $V_{2-x}Ni_{2x}Sb_xO_{5-\delta}$ and g-C_3N_4 taken in the ratio 1:1 [16].

6.2.4. Characterizations

Crystallographic analyses of the samples were conducted using X-ray diffractometry (XRD) with AERIS PANalytical equipment, employing copper K-alpha radiation with a wavelength of 1.5406 Å. Scanning electron microscopy (SEM) and energy-dispersive spectroscopy (EDS) were performed using a Gemini SEM 300 by Carl Zeiss, with a resolution of 0.8 nm at 15 kV, and a VEGA-TESCAN analyzer with a 30 keV accelerating voltage, respectively. Optical properties were studied using UV-Vis diffuse reflectance spectra obtained from Perkin Elmer Lambda 365 spectrophotometer. Photoluminescence (PL) measurements were carried out using an FP-8300 JASCO spectrofluorometer with an excitation wavelength of 330 nm. XPS analysis was recorded with a Thermo Scientific ESCA instrument using an Al *Kα* monochromator at 1486 Å. Survey scans were performed at a constant pass energy of

100 eV, and high-resolution measurements at 20 eV. Data analysis was conducted using Casa XPS software, with mixed Lorentzian-Gaussian curves used to fit the spectra. FTIR studies were performed using an IRAffinity-1S (document number 1), a Shimadzu spectrometer, within the range of 500-4000 cm^{-1}.

6.2.5. Photocatalytic experiments

The photocatalytic performance of the synthesized samples was evaluated through the degradation of Methylene Blue (MB) under visible light irradiation. For each experiment, 10 mg of the photocatalyst was dispersed in 50 mL of a 10 ppm MB dye solution. Before illumination, the suspension was magnetically stirred in the dark for 40 minutes to establish adsorption–desorption equilibrium between the dye molecules and the catalyst surface. Upon exposure to natural sunlight, the degradation process was monitored by withdrawing 3 mL aliquots from the suspension at 10-minute intervals. Each sample was immediately centrifuged at 10000 rpm for 10 minutes to separate the photocatalyst before recording the absorbance spectra using a visible spectrophotometer. All photocatalytic tests were conducted under consistent sunlight conditions during midday hours on cloudless days, with an average light intensity of approximately 100,000 lux. To assess the reusability and photostability of the catalysts, recycling experiments were also performed. After each photocatalytic cycle, the used catalyst was recovered via centrifugation, rinsed thoroughly with double-distilled water to eliminate residual dye, and dried overnight at 80 °C for subsequent use. This protocol ensured the evaluation of catalyst durability under repeated solar exposure.

6.2.6. Photocatalytic efficiency and Kinetic study

The progression of MB degradation during the photocatalytic decolorization process was monitored by measuring the absorbance of the reaction mixture at characteristic wavelengths using a UV–Vis spectrophotometer. The recorded absorbance values were subsequently converted to concentration values (C) based on a pre-established calibration curve. The photocatalytic efficiency of the process was quantified using the following relation:

$$\text{MB colour removal (\%)} = (C_o - C_t)/C_o \times 100 \quad (1)$$

where C_0 and C_t (in $mg \cdot L^{-1}$) denote the initial dye concentration and the concentration at a given irradiation time t (in minutes), respectively. To understand the kinetics of the photocatalytic reaction, the data were analyzed using the Langmuir-Hinshelwood (L-H) kinetic model, which assumes a pseudo-first-order reaction with respect to the dye concentration under low initial concentrations.

$$\ln(C_o/C_t) = k_{app} t \quad (2)$$

The rate constant k_{app} (min^{-1}) was determined from the linear fitting of the experimental data plotted as $\ln(C_0/C_t)$ versus irradiation time. The slope of this linear plot corresponds to the apparent first-order rate constant, providing insight into the efficiency and reaction rate of the photocatalytic system [47].

6.2.7. Active species trapping experiments

To identify the primary reactive species involved in the photocatalytic degradation process over the synthesized Sb-Ni-V_2O_5/g-C_3N_4 heterostructures, radical trapping experiments were conducted under standard photocatalytic reaction conditions. It is well established that photogenerated holes (h^+), superoxide radicals ($\bullet O_2^-$), and hydroxyl radicals (•OH) are the major oxidative species in visible light-driven photocatalysis. To selectively quench each of these species, isopropanol (IPA, 1 mM) was used as a scavenger for •OH, ethylenediaminetetraacetic acid (EDTA, 1 mM) for h^+, and 1,4-benzoquinone (BQ, 1 mM) for $\bullet O_2^-$. The scavengers were introduced into the photocatalytic system in separate trials, and their impact on the degradation efficiency was analyzed to determine the dominant reactive species responsible for the observed photocatalytic activity.

6.2.8. Antimicrobial studies

The visible-light-induced antimicrobial activity of the synthesized $V_{2-x}Ni_{2x}Sb_xO_{5-\delta}$/g-$C_3N_4$ heterostructure was evaluated against both bacterial and fungal pathogens using standard diffusion methods. Antibacterial efficacy was tested against Gram-positive bacteria (*Staphylococcus aureus, Bacillus cereus*) and Gram-negative

bacteria (*Escherichia coli*, *Pseudomonas aeruginosa*, *Vibrio sp*.) using the agar well diffusion method on Mueller-Hinton Agar (MHA) plates. Bacterial cultures grown in Luria Bertani broth were swabbed onto MHA, and 7 mm wells were loaded with 50-200 μL of the composite dispersed in DMSO. Streptomycin and DMSO served as positive and negative controls, respectively. In parallel, antifungal activity was assessed against *Penicillium* spp. and *Aspergillus niger* using the disc diffusion method on Sabouraud Dextrose Agar (SDA) plates. Fungal suspensions were adjusted to a 0.5 McFarland standard and spread on SDA plates, followed by placement of sterile filter paper discs loaded with the composite extract, along with fluconazole and DMSO as controls. Both the plates were kept in visible light for one hour and then incubated at 37°C for 48 h, after which the inhibition zones were recorded. Both sets of experiments were performed in triplicate, and the heterostructures demonstrated significant antimicrobial effects under visible light, indicating efficient generation of reactive oxygen species and strong potential for applications in antibacterial and antifungal treatments.

6.3. Result and Discussion

6.3.1. Structural Analysis: X-ray Diffractogram

XRD analysis was employed to identify the crystalline phases of the synthesized samples. As shown in Figure. 6.1(a), the pure g-C_3N_4 sample exhibits diffraction peaks at 13.0° and 27.25°, corresponding to the (100) and (002) planes, respectively [39], [48]. These reflections are indicative of the in-plane structural motif and interlayer stacking of graphitic carbon nitride with a hexagonal structure, consistent with JCPDS Card No. 87-1526 [14], [49]. The (100) plane is indicative of the 3-s-triazine ring structure of g-C_3N_4. The (002) reflection observed in the XRD pattern is characteristic of graphitic materials and arises from interlayer stacking within the conjugated aromatic framework. This feature confirms the successful formation of a layered graphitic structure, resulting from the thermal

polycondensation of urea at 550 °C [14], [50]. Our previous studies confirmed the coexistence of triple phases in the $V_{2-x}Ni_{2x}Sb_xO_{5-\delta}$ sample (Fig. 6.1b) [46], with the dominant phase identified as α-V_2O_5 (ICDD: 41-1426) [41], [51].

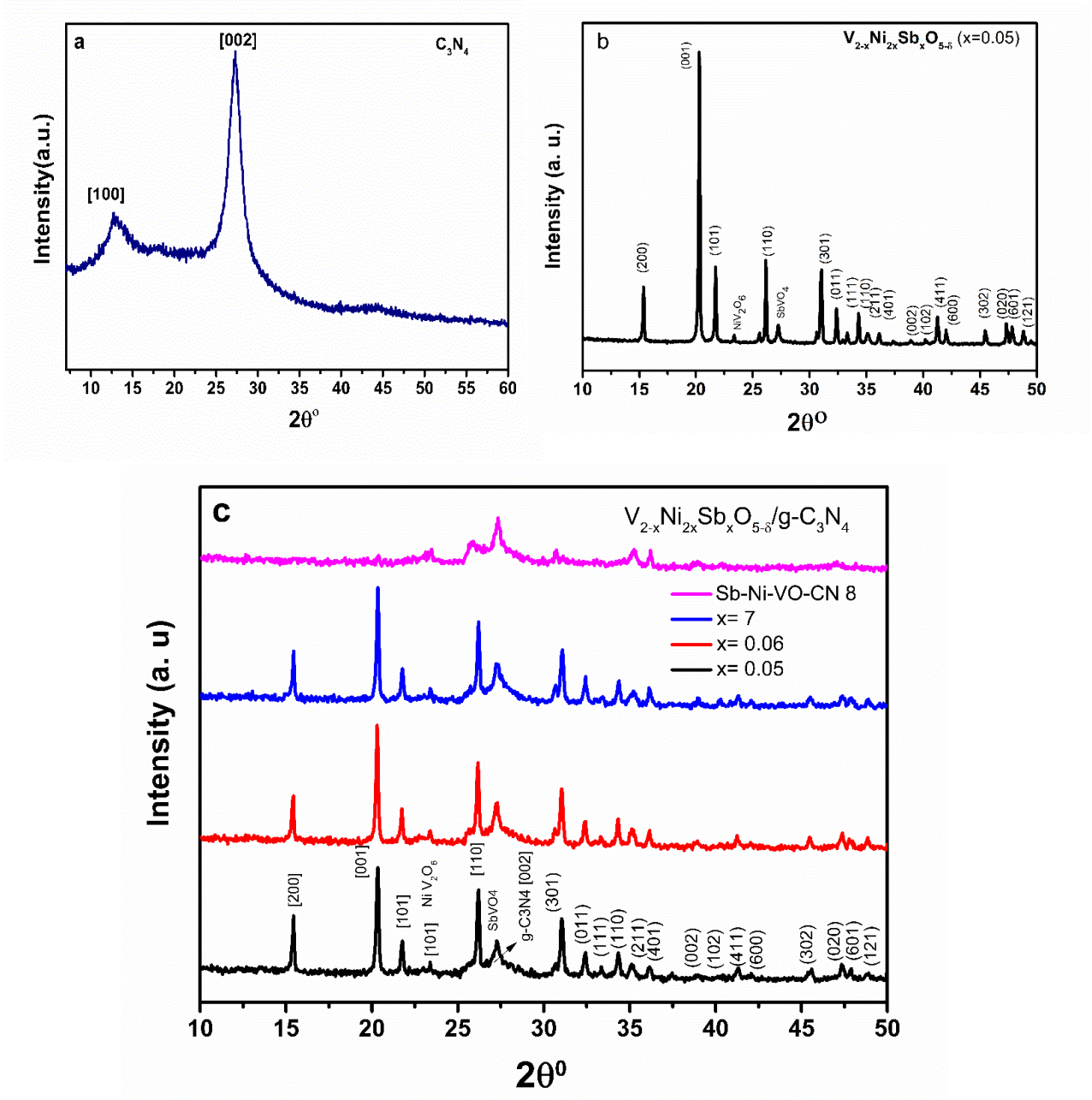

Figure. 6.1(a) representing XRD pattern of as prepared hexagonal phase of g-C_3N_4, (b)Mixed phase $V_{2-x}Ni_{2x}Sb_xO_{5-\delta}$; $x = 0.05$ & (c)$V_{2-x}Ni_{2x}Sb_xO_{5-\delta}$/g-$C_3N_4$ heterostructures for $0.05 \leq x \leq 0.08$

Detailed examination of the X-ray diffraction pattern of the calcined powder reveals a weak reflection at approximately $2\theta = 23.34°$, corresponding to the (101) crystallographic plane, indicative of the presence of a triclinic NiV_2O_6 phase having a monoclinic structure with space group (ICSD:33881) [52], [46]. Moreover, the XRD peak at 27.3^0 is distinctly indicative of (110) plane of the $SbVO_4$ species distinguished by a tetragonal structure with space group P42/mnm (CCDC: 2357624-2357627) [44], [53-54]. Both these extraneous peaks, along with the NiV_2O_6 and $SbVO_4$ phases, have been previously reported in NiO- and Sb_2O_3-incorporated V_2O_5 compounds [44], [46]. Figure 6.1c depicts the XRD pattern of $V_{2-x}Ni_{2x}Sb_xO_{5-\delta}$/g-$C_3N_4$ obtained by sonication and hydrothermal treatment [55]. The results reveal that the as-prepared heterostructures with various mol fractions are well crystallized, except for $V_{2-x}Ni_{2x}Sb_xO_{5-\delta}$/g-$C_3N_4$ at x = 0.08. For the composite sample, the characteristic peak of g-C_3N_4 corresponding to the (002) plane is distinctively evident for all mol fractions. In contrast, the peak intensities of $V_{2-x}Ni_{2x}Sb_xO_{5-\delta,}$ indicating reflections from V_2O_5, $NiV_2O_{6,}$ and $SbVO_4$ planes, are exhibited clearly for all compositions except for mol fraction x =0.08. In the heterostructure with x = 0.08, the characteristic reflection from the stable V_2O_5 (001) plane is notably absent, but distinct reflections corresponding to the (301), (211), and (401) planes of V_2O_5, along with a prominent (002) plane indicative of g-C_3N_4, confirming the successful formation of the composite is present (Fig.6.1c). Furthermore, the absence of extraneous diffraction peaks confirms the high phase purity of the synthesized $V_{2-x}Ni_{2x}Sb_xO_{5-\delta}$/g-$C_3N_4$ heterostructured photocatalysts, substantiating the formation of a well-defined four-phase hybrid architecture. For all mol fractions, the compositional percentage taken during the synthesis was 50% Sb-Ni-V_2O_5+50% C_3N_4 [14].

6.3.2 FTIR Spectroscopy

Figure 6.2(a) presents the comparison of FTIR spectra of pristine g-C_3N_4, the ternary oxide $V_{2-x}Ni_{2x}Sb_xO_{5-\delta}$ at x = 0.08, and their corresponding heterostructure, $V_{2-x}Ni_{2x}Sb_xO_{5-\delta}$/g-$C_3N_4$, synthesized at the same composition. In the spectrum of pure g-C_3N_4, the broad absorption band spanning 3000-3500 cm^{-1} is attributed to the stretching vibrations of residual N-H bonds from uncondensed amino groups, as well

as surface-adsorbed hydroxyl groups (O-H). The pronounced peaks observed at 805 cm^{-1} and 894 cm^{-1} correspond to the characteristic breathing modes of s-triazine ring structures, which are the fundamental building blocks of the graphitic carbon nitride framework [11], [14]. Additionally, a series of absorption features located between 1200 and 1650 cm^{-1}, specifically at 1234, 1315, 1403, 1553, and 1620 cm^{-1}, are attributed to the stretching vibrations of aromatic C-N and C=N bonds within the heptazine-based heterocyclic backbone.

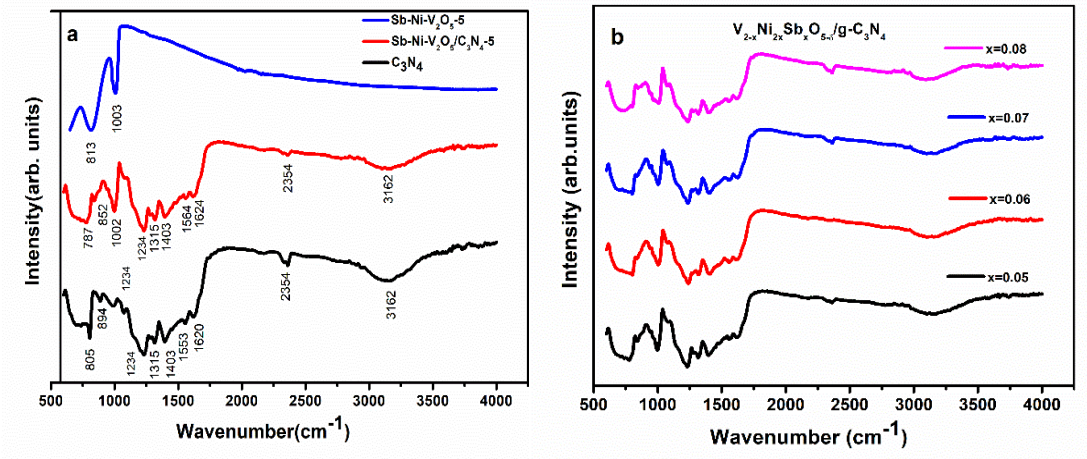

Figure 6.2. (a) depicts the FTIR spectrum showing pure g-C_3N_4, $V_{2-x}Ni_{2x}Sb_xO_{5-\delta}$ & $V_{2-x}Ni_{2x}Sb_xO_{5-\delta}$ /g-C_3N_4 at x=0.05 compounds (b) shows up $V_{2-x}Ni_{2x}Sb_xO_{5-\delta}$ /g-C_3N_4 heterostructures for $0.05 \leq x \leq 0.08$

These spectral signatures collectively confirm the structural integrity of the g-C_3N_4 matrix [48]. For the $V_{2-x}Ni_{2x}Sb_xO_{5-\delta}$ compound at x = 0.08, the distinct band at 1010 cm^{-1} is characteristic of terminal V=O stretching vibrations, while the peak centered around 813 cm^{-1} is associated with V–O–V bridging vibrations, indicative of the vanadate lattice framework [43], [56]. After the hybridization of Sb-Ni-V_2O_5 and g-C_3N_4, in addition to characteristic peaks of g-C_3N_4, a small additional peak occurs at 852 cm^{-1}, and a prominent, distinctive peak occurs at 1002 cm^{-1}, both indicative of the stretching vibrations in vanadium pentoxide-based compounds [39]. But the well-resolved intense peak at 805 cm^{-1} in pristine g-C_3N_4, relating to the breathing mode of triazine units, seems to be absent in the newly formed heterostructures. The FTIR spectra of the Sb–Ni–V_2O_5/g–C_3N_4 composites for all mol fraction x, as illustrated in

Figure 6.2(b), clearly exhibit a superimposition of the characteristic vibrational bands corresponding to both g–C_3N_4 and the Sb–Ni–V_2O_5 phase, without any detectable signals indicative of secondary or impurity phases [62]. The retention of all signature peaks associated with the individual components in the composite spectrum confirms the successful integration of the two materials [55].

From the FTIR results, we expect strong interfacial coupling between C_3N_4 and Sb-Ni-V_2O_5, which could promote the separation and transfer of photogenerated electron-hole pairs and further enhance the photocatalytic performance of Sb-Ni-V_2O_5/C_3N_4 composites [16].

6.3.3. Surface Morphology and Chemical Composition

Figure 6.3(a) displays the SEM micrograph of the pristine g-C_3N_4 with structural features clearly discernible at a magnification of 2 µm. The bulk g-C_3N_4 sample reveals heterogeneously distributed and agglomerated structures still maintaining loose and irregular tissue-like 2D nanosheet morphology with wrinkles and irregular folding structures [11], [50], [57].

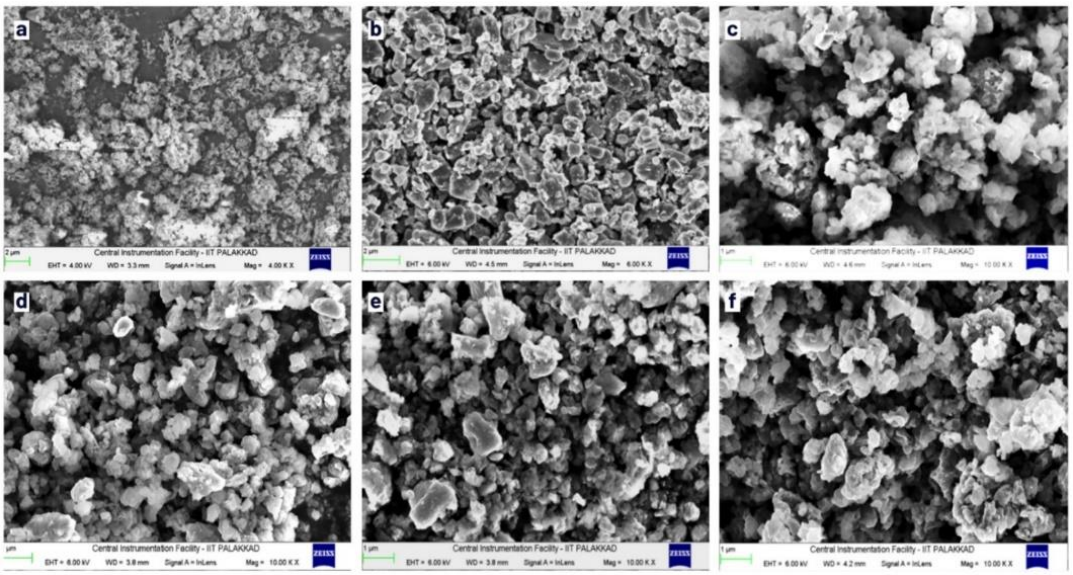

Figure 6.3(a) SEM image of pure g-C_3N_4, (b) SEM image of Sb-Ni-V_2O_5-5 triple phase composite, (c, d, e & f) present the SEM images of $V_{2-x}Ni_{2x}Sb_xO_{5-d}$ /g-C_3N_4 heterostructures for $0.05 \leq x \leq 0.08$

Figure 6.3(b) shows the Sb–Ni–V_2O_5-5 triple-phase composite at 2 µm magnification, illustrating flake or plate-like Sb-Ni-V_2O_5 particles with dimensions

ranging from 20 to 30 nm, as determined using ImageJ in accordance with prior reports [45]. In contrast, images 3(c–f) show SEM micrographs of the $V_{2-x}Ni_{2x}Sb_xO_{5-\delta}$/g-$C_3N_4$ heterostructures corresponding to $0.05 \leq x \leq 0.08$, recorded at a higher magnification of 1 µm.

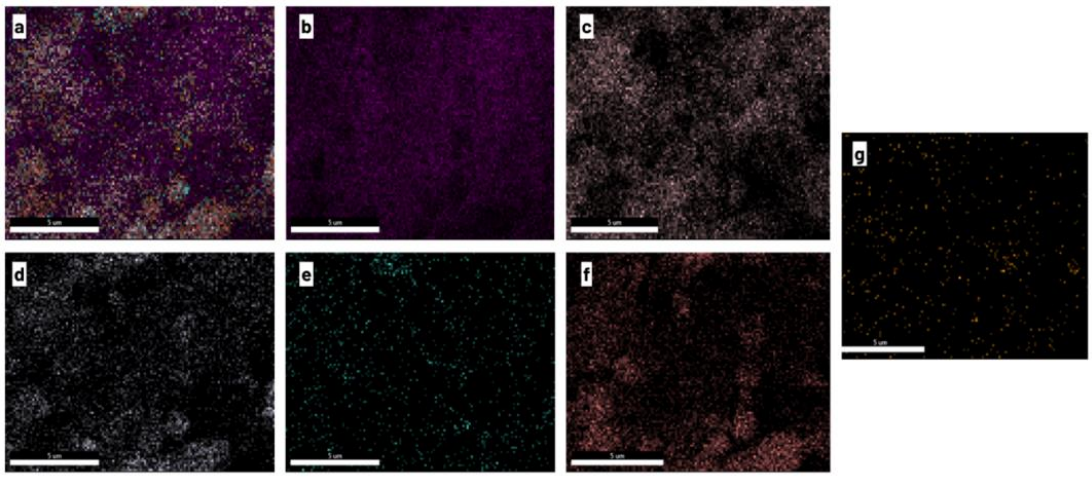

Fig.6.4(a-g) representing the elemental overlay image of Sb-Ni-V_2O_5/g-C_3N_4-5, Carbon, Nitrogen, Oxygen, Antimony, Vanadium, and Nickel, respectively

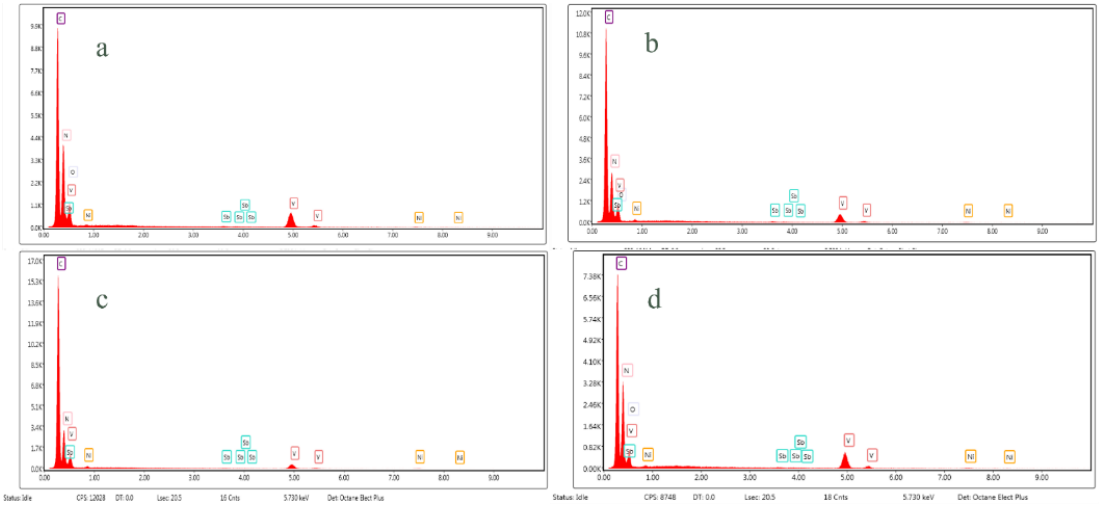

Figure. 6.5(a-d) reveals the EDS spectrum representing the presence of Sb, Ni, V, O, C, and N elements in $V_{2-x}Ni_{2x}Sb_xO_{5-\delta}$ / C_3N_4 heterostructures for $0.05 \leq x \leq 0.08$

The presence of both Sb-Ni-V_2O_5 and g-C_3N_4 in the newly formed heterostructure composites was analyzed through elemental mapping, which revealed the elemental composition and uniform distribution of constituent atoms. The elemental mapping for the selected region in the $V_{2-x}Ni_{2x}Sb_xO_{5-\delta}$/g-$C_3N_4$ composite at

x = 0.05, as shown in Figure. 6.4 (a–g), indicates a consistent spatial distribution of Sb, Ni, V, O, C, and N elements, respectively, throughout the sample

This uniform dispersion confirms the close integration of the Sb–Ni–V_2O_5 phase within the g–C_3N_4 matrix, which facilitates the formation of well-coupled heterojunction architectures. Additionally, energy-dispersive X-ray spectroscopy provides further support for the elemental composition of the heterostructures, clearly verifying the presence of all constituent elements Sb, Ni, V, O, C, and N in the synthesized composites for the range $0.05 \leq x \leq 0.08$, as in figure 6.5(a-d) [63]. Table 6.1 summarizes the elemental composition of the $V_{2-x}Ni_{2x}Sb_xO_{5-\delta}$/g-$C_3N_4$ heterostructures ($0.05 \leq x \leq 0.08$) as determined by EDS analysis, confirming the successful incorporation of vanadium, nickel, antimony, oxygen, carbon, and nitrogen in stoichiometric proportions within the synthesized compounds.

Table 6.1: Elemental Constituents of $V_{2-x}Ni_{2x}Sb_xO_{5-\delta}$/g-$C_3N_4$ compounds obtained from the EDS spectrum

$V_{2-x}Ni_{2x}Sb_xO_{5-\delta}$/g-$C_3N_4$	**x=0.05**		**x=0.06**		**x=0.07**		**x=0.08**	
Constituent Elements	Wt %	At%	Wt %	At %	Wt %	At%	Wt %	At %
Sb	0.78	0.11	1.04	0.95	1.52	1.12	1.67	1.39
Ni	0.57	0.16	1.70	0.42	1.96	0.98	2.05	1.45
V	23.52	7.67	19.15	6.26	17.67	6.12	14.87	5.49
O	13.22	13.73	15.03	13.98	19.41	17.67	19.56	19.33
C	24.67	34.14	27.97	35.41	26.35	36.66	26.08	31.56
N	37.24	44.19	35.11	42.98	33.09	37.45	35.77	40.78

6.3.4. X-ray photoelectron spectroscopy (XPS)

The chemical bonding interactions among vanadium, nickel, antimony, carbon, and nitrogen can be analyzed by deconvoluting the core-level XPS spectra, specifically the V*2p*, Ni*2p*, Sb*3d*, C*1s*, and N*1s* regions into Gaussian-shaped components, as shown in the Figure 6.6. The binding energy of the V*2p* core level in the $V_{2-x}Ni_{2x}Sb_xO_{5-\delta}$/g-$C_3N_4$ heterostructure is strongly influenced by the oxidation state of vanadium cations. Therefore, curve fitting of the V*2p* XPS signal serves as a reliable method to identify the different oxidation states of vanadium present in the

oxide matrix. The binding energy of the V*2p* core level is influenced by the oxidation state of the vanadium cation in $V_{2-x}Ni_{2x}Sb_xO_{5-\delta}$/g-$C_3N_4$ heterostructures, making curve fitting of the V*2p* signal an effective approach to identifying various vanadium oxidation states present in vanadium oxides. By employing a V_2O_5 reference, it is demonstrated that incorporating the O*1s* signal is crucial for accurate determination of the Shirley background, as the proximity of the O1s signal to the V$2p_{1/2}$ signal significantly influences the background associated with the V*2p* spectrum. The spectra revealed three distinct peaks at 515.5, 516.9, and 517.7 eV, with corresponding FWHM values of 1.3, 3.2, and 1.01 eV, respectively, which were attributed to the V^{4+}, V^{5+}, and V^{3+} oxidation states of vanadium. Notably, these binding energy values were higher than those reported in the literature. However, the Δ value for the V^{5+} oxidation state was determined to be 12.6 eV, consistent with the findings of Mendialdua et. al. [58-60]. The V$2p_{1/2}$ components, exhibiting energies of 525.04 eV and 523.53 eV, can be similarly characterized [61].

The presence of oxygen species within the V_2O_5 lattice is further substantiated by the deconvolution of the O*1s* XPS spectrum, as illustrated in Figure 6.6(a). The spectrum reveals distinct peaks centered at binding energies of 529.8, 530.68, and 532.01 eV. The first peak at 529.8 eV is attributed to lattice oxygen (O^{2-}) bonded to vanadium in the V_2O_5 framework, while the second component at 530.68 eV corresponds to surface hydroxyl groups (C-OH). The third peak, positioned at 532.01 eV, is generally ascribed to physisorbed molecular water or oxygen atoms involved in O-C bonding environments [62-63]. Additionally, the C*1s* spectrum exhibits characteristic peaks within the binding energy range of 282–288 eV, indicating the presence of various carbon–oxygen bonding configurations, further supporting the interaction between carbon and oxygen species on the material's surface. The peak with the highest intensity is observed at 286 eV, which is associated with the C=O bond [64]. As shown in Figure 6.6(b), the deconvoluted C*1s* spectrum shows peaks at 282.5 eV, 284.2 eV, 286.2 eV, and 287.8 eV, attributed to C=C, C=N (N-sp^2 C type, a defect-containing sp^2 hybridized carbon), C–N (N-sp^3 C configurations, sp^3-hybridized carbon atoms), and C–O bonds, respectively [65].

Further insights are obtained from the high-resolution analysis of the N*1s* spectrum, which has been deconvoluted to show distinct peaks. Notably, the N*1s* spectrum exhibits three peaks, with the most prominent ones located at binding energies of 395.2 eV and 399.7 eV as in figure 6.6(c). These peaks are attributed to the chemical states corresponding to C–N or C≡N bonds and C=N bonds, respectively.

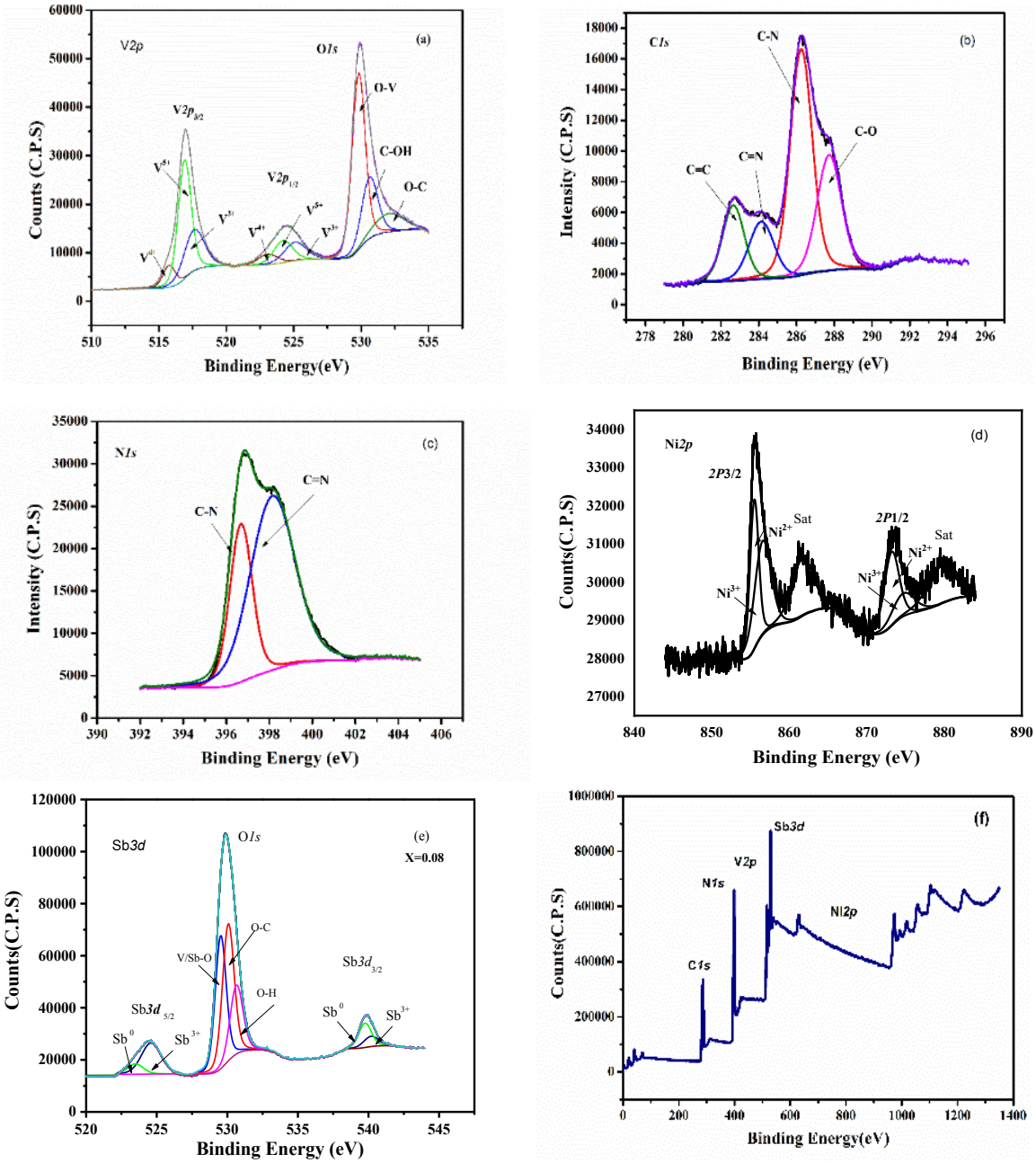

Figure 6.6 : High-resolution XPS spectra of (a) V2p (b)C1s (c)N1s (d)Ni2p (e)Sb 3d and (f) Survey spectrum in $V_{2-x}Ni_{2x}Sb_xO_{5-d}$/g-$C_3N_4$ heterostructure for x=0.08

This observation suggests the presence of well-defined chemical bonding environments for nitrogen in the material, which could significantly influence its structural, chemical, and functional properties [66]. Figure 6.6(d) focuses on the Ni*2p* region, providing insights into the chemical state of nickel in the sample. Two significant peaks are identified at binding energies of approximately 855.5 eV and 873.1 eV, which correspond to the Ni$2p_{3/2}$ and Ni$2p_{1/2}$ spin-orbit components, respectively. These peak locations are indicative of Ni^{2+} species, implying that Ni predominantly exists in the +2 oxidation state [67-68]. Alongside the primary peaks, distinct satellite features are observed near 861 eV and 879 eV, which suggest a high-spin Ni^{2+} configuration typically associated with NiO or Ni-substituted oxides. The lack of a peak around 852.6 eV confirms the absence of metallic Ni^{0}. The clear detection of these satellite peaks reinforces the conclusion that nickel is in an oxidized state, likely integrated into the oxide matrix, which may affect the electronic and optical properties of the material. Figure 6.6(e) presents the XPS spectrum within the binding energy range of 520-545 eV, providing detailed insights into the oxidation states and chemical environments of antimony (Sb) and oxygen (O) in the sample. The spectrum reveals distinct peaks corresponding to the Sb *3d* and O*1s* regions. The Sb$3d_{5/2}$ and Sb$3d_{3/2}$ peaks indicate the presence of both Sb^{3+} and Sb^{0} states, suggesting a mixed-valence environment that is commonly observed in doped or non-stoichiometric oxides [69-70].

The O*1s* region exhibits multiple components, a prominent peak around 530.0 eV corresponds to lattice oxygen (metal–oxygen bonds such as V-O or Sb-O), while peaks near 531.5 eV and 532.5 eV are attributed to surface hydroxyl (O–H) groups and carbonate or organic oxygen species (O-C), respectively. These characteristics indicate surface adsorption of moisture and carbon dioxide, resulting in the formation of hydroxylated and carbonate compounds [71-72]. Survey scan spectrum, as illustrated in Figure 6.6(f), the survey spectrum clearly indicates the presence of vanadium, antimony, carbon, nitrogen and nickel elements.

6.3.5. Optical Analysis: UV- Visible Spectroscopy

The optical absorption characteristics of the synthesized materials were examined through UV–Visible diffuse reflectance spectroscopy (UV–Vis DRS), with the resulting absorption profiles depicted in Figure 6.7(a). The bulk *g*-C_3N_4 exhibits a characteristic absorption edge around 440 nm, consistent with its semiconducting nature and direct band gap transition. This absorption feature originates from π–π* transitions within the sp^2-hybridized aromatic C–N framework.

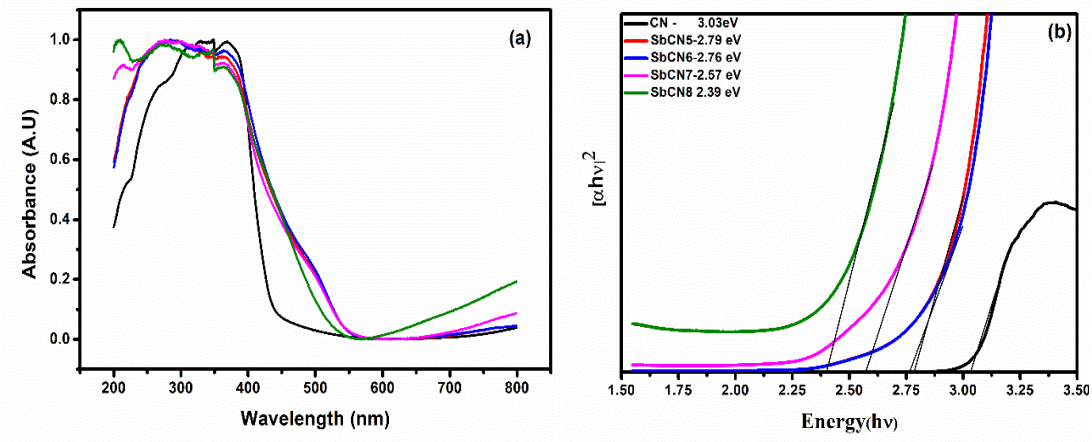

Figure. 6.7(a). Absorbance spectrum and (b)Tauc plot of pure g-C_3N_4 and $V_{2-x}Ni_{2x}Sb_xO_{5-d}$/g-$C_3N_4$ heterostructures

Upon photoexcitation, electrons are promoted from the valence band (VB), primarily composed of N*2p* orbitals, to the conduction band (CB) consisting of C*2p* orbitals, facilitating efficient charge separation under visible light. In contrast, $V_{2-x}Ni_{2x}Sb_xO_{5-\delta}$/g-$C_3N_4$ heterostructures for $0.05 \leq x \leq 0.08$ display significant redshifts in their absorption edges compared to pristine *g*-C_3N_4, extending up to approximately 560 nm, as seen in Figure. 6.7(a). This shift is attributed to the synergistic electronic interaction between *g*-C_3N_4 and the multi-cation incorporated vanadium pentoxide species, which enhances visible light harvesting. A noticeable darkening in sample color, from light yellow (*g*-C_3N_4) and greenish-yellow (Sb-Ni-V_2O_5) to dark grey in the heterostructures, further corroborates the spectral shift. Additionally, the intensity of absorption in the visible region increases progressively with increasing dopant concentration, confirming improved solar responsiveness due to the formation of interfacial charge-transfer complexes. These observations

collectively indicate that all synthesized heterostructures possess strong absorption in the visible region, enabling their potential as efficient photocatalysts under solar illumination [38-39], [50]. To estimate the optical band gap energies of the as-synthesized compounds, Tauc plots were constructed based on the Kubelka–Munk-transformed reflectance data. For direct band gap semiconductors, the optical band gap (Eg) is evaluated using the Tauc relation given by equation 3 [11].

$$(\alpha h\nu) = C(h\nu - Eg)^n \quad (3)$$

In this context, α denotes the absorption coefficient, h represents Planck's constant, ν is the frequency of the incident light, and C is a material-specific proportionality constant. For direct allowed electronic transitions, the exponent n takes a value of ½. The optical band gap energy was estimated by extrapolating the linear portion of the Tauc plot, i.e., $(\alpha h\nu)^2$ versus photon energy (hν), to the intercept on the energy axis where $(\alpha h\nu)^2$ approaches zero, as illustrated in Figure 6.7(b) [38], [50], [55]. The estimated band gap of pristine *g*-C_3N_4 from the Tauc plot is 3.03 eV, which is within the expected range (2.7–3.0 eV) for samples synthesized from urea under various processing conditions, including calcination temperature, atmosphere, and precursor choice [50]. The band gap of pure Sb-Ni-V_2O_5-5 has been reported as approximately 2.2 eV [47]. A systematic reduction in the optical band gap was observed for the $V_{2-x}Ni_{2x}Sb_xO_{5-\delta}$/g-$C_3N_4$ heterostructures with increasing dopant concentration, with values decreasing from 2.79 eV at x = 0.05 to 2.76 eV (x = 0.06), 2.57 eV (x = 0.07), and reaching 2.39 eV at x = 0.08 (Table 6.3). This trend indicates enhanced band alignment and charge transfer interactions between the two components, leading to narrowed band gaps and improved visible-light activity. Similar observations were made by S.M. Saleh *et al.* [48], who reported a reduction in band gap from 2.84 to 2.41 eV upon incorporation of V_2O_5 nanoparticles into *g*-C_3N_4 matrices.

6.3.6. Photoluminescence Spectroscopy

Photoluminescence (PL) spectroscopy is commonly utilized to evaluate the charge carrier dynamics, specifically the separation efficiency and recombination behavior of photoexcited electron–hole pairs in heterojunction-based photocatalysts. Generally, a lower PL signal indicates a higher efficiency of photo-induced electron–

hole pair separation. In this study, PL measurements were conducted to examine the electron–hole separation process in Sb-Ni-V_2O_5/g-C_3N_4 samples, with all samples excited using a laser at a wavelength of 360 nm [57]. Figure 6.8 illustrates the PL emission spectra of the synthesized photocatalysts. Pristine g-C_3N_4 exhibits a distinct emission peak centered around 420 nm, which is indicative of its intrinsic band-to-band recombination process. This emission corresponds to an optical band gap of approximately 3.0 eV, as determined from Tauc plot analysis in Figure 6.7(b).

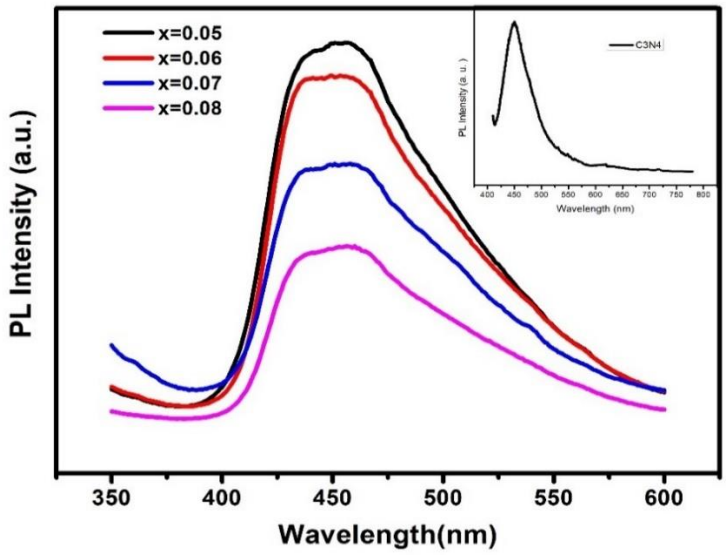

Figure 6.8. Photoluminescence spectrum of $V_{2-x}Ni_{2x}Sb_xO_{5-\delta}$ /g-C_3N_4 heterostructures for $0.05 \leq x \leq 0.08$ and pristine g-C_3N_4(inset)

This emission is attributed to the band-to-band PL phenomenon, where the emitted photon's energy closely matches the band gap energy of g-C_3N_4 [55]. The pronounced photoluminescence (PL) intensity observed in pristine g-C_3N_4 reflects a high rate of radiative recombination of photogenerated electron–hole pairs, with an intensity nearly fourfold higher than that of the Sb–Ni–V_2O_5/g-C_3N_4 heterostructures. In contrast, the heterostructured composites exhibit a marked decrease in PL intensity with increasing Ni and Sb content, suggesting a significant suppression of charge carrier recombination. This reduced PL intensity signifies improved charge carrier separation, crucial for enhanced photocatalytic efficiency. Notably, the Sb–Ni–V_2O_5/g-C_3N_4-8 composite displays the weakest PL emission, corresponding to a narrowed band gap of 2.37 eV. This significant fluorescence quenching reflects effective suppression of electron-hole recombination and efficient interfacial charge

transfer to the catalyst surface [73]. The marked suppression of radiative recombination arises from efficient charge transfer across the heterojunction, facilitated by strong electronic interactions between the integrated phases. This behavior supports a direct Z-scheme mechanism, enhancing carrier lifetimes and redox capability. Consequently, the Sb–Ni–V_2O_5/g-C_3N_4 system exhibits superior photocatalytic performance under visible light compared to pure g-C_3N_4 [38], [73].

6.3.7 Photocatalytic performance

The photocatalytic performance of the synthesized Sb–Ni–V_2O_5/g-C_3N_4 heterostructures was assessed via the degradation of Methylene Blue (MB) under sunlight for 60 minutes. Negligible self-degradation of MB in the absence of a catalyst confirms the necessity of a photocatalyst for effective photodegradation. Figure 6.9(a) presents the time-resolved UV–Visible absorption spectra of MB during its degradation using the Sb–Ni–V_2O_5/g-C_3N_4-5 heterostructure. The characteristic absorption peak intensity at 664 nm markedly diminishes with prolonged irradiation, indicating efficient photocatalytic activity under visible light. This progressive attenuation indicates effective photodegradation of the dye, with approximately 75% degradation achieved after 60 minutes of exposure, confirming the photocatalytic efficiency of the material.

The adsorption performance of all samples was evaluated in the dark for 60 minutes prior to light irradiation, as illustrated in Figure 6.9(b). The results showed that the adsorption equilibrium was nearly achieved within 40 minutes. Furthermore, increasing the Sb and Ni content in V_2O_5 enhanced the adsorption capacity of the resulting Sb-Ni-V_2O_5/g-C_3N_4 heterojunction photocatalysts compared to pure g-C_3N_4. This improved adsorption facilitates more effective interaction between MB molecules and the photocatalyst surface, thereby promoting enhanced photocatalytic activity. As expected, all Sb-Ni-V_2O_5/g-C_3N_4 composites exhibited improved photocatalytic activities than the pure C_3N_4 and Sb-Ni-V_2O_5 as shown in Figure 6.9(b). Figure 6.9(c) depicts the bar diagram illustrating the percentage of dye removal by V_2O_5, g-C_3N_4, and $V_{2-x}Ni_{2x}Sb_xO_{5-\delta}$/g-$C_3N_4$ composites (for $0.05 \leq x \leq 0.08$) under visible light irradiation, comparing degradation efficiencies at 30-minute

and 60-minute time intervals. Compared to V_2O_5 and Sb-Ni-V_2O_5, pure g-C_3N_4 demonstrated higher photocatalytic activity, likely due to its larger specific surface area and increased number of active sites (Fig. 6.9c).

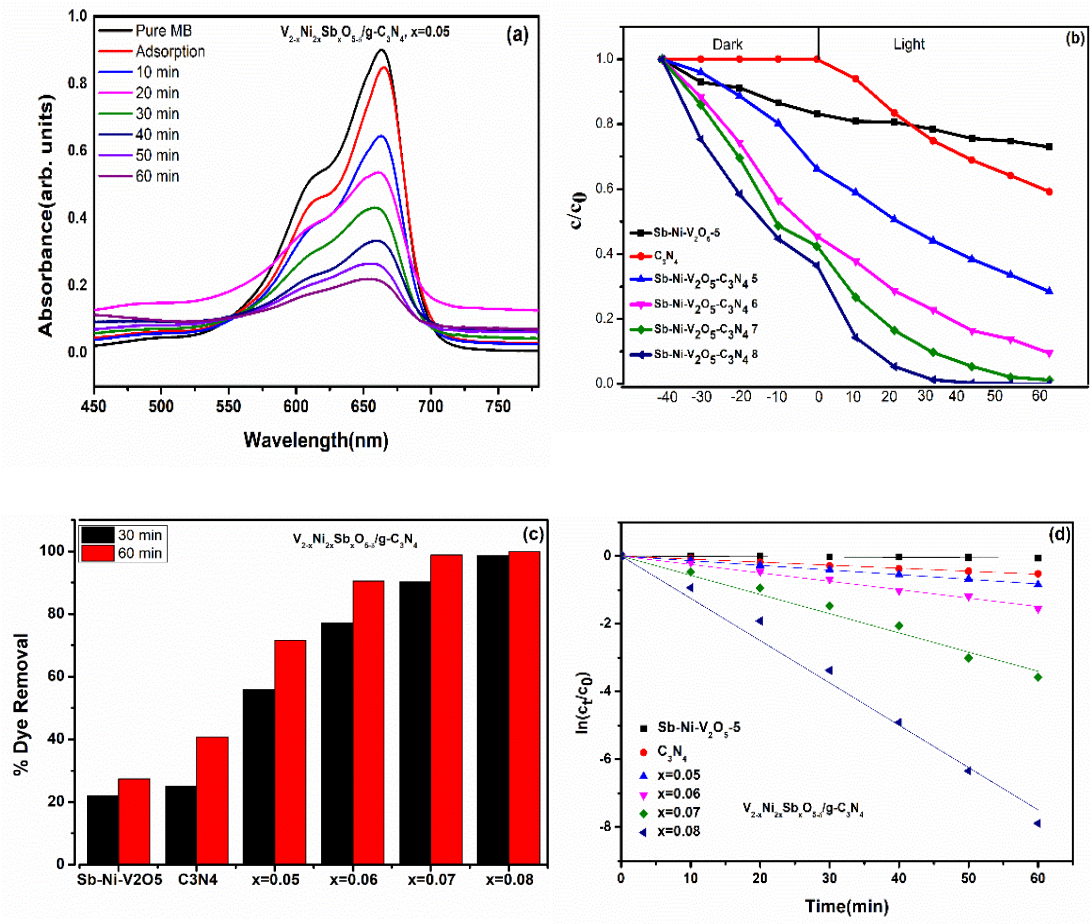

Fig.6.9. a) UV–Vis absorption spectra of methylene blue (MB) solution during photodegradation using Sb–Ni–V_2O_5/C_3N_4-5 under visible light irradiation. b) The photodegradation performance of the photocatalyst and its precursors for MB dye degradation. c)Bar Diagram depicting % Dye removal and d) Pseudo-first-order reaction kinetics of Sb-Ni-V_2O_5, C_3N_4, $V_{2-x}Ni_{2x}Sb_xO_{5-\delta}$ /g-C_3N_4 compounds for 0.05 ≤ x ≤ 0.08

The enhanced photocatalytic performance of the composite materials can be attributed to the efficient separation of photogenerated electron–hole pairs facilitated by the formation of heterojunctions between Sb-Ni-V_2O_5 and g-C_3N_4. Additionally, the photocatalytic activity of the composites improved with increasing Sb and Ni content, with the $V_{2-x}Ni_{2x}Sb_xO_{5-\delta}$/g-$C_3N_4$ composite achieving optimal performance at a mole fraction of $x = 0.08$. This suggests that an optimal Sb and Ni doping level is

crucial for maximizing photocatalytic efficiency. The degradation kinetics of MB by the synthesized photocatalysts were analyzed using a pseudo-first-order model, represented by the equation $\ln(C/C_0) = -kt$, where k is the rate constant, C_0 is the initial MB concentration, and C is the concentration at time t (Fig. 6.9. d) [48], [74]. The k value can be determined by a linear fit of the plot of $\ln (C/C_0)$ versus reaction time (t) [75]. As shown in the bar diagram in Figure. 6.10, the determined k values for MB degradation are 0.000949, 0.00895, 0.01372, 0.02483, 0.05669, 0.12485 for Sb-Ni-V_2O_5, C_3N_4, $V_{2-x}Ni_{2x}Sb_xO_{5-}$ /g-C_3N_4 heterostructures for $0.05 \leq x \leq 0.08$, respectively.

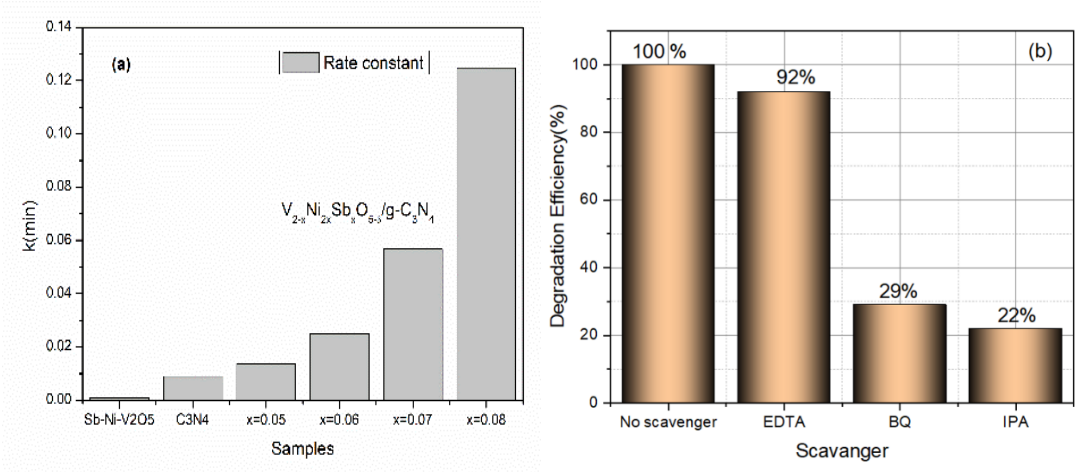

Figure 6.10(a). Rate constants for MB degradation (b). Reactive species trapping experiments for the Sb–Ni–V_2O_5/g-C_3N_4-8 photocatalyst showing dye removal efficiency after 1 hour of visible light irradiation.

Among the heterostructures, the sample with x=0.08 exhibited the highest rate constant for MB degradation, surpassing that of Sb-Ni-V_2O_5 and g-C_3N_4 by approximately 132 and 14 times, respectively. This substantial improvement highlights the synergistic effect of the heterojunction structure, revealing that the formation of the heterostructure greatly influences the photocatalytic performances of the composites [39], [76]. Table 6.2 presents a comparative analysis of the photocatalytic performance of the synthesized heterostructures with previously reported studies. The Sb–Ni–V_2O_5/g-C_3N_4 heterostructure completely degraded MB within 30 min using only 10 mg of catalyst, achieving the shortest reaction time with the lowest catalyst dosage reported to date.

Table. 6.2. Comparison of photocatalytic performance of V_2O_5 and g-C_3N_4-based heterostructures.

SL. No.	Photocatalyst	Name and Concentration of pollutants	Volume of pollutant	Amount of catalyst	Degradation %	Light Source	Illumination Time	Ref
1.	Sb–Ni–V_2O_5/g-C_3N_4-8	Methylene Blue 10mg/L	50 ml	10mg	100%	Sunlight	30 minutes	Present work
2.	C_3N_4(60.3%) /V_2O_5	Rhodamine-B 10mg/L	50 ml	50 mg	100%	200W Xenon Lamp	80 minutes	[55]
3.	C_3N_4/V_2O_5(1.0%)	Rhodamine-B Methylene Blue 10mg/L	100ml	50 mg	100%	250 W Xenon lamp	60 minutes (RhB) 120 minutes (MB)	[38]
3.	VO/CN	Rhodamine B 10 mg/L	100 ml	-	100%	Xenon Lamp	60 minutes	[16]
4.	V_2O_5@g-C_3N_4	Rhodamine B 25 ml/L		75 mg	93.4%	UV radiation	60 minutes	[48]
6.	V_2O_5/g-C_3N_4/ZnO	Methylene Blue 20mg/L	100 ml	50 mg	93.23%	300 W Xenon lamp	90 minutes	[77]
7.	MnV_2O_6/V_2O_5/g-C_3N_4	Methylene Blue 10mg/L	50 mL	50 mg	89%	Sun Lamp	30 minutes	[76]
8.	V_2O_5(4%)/g-C_3N_4	Congo Red 20 mg/L	50 ml	50 mg	99.8%	Sun light	90 minutes	[39]

6.3.8. Scavenger testing

Active species trapping experiments were initially conducted to elucidate the enhanced photocatalytic mechanism underlying MB degradation over pure g-C_3N_4, Sb-Ni-V_2O_5, and $V_{2-x}Ni_{2x}Sb_xO_{5-\delta}$/g-$C_3N_4$ heterostructures within the compositional range $0.05 \leq x \leq 0.08$ [3]. The intimate coupling within the Sb-Ni-V_2O_5/g-C_3N_4 heterostructure facilitates efficient electron transfer across the interface while suppressing recombination of photoinduced charge carriers. In photocatalytic systems, holes (h^+), hydroxyl radicals, and superoxide radicals typically drive the degradation of organic pollutants. To identify the dominant reactive species, isopropyl alcohol, ethylenediaminetetraacetic acid and p-benzoquinone were employed as scavengers for •OH, h^+, and $•O_2^-$, respectively. Under scavenger-free conditions, the g-C_3N_4/Sb-Ni-V_2O_5-8 photocatalyst achieved maximum methylene blue degradation

under visible light within 30 minutes. Prior studies confirm that •OH and $•O_2^-$ play a crucial role in the degradation pathways of C_3N_4 and V_2O_5/g-C_3N_4 heterostructures [78-81]. As illustrated in Figure 6.10(b), the introduction of EDTA (a hole scavenger) had minimal impact on the photocatalytic performance of the $V_{2-x}Ni_{2x}Sb_xO_{5-\delta}$ /g-C_3N_4-8 composite, with MB degradation remaining at 92 % compared to 100 % in the absence of scavengers. However, the addition of p-benzoquinone, a superoxide radical scavenger, led to a 29 % reduction in degradation efficiency, highlighting the significant role of $•O_2^-$ in the process. Similarly, incorporating isopropyl alcohol as a hydroxyl radical scavenger caused a sharp decline in MB degradation to 22 %, indicating that •OH is a primary reactive species. These results confirm that both $•O_2^-$ and •OH play pivotal roles in the photocatalytic degradation mechanism of the present heterostructure.

6.3.9 Discussion of catalytic reaction mechanism

The Sb-Ni-V_2O_5/g-C_3N_4-8 heterostructure demonstrates exceptional photocatalytic activity toward the degradation of MB dye, achieving complete (100%) degradation within a short contact time of 30 minutes under visible light irradiation. This superior performance is attributed to the efficient charge separation and enhanced redox potential provided by the Z-scheme charge transfer mechanism inherent to the heterostructure architecture. The absolute electronegativity of $V_{2-x}Ni_{2x}Sb_xO_{5-\delta}$ is estimated from the weighted arithmetic mean of Mulliken electronegativities for the heterostructures as given in Table 6.3 for all mol fractions [82-86]. The absolute electronegativity of g-C_3N_4 from previous reports is 4.73 [38], [87-89]. The conduction band and valence band edge positions were calculated using equations (4) and (5) [86], [39].

$$VB = \chi - E_e + 0.5 * E_g \quad (4)$$

$$CB = VB - E_g \quad (5)$$

χ = Absolute electronegativity of the semiconductor

E_e = Energy of free electrons on the hydrogen scale (approximately 4.5 eV)

E_g = Band gap energy of the semiconductor.

The $V_{2-x}Ni_{2x}Sb_xO_{5-\delta}$/g-$C_3N_4$ composite forms a direct Z-scheme interface, leveraging the staggered band positions of the two semiconductors. g-C_3N_4 has a CB at –1.27 eV and VB at +1.73 eV (vs. NHE), whereas at x=0.08, $V_{2-x}Ni_{2x}Sb_xO_{5-\delta}$ has a CB at +0.851 eV and VB at +3.071 eV (Table 6.3). In this alignment, the CB of g-C_3N_4 is much more negative (higher in energy) than that of Sb–Ni–V_2O_5, and the VB of Sb–Ni–V_2O_5 is much more positive (deeper in energy) than that of g-C_3N_4. These offsets drive a Z-scheme charge flow, photogenerated electrons on Sb–Ni–V_2O_5 (CB) tend to recombine with holes on g-C_3N_4 (VB), leaving the most energetic carriers on opposite side.

In effect, electrons remain in the highly reductive CB of g-C_3N4 (– 1.27 eV) and holes remain in the highly oxidizing VB of Sb–Ni–V_2O_5 (+3.071 eV). This preserves strong redox potentials, much like those reported for V_2O_5/g-C_3N_4 Z-schemes and greatly suppresses charge recombination [39]. Specifically, electrons from the conduction band of g-C_3N_4 reduce dissolved O_2 to form $\bullet O_2^-$. Thermodynamically, $O_2/\bullet O_2^-$ requires about –0.33 eV, and –1.27 eV is far more negative, so the reaction is strongly favored [16], [38], [73]. The VB holes of Sb–Ni–V_2O_5 (+3.071 eV) oxidize surface water or hydroxide to •OH. The standard potential for $\bullet OH/H_2O$ is 2.40 V vs. NHE and +3.071 eV greatly exceeds this [16], [38]. Thus, holes in Sb-Ni-V_2O_5 can oxidize H_2O or OH^- to •OH. Since g-C_3N_4's VB holes (+1.73 eV) are insufficient to generate •OH (1.73 < 2.40 eV), only the Sb-Ni-V_2O_5 VB holes produce •OH. Both $\bullet O_2^-$ and •OH are highly reactive ROS capable of decomposing MB dye.

Therefore, the favorable alignment of CB and VB edges in the Z-scheme system confirms the thermodynamic feasibility of ROS production, facilitating efficient visible-light-driven degradation of MB dye [76], [90]. Scavenger studies also confirm that •OH and $\bullet O_2^-$ dominate in this system. Once generated, $\bullet O_2^-$ and •OH rapidly attack the methylene blue (MB) dye, leading to its complete degradation [38]. The radicals oxidize the chromophore and aromatic rings of MB stepwise, ultimately mineralizing the dye to CO_2, H_2O, and inorganic ions. In general, •OH (a very strong oxidant) abstracts hydrogen atoms or adds to aromatic

C=C bonds, breaking conjugation in MB and forming intermediate radicals or quinone-like products. $\bullet O_2^-$ or its downstream products like H_2O_2 also oxidizes the dye or promotes further •OH generation (e.g. via $O_2^- + H^+ \rightarrow HO_2$, then $HO_2 + e^- \rightarrow OH^- + \bullet OH$) [38], [74]. Analogous Z-scheme systems of g-C_3N_4 coupled with a metal oxide have shown that MB and related dyes undergo rapid decolorization via $\bullet O_2^-$/•OH attack [38-39]. As both radicals are present in large amounts due to efficient Z-scheme separation, MB is fully degraded within 30 min under sunlight. Figure 6.11 presents the possible photocatalytic mechanism of Sb-Ni-V_2O_5/g-C_3N_4 heterojunction photocatalysts for the degradation of MB under solar light irradiation.

.

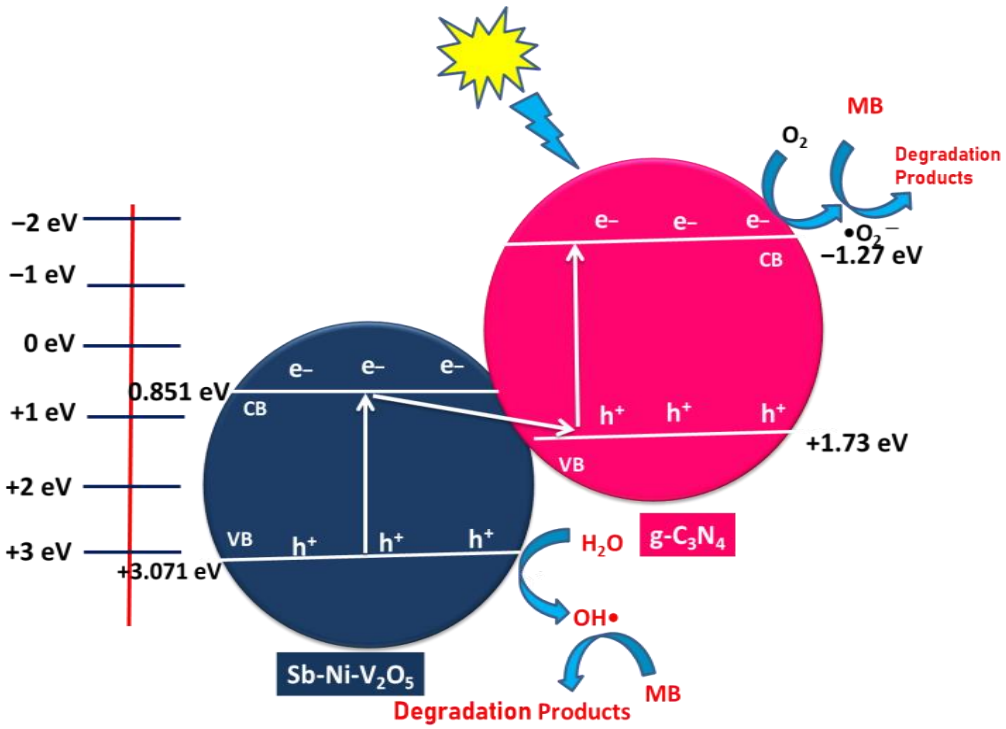

Figure. 6.11: The possible photocatalytic mechanism of Sb-Ni-V_2O_5/g-C_3N_4 heterojunction photocatalysts at x=0.08, for degradation of MB under solar light irradiation

The sequential equations (6) to (11) delineate the complete photocatalytic degradation mechanism of methylene blue (MB) facilitated by the Z-scheme Sb–Ni–V_2O_5/g-C_3N_4 heterojunction system.

*Table 6.3 presents the absolute electronegativity (χ), band gap energy (Eg), and the calculated valence band (E_{VB}) and conduction band (E_{CB}) edge potentials (vs. NHE) for each molar fraction (**x**) of the compound $V_{2-x}Ni_{2x}Sb_xO_{5-\delta}$, along with the corresponding values for g-C_3N_4.*

x	Absolute Electronegativity of $V_{2-x}Ni_{2x}Sb_xO_{5-\delta}$	Absolute Electronegativity of C_3N_4	Eg of $V_{2-x}Ni_{2x}Sb_xO_{5-\delta}$ *eV* [46]	g-C_3N_4		$V_{2-x}Ni_{2x}Sb_xO_{5-\delta}$		Eg of $V_{2-x}Ni_{2x}Sb_xO_{5-\delta}$/g-$C_3N_4$
				E_{VB} *eV*	E_{CB} *eV*	E_{VB} *eV*	E_{CB} *eV*	From the Tauc plot (*eV*)
0.05	6.440	4.73	2.28	1.73	-1.27	3.083	0.803	2.79
0.06	6.448	4.73	2.26	1.73	-1.27	3.080	0.820	2.76
0.07	6.452	4.73	2.24	1.73	-1.27	3.074	0.834	2.57
0.08	6.460	4.73	2.22	1.73	-1.27	3.071	0.851	2.39

$g\text{-}C_3N_4 + h\upsilon \longrightarrow e^- _{(CB,\ -1.27eV)} + h^+ _{(VB,\ +1.73eV)}$ (6)

$Sb\text{-}Ni\text{-}V_2O_5 + h\upsilon \longrightarrow e^- _{(CB,+0.851eV)} + h^+ _{(VB,+3.071eV)}$ (7)

$e^-(Sb\text{-}Ni\text{-}V_2O_5) + h^+(g\text{-}C_3N_4) \longrightarrow$ recombination *(Z-Scheme)* (8)

$e^-(g\text{-}C_3N_4) + O_2 \longrightarrow \cdot O_2 (E^o \approx -0.33\ eV:\ -1.27\ eV < -0.33\ eV)$ (9)

$h^+(Sb\text{-}Ni\text{-}V_2O_5) \longrightarrow \cdot OH + H^+ (E^o_{\cdot OH/H2O} = +2.40\ eV,\ VB = +3.071\ eV)$ (10)

$\cdot OH/\cdot O_2^- + MB \longrightarrow$ oxidized products $\longrightarrow CO_2 + H_2O +$ ions (11)

6.3.10. Cycling Stability

The long-term stability of heterostructured photocatalysts is crucial for their practical deployment in environmental remediation. To evaluate the durability of the $Sb\text{-}Ni\text{-}V_2O_5/g\text{-}C_3N_4$-heterostructure, cyclic photocatalytic degradation tests of MB were performed under sunlight irradiation, with each cycle lasting 30 minutes, as shown in Figure 6.12.

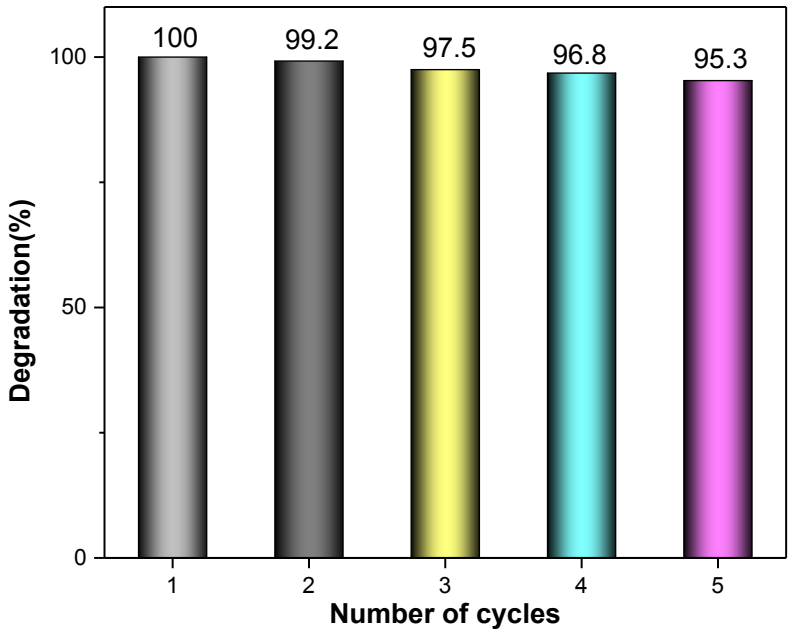

Figure. 6.12. Recyclability test of Sb–Ni–V_2O_5/g-C_3N_4-8 showing a slight reduction in MB degradation efficiency from 100% to 95.3% over five 30-minute sunlight irradiation cycles.

The results reveal that the degradation efficiency decreased only marginally from 100 % in the first cycle to 95.3 % by the fifth cycle, demonstrating excellent photocatalytic stability and reusability of the heterostructure over repeated use.

6.3.11. Visible light-induced antimicrobial applications of $V_{2-x}Ni_{2x}Sb_xO_{5-\delta}$/g-$C_3N_4$ heterostructures

The synthesized heterostructure exhibits pronounced photocatalytic antimicrobial activity with a sunlight illumination of 1 hour, via a Z-scheme charge transfer mechanism, augmented by multivalent cation synergy. Upon solar irradiation, as mentioned earlier, residual electrons in g-C_3N_4 reduce O_2 to $\bullet O_2^-$, while holes in Sb-Ni-V_2O_5 oxidize H_2O/OH^- to •OH. These reactive oxygen species inflict oxidative damage on microbial membranes, proteins, and nucleic acids, culminating in cell lysis. XPS analysis reveals the presence of multiple valence states like V^{5+}, V^{4+}, V^{3+}, Ni^{2+}, Ni^{3+}, and Sb^{3+} along with metallic Sb, indicating abundant defect sites and internal charge reservoirs. These multivalent centers serve as charge-transfer bridges and trap states that prolong charge separation.

Gram-negative pathogens like *E. coli*, *P. aeruginosa*, *V. harveyi,* and *V. cholerae* possess an additional outer membrane rich in lipopolysaccharide (LPS) and proteins. This LPS-layered envelope acts as a strong permeability barrier that protects against toxins and hydrophobic or charged agents [91]. However, the as-prepared photocatalyst still produced clear inhibition zones of 24 mm for *E. coli*, 16 mm for *P. aeruginosa*, 18 mm for *V. harveyi,* and 19 mm for *V. cholerae*, reflecting its antimicrobial effect despite this barrier for the heterostructures at mol fraction x=0.08 (fig. 6.13). These zone sizes suggest differences in susceptibility; for example, *P. aeruginosa* often exhibits stronger efflux and lower permeability, giving a smaller zone. Photocatalytically generated $\bullet O_2^-$ and •OH can inflict oxidative stress on the outer membrane and periplasm, damaging lipids and proteins. In addition, the Sb–Ni–V_2O_5/g-C_3N_4 surface carries positively charged metal centers as evident from XPS that electrostatically adhere to the negatively charged bacterial surface, including LPS and membrane phosphates [92]. Such adhesion concentrates the reactive species at the

membrane, enhancing cell envelope disruption in Gram-negatives despite their protective layer [93].

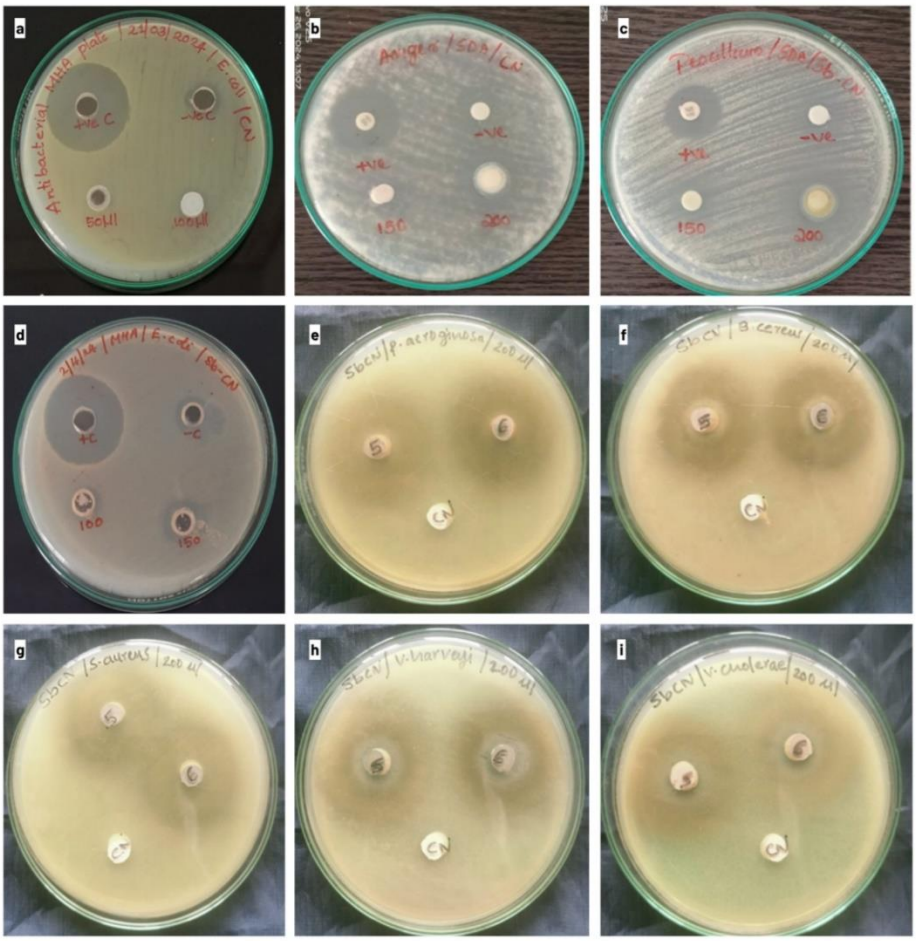

Figure.6.13(a-i). Representative images depicting microbial growth inhibition zones induced by Sb–Ni–V_2O_5/g-C_3N_4 heterostructures at x=0.08, against selected bacterial and fungal strains, compared to standard positive controls (streptomycin for bacteria, fluconazole for fungi) and a DMSO negative control, (a)g-C_3N_4: E.Coli(50 & 100µl),(b)g-C_3N_4: A. Niger(150 & 200 µl),and Sb-Ni-V_2O_5/g-C_3N_4 against(c) Pencillium(150 & 200 µl), (d)A.Niger(100 &150 µl), e)P. Aeroginosa(200 µl) (f)B. Cereus(200 µl), (g)S. Aureus (200 µl) (h) V. Harveyi (200 µl), (i)V. Cholerae (200 µl)

Gram-positive bacteria like *S. aureus* and *B. cereus* lack an outer membrane, but feature a thick peptidoglycan (PG) layer interwoven with teichoic acids. These teichoic acids are linear polyphosphate polymers that impart a strong negative charge to the cell surface [91]. The dense PG mesh provides rigidity but is relatively porous to ROS compared to a Gram-negative outer membrane. As a result, gram-positives tend to be more vulnerable to oxidative attack. Sb–Ni–V_2O_5/g-C_3N_4 at mol fraction

x=0.08, showed large inhibition zones of 22 mm for *S. aureus* and 18 mm for *B. cereus*, indicating effective killing (Fig. 6.13). The combination of strong oxidative radicals and metal interactions is important, ie, the cationic dopants on the photocatalyst surface bind tightly to the anionic gram-positive wall [94]. This enhances adhesion of the photocatalyst and localizes •OH production at the cell wall. Once localized, •OH can peroxidize the PG and membrane lipids, while $\bullet O_2^-$ causes additional oxidative damage. In sum, the negative teichoic-acid-rich wall of Gram-positives favors attraction of V^{5+}, V^{4+}, V^{3+}, Ni^{2+}, Ni^{3+}, Sb^{3+} sites on the catalyst, and the ensuing ROS-induced lipid and protein oxidation overwhelms the bacteria, leading to the observed high susceptibility.

Table 6.4. ZOI values (in mm) for Gram-positive bacteria, Gram-negative bacteria, and fungi treated with Sb–Ni–V_2O_5/g-C_3N_4 compound at 50, 100, 150, and 200 µL concentrations, including positive and negative controls

SI. No.	Name of Bacteria/Fungus	50 µl	100 µl	150 µl	200 µl	+ve	-ve
7.	*Escherichia coli*	R	13	18	24	23	7
8.	*Staphylococus aureus*	12	14	18	22	25	7
9.	*Pseudomonas aeroginosa*	R	13	14	16	22	7
10.	*Bacillus cereus*	R	15	17	18	19	7
11.	*Vibrio harveyi*	R	12	15	18	19	7
12.	*Vibrio cholerae*	R	13	16	19	19	7
13.	*Pencillium*	R	R	12	17	20	7
14.	*Aspergillus niger*	R	R	15	21	23	7

A multilayered wall of polysaccharides and glycoproteins encloses fungal cells, such as those of *Penicillium sp*. and *Aspergillus niger*. The inner core is a covalently linked matrix of branched β-1,3-glucans and chitin, overlaid by an outer layer of glycoproteins [94-95]. This network provides structural strength and some barrier function, but it is permeable to small reactive species. Photogenerated •OH radicals, in particular, are highly damaging and they abstract hydrogen from lipids and carbohydrates, initiating lipid peroxidation and cleavage of cell-wall polysaccharides. Experimentally, though the disc diffusion method, Sb–Ni–V_2O_5/g-C_3N_4 produced measurable antifungal inhibition of 17 mm zone for *Penicillium* and 21 mm for *A.*

niger, indicating moderate susceptibility for mol fraction x=0.08. The larger effect on *A. niger* may reflect differences in wall thickness or surface properties.

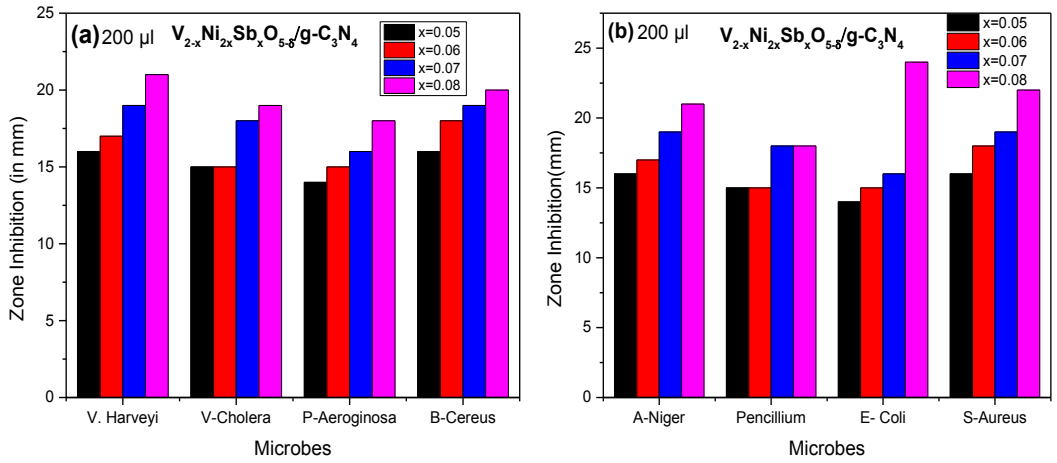

Figure 6.14. a & b. Comparative bar charts illustrating the antimicrobial efficacy of Sb–Ni–V_2O_5/g-C_3N_4 heterostructures with varying mol fraction x ($0.05 \leq x \leq 0.08$), assessed through zone of inhibition measurements (mm) at a standardized dose of 200 µL encompassing activity against gram-positive and gram-negative bacterial strains and fungal species.

Here also •OH attacks fungal membranes and wall components, causing membrane rupture and leakage. Overall, the photocatalytic •OH and $\bullet O_2^-$ disrupt fungal hyphae and inhibit growth, even though fungal walls lack LPS. Figure 6.14(a&b) displays comparative bar graphs illustrating the antimicrobial performance of Sb–Ni–V_2O_5/g-C_3N_4 heterostructures with varying dopant concentrations ($0.05 \leq x \leq 0.08$), evaluated via zone of inhibition (ZOI) measurements in millimeters at a fixed dosage of 200 µL. Table 6.4 shows the measured ZOI, in mm, against Gram-positive and Gram-negative bacteria, as well as fungal strains, for Sb–Ni–V_2O_5/g-C_3N_4 composite at varying concentrations (50, 100, 150, and 200 µL), alongside standard positive and negative controls [45].

6.4. Conclusion

The structural characterization by XRD confirmed that the $V_{2-x}Ni_{2x}Sb_xO_{5-\delta}$/g-$C_3N_4$ compounds for $0.05 \leq x \leq 0.08$ exhibited crystallinity of all constituent phases, with no impurity peaks detected, ensuring compositional uniformity and phase

integrity. The absence of the V_2O_5 (001) reflection at $x = 0.08$ suggests lattice rearrangement, while the retained (002) plane of g-C_3N_4 across all compositions validates the formation of a robust Z-scheme photocatalytic hybrid. The FTIR spectra of the Sb–Ni–V_2O_5/g-C_3N_4 heterostructures confirmed the presence of key functional groups from both constituents while indicating strong interfacial coupling. The formation of a nanoscale interface between the Sb–Ni–V_2O_5 and g-C_3N_4 components was validated by SEM, EDS, and elemental mapping, confirming uniform incorporation of all six elements and supporting the successful synthesis of a stoichiometrically stable multi-phase heterojunction system. The deconvoluted core-level XPS spectra revealed mixed valence states and well-defined bonding environments among V, Sb, Ni, C, N, and O, affirming the formation of a multi-cation, oxygen-deficient, and chemically integrated heterostructure conducive to enhanced electronic and photocatalytic behavior. Progressive Sb and Ni incorporation narrows the band gap of $V_{2-x}Ni_{2x}Sb_xO_{5-\delta}$/g-$C_3N_4$ from 3.03 eV to 2.39 eV, evidencing favorable heterojunction interfaces that enhance visible-light absorption and charge mobility. The pronounced PL quenching in Sb–Ni–V_2O_5/g-C_3N_4-8 confirms efficient direct Z-scheme charge transfer, extended carrier lifetimes, and suppressed recombination, optimizing photocatalytic performance. This Z-scheme heterostructure maximizes charge carrier separation and redox potential, thereby facilitating complete mineralization of methylene blue within a contact time of 30 minutes for mol fraction x=0.08, via synergistic action of $\bullet O_2^-$ and •OH radicals. The Sb–Ni–V_2O_5/g-C_3N_4 heterostructure demonstrates potent sunlight-driven antimicrobial activity via a Z-scheme charge transfer mechanism, wherein photogenerated •OH and $\bullet O_2^-$ radicals, augmented by surface-bound multivalent dopants, induce oxidative stress and structural disruption in a broad spectrum of bacterial and fungal pathogens.

References

[1] N. Serpone and A. V. Emeline, "Semiconductor Photocatalysis — Past, Present, and Future Outlook," *J. Phys. Chem. Lett.*, vol. 3, no. 5, pp. 673–677, Mar. 2012, doi: 10.1021/jz300071j.

[2] I. Ahmad *et al.*, "Semiconductor photocatalysts: A critical review highlighting the various strategies to boost the photocatalytic performances for diverse applications," *Adv. Colloid Interface Sci.*, vol. 311, p. 102830, Jan. 2023, doi: 10.1016/j.cis.2022.102830.

[3] R. C. Ngullie, S. O. Alaswad, K. Bhuvaneswari, P. Shanmugam, T. Pazhanivel, and P. Arunachalam, "Synthesis and Characterization of Efficient ZnO/g-C3N4 Nanocomposites Photocatalyst for Photocatalytic Degradation of Methylene Blue," *Coatings*, vol. 10, no. 5, p. 500, May 2020, doi: 10.3390/coatings10050500.

[4] S. Peiris, H. B. De Silva, K. N. Ranasinghe, S. V. Bandara, and I. R. Perera, "Recent development and future prospects of TiO_2 photocatalysis," *J. Chin. Chem. Soc.*, vol. 68, no. 5, pp. 738–769, May 2021, doi: 10.1002/jccs.202000465.

[5] Y. Sari, P. L. Gareso, B. Armynah, and D. Tahir, "A review of TiO2 photocatalyst for organic degradation and sustainable hydrogen energy production," *Int. J. Hydrog. Energy*, vol. 55, pp. 984–996, Feb. 2024, doi: 10.1016/j.ijhydene.2023.11.126.

[6] N. Roy and S. Chakraborty, "ZnO as photocatalyst: An approach to waste water treatment," *Mater. Today Proc.*, vol. 46, pp. 6399–6403, 2021, doi: 10.1016/j.matpr.2020.06.264.

[7] A. M. Al-Hamdi, U. Rinner, and M. Sillanpää, "Tin dioxide as a photocatalyst for water treatment: A review," *Process Saf. Environ. Prot.*, vol. 107, pp. 190–205, Apr. 2017, doi: 10.1016/j.psep.2017.01.022.

[8] K. Qi, S. Liu, and A. Zada, "Graphitic carbon nitride, a polymer photocatalyst," *J. Taiwan Inst. Chem. Eng.*, vol. 109, pp. 111–123, Apr. 2020, doi: 10.1016/j.jtice.2020.02.012.

[9] D. Bhanderi, P. Lakhani, and C. K. Modi, "Graphitic carbon nitride (g-C_3 N_4) as an emerging photocatalyst for sustainable environmental applications: a comprehensive review," *RSC Sustain.*, vol. 2, no. 2, pp. 265–287, 2024, doi: 10.1039/D3SU00382E.

[10] H. Li, Z. Zhang, Y. Liu, W. Cen, and X. Luo, "Functional Group Effects on the HOMO–LUMO Gap of g-C3N4," *Nanomaterials*, vol. 8, no. 8, p. 589, Aug. 2018, doi: 10.3390/nano8080589.

[11] S. P. Pattnaik, A. Behera, S. Martha, R. Acharya, and K. Parida, "Facile synthesis of exfoliated graphitic carbon nitride for photocatalytic degradation of ciprofloxacin under solar irradiation," *J. Mater. Sci.*, vol. 54, no. 7, pp. 5726–5742, Apr. 2019, doi: 10.1007/s10853-018-03266-x.

[12] M. Majdoub, D. Sengottuvelu, S. Nouranian, and A. Al-Ostaz, "Graphitic Carbon Nitride Quantum Dots (g-C_3 N_4 QDs): From Chemistry to Applications," *ChemSusChem*, vol. 17, no. 13, p. e202301462, July 2024, doi: 10.1002/cssc.202301462.

[13] M. Y. Emran *et al.*, "Tailored portable electrochemical sensor for dopamine detection in human fluids using heteroatom-doped three-dimensional g-C3N4 hornet nest structure," *Anal. Chim. Acta*, vol. 1320, p. 342985, Sept. 2024, doi: 10.1016/j.aca.2024.342985.

[14] E. V. Rosa *et al.*, "Carbon nitride nanosheets magnetically decorated with Fe3O4 nanoparticles by homogeneous precipitation: Adsorption-photocatalytic performance and acute toxicity assessment," *Environ. Nanotechnol. Monit. Manag.*, vol. 16, p. 100549, Dec. 2021, doi: 10.1016/j.enmm.2021.100549.

[15] M. A. Ahmed, S. A. Mahmoud, and A. A. Mohamed, "Unveiling the photocatalytic potential of graphitic carbon nitride (g-C_3 N_4): a state-of-the-art review," *RSC Adv.*, vol. 14, no. 35, pp. 25629–25662, 2024, doi: 10.1039/D4RA04234D.

[16] Y.-N. Zang *et al.*, "A biochar-promoted V_2 O_5 /g-C_3 N_4 Z-Scheme heterostructure for enhanced simulated solar light-driven photocatalytic activity," *RSC Adv.*, vol. 11, no. 25, pp. 15106–15117, 2021, doi: 10.1039/D1RA02712C.

[17] H. Tran Huu *et al.*, "One-pot synthesis of S-scheme MoS2/g-C3N4 heterojunction as effective visible light photocatalyst," *Sci. Rep.*, vol. 11, no. 1, p. 14787, July 2021, doi: 10.1038/s41598-021-94129-0.

[18] X. Jin, X. Fan, J. Tian, R. Cheng, M. Li, and L. Zhang, "MoS_2 quantum dot decorated g-C_3 N_4 composite photocatalyst with enhanced hydrogen evolution performance," *RSC Adv.*, vol. 6, no. 58, pp. 52611–52619, 2016, doi: 10.1039/C6RA07060D.

[19] N. Sujatha, M. Meenachi, S. M. Harshulkhanb, and H. H. Hegazy, "Design and fabrication of Ag3VO4/g-C3N4 heterostructure photocatalyst for enhanced visible light degradation of various organic pollutants," Mar. 29, 2021, *In Review*. doi: 10.21203/rs.3.rs-329610/v1.

[20] R. Manimozhi, M. Mathankumar, and A. P. G. Prakash, "Synthesis of g-C3N4 / ZnO heterostructure photocatalyst for enhanced visible degradation of organic dye," *Optik*, vol. 229, p. 165548, Mar. 2021, doi: 10.1016/j.ijleo.2020.165548.

[21] Z. Zhang, K. Liu, Z. Feng, Y. Bao, and B. Dong, "Hierarchical Sheet-on-Sheet ZnIn2S4/g-C3N4 Heterostructure with Highly Efficient Photocatalytic H2 production Based on Photoinduced Interfacial Charge Transfer," *Sci. Rep.*, vol. 6, no. 1, p. 19221, Jan. 2016, doi: 10.1038/srep19221.

[22] C. He, J. H. Zhang, W. X. Zhang, and T. T. Li, "Type-II InSe/ *g* -C_3 N_4 Heterostructure as a High-Efficiency Oxygen Evolution Reaction Catalyst for Photoelectrochemical Water Splitting," *J. Phys. Chem. Lett.*, vol. 10, no. 11, pp. 3122–3128, June 2019, doi: 10.1021/acs.jpclett.9b00909.

[23] H. Zhang, T. Ouyang, J. Li, M. Mu, and X. Yin, "Dual 2D CuSe/g-C3N4 heterostructure for boosting electrocatalytic reduction of CO2," *Electrochimica Acta*, vol. 390, p. 138766, Sept. 2021, doi: 10.1016/j.electacta.2021.138766.

[24] G. Liu *et al.*, "Enhanced removal and selective conversion for NO with N-vacancies g-C3N4\BaTiO3 by piezo-photocatalysis," *Sep. Purif. Technol.*, vol. 360, p. 130914, July 2025, doi: 10.1016/j.seppur.2024.130914.

[25] B. Shao *et al.*, "Nitrogen-Doped Hollow Mesoporous Carbon Spheres Modified g-C_3N_4 /Bi_2O_3 Direct Dual Semiconductor Photocatalytic System with Enhanced Antibiotics Degradation under Visible Light," *ACS Sustain. Chem. Eng.*, vol. 6, no. 12, pp. 16424–16436, Dec. 2018, doi: 10.1021/acssuschemeng.8b03480.

[26] J. Lv, K. Dai, J. Zhang, Q. Liu, C. Liang, and G. Zhu, "Facile constructing novel 2D porous g-C3N4/BiOBr hybrid with enhanced visible-light-driven photocatalytic activity," *Sep. Purif. Technol.*, vol. 178, pp. 6–17, May 2017, doi: 10.1016/j.seppur.2017.01.019.

[27] J. Li, H. Yuan, and Z. Zhu, "Improved photoelectrochemical performance of Z-scheme g-C3N4/Bi2O3/BiPO4 heterostructure and degradation property," *Appl. Surf. Sci.*, vol. 385, pp. 34–41, Nov. 2016, doi: 10.1016/j.apsusc.2016.05.065.

[28] R. Ye, H. Fang, Y.-Z. Zheng, N. Li, Y. Wang, and X. Tao, "Fabrication of $CoTiO_3$ /g-C_3N_4 Hybrid Photocatalysts with Enhanced H_2 Evolution: Z-Scheme Photocatalytic Mechanism Insight," *ACS Appl. Mater. Interfaces*, vol. 8, no. 22, pp. 13879–13889, June 2016, doi: 10.1021/acsami.6b01850.

[29] B. Zhu, P. Xia, Y. Li, W. Ho, and J. Yu, "Fabrication and photocatalytic activity enhanced mechanism of direct Z-scheme g-C 3 N 4 /Ag 2 WO 4 photocatalyst," *Appl. Surf. Sci.*, vol. 391, pp. 175–183, Jan. 2017, doi: 10.1016/j.apsusc.2016.07.104.

[30] N. Li *et al.*, "Z-scheme 2D/3D g-C3N4@ZnO with enhanced photocatalytic activity for cephalexin oxidation under solar light," *Chem. Eng. J.*, vol. 352, pp. 412–422, Nov. 2018, doi: 10.1016/j.cej.2018.07.038.

[31] J. Yan, H. Wu, H. Chen, Y. Zhang, F. Zhang, and S. F. Liu, "Fabrication of TiO2/C3N4 heterostructure for enhanced photocatalytic Z-scheme overall water splitting," *Appl. Catal. B Environ.*, vol. 191, pp. 130–137, Aug. 2016, doi: 10.1016/j.apcatb.2016.03.026.

[32] Y. Gong, X. Quan, H. Yu, S. Chen, and H. Zhao, "Enhanced photocatalytic performance of a two-dimensional BiOIO3/g-C3N4 heterostructured composite with a Z-scheme configuration," *Appl. Catal. B Environ.*, vol. 237, pp. 947–956, Dec. 2018, doi: 10.1016/j.apcatb.2018.06.060.

[33] J. Zhang, Y. Hu, X. Jiang, S. Chen, S. Meng, and X. Fu, "Design of a direct Z-scheme photocatalyst: Preparation and characterization of Bi2O3/g-C3N4 with high visible light activity," *J. Hazard. Mater.*, vol. 280, pp. 713–722, Sept. 2014, doi: 10.1016/j.jhazmat.2014.08.055.

[34] Y. Yang, W. Guo, Y. Guo, Y. Zhao, X. Yuan, and Y. Guo, "Fabrication of Z-scheme plasmonic photocatalyst Ag@AgBr/g-C3N4 with enhanced visible-light photocatalytic activity," *J. Hazard. Mater.*, vol. 271, pp. 150–159, Apr. 2014, doi: 10.1016/j.jhazmat.2014.02.023.

[35] S. H. Ammar, Y. R. Abdulmajeed, H. J. Khadim, Z. H. Jabbar, and E. M. Khudhair, "Rational assembly of Z-scheme FeTiO3/Fe-doped g-C3N4 photocatalytic heterojunctions: Photodegradation behavior and mechanism insight," *J. Water Process Eng.*, vol. 61, p. 105275, May 2024, doi: 10.1016/j.jwpe.2024.105275.

[36] A. Hamza and H. Alshamsi, "Novel Z-Scheme g-C3N4/TiO2/NiCo2O4 Heterojunctions for Efficient Photocatalytic Degradation of Rhodamine B under

Visible Light Irradiation," *J. Clust. Sci.*, vol. 35, no. 7, pp. 2539–2556, Oct. 2024, doi: 10.1007/s10876-024-02688-9.

[37] W. Muhammad *et al.*, "Construction of visible-light-driven 2D/2D NiFe2O4/g-C3N4 Z-scheme heterojunction photocatalyst for effective degradation of organic pollutants and CO2 reduction," *J. Environ. Chem. Eng.*, vol. 12, no. 5, p. 113409, Oct. 2024, doi: 10.1016/j.jece.2024.113409.

[38] Y. Hong *et al.*, "In-situ synthesis of direct solid-state Z-scheme V2O5/g-C3N4 heterojunctions with enhanced visible light efficiency in photocatalytic degradation of pollutants," *Appl. Catal. B Environ.*, vol. 180, pp. 663–673, Jan. 2016, doi: 10.1016/j.apcatb.2015.06.057.

[39] R. Dadigala, R. Bandi, B. R. Gangapuram, A. Dasari, H. H. Belay, and V. Guttena, "Fabrication of novel 1D/2D V2O5/g-C3N4 composites as Z-scheme photocatalysts for CR degradation and Cr (VI) reduction under sunlight irradiation," *J. Environ. Chem. Eng.*, vol. 7, no. 1, p. 102822, Feb. 2019, doi: 10.1016/j.jece.2018.102822.

[40] K. Yan, C. Mu, L. Meng, Z. Fei, and P. J. Dyson, "Recent advances in graphite carbon nitride-based nanocomposites: structure, antibacterial properties and synergies," *Nanoscale Adv.*, vol. 3, no. 13, pp. 3708–3729, 2021, doi: 10.1039/D1NA00257K.

[41] M. Sabna, K. Safna, J. Mayandi, S. Zh. Karazhanov, and P. Jayaram, "Microstructure profiling and photoluminescence characteristics of V(1-x)2 Ni3xO5-δ compound systems," *Mater. Lett.*, vol. 266, p. 127507, May 2020, doi: 10.1016/j.matlet.2020.127507.

[42] M. Sabna and P. Jayaram, "Reformed dielectric features in single phase orthorhombic nickel vanadate complex oxides and the significance of the lattice dynamics in the optoelectrical features," *J. Phys. Chem. Solids*, vol. 180, p. 111428, Sept. 2023, doi: 10.1016/j.jpcs.2023.111428.

[43] M. Sabna, K. Safna, S. C P, and P. Jayaram, "Surface-Modified Mesoporous $V_{2-x}Sb_{2x}O_{5-\delta}$ Ceramics for Improving the Electrostatic Chemisorption of Methylene Blue," *ChemistrySelect*, vol. 9, no. 29, p. e202400862, Aug. 2024, doi: 10.1002/slct.202400862.

[44] M. Sabna, P. Jayaram, K. Safna, Riyas. K. M, Sona. C. P, and S. Sreedevi, "Crystallographic Profiling, Core-Shell Electronic Configurations, and Investigations of Frequency-Dependent Dielectric Characteristics of Sb2O3-V2O5 Micro Ceramics," *Mater. Chem. Phys.*, p. 130172, Nov. 2024, doi: 10.1016/j.matchemphys.2024.130172.

[45] M. Sabna, P. Jayaram, K. R. Aneesa, and K. M. M. Rahiman, "Investigations on the Antimicrobial Activity of V2–xSb2xO5–δ Compound Systems Against the Gram-Positive, Gram-Negative Bacteria, Penicillium, and Aspergillus niger Fungi," *J. Appl. Spectrosc.*, July 2025, doi: 10.1007/s10812-025-01958-2.

[46] M. Sabna, P. Jayaram, K. Safna, S. Sreedevi, and F. S, "Correlating structural and electronic properties with energy dissipation, polarization dynamics, and dielectric responses in V2O5-NiO-Sb2O3 micro-ceramics," *Phys. B Condens. Matter*, vol. 704, p. 417010, May 2025, doi: 10.1016/j.physb.2025.417010.

[47] A. H. Jawad, N. S. A. Mubarak, M. A. M. Ishak, K. Ismail, and W. I. Nawawi, "Kinetics of photocatalytic decolourization of cationic dye using porous TiO_2 film," *J. Taibah Univ. Sci.*, vol. 10, no. 3, pp. 352–362, July 2016, doi: 10.1016/j.jtusci.2015.03.007.

[48] S. M. Saleh, A. E. A. E. Albadri, M. A. B. Aissa, and A. Modwi, "Fabrication of Mesoporous V2O5@g-C3N4 Nanocomposite as Photocatalyst for Dye Degradation," *Crystals*, vol. 12, no. 12, p. 1766, Dec. 2022, doi: 10.3390/cryst12121766.

[49] Y. Tian, L. Ge, K. Wang, and Y. Chai, "Synthesis of novel MoS2/g-C3N4 heterojunction photocatalysts with enhanced hydrogen evolution activity," *Mater. Charact.*, vol. 87, pp. 70–73, Jan. 2014, doi: 10.1016/j.matchar.2013.10.020.

[50] Y. Guo, J. Sun, H. Chang, and X. Zhao, "Direct Exfoliation of g-C3N4 with Addition of NaOH for Enhanced Photocatalytic Cr(VI) Reduction," Apr. 11, 2018. doi: 10.20944/preprints201804.0155.v1.

[51] D. Tadeu Cestarolli and E. Maria Guerra, "Vanadium Pentoxide (V_2O_5): Their Obtaining Methods and Wide Applications," in *Transition Metal Compounds - Synthesis, Properties, and Application*, S. Haider and A. Haider, Eds., IntechOpen, 2021. doi: 10.5772/intechopen.96860.

[52] M. Atikur Rahman, M. R. Akter, M. R. Khatun, R. Sultana, and M. A. R. Sarker, "Synthesis and Characterization of High-Quality Polycrystalline Sample NiV2O6 by Solid-State Reaction Technique," *Phys. Solid State*, vol. 62, no. 6, pp. 1024–1032, June 2020, doi: 10.1134/S1063783420060049.

[53] D. Errandonea, "High pressure crystal structures of orthovanadates and their properties," *J. Appl. Phys.*, vol. 128, no. 4, p. 040903, July 2020, doi: 10.1063/5.0016323.

[54] R. Ran, J. G. McEvoy, and Z. Zhang, "Synthesis and Optimization of Visible Light Active $BiVO_4$ Photocatalysts for the Degradation of RhB," *Int. J. Photoenergy*, vol. 2015, pp. 1–14, 2015, doi: 10.1155/2015/612857.

[55] Q. Liu, C. Fan, H. Tang, X. Sun, J. Yang, and X. Cheng, "One-pot synthesis of g-C3N4/V2O5 composites for visible light-driven photocatalytic activity," *Appl. Surf. Sci.*, vol. 358, pp. 188–195, Dec. 2015, doi: 10.1016/j.apsusc.2015.09.010.

[56] M. Farahmandjou, "Chemical Synthesis of Vanadium Oxide (V2O5) Nanoparticles Prepared by Sodium Metavanadate," *J. Nanomedicine Res.*, vol. 5, no. 1, Jan. 2017, doi: 10.15406/jnmr.2017.05.00103.

[57] S. Zhou *et al.*, "Facile in situ synthesis of graphitic carbon nitride (g-C3N4)-N-TiO2 heterojunction as an efficient photocatalyst for the selective photoreduction of CO2 to CO," *Appl. Catal. B Environ.*, vol. 158–159, pp. 20–29, Oct. 2014, doi: 10.1016/j.apcatb.2014.03.037.

[58] J. Mendialdua, R. Casanova, and Y. Barbaux, "XPS studies of V2O5, V6O13, VO2 and V2O3," *J. Electron Spectrosc. Relat. Phenom.*, vol. 71, no. 3, pp. 249–261, Apr. 1995, doi: 10.1016/0368-2048(94)02291-7.

[59] M. N. F. Hoque, G. Karaoglan-Bebek, M. Holtz, A. A. Bernussi, and Z. Fan, "Exploiting the Metal-Insulator Transition of VO_2 Thin Films for Terahertz Wave Modulation and Switching," *MRS Proc.*, vol. 1805, pp. mrss15-2134529, 2015, doi: 10.1557/opl.2015.594.

[60] C. Chen *et al.*, "Influence of defects on structural and electrical properties of VO2 thin films," *J. Appl. Phys.*, vol. 110, no. 2, p. 023707, July 2011, doi: 10.1063/1.3609084.

[61] V. Bondarenka, S. Grebinskij, S. Mickevičius, H. Tvardauskas, and S. Kačiulis, "Determination of vanadium valence in hydrated compounds," *J. Alloys Compd.*, vol. 382, no. 1–2, pp. 239–243, Nov. 2004, doi: 10.1016/j.jallcom.2004.06.005.

[62] V. Bondarenka, V. Jasulaitienė, R. Sereika, and A. Stirkė, "Sol–gel synthesis and XPS study of vanadium pentoxide xerogels intercalated with glucose," *J. Sol-Gel Sci. Technol.*, vol. 71, no. 3, pp. 385–390, Sept. 2014, doi: 10.1007/s10971-014-3385-6.

[63] S. D. Gardner, C. S. K. Singamsetty, G. L. Booth, G.-R. He, and C. U. Pittman, "Surface characterization of carbon fibers using angle-resolved XPS and ISS," *Carbon*, vol. 33, no. 5, pp. 587–595, 1995, doi: 10.1016/0008-6223(94)00144-O.

[64] R. Mehek, N. Iqbal, T. Noor, Z. A. Ghazi, and M. Umair, "Metal–organic framework derived vanadium oxide supported nanoporous carbon structure as a bifunctional electrocatalyst for potential application in metal air batteries," *RSC Adv.*, vol. 13, no. 1, pp. 652–664, 2023, doi: 10.1039/D2RA06688B.

[65] X. Yan, T. Xu, G. Chen, S. Xu, and S. Yang, "Field-emission properties of diamond-like-carbon and nitrogen-doped diamond-like-carbon films prepared by electrochemical deposition," *Appl. Phys. A*, vol. 81, no. 1, pp. 41–46, June 2005, doi: 10.1007/s00339-004-3069-0.

[66] X. Yan, T. Xu, G. Chen, S. Yang, H. Liu, and Q. Xue, "Preparation and characterization of electrochemically deposited carbon nitride films on silicon substrate," *J. Phys. Appl. Phys.*, vol. 37, no. 6, pp. 907–913, Mar. 2004, doi: 10.1088/0022-3727/37/6/015.

[67] M. Cheng, H. Fan, Y. Song, Y. Cui, and R. Wang, "Interconnected hierarchical $NiCo_2O_4$ microspheres as high-performance electrode materials for supercapacitors," *Dalton Trans*, vol. 46, no. 28, pp. 9201–9209, 2017, doi: 10.1039/C7DT01289F.

[68] X. Hu, X. Tian, Y.-W. Lin, and Z. Wang, "Nickel foam and stainless steel mesh as electrocatalysts for hydrogen evolution reaction, oxygen evolution reaction and overall water splitting in alkaline media," *RSC Adv.*, vol. 9, no. 54, pp. 31563–31571, 2019, doi: 10.1039/C9RA07258F.

[69] N. Bhatt, S. Parveen, A. Whab, and P. Munga, "Reduction of write current with improved thermal stability in $GeSe_2$ doped Sb_2Te_3 films for phase change memory applications," *J. Phys. Appl. Phys.*, vol. 57, no. 36, p. 365306, Sept. 2024, doi: 10.1088/1361-6463/ad5605.

[70] H. Zhang *et al.*, "A Visual Color Response Test Paper for the Detection of Hydrogen Sulfide Gas in the Air," *Molecules*, vol. 28, no. 13, p. 5044, June 2023, doi: 10.3390/molecules28135044.

[71] M. Aronniemi, J. Sainio, and J. Lahtinen, "XPS study on the correlation between chemical state and oxygen-sensing properties of an iron oxide thin film," *Appl. Surf. Sci.*, vol. 253, no. 24, pp. 9476–9482, Oct. 2007, doi: 10.1016/j.apsusc.2007.06.007.

[72] K. Pfeifer, M. F. Greenstein, D. Aurbach, X. Luo, H. Ehrenberg, and S. Dsoke, "Interaction between Electrolytes and Sb_2O_3 -Based Electrodes in Sodium Batteries: Uncovering the Detrimental Effects of Diglyme," *ChemElectroChem*, vol. 7, no. 16, pp. 3487–3495, Aug. 2020, doi: 10.1002/celc.202000894.

[73] X. Zou, Y. Dong, S. Li, J. Ke, Y. Cui, and X. Ou, "Fabrication of V2O5/g-C3N4 heterojunction composites and its enhanced visible light photocatalytic performance for degradation of gaseous ortho-dichlorobenzene," *J. Taiwan Inst. Chem. Eng.*, vol. 93, pp. 158–165, Dec. 2018, doi: 10.1016/j.jtice.2018.05.041.

[74] M. Rafique, M. Hamza, M. Shakil, M. Irshad, M. B. Tahir, and M. R. Kabli, "Highly efficient and visible light–driven nickel–doped vanadium oxide photocatalyst for degradation of Rhodamine B Dye," *Appl. Nanosci.*, vol. 10, no. 7, pp. 2365–2374, July 2020, doi: 10.1007/s13204-020-01429-4.

[75] X. Liu, N. Chen, Y. Li, D. Deng, X. Xing, and Y. Wang, "A general nonaqueous sol-gel route to g-C3N4-coupling photocatalysts: the case of Z-scheme g-C3N4/TiO2 with enhanced photodegradation toward RhB under visible-light," *Sci. Rep.*, vol. 6, no. 1, p. 39531, Dec. 2016, doi: 10.1038/srep39531.

[76] S. Yan, Z. Cai, D. Wu, Y. Yu, S. Huang, and Y. Cao, "Z-scheme interface modification by MnV2O6 for V2O5/g-C3N4 heterostructure towards efficient visible photocatalytic activity," *J. Alloys Compd.*, vol. 882, p. 160751, Nov. 2021, doi: 10.1016/j.jallcom.2021.160751.

[77] P. Vijayalakshmi, P. Shanmugavelan, and P. MuthuMareeswaran, "Enhanced photocatalytic activity of V2O5 /g-C3N4 /ZnO nanocomposite for efficient degradation of Amoxicillin, Chlorpyrifos and Methylene blue," July 17, 2024, *In Review*. doi: 10.21203/rs.3.rs-4635489/v1.

[78] H. D. Weldekirstos, T. Mengist, N. Belachew, and M. L. Mekonnen, "Enhanced photocatalytic degradation of methylene blue dye using fascily synthesized g-C3N4/CoFe2O4 composite under sun light irradiation," *Results Chem.*, vol. 7, p. 101306, Jan. 2024, doi: 10.1016/j.rechem.2024.101306.

[79] D. Yang *et al.*, "V2O5/BiVO4 nanowires with enhanced photocatalytic activity for degradation of methylene blue," *Inorg. Chem. Commun.*, vol. 155, p. 111135, Sept. 2023, doi: 10.1016/j.inoche.2023.111135.

[80] N. N. Ilkhechi, M. Mozammel, and A. Y. Khoroushahi, "Antifungal effects of ZnO, TiO2 and ZnO-TiO2 nanocomposite on Aspergillus flavus," Dec. 10, 2020. doi: 10.21203/rs.3.rs-123795/v1.

[81] A. Jenifer, M. L. S. Sastri, and S. Sriram, "Photocatalytic dye degradation of V2O5 Nanoparticles—An experimental and DFT analysis," *Optik*, vol. 243, p. 167148, Oct. 2021, doi: 10.1016/j.ijleo.2021.167148.

[82] R. G. Pearson, "Absolute electronegativity and absolute hardness of Lewis acids and bases," *J. Am. Chem. Soc.*, vol. 107, no. 24, pp. 6801–6806, Nov. 1985, doi: 10.1021/ja00310a009.

[83] J. Mullay, "Calculation of group electronegativity," *J. Am. Chem. Soc.*, vol. 107, no. 25, pp. 7271–7275, Dec. 1985, doi: 10.1021/ja00311a008.

[84] X. Ou, P. Chen, K. Zhao, and C. Xia, "Fabrication of Z-scheme ZnO/g-C3N4 heterojunction modified by silver nanoparticles for photocatalytic removal of Norfloxacin and Rhodamine B," *Opt. Mater.*, vol. 144, p. 114305, Oct. 2023, doi: 10.1016/j.optmat.2023.114305.

[85] Q. Luo, Y. Sun, X. Lv, L. Huang, L. Fang, and R. Wang, "Creation of direct Z-scheme Al/Ga co-doping biphasic ZnO/g-C3N4 heterojunction for the sunlight-driven

photocatalytic degradations of methylene blue," *J. Sol-Gel Sci. Technol.*, vol. 103, no. 3, pp. 876–889, Sept. 2022, doi: 10.1007/s10971-022-05865-2.

[86] M. A. Butler, "Photoelectrolysis and physical properties of the semiconducting electrode WO2," *J. Appl. Phys.*, vol. 48, no. 5, pp. 1914–1920, May 1977, doi: 10.1063/1.323948.

[87] S. Xiong *et al.*, "One-step preparation of well-dispersed spindle-like Fe2O3 nanoparticles on g-C3N4 as highly efficient photocatalysts," *Ecotoxicol. Environ. Saf.*, vol. 208, p. 111519, Jan. 2021, doi: 10.1016/j.ecoenv.2020.111519.

[88] R. R. Shamilov *et al.*, "Photocatalytic Materials Based on g-C3N4 Obtained by the One-Pot Calcination Method," *C*, vol. 9, no. 3, p. 85, Sept. 2023, doi: 10.3390/c9030085.

[89] L. Dai, F. Sun, P. Fu, and H. Li, "Enhanced photocatalytic hydrogen evolution and ammonia sensitivity of double-heterojunction g-C_3 N_4 /TiO_2 /CuO," *RSC Adv.*, vol. 12, no. 21, pp. 13381–13392, 2022, doi: 10.1039/D2RA01918C.

[90] K. Kalidasan, S. Mallapur, C. P. Prathibha, S. Kandaiah, S. Gopinathan, and S. G. Kumar, "Visible light driven Dy-V2O5/g-C3N4 Z-scheme heterojunction: Insight into the role of Dy modification and enhanced photocatalytic activity," *Sep. Purif. Technol.*, vol. 364, p. 132442, Aug. 2025, doi: 10.1016/j.seppur.2025.132442.

[91] L. C. Ann *et al.*, "Antibacterial responses of zinc oxide structures against Staphylococcus aureus, Pseudomonas aeruginosa and Streptococcus pyogenes," *Ceram. Int.*, vol. 40, no. 2, pp. 2993–3001, Mar. 2014, doi: 10.1016/j.ceramint.2013.10.008.

[92] Z. Wang, W. Zhou, H. Yang, L. Wang, X. Li, and Z. Zhou, "MXenes: next-generation 2D nanomaterials for effective antimicrobial applications," *Chem. Eng. J.*, vol. 516, p. 163681, July 2025, doi: 10.1016/j.cej.2025.163681.

[93] M. Ikram *et al.*, "Graphitic-carbon nitride and poly acrylic acid doped vanadium oxide for efficient catalytic and antimicrobial activity: In silico molecular docking studies," *J. Photochem. Photobiol. Chem.*, vol. 443, p. 114835, Sept. 2023, doi: 10.1016/j.jphotochem.2023.114835.

[94] C. Sridhar, N. Gunvanthrao Yernale, and M. V. N. A. Prasad, "Synthesis, Spectral Characterization, and Antibacterial and Antifungal Studies of PANI/V_2 O_5 Nanocomposites," *Int. J. Chem. Eng.*, vol. 2016, pp. 1–6, 2016, doi: 10.1155/2016/3479248.

[95] R. Garcia-Rubio, H. C. De Oliveira, J. Rivera, and N. Trevijano-Contador, "The Fungal Cell Wall: Candida, Cryptococcus, and Aspergillus Species," *Front. Microbiol.*, vol. 10, p. 2993, Jan. 2020, doi: 10.3389/fmicb.2019.02993.

[96] L. Sun *et al.*, "Antibacterial Activity of Graphene Oxide/g-C_3 N_4 Composite through Photocatalytic Disinfection under Visible Light," *ACS Sustain. Chem. Eng.*, vol. 5, no. 10, pp. 8693–8701, Oct. 2017, doi: 10.1021/acssuschemeng.7b01431.

[97] I. N. Reddy *et al.*, "Vanadium-doped graphitic carbon nitride for multifunctional applications: Photoelectrochemical water splitting and antibacterial activities," *Chemosphere*, vol. 264, p. 128593, Feb. 2021, doi: 10.1016/j. chemosphere.2020.128593.

Chapter VII

General Conclusion

- Multi-cation incorporation of Ni^{2+} and Sb^{3+} into the V_2O_5 lattice was successfully achieved via high-temperature solid-state reaction, resulting in multi-phase and structurally stable compounds with controlled lattice distortions and enhanced defect density.

- Rietveld refinement, XRD, and Raman analyses confirmed the coexistence of orthorhombic V_2O_5, monoclinic NiV_2O_6, and tetragonal $SbVO_4$ phases, demonstrating precise dopant incorporation and tunable crystal structure.

- XPS studies revealed mixed oxidation states (V^{4+}/V^{5+}, Ni^{2+}/Ni^{3+}, Sb^{3+}/Sb^{0}) and oxygen vacancies, which collectively contribute to enhanced electron hopping and redox activity, critical for AC conductivity and photocatalysis.

- SEM analysis reveals flake like morphology with particles falling in the micrometer regime and EDS spectrum projects the presence of all the constituent elements in the prepared complex compounds and heterostructures.

- Optical studies using UV-visible diffuse reflectance spectra revealed band gap restructuring via KM plot for multi-cation incorporated compounds and Tauc plot for the heterostructures and Photoluminescence studies indicated blue-green transitions due to symmetry distortions and multication-induced defects

- The dielectric measurements exhibited frequency-dependent behavior, with a decreasing dielectric constant at higher frequencies, consistent with dipolar relaxation and space charge polarization effects, while low tangent loss highlighted the suitability of these materials for high-frequency applications.

- AC conductivity increased with frequency due to improved polaronic hopping between V^{4+} and V^{5+} sites, while higher dopant concentrations introduced defects that moderated charge carrier mobility, demonstrating the tunable electronic properties of Sb-Ni-V-O.

- g-C_3N_4 is prepared from the polycondensation of urea, and $V_{2-x}Ni_{2x}Sb_xO_{5-\delta}$/g-$C_3N_4$ (0.05<=x<=0.08). heterostructures were formed by sonication-hydrothermal method

- XRD reveals the formation of heterostructures including V_2O_5 orthorhombic, NiV_2O_6 triclinic, $SbVO_4$ tetragonal phase along with the g-C_3N_4 phase and FTIR results reveals the strong interfacial coupling effect between C_3N_4 and Sb-Ni-V-O.

- EDS spectrum projects the presence of Sb, Ni, V, O, C, and N elements in the as prepared heterostructures of $V_{2-x}Ni_{2x}Sb_xO_{5-d}/C_3N_4$ heterostructures for $0.05 \leq x \leq 0.08$

- The deconvoluted core-level XPS spectra revealed mixed valence states and well-defined bonding environments among V, Sb, Ni, C, N, and O, affirming the formation of a multi-cation, oxygen-deficient, and chemically integrated heterostructure

- The band gap energy of $V_{2-x}Ni_{2x}Sb_xO_{5-d}$ /g-C_3N_4 heterostructures formed from both ranges between 2.79 eV, 2.76 eV, 2.57 eV and reached up to 2.39 eV for x=0.05, 0.06, 0.07 & 0.08 respectively

- Photocatalytic studies using Methylene Blue demonstrated that Sb-Ni-V-O/g-C_3N_4 heterostructures enhance visible-light absorption and promote Z-scheme charge separation, achieving rapid and efficient degradation of dyes through •OH and $O_2•^-$ radicals.

- Antimicrobial studies showed broad-spectrum activity against Gram-positive and Gram-negative bacteria, as well as fungi, attributable to ROS generation, membrane disruption, and electrostatic interactions, which were significantly enhanced in heterostructured systems.

- The synergistic effect of multi-cation doping and heterostructure formation resulted in improved photocatalytic efficiency and antimicrobial performance, highlighting the versatility of composites for multifunctional applications

Chapter VIII

Future Prospects

- **Optimization of Dopant Concentration**: Further studies can explore fine-tuning of Ni and Sb concentrations to maximize electron hopping, dielectric response, and ROS generation, enabling precise control over photocatalytic and antimicrobial performance.
- **High-Frequency Device Applications**: Low tangent loss and stable dielectric properties make Sb-Ni-V_2O_5 suitable for microwave absorbers, RF components, and capacitors.
- **Supercapacitors**: High dielectric constant and AC conductivity makes Sb-Ni-V_2O_5 excellent candidates for supercapacitor electrodes applications
- **Device Integration**: Sb-Ni-V-O and its g-C_3N_4 heterostructures can be incorporated into antimicrobial coatings, photocatalytic reactors
- **Extended Photocatalytic Applications**: The heterostructures can be evaluated for degradation of more complex industrial dyes, pharmaceuticals, and organic pollutants under natural sunlight or simulated solar irradiation.
- **Biomedical Applications**: Owing to their ROS-mediated antimicrobial activity, these materials have potential for biofilm inhibition, wound dressing, and infection control, subject to cytotoxicity assessments.
- **Theoretical Modeling and DFT Studies**: Computational studies could provide insights into charge carrier dynamics, band alignment, and defect states, guiding the rational design of next-generation multi-cation metal oxides.

Appendix

Papers Published

1. **Melethil Sabna,** Peediyekkal Jayaram, Vandana P. Viswanathan, S. Sreedevi, K. Safna, Development of Z-scheme Sb_2O_3–NiO–V_2O_5/g-C_3N_4 heterostructures for visible light photocatalysis and antimicrobial applications, **Journal of the Indian Chemical Society**, Volume 103, Issue 6, 2026, 102637, ISSN 0019-4522. **(Publisher: Elsevier)**

2. **Sabna, Melethil**, Jayaram, P., Safna, K. et al. Synergistic Effects of Nickel and Antimony Integration into V2O5 Matrix: Insights into Microstructural Evolution, Oxygen Defect-Mediated Photoluminescence, Lattice Dynamics and Enhanced Antimicrobial Activity. **J Inorg Organomet Polym** (2026) https://doi.org/10.1007/s10904-026-04317-6. **(Publisher: Springer)**

3. **Melethil Sabna**, K Safna, Sona C P, P Jayaram, Surface-Modified Mesoporous $V_{2-x}Sb_{2x}O_{5-\delta}$ Ceramics for Improving the Electrostatic Chemisorption of Methylene Blue, **Chemistry Select** 9(29), e202400862 29/2024. **(Publisher: Wiley)**

4. **Melethil Sabna**, Peediyekkal Jayaram, Reformed dielectric features in single phase orthorhombic nickel vanadate complex oxides and the significance of the lattice dynamics in the optoelectrical features, **Journal of Physics and Chemistry of Solids**, Volume 180,2023,111428,ISSN 00223697. **(Publisher: Elsevier)**

5. **Melethil Sabna**, Peediyekkal Jayaram, K. Safna, Riyas K. M, Sona C. P, S. Sreedevi, Crystallographic profiling, core-shell electronic configurations, and investigations of frequency-dependent dielectric characteristics of Sb_2O_3–V_2O_5 micro ceramics, **Materials Chemistry and Physics**, Volume 332, 2025, 130172, ISSN 0254-0584, j.matchemphys.2024.130172. **(Publisher: Elsevier)**

6. **Melethil. Sabna**, K. Safna, J Mayandi , S.Zh. Karazhanov P Jayaram, Microstructure profiling and photoluminescence characteristics of $V_{(1-x)2}$ $Ni_{3x}O_{5-\delta}$ compound systems, **Materials Letters** 266 (2020) 127507, **(Publisher: Elsevier)**

7. **Melethil Sabna**, Peediyekkal Jayaram, K. Safna, S. Sreedevi, Faheema S, Correlating structural and electronic properties with energy dissipation,

polarization dynamics, and dielectric responses in V2O5-NiO-Sb2O3 micro-ceramics, **Physica B: Condensed Matter**, Volume 704, 2025, 417010, ISSN 0921, **(Publisher: Elsevier)**

8. **Sabna, Melethil**, Jayaram, Peediyekkal, Sreedevi, Vanga, Pradeep Reddy, S. Sreejalakshmi, Aneesa K, Mujeeb Rahiman K and Safna, Kakkattil. "Phase evolution, surface chemistry, and antimicrobial performance of Ni-incorporated vanadium pentoxide complex oxides" **Zeitschrift für Physikalische Chemie**, vol. 240, no. 1-2, 2026, pp. 219-237**. (Publisher: De Gruyter)**

9. **Sabna, Melethil.,** Jayaram, P., Aneesa, K.R. et al. Investigations on the Antimicrobial Activity of $V_{2-x}Sb_{2x}O_{5-\delta}$ Compound Systems Against the Gram-Positive, Gram-Negative Bacteria, Penicillium, and Aspergillus niger Fungi. **J Appl Spectrosc** 92,680–687, 2025, **(Publisher: Springer)**

10. Safna K, Jayaram P, **Sabna Melethil,** Sreedevi S, Madhu Chennabasappa, Rietveld refinement, core level electron shell structure and frequency-dependent dielectric behavior of vanadium bismuth oxide microstructures, **Physica B: Condensed Matter**, Volume 691,2024,416318,ISSN0921-4526, (**Publisher: Elsevier**)

11. Safna, K., Jayaram, P, **Sabna, M**, Microstructure profiling, lattice dynamics, and morphological studies on multi-excitonic vanadium bismuth oxide compound systems. **J Aust Ceram Soc** 58, 1129–1136 (2022). **(Publisher: Springer**)

12. Lakshmi S., Sreeja, Jahan Elamkulavan, Hasana, Keloth, Chandrasekharan, Peediyekkal, Jayaram, **Melethil Sabna** and P. Sudheesh. "Third-order nonlinear optical characteristics of natural dye anthocyanin extracted from Ixora coccinea" **Zeitschrift für Physikalische Chemie,** 2025. (**Publisher: De Gruyter**)

13. Riyas, K.M., Sreedevi, S. **Sabna. Melethil,** Jayaram, P. et al. Structural Refinement, Core–Shell Electron Structure, Enhanced Phosphorescence, and Splitting of $5D0 \rightarrow 7F2$ Transitions in Li-doped Rare Earth Oxide Systems**. J. Electron. Mater**. 54, 1369–1380 (2025). 11651-3. (**Publisher: Springer**)

14. S. Sreedevi, Jayaram Peediyekkal, **Sabna Melethil,** Anandalli Mallikarjun, A.

Biju, Nandakumar Kalarikkal, Microstructure, fluorescence emission, and nonlinear optical limiting properties of ZnO-Bi_2O_3-Nb2O5 compound systems, **Ceramics International**, Volume 51, Issue 3, 2025, 2985-2995, ISSN 0272-8842. **(Publisher: Elsevier)**

15. Safna, K., Jayaram, P., **Sabna Melethil.** et al. Structural Profile, Lattice Dynamics, Broad Frequency Dielectric Responses, and Tuning of Optoelectronic Properties of Multiphase $V_{2-x}Mn_xO_{5-\delta}$ Compounds Systems. **J. Electron. Mater**. 54, 4918–4930 (2025) **(Publisher: Springer)**

16. Riyas K M, Peediyekkal Jayaram, Prasoon Prasannan, **Melethil Sabna**, Pradeep Reddy Vanga,Investigation of structural profiles and lattice dynamics in Gd2O3-Based multication phosphorescent materials: Studies on crystal field splitting and photoluminescence characteristics, Journal of **Solid State Chemistry**,Volume 352,2025,125571, ISSN 0022-4596, (**Publisher: Elsevier**)

17. Sona C. P, Peediyekkal Jayaram, Aryamol Stephen, A. Biju, **Sabna M**, Faheema S, Synergistic effect of multication incorporation on phase transition and dielectric relaxation behavior in Nb_2O_5-SnO_2-MoO_3 composite system, **Journal of Alloys and Compounds**, Volume 1037, 2025, 182320, ISSN 0925-8388. (**Publisher: Elsevier**)

18. S. Sreeja Lakshmi, Safna Hussan, Kodakkat Parambil, Jayaram, Peediyekkal, **Melethil, Sabna** and Sudheesh, Palengara. "Comparative analysis of nonlinear optical properties in santalin A and santalin B: a density functional theory approach" **Zeitschrift für Physikalische Chemie**. https://doi.org/ 10.1515/zpch-2025-0060. **(Publisher: De Gruyter)**

19. K. Safna, Peediyekkal Jayaram, **M. Sabna**, Madhu Chennabasappa, A.K. Sivadasan, Structural refinement of vanadium pentoxide with manganese incorporation and the correlation of structural modification with the magnetic and optical properties, **Physica B: Condensed Matter**, Volume 737, 2026, 418689, ISSN 0921-4526. (**Publisher: Elsevier**)

20. Safna, Kakkattil, Jayaram, Peediyekkal, Sasi, Sreedevi, **Sabna, Melethil**, Srankite, Faheema and Mayandi, Jeyanthinath. "Electrochemical performance of complex oxides of manganese incorporated vanadium pentoxide-based electrode materials for energy storage applications" **Zeitschrift für**

Physikalische Chemie, vol. 240, no. 1-2, 2026, pp. 191-217**. (Publisher: De Gruyter)**

21. K. Safna, Peediyekkal Jayaram, S. Sreedevi, **M. Sabna**, Engineering oxides of bismuth manganese vanadate electrodes for enhanced charge transport and stable high-performance supercapacitors**, Journal of the Indian Chemical Society,** Volume 103, Issue 9, 2026,102945, ISSN 0019-4522, https://doi.org/10.1016/j.jics.2026.102945. **(Publisher: Springer)**

Papers Presented

1. Synthesis, Microstructure Analysis and Optical Studies On $V_{(1-x)2}Ni_{3x}O_{5-\delta}$ Complex Systems, Sabna. M, Dr. P Jayaram, International Conference On Energy And Environment, (ICEE 2k19), 12-14 December 2019, TKM College, Kollam.

2. Microstructural Profiling And Optical Characterizations On Complex $V_{2-x}Sb_{2x}O_{5-\delta}$ Solid Solutions, Sabna. M, Safna. K, Dr. P. Jayaram, International Conference on Theoritical And Experimental Physics (ICTEP 2020), 5-6 February 2020, Farook College, Calicut.

3. Lattice Dynamics and Optical Characterization of $V_{(1-x)2}Ni_{3x}O_{5-\delta}$ Multi-cation Complex Compounds" In "International Conference On Recent Trends In Theoretical And Applied Physics" Organized By Post Graduate And Research Department Of Physics, Sree Narayana College, Kollam In Academic Collaboration With The Kerala State Higher Education Council 'From 14th - 16th December, 2020.

4. 'Synthesis Structural Investigation and Optical Characterizations in Ternary Microstructures of $V_{2-x}Ni_{2x}Sb_xO_{5-\delta}$ for 0.05>=x>=0.09', International Conference On Nanoscience 2021 on 28-30 July 2021, Organized by Christian College, Kattakkada, Trivandrum

5. "Electric Conductivity and Dielectric Studies Of $V_{(1-x)2}Ni_{3x}O_{5-\delta}$ Complex Compounds" In The 9th National Conference on Condensed Matter and Applications On 16th And 17th September 2021 Organized by Manipal Institute of Technology, Manipal.

6. Presented A Research Paper Titled Crystallographic Profiling, AC Conductivity and Dielectric Studies of $V_{(1-x)2}Ni_{3x}O_{5-\delta}$ Multi-cation

Compounds in the 9th National Conference on Condensed Matter Physics And Applications (CMPA-2021) held at Manipal Institute of Technology, Mahe, Manipal During September 16-17, 2021.

7. Multi-Valent Cation Induced Band Gap Restructuring of Vanadium Pentoxide Based Compounds in The International Conference on Advanced Research: INSIGHT 2022 Organized by The Internal Quality Assurance Cell, MES KVM College Valanchery in Association with Kerala State Higher Education Council (KSHEC) From 11th To 14th January 2022.

8. Substitutional effect of Sb^{3+} ions on the Lattice dynamics, Surface Chemical states and Optical Properties of Vanadium Pentoxide at the Indo-Norwegian Online Conference, organized by Institute for Energy Technology (IFE), University of Oslo, Norway and Madurai Kamaraj University (MKU) on 02-04 February 2022

9. Adsorption Of Methylene Blue Using Vanadium-molybdenum Oxide Compounds And their Structural-Optical Properties at ICMM 2022- International Conference On Recent Multifunctional Materials, 22-24 December, Hyderabad

10. Effect of Divalent Nickel ion On The Structure, Lattice Dynamics, Surface Morphology, Optical Features And Adsorptive Performance Of Single Phased Ni-V_2O_5 Compounds, International Conference On Functional Materials For Advanced Technology (ICFMAT 2023), 02-04 January, Central University of Kerala

11. Effect Of Trivalent Antimony ion On The Adsorptive Features Of Vanadium Pentoxide, International Conference On Materials For Advanced Technologies, Materials Research Society, ICMAT-2023, 26-30 June, 2023, Suntec, Singapore

12. Synthesis, Structural Elucidation And Photoluminescence Characteristics Of Multi-phase Sb-Ni-V-O Ceramics, ICAM 2024- International Conference On Advanced Materials, Marymatha College, Kuruvilangad, 03 January 2024

13. Sb-Ni-V-O/g-C_3N_4 Heterostructures for Enhanced Antimicrobial Applications, ICAFMC-2024 International Conference on Advances In

Functional Materials And Coatings, 14-16 February, 2024, Department Of Physics, MES Ponnani College

14. "Reitveld Refinement, Core Level Electron Shell Structure and Optical Properties of Sb_2O_3-NiO-V_2O_5 Compound Systems: Study of Enhanced Photocatalysis and Anti-microbial Application" 2nd International Conference On Recent Trends In Applied Physics & Material Science (RAM 2024), 15-16, November, 2024. Bikaner Technical University, Bikaner - Rajasthan, India.

15. 'Sb_2O_3-NiO-V_2O_5/g-C_3N_4 Heterostructures for Enhanced Sunlight Assisted Z-Scheme Photocatalysis', National Seminar on Frontiers In Materials Science, S. H. Thevara, 27– 28 November 2024.

16. 'Sunlight-Driven $V_{2-x}Ni_{2x}Sb_xO_{5-\delta}$/g-$C_3N_4$ Z-Scheme Heterojunctions: A Dual-Functional Catalyst for Rapid Dye Degradation and Environmental Disinfection'**,** Centum Doctorates: Celebrating 100 PhDs@Devagiri instituted by St. Joseph's College, Kozhikode on 19 June 2026.

Awards and Recognition

1. **Received Best Paper Award** for paper titled "Lattice Dynamics And Optical Characterization Of $V_{(1-x)2}Ni_{3x}O_{5-\delta}$ Multi-cation Complex Compounds" In "International Conference On Recent Trends In Theoretical And Applied Physics" Organized By Post Graduate And Research Department Of Physics, Sree Narayana College, Kollam In Academic Collaboration With The Kerala State Higher Education Council From 14th -16th December, 2020

2. Presented a paper on Effect Of Trivalent Antimony ion on the Adsorptive Features of Vanadium Pentoxide, International Conference On Materials for Advanced Technologies, Materials Research Society**, ICMAT – 2023**, 26-30 June, 2023, **Suntec, Singapore**

3. Received **Eurudito Outstanding Research Scholar Award -2024** instituted by IQAC, MES Ponnani College

4. Received **Eurudito Outstanding Research Scholar Award -2025** instituted by IQAC, MES Ponnani College

5. Received **Inquisito Outstanding Research Scholar Award -2026**, instituted by RPC-IQAC, MES Ponnani College

6. Received **Best All Kerala Science Faculty Researcher award 2026** April: Instituted by MES Kerala

7. Received **First Prize** in the **Research presentation challenge** in the Centum Doctorates: Celebrating 100 PhDs@Devagiri instituted by St. Joseph's College, Kozhikode on 19/06/2026